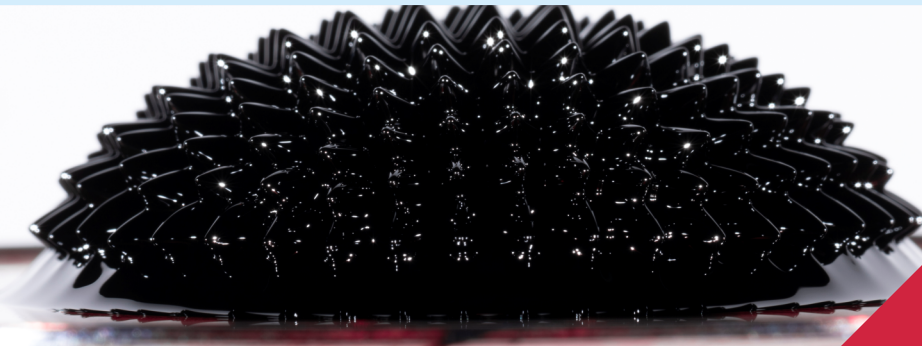
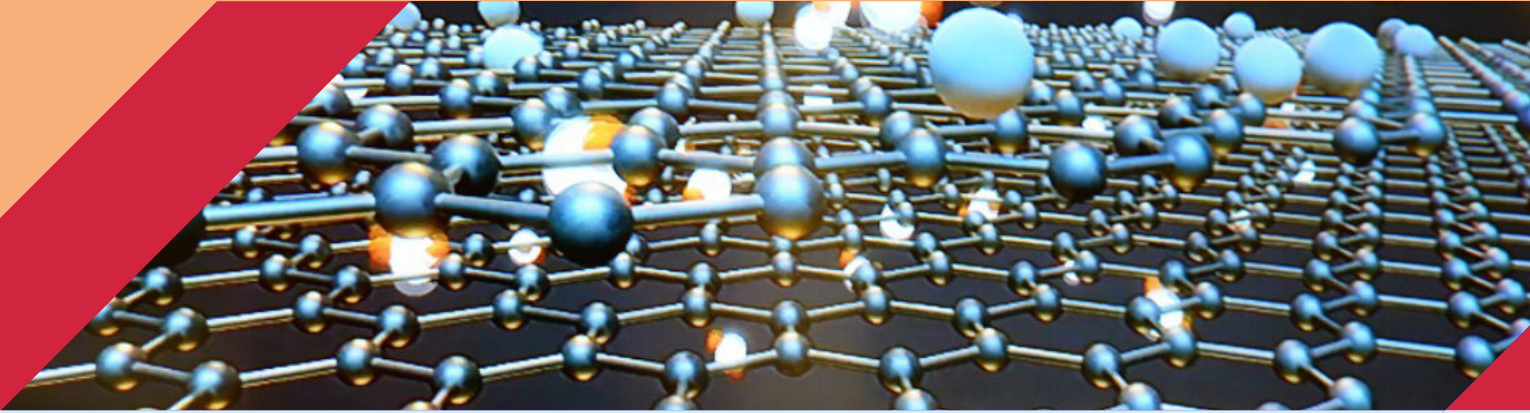




**INTERNATIONAL CONFERENCE ON ADVANCED MATERIALS  
SCIENCE & ENGINEERING AND HIGH TECH DEVICE APPLICATIONS**

# **PROCEEDINGS BOOK**



**October 27- 29 2022**

**Ankara / TURKEY**

**[icmatse.org](http://icmatse.org)**

**ISBN: 978-625-00-1052-5**



**NANOSENSOR**

INTERNATIONAL CONFERENCE ON  
ADVANCED MATERIALS SCIENCE &  
ENGINEERING AND  
HIGH TECH DEVICE APPLICATIONS



**HAVELSAN**



**October 27- 29 2022 Ankara / TURKEY**

**icmatse.org**

# International Conference on Advanced Materials Science and Engineering and High Tech Device Applications (ICMATSE 22)

**October 27 – 29 2022, Ankara/TURKEY**

## EDITORS

**Prof. Dr. Hakan ATES/Gazi University**

**Prof. Dr. Munir H. NAYFEH/University of Illinois at Urbana-Champaign**

**Assoc. Prof. Dr. Ersin BAHCECI/Iskenderun Technical University**

## EDITORIAL BOARD

**Prof. Dr. Munir H. NAYFEH/University of Illinois at Urbana-Champaign**

**Dr. Irfan AHMAD/University of Illinois at Urbana-Champaign**

**Prof. Dr. Ammar NAYFEH/Khalifa University, UAE**

**Assoc. Prof. Dr. Ersin BAHCECI/Iskenderun Technical University**

**Prof. Dr. Necdet SAGLAM/Hacettepe University**

**Assoc. Prof. Dr. Gokhan SURUCU/Gazi University**

**Prof. Dr. Behcet GULENC/Gazi University**

**Prof. Dr. Irshad HUSSAIN/Lahore University, Pakistan**

**Prof. Dr. Dmitri GORIN/SCP& QM Skolkovo Inst. of Sci. and Tech., Russia**

**Assoc. Prof. Dr. Zuhale ER/Istanbul Technical University**

**Assoc. Prof. Dr. Ozge SURUCU/Atilim University**

**Dr. Bilge IMER/Middle East Technical University**

**Dr. Sahin COSKUN/Eskisehir Osmangazi University**

**Dr. Mete Bakir/TAI / A. Yildirim Beyazid University**

ANKARA

SEPTEMBER 2022

**Proceedings Book**

**Online: ISBN: 978-625-00-1052-5**

**Contact Address**

Gazi University, Faculty of Technology, Dept. of Metallurgy and Materials Engineering,  
Yenimahalle/Ankara/TURKEY

[icmatse.org](http://icmatse.org), [icmatse@gmail.com](mailto:icmatse@gmail.com)

# International Conference on Advanced Materials Science and Engineering and High Tech Device Applications (ICMATSE 2022)

**October 27 – 29 2022, Ankara/TURKEY**

## CHAIRMAN

**Munir H. NAYFEH (Prof. Dr)/**University of Illinois

**Hakan ATES (Prof. Dr)/** Gazi University

## SCIENTIFIC COMMITTEES

**Prof. Dr. Ayhan EROL/Afyon Kocatepe University**

**Prof. Dr. Ahmad I. AYESH/Qatar University, Qatar**

**Prof. Dr. Ali GUNGOR/Karabük University**

**Assoc. Prof. Dr. Aisha IHSAN/National Inst. Of  
Biotech and Eng, Pakistan**

**Assoc. Prof. Dr. Alpay OZER/Gazi University**

**Prof. Dr. Ammar NAYFEH/Khalifa University, UAE**

**Assoc. Prof. Dr. Ayhan ORHAN/Firat University**

**Assoc. Prof. Dr. Gokhan SURUCU/Gazi University**

**Assoc. Prof. Dr. Ersin BAHCECI/Iskenderun Technical  
University**

**Dr. Aysun AYDAY/Sakarya University**

**Prof. Dr. Aytunç ATES/A. Yıldırım Beyazıt University**

**Assoc. Prof. Dr. Babek ERDEBILLI/A. Yıldırım Beyazıt  
University**

**Prof. Dr. Bekir OZCELIK/Cukurova University**

**Dr. Bilge IMER/Middle East Technical University**

**Prof. Dr. Bilge DEMIR/Karabuk University**

**Prof. Dr. Bulent YESILATA/A. Yıldırım Beyazıt  
University**

**Prof. Dr. C. SURYANARAYANA/University of Central  
Florida, Orlando, USA**

**Prof. Dr. Cetin KARATAS/Gazi University**

**Prof. Dr. Canan VARLIKLI/Izmir Institute of  
Technology**

**Prof. Dr. Dmitri GORIN/SCP& QM Skolkovo Inst. of  
Sci. and Tech., Russia**

**Prof. Dr. Erol KURT/Gazi University**

**Prof. Dr. Guven CANKAYA/A. Yıldırım Beyazıt  
University / Roketsan**

**Prof. Dr. Fahrettin YAKUPHANOGLU/Firat  
University**

**Assoc. Prof. Dr. Fatih CALISKAN/Sakarya University  
of Applied Sciences**

**Prof. Dr. Feza KORKUSUZ/Hacettepe University /  
TUBITAK**

**Prof. Dr. Francesco COTTONE/Perugia University,  
Italy**

**Assoc. Prof. Dr. Gokhan KUCUKTURK/Gazi  
University**

**Prof. Dr. Haitham Abu-RUB/Texas A&M University,  
Qatar**

**Prof. Dr. C. Hakan GUR/Middle East Technical  
University**

**Dr. Hasan M. NAYFEH/IBM, USA**

**Prof. Dr. Husnu Emrah UNALAN/Middle East  
Technical University**

**Dr. Halit KALEBOZAN/GM at Kalebozan Dış Tic. A.S.**

**Assoc. Prof. Dr. Hakan GURUN/Gazi University**

**Prof. Dr. Ahmet DURGUTLU/Gazi University**

**Prof. Dr. Hanan Issa MALKAWI/Yarmouk  
University, Jordan**

**Assoc. Prof. Dr. Hanifi CINICI/Gazi University**

**Prof. Dr. Hasan SAHIN/Izmir Institute of Technology**

**Prof. Dr. Hussein MOHAMED/Helwan University  
Cairo, Egypt**

**Prof. Dr. H. HADIYANTOI/Diponegoro University,  
Indonesia**

**Prof. Dr. Ilyas UYGUR/Duzce University**

**Assoc. Prof. Dr. Ihsan TOKTAS/A. Yıldırım Beyazıt  
University**

**Prof. Dr. Irshad HUSSAIN/Lahore University,  
Pakistan**

**Prof. Dr. Idris AKYUZ/Eskisehir Osmangazi  
University**

**Prof. Dr. Irfan AR/Gazi University**

**Prof. Dr. Kadir KOCATEPE/Gazi University**

**Prof. Dr. L. Cenk KUMRUOGLU/Iskenderun Technical  
University**

**Prof. Dr. Madjid FATHI/Inst. For Knowledge Based  
Sys., Germany**

**Prof. Dr. Laila H. Abu Hassan/University of Jordan,  
Jordan**

**Prof. Dr. Liviu Brandusan (Retired)/Technical  
University Cluj-Napoca, Romania**

**Prof. Dr. Muhammad Faizal Bin A. Gani/University  
of Malaya, Malaysia**

**Dr. Melika OZER/Gazi University**

**Assoc. Prof. Dr. Xiaotian WANG/Southwest  
University / China**

**Prof. Dr. Mehmet EROĞLU**/Firat University  
**Prof. Dr. Metin BEDİR**/Gaziantep University  
**Prof. Dr. Mustafa ACARER**/Selcuk University  
**Prof. Dr. Habib RACHED**/Benbouali University  
 Algeria  
**Prof. Dr. Meena LAAD**/Symbiosis International  
 University, India  
**Prof. Dr. M. Ishaque KHAN**/Illinois Institute of  
 Technology, USA  
**Prof. Dr. N. Fazil YILMAZ**/Gaziantep University  
**Dr. H. İbrahim EFKERE**/Gazi University  
**Prof. Dr. Nizamettin KAHRAMAN**/Karabuk  
 University  
**Prof. Dr. Noha ELHALAWANI**/NRC, Cairo, Egypt  
**Assoc. Prof. Dr. Sedat SURDEM**/Gazi University  
**Prof. Dr. Oguzhan YILMAZ**/Gazi University  
**Prof. Dr. Olena S. Melnyk**/Oleksandr D Dovzhenko  
 HNP University, Ukraine  
**Prof. Dr. Rahmi UNAL**/Gazi University  
**Prof. Dr. Ramazan BAYINDIR**/Gazi University  
**Prof. Dr. Ramazan KACAR**/Karabuk University  
**Prof. Dr. Rasid Ahmad**/Kashmeer University,  
 Pakistan  
**Prof. Dr. Raul MITRA**/Indian Institue of Technology,  
 India  
**Assoc. Prof. Dr. Recep ZAN**/N. Omer Halis Demir  
 University

**Prof. Dr. Saffa RIFFAT**/University of Nottingham, UK  
**Prof. Dr. Shadia IKHMAYIES**/Al Isra University,  
 Jordan  
**Assoc. Prof. Dr. Salih KOSE**/Eskisehir Osmangazi  
 University  
**Prof. Dr. Salim ARSLANLAR**/Sakarya University of  
 Applied Sciences  
**Prof. Dr. Serdar SALMAN**/Marmara University  
**Prof. Dr. Servet TURAN**/Eskişehir Technical  
 University  
**Prof. Dr. Semra IDE**/Hacettepe University  
**Prof. Dr. Sezai ELAGOZ**/ASELSAN  
**Prof. Dr. Suleyman GUNDUZ**/Karabuk University  
**Assoc. Prof. Dr. Aysenur GENCER**/Karamanoglu  
 Mehmetbey University  
**Assoc. Prof. Dr. Tarik ASAR**/Gazi University  
**Prof. Dr. Ramazan AKCAN**/Hacettepe University  
**Prof. Dr. Suleyman OZCELIK**/Gazi University  
**Prof. Dr. Sukru CAVDAR**/Gazi University  
**Prof. Dr. Takashige OMATSU**/Chiba University,  
 Japan  
**Prof. Dr. Temel KOTIL**/TAI  
**Prof. Dr. Tolga DEPCI**/Iskenderun Technical  
 University  
**Dr. Tugrul IMER**/Gazi University  
**Dr. Ugur ARABACI**/Gazi University  
**Dr. Volkan KILICLI**/Gazi University

## ORGANIZING COMMITTEE

**Prof. Dr. Hakan ATEŞ** -/Gazi University  
**Prof. Dr. Munir H. NAYFEH**/University of Illinois at  
 Urbana-Champaign, USA  
**Dr. Irfan AHMAD**/University of Illinois at Urbana-  
 Champaign, USA  
**Assoc. Prof. Dr. Ersin BAHCECI**/Iskenderun Technical  
 University  
**Prof. Dr. Ammar NAYFEH**/Khalifeh University, UAE  
**Prof. Dr. H. I. UNAL**/Gazi University  
**Dr. H. M. NAYFEH**/IBM, USA  
**Prof. Dr. C. Hakan GUR**/Middle East Technical  
 University  
**Prof. Dr. H. E. UNALAN**/Middle East Technical  
 University  
**Prof. Dr. Yusuf Z. MENCELOGLU**/Sabanci University  
**Prof. Dr. Dmitri GORIN**/SCP& QM Skolkovo Inst. of Sci.  
 and Tech., Russia  
**Prof. Dr. Adem KURT**/Gazi University  
**Prof. Dr. Ahmet KARAASLAN**/Yildiz Technical  
 University  
**Prof. Dr. Ali Arslan KAYA**/Mugla Sitki Kocman  
 University

**Prof. Dr. Canan VARLIKLI**/Izmir Institute of Technology  
**Prof. Dr. H. Ozkan GULSOY**/Marmara University  
**Assoc. Prof. Dr. Gokhan SURUCU**/Gazi University  
**Prof. Dr. Liviu Brandusan**/Technical University Cluj-  
 Napoca, Romania  
**Prof. Dr. Mehmet OZALP**/Karabuk University  
**Prof. Dr. Irfan AR**/Gazi University  
**Prof. Dr. Metin GURU**/Gazi University  
**Prof. Dr. Necdet SAGLAM**/Hacettepe University  
**Prof. Dr. Niyazi OZDEMİR**/Firat University  
**Prof. Dr. Olena S. Melnyk**/Summy University, Ukraine  
**Assoc. Prof. Dr. R. KARSLIOGLU**/A. Yıldırım Beyazid  
 University  
**Dr. Sahin COSKUN**/Eskisehir Osmangazi University  
**Dr Sema VURAL**/Necmettin Erbakan University  
**Prof. Dr. Sinan AKGOL**/Ege University  
**Prof. Dr. Sukru TALAS**/Afyon Kocatepe University  
**Prof. Dr. Zafer TATLI**/Sakarya University of Applied  
 Sciences  
**Assoc. Prof. Dr. Zuhale ER**/Istanbul Technical University  
**Dr. Melika OZER**/Gazi University

**TECHNICAL COMMITTEE**

**Prof. Dr. Munir H. NAYFEH**/University of Illinois at Urbana-Champaign

**Prof. Dr. Necdet SAGLAM**/Hacettepe University

**Assoc. Prof. Dr. Gokhan SURUCU**/Gazi University

**Assoc. Prof. Dr. Ersin BAHCECI**/Iskenderun Technical University

**Assoc. Prof. Dr. Aysenur GENCER**/Karamanoglu Mehmet Bey University

**Assoc. Prof. Dr. Hakan GURUN**/Gazi University

**Dr. H. Ibrahim EFKERE**/Gazi University

**PUBLICATION COMMITTEE**

**Assoc. Prof. Dr. Tarik ASAR**/Gazi University

**Assoc. Prof. Dr. Gokhan SURUCU**/Gazi University

**Assoc. Prof. Dr. Zuhall ER**/Istanbul Technical University

**Assoc. Prof. Dr. Ersin BAHCECI**/Iskenderun Technical University

**Assoc. Prof. Dr. Ramazan KARSLIOGLU**/A. Yıldırım Beyazid University

**Assoc. Prof. Dr. Gokhan KUCUKTURK**/Gazi University

**Erdem MERMER**/TAI

**SPONSORSHIP AND EXHIBITION COMMITTEE**

**Assoc. Prof. Dr. Gokhan SURUCU**/Gazi University

**Assoc. Prof. Dr. Zuhall ER**/Istanbul Technical University

**Assoc. Prof. Dr. Ersin BAHCECI**/Iskenderun Technical University

**Halil I. EFKERE**/Gazi University

**Erdem MERMER**/TAI

**Gizem C. DELİBALTA**/Mugla Sıtkı Kocman University

**Berkcan ERENLER**/Gazi University

**EVENTS AND ACTIVITIES COMMITTEE**

**Assoc. Prof. Dr. Ayhan ORHAN**/Firat University

**Assoc. Prof. Dr. Zuhall ER**/Istanbul Technical University

**Dr. Bugra YILDIZ** /Hacettepe University

**Oykum BASGOZ**/Mersin University

**Dr. Halil I. EFKERE**/Gazi University

**Erdem MERMER** TAI

**Ilayda DEMIRDİS**/Hacettepe University

**Gizem C. DELİBALTA**/Mugla Sıtkı Kocman University

**Berkcan ERENLER**/Gazi University

**MEDIA AND INTERNATIONAL RELATIONS COMMITTEE**

**Assoc. Prof. Dr. Zuhall ER**/Istanbul Technical University

**Dr. Bugra YILDIZ**/Hacettepe University

**Erdem MERMER**/TAI

**Gizem C. DELİBALTA**/Mugla Sıtkı Kocman University

**Berkcan ERENLER**/Gazi University

**Notice:** The conference has attended by academics about 20 different countries. 52.2% of conference participants are foreign authors and / or his work with researchers in Turkiye of these authors. Publications selected from the ICMATSE 2022 conference to the journals will not be included in the papers in the proceedings book. All responsibility for references, text and citations belong to the authors.

Proceedings Book

Online: ISBN: 978-625-00-1052-5

## PREFACE

As organizing this event of ICMATSE in 2022, we are excited and proud to have a magnificent scientific program, publish the main developments in the field in the form of 38 keynote/invited talks, a distinguished of 12 session presentations with recent advances. This book presents the abstracts of material science focused on advanced materials and nanotechnology having in energy conversion and storage and LED lighting, optoelectronics, biomedical, agricultural and food and mechanical and thermal applications as well as commercialization issues. In addition to these, powder metallurgy, additive manufacturing, advanced manufacturing and joining techniques are also included. A committee discussed and determined the conference topics that constituted of renowned representatives of academia from Turkey, several European and Asian countries and the USA.

Our world-renowned and top-ranked sponsors enriched our conference by opening exhibitions. They deserve all the thanks.

The academician organizers of the conference, from Gazi University, Iskenderun Technical University, other Universities from Turkey, in collaboration with experts and academician from the University of Illinois at Urbana-Champaign/USA are planning to publish a printed proceedings version after the conference, as well. This will be prepared depends on presenting and selected papers for journals. Papers that are not presented or registered were not included in the proceedings book. Latest news is being announced by the conference website.

Our world-renowned and top-ranked sponsors enriched our conference by opening exhibitions. They deserve all the thanks.

Due to the COVID - 19 outbreak, one – on - one contact events were carried out through online platforms at ICMATSE 2020. Although we missed the face – to - face activities and there was a distance between them for public health, virtual meetings were considered to be used. The virtual meeting took place between 2 –4 October 2020. Remote/virtual presentations sessions were allowed for live interaction. But, now ICMATSE 2022 was held as hybrid format. The longing for face-to-face conferences is evident from the participation of a large number of audiences. We are proud to be able to achieve this.

See you at ICMATSE 2024; Wishing you a healthy and successful life. All this has been possible thanks to your participation, to our sponsors' support, and to our colleagues' involvement. We would like to thank to keynote/invited speakers, participants and all sponsors.

**Hakan ATES (Prof. Dr)**

**Ersin BAHCECI (Assoc. Prof. Dr)**

## **CONTENTS**

<b>Effect of Circular Tool Shoulder End Features on Mechanical Properties of Friction Stir Welded Aluminum 6061 Alloy.....</b>	<b>6</b>
Tolga Arıbal, Duran Kaya, Gökhan Kücükürk	
<b>EU-Materials on and relevant to Nanomaterials: Definition, Regulation and Restrictions.....</b>	<b>12</b>
Natalia Charalampidou	
<b>Optical Properties of BaLiF<sub>3</sub> Single Crystal: Ab Initio Investigation.....</b>	<b>17</b>
Shadia J. Ikhmayies	
<b>Absorption edge of CdTe thin Films Prepared by Thermal Evaporation .....</b>	<b>18</b>
Shadia J. Ikhmayies	
<b>Functional Nanomaterials – Tuning the Size and Surface Chemistry for Applications in Catalysis, Biomedical and Environmental Sciences .....</b>	<b>19</b>
Irshad Hussain	
<b>Non-Destructive Methods for Assessment and Qualification of Metallic Components Additively Manufactured by Powder Bed Fusion Processes .....</b>	<b>22</b>
C. Hakan Gür	
<b>THERMOPHYSICAL PROPERTIES OF 2-PENTANONE AND 2-HEPTANONE + AROMATIC AMINES AT THREE DIFFERENT TEMPERATURES .....</b>	<b>28</b>
Aditi Prabhune, Ranjan Dey	
<b>Strategies for improving mechanical properties and high temperature oxidation resistance in silicides and ceramic composites for ultra-high temperature applications .....</b>	<b>36</b>
Rahul Mitra	
<b>Effect of graphene nanoribbon modification by metal oxide cluster on its adsorption for hydrogen sulfide.....</b>	<b>37</b>
Ahmad I. Ayesb	
<b>Precision Medicine Today .....</b>	<b>38</b>
Sabina Semiz	
<b>Recent findings on gas sensors based on metal-oxide nanoparticles.....</b>	<b>39</b>
Ahmad I. Ayesb	
<b>Functional Materials for Sustainable Development.....</b>	<b>40</b>
M. Ishaque Khan	
<b>Helical light fields revolve materials science .....</b>	<b>41</b>
Takashige Omatsu , Katsuhiko Miyamoto	
<b>Metal Additive Manufacturing: Trends, Oppurtunities and Challanges .....</b>	<b>42</b>
Oguzhan Yilmaz	
<b>Combination of Photonic Tools and Nanostructured Materials for Biomedical Applications .....</b>	<b>43</b>
D.A.Gorin	
<b>Ukrainian track to the green energy transition.....</b>	<b>45</b>
Olena Melnyk, Iryna Vaskina	
<b>Effect of Alignment on Infrared Emissivity for Electrospun Nanofibers .....</b>	<b>46</b>
Osman Safa ÇİFÇİ	

<b>Scaling up Superconducting Quantum Processors: Materials and Fabrication Challenges .....</b>	<b>50</b>
H. M. Nayfeh, D. T. McClure	
<b>First principles study of structural, elastic and mechanical properties of Ti-(44-x)Al-5Zr-xNb alloys .....</b>	<b>55</b>
Erdem Mermer, Hanifi Çinici, Gökay Uğur, Rahmi Ünal	
<b>The Use of Chitosan as a Corrosion Inhibitor with Graphene Oxide .....</b>	<b>60</b>
Narmina Guliyeva, Elshan Aliyev, Aynur Mammadova, Elsun Azizov	
<b>The Use of Chitosan with Graphene Oxide to Create a Membrane for Water Purification .....</b>	<b>63</b>
Narmina Guliyeva	
<b>Utilization of biomass-based hard carbon in energy storage.....</b>	<b>66</b>
Tolga Depci , Yunus Onal, Mustafa Goktan Aydin Emine Yalman	
<b>An investigation of the biomass-derived carbon for next-generation energy storage systems .....</b>	<b>73</b>
Tolga Depci, Yunus Onal, Emine Yalman, Ersin Bahceci	
<b>Tuning the Properties of Spray-Deposited Zinc Oxide (ZnO) for Solar Cells and Optoelectronic Applications: A Review.....</b>	<b>89</b>
Shadia J. Ikhmayies	
<b>Investigation of The Effect of Leaching Applied To Rice Hull Ash On Silica Content and BET Surface Area .....</b>	<b>90</b>
Oykum BASGOZ, Ali Oktay GUL, Ersin BAHCECI, Tolga DEPCI, Omer GULER	
<b>Synthesis of Three-Dimensional Graphene Coated, Molybdenum Loaded Electrode as Microbial Fuel Cell Anode.....</b>	<b>98</b>
Habib Akyazi, Çiğdem Güldür	
<b>Characterization of Radar Absorption Performance of Polyurethane Paint Combined With Different Reinforcements.....</b>	<b>105</b>
Ipek ALISKIN, Ali Oktay GUL, Ersin BAHCECI	
<b>Advanced Materials and Manufacturing Concepts for Next-Generation Aircraft Development Programs ...</b>	<b>115</b>
Mete Bakir	
<b>Development and Characterization Of 3d Printed Frequency Selective Surface Structures in Aerospace Applications.....</b>	<b>119</b>
Omer Ziyaeddin Alaboyun, Mete Bakir, Oguzhan Akgol	
<b>Processing and material design approaches for advanced oxide thermoelectrics: representative cases .....</b>	<b>124</b>
Andrei V. Kovalevsky, Gabriel Constantinescu, Diogo Lopes, Tiago Paulino, Kiryl V. Zakharchuk, Nuno M. Ferreira, Florinda M. Costa, Wenjie Xie, Anke Weidenkaff	
<b>Microstructural and Mechanical Effects of Intercritical Annealing on Mid-Mn Steels .....</b>	<b>126</b>
Mehmet Eroglu, Fatih Demir	
<b>THE PREPARATION OF Al<sub>2</sub>O<sub>3</sub>-Ag CORE-SHELL MICROSPHERES BY USING SEED MEDIATED GROWTH ELECTROLESS PLATING .....</b>	<b>131</b>
Meryem BOZKAYA, Hakan ATEŞ, Ramazan KARSLIOĞLU	
<b>Laser Technologies to fabricate Large Scale Bi-2212 Superconducting Plates.....</b>	<b>135</b>
C. Özçelik, H. Amaveda, M. Mora, E. Martínez, B. Özçelik, G.F. de la Fuente, L. A. Angurel	
<b>Fabrication of spinel ferrite nanoparticles via laser ablation.....</b>	<b>137</b>
B. Özçelik, H. Amaveda, L. A. Angurel, G.F. de la Fuente	

<b>Hybrid Terminal Block Design With Two Different Connection Types.....</b>	<b>138</b>
Burak Karaca, Orhan Kara, Aydın Şık,	
<b>Exciton optoelectronics in two-dimensional monolayer interfaces .....</b>	<b>141</b>
Chandan Biswas	
<b>Study of the effect of pressure and temperature on the microstructure and thermoelectric performances of hot-pressed Sr-doped <math>\text{Ca}_3\text{Co}_4\text{O}_9</math> .....</b>	<b>143</b>
A. Sotelo, M. A. Madre, O. J. Dura, G. García, S. Marinell, P. Martinez-Filgueira, M. A. Torres	
<b>Laser Zone Melting Process for fabricating <math>\text{MnFe}_2\text{O}_4</math> spinel ferrites .....</b>	<b>144</b>
L. A. Angurel, B. Özçelik, H. Amaveda, G.F. de la Fuente	
<b>The investigation of <math>\text{Pd}_2\text{Si}/\text{n-Si}(111)</math> Schottky barrier diodes (SBDs) from <math>C - V - T</math> and <math>G/\omega - V - T</math> measurements on the basis the generalized model.....</b>	<b>145</b>
Izzat Afandiyeva	
<b>Microfluidic Human Placenta DNA purification using superparamagnetic microbeads .....</b>	<b>154</b>
Güneş Kibar, Serkan Doğanay, Mikail Yıldız, Barbaros Çetin	
<b>Superconducting Base Elements for Artificial Neural Network.....</b>	<b>157</b>
Anatolie Sidorenko, Nikolai Klenov, Igor Soloviev, Sergey Bakurskiy, Vladimir Boian, Cezar Casian Malcoci, Roman Morari, Yurii Savva, Alexander Vakhrushev	
<b>Direct and Continuous Routes for the Synthesis of Complex Advanced Functional Ceramic Materials .....</b>	<b>158</b>
Prof Jawwad A. Darr	
<b>Coating glass polycapillary optic with luminescent silicon nanoparticle to enhance the optical characteristics in the EUV/X-ray regime.....</b>	<b>159</b>
Jiacheng Xu, Dmitry Gorin, Julia Skibina, Ammar M. Nayfeh, Mete Bakir, Ersin Bahceci, Hakan Ates, Munir H. Nayfeh	
<b>EFFECTS OF UNDERCUT DEPTH AND LENGTH ON WELD STATIC STRESS CONSANTRATION AND DUCTILITY.....</b>	<b>171</b>
Memduh KURTULMUŞ, Ezgi DOĞAN,	
<b>ACTIVATING FLUX GAS METAL ARC WELDING PROCESS .....</b>	<b>175</b>
Memduh KURTULMUS, Ezgi DOGAN	
<b>Enhanced VGG16 Deep Learning Network for Classification of Deformation Rate from Microstructure Images .....</b>	<b>179</b>
Selim Özdem, İlhami Muharrem Orak	
<b>Thermodynamic Properties of Half –Heusler Semiconductor <math>\text{RhTiSb}</math> Compound .....</b>	<b>186</b>
İlknur Kars Durukan, Yasemin Oztekin Ciftci	
<b>Laser Induced Reverse Transfer .....</b>	<b>191</b>
F. Rey-García, C. Bao, L. A. Angurel, G.F. de la Fuente	
<b>In Situ SEM Scratch Testing to Evaluate Wear Mechanisms of <math>\text{TiC-Ti6Al4V}</math> Nanocomposites Manufactured by Selective Laser Melting .....</b>	<b>192</b>
Beverley J Inkson, İdris Tuğrul Gülenç, Shaumik Lenka	
<b>In situ X-ray Microscopy tensile testing of <math>\text{Ti6Al4V}</math> Parts Manufactured by Selective Laser Melting .....</b>	<b>193</b>
İdris Tuğrul Gülenç, Hongbo Shi, Ria Mitchell, Beverley J Inkson	
<b>A review of the microstructural evolution of the parts which produced with wire arc additive manufacturing technique .....</b>	<b>194</b>
Adem KAYADELEN, Oguzhan YILMAZ, Hakan ATES	

<b>Electrodeposition of Dense Lithium and Sodium Battery Cathodes for Solid-State Batteries.....</b>	<b>209</b>
Paul V. Braun	
<b>The role of defects on structural and optical properties of ZnO nanorods synthesized by a hydrothermal route at various growth times and temperatures.....</b>	<b>210</b>
Şefda Kaya, Ozgür Özturk, A. T. Tasci, F. Bulut, D. Akcan, L. Arda	
<b>Carbide-Free Bainitic Steels-A Short Review .....</b>	<b>226</b>
Omer SAHIN, Volkan KILICLI	
<b>DEVELOPMENT OF CONTINUOUS COLOR COATING LINE FOR STEEL &amp; ALUMINUM STRIP.....</b>	<b>230</b>
Emrullah ÇAYIR, Mehmet YAVUZ, Fevzi ÖZÇELİK, Abdülkadir ÖZÇELİK, Mehmet UÇKAN, İlhami Muharrem ORAK, Ali Yavuz GÜNDOĞDU	
<b>2D MoS<sub>2</sub> Nanoparticle Based Solar Cell on Si.....</b>	<b>237</b>
Ammar Nayfeh	
<b>Solar Energy Forecasting Using Machine Learning Models.....</b>	<b>239</b>
Yusuf Gencer, Zuhale ER	
<b>Presentation Real time microstructural control for product quality and new steel grade development using electromagnetic sensors .....</b>	<b>243</b>
Claire Davis	
<b>Boron R&amp;D Activities and TENMAK BOREN .....</b>	<b>244</b>
Abdulkerim YORUKOGLU	
<b>Development of a New Lining Material with Boron Addition.....</b>	<b>245</b>
Sirma Nur DINLER, Sedat SURDEM, Hakan ATES	
<b>Design, Fabrication and Characterization of Tunable Metamaterials .....</b>	<b>249</b>
Buse Budak, Hakan Ates, Mutlu Gokkavas, Seval Donertas, Ekmel Ozbay	
<b>Highly efficient Cr(VI) removal from aqueous solution by SnO<sub>2</sub> loaded wild plumb kernel shell biochar composite .....</b>	<b>253</b>
Md Mehedi Hasan, Elif Gezgin, Ozlem Altintas Yildirim, Erol Pehlivan	
<b>High throughput DFT calculations and UHS sintering on high entropy diboride ceramics.....</b>	<b>258</b>
Mubashir Mansoor, Sina Kavak, Amir Akbari, Mehya Mansoor, Maryam Mansoor, Volkan Dedeoğlu, Zuhale Er, Kamil Czelej, Lütfi Öveçoğlu, Mustafa Ürgen, Duygu Ağaoğulları	
<b>OPERATION of PbSe DETECTORS IN THE PLASMIC MEDIA.....</b>	<b>259</b>
H. Hilal Yücel KURT, Selçuk UTAŞ	
<b>UNDER ATMOSPHERIC PRESSURE PLASMA RESULTS OF THE MICRODISCHARGE CELL WITH GaSb CATHODE.....</b>	<b>263</b>
H. Hilal Yücel KURT, Selçuk UTAŞ	
<b>ENERGY EXCHANGE VIA GaAs ELECTRODE IN A PLASMA SYSTEM .....</b>	<b>267</b>
H. Hilal Yücel KURT, Selçuk UTAŞ	
<b>Production and Characterization of Commercially Pure (Cp-Ti) and Alloy (Ti64) Porous Titanium Medical Implants using Laser Powder Bed Fusion (L-PBF) Technology Surgery .....</b>	<b>271</b>
Fatma Nur Depboylu, Özgür Poyraz, Evren Yasa, Feza Korkusuz	
<b>Creating an innovation culture in research and development in a volatile world.....</b>	<b>273</b>
Dr Nasar Ali, Dr Mikael Syväjärvi	

**Hyaluronate-Based Thermo-sensitive Hydrogel for Vitreous Body Substitute .....274**  
Feng-Huei Lin (double)

ICMATSE 2022

## Effect of Circular Tool Shoulder End Features on Mechanical Properties of Friction Stir Welded Aluminum 6061 Alloy

**Tolga Arıbal**

Gazi University Graduate School of Natural and Applied Sciences Department of Mechanical Engineering, 06570, Ankara, Turkey, [tolga.aribal@gazi.edu.tr](mailto:tolga.aribal@gazi.edu.tr)  
ORCID: 0000-0001-7814-5208

**Duran Kaya**

Gazi University Project Coordination Implementation and Research Center, 06560, Ankara, Turkey, [durankaya@gazi.edu.tr](mailto:durankaya@gazi.edu.tr)  
ORCID: 0000-0003-3102-9204

**Gökhan Küçüktürk**

Gazi University-Faculty of Engineering Department of Mechanical Engineering, 06570, Ankara, Turkey, [gkucukturk@gazi.edu.tr](mailto:gkucukturk@gazi.edu.tr)  
ORCID: 0000-0002-2978-8968

*Cite this paper as: Arıbal, T, Kaya, D, Küçüktürk, G. Effect of Circular Tool Shoulder End Features on Mechanical Properties of Friction Stir Welded Aluminum 6061 Alloy. Int. Conf. Advanced. Mater. Sci. & Eng. HiTech.and Device Appl.Oct. 27-29 2022, Ankara, Turkey*

**Abstract.** Friction Stir Welding (FSW) is solid-state welding that uses non-consumable tools traversing and rotating along the interface of the materials to be welded. Heat generation by friction and shear deformation is one of the critical characteristics of the formation of bonds. The study aims to understand temperature characteristics, weld zone formation and tensile strength properties of Aluminium 6061-T6 Alloy during the FSW process for different shoulder end features. In this study, three FSW tools, each having various shoulder end features, were designed. The tools were made from AISI 4140 steel and used in a condition of 40 mm/min tool travel speed at 800 rpm. Friction stir welding experiments were performed, and the temperature during welding was measured with the thermal imaging camera. In addition, tensile testing was conducted, and the results were presented. Design with raised shoulder end tool has shown better performance in tensile testing and giving 190.1 MPa as UTS. A numerical model will be developed to deeply understand the effect of the new feature design for further improvement of tool pin design.

**Keywords:** Friction stir welding, aluminium 6061 alloys, ultimate tensile strength, shoulder end features

© 2022 Published by ICMATSE

### 1. Introduction

Friction stir welding (FSW) is a solid-state welding process which occurs below the melting point of the base material. Since it is solid-state welding defects seen in fusion weldings such as cracking, porosity, and alloying element loss can be minimized [1, 2]. FSW enables improvement in tensile strength, hardness, toughness, fatigue and ductility of the welding zone[3]. Moreover, in industries, FSW can be used to minimize the manufacturing period with improved dimensional accuracy [4]. FSW allows

welding of the ferrous and non-ferrous materials such as aluminium, copper, nickel, titanium [4], magnesium, copper, steel and polymers [5]. It is reported by many researchers that FSW has advantages over conventional fusion welding processes, especially for the fields using aluminium alloys [2]. Moreover, FSW is showed an efficient way of refining the grain size over recrystallization, therefore, it has a big potential to join low melting point non-ferrous metals [6].

In this welding technology, the rotating tool moves along the interface of the workpieces to be joined. The plunge of the rotating tool, dwelling specific time and then traversing along the weld line are the three main phases that exist in FSW[5]. The process is either controlled by a predetermined amount of force (load control) applied by the shoulder or with the plunged depth of the tool (displacement control). A schematic of the process can be seen in Figure 1.

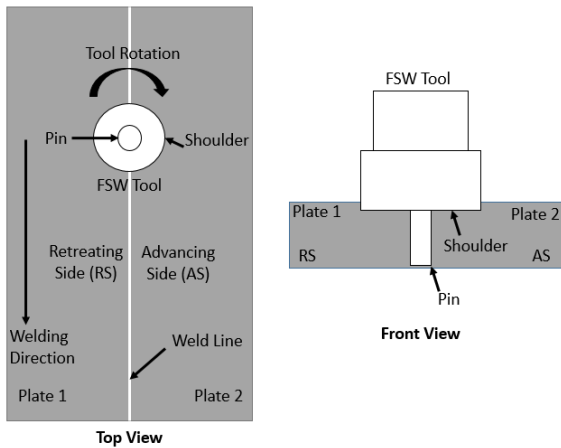


**Figure 1.** Schematic of friction stir welding process

Bond formation in FSW is related to frictional heat generation and shear deformation created by the tool is a measure of quality in friction stir welding. Therefore; tool design is an important parameter in this welding process and the tool is required to provide a sufficient amount of heat underneath the shoulder for bonding [5]. Tool plasticizes the workpiece by frictional heat and deformational heat provides the bonding. The tool is plunged into a workpiece mainly comprised of a shoulder and pin [7].

Most of the frictional heat is generated by the shoulder. The shoulder keeps the plasticized material under the tool [8] and moves the material from the advancing side to the retreating side [3]. Additionally, tool shoulders generate downward forging which is required for welding consolidation [1].

In literature there have been limited studies published with the use of shoulder end surface features such as concentric circle featured tool, ridge featured tool, knurling featured tool and scroll featured tool and limited investigation work has been done for comparison of raised and recessed shoulder end features. In this study raised and recessed circular shoulder end tools were designed and compared with the featureless shoulder end tool in terms of tensile strength in FSW of 6061-T6 aluminium alloy.

## 2. Experimental Work

The base material welded in the experiment was a 6061-T6 aluminium alloy plate. To increase ductility and toughness 6061 aluminium alloys contain manganese.

**Table 1.** Chemical Composition of Al 6061-T6 [9]

Component	Chemical Composition %
<b>Al</b>	95.8 - 98.6
<b>Mg</b>	0.8 - 1.2
<b>Si</b>	0.4 - 0.8
<b>Fe</b>	Maximum 0.7
<b>Cu</b>	0.15 - 0.4
<b>Cr</b>	0.04 - 0.35
<b>Zn</b>	Maximum 0.25
<b>Mn</b>	Maximum 0.15
<b>Ti</b>	Maximum 0.15

Two aluminium 6061-T6 plates each of them 280 mm long, 70 mm wide and 5 mm thick are butt welded by specially designed FSW tools.

Three types of FSW tools with a conical pin were designed and manufactured to weld aluminium 6061-T6. All FSW tools used in experimentation were fabricated from AISI 4140 steel.

**Table 2.** Chemical Composition of AISI4140 [10]

Component	Chemical Composition %
<b>Fe</b>	96.785 - 97.77
<b>Cr</b>	0.80 - 1.1
<b>Mn</b>	0.75 - 1.0
<b>C</b>	0.38 - 0.43
<b>Mo</b>	0.15 - 0.25
<b>P</b>	<= 0.035
<b>Si</b>	0.15 - 0.30
<b>S</b>	<= 0.040

The major dimensions of the FSW tools are given in figure 2.

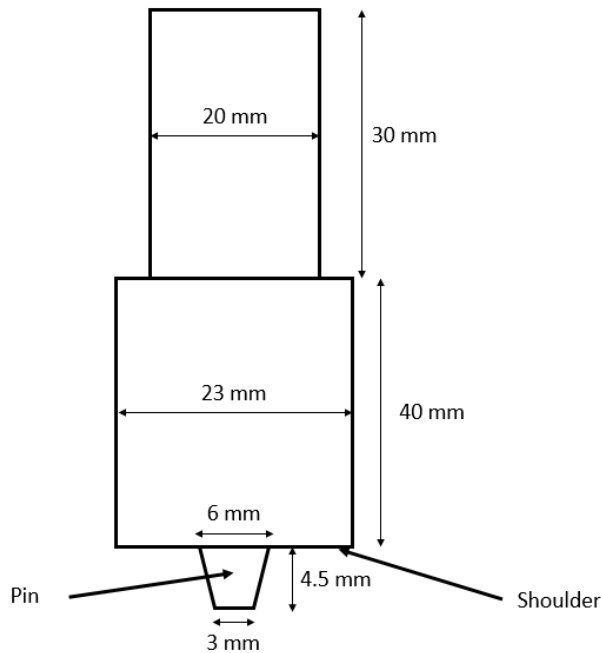


**Figure 2.** Major dimensions of the FSW tools used in the study

The difference among the FSW tools is the type of shoulder end feature. Featureless shoulder end tools in which no features exist raised circular shoulder end tools and recessed circular shoulder end tools were machined using a 1.5 mm drill bit. The distance between the shoulder base surface to raised and recessed features was designed as 0.5 mm. Tool rotational speed was set to 800 rpm and traversing along the weld line around 40 mm/min with a plunge depth of 4.7 mm.

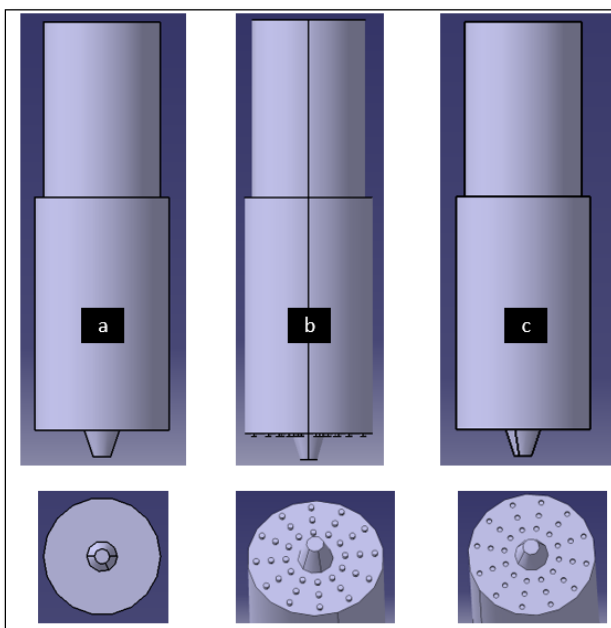


**Figure 3.** Shoulder end features. a Featureless Shoulder end tool b Raised circular shoulder end tool c Recessed circular shoulder end tool



**Figure 4.** From left to right featureless shoulder, raised circular shoulder and recessed circular shoulder end FSW tool

Experiments were carried out in 3 axes vertical machining centre. During the experiment temperature data was recorded with the thermal imaging camera.

Optical microscopy was used to check the stability of the weld zone at different sections along the weld line.

Tensile tests of the welded specimens were done to check the strength at the welding zone. Hand machining was performed to clear flash/crowns on the top surface of the plates. Two types of tensile test specimens; sub-size and mid-size tensile test specimens; mid-size of gauge length of 50 mm, a radius of 12.5 mm, and web of 12.5 mm and sub-size of gauge length of 25 mm, a radius of 6 mm and web of 6 mm as per ASTM E8 standard[11] were sectioned from the middle section of the plates perpendicular to the welding direction.

### 3. Results and Discussion

#### 3.1 Visual Inspection

By visual inspection, all the FSW tools used in the experiment resulted in flash generation and crowns on the retreating side. However, the minimum amount of flash was seen on the advancing side. Keyhole geometry was observed where the tool exits the material due to the withdrawal motion of the FSW tool. Additionally, excessive material was gathered at the exit for all the FSW tools. Crowns produced by the FSW tools can be seen in figure 5. The quality of the top surface of the weld found by the recessed circular shoulder end tool is better based on the visual inspection.

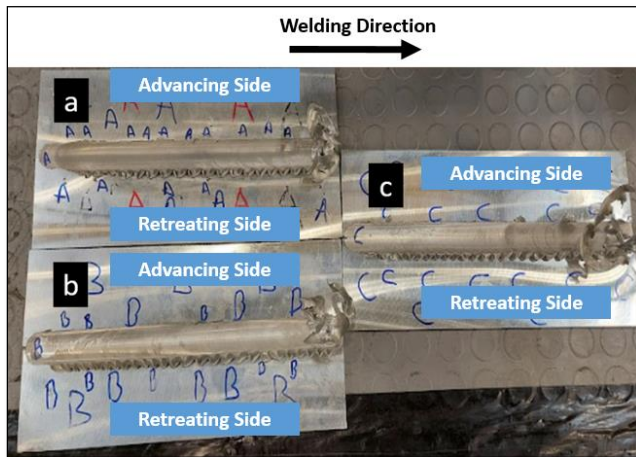


**Figure 5.** The top surface of the welded plates  
*a.* Featureless shoulder end tool *b.* Raised shoulder end tool *c.* Recessed shoulder end tool

On the other hand, it was detected during the sectioning of the test samples, defects were seen in the welds with recessed shoulder end tool at the cross-section of the weld, especially for the samples sliced around the tool plunge region and tool exit region. It is possible to say by visual inspection that recessed shoulder end features could not provide similar structures at the cross-section of the weld.



**Figure 6.** Example of the defect seen in FSW, both samples welded with recessed shoulder end tool during the same welding process

### 3.2 Optical Microscopy

As observed from the experiments, cross-sections of the welds do not exhibit similar structures along the weld line. To validate this unstable situation, two rectangular weld specimens belonging to the featureless shoulder end tool, perpendicularly sliced from the welding direction at different locations were used for optical microscopy as shown in figure 7.



**Figure 7.** Rectangular test specimens for optical microscopy

As it is inferred from the weld zone images, dimensions of the heat-affected zones and voids/defects at the entrance/exit of each specimen show differences.

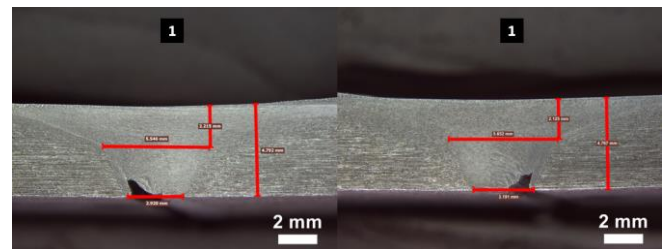


**Figure 8.** Optical microscopy of specimen 1

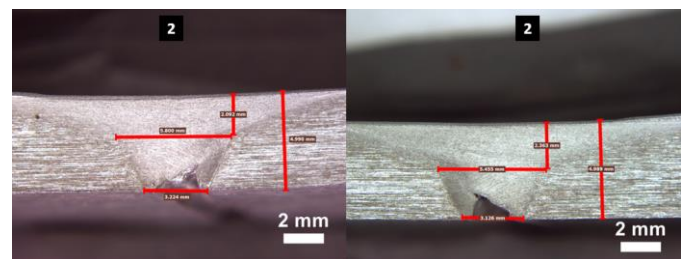


**Figure 9.** Optical microscopy of specimen 2

Void formations occurred at the advancing side of the tool for specimen 1. However, it was not so clear for specimen 2.

### 3.3 Temperature

Maximum temperature in friction stir welding occurs underneath the shoulder. However, in this study maximum temperature recorded was measured around the shoulder periphery because the thermal imaging camera measures the temperature where it sees. Temperatures recorded were higher in the featureless shoulder end tool compared with the

featured tools which are fluctuating around 250 Celcius when it reaches steady conditions.

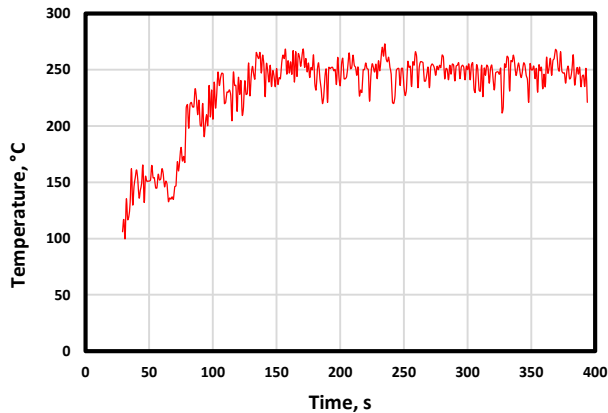


Figure 10. Temperature graph for the featureless shoulder end tool

### 3.4 Tensile Testing

Tensile tests were carried out at room temperature. All the welded samples with the featureless raised and recessed shoulder end feature tools were broken in the tensile testing in heat affected zone at the shoulder/workpiece interface which was the expected location due to the hardness decrease in the heat-affected zone. In figure 11, two samples (midsize and sub-size specimens) from each shoulder end tool were shown.

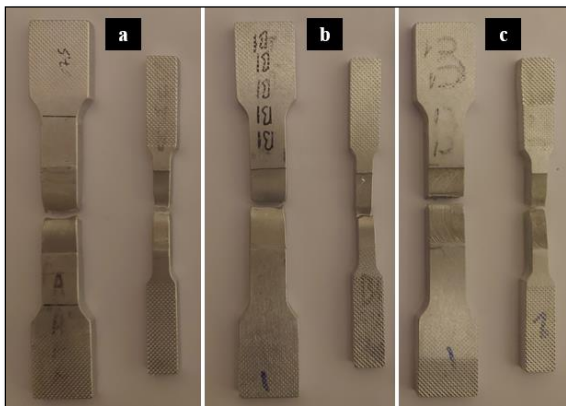


Figure 11. Midsize and sub-size tension test samples a.welded with featureless b.welded with raised c. welded with recessed shoulder end tool

Among the mid-size specimens, maximum ultimate tensile strength was obtained in raised shoulder end tool as in the sub-size specimens which are 187.3 Mpa. Due to the unstable structure observed at different cross-sections of the welded specimens explained previously in terms of defects/voids, especially for the weld with recessed shoulder end tool, comparisons have been done between the sub-size

specimens according to the radiography testing results and by visual examination.

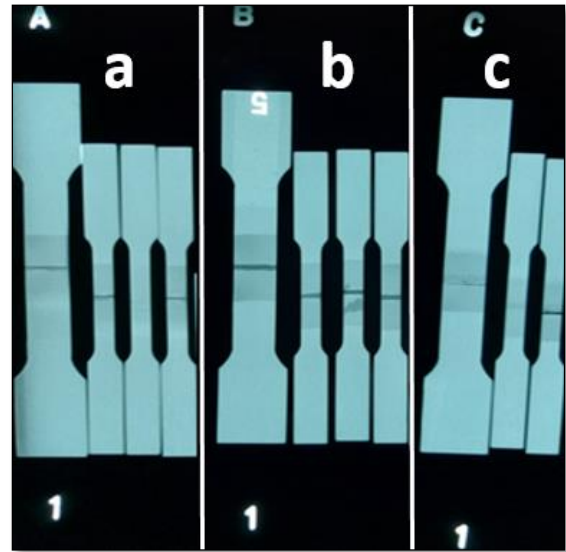


Figure 12. Radiography results of a.welded with featureless b.welded with raised c. welded with recessed shoulder end tool

The maximum ultimate tensile strength (UTS) obtained was recorded as 190.1 Mpa which belongs to specimen weld with raised shoulder end tool. Intermediate UTS was recorded as 174.3 MPa for the recessed shoulder end tool and the lowest was obtained in the featureless shoulder end tool as 163.4 MPa.

### 4. Conclusion

Friction stir welding of Al6061-T6 has been investigated during this study. As a result, a novel tool pin design has been developed to enhance the mechanical properties of the welded sample. This novel design is a form of the raised feature of a small cylindrical shape. Different samples have been welded with different tool pin designs, including the developed novel design. In addition, tensile testing was used to evaluate welded samples with the investigated structures. The developed novel design showed higher performance in tensile testing than other designs and achieved 190.1 MPa UTS. Future work will focus on developing a numerical model to deeply understand the effect of raised features to enhance further the mechanical performance of Al6061-T6 welded FSW.

## References

1. Zhang YN, Cao X, Larose S, Wanjara P (2012) Review of tools for friction stir welding and processing. *Canadian Metallurgical Quarterly* 51:250–261. <https://doi.org/10.1179/1879139512Y.0000000015>
2. Ramanjaneyulu K, Madhusudhan Reddy G, Venugopal Rao A (2014) Role of Tool Shoulder Diameter in Friction Stir Welding: An Analysis of the Temperature and Plastic Deformation of AA 2014 Aluminium Alloy. *Trans Indian Inst Met* 67:769–780. <https://doi.org/10.1007/s12666-014-0401-z>
3. Joshi S, Namjoshi S, Paliwal D (2020) Effect of Tool Geometry on Friction Stir Welded 6061 Aluminum Alloy. *Materials Today: Proceedings* 24:738–745. <https://doi.org/10.1016/j.matpr.2020.04.330>
4. Asmare A, Al-Sabur R, Messele E (2020) Experimental Investigation of Friction Stir Welding on 6061-T6 Aluminum Alloy using Taguchi-Based GRA. *Metals* 10:1480. <https://doi.org/10.3390/met10111480>
5. Mugada KK, Adepu K (2018) Influence of tool shoulder end features on friction stir weld characteristics of Al-Mg-Si alloy. *Int J Adv Manuf Technol* 99:1553–1566. <https://doi.org/10.1007/s00170-018-2602-9>
6. Joshi SK, Gandhi JD Influence of Tool Shoulder Geometry on Friction Stir Welding: A Literature Review. 4
7. Trueba L, Heredia G, Rybicki D, Johannes LB (2015) Effect of tool shoulder features on defects and tensile properties of friction stir welded aluminum 6061-T6. *Journal of Materials Processing Technology* 219:271–277. <https://doi.org/10.1016/j.jmatprotec.2014.12.027>
8. Nandan R, Debroy T, Bhadeshia H (2008) Recent advances in friction-stir welding – Process, weldment structure and properties. *Progress in Materials Science* 53:980–1023. <https://doi.org/10.1016/j.pmatsci.2008.05.001>
9. ASM Material Data Sheet. <https://asm.matweb.com/search/SpecificMaterial.asp?bassnum=ma6061t6>. Accessed 18 Sep 2022
10. AISI 4140 Steel, normalized at 870°C (1600°F), air cooled, 25 mm (1 in.) round. <https://www.matweb.com/search/DataSheet.aspx?MatGUID=8b43d8b59e4140b88ef666336ba7371a&ckck=1>. Accessed 18 Sep 2022
11. E28 Committee Test Methods for Tension Testing of Metallic Materials. ASTM International

## EU-Materials on and relevant to Nanomaterials: Definition, Regulation and Restrictions

**Natalia Charalampidou**

*Democritus University of Thrace – Faculty of Law, Department of International Relations,  
GR-69100 Komotini, Greece, natalia.charalampidou@gmail.com*

ORCID: 0000-0001-9792-0222

*Cite this paper as: Charalampidou, Natalia, EU-Materials on and relevant to Nanomaterials: Definition, Regulation and Restrictions, Conf. Advanced. Mater. Sci. & Eng. HiTech. and Device Appl. Oct. 27-29 2022, Ankara, Turkey*

**Abstract.** This paper shall analyse the legal aspects related to nanomaterials under EU Law from three perspectives. At the outset it shall outline the EU's understanding of nanomaterials [1]. In this part, it shall be interesting to see how legal instruments define nanomaterials, which in essence is the result of a technological process that evolves with high velocity and by its nature stands in contradiction to the rigidity of legal definitions. Thereafter, it shall elucidate whether the EU has introduced any regulatory provisions on nanomaterial [2]. Finally, in view of the fact that nanomaterials have a wide spectrum of application, the paper shall focus on restrictions introduced by Brussels imposing restrictive measures (sanctions) and in particular restrictions related to military material [3], equipment for internal repression [4], dual-use goods and technology [5] and other equipment, technology and software [6]. This paper aims to producing the result of presenting to scientists who develop this technology, the legal frame that EU instruments create, and portray possible implications that can arise due to the imposed restrictive measures, once the technology has reached the commercialization stage.

**Keywords:** nanomaterials, legal definition, regulatory framework, sanctions

© 2022 Published by ICMATSE

### I. Introduction

This paper examines the legal instruments of the European Union ('EU') in relation to nanomaterial. Mention is made on *legal instruments*, and not *laws*, as some of them are not binding and they therefore lack the mandatory legal effect that a law ordinarily has. The paper is divided in three main parts. The first one shall examine the legal definition of nanomaterials that Brussels has chosen to enact. The second shall set out the regulatory frame that applies on nanomaterials, whereas the third one shall portray the restrictions on the trade, supply and export that certain items and materials face, when they fall under the restrictive measures (sanctions) imposed by the EU in view of the situation in certain countries. The sanctions that the United Nations ('UN') impose are not within the scope of the present paper.

### II. The Definition of *Nanomaterial* and its Legal Effect

It has been a decade since the EU has undertaken the task to legally define *nanomaterial*, initially at the request of the European Parliament. In doing so,

it deviated from the generic definition adopted by the International Organisation for Standardisation that reads 'material with any external dimension in the nanoscale or having internal structure or surface structure in the nanoscale' [7] and opted for the ensuing definition which consisted of one main rule and two subsequent ones, that under circumstances offered flexibility and could broaden the definition that the main rule had set. Accordingly, '*nanomaterial* means a natural, incidental or manufactured material containing particles, in an unbound state or as an aggregate or as an agglomerate and where, for 50 % or more of the particles in the number size distribution, one or more external dimensions is in the size range 1 nm-100 nm.' At the same time, the subsequent rule allowed for a broader definition where the number size distribution threshold of 50 % is replaced by a threshold between 1 and 50 %, under circumstances that justified this in view of concerns for the environment, health, safety or competitiveness. Furthermore, the EU offered the possibility to consider as nanomaterials 'fullerenes, graphene flakes and single wall carbon nanotubes with one or

more external dimensions below 1 nm'. In adopting this threefold definition, the EU acknowledged the necessity of available scientific knowledge being its cornerstone and the speed inherent to technological development, which necessitates review of the relevant legal instruments in order to ensure that they correspond to 'the needs' [8], although it did fail to clarify both the nature and the scope of said needs.

Almost a decade later, the EU concluded the review of the aforementioned definition, reiterating the effect that progress and technological innovation have on legislative material and the need for frequent review [1 p. 5], while explaining its findings. At the outset, it took the approach that the definition should be grounded on the 'relative fraction of particles in a defined range within the particle number-based distribution of the external dimension of the constituent particles of a material' and not relate to any hazardous properties or risks that it may have for human health or the environment [1 p. 2]. Further, it thought that the definition should address materials *consisting* of particles in solid state, present on their own or bound as constituent parts of aggregates or agglomerates, where the specifically chosen term *consists* denotes acknowledging that particles form the principal component [*ibid*]. In addition, the definition should include solely solid particles, excluding non-solid ones [*ibid*] as well as large solid products or components, even when an internal structure or a surface structure is at nanoscale [*ibid*]. Moreover, it should cover particles on their own as well as identifiable constituent particles in agglomerates or aggregates [1 p. 3]. Then the EU took the view that the default threshold of 50% should be maintained and the flexibility option established with the aforesaid subsequent rules should be abolished for the sake of regulatory consistency and coherence [*ibid*]. Accordingly, the reviewed definition of nanomaterial, which was considered appropriate in the general context of Union policy and legislation, [*ibid*] reads:

'*nanomaterial* means a natural, incidental or manufactured material consisting of solid particles that are present, either on their own or as identifiable constituent particles in aggregates or agglomerates, and where 50 % or more of these particles in the number-based size distribution fulfil at least one of the following conditions:

- (a) one or more external dimensions of the particle are in the size range 1 nm to 100 nm;
- (b) the particle has an elongated shape, such as a rod, fibre or tube, where two external dimensions

are smaller than 1 nm and the other dimension is larger than 100 nm;

(c) the particle has a plate-like shape, where one external dimension is smaller than 1 nm and the other dimensions are larger than 100 nm.

In the determination of the particle number-based size distribution, particles with at least two orthogonal external dimensions larger than 100  $\mu\text{m}$  need not be considered.

However, a material with a specific surface area by volume of  $< 6 \text{ m}^2 / \text{cm}^3$  shall not be considered a nanomaterial.' [1 p. 5&6]

Finally, although the European Commission that penned this definition, proposes that it may serve policy, legislative and research purposes [1 p. 5], one should underline that, from a legal viewpoint, this definition is merely suggested and lacks any legally binding effect, in the sense that its application may merely be argued and may not be enforced, although policy and politics may suggest otherwise.

### III. The Regulatory Frame Related to Nanomaterial

The EU legislator, despite his aforementioned effort to specify and determine nanomaterial, has not proceeded with adopting a regulatory frame on nanomaterial that would apply horizontally across all areas and industries, as for example the case has been with mercury [9]. Therefore, nanomaterial, just like ordinary material, are subject to the regulatory norms and rules that are applicable in industries and sectors, albeit not *per se*, but as part of a product. For example, if nanomaterial is included in *substances* and *mixtures* in the sense of their statutory definition under EU law [2 Arts 1(2) and 3(1)&(2)], this law on chemicals shall be applicable. Similarly, if nanomaterial is included in *medicinal product* either for human or for veterinary use [10], this law on medicinal product shall be applicable.

### IV. Nanomaterial and Restrictive Measures

In view of the wide applicability of nanomaterial and the lack of horizontal regulatory frame for such under EU law, it is significant to refer to restrictive measures as these prohibitions may, and do, have impact on nanomaterial contained in such equipment and items.

Restrictive measures, also widely known as sanctions, traditionally involved freezing funds targeting specific individuals [11]. However, over the years they have become more sophisticated and have split over other areas of commercial transactions. In the ensuing paragraphs it shall be described how sanctions impose restrictions on the trade of military

materials and equipment, equipment for internal repression, as well as the dual use items and other equipment, technology and software, as they involve products that may contain nanomaterials.

*Military materials and equipment* that can be subject to restrictive measures, as the case is in view of the situation in Belarus [12] and South Sudan [3], are specified throughout the EU and set out in detail in the Common Military List [13]. The Common Military List includes smooth-bore weapons and other arms and weapons [13 p. 1-3], ammunition, fuze setting devices and specially designed components therefor [13 p. 4], bombs, torpedoes, rockets, missiles, other explosive devices and charges [13 p. 4-5], fire control, surveillance and warning equipment, and related systems, test and alignment and countermeasure equipment [13 p. 5-6], ground vehicles and components [13 p. 6-7], chemical agents, "biological agents", "riot control agents", radioactive materials [13 p. 7-10], "energetic materials" [13 p. 10-20], vessels of war (surface or underwater), special and naval equipment and other surface vessels [13 p. 20-22], "aircraft", "lighter-than-air vehicles", "Unmanned Aerial Vehicles", aero-engines and "aircraft" equipment, related equipment, and components [13 p. 22-23], electronic equipment, "spacecraft" and components, not specified elsewhere on the EU Common Military List [13 p. 24], high velocity kinetic energy weapon systems and related equipment [13 p. 24-25], armoured or protective equipment, constructions and components [13 p. 25-26], 'specialised equipment for military training' or for simulating military scenarios, simulators specially designed for training in the use of firearm or weapon [13 p. 26], imaging or countermeasure equipment [*ibid*], forgings, castings and other unfinished products, specially designed for certain aforementioned items [*ibid*], miscellaneous equipment, materials and "libraries" in the sense of collections of technical information, reference to which may enhance the performance of relevant systems, equipment or components [13 p. 27-28 & 34], "production" equipment, environmental test facilities and components [13 p. 28], Directed Energy Weapon (DEW) systems, related or countermeasure equipment and test models [13 p. 29], cryogenic and "superconductive" equipment [13 p. 29-30] and finally related software and technology [13 p. 30-31]. These items, which here have been merely briefly mentioned and are described in detail in the legal material, have the common component that they are specifically designed or modified for military use or for use in a combat zone.

*Equipment that might be used for internal repression*, is similarly specified in EU legal material, albeit less specifically, and consists mostly of material not controlled by the Common Military List. Further, unlike the Common Military List, which is listed in a single legal instrument, this equipment is set out in each EU legislation imposing such sanctions as an annex thereto, i.e. the laws imposing restrictive measures in view of the situation in Venezuela [4], Iran [14] and Myanmar/Burma [5]. In most cases, this list includes firearms, ammunition and related accessories, bombs and grenades, vehicles, explosive substances, protective equipment, simulators, night vision, razor barbed wire, military knives, combat knives and bayonets with blade lengths in excess of 10 cm, related production equipment and related specific technology [4 p. 30-31] [d] [5 p. 4-5].

*Dual-use items* are items, including software and technology that can be used for both civil and military purposes and include all goods which can be used for both non-explosive uses and assisting in any way in the manufacture of nuclear weapons or other nuclear explosive devices [15 Art. 2(1)]. Under the imposed sanctions, in a fashion similar to the Common Military List, it is prohibited to sell, supply, transfer and export such dual-use items that specifically fall under ten categories of goods, material and equipment, those being nuclear, special material, materials processing, electronics, computers, telecommunications and "information security", sensors and lasers, navigation and avionics, marine and aerospace and propulsion. The specific goods, along with technology notes are described in much detail in the relevant legal instruments [15 Annex I] [16].

Finally, certain legal instruments prohibit the act of selling, supplying, transferring or exporting of specific equipment, technology and software. This is for example the case in relation to sanctions imposed in view of the situation in Syria [6 Art. 4 & Annex V]. The prohibited equipment, technology and software, as specified in the apposite legal instrument includes various equipment such as equipment for radio frequency monitoring, remote infection and interception [6 Annex V points A, D & E]. Another example constitute the restrictive measures imposed against North Korea [17]. In this law, the specific items, materials, equipment, goods and technology that are prohibited have been identified and designated by the Security Council of the United Nations [18] [19]. They are set out in a long and detailed list which ranges from nuclear

materials, facilities and equipment to sensors, lasers and propulsion [17 Annex II Parts IV-VII].

## V. Conclusions

The EU has attempted to specify and define nanomaterials from a legal perspective and it has agreed to a definition, which was subsequently amended in order to reflect the technological development that inevitably has an effect on legal instruments, as the EU has explicitly acknowledged. However, the agreed definition although perhaps accurate, is not legally binding. Further, the EU has refrained from regulating nanomaterial *per se*, in the sense that a legally binding document specifying registration and authorization of nanomaterials throughout the common market is absent. Still, as

they form part of materials, items and equipment, in a legal sense, their trade, supply and export is regulated under the provisions applicable on such material, items and equipment, i.e. chemicals or medicinal products, or prohibited, when they constitute materials, items and equipment that fall under the sanctions lists that have been drawn by the EU in view of the situation in certain countries. The present paper has merely scratched the surface of the items listed in the sanctions lists which set out in much detail and precision what may not be sold, traded or supplied to the relevant countries. Much caution is necessary in order to ensure that the sanctions are not violated, as the consequences are dire.

## References

1. European Commission, Commission Recommendation of 10.6.2022 on the definition of nanomaterial, C(2022) 3689 final, [https://ec.europa.eu/environment/chemicals/nanotech/pdf/C\\_2022\\_3689\\_1\\_EN\\_ACT\\_part1\\_v6.pdf](https://ec.europa.eu/environment/chemicals/nanotech/pdf/C_2022_3689_1_EN_ACT_part1_v6.pdf)
2. See in particular Regulation (EC) No 1907/2006 of the European Parliament and of the Council of 18 December 2006 concerning the Registration, Evaluation, Authorisation and Restriction of Chemicals (REACH), establishing a European Chemicals Agency, amending Directive 1999/45/EC and repealing Council Regulation (EEC) No 793/93 and Commission Regulation (EC) No 1488/94 as well as Council Directive 76/769/EEC and Commission Directives 91/155/EEC, 93/67/EEC, 93/105/EC and 2000/21/EC, OJ 396, 30.12.2006, p. 1, as last amended by Commission Regulation (EU) 2022/586 of 8 April 2022 amending Annex XIV to Regulation (EC) No 1907/2006 of the European Parliament and of the Council concerning the Registration, Evaluation, Authorisation and Restriction of Chemicals (REACH), OJ L 112, 11.4.2022, p. 6.
3. See for example Council Regulation (EU) 2015/735 of 7 May 2015 concerning restrictive measures in respect of the situation in South Sudan, and repealing Regulation (EU) No 748/2014, OJ L 117, 8.5.2015, p. 13, as last amended by Council Implementing Regulation (EU) 2022/748 of 16 May 2022 implementing Regulation (EU) 2015/735 concerning restrictive measures in respect of the situation in South Sudan, OJ L 138, 17.5.2022, p. 1.
4. See for example Council Regulation (EU) 2017/2063 of 13 November 2017 concerning restrictive measures in view of the situation in Venezuela, OJ L 295, 14.11.2017, p. 21, as last amended by Commission Implementing Regulation (EU) 2022/595 of 11 April 2022 amending certain Regulations concerning restrictive measures and setting out a single list for the Annexes to those Regulations containing the contact details of Member States' competent authorities and the address for notifications to the European Commission, OJ L 114, 12.4.2022, p. 60.
5. See for example Council Regulation (EU) No 401/2013 concerning restrictive measures in view of the situation in Myanmar/Burma and repealing Regulation (EC) No 194/2008, OJ L 121, 3.5.2013, p. 13, as last amended by Council Implementing Regulation (EU) 2022/662 of 21 April 2022 implementing Regulation (EU) No 401/2013 concerning restrictive measures in view of the situation in Myanmar/Burma, OJ L 121, 22.4.2022, p. 1.
6. See for example Council Regulation (EU) No 36/2012 of 18 January 2012 concerning restrictive measures in view of the situation in Syria and repealing Regulation (EU) No 442/2011, OJ L 16, 19.1.2012, p. 1, as last amended by Regulation (EU) 2022/595 (n 4 above).
7. International Organisation for Standardisation, Online Browsing Platform, <https://www.iso.org/obp/ui/#home>
8. Commission, Recommendation of 18 October 2011 on the definition of nanomaterial, OJ L 275, 20.10.2011, p. 38.
9. Regulation (EU) 2017/852 of the European Parliament and of the Council of 17 May 2017 on mercury, and repealing Regulation (EC) No 1102/2008, OJ L 137, 24.5.2017, p. 1, as amended.
10. Regulation (EC) No 726/2004 of the European Parliament and of the Council of 31 March 2004 laying down Community procedures for the authorisation and supervision of medicinal products for human and veterinary use and establishing a European Medicines Agency, OJ L 136, 30.4.2004, p. 1, as amended.
11. See for example Council Regulation (EC) No 881/2002 of 27 May 2002 imposing certain specific restrictive measures directed against certain persons and entities associated with Usama bin Laden, the Al-Qaida network and the Taliban, and repealing Council Regulation (EC) No 467/2001 prohibiting the export of certain goods and services to Afghanistan, strengthening the flight ban and extending the freeze of funds and other financial resources in respect of the Taliban of Afghanistan, OJ L 139, 29.5.2002, p. 9, as amended.
12. Council Regulation (EC) No 765/2006 of 18 May 2006 concerning restrictive measures against President Lukashenko and certain officials of Belarus, OJ L 134, 20.5.2006, p. 1, as amended.

13. Common Military List of the European Union, OJ C 85, 13.3.2020, p.1, as amended.
14. Council Regulation (EU) No 359/2011 of 12 April 2011 concerning restrictive measures directed against certain persons, entities and bodies in view of the situation in Iran, OJ L 100 14.4.2011, p. 1, as last amended by Commission Implementing Regulation (EU) 2022/595 of 11 April 2022 amending certain Regulations concerning restrictive measures and setting out a single list for the Annexes to those Regulations containing the contact details of Member States' competent authorities and the address for notifications to the European Commission, OJ L 114, 12.4.2022, p. 60.
15. Council Regulation (EC) No 428/2009 of 5 May 2009 setting up a Community regime for the control of exports, transfer, brokering and transit of dual-use items (recast), OJ L 134, 29.5.2009, p. 1, as amended.
16. Commission Delegated Regulation (EU) 2020/1749 of 7 October 2020 amending Council Regulation (EC) No 428/2009 setting up a Community regime for the control of exports, transfer, brokering and transit of dual-use items, OJ L 421, 14.12.2020, p. 1.
17. Council Regulation (EU) 2017/1509 of 30 August 2017 concerning restrictive measures against the Democratic People's Republic of Korea and repealing Regulation (EC) No 329/2007, OJ L 224 31.8.2017, p. 1, as amended.
18. UN Security Council Resolution 2270 (2016).
19. UN Security Council Resolution 2321 (2016).

## Optical Properties of BaLiF3 Single Crystal: Ab Initio Investigation

**Shadia J. Ikhmayies**

*Jabal El-Hussain,, Amman 11121, Jordan, shadia\_ikhmayies@yahoo.com, ORCID: 0000-0002-2684-3300*

*Cite this paper as: Ikhmayies,S., Optical Properties of BaLiF3 Single Crystal: Ab Initio Investigation.Int. Conf. Advanced. Mater. Sci.& Eng. HiTech.and Device Appl.Oct. 27-29 2022,Ankara, Turkey*

**Abstract.** Cubical perovskite LiBaF<sub>3</sub> is a promising material for various applications such as scintillators, dosimeters, and other optical industries. In addition this crystal is a potential laser material when it is doped with divalent cations. In this work the full-potential linearized augmented plane wave method (FP-LAPW) based on the density functional theory (DFT) were used to perform the calculations to investigate the optical properties of BaLiF<sub>3</sub> single crystal. The generalized gradient approximation (GGA) implemented in Wein2K code was used as the exchange correlation potential. The density of states, real and imaginary parts of the complex dielectric function, refractive index, extinction coefficient, reflectance, absorbance, real and imaginary parts of the optical conductivity, and energy loss of BaLiF<sub>3</sub> single crystal are computed and discussed.

**Keywords:** Cubical perovskite LiBaF<sub>3</sub>, Density functional theory (DFT), band structure, Optical properties  
© 2022 Published by ICMATSE

Cubical perovskite BaLiF<sub>3</sub> is one of the interesting mixed metal fluorides (e.g. BaLiF<sub>3</sub>, BaY<sub>2</sub>F<sub>8</sub>, YLiF<sub>4</sub>, LiCaAlF<sub>6</sub>, LiSrAlF<sub>6</sub>) [1] with a wide energy band gap. So, they have great potential for a variety of device applications in optical, ferroelectric, antiferromagnetic systems [2,3]. In this work the the density of states, band structure, and other optical properties were determined.

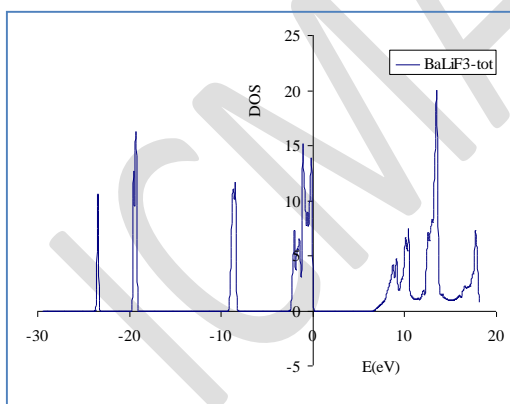


**Figure 1.** Total density of states of BaLiF<sub>3</sub> single crystal.

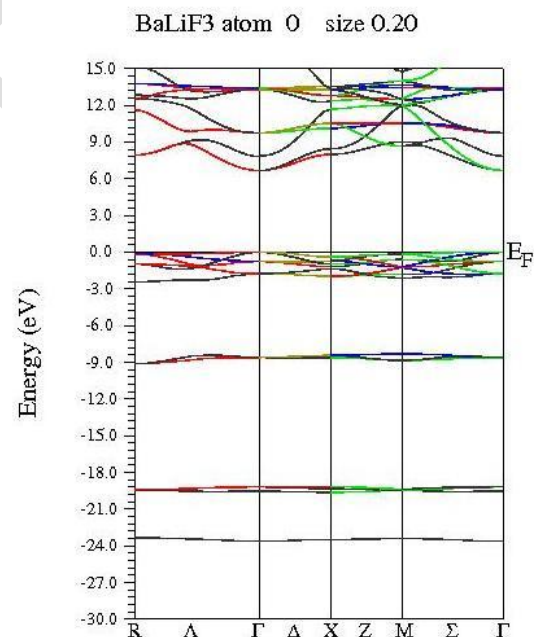


**Figure 2.** Band structure of BaLiF<sub>3</sub> single crystal.

### References

1. Robert A. Jackson, Mario E. G. Valerio, Marcos A. Couto dos Santos, Jomar B. Amaral. Computer modelling of mixed metal fluorides for optical applications. Dalton Trans. , (2004), pp. 3098-3100, <https://doi.org/10.1039/B401220H>
2. K. Neupane and R. K. Thapa. Study of electronic properties of fluoride perovskite BaLiF<sub>3</sub> using FP-LAPW method. Journal of Materials Science and Engineering A., 7 (11-12) (2017), pp. 311-314, Doi: 10.17265/2161-6213/2017.11-12.005
3. R.E. Ouenzerfi, S. Ono, A. Quema, M. Goto, M. Sakai, N. Sarukura, Design of wide-gap fluoride heterostructure for deep ultraviolet optical devices, J. Appl. Phys. 96 (2004), pp. 7655-59, <https://doi.org/10.1063/1.1808474>

## Absorption edge of CdTe thin Films Prepared by Thermal Evaporation

**Shadia J. Ikhmayies**

*Jabal El-Hussain,, Amman 11121, Jordan, shadia\_ikhmayies@yahoo.com, ORCID: 0000-0002-2684-3300*

*Cite this paper as: Ikhmayies SJ. Absorption edge of CdTe thin Films Prepared by Thermal Evaporation.Int. Conf. Advanced. Mater. Sci.& Eng. HiTech.and Device Appl.Oct. 27-29 2022,Ankara, Turkey*

**Abstract.** Cadmium telluride (CdTe) is an important semiconductor that has applications in photovoltaic cells and optoelectronic industries. In this work, thin films of CdTe were deposited by thermal evaporation at ambient temperature on glass substrates. From the x-ray diffraction (XRD) measurements it is found that the films are polycrystalline with zinc-blende structure. Scanning electron microscopy supported by x-ray energy dispersive spectroscopy (SEM-EDS) was used to observe the morphology and composition of the films. Polycrystalline nature was confirmed through SEM micrographs, and the films showed stoichiometric composition. Transmittance of the films was measured at room temperature in the wavelength range 770-1100 nm and used to deduce the absorbance. The second derivative of the absorbance was used to detect the peaks in the near band-edge region. The most relevant peaks are discussed and explained.

**Keywords:** Cadmium telluride, Solar cells, Absorption edge

© 2022 Published by ICMATSE

Cadmium telluride (CdTe) is an important II-VI compound semiconductor that can be used as an absorber in photovoltaic devices [1]. It has a band gap of about 1.5 eV at room temperature, which is in the middle of the solar spectrum. It has applications in photovoltaics and optoelectronic industries such as infrared and x-ray detectors. Besides, it has a large absorption coefficient large absorption coefficient ( $\alpha > 10^4 \text{ cm}^{-1}$ ) for the visible solar spectrum [1].

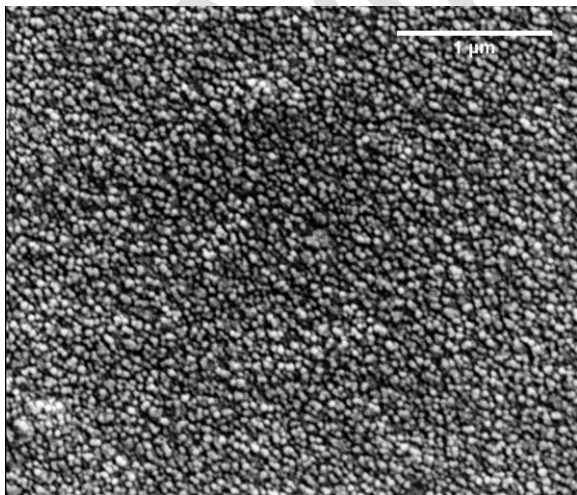


**Figure 1.** SEM image of vacuum deposited CdTe thin film of thickness about 1  $\mu\text{m}$ .

### References

1. A. A. J. Al-Douri, F. Y. Al-Shakily, M. F. A. Alias, A. A. Alnajjar. Optical properties of Al- and Sb-doped CdTe thin films. *Advances in Condensed Matter Physics*. (2010), Article ID 947684, 5 pages, doi:10.1155/2010/947684

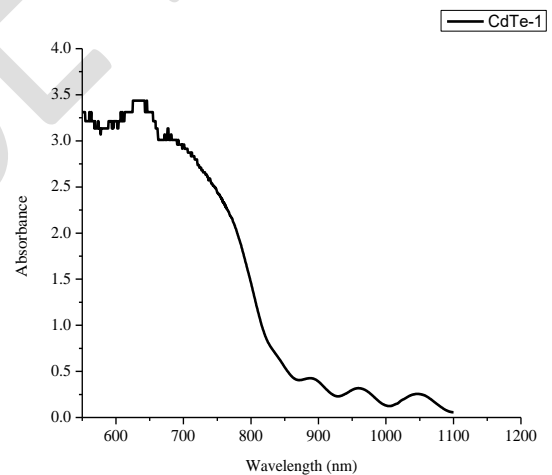


**Figure 2.** Absorbance of thermally evaporated CdTe thin film

Transmittance of the films was measured at room temperature in the wavelength range 770-1100 nm and used to deduce the absorbance. The second derivative of the absorbance was used to detect the peaks in the near band-edge region. The most relevant peaks are discussed and explained.

## **Functional Nanomaterials – Tuning the Size and Surface Chemistry for Applications in Catalysis, Biomedical and Environmental Sciences**

***Irshad Hussain***

*Department of Chemistry & Chemical Engineering, SBA School of Science & Engineering (SSE), Lahore University of Management Sciences (LUMS), DHA, Lahore Cantt-54792, Pakistan*

ORCID: 0000-0001-5498-1236

*Cite this paper as: HUSSAIN, I., Functional Nanomaterials – Tuning the Size and Surface Chemistry for Applications in Catalysis, Biomedical and Environmental Sciences , Int. Conf. Advanced. Mater. Sci. & Eng. HiTech.and Device Appl.Oct. 27-29 2022,Ankara, Turkey*

**Abstract.** Abstract. The unique chemical and physical properties of nanoscale materials have triggered much scientific interest to explore their potential applications in biomedical sciences, energy technologies, agriculture, environment, catalysis and industry etc. The chemical and physical properties of metal/ metal oxide nanoparticles can generally be tuned by controlling their size, shape and surface chemistry. In this regard, we have developed several reproducible protocols to prepare functionalized metal/metal oxide nanoparticles from subnanometer to over 100 nm in aqueous/organic media with a decent control over their size, shape, and surface chemistry. We generally used chemical reduction approach for the synthesis of metal nanoparticles, where metal salts are reduced in the presence of stabilizers that can coat the initially formed metal nuclei at different stages of their growth depending on the nature of metal and the stabilizing ligand. Depending on the nature of ligands, nanoparticles stay away from each other due to electrostatic repulsion and steric repulsion. Many of these metal nanoparticles have been used as building blocks to design/synthesize new nanostructured materials using template-based and template-less strategies. Template-based strategies have particularly been employed to form hierarchically porous nanocomposite materials for water remediation and inorganic oxide based porous catalysts (after removing the sacrificial template by calcination) for various catalytic applications.

The functionalized metal/metal oxide nanoparticles/nanoclusters possess interesting optical, recognition and catalytic/bio-catalytic properties. For example, we have used some of the fluorescent metal nanoclusters for the sensing of biomolecules and even explosives due to the quenching of fluorescence in the presence of analytes. Similarly, we have produced cationic iron oxide nanoparticles that mimic horseradish peroxidase enzyme and used them as artificial enzymes for the detection of bacteria. We have also used silver nanoparticles and nanoclusters (both cationic and anionic) to kill resistant bacteria and tried to understand how the size and surface chemistry of nanoparticles affect their antimicrobial properties. We have also developed various metal nanoclusters based electrocatalysts (both homogeneous and heterogeneous catalysts) for electrocatalytic and photocatalytic splitting of water. Having developed some interesting electrocatalysts in this regard, we are now further extending their scope to be used as electrode materials for aqueous sodium ion batteries. In yet another project, we are developing graphene-photocatalysts nanocomposites on which hypercrosslinked polymers can be grown to facilitate the adsorption of CO<sub>2</sub> and its subsequent conversion to the hydrocarbon fuel.

This talk would, therefore, be an overview of interdisciplinary research activities of Functional Nanomaterials Group at LUMS to synthesize customized inorganic/organic nanoparticles with tunable size and surface chemistry, and their composites having unique chemical and physical properties, and subsequent applications in biomedical sciences, environment, catalysis and renewable energy technologies.

**Keywords:** Green chemistry, Green deal, Sustainable development, Polymers

© 2022 Published by ICMATSE

..

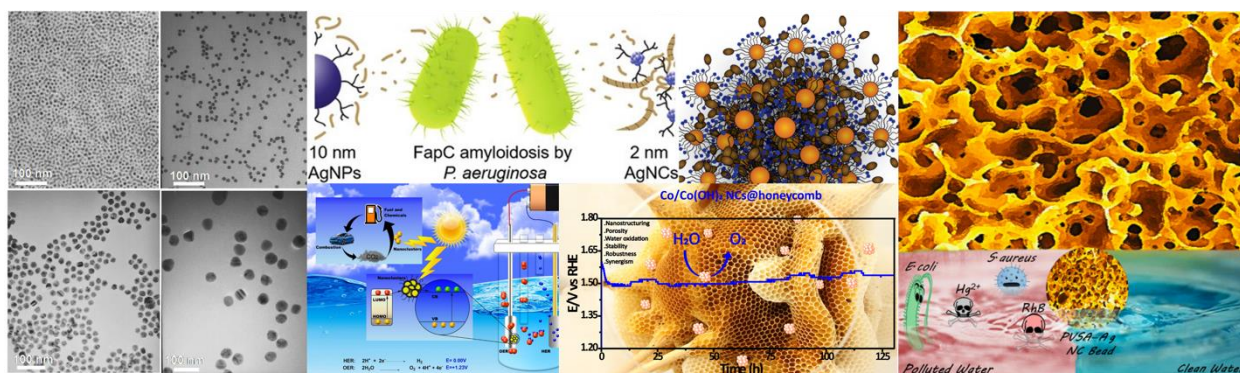


**Fig. 01:** A representative image showing the electron microscopic images, and cartoons for some of the nanomaterials being routinely prepared/used in Functional Nanomaterials Group at LUMS.

## References

### Selected References:

1. Immobilized covalent triazine frameworks films as effective photocatalysts for hydrogen evolution reaction. Xunliang Hu, Zhen Zhan, Jianqiao Zhang, Irshad Hussain, Bien Tan. *Nature Communications*, 2021, 12, 1.
2. Fundamentals and design-led synthesis of emulsion-templated porous materials for environmental applications. Muhammad Ahmad Mudassir, Tariq Mahmood Ansari, Haifei Zhang and Irshad Hussain\*. *Advanced Science* 2021, 8, 2102540.
3. Recent advances in the electrocatalysts towards alcohols assisted energy-saving hydrogen production. Farhan Arshad, Tanveer ul Haq, Irshad Hussain\*, Falak Sher\*. *ACS Applied Energy Materials* 202, 4 (9), 8685.
4. Facile preparation of silver nanocluster self-assemblies with aggregation-induced emission by equilibrium shifting. Lianyu Li, Weiyao Xi, Irshad Hussain, Meiling Chen, Bien Tan. *Nanoscale* 2021, 13, 14207
5. Hyperbranched polyethylenimine-tethered multiple emulsion-templated hierarchically microporous poly(acrylic acid)-Al<sub>2</sub>O<sub>3</sub> nanocomposite beads for water purification. Muhammad Ahmad Mudassir, Syed Zajif Hussain, Shazia Kousar, Haifei Zhang, Tariq Mahmood Ansari and Irshad Hussain\*. *ACS Applied Materials and Interfaces* 2021, 13 (23), 27400.
6. Bactericidal effect of 5-mercapto-2-nitrobenzoic acid coated silver nanoclusters against multidrug-resistant *Neisseria gonorrhoeae*. Maria Isabel Lucio, Maria-Eleni Kyriazi, Joshua Hamilton, Diego Batista, Alexander Sheppard, Elisabeth Sams-Dodd, Maria Humbert, Irshad Hussain, Myron Christodoulides, Antonios Kanaras\*. *ACS Applied Materials & Interfaces*, 2020, 12 (25), 27994.
7. Nanosilver mitigates biofilm formation via FapC Amyloidosis Inhibition. Zil-e Huma, Ibrahim Javed, Zhenzhen Zhang, Hajira Bilal, Yunxiang Sun, Syed Zajif Hussain, Thomas P. Davis,†, Daniel E. Otzen, Cornelia B. Landersdorfer, Feng Ding, Irshad Hussain\* and Pu Chun Ke\*. *Small*, 2020, 16, 1906674.
8. Controlled Assembly of Cu/Co-oxide Beaded Nanoclusters on Thiolated Graphene Oxide Nanosheets for High Performance Oxygen Evolution Reaction. Akhtar Munir, Tanveer Ul Haq, Iqtidar Hussain, Irfan Ullah, Syed Zajif Hussain, Javed Iqbal, Ahsanulhaq Qurashi, Asma Rehman, Irshad Hussain\*. *Chemistry – A European Journal*, 2020, 26(49), 11209.
9. Controlled Engineering of Nickel Carbide Induced N-Enriched Carbon Nanotubes for Hydrogen and Oxygen Evolution Reactions in Wide pH Range. Akhtar Munir, Tanveer-ul-Haq, Murtaza Saleem, Anwar-UI-Hamid, Syed Zajif Hussain, Falak Sher, Ahsanulhaq Qurashi, Asim Jalani, Irshad Hussain\*. *Electrochimica Acta*, 2020, 341, 136032.
10. Controlled Development of Higher-Dimensional Nanostructured Copper Oxide Thin Films as Binder Free Electrocatalysts for Oxygen Evolution Reaction. Farhan Arshad, Akhtar Munir, Qasim Qayyum Kashif, Tanveer ul Haq, Javed Iqbal, Falak Sher, Irshad Hussain\*. *International Journal of Hydrogen Energy*, 2020, 45(23), 16583.
11. A proactive model on innovative biomedical applications of gold nanoparticles. Asma Irshad\*, Maira Zahid, Tayyab Husnain, Abdul Qayyum Rao, Nadeem Sarwar, Irshad Hussain. *Applied Nanoscience* 2020, 10, 2453.
12. Ultrasmall Co@Co(OH)<sub>2</sub> Nanoclusters Embedded in N-Enriched Mesoporous Carbon Network as Efficient Electrocatalysts for Durable Water Oxidation. Akhtar Munir, Tanveer ul Haq, Iqtidar Hussain, Ahsanulhaq Qurashi, Ubaid Ullah, Muhammad J. Iqbal, Irshad Hussain\*. *ChemSusChem*, 2019, 12, 5117.
13. Fabrication of Emulsion-Templated Poly(vinylsulfonic acid)-Ag Nanocomposite Beads with Hierarchical Multimodal Porosity for Water Cleanup. Muhammad A. Mudassir, Syed Zajif Hussain, Syeda T. Asma, Haifei Zhang, Tariq M. Ansari\*, Irshad Hussain\*. *Langmuir* 2019, 35. 40, 13165.
14. Porous hypercrosslinked polymer-TiO<sub>2</sub>-graphene composite photocatalysts for visible-light-driven CO<sub>2</sub> conversion. Shaolei Wang, Min Xu, Tianyou Peng, Chengxin Zhang, Tao Li, Irshad Hussain, Jingyu Wang and Bien Tan\*. *Nature Communications*, 2019, 10, 676.

15. Combatting antibiotic-resistant bacteria using nanomaterials. Akash Gupta, Shazia Mumtaz, Cheng-H. Li, Irshad Hussain\* and Vincent M. Rotello\*. *Chemical Society Reviews*, 2019, 48, 415.
16. Metal Nanoclusters: New Paradigm in Catalysis for Water Splitting, Solar and Chemical Energy Conversion. Akhtar Munir, Khurram Joya, Syed Z. Hussain, Noor UA. Babar, Najeeb Ullah, Ahsanulhaq Qureshi, and Irshad Hussain\*. *ChemSusChem*, 2018 (In press).
17. Dopamine coated Fe<sub>3</sub>O<sub>4</sub> nanoparticles as enzyme mimics for the sensitive detection of bacteria. Shazia Mumtaz, Li-Sheng Wang, Syed Zajif Hussain, Muhammad Abdullah, Zill-e- Huma, Zafar Iqbal, Brian Creran, Vincent M. Rotello\* and Irshad Hussain.\* *Chemical Communications*, 2017, 53, 12306.
18. Development of silver nanoparticles decorated emulsion-templated hierarchically porous poly(1-vinylimidazole) beads for water treatment. Muhammad Ahmad Mudassir, Syed Zajif Hussain, Asma Rehman, Wasif Zaheer, Syeda Tasmia Asma, Asim Jilani, Mohammad Aslam, Haifei Zhang, Tariq Mahmood Ansari,\* Irshad Hussain.\* *ACS Applied Materials & Interfaces*, 2017, 9, 24190.
19. Layered microporous polymers by solvent knitting method. Shaolei Wang, Chengxin Zhang, Yu Shu, Shulan Jiang, Qi Xia, Linjiang Chen, Shangbin Jin, Irshad Hussain, Andrew I. Cooper, Bien Tan\*. *Science Advances*, 2017, 3, e1602610.
20. Synthesis, characterization and evaluation of lecithin based nanocarriers for enhanced pharmacological and oral pharmacokinetic profile of amphotericin B. Ibrahim Javed, Syed Zajif Hussain, Irfan Ullah, Imran Khan, Muhammad Ateeq, Gul Shahnaz, Habib ur Rehman, Muhammad T. Razi, Raza Shah and Irshad Hussain.\* *Journal of Materials Chemistry B*, 2015, 3, 8359.
21. Synthesis of highly stable and water dispersible Ag<sub>44</sub>(SR)<sub>30</sub> nanoclusters. Lina G. Abdulhalim, Sumaira Ashraf, Nuwan Kothalawala, Khabiboulakh Katsiev, Dalaver H. Anjum, Sikandar Abbas, Francesco Stellacci, Amala Dass, Irshad Hussain,\* and Osman M. Bakr.\* *Journal of Materials Chemistry A*, 2013, 01, 10148.
22. Facile and surfactant-free preparation of highly blue fluorescent gold nanoclusters in organic media. Xin Huang, Buyi Li, Luo Li, Hui Zhang, Irfan Majeed, Irshad Hussain\* and Bien Tan.\* *Journal of Physical Chemistry C*, 2012, 116, 448.
23. Formation of spherical nanostructures by controlled aggregation of gold colloids. Irshad Hussain,\* Zhenxin Wang, Andrew I. Cooper and Mathias Brust. *Langmuir*, 2006, 22, 2941.
24. Synthesis of hierarchically porous inorganic–metal site-isolated nanocomposites. Haifei Zhang, Irshad Hussain, Mathias Brust, and Andrew I. Cooper\*. *Chemical Communications*, 2006, 24, 2539.
25. Aligned two and three-dimensional structures by directional freezing of polymers and nanoparticles. Haifei Zhang, Irshad Hussain, Mathias Brust, Micheal F. Butler, Steven P. Rannard and Andrew I. Cooper\*. *Nature Materials*, 2005, 4, 787.
26. A new Pt-Ru model system to study the bifunctional mechanism of electrocatalysis. Christina Roth, Adam J. Papworth, Irshad Hussain, Richard J. Nichols and David J. Schiffrin. *Journal of Electro-Analytical Chemistry*, 2005, 581, 79.
27. Size-controlled synthesis of near-monodisperse gold nanoparticles in the 1-4 nm range using polymeric stabilizers. Irshad Hussain, Susan Graham, Zhenxin Wang, Bien Tan, Steven P. Rannard, David C. Sherrington, Andrew I. Cooper\* and Mathias Brust\*. *Journal of the American Chemical Society*, 2005, 127, 16398.
28. Emulsion-templated gold beads using gold nanoparticles as building blocks. Haifei Zhang, Irshad Hussain, Mathias Brust and Andrew I. Cooper\*. *Advanced Materials*, 2004, 16, 1, 27 (Front cover art).
29. Fullerene-linked Pt nanoparticle assemblies. Christina Roth, Irshad Hussain, Maryam Bayati, Richard J. Nichols and David J. Schiffrin\*. *Chemical Communications*, 2004, 1532.
30. Rational and combinatorial design of peptide capping ligands for gold nanoparticles. Raphael Levy, Nguyen T. K. Thanh, Christopher R. Doty, Irshad Hussain, Richard J. Nichols, David J. Schiffrin, Mathias Brust, and David G. Fernig\*. *Journal of the American Chemical Society*, 2004, 126, 10076.
31. Preparation of acrylate-stabilized gold and silver hydrosols and gold-polymer composite films. Irshad Hussain, Mathias Brust\*, Adam J. Papworth and Andrew I. Cooper\*. *Langmuir*, 2003, 19, 4831.

## **Non-Destructive Methods for Assessment and Qualification of Metallic Components Additively Manufactured by Powder Bed Fusion Processes**

**C. Hakan Gür**

*Middle East Technical University (METU) – Department of Metallurgical and Materials Engineering  
Middle East Technical University (METU) – Welding Tech. & Non-Destructive Testing Res./Appl. Center  
06800, Ankara, TR, chgur@metu.edu.tr  
ORCID: 0000-0002-4884-9818*

*Cite this paper as: Gür, CH. Nondestructive Methods for Assessment and Qualification of Metallic Components Additively manufactured by Powder Bed Fusion Processes. Int. Conf. Advanced Mater. Sci. & Eng. HiTech. and Device Appl., Oct. 27-29 2022, Ankara, Turkey*

**Abstract.** Additive manufacturing (AM) has created the possibility of producing high-value, complicated, and customized components that would not be feasible to build using conventional routes. In powder bed fusion type processes, laser or electron beams are used to melt and fuse the metal powder. Significant uncertainties, such as dimensional inaccuracy, discontinuities, nonhomogeneous microstructure, and anisotropic mechanical behavior, are typically brought on by variations in raw materials and process conditions. Thus, the qualification of AM components requires extra effort to verify their structural integrity and performance. Since the variations inside the volume, between build lots, and between platforms make destructive testing for qualification less effective with AM techniques, non-destructive (ND) techniques have become more prevalent. But because of complex geometry and significant microstructural variability, AM parts are difficult to inspect using many traditional ND techniques. Therefore, it is crucial to develop innovative ND techniques that are matched to AM processes and components. This paper reviews the current status of the ND methods used for the assessment and qualification of metallic components additively manufactured by powder bed fusion processes.

**Keywords:** Additive manufacturing, Powder Bed Fusion, Quality control, Assessment, Nondestructive methods  
© 2022 Published by ICMATSE

### **1. Introduction**

Powder bed fusion (PBF) type additive manufacturing (AM) processes, such as Direct Metal Laser Sintering, Electron Beam Melting, and Selective Laser Melting provide exceptional possibilities for the fabrication of metal parts with complex geometries. They utilize a moving electron or laser beam to selectively melt the metal powder to build the final component in a layer-by-layer manner. Nevertheless, they are constrained by dimensional inaccuracy, anisotropic behavior, and flaws that could seriously impair the product's structural integrity and functionality.

The efficient application of diverse quality control and characterization techniques is necessary for the identification and precise evaluation of defects, the determination of material properties, and the assurance of the integrity of AM parts. Material, equipment, and processes must be qualified and certified using reliable tests with a sufficient level of

confidence to produce high-quality AM parts. Moreover, in-process feedback and closed-loop systems are necessary for the control of process variability and performance [1,2]. Due to the nonuniformity and anisotropy inside the as-built volume as well as the differences in the production lots, the results of typical mechanical testing may not be sufficiently accurate for the AM parts. Additionally, due to changes in thermal history caused by geometrical and manufacturing variances, test specimens that are created separately might not accurately represent the AM product. Non-destructive (ND) techniques offer solutions to these challenges and have a critical role in establishing a closed-loop diagnostic system for monitoring and predicting structure properties and the occurrence of defects throughout AM processes. It is also possible to use ND techniques to determine microstructure, mechanical properties, and residual stress [3].

## 2. Typical defects and anomalies

The typical defects and anomalies include porosity (gas, lack-of-fusion, keyhole), balling, cracking, delamination, microstructural inhomogeneity, dimensional inaccuracy, surface roughness, distortion, and residual stress. They arise from part design, equipment, build direction, base plate, properties of the feedstock powder (aspect ratio, mean size, size range, surface contamination, trapped gases, impurities, internal voids, moisture, flowability, spreadability, etc.), powder spattering, process parameters (atmosphere of the building chamber, powder spreading, beam power, beam profile, scan speed, layer thickness, hatch spacing, scan strategy), and post-processes (HIP, heat treatment). Imperfections at the crystal structure scale such as dislocations and grain boundaries may also affect the final properties. Detailed reviews on the metal powder bed fusion AM defects and their formation mechanisms exist in the literature [4,5].

In conventionally manufactured parts, non-destructive (ND) methods have been used to detect surface and internal flaws, characterize microstructure, determine mechanical properties and residual stress, as well as for long-term structural monitoring to prevent failures. However, due to the micron-scale layer-wise manufacturing, high geometric complexity, and microstructural non-uniformity, their application for the inspection of PBF-AM parts is a difficult task. Thus, there is a need to detect and evaluate the defects in AM parts by novel ND techniques at a certain confidence level. Recent years have seen the publication of certain reviews regarding the application of ND techniques in the AM industry [6-9].

### 3. Control of raw material

The quality and properties of the raw material (feedstock powder) directly influence the final product. Various methods have been used to characterize powders such as gas pycnometry to measure the powder density; scanning electron microscopy to measure the shape, size, aspect ratio, etc.; energy dispersive X-ray analysis to identify chemical composition and microstructure [10]. A recent study has reported the results of the studies on stainless steel and Co-Cr powders by utilizing laser diffraction, X-ray computed tomography, optical and scanning electron microscopy, X-ray diffraction, energy dispersive analytical X-ray analysis, and X-Ray photoelectron spectroscopy [11].

## 4. In situ monitoring of the process

Since any anomalies in the melt pool might be related to the defect formation, in situ monitoring will be advantageous for observing defect formation in real time. This approach enables the reduction of defects by controlling the process parameters, and also, enforces the further improvement of ND qualification methods. Using this approach, powder bed anomaly, spattering, powder melting, consolidation have been detected via visible-light high-speed imaging [12,13]; high-speed IR imaging, i.e., active thermography [14-16]; high-speed synchrotron/x-ray imaging, and diffraction [17-20]; 3D synchrotron x-ray microtomography [21]; ultrasonic wave scattering [22]; and acoustic emission testing [23-26]. These techniques have recently been combined with neural network models and machine learning approaches. More thorough studies about in-situ monitoring techniques for additive manufacturing processes can be found elsewhere [27,28].

## 5. Control of the final product

### 5.1. Density, dimensional accuracy, roughness

The density of the AM parts is determined using the Archimedean method, or cross-sectioning to compare pore volume to total bulk volume [29]. Dimensional accuracy can be controlled via a coordinate measuring machine, a structural light 3D scanner, or a 3D laser scanner [30]. Surface roughness is determined by using contact surface profilometry, optical profiling, etc. [31,32]. The ability to detect every micro-notch on as-built surfaces using standard profilometry techniques and average roughness values, however, is in question. Recently, 3D surface and subsurface features of as-built AM materials have been captured using the XCT method [33].

### 5.2. Residual stress

Due to the severe temperature gradients produced by rapid melting, solidification, and re-melting of underlying previously solidified layers during the layer-by-layer assembly at the micrometer scale, complex patterns of residual stress are developed in the AM parts. Volume changes brought on by phase transformations may also have an impact on the residual stress state. The end-use parts' mechanical properties and performance (e.g., fatigue behavior) may diminish due to residual stresses, which may also cause deformation and lower dimensional

accuracy [34,35]. The research about residual stress measurement in AM parts has usually focused on X-ray and neutron diffraction methods. Recent research has found high agreement between X-ray and neutron diffraction and contour methods when measuring residual stress in an as-built component [36]. Due to its greater penetration depth and ability to quantify all three orthogonal strains, neutron diffraction allows for stress estimates at a larger variety of positions than other methods. However, when there is a considerable stress gradient at a shallow depth, a higher-resolution technique like XRD is suggested to gather crucial data, for instance for fatigue applications.

### 5.3. Detection and evaluation of defects

Since many factors such as roughness, anisotropy, complicated geometry, and defect nature make it challenging for reliable ND evaluation, the ND techniques have not yet been thoroughly validated to capture standard-sized flaws in the AM components at a defined probability and confidence level.

#### 5.3.1. Computed tomography method

X-ray computed tomography (XCT) has been efficiently used in analyzing defects in AM parts [37]. It can be used to probe the sub-surface porosity and features that may be inaccessible through other techniques. It provides information about the individual pore sizes and shapes in 3D, along with the bulk porosity values by the reconstruction of a series of radiographic images taken as the component or the source-detector pair rotates with small angle steps till 180° or 360°. Then, computational algorithms reconstruct the 3D volume by using the recorded data [38-40]. Data acquisition at each scan takes several hours. On the other hand, synchrotron-based XCT enables fast data recording within a few minutes, improved spatial contrast and resolution to micro-XCT methods, and sub-micron voxel resolution. Recently, advanced in situ x-ray technologies have been used to generate important insights into defect formation during AM process [41,42].

#### 5.3.2. Ultrasonic methods

Since ultrasonic waves can propagate through thick solid parts, ultrasonic testing is suitable for the detection of various types of defects in a wide range of materials, far beneath the inspection surface [43]. With pulse-echo ultrasonic testing, the same transducer emits and receives very short ultrasonic

pulses with frequencies usually ranging from 1 to 10 MHz. This method uses echo signals at an imperfection interface to reflect the waves. The C-scan ultrasonic method, in which the data collected from an ultrasonic inspection is plotted on a plan view of the component parallel to the scanning surface, provides 3D images of the surface and the inside features. The measurements are much faster than XCT, however, not suitable for complex shaped parts and less accurate than XCT [44].

Non-contact ultrasonic techniques have been developed since conventional ultrasonic testing transducers aren't always appropriate for the inspection of complex shaped parts. As a potential method to monitor AM parts for porosities, lack of fusion, etc., laser ultrasonics creates and detects ultrasonic signals remotely. An infrared Nd:YAG pulsed laser's nanosecond impulses cause a reversible thermoelastic deformation and the development of surface and volume waves (compressional and transverse) in the component. Then, laser interferometry can detect surface displacements caused by the interactions of waves with defects [45]. During the inspection, the A-scans are acquired along a line on the sample surface, and the B-scan image is analyzed to determine the position, size, and depth of the flaw [46].

The spatially resolved acoustic spectroscopy (SRAS) technique can identify faults in AM parts, according to a recent study [47]. It probes the part with surface waves to a few micrometers in depth, providing details on the microstructure and surface and subsurface flaws. SEM images have been used to confirm the surface pores that were discovered using this approach. Additionally, XCT images taken up to a depth of 25 μm have verified subsurface pores discovered by SRAS analysis.

The efficiency of the resonant acoustics method (RAM) and phased array ultrasonic testing (PAUT) in AM parts have been evaluated by using artificial defects simulating typical AM flaws lying between 100 and 700 μm [48]. The RAM is based on an analysis of the component's natural resonant frequencies. The PAUT steers the ultrasonic beam without moving the probe to produce 3D images of the part. It also involves a full matrix capture acquisition procedure and a fully focused method for post-processing the data and reconstructing the images. Although the RAM is quite effective at sorting defective parts, PAUT is preferable if the flaws need to be identified and located.

In addition to being successfully used for in-situ monitoring of AM processes, acoustic emission testing can also be used for volumetric fast inspection of as-built parts by mounting multiple sensors on the part to gather data on the location of discontinuities and the structural integrity. Discontinuities present in the component cause the release and propagation of elastic energy (i.e., crack propagation) in the form of stress waves, which may be observed by sensors when the component is subjected to a change in load. However, further NDT techniques are required to acquire quantitative conclusions regarding size and depth.

### 5.3.3. Eddy current method

By measuring the apparent electrical conductivity of the AM components, it has been reported that a multi-frequency eddy current approach enables the differentiation of various surface textures and various pore-size lattice architectures. These measurements, however, are restricted to a

relatively shallow depth and are inappropriate for components with volumes lower than 1 cm<sup>3</sup> [44].

## 6. Conclusions

Non-destructive (ND) techniques are promising tools for the qualification and certification tasks in the AM industry. Although some effective applications of ND techniques to PBF-AM processes, such as in-situ monitoring and flaw identification in the as-built parts, have been shown, there remain significant difficulties in the detection, characterization, and precise evaluation of the defects at a particular confidence level. Because of their intricate geometries and high levels of microstructural variability, AM parts are difficult to control with typical ND approaches. To optimize the in situ AM process control and inspection of the as-built products, cutting-edge ND techniques are required. Additionally, the combination of ND techniques and the machine learning approach would open up amazing possibilities for the control and improvement of AM processes and products.

## References

1. Energetics Incorporated, Summary Report: Roadmap Workshop on Measurement Science for Metal-Based Additive Manufacturing, Dec 4–5, 2012 Gaithersburg, Maryland, May 2013
2. M. Seifi, A. Salem, J. Beuth, O. Harrysson, J.J. Lewandowski, Overview of materials qualification needs for metal additive manufacturing, *JOM*, 68 (3) (2016), pp. 747-764, 10.1007/s11837-015-1810-0
3. Materials Characterization Using Nondestructive Evaluation Methods, Eds: Gerhard Huebschen, Iris Altpeter, Ralf Tschuncky, Hans-Georg Herrmann, Woodhead Publishing (2016), ISBN: 9780081000403
4. H. Taheri, M.R.M. Shoaib, L.W. Koester, T.A. Bigelow, P.C. Collins, L.J. Bond, Powder-based additive manufacturing - A review of types of defects, generation mechanisms, detection, property evaluation, and metrology, *International Journal of Additive and Subtractive Materials Manufacturing*, 1 (2) (2017), pp. 172-209, 10.1504/IJASMM.2017.10009247
5. A. Mostafaei, C. Zhao, Y. He, S.R. Ghiaasiaan, B. Shi, S. Shao, N. Shamsaei, Z. Wu, N. Kouraytem, T. Sun, J. Pauza, B. Webler, N.D. Parab, M. Asherloo, Q. Guo, L. Chen, A.D. Rollett, Defects and anomalies in powder bed fusion metal additive manufacturing, *Current Opinion in Solid State and Materials Science*, 26 (2) (2022), Article no. 100974, 10.1016/j.cossms.2021.100974
6. J.M. Waller, H. Parker, K.L. Hodges, E.R. Burke, J.L. Walker, NASA/TM-2014-218560, Nondestructive evaluation of additive manufacturing: State-of-the-discipline report, NASA/TM-2014–218560, (2014), 10.13140/RG.2.1.1227.9844
7. Q.Y. Lu and C.H. Wong, Additive manufacturing process monitoring and control by non-destructive testing techniques: Challenges and in-process monitoring, *Virtual and Physical Prototyping*, 13 (2) (2018), pp. 39-48, 10.1080/17452759.2017.1351201
8. L.W. Koester, L.J. Bond, H. Taheri, P.C. Collins, Nondestructive evaluation of additively manufactured metallic parts: In situ and post-deposition, in *Additive Manufacturing for the Aerospace Industry*, Eds. F. Froes and R. Boyer, Elsevier (2019), pp. 401-417, ISBN 9780128140635, 10.1016/B978-0-12-814062-8.00020-0
9. P. Charalampous, I. Kostavelis, D. Tzovaras, Non-destructive quality control methods in additive manufacturing: A survey, *Rapid Prototyping Journal*, 26 (4) (2020), pp. 777–790, 10.1108/RPJ-08-2019-0224
10. V.V. Popov, M.L. Grilli, A. Koptuyug, L. Jaworska, A. Katz-Demyanetz, D. Klobčar, S. Balos, B.O. Postolnyi, S. Goel, Powder bed fusion additive manufacturing using critical raw materials: A review, *Materials*, 14 (2021), No. 4, Article no. 909, 10.3390/ma14040909
11. J.A. Slotwinski, E.J. Garboczi, P.E. Stutzman, C.F. Ferraris, S. S. Watson, and M. A. Peltz, Characterization of metal powders used for additive manufacturing, *Journal of Research of the National Institute of Standards and Technology*, 119 (2014), pp. 460-493, 10.6028/jres.119.018

12. G. Repossini, V. Laguzza, M. Grasso, B.M. Colosimo, On the use of spatter signature for in-situ monitoring of Laser Powder Bed Fusion, *Additive Manufacturing*, 16 (2017), pp. 35-48, 10.1016/j.addma.2017.05.004
13. U.S. Bertoli, G. Guss, S. Wu, M.J. Matthews, J.M. Schoenung, In-situ characterization of laser-powder interaction and cooling rates through high-speed imaging of powder bed fusion additive manufacturing, *Materials, and Design*, 135 (2017), pp. 385-396, 10.1016/j.matdes.2017.09.044
14. H. Krauss, T. Zeugner, M.F. Zaeh, Layerwise monitoring of the selective laser melting process by thermography, *Physics Procedia*, (56) 2014, pp. 64-71, 10.1016/j.phpro.2014.08.097
15. J.L. Bartlett, F.M. Heim, Y.V. Murty, X. Li, In situ defect detection in selective laser melting via full-field infrared thermography, *Additive Manufacturing*, 24 (2018), pp. 595-605, 10.1016/j.addma.2018.10.045
16. J.L. McNeil, K. Sisco, C. Frederick, M. Massey, K. Carver, F. List, C. Qiu, M. Mader, S. Sundarraj, and S.S. Babu, In situ monitoring for defect identification in Nickel alloy complex geometries fabricated by L-PBF additive manufacturing, *Metall Mater Trans A*, 51 (2020), pp. 6528-6545, 10.1007/s11661-020-06036-0
17. C. Zhao, K. Fezzaa, R.W. Cunningham, H. Wen, F. De Carlo, L. Chen, A.D. Rollett, T. Sun, Real-time monitoring of laser powder bed fusion process using high-speed X-ray imaging and diffraction, *Sci Rep*, 7 (2017), pp. 1-11, 10.1038/s41598-017-03761-2
18. Q. Guo, C. Zhao, L.I. Escano, Z. Young, L. Xiong, K. Fezzaa, W. Everhart, B. Brown, T. Sun, L. Chen, Transient dynamics of powder spattering in laser powder bed fusion additive manufacturing process revealed by in-situ high-speed high-energy x-ray imaging, *Acta Mater*, 151 (2018), pp. 169-180, 10.1016/j.actamat.2018.03.036
19. R. Cunningham, C. Zhao, N. Parab, C. Kantzos, J. Pauza, K. Fezzaa, T. Sun, A.D. Rollett, Keyhole threshold and morphology in laser melting revealed by ultrahigh-speed x-ray imaging, *Science*, 80 (363) (2019), pp. 849-52, 10.1126/science.aav4687
20. A.A. Martin, N.P. Calta, J.A. Hammons, S.A. Khairallah, M.H. Nielsen, R.M. Shuttlesworth, N. Sinclair, M.J. Matthews, J.R. Jeffries, T.M. Willey, J.R.I. Lee, Ultrafast dynamics of laser-metal interactions in additive manufacturing alloys captured by in situ X-ray imaging, *Mater Today Adv*, 1 (2019), Article 100002, 10.1016/j.mtadv.2019.01.001
21. P. Lhuissier, X. Bataillon, C. Maestre, J. Sijobert, E. Cabrol, P. Bertrand, E. Boller, A. Rack, J.J. Blandin, L. Salvo, G. Martini, In situ 3D X-ray microtomography of laser-based powder-bed fusion (L-PBF) - A feasibility study, *Additive Manufacturing*, 34 (2020), Article no. 101271, 10.1016/j.addma.2020.101271
22. C.M. Kube, Y. Shu, A.J. Lew, and D. Galles, Real-time characterization of laser-generated melt pools using ultrasound, *Materials Evaluation*, 76 (4) (2018), pp. 525-534
23. M.R. Redding, S.A. Gold, and T.G. Spears, Non-contact acoustic inspection method for additive manufacturing processes, US Patent 20,170,146,489, 2017
24. H. Gaja, F. Liou, Defects monitoring of laser metal deposition using acoustic emission sensor, *Int J Adv Manuf Technol*, 90 (1-4) (2017), pp. 561-574, 10.1007/s00170-016-9366-x
25. S.A. Shevchik, C. Kenel, C. Leinenbach, K. Wasmer, Acoustic emission for in situ quality monitoring in additive manufacturing using spectral convolutional neural networks, *Additive Manufacturing*, 21 (2018), pp. 598-604, 10.1016/j.addma.2017.11.012
26. D. Kouprianoff, I. Yadroitsava, A. du Plessis, N. Luwes, and I. Yadroitsev, Monitoring of laser powder bed fusion by acoustic emission: Investigation of single tracks and layers, *Front Mech Eng*, 7 (2021), Article no. 678076, 10.3389/fmech.2021.678076
27. S.K. Everton, M. Hirsch, P.I. Stavroulakis, R.K. Leach, A.T. Clare, Review of in-situ process monitoring and in-situ metrology for metal additive manufacturing, *Mater Des*, 95 (2016), pp. 431-445, 10.1016/j.matdes.2016.01.099
28. M. Grasso and B.M. Colosimo, Process defects and in situ monitoring methods in metal powder bed fusion: A review, *Meas Sci Technol*, 28 (2017), Article no. 044005, 10.1088/1361-6501/aa5c4fdes.2017.09.044
29. A.B. Spierings, M. Schneider, R. Eggenberger, Comparison of density measurement techniques for additive manufactured metallic parts, *Rapid Prototyping Journal*, 17 (5) (2011), pp. 380-386, 10.1108/13552541111156504
30. P.I. Stavroulakis, R.K. Leach, Review of post-process optical form metrology for industrial-grade metal additive manufactured parts, *Rev Sci Instrum*, 87 (4) (2016), Article no. 041101, 10.1063/1.4944983
31. A. Townsend, N. Senin, L. Blunt, R.K. Leach, J.S. Taylor, Surface texture metrology for metal additive manufacturing: A review, *Precis Eng*, 46 (2016), pp. 34-47, 10.1016/j.precisioneng.2016.06.001
32. M. Heinel, S. Greiner, K. Wudy, C. Pobel, M. Rasch, F. Huber, T. Papke, M. Merklein, M. Schmidt, C. Körner, D. Drummer and T. Hausotte, Measuring procedures for surface evaluation of additively manufactured powder bed-based polymer and metal parts, *Meas Sci Technol*, 31 (9) 2020, Article no. 095202, 10.1088/1361-6501/ab89e2
33. C.A. Kantzos, R.W. Cunningham, V. Tari, A.D. Rollett, Characterization of metal additive manufacturing surfaces using synchrotron XCT and micromechanical modeling, *Comput Mech*, 61 (2018), pp. 575-580, 10.1007/s00466-017-1531-z
34. C. Li, Z.Y. Liu, X.Y. Fang, Y.B. Guo, Residual stress in metal additive manufacturing, *Procedia CIRP*, 71 (2018), pp. 348-353, 10.1016/j.procir.2018.05.039
35. J.L. Bartlett, B.P. Croom, J. Burdick, D. Henkel, X. Li, Revealing mechanisms of residual stress development in additive manufacturing via digital image correlation, *Additive Manufacturing*, 22 (2018), pp. 1-12, 10.1016/j.addma.2018.04.025

36. T.Q. Phan, M. Strantz, M.R. Hill, T.H. Gnaupel-Herold, J. Heigel, R.D. Christopher, T.D. Adrian, B. Clausen, D.C. Pagan, J.Y.P. Ko, D.W. Brown, L.E. Levine, Elastic residual strain and stress measurements and corresponding part deflections of 3D additive manufacturing builds of IN625 AM-bench artifacts using neutron diffraction, synchrotron X-ray diffraction, and contour method, *Integr Mater Manuf Innov*, 8 (2019), pp.318-334, 10.1007/s40192-019-00149-0
37. A. Thompson, I. Maskery, R.K. Leach, X-ray computed tomography for additive manufacturing: A review, *Meas Sci Technol*, 27 (2016), No. 072001, 10.1088/0957-0233/27/7/072001
38. P. Shah, R. Racasan, P. Bills, Comparison of different additive manufacturing methods using computed tomography, *Case Studies in Nondestructive Testing and Evaluation*, 6 Part B (2016), pp. 69-78, 10.1016/j.csnndt.2016.05.008
39. A. Du Plessis, I. Yadroitsev, I. Yadroitsava, and S.G. Le Roux, X-ray microcomputed tomography in additive manufacturing: A review of the current technology and applications, *3D Printing and Additive Manufacturing*, 5 (3) (2018), pp. 227-247, 10.1089/3dp.2018.0060
40. Filippo Zanini, Elia Sbettega, Simone Carmignato, X-ray computed tomography for metal additive manufacturing: challenges and solutions for accuracy enhancement, *Procedia CIRP*, 75 (2018), pp. 114-118, 10.1016/j.procir.2018.04.050.
41. R. Cunningham, S.P. Narra, T. Ozturk, J. Beuth, and A.D. Rollet, Evaluating the effect of processing parameters on porosity in electron beam melted Ti-6Al-4V via synchrotron x-ray microtomography, *JOM*, 68 (3) (2016), pp. 765-771, 10.1007/s11837-015-1802-0
42. M.S. Xavier, S. Yang, C. Comte, A. Bab-Hadiashar, N. Wilson, I. Cole, Nondestructive quantitative characterization of material phases in metal additive manufacturing using multi-energy synchrotron X-rays microtomography, *Int J Adv Manuf Technol*, 106 (2020), pp. 1601-1615, 10.1007/s00170-019-04597-y
43. M.V. Felice, Z. Fan, Sizing of flaws using ultrasonic bulk wave testing: A review, *Ultrasonics*, 88 (2018), pp. 26-42, 10.1016/j.ultras.2018.03.003
44. A-F. Obaton, M.Q. Le, V. Prezza, D. Marlot, P. Delvart, A. Huskic, S. Senck, E. Mahé, C. Cayron, Investigation of new volumetric non-destructive techniques to characterize additive manufacturing parts, *Weld World*, 62 (2018), pp. 1049-1057, 10.1007/s40194-018-0593-7
45. C. Millon, A. Vanhoye, A-F. Obaton, J-D. Penot, Development of laser ultrasonics inspection for online monitoring of additive manufacturing, *Weld World*, 62 (2018), pp. 653-661, 10.1007/s40194-018-0567-9
46. D. Cerniglia, N. Montinaro, Defect detection in additively manufactured components: Laser ultrasound and laser thermography comparison, *Procedia Struct Integr*, 8 (2018), pp. 154-162, 0.1016/j.prostr.2017.12.016
47. R.J. Smith, M. Hirsch, R. Patel, W. Li, A.T. Clare, S.D. Sharples, Spatially resolved acoustic spectroscopy for selective laser melting, *J Mater Process Technol*, 236 (2016), pp. 93-102, 10.1016/j.jmatprotec.2016.05.005
48. A-F. Obaton, B. Butsch, E. Carcreff, N. Laroche, J. Tarr, A. Donmez, Efficient volumetric nondestructive testing methods for additively manufactured parts, *Weld World*, 64 (2020), pp. 1417-1425, 10.1007/s40194-020-00932-0

## **THERMOPHYSICAL PROPERTIES OF 2-PENTANONE AND 2-HEPTANONE + AROMATIC AMINES AT THREE DIFFERENT TEMPERATURES**

**Aditi Prabhune**

*Department of Chemistry, Birla Institute of Technology and Science (BITS) - Pilani,  
K. K. Birla Goa Campus, Zuarinagar, Goa, India-403726.*

[P20180431@goa.bits-pilani.ac.in](mailto:P20180431@goa.bits-pilani.ac.in)

ORCID: 0000-0003-4899-3825

**Ranjan Dey**

*Department of Chemistry, Birla Institute of Technology and Science (BITS) - Pilani,  
K. K. Birla Goa Campus, Zuarinagar, Goa, India-403726.*

[ranjandey@goa.bits-pilani.ac.in](mailto:ranjandey@goa.bits-pilani.ac.in)

ORCID: 0000-0001-8914-8519

*Cite this paper as Prabhune, Aditi, Dey, Ranjan. Thermophysical Properties of 2-Pentanone and 2-Heptanone + Aromatic amines at Three Different Temperatures. Int. Conf. Advanced. Mater. Sci. & Eng. HiTech. and Device Appl. Oct. 27-29 2022, Ankara, Turkey*

**Abstract.** Proteins are polymers of amino acids linked to each other by a peptide bond. The study of these amino acids, amides, peptides and their derivatives is very interesting for knowledge of complex biological molecules. The carbonyl and amide groups present in the Alkanone and Aromatic amine mixtures are of interest to study their effect on the interactions. Furthermore, alkanone and amine have wide commercial applications and amines play an important role in advanced processes like carbon dioxide capture when used with ionic liquids. In the present investigation, an attempt has been made to evaluate the energy ( $\Delta E_{vap}$ ) and enthalpy of vaporization ( $\Delta H_{vap}$ ), internal pressure ( $P_i$ ), isothermal compressibility and their corresponding excess parameters i. e. excess internal pressure ( $P_i^E$ ) and excess isothermal compressibility ( $\beta_T^E$ ) and interaction parameter ( $\chi$ ) for binary solutions of alkanones (2-Pentanone, 2-Heptanone) and aromatic amines (Aniline, N-Methylaniline, Pyridine) at 293.15, 298.15 and 303.15 K. Coefficient of thermal expansion ( $\alpha$ ) and isothermal compressibility ( $\beta_T$ ) have also been computed and subjected to extensive applications to evaluate the aforementioned parameters. All the properties and their excess counterparts have been used to understand the nature of intermolecular interactions taking place.

**Keywords:** Internal pressure, Excess properties, Isothermal compressibility, Binary

© 2022 Published by ICMATSE

### **Introduction:**

The study of thermophysical properties of liquid mixtures holds utmost importance due to their large applications in the chemical, paints, and pharmaceutical industries. These properties play a vital role in design processing and engineering calculations [1–3]. The nature and extent of interactions can be well understood with thermophysical and their excess properties. Amines hold a significant role in metabolic and physiological functions in biological systems. They also have numerous applications in chemical, pharmaceutical, dye, and polymer industries. Aniline is widely used in the manufacturing of various chemicals and intermediates. It plays a major role in the rubber

industry, dye and pigments, drugs and agriculture products [4]. N-methylaniline is a secondary amine and is used as a solvent and coupling agent in various chemical reactions, and as an intermediate in dye manufacturing and the agrochemical industry [5]. Pyridine is largely used as a solvent for anhydrous mineral salts, in organic synthesis and various analytical techniques [6]. 2-Pentanone is widely used as a solvent in the paint, resin, and oil industries and is also used as a flavouring agent and in the synthesis of the essence [7,8]. 2-Heptanone is used as solvents, cleansing products and adhesives [9,10]. The amide functional group plays a very important role in biologically complex molecules. The understanding of interactions between the

amine and the carboxylic group provides a better insight into the amide functional group which is part of biologically complex molecules. Amides also have In the current investigation, the molecular interactions between 2-Pentanone and 2-Heptanone with amines such as pyridine, N-methylaniline and aniline have been studied between the temperature range of 293.15 K-303.15 K using standard thermodynamic equations and properties to understand their interactive behaviour in a liquid state. The necessary data required for the evaluation of thermophysical properties are taken from the literature [13–18].

### Materials and methods:

The isobaric thermal expansivity ( $\alpha$ ) is the relative change in the volume with the temperature at constant pressure and it is represented below [19]:

$$\alpha = \frac{1}{V} \left( \frac{\partial V}{\partial T} \right)_P \quad (1)$$

Isothermal Compressibility ( $\beta_T$ ) is the relative change in the volume with pressure at constant temperature conditions and it is given as [19]:

$$\beta_T = -\frac{1}{V} \left( \frac{\partial V}{\partial P} \right)_T \quad (2)$$

Internal pressure ( $P_i$ ) is the variation in internal energy due to volume changes under isothermal conditions i. e.  $(dU/dV)_T$ . It occurs due to the presence of attractive forces, dispersion, ion-dipole interactions, dipole-dipole interactions and repulsive forces within the liquid. The cohesion within liquid exhibits high pressure. This pressure is experienced by solute when dissolved in the solvent and a change in internal energy is caused due to interactions taking place between solute-solvent molecules. It is expressed as [20,21]:

$$P_i = \frac{\alpha T}{\beta_T} - P \quad (3)$$

The energy of vapourization ( $\Delta E_{vap}$ ) is the energy utilized in the evaporation of one mole of the liquid by breaking all the associated forces with it. Enthalpy of vapourization ( $\Delta H_{vap}$ ) is a sum of pressure-volume work done and the internal energy of the system. Both thermodynamic properties are expressed below [22];

$$(\Delta E_{vap}) = P_i \cdot V_m \quad (4)$$

$$(\Delta H_{vap}) = (\Delta E_{vap}) + RT \quad (5)$$

where all symbols have their usual meaning.

The cohesive energy density (CED) represents the total cohesion present within a unit volume of the liquid which arises due to specific and non-specific interactions. These specific and non-specific interactions include attractive forces, hydrogen bonding, ion-ion, ion-dipole, dipole-dipole interactions, repulsive forces, dispersion etc. The

many applications in the medicinal industries [11,12].

pressure is experienced by a solute molecule while dissolution takes place and this pressure is varied as solute-solvent interactions changes. It is given by the equation [22,23];

$$CED = \frac{\Delta E_{vap}}{V_m} \quad (6)$$

Free volume ( $V_f$ ) represents the free space between the molecules in the liquid. The interactions between solvent and solute molecules cause either an increase or decrease in the free volume. Free volume is interdependent on internal pressure which shows the cohesion within the liquid mixture. It is evaluated using the equation [23]:

$$V_f = \frac{RT}{(P+P_i)} \cong \frac{RT}{P_i} \quad \text{as } P_i \gg P; \text{ hence } P + P_i \cong P_i \quad (7)$$

where all symbols have their usual meaning.

The interaction parameter ( $\chi$ ) is evaluated using the expression [24]:

$$\chi = \left( \frac{u}{u_{id}} \right)^2 - 1 \quad \text{where } u \text{ is ultrasonic velocity and } u_{id} = \left( \frac{1}{\rho^{id} \cdot \beta_s^{id}} \right)^{1/2} \quad (8)$$

The values of ideal thermodynamic properties in the above equations are calculated using:

$$\rho^{id} = x_1 \rho_1 + x_2 \rho_2 \quad \text{and} \quad \beta_s^{id} = \phi_1 \beta_{s,1} + \phi_2 \beta_{s,2}$$

where  $\phi_i$  is volume fraction,  $x_i$ , mole fraction,  $\beta_{s,i}$ , isentropic compressibility,  $\rho_i$ , the density of the constituent components.

The required data of pure components for the evaluation of thermophysical properties have been taken from the literature [13–18].

### Results and Discussion:

Thermodynamic properties like the energy and enthalpy of vapourization, cohesive energy density, internal pressure, free volume, solubility parameter along with excess isothermal compressibility and interaction parameter have been evaluated and compared for 2-Pentanone and 2-Heptanone with various aromatic amines like Aniline, N-methylaniline, Pyridine at 293.15 K -303.15 K temperature range.

The thermal expansivity ( $\alpha$ ) and isothermal compressibility ( $\beta_T$ ) are two vital thermodynamic properties and they have been evaluated using the requisite data of components from the literature. Both properties show increasing values with the addition of alkanone. It indicates the presence of a higher degree of interactions and the increasing value of compressibility denotes that liquid became

more compressible with an increased concentration of alkanone at 298.15 K. Thermal expansivity ( $\alpha$ ) and isothermal compressibility ( $\beta_T$ ) have also been computed at 298.15 K using the empirical equation given below [25] which incorporates ultrasonic velocity ( $u$ ) and density ( $\rho$ ) of liquid mixtures.

$$\alpha = \frac{75.6 \times 10^{-3}}{T^{1/9} u^{1/2} \rho^{1/3}} \quad \text{and} \quad \beta_T = \frac{17.1 \times 10^{-3}}{T^{4/9} \rho^{4/3} u^2}$$

The resultant values are in good agreement with experimental values of corresponding properties at 298.15 K. This prompted to use of these empirical equations further for evaluation of the same properties at 293.15 K and 303.15 K due to the unavailability of experimental data at these

temperatures. The obtained results show a similar increasing trend of values indicating the extent of interactions within liquid at remaining temperatures.

Isothermal compressibility relates to the volume of liquid components. The excess isothermal compressibility is computed using the following equations. The evaluated  $\beta_T^E$  values are tabulated in Table 1 for alkanone + aromatic amine mixtures at 298.15 K [13].

$$\beta_T^E = \beta_T - \beta_T^{id} \quad \text{and} \quad \beta_T^{id} = \phi_1 \beta_{T,1} + \phi_2 \beta_{T,2}$$

where  $\phi_i$  is volume fraction and  $\beta_{T,i}$  is isothermal compressibility of constituent components.

Table 1: Excess Isothermal Compressibility of Alkanone + Aromatic amine mixtures at 298.15 K.

$x_1$	$\beta_T^E / \text{TPa}^{-1}$	$x_1$	$\beta_T^E / \text{TPa}^{-1}$	$x_1$	$\beta_T^E / \text{TPa}^{-1}$
2-Pentanone + Aniline					
0.0000	0.08	0.3536	-124.88	0.6963	-132.93
0.0446	-18.60	0.4058	-135.44	0.7441	-120.87
0.0948	-39.21	0.4507	-142.26	0.7943	-104.42
0.1497	-60.82	0.5005	-147.16	0.8393	-86.41
0.1939	-77.21	0.5511	-148.74	0.8890	-63.50
0.2513	-96.64	0.6055	-146.13	0.9390	-35.30
0.2993	-110.77	0.6477	-141.67	1.0000	0.15
2-Pentanone + N-methylaniline					
0.0000	0.09	0.3498	-65.85	0.6985	-73.98
0.0507	-11.78	0.4037	-71.84	0.7384	-69.47
0.1000	-22.74	0.4544	-76.00	0.7949	-60.37
0.1442	-31.92	0.5014	-78.65	0.8385	-51.43
0.1980	-42.34	0.5480	-80.06	0.8894	-38.39
0.2491	-51.24	0.6052	-79.69	0.9416	-22.11
0.3057	-60.04	0.6530	-77.52	1.0000	0.15
2-Pentanone + Pyridine					
0.0000	-0.12	0.3550	-44.06	0.6954	-37.11
0.0481	-9.73	0.4007	-45.55	0.7400	-33.23

0.0984	-18.48	0.4506	-46.47	0.7953	-27.72
0.1469	-25.67	0.5026	-46.20	0.8468	-21.72
0.2033	-32.61	0.5546	-45.00	0.8786	-17.69
0.2515	-37.34	0.6048	-42.97	0.9332	-10.37
0.3006	-41.05	0.6455	-40.73	1.0000	0.14
2-Heptanone + Aniline					
0.0000	-0.09	0.3638	-67.23	0.7057	-57.07
0.0619	-15.54	0.4002	-70.19	0.7584	-49.03
0.1115	-27.14	0.4537	-72.38	0.8041	-41.09
0.1601	-37.39	0.5092	-72.68	0.8515	-32.00
0.2133	-47.39	0.5430	-71.77	0.9033	-21.51
0.2575	-54.73	0.5964	-68.72	0.9467	-12.57
0.3064	-61.27	0.6599	-62.81	1.0000	-0.90
2-Heptanone + N-methylaniline					
0.0000	1.19	0.3448	-44.58	0.6904	-40.97
0.0583	-11.39	0.3994	-46.95	0.7506	-36.08
0.1032	-19.09	0.4452	-48.11	0.8023	-30.62
0.1524	-26.40	0.4949	-48.52	0.8499	-24.85
0.2036	-32.72	0.5465	-47.82	0.8989	-18.01
0.2475	-37.33	0.5977	-46.33	0.9494	-10.01
0.2987	-41.53	0.6464	-43.87	1.0000	-2.13
2-Heptanone + Pyridine					
0.0000	0.10	0.3542	-23.09	0.7047	-16.64
0.0553	-7.01	0.3994	-23.48	0.7500	-14.63
0.1034	-11.91	0.4544	-23.40	0.8056	-11.84
0.1543	-15.82	0.5053	-22.78	0.8528	-9.29
0.2032	-18.58	0.5544	-21.82	0.8956	-6.91
0.2521	-20.71	0.6019	-20.53	0.9444	-4.03

0.3042                      -22.23                      0.6671                      -18.25                      1.0000                      -0.90

Table 1 shows that the excess isothermal compressibility ( $\beta_T^E$ ) values are negative for systems under study and the trends are decreasing and then increasing with the gradual addition of alkanone in liquid mixtures. It shows the highest values for Aniline and the least value for Pyridine for a particular alkanone at 298.15 K. The higher value of excess compressibility causes due to higher interactions between unlike molecules which may have risen due to the geometric fitting of constituent components. The excess isothermal compressibility values for 2-Pentanone are higher than 2-Heptanone for a set of aromatic amine at 298.15 K. The overall order of molecular interactions is observed to be Aniline > N-methylaniline > Pyridine at 298.15 K.

The internal pressure ( $P_i$ ) represents the change in internal energy with volume under isothermal conditions. It is produced due to the presence of various attractive and repulsive forces like dispersion, ion and dipole interactions, van der Waal forces, etc. It contributes to the overall cohesion it shows increasing values. . The decrease in the values suggests the decrease in the cohesive forces present within the liquid mixtures.

present within the liquid. The literature reveals that the  $P_i$  values decrease with the addition of the first component i. e. alkanone at all temperatures. The  $P_i$  values for an alkanone with Aniline and N-methylaniline show higher variation relative to Pyridine. Also,  $P_i$  values for 2-Pentanone + Aromatic amines are higher than that of 2-Heptanone + Aromatic amines at 298.15 K. These observed trends reveal that the extent of interactions follows order as Aniline > N-methylaniline > Pyridine for constant alkanone [17,18].

The energy ( $\Delta E_{vap}$ ) and enthalpy of vapourization ( $\Delta H_{vap}$ ) have been evaluated at all temperatures [17,18]. The values of both the properties are observed to be decreasing with the addition of alkanone. The decrease in values of  $\Delta E_{vap}$  and  $\Delta H_{vap}$  for 2-Pentanone + Pyridine system is relatively less than that of 2-Pentanone with Aniline and N-methylaniline. The values of 2-Heptanone with Aniline and N-methylaniline are observed to be decreasing while with Pyridine

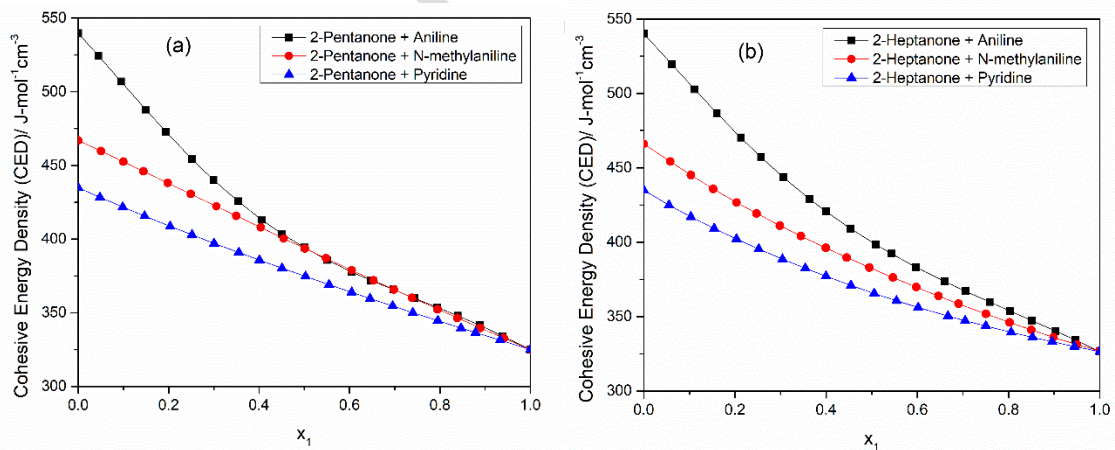


Fig. 1: Cohesive Energy Density of (a) 2-Pentanone and (b) 2-Heptanone with Aromatic amines at 298.15 K.

The cohesive energy density (CED) has been evaluated using equation (6) which incorporates the energy of vapourization and molar volume. The results are represented in fig.1 (a) and (b) at 298.15 K for Alkanone + Aromatic amine mixtures. The CED values for 2-Pentanone + aromatic amines lie between 539.62 J·mol<sup>-1</sup>·cm<sup>-3</sup> to 325.07 J·mol<sup>-1</sup>·cm<sup>-3</sup> and for 2-Heptanone + Aromatic amines from 540.11 J·mol<sup>-1</sup>·cm<sup>-3</sup> to 326.48 J·mol<sup>-1</sup>·cm<sup>-3</sup> at 298.15 K [17,18]. It is seen from Fig.1 that the values of CED

are decreasing gradually as the concentration of alkanone is increasing for all systems under study. The decreasing values of CED suggest a decrease in the cohesion present within the liquid mixture. Similar behaviour of CED values have been observed for the other two temperatures (293.15 K and 303.15 K) for 2-Pentanone and 2-Heptanone with various amines. Even though CED and internal pressure values are almost similar but both properties signify different physical properties of a

liquid. The internal pressure is a measure of non-specific interaction energy within the liquid while the CED measures the total intermolecular interaction energy which includes both specific and non-specific interaction energies within the liquid mixture [20,23]. The solubility parameter is the square root of CED i. e.  $\delta = \sqrt{CED}$  and it indicates

the strength of intermolecular interactions between solute and solvent molecules [26]. It is observed that solubility parameter values are decreasing with increasing concentration of alkanone at all temperatures. For an alkanone, Aniline shows the highest value of solubility parameter which is followed by N-methylaniline and then Pyridine at all temperatures [17,18].

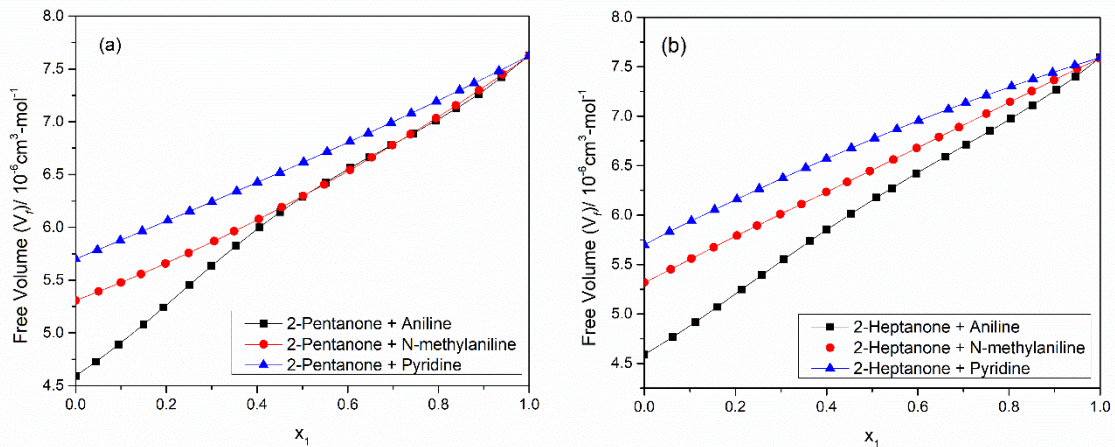


Fig. 2: Free volume ( $V_f$ ) of (a) 2-Pentanone and (b) 2-heptanone with aromatic amine mixtures at 298.15 K.

Free volume ( $V_f$ ) indicates the existing free space within the liquid molecules and it depends on the internal pressure of the liquid. It is affected by the molecular association, interactions present between the constituent molecules of liquid mixture. In Fig.2, free volume is observed to be

increasing for both alkanone + aromatic amine mixtures at all temperatures. Internal pressure and free volume show opposite trends as they are inversely related. Hence, an increasing value of  $V_f$  suggests an increase in free molecular space indicating a decrease in molecular cohesion.

Fig. 3 represents the interaction parameter ( $\chi$ ) at 298.15 K for the system under study. Here the highest interactions are seen between Aniline and Alkanones while the lowest are between Pyridine and Alkanones. Also, the interaction parameter values for 2-Pentanone are higher compared to 2-

Heptanone suggesting more interactions between 2-Pentanone and amines at 298.15 K. An overall observation of Fig.2 suggests that for a particular alkanone, interactions are in order of Aniline > N-methylaniline > Pyridine for all three temperatures.

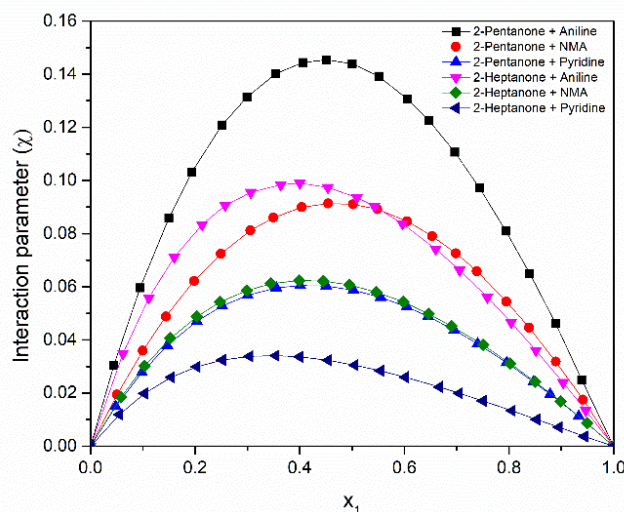


Fig. 3: Interaction parameter of alkanone + Aromatic amines at 298.15 K

A perusal of figures, tables and literature [17,18] points towards order interactions as Aniline > N-

methylaniline > Pyridine for a constant alkanone at various temperatures. The molecular interactions

are readily formed between Aniline and alkanone which is followed by N-methylaniline and then Pyridine. This may be attributed to the geometry of aromatic amines and their ability to form hydrogen bonding. Aniline, N-methylaniline and Pyridine are primary, secondary and tertiary amines respectively. The tendency to form H-bonding decreases from primary to tertiary amine [13]. Furthermore, Pyridine is highly self-associated, a cyclic carbon compound with the Nitrogen atom in the ring. The aromatic character and high stability of Pyridine have been governed by a hybrid resonance structure and the basic nature is due to the presence of lone pair of electrons on the nitrogen atom [27]. This indicates the presence of less interaction between alkanone and Pyridine at various temperatures. An overview of all properties suggests that for a fixed amine, alkanones show the order of interactions as 2-Pentanone > 2-Heptanone at all three temperatures. The chain length in the alkanone compound also seems to affect the molecular interactions as an increase in the alkyl chain length reduces its ability to form hydrogen bonding with amines. The polar nature of the oxygen atom in the carbonyl group is reduced due to the presence of more methyl groups. Also, spatial accommodation, geometric fitting and steric

hindrance affect the interaction taking place within the liquid.

### Conclusion:

In current studies, Energy and Enthalpy of vapourization ( $\Delta E_{vap}$  and  $\Delta H_{vap}$ ), Cohesive energy density (CED), Internal pressure ( $P_i$ ), free volume ( $V_f$ ), Solubility parameter ( $\delta$ ), along with excess isothermal compressibility ( $\beta_T^E$ ) and interaction parameter ( $\chi$ ) have been evaluated. A strong tendency of Aniline to form hydrogen bonds causes maximum interactions. The stability of Pyridine is governed by Nitrogen atom present in the ring thereby restricting its interaction capability; which is exhibited in all the interactions of systems involving Pyridine. An increase in the number of methyl groups in alkanones affects the interactions for a particular amine due to steric hindrance and polar nature of oxygen atom in the carbonyl group. It can thus be concluded that thermodynamic properties along with excess properties can be used as an effective tool to understand the nature and extent of intermolecular interactions in liquid mixtures.

### References:

- [1] S. Malik, H. Gupta, V.K. Sharma, Molecular interactions in ternary liquid mixtures containing alkyl imidazolium tetrafluoroborates and cyclic ketones: Excess molar volumes and excess isentropic compressibilities, *Chemical Data Collections*. 31 (2021) 100603. <https://doi.org/10.1016/J.CDC.2020.100603>.
- [2] E.A. Crespo, L.P. Silva, P.J. Carvalho, J.A.P. Coutinho, The excess volumes of protic ionic liquids and its significance to their thermodynamic modelling, *Fluid Phase Equilib.* 552 (2022) 113277. <https://doi.org/10.1016/j.fluid.2021.113277>.
- [3] M. Popovic, Thermodynamic properties of microorganisms: determination and analysis of enthalpy, entropy, and Gibbs free energy of biomass, cells and colonies of 32 microorganism species, *Heliyon*. 5 (2019) e01950. <https://doi.org/10.1016/J.HELIYON.2019.E01950>.
- [4] R.G. Arokiaraj, R. Raju, S. Ravikumar, K. Sivakumar, P. Bhanuprakash, V. Pandiyan, Excess thermodynamic properties and FTIR studies of binary mixtures of aniline with esters at different temperatures, *Chemical Data Collections*. 37 (2022) 100807. <https://doi.org/10.1016/j.cdc.2021.100807>.
- [5] M. Gowrisankar, P. Venkateswarlu, K. Sivakumar, S. Sivarambabu, Ultrasonic studies on molecular interactions in binary mixtures of N-methyl aniline with methyl isobutylketone, +3-pentanone, and +cycloalkanes at 303.15 K, *J Solution Chem*. 42 (2013) 916–935. <https://doi.org/10.1007/S10953-013-0003-0/FIGURES/10>.
- [6] S. Malik, P.J. Darolia, D. Sharma, V.K. Sharma, Densities, speeds of sound and molar heat capacities of solvent mixtures containing cyclic ethers and piperidine, *Chemical Data Collections*. 31 (2021) 100596. <https://doi.org/10.1016/J.CDC.2020.100596>.
- [7] L. Wei, C.Y. Zeng, H.J. Xie, Y.Q. Wu, Study on the formation of 2-pentanone from ethanol over K-CuZrO<sub>2</sub> catalysts, *Journal of Fuel Chemistry and Technology*. 49 (2021) 80–87. [https://doi.org/10.1016/S1872-5813\(21\)60008-7](https://doi.org/10.1016/S1872-5813(21)60008-7).
- [8] K. Sun, M. Li, Y. Song, J. Tang, R. Liu, Organism and molecular-level responses of superoxide dismutase interaction with 2-pentanone, *Chemosphere*. 286 (2022) 131707. <https://doi.org/10.1016/J.CHEMOSPHERE.2021.131707>.
- [9] National Center for Biotechnology Information. PubChem Compound Summary for CID 8051, 2-Heptanone., (2022). <https://pubchem.ncbi.nlm.nih.gov/compound/2-Heptanone>.
- [10] National Center for Biotechnology Information. PubChem Compound Summary for CID 6569, Methyl ethyl ketone., (2022). <https://pubchem.ncbi.nlm.nih.gov/compound/6569>.
- [11] F. Zhang, L. Li, J. Zhang, H. Gong, Metal- and solvent-free synthesis of amides using substitute formamides as an amino source under mild conditions, *Scientific Reports* 2019 9:1. 9 (2019) 1–6. <https://doi.org/10.1038/s41598-019-39240-z>.

- [12] P.W. Seavill, J.D. Wilden, The preparation and applications of amides using electrosynthesis, *Green Chemistry*. 22 (2020) 7737–7759. <https://doi.org/10.1039/D0GC02976A>.
- [13] I. Alonso, V. Alonso, I. Mozo, I.G. de La Fuente, J.A. González, J.C. Cobos, Thermodynamics of ketone + amine mixtures. I. Volumetric and speed of sound data at (293.15, 298.15, and 303.15) K for 2-propanone + aniline, + N-methylaniline, or + pyridine systems, *J Chem Eng Data*. 55 (2010) 2505–2511. <https://doi.org/10.1021/je900874z>.
- [14] I. Alonso, I. Mozo, I.G. de La Fuente, J.A. González, J.C. Cobos, Thermodynamics of ketone + amine mixtures 7. Volumetric and speed of sound data at (293.15, 298.15 and 303.15) K for 2-pentanone + aniline, + N-methylaniline, or + pyridine systems, *J Mol Liq*. 160 (2011) 180–186. <https://doi.org/10.1016/J.MOLLIQ.2011.03.015>.
- [15] I. Alonso, I. Mozo, I.G. de La Fuente, J.A. González, J.C. Cobos, Thermodynamics of ketone + amine mixtures. part III. Volumetric and speed of sound data at (293.15, 298.15, and 303.15) K for 2-Butanone + Aniline, + N- Methylaniline, or + Pyridine systems, *J Chem Eng Data*. 55 (2010) 5400–5405. <https://doi.org/10.1021/je100472t>.
- [16] I. Alonso, I. Mozo, I.G. de La Fuente, J.A. González, J.C. Cobos, Thermodynamics of ketone + amine mixtures part V. Volumetric and speed of sound data at (293.15, 298.15 and 303.15) K for mixtures of 2-heptanone with aniline, N-methylaniline or pyridine, *J Solution Chem*. 40 (2011) 2057–2071. <https://doi.org/10.1007/s10953-011-9774-3>.
- [17] A. Prabhune, A. Natekar, R. Dey, Thermophysical Properties of Alkanone + Aromatic Amine Mixtures at Varying Temperatures, *Front Chem*. 10 (2022) 868836. <https://doi.org/10.3389/FCHEM.2022.868836>.
- [18] A. Prabhune, R. Dey, Physicochemical Behaviour of 2-Pentanone + Amine Mixtures at Three Temperatures, Communicated.
- [19] H. Shekaari, M.T. Zafarani-Moattar, M. Mokhtarpour, S. Faraji, Volumetric and compressibility properties for aqueous solutions of choline chloride based deep eutectic solvents and Prigogine–Flory–Patterson theory to correlate of excess molar volumes at  $T=(293.15$  to  $308.15)$  K, *J Mol Liq*. 289 (2019) 111077. <https://doi.org/10.1016/J.MOLLIQ.2019.111077>.
- [20] M.R.J. Dack, The importance of solvent internal pressure and cohesion to solution phenomena, *Chem Soc Rev*. 4 (1975) 211–229. <https://doi.org/10.1039/CS9750400211>.
- [21] Y. Marcus, Internal pressure of liquids and solutions, *Chem Rev*. 113 (2013) 6536–6551. <https://doi.org/10.1021/cr3004423>.
- [22] Ramakant, S. Chandra Shrivastava, S. Srivastava, J.D. Pandey, Applications of Flory’s statistical theory to pure ionic liquids – Estimation of useful and important thermodynamic and thermo acoustic properties, *J Mol Liq*. 336 (2021) 116316. <https://doi.org/10.1016/j.molliq.2021.116316>.
- [23] M. Almasi, Cohesive energy density and internal pressure of benzene and 1-alkanol binary mixtures, *J Mol Liq*. 313 (2020) 113459. <https://doi.org/10.1016/J.MOLLIQ.2020.113459>.
- [24] A. Saini, A. Harshvardhan, R. Dey, Thermophysical, excess and transport properties of organic solvents with imidazolium based ionic liquids, 2017.
- [25] V. Sanguri, R. Sethi, Sunil, J.D. Pandey, Thermodynamic and interaction studies of binary liquid mixtures on the basis of Flory’s statistical theory and empirical relations, *J Mol Liq*. 271 (2018) 892–906. <https://doi.org/10.1016/J.MOLLIQ.2018.09.039>.
- [26] P. Weerachanchai, Z. Chen, S.S.J. Leong, M.W. Chang, J.M. Lee, Hildebrand solubility parameters of ionic liquids: Effects of ionic liquid type, temperature and DMA fraction in ionic liquid, *Chemical Engineering Journal*. 213 (2012) 356–362. <https://doi.org/10.1016/J.CEJ.2012.10.012>.
- [27] P.W.G. Smith, A.R. Tatchell, *Heterocyclic Chemistry, I, Aromatic Chemistry*. (1969) 222–247. <https://doi.org/10.1016/B978-0-08-012948-8.50013-9>.

## Strategies for improving mechanical properties and high temperature oxidation resistance in silicides and ceramic composites for ultra-high temperature applications

**Rahul Mitra**

Department of Metallurgical and Materials Engineering, Indian Institute of Technology Kharagpur,  
721302, Kharagpur, India, rahul@metal.iitkgp.ac.in  
ORCID: 0000-0002-2908-1479

*Cite this paper as: Mitra, Rahul. Strategies for improving mechanical properties and high temperature oxidation resistance in silicides and ceramic composites for ultra-high temperature applications. Int. Conf. Advanced Mater. Sci. & Eng. HiTech.and Device Appl. Oct. 27-29 2022,Ankara, Turkey*

**Abstract.** Molybdenum and niobium silicide based multiphase intermetallic alloys, C<sub>f</sub>-SiC and ZrB<sub>2</sub>-SiC based ultra-high temperature ceramic (UHTC) composites have received significant attention for use at temperatures well beyond the limit for the Ni-based superalloys. These materials are being designed with the objective of simultaneously achieving specified high temperature strength along with adequate fracture toughness at the ambient temperature, as well as an impressive resistance to environmental degradation against oxidation and ablation. Whereas the silicide based intermetallic alloys have use in hot-end components of aero-engines, the UHTCs have potential applications in nose-cones and leading edges of hypersonic vehicles. In the multiphase silicide based alloys, the microstructures containing a mixture of ductile and hard phases ensure adequate fracture toughness at room temperature besides high temperature strength, whereas Si-containing phases contribute to formation of protective oxide scales. The C<sub>f</sub>-SiC composites exhibits a typical damage tolerant behavior caused by crack bridging and closure by the partially debonded fibres, whereas the SiC seal-coating develops a self-healing coating of SiO<sub>2</sub> at high temperature. The ZrB<sub>2</sub>-SiC composites are protected from damage by oxidation till 1500oC and ablation at ~2000°C by formation of borosilicate and ZrO<sub>2</sub> scales respectively, whereas creep resistance in air is improved with oxidation resistance.

**Keywords:** Silicides, C<sub>f</sub>-SiC composites, Ultra-high temperature ceramic composites, mechanical properties, oxidation resistance

© 2020 Published by ICMATSE

## Effect of graphene nanoribbon modification by metal oxide cluster on its adsorption for hydrogen sulfide

**Ahmad I. Ayesh**

Physics Program, Department of Mathematics, Statistics and Physics, College of Arts and Sciences,  
Qatar University, P. O. Box 2713, Doha, Qatar  
ORCID: 0000-0002-0442-5941

e-mail address: [ayesh@qu.edu.qa](mailto:ayesh@qu.edu.qa)

**Abstract.** In this work, a first principles investigation is exceeded to examine the adsorption of H<sub>2</sub>S gas on pure and modified armchair-graphene nanoribbon (AGNR) [1]. CuO<sub>x</sub> ( $x = 0, 1, \text{ or } 2$ ) cluster is introduced to AGNR by either substitution of carbon atoms or through the decoration on their surfaces. The influence of modification on H<sub>2</sub>S adsorption is examined using density functional theory (DFT) computations of band structure, adsorption energy ( $E_{Ads}$ ), charge transferred ( $\Delta Q$ ), adsorption length, as well as density of states (DOS) [2, 3]. The results present decent enhancement towards H<sub>2</sub>S adsorption upon modification. In general, the adsorption energy of H<sub>2</sub>S is greater for doped AGNR structures as compared with the decorated structures. The results reveal that AGNR doped with CuO<sub>2</sub> have the maximum adsorption energy, followed by AGNR doped with CuO. AGNR doped with Cu or decorated with Cu, CuO, or CuO<sub>2</sub> have lower adsorption energy for H<sub>2</sub>S. Lastly, the obtained results designate that AGNR doped with CuO<sub>2</sub> or CuO exhibit potential for H<sub>2</sub>S sensor applications.

**Keywords:** H<sub>2</sub>S gas sensor; DFT; graphene nanoribbon; CuO<sub>x</sub>, doping.

© 2022 Published by ICMATSE

### References

- [1] A.I. Ayesh, Effect of CuO<sub>x</sub> additive site to graphene nanoribbon on its adsorption for hydrogen sulfide, Results in Physics, 24 (2021) 104199.
- [2] A.I. Ayesh, H<sub>2</sub>S and SO<sub>2</sub> adsorption on Cu doped MoSe<sub>2</sub>: DFT investigation, Physics Letters A, 422 (2022) 127798.
- [3] A.I. Ayesh, The effect of doping MoSe<sub>2</sub> by clusters of noble metals on its adsorption for NH<sub>3</sub>, Physics Letters A, (2022) 128163.

## Precision Medicine Today

**Sabina Semiz**

*College of Medicine & Health Sciences, Khalifa University, Abu Dhabi, United Arab Emirates*

*sabina.semiz@ku.ac.ae*

*ORCID: 0000-0003-2629-4660*

*Cite this paper as: Sabina Semiz, Precision Medicine Today, Int. Conf. Advanced. Mater. Sci. & Eng. HiTech. and Device Appl. Oct. 27-29 2022, Ankara, Turkey*

**Abstract:** Precision medicine has the potential to revolutionize the healthcare, where a patient's unique genetic profile can be used to detect the disease's onset, prevent its progression, and optimize its treatment. If genetic testing could be used to predict drug response, appropriate measures could be taken to more efficiently treat diseases, such as cancer, cardiovascular disease, and diabetes. Use of an individual's genetic information to select treatment options is already in practice, such as in the case of treatment with clopidogrel and other cardiovascular and anticancer drugs that will be discussed here in more details. Furthermore, there are regulatory, economic, social and ethical challenges, which are highly interlinked and often represent an obstacle in efficient transfer of precision medicine to the clinic. Continued professional education is another essential factor for the successful development and application of precision medicine today. Thus, transdisciplinary collaboration between healthcare institutions, academia, pharmaceutical and biotech companies, regulatory agencies, policy-makers, and other relevant stakeholders is essential for an effective translation of precision medicine in the current clinical practice.

**Keywords:** Precision medicine, pharmacogenomics, effective treatment, side-effects, professional education

## Recent findings on gas sensors based on metal-oxide nanoparticles

**Ahmad I. Ayesh**

*Physics Program, Department of Math., Stat and Physics, College of Arts and Sciences, Qatar  
University, Doha, Qatar  
[ayesh@qu.edu.qa](mailto:ayesh@qu.edu.qa)*

**Abstract:** This presentation reports on our recent findings of gas sensors based on metal-oxides nanoparticles. The focus of the presentation will be on two gases: H<sub>2</sub>S gas that is highly toxic and results from petroleum extraction and refining activities, and H<sub>2</sub> that is promoted as a carbon-free and clean fuel for vehicles. The fabricated sensors are conductometric sensors where their response is indicated by the change in their electrical resistance. The nanoparticles are synthesized by chemical routes, and they include CuO, SnO<sub>2</sub>, and PdO as well as their composites with magnetic nanoparticles such as Fe<sub>2</sub>O<sub>4</sub> and Fe<sub>3</sub>O<sub>4</sub> [1-6]. The metal-oxide nanoparticles exhibit semiconducting characteristics. Adsorption of the gas on nanoparticles modifies the concentration of free electrons thus their electrical conductance. The incorporation of two types of nanoparticles allows the formation of p-n junctions that boost the gas response signal. The morphology and composition of nanoparticles are characterized by different techniques including transmission electron microscopy, scanning electron microscopy, Fourier transform infrared spectroscopy, energy dispersive x-ray analysis, and x-ray diffraction. The charge transport and sensor response are characterized by dc electrical conductance measurements and ac impedance spectroscopy. The fabricated sensors are practical to fabricate on large scale with low cost and have low power requirements, thus, they qualify for practical device utilization in the hazardous gas sensor sector.

- [1] A.I. Ayesh, A.A. Alyafei, R.S. Anjum, R.M. Mohamed, M.B. Abuharb, B. Salah, M. El-Muraikhi, Production of sensitive gas sensors using CuO/SnO<sub>2</sub> nanoparticles, *Applied Physics A*, 125 (2019) 1-8.
- [2] A.I. Ayesh, R.E. Ahmed, M.A. Al-Rashid, R.A. Alarrouqi, B. Saleh, T. Abdulrehman, Y. Haik, L.A. Al-Sulaiti, Selective gas sensors using graphene and CuO nanorods, *Sensors and Actuators A: Physical*, 283 (2018) 107-112.
- [3] A.I. Ayesh, A.F.S. Abu-Hani, S.T. Mahmoud, Y. Haik, Selective H<sub>2</sub>S sensor based on CuO nanoparticles embedded in organic membranes, *Sensors and Actuators B: Chemical*, 231 (2016) 593-600.
- [4] A.I. Ayesh, B. Salah, Production of selective gas sensors based on nanoparticles of PdO/Fe<sub>3</sub>O<sub>4</sub>, *Applied Physics A*, 127 (2021) 1-9.
- [5] B. Salah, A.I. Ayesh, Fabrication of H<sub>2</sub>S sensitive gas sensors formed of SnO<sub>2</sub>-Fe<sub>2</sub>O<sub>3</sub> composite nanoparticles, *Materials Chemistry and Physics*, (2021) 124597.
- [6] A.I. Ayesh, S.T. Mahmoud, S.J. Ahmad, Y. Haik, Novel hydrogen gas sensor based on Pd and SnO<sub>2</sub> nanoclusters, *Materials Letters*, 128 (2014) 354-357.

## Functional Materials for Sustainable Development

*M. Ishaque Khan*

*Illinois Institute of Technology, Department of Chemistry, Chicago, IL 60616, USA; khan@iit.edu*  
ORCID: 0000-0002-8799-5738

**Abstract.** Materials are chemical substances that derive the modern society. Materials enable technology for making beneficial devices. And chemical sciences play a central role in making these materials. There is an ever increasing demand for newer and better functional materials for performing technological operations to address many of the modern technological and environmental challenges facing the society. Sustainable development calls for environmentally benign and inexpensive materials. UN Brundtland Commission's definition of sustainable development is 'meeting the needs of the present without compromising the ability of future generations to meet their own needs'.

Transition metal oxide clusters or polyoxometalates (POMs) and their derivatives offer unprecedented variety of versatile building blocks for making functional materials with properties suitable for application in such areas as catalysis, sensing, membrane technology, pollution control, energy storage, and biomedical usage. POMs, which are molecular systems of sizes up to several nanometer diameter and molecular weight at par with small proteins, can be made relatively inexpensively by employing environmentally benign 'green' synthetic methods. POMs can be functionalized readily and used as structural motifs for making new materials whose properties can be varied systematically and correlated with their constituents at the molecular level. It offers an attractive and sustainable approach to new materials of desirable properties and functions.

**Keywords:** Sustainability, functional materials, polyoxometalates, catalysis, sensors.

## Helical light fields revolve materials science

**Takashige Omatsu**

*Graduate School of Engineering, Chiba University, Japan*

[omatsu@faculty.chiba-u.jp](mailto:omatsu@faculty.chiba-u.jp)

ORCID: 0000-0003-3804-4722

**Katsuhiko Miyamoto**

*Molecular Chirality Research Center, Chiba University, Japan*

\*

*Cite this paper as: O OMATSU, Keynote Talk. Int. Conf. Advanced. Mater. Sci. & Eng. HiTech.and Device Appl.Oct. 27-29 2022,Ankara, Turkey*

**Abstract.** We review advanced materials sciences and technologies with helical light fields, that is optical vortices. The optical vortex possesses an orbital angular momentum (OAM) owing to its helical wavefront, and it enables the twist of materials, such as metals, polymers, and even ultrahigh viscosity liquids to form versatile helical structures on nano/micro-scale. Such optical vortex materials processing should offer new advanced material sciences and technologies.

**Keywords:** Optical Vortex, Helical Light Fields, Laser Materials Processing, Laser Induced Forward Transfer

© 2022 Published by ICMATSE

Helical light fields, that is optical vortices, carry unique physical properties, such as a donut-shaped spatial profile and an orbital angular momentum, arising from their helical wavefronts. They have been widely studied in versatile fields, including optical tweezers/manipulations, optical/quantum communications, and scanning microscopes.

In recent years, optical vortex materials processing has been proposed, and it enables the fabrication of a variety of nano/micro-scale chiral structures owing to the orbital angular momentum transfer. Extending beyond the conventional laser materials processing technologies, the optical vortex materials processing should open the door towards advanced materials science and technology, such as chiral photonics, plasmonics and metamaterials at high efficiencies.

### References

1. T. Omatsu, K. Miyamoto, K. Toyoda, R. Morita, Y. Arita, K. Dholakia, A new twist for materials science: the formation of chiral structures using the angular momentum of light, *Adv Opt Mater*, 7 (2019), 1801672, doi.org/10.1002/adom.201801672
2. T. Omatsu, K. Masuda, K. Miyamoto, K. Toyoda, N. M. Litchinitser, Y. Arita, K. Dholakia, Twisted mass transport enabled by the angular momentum of light, *J Nanophotonics* 14 (2020), 010901, doi.org/10.1117/1.JNP.14.010901
3. T. Omatsu, K. Miyamoto, K. Yuyama, K. Yamane, R. Morita, Laser-Induced Forward-Transfer with Light possessing Orbital Angular Momentum, *J Photochem. Photobiol. C* 52 (2022), 100535, doi.org/10.1016/j.jphotochemrev.2022.100535

Also, an optical vortex laser induced forward transfer technology, that is an entirely exotic non-contact printing technology with an optical vortex, allows the direct print of solids and even ultrahigh viscosity liquids at high spatial and pointing resolutions without any nozzle clogging. This technology will pave the way towards next generation printed photonics/electronics and bioprinting as a non-contact and cost/energy-saving process.

In this paper, we report on the review of the state-of-art of the optical vortex materials processing and optical vortex laser induced forward transfer technologies.

[1-3].

## Metal Additive Manufacturing: Trends, Opportunities and Challenges

Oguzhan Yilmaz

Advanced Manufacturing Technologies Research Group (AMTRG), Faculty of Engineering, Gazi University, Celal Bayar Boulevard, 06570, Maltepe, Ankara, Turkiye  
ORCID: 0000-0002-2641-2324

Cite this paper as: Yilmaz, O., Metal Additive Manufacturing: Trends, Opportunities and Challenges, Int. Conf. Advanced. Mater. Sci. & Eng. HiTech. and Device Appl. Oct. 27-29 2022, Ankara, Turkey

**Abstract.** Additive Manufacturing (AM) draws great attention from both academia and industry due to its flexibilities in productions steps and design. Although, AM has began its journey with rapid prototyping using polymeric materials, in the last decade AM became an alternative manufacturing method for metal parts with higher design complexities and efficient material use. This presentation implies with trends, opportunities and challenges in metal additive manufacturing. Metal AM is highly crucial for many industries since it facilitates design complexities, multiple material use, large and dense part production and so on. The recent studies which have been appear in the literature are mainly about metal AM. Besides, the most mature and costly machines are delivered for metal AM industry. However, there are still many gaps and research topics in metal AM, such as microstructure control, alloying, anisotropy, process monitoring and control etc.

**Keywords:** Additive Manufacturing, Metals, Digital Manufacturing  
© 2022 Published by ICMATSE

Metal Additive Manufacturing (AM) methods can be classified as powder bed and material fed methods. Powder bed methods use powders and laser-electron beam as energy source to melt the powder layer upon layer. Material fed methods use laser, electron beam and welding arc as energy source directed to material which is fed through as powder and wire form. In both cases, metal raw material melts and solidifies in a short time and produces layers [1,2].

Figure 1. Comparison of Metal AM methods

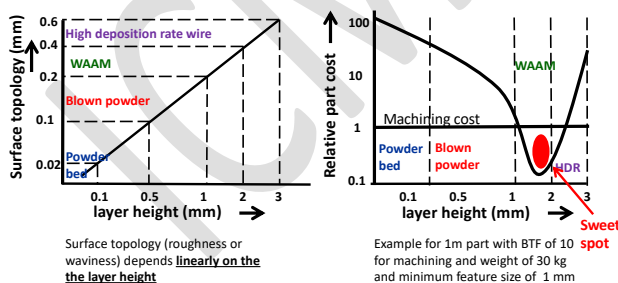


Figure 2. WAAM: Wire Arc Additive Manufacturing

Figure 1 depicts the differences of metal AM methods in terms of surface topology and relative part cost. Wire arc additive manufacturing (WAAM) is clearly having less part cost and higher deposition rates. However, WAAM produces higher surface roughness compared to other metal AM methods. Figure 2 shows a typical WAAM unit [1].

Metal AM methods are capable of producing both large-dense parts and complex lattice structures. It gives great potential for critical sectors, such as aerospace, to produce metal parts with low investment cost, light weight parts with higher design complexities.

### References

1. AS Yildiz, K Davut, B Koc, O Yilmaz, Wire arc additive manufacturing of high-strength low alloy steels: study of process parameters and their influence on the bead geometry and mechanical characteristics, Int. J. Adv. Manuf. Tech., 11, 108 (2020), pp. 3391-3404, doi.org/10.1007/s00170-020-05482-9
2. Mustafa Kas, Oguzhan Yilmaz, Radially graded porous structure design for laser powder bed fusion additive manufacturing of Ti-6Al-4V alloy, J Mater Proc Tech 296 (2021), doi.org/10.1016/j.jmatprotec.2021.117186

## Combination of Photonic Tools and Nanostructured Materials for Biomedical Applications

**D.A.Gorin**

*Skolkovo Institute of Science and Technology, Moscow, Russia*  
ORCID: 0000-0001-8760-615X

*Cite this paper as: Gorin, D. Combination of Photonic Tools and Nanostructured Materials for Biomedical Applications, Int. Conf. Advanced. Mater. Sci. & Eng. HiTech.and Device Appl.Oct. 27-29 2022,Ankara, Turkey*

**Abstract.** The presentation text starts here and continues. The abstract should be prepared via Calibri (Font) and 10 pts, single spaced with 2 cm margins on all sides and align full. The length of Abstract should be between 150 and 200 words. The abstract should be informative by referring study aims, the methodology, the instruments, the major findings and the implications of the study. This talk will review the combination of nanostructured materials and photonic tools that can be used for their visualization, navigation and remote-controlled release of bioactive substances, and last but not least, the application of optical sensors for early diagnosis and evaluation treatment efficiency. There are many biological objects that can be used as markers of various pathological states including cancer. These comprise, but are not limited to, proteins, exosomes, and circulation tumor cells. Exosomes are a very promising marker for early cancer diagnosis and even for evaluating treatment efficiency. An exosome is a small vesical at 100 nm size produced by a cell. Exosomes contain specific proteins and are distributed on the surface of cell membrane. The exosomes can be sent by both normal and pathological cells. It can be used for early diagnosis of neuro, cardio, and onco-diseases [1]. We have already elaborated a different types of photonic based sensors including SERS [2], nanozyme based optical sensor [3,4], hollow-core microstructured fibres [5], and photonic integrated circuits [6]. The combination of a photonic integrated circuits (PIC), a microfluidic devices (MF) and a surface modification can improve not only the sensitivity but also the specificity of exosomes' detection .

Additionally, the application of photonic and acoustic tools can be used for visualization, navigation of multimodal and multifunctional carriers and remote-controlled release of bioactive substances. These particles will combine the ability to deploy drugs in a controllable manner with physical triggering, multimodal detection, and visualization as well as sensing of important biological markers. It was required to apply a new bottom-up method as layer by layer assembly [7] and freezing induced loading [8] and their combination [9,10]. It can be allowed us to vary the volume fraction of components and their chemical composition led to the control of the optical and thermal properties of multifunctional carriers [11]. Raman spectroscopy is perspective method for *in situ* monitoing of freezing induced loading method [12]. Physical targeting of carriers was realized by the gradient of the magnetic field [13], optical tweezers approach [14]. Acoustics has a good perspective for the same purpose. The carrier sensitivity to external influences such as laser irradiation, ultrasound treatment can be changed by variation of volume fraction and chemical composition of inorganic nanoparticles and/or organic dyes in the carrier shells. The same approach is applied for drug delivery carriers imaging by MRI, FT, US and optoacoustics using inorganic nanoparticles and/or organic dyes as contrast or functional agents [4,9,10]. Photonic tools are also promising method for the monitoing of the diatom colonies growth [15]. The diatom algae is responsible for 20 % oxygen at our planet. Thus, the combination of photonic tools with microstructured materials has a good perspective for application in biology and medicine.

This work was partly supported by RSF Project 22-14-00209.

**Keywords:** Fotonic Tools, Nanostructured materials, Biomedical Applicatrion,  
© 2022 Published by ICMATSE

### References

1. A.A. Merdalimova, et al, Applied Sciences-Basel, 2019, 9,6, 1135

2. J. Cvjetinovic, et al, Phys. Chem. Chem. Phys. 2022, **24**, 8901
3. M. Slyusarenko et al, Biosensors, 2022, **12**, 23.
4. J. Mujtaba et al, Advanced Materials, 2021, 2007456, 1
5. T. Ermatov et al, Light: Science & Applications, 2020,**9**, 173
6. A. Kuzin, et al, Optics Letters, 2022, **47**, 9, 2358
7. M.V. Novoselova *et al*, J. Biophotonics, 2019, **12** (4), e201800265
8. S.V. German, et al. Scientific Reports, 2018, **8**, 17763
9. M.D. Mokrousov, et al., Biomedical Optical Express, 2019, **10**, 9, 4775
10. M.V. Novoselova, et al, Colloids and Surfaces B, 2021, 111576
11. R. E. Noskov, et al, Adv. Mater., 2021, 2008484
12. S.V. German, et al, Langmuir, 2021, **37**,4, 1365
13. D.V. Voronin *et al*, ACS Applied Materials & Interfaces, 2017, **9**, 6885
14. I.Y. Stetciura *et al*, Analyst, **140**, 2005, 4981
15. J. Cvjetinovic, et al, Photoacoustics, 2020, 100171

ICMATSE 2022

## Ukrainian track to the green energy transition

***Olena Melnyk***

*ETH Zurich, Department of Environmental Systems Science, 8092, Zurich, Switzerland,  
SNAU, Department of Ecology and Botany, 40000, Sumy, Ukraine  
olena.melnyk@usys.ethz.ch  
ORCID: 0000-0001-5763-0431*

***Iryna Vaskina***

*SSU, Department of Ecology and Environmental Protection Technologies, 40000, Sumy, Ukraine,  
i.vaskina@ecolog.sumdu.edu.ua  
ORCID: 0000-0001-5904-9640*

*Cite this paper as: Melnyk, O, Vaskina, I. Ukrainian track to the green energy transition. Int. Conf. Advanced Mater. Sci. & Eng. HiTech.and Device Appl. Oct. 27-29 2022, Ankara, Turkey*

**Abstract.** The article observes solutions for energy safety in the global climate context of the war in Ukraine. The new opportunities for renewable energy sources (RES) and low-carbon post-war development in Ukraine are being considered.

**Keywords:** RES, green transition, electricity.

© 2022 Published by ICMATSE

In spite of the full scale Russian invasion, Ukraine has a significant potential for investments in energy sector, moreover energy can become one of the drivers of the recovery of the Ukrainian economy. Electricity exports from Ukraine could replace 17% of Russian natural gas consumed by the European Union countries. In the context of the strategy of transition to climate neutral development of the EU, it is important that a significant part of the exported electricity should come from RES, moreover it's more profitable now to build new renewable energy power plants. According to some investigation electricity assumes a share of RES in 83% by 2050 [1]. At the same time, today, in the conditions of electricity produced by nuclear power stations surplus, owners of solar power plants are forced to reduce the volume of electricity production. Such modes of operation significantly reduce the productivity of solar stations and jeopardize their economic profitability. According to the calculations, the amount of system restrictions

of only the SPSs is 573 GW/h, or approximately 30% of the potential generation. Instead of restrictions and underproduction, "green" energy can be exported to the EU countries in the future, reducing the financial burden and payments of the "green" tariff for the system restrictions. The electricity surplus Ukraine currently has, will allow individual countries to quickly abandon Russian gas. To support the energy sector Ukraine has joined the unified continental European electricity system ENTSO-E and completed an emergency synchronisation of its power grids with the ENTSO-E; on June 30th 2022, Ukraine started selling electricity to Romania and in July to Slovakia. Currently, Ukraine has the following interconnections with the ENTSO-E countries with about 1850 MW export and 1500 MW import capacities. The energy sector in Ukraine is on the brink of the major change. These changes are made to provide energy transition and favourable investment climate for RES enlargement in the after war period [2].

### **Acknowledgement**

The article is written in the projects framework 620031-EPP-1-2020-1-UA-EPPJMO-CHAIR: "EU Climate Leadership", with the support of the EU.

### **References**

1. Andersson, Jan and Petryk Igor SolutionsFlexibility to future-proof the Ukrainian power system Solving the Ukrainian Green-Coal paradox. *Wärtsilä Energy* 11, (2018), 24 p.
2. REPowerEU: A plan to rapidly reduce dependence on Russian fossil fuels and fast forward the green transition, 18 May 2022 Brussels.

## Effect of Alignment on Infrared Emissivity for Electrospun Nanofibers

**Osman Safa ÇİFÇİ**

Yozgat Bozok University, Electrical-Electronics Engineering Department 66900, Yozgat

[o.safa.cifci@yobu.edu.tr](mailto:o.safa.cifci@yobu.edu.tr)

ORCID: 0000-0003-4431-0783

*Cite this paper as: Cifci, Osman S. Effect of Alignment on Infrared Emissivity for Electrospun Nanofibers. Int. Conf. Advanced. Mater. Sci. & Eng. HiTech.and Device Appl.Oct. 27-29 2022,Ankara, Turkey*

**Abstract.** Besides radar, the infrared signature is one of the most widely exploited characteristics of military targets, as objects with a temperature above absolute zero emit light mostly in infrared (IR) wavelengths. Hence, the concealment of highly precious components is desirable, and materials with low absorptivity and high reflectivity can satisfy such demands. Metal or semiconductor filler materials and micropatterned structures are proposed for low emissivity systems, but they suffer from significantly increased weight and cost/labor, respectively. Electrospun fiber-based composites (produced through electrospinning, physical, and chemical deposition methods) are more recently introduced IR stealth material alternatives with lightweight and multifunctional properties. Nanofibers' directionality influences optical (e.g., transmittance) and mechanical (e.g., strength and toughness) properties. However, how directionality changes with IR emissivity has yet to be established in the literature. Hence, in this study, we perform electromagnetic simulations to determine the effect of alignment (non-aligned, moderately aligned, and highly aligned) on the IR emissivity of fibrous nanocomposites for different polarization states of light. The findings can be significant to the concealment and detection of strategic assets.

**Keywords:** Electrospun nanofibers, infrared emissivity, polarization, computational electrodynamics, directionality

© 2022 Published by ICMATSE

**Introduction.** Stealth technology deals with concealing assets of interest across multiple frequencies. One such frequency range is the infrared region, precisely 8-14  $\mu\text{m}$  waveband for objects at or close to room temperature, where highly developed detectors are available [1]. Stefan-Boltzmann law dictates that to reduce the thermal energy emission, emissivity or temperature has to decrease [2]. In the literature, multiple ways of reducing emissivity, a value between 0 and 1, have been proposed. Some of these approaches involve using fillers made of metals, metal oxides, or semiconductors. However, these fillers increase the weight, and in the case of metals, oxidation is a major concern [3]. Another approach involves having periodic structures, such as photonic crystals or metasurfaces, which exhibit excellent performance at the expense of significant labor and cost [4]. Nanofibers made of polymers and coated with semiconductors or metals have recently emerged as lightweight, flexible, and high-performance infrared camouflage material. Numerous techniques can produce nanofibers. Electrospinning, fabricating polymer fibers with

sizes ranging from tens of nanometers to a few micrometers via the application of an electric field to the tip of a sharp orifice in front of a syringe with polymer solution inside, is a simple, effective and versatile technique. Electrospun fibers can act as a scaffold for the further deposition of semiconductors or metals. An added advantage of the electrospinning method is the ability to orient the nanofibers by slightly modifying the setup. Alignment induces optical and mechanical anisotropies and has found applications in tissue engineering [5,6]. Optical anisotropy effects have been known for decades in the case of wire-grid polarizers, where transverse electric (TE) and transverse magnetic (TM) light behave differently [7]. Thermal emission is randomly polarized but can be regarded as the average of TE and TM polarized light. Unfortunately, the literature has yet to study how the alignment of nanofibers influences infrared emissivity at different polarization states of light. Thus, the focus of this study is to computationally obtain infrared emissivity values of coated nanofibers at different alignment degrees for TE and TM polarized light

incidence. The findings could shed light on the design of more efficient thermal camouflage fabric in the defense industry.

### Materials and Methods.

**Simulation Design.** Computational studies were conducted to compute emissivity values for TE and TM polarized light. Kirchoff's law states that under thermodynamic equilibrium, absorption equals emissivity. Hence, in the computational studies, reflectance and transmittance values were obtained, and the summation of these values was deducted from 1 to obtain absorbance. The finite difference time domain method was utilized to simulate a periodic nanofiber array [8] under TE and TM polarized light incidence.

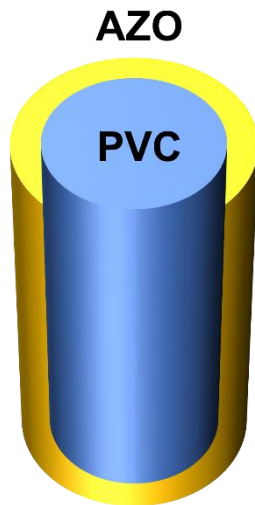


**Figure 1.** The material system under study is a 75 nm radius Polyvinyl chloride (PVC) core with a 30 nm thick Aluminum-doped Zinc Oxide (AZO) coating.

**Materials Selection and Parameters.** The nanofiber under study has a 75 nm radius and made of polyvinyl chloride (PVC), and has 30 nm thick aluminum-doped zinc oxide (AZO) around it, as shown in Fig. 1. These thickness values are similar to the values found in the literature. The fill ratio of the nanofiber array was chosen to be 0.9, which means only 10% of the area of interest is air, whereas the rest of the area is filled with nanofibers. An average of ten simulations, each with a fiber oriented at a specific angle for each polarization state incidence, was used to report emissivity values.

**Alignment and Anisotropy Quantification.** Three nanofiber arrays with different alignment degrees were studied: randomly aligned (each fiber has a random orientation between  $-90^\circ$  and  $90^\circ$ ), moderately aligned (75% of fibers within  $20^\circ$  orientation), and highly aligned (95% of fibers

within  $10^\circ$  orientation) based on the reports from the literature [9]. Orientational anisotropy, denoted as  $r$ , is a parameter borrowed from the fluorescence spectroscopy domain and defined as emission intensities with polarizations in parallel and perpendicular excitation [10]. The formula is given in Eq. [1]. For randomly aligned nanofibers, ten samples were drawn from a uniform distribution between  $-90^\circ$  and  $90^\circ$  to determine the nanofiber orientation angle. Moderately and highly aligned nanofibers' orientation angles were selected by first modeling a Gaussian distribution that matches the given constraint and subsequently drawing ten samples from the distribution using the R programming language.

### Equation 1. Orientational anisotropy

$$r = \frac{\epsilon_{TM} - \epsilon_{TE}}{\epsilon_{TM} + 2 * \epsilon_{TE}}$$

### Results.

The simulation results, including emissivity and orientational anisotropy for three different alignment degrees, were given below in Table 1 for the randomly aligned case, Table 2 for the moderately aligned case, and Table 3 for the highly aligned case.

**Table 1.** Emissivity and orientational anisotropy values for randomly aligned nanofibers

Angle	$\epsilon_{TM}$	$\epsilon_{TE}$	$r$
55.4	0.463	0.469	-0.004
-89.4	0.472	0.472	0
-45.6	0.449	0.469	-0.015
-66.3	0.469	0.470	-0.001
58.1	0.465	0.469	-0.003
72.0	0.470	0.470	0
-29.4	0.441	0.471	-0.022
36.9	0.442	0.471	-0.021
43.4	0.446	0.47	-0.017
59.1	0.466	0.469	-0.002

The average reported values of emissivities when the incident light is TE or TM polarized (left side) and corresponding orientational anisotropy values (right side) were given in Fig. 2. Average emissivity

value for TM polarized light was 0.458, and the value for TE polarized light was 0.47 when there was no alignment. For moderately aligned nanofibers, infrared emission was found to be 0.451 under TM polarization which is not significantly different compared to randomly aligned nanofibers. However, emissivity sharply decreased to 0.217 under TE-polarized light. Moderate alignment decreases the emissivity down to 0.334. Under high alignment conditions, the nanofibers' emission under TE-polarized light was found to be 0.179, while having 0.452 for TM-polarized light. The average emissivity then was found to be 0.315.

**Table 2.** Emissivity and orientational anisotropy values for moderately aligned nanofibers

Angle	$\epsilon_{TM}$	$\epsilon_{TE}$	$r$
-1.6	0.452	0.177	0.341
4.9	0.452	0.180	0.335
3.6	0.452	0.179	0.338
-21.6	0.446	0.383	0.051
7.9	0.452	0.197	0.302
1.0	0.452	0.177	0.341
16.7	0.449	0.273	0.176
-1.3	0.452	0.177	0.341
15.3	0.450	0.252	0.207
3.9	0.452	0.179	0.338

Orientalional anisotropy was obtained as -0.009 for the randomly aligned case, 0.277 for the moderately aligned fibers, and 0.338 for the highly aligned fibers.

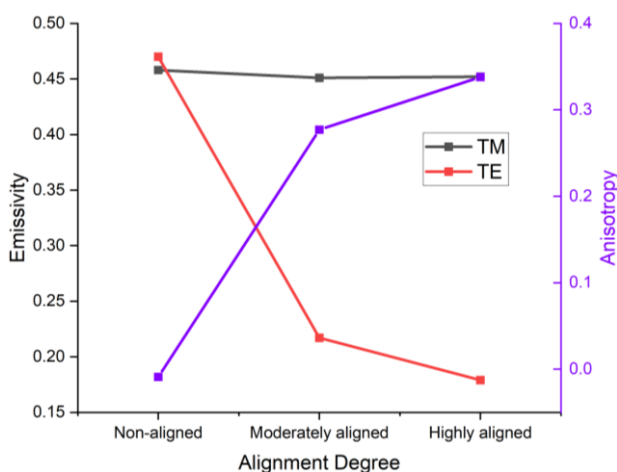


**Figure 2.** Nanofiber alignment degree's effect on IR emissivity and orientational anisotropy.

**Table 3.** Emissivity and orientational anisotropy values for highly aligned nanofibers

Angle	$\epsilon_{TM}$	$\epsilon_{TE}$	$r$
3.5	0.452	0.178	0.339
2.9	0.452	0.179	0.338
3.9	0.452	0.179	0.338
-1.2	0.452	0.177	0.341
6.1	0.452	0.186	0.323
0.7	0.452	0.177	0.341
1.4	0.452	0.177	0.341
-4.0	0.452	0.179	0.338
0.3	0.452	0.177	0.342
1.0	0.452	0.177	0.341

**Discussion.** The key finding in this study was the alignment effects on infrared emission. As can be seen in the results section, the infrared emissivity tends to decrease with a higher alignment degree. The phenomenon at play here is no different from the operation of a wire-grid polarizer which works when the incoming light has a wavelength longer than the nanowires. In a wire grid polarizer, electrons at the surface of the (semi)conductor can be excited with one state of light polarization but not with the opposite state of polarization.

**Conclusion.**

In this work, we studied the emissivity values of polymer nanofibers that can be produced by electrospinning with thin semiconductor coating under TE- and TM-polarized light. Three different fiber alignment degrees were studied using FDTD simulations. A significant (up to 62%) reduction in infrared emissivity was observed for highly aligned nanofibers under TE-polarized light. However, no change was observed in all three different alignments under TM-polarized light. Overall emissivity reduction compared to randomly aligned fibers was 28% for moderately aligned fibers and 32% for highly aligned fibers. Based on the results, nanofibers should be made as aligned as possible to diminish infrared emissivity, which is highly desirable to protect assets of interest such as military tanks or soldiers.

## References

- [1] Fang KY, Fang F. Au-decorated SWNT/PVDF electrospun films with enhanced infrared stealth performance. *Mater Lett* 2018. <https://doi.org/10.1016/j.matlet.2018.07.116>.
- [2] Liu XF, Lai YK, Huang JY, Al-Deyab SS, Zhang KQ. Hierarchical SiO<sub>2</sub>@Bi<sub>2</sub>O<sub>3</sub> core/shell electrospun fibers for infrared stealth camouflage. *J Mater Chem C* 2015. <https://doi.org/10.1039/c4tc01873g>.
- [3] Wang H, Ma Y, Qiu J, Wang J, Zhang H, Li Y, et al. Multifunctional PAN/Al–ZnO/Ag Nanofibers for Infrared Stealth, Self-Cleaning, and Antibacterial Applications. *ACS Appl Nano Mater* 2022. <https://doi.org/10.1021/acsanm.1c03518>.
- [4] Xu C, Wang B, Yan M, Pang Y, Meng Y, Wang W, et al. An optically transparent sandwich structure for radar-infrared bi-stealth. *Infrared Phys Technol* 2020. <https://doi.org/10.1016/j.infrared.2019.103108>.
- [5] Li B, Pan S, Yuan H, Zhang Y. Optical and mechanical anisotropies of aligned electrospun nanofibers reinforced transparent PMMA nanocomposites. *Compos Part A Appl Sci Manuf* 2016. <https://doi.org/10.1016/j.compositesa.2016.07.024>.
- [6] Ayres C, Bowlin GL, Henderson SC, Taylor L, Shultz J, Alexander J, et al. Modulation of anisotropy in electrospun tissue-engineering scaffolds: Analysis of fiber alignment by the fast Fourier transform. *Biomaterials* 2006. <https://doi.org/10.1016/j.biomaterials.2006.06.014>.
- [7] Verrier I, Kämpfe T, Celle F, Cazier A, Guttmann M, Matthis B, et al. Wire-grid polarizer using galvanic growth technology: demonstration of a wide spectral and angular bandwidth component with high extinction ratio. *Opt Eng* 2015. <https://doi.org/10.1117/1.oe.54.4.047105>.
- [8] Taflove A, Hagness SC. *Computational Electrodynamics: The Finite-Difference Time-Domain Method*, Third Edition. 2005.
- [9] Vimal SK, Ahamad N, Katti DS. A simple method for fabrication of electrospun fibers with controlled degree of alignment having potential for nerve regeneration applications. *Mater Sci Eng C* 2016. <https://doi.org/10.1016/j.msec.2016.03.008>.
- [10] Gao Y, Ta VD, Zhao X, Wang Y, Chen R, Mutlugun E, et al. Observation of polarized gain from aligned colloidal nanorods. *Nanoscale* 2015. <https://doi.org/10.1039/c4nr07395a>.

## Scaling up Superconducting Quantum Processors: Materials and Fabrication Challenges

**H. M. Nayfeh, D. T. McClure**

IBM Quantum, T.J. Watson Research Center 1101 Kitchawan Rd. Yorktown Heights, NY 10598, U.S.A.  
[hasan.munir.nayfeh@ibm.com](mailto:hasan.munir.nayfeh@ibm.com)

*Cite this paper as: H. M. Nayfeh, D. T. McClure. Scaling up Superconducting Quantum Processors: Materials and Fabrication Challenges. Int. Conf. Advanced. Mater. Sci. & Eng. HiTech. and Device Appl. Oct. 27-29 2022, Ankara, Turkey*

**Abstract.** Scaling up quantum processors based on superconducting qubits will require continued technology improvements in the areas of qubit quality, gate performance, and scalable microwave signal generation and delivery. In recent years at IBM, we have delivered the first gate-based superconducting processor to break the 100-qubit barrier and have demonstrated coherence time approaching 1 msec on test devices. Despite these positive developments, there are two key challenges that need to be overcome to reduce noise and errors and as a result enable continued scaling- (1) coherence stability versus time due primarily to qubit interactions with two-level systems (TLS) that are attributed to defects in amorphous materials and (2) frequency collisions due to variability in Josephson junction (JJ) fabrication. Overcoming these will require work to identify the microscopic origin of the defects and eliminate them through materials and process improvements that achieve cleaner surfaces/interfaces combined with improved fabrication control.

**Keywords:** quantum processors, superconducting qubits

**Introduction:** Delivering a universal fault-tolerant quantum computer will enable advantages over classical computation in molecular simulation, search algorithms, and algebraic algorithms used for machine learning [1-4]. Superconducting qubits are a leading candidate due to advantages in the three key performance categories of scale, quality, and speed. From the major types of superconducting qubits, quantum processor units (QPU's) based on fixed-frequency transmons are attractive due to simplicity of fabrication and operation as well as low charge noise sensitivity which has helped enable coherence times approaching the 1 msec regime on test devices [5]. The transmon qubit is a quantum non-linear low-loss resonator operating in the microwave frequency range and is comprised of a superconducting Josephson junction (JJ), which behaves like a non-linear inductor, shunted by a large capacitance [6]. Due to this non-linearity the energy separation of the two lowest levels  $|0\rangle$  and  $|1\rangle$  are distinct with typical frequency of  $f = \frac{E}{h} \sim 5$  GHz corresponding to  $T = \frac{E}{k_b} = 240$  mK. Superconducting coplanar waveguide resonators that couple to the qubits enable fast, high-fidelity state measurement especially when mated to a readout chain incorporating quantum-limited amplifiers. Dilution refrigerators are needed in

order to reach low enough temperatures to avoid significant thermal population of the qubits and resonators. The fabrication process lends itself well to scaling up as it leverages the extensive experience from semiconductor devices in terms of surface cleaning, metal deposition (sputtering and evaporation), lithographic patterning (optical and electron beam), liftoff and 3-D chip packaging with advanced backend of the line (BEOL) wiring. This paper will describe the following key-challenges to scaling up further: variability of qubit coherence versus time and overcoming quantum crosstalk errors from frequency collisions that occur because of imprecise setting of qubit resonance frequencies.

**Results and Discussion:** We have demonstrated excellent device metrics on our 27-qubit cloud-accessible systems that employ our Falcon rev. 5.11 QPU design and fabrication process. For instance, *ibm\_auckland's* median single qubit error per gate (EPG) is  $\sim 0.03\%$  (fidelity=99.97%), state measurement error is  $\sim 1\%$  (fidelity=99%), and two-qubit entangling (CNOT) gate EPG is 0.7% (fidelity= 99.30%). This entangling gate used here, known as the cross-resonance gate works by applying a microwave excitation drive signal on the

control qubit at the transition frequency of the target qubit as shown in Fig. 1.

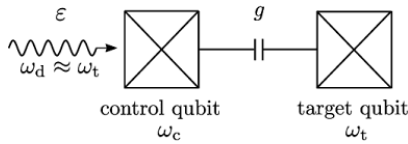


Fig. 1 The cross-resonance gate for generating entanglement works by applying a microwave drive on the control qubit at the target qubit's resonance frequency.

This results in an interaction between the two coupled qubits that is tunable by simply varying the amplitude of the drive signal [7].

Despite these promising results, maintaining stable high performance across an entire quantum processor remains difficult. Qubit coherence fluctuates with time with a distribution that is ~normal with  $-2\sigma$  at  $\sim 0.5X$  median with some data points as low as  $0.10X$  as shown in Fig. 2.

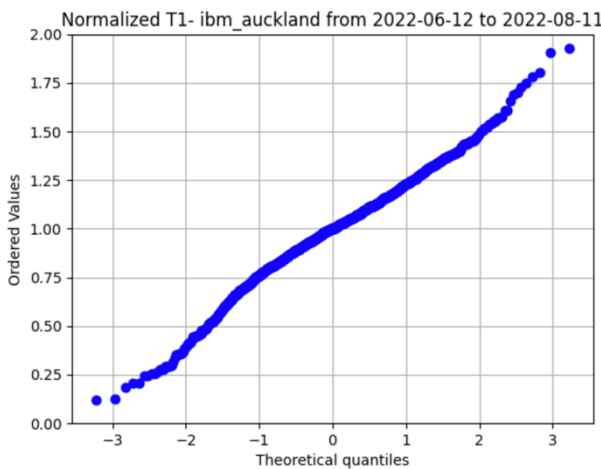


Fig. 2. Statistical distribution of  $T_1$  for a 2-month time window normalized to the median over this time. Each qubit's  $T_1$  is normalized to their own median. The distribution is  $\sim$  normal with  $-2$  sigma at  $\sim 0.5X$  median.

These fluctuations are primarily due to two-level system (TLS) defects in the vicinity of the transmon diffusing to a frequency resonant with the qubit [8]. The resulting interaction causes lower  $T_1$  energy relaxation time and degraded gate performance. Fig. 3 shows a particular example of a CNOT entangling gate showing  $\sim 6$ -fold increase in EPG for two different days labeled as A and B.  $T_1$  of the target qubit shows a drop from  $43 \mu\text{sec}$  on day A to  $9 \mu\text{sec}$  on day B. Spectroscopy was performed by preparing the qubit in the  $|1\rangle$  state and then shifting the qubit frequency using a Stark tone and measuring the probability remaining in this state,  $P(1)$  after a fixed delay time of  $20 \mu\text{sec}$

as a function of qubit frequency [9]. The results shown in Fig. 4a-b demonstrate strong qubit-TLS interaction for day B but not day A

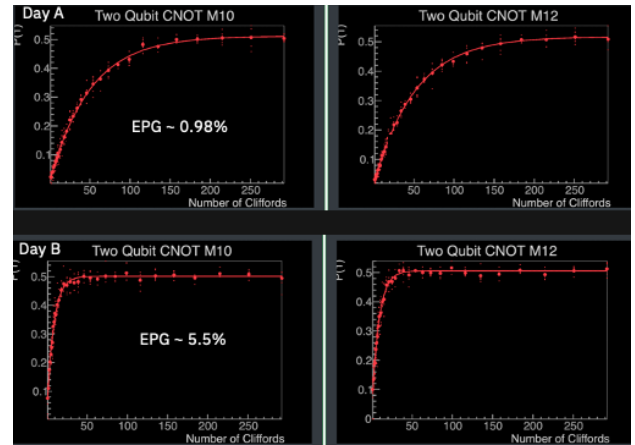


Fig. 3. Randomized benchmarking data from the CNOT entangling gate for two different days A and B showing large error increase for day-B. This is associated with a reduction in  $T_1$  of the target qubit Q12 from  $43 \mu\text{sec}$  to  $9 \mu\text{sec}$

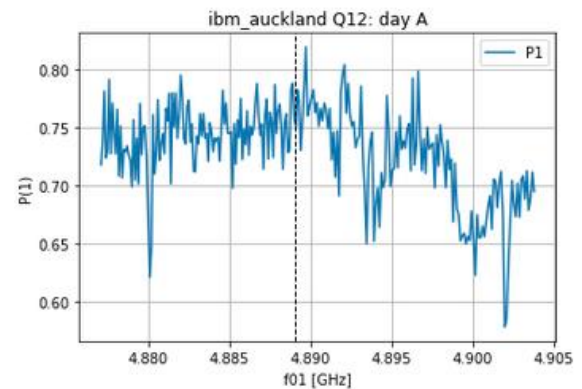


Fig. 4a. TLS spectroscopy for day A. The dashed line is the qubit resonance frequency. As seen here,  $P(1)$  is at  $\sim 0.75$  indicating no TLS-qubit interaction

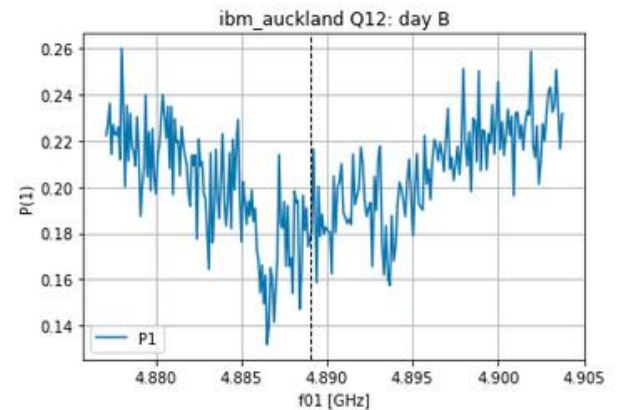


Fig. 4b. TLS spectroscopy for day B. The dashed line is the qubit resonance frequency. As seen here,  $P(1)$  is at  $\sim 0.18$  at the qubit resonance frequency indicating strong TLS-qubit interaction

Furthermore, as shown in Fig. 5, some qubits from *ibm\_auckland* show  $T_2$  decoherence time significantly below the limit of  $2T_1$  set by relaxation. This indicates the presence of elevated dephasing noise for these qubits.

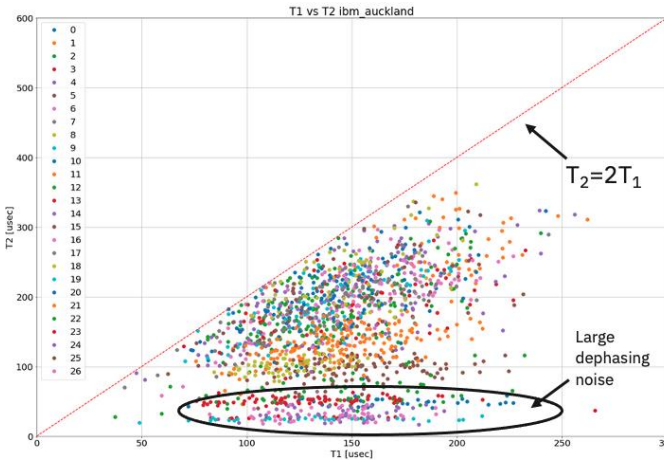


Fig. 5  $T_2$  decoherence time versus  $T_1$  relaxation time for a 2 month time range. The red dotted line corresponds to the relaxation energy limit of  $T_2=2T_1$ . Some qubits show data that is significantly below this line indicating high dephasing noise.

We show that by applying a Carr-Purcell-Meiboom-Gill (CPMG) pulse sequence [10] with up to 101 decoupling  $\pi$  pulses to such low  $T_2$  qubits that this noise is mitigated resulting in significant increase in  $T_2$  with a particular example here from Q13 showing  $\sim 4.2$ -fold  $T_2$  increase as shown in Fig. 6. This pulse sequence essentially applies bandpass filtering to the frequency domain that shapes the noise spectrum seen by the qubit. With a larger number of pulses, the centroid of the filter shifts to higher frequency. This result suggests that the dephasing comes primarily from  $1/f$ -like noise, likely arising from material defects [11].

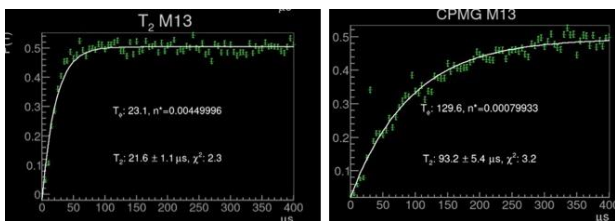


Fig. 6 Carr-Purcell-Meiboom-Gill (CPMG) pulse sequence with 101 decoupling  $\pi$ -pulses applied to the qubit with high dephasing noise, Q13. The data shows a significant improvement in  $T_2$  from  $\sim 22$   $\mu$ sec to 93  $\mu$ sec

The next challenge for scaling up is achieving improved frequency control or less variability. Since our traditional architecture uses fixed-frequency qubits and couplers, there is a static ZZ interaction

between two coupled qubits ( $Q_1$  and  $Q_2$ ). This interaction is the amount the frequency of a qubit shifts due to the state of the neighboring coupled qubit and is dependent on the frequency delta between them (detuning),  $\Delta$ , their non-linearity or anharmonicity:  $\delta_1, \delta_2$  defined as the delta of the frequency transition of the 1<sup>st</sup> to 2<sup>nd</sup> excited state and the ground to 1<sup>st</sup> excited state, and the exchange coupling energy  $J$  as such [12]

$$ZZ = \frac{J^2(\delta_1 + \delta_2)}{(\Delta + \delta_1)(\delta_2 - \Delta)}$$

As shown in Fig. 7, the distribution of this interaction for *ibm\_auckland* for all coupled qubits is min/median/max: 37/53/106 kHz.

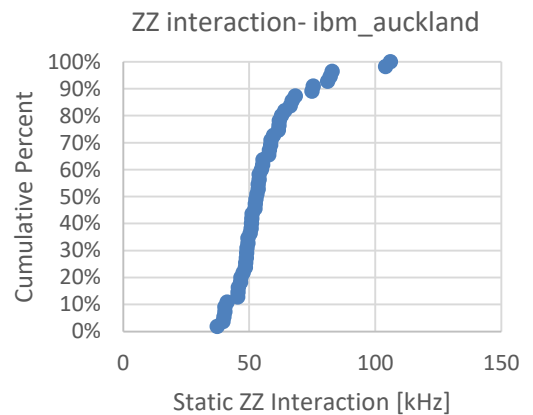


Fig. 7. Static ZZ interaction distribution across all coupled qubits in *ibm\_auckland* shows the following: min/median/max: 37/53/106 kHz. This interaction is an example of quantum crosstalk that can result in elevated gate errors even in the absence of decoherence.

This interaction results in quantum crosstalk and therefore increased errors [13]. Therefore, precise frequency settings are needed to achieve predictable interactions. Another source of error related to frequency variability is hybridization between pairs of coupled qubits that occurs for small  $\Delta$ , resulting in elevated control errors. To study this, we investigated the impact of  $\Delta$  from 95 MHz to 15 MHz on single qubit EPG. As shown in Fig. 8, for  $\Delta < 50$  MHz, EPG increases exponentially with decreasing  $\Delta$ .

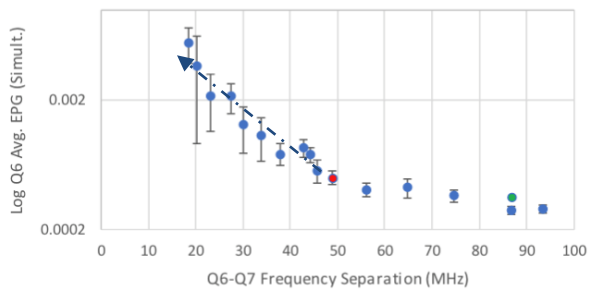


Fig. 8 log(EPG) for qubit Q6 vs the resonance frequency detuning,  $\Delta$  with coupled qubit Q7. The data shows that for  $\Delta < 50$  MHz, EPG increases exponentially with decreasing  $\Delta$ .

To mitigate certain types of errors such as those from the ZZ interaction, we can insert decoupling pulses during the idle time of qubits [14] and increase circuit speed by shortening the gate length of CNOT operations down to the 200-300 nsec regime [15]. Such measures were key to improving circuit performance resulting in demonstrating quantum volume of 64. Less variation in setting qubit resonance frequency can help to prevent quantum crosstalk further by decreasing collisions. Such variation is dominated by statistical variability of the JJ tunneling resistance. Tighter control of the fabrication process in terms of metal and barrier layer deposition and lithographic patterning are needed to reduce such variability.

An alternative approach we have recently pursued to mitigate problems stemming from frequency

allocation is implementation of a novel entangling gate employing a tunable qubit-qubit coupler. In contrast to the cross-resonance gate, where the drive tone can induce unwanted rotations especially if the qubit frequencies align in undesirable ways and the always-on ZZ interaction must be canceled with dynamic decoupling, this coupler enables a gate operation that is less sensitive to qubit frequency alignment and works by quickly turning the ZZ interaction on to achieve a fast CPHASE gate and leaving it off when not driving the gate [16]. The highest gate fidelity demonstrated using these couplers is 99.85% with gate length of 46 nsec. Even with this more robust architecture, however, achieving uniformly high performance across ever larger quantum processors will still benefit from improvements in the ability to target qubit frequencies precisely during fabrication.

**Conclusions:** This is an exciting time to work on scaling up QPU's based on superconducting qubits as it will require technology improvements in a broad range of areas to reduce noise and errors. QPU performance will likely be determined by how well we can overcome material and fabrication challenges. This is necessary in order to execute our roadmap to continue scaling up with the goal of demonstrating practical advantages over classical computers for select algorithms [17].

## References:

- [1] A. Adedoyin, et al. "Quantum Algorithm Implementations for Beginners", arXiv: 1804.03719, March 18 2020.
- [2] A. Eddins, M. Motta, T. P. Gujarati, S. Bravyi, A. Mezzacapo, C. Hadfield, S. Sheldon, "Doubling the Size of Quantum Simulators by Entanglement Forging, PRX Quantum Vol. 3, 010309, 2022.
- [3] B. Parney, J. Garcia, D. Womack, "Exploring Quantum Use Cases for Chemicals and Petroleum" IBM Expert Insights.
- [4] J. R. Glick, T. Guarati, A. Corcoles, Y. Kim, A. Kandala, J. M. Gambetta, K. Temme, "Covariant Quantum Kernels for Data with Group Structure. arXiv: 2105.03406, March 21, 2022.
- [5] J. M. Gambetta: "Breaking Through the millisecond barrier with our single junction transmon", May 20, 2021.
- [6] J. Koch, T. Yu, J. Gambetta, A.A. Houck, D.I. Schuster, J. Major, A. Blais, M.H. Devoret, S.M.Girvin, R.J. Schoelkopf, "Charge insensitive qubit design derived from the Cooper pair box, phys. Rev.A. vol. 76, issue 4, October 12, 2007.
- [7] J. M. Chow, A.D. Corcoles, J.M. Gambetta, C. Rigetti, B.R. Johnson, J. A. Smolin, J.R. Rozen, G.A. Keefe, M.B. Rothwell, M.B. Ketchen, M. Steffen, "Simple All Microwave Entangling Gate for Fixed Frequency Superconducting Qubits", Phys. Rev. Lett. Vol. 107, 080502, Aug. 17, 2011
- [8] M. Carroll, S. Rosenblatt, P. Jurcevic, I. Lauer, A. Kandala, "Dynamics of Superconducting Qubit Relaxation Times". arXiv: 2105.1520, March 31, 2021.
- [9] C. Muller, J. Cole, J. Lisenfeld, "Towards Understanding two-level-systems in amorphous solids—insights from quantum circuits". arXiv: 1705.01108, May 2, 2017.
- [10] Meiboom, S. & Gill, D. Modified spin-echo method for measuring nuclear relaxation times. Rev. Sci. Instrum. 29, 688–691 (1958).
- [11] P. Krantz, M. Kjaergard, F. Yang, T.P. Orlando, S. Gustavson, W.L. Oliver, "A Quantum Engineer's Guide to Superconducting Qubits", Applied Physics Reviews, vol. 6, 021318, 2019.
- [12] E. Magesan, J.M. Gambetta, "Effective Hamiltonian models of the cross-resonance gate, arXiv. 1804.04073, April 11, 2018.
- [13] J. Hertzberg, E.J. Zhang, S. Rosenblatt, E. Magesan, J. Smolin, J.-B. Yau, V. Adiga, M. Sandberg, M. Brink, J. M. Chow, J. Orcutt, "Laser-Annealing Josephson Junctions for Yielding Scaled-up Superconducting Quantum Processors, npj Quantum Information, vol. 129, Aug. 19, 2021.
- [14] P. Jurcevic, et al. "Demonstration of Quantum Volume 64 on a Superconducting Quantum Computing System", Quantum Science and Technology, Vol. 6, No. 2.

- [15] N. Sundaresan, I. Lauer, E. Pritchett, E. Magesan, P. Jurcevic, J. M. Gambetta “Reducing unitary and spectator errors in cross resonance with optimized rotary echoes”, arXiv: 2007.02925, July 6, 2020.
- [16] J. Stehlik, D.M. Zajac, D.L. Underwood, T. Phung, J. Blair, S. Carnevale, D. Klaus, G. A. Keefe, A. Carniol, M. Kumph, M. Steffen, O. Dial, “Tunable Coupling Architecture of Fixed-Frequency Transmon Superconducting Qubits”, Phs. Rev. Letter vol. 127, 080505, August 20, 2021.
- [17] J. Gambetta, “IBM’s Roadmap for Scaling Quantum Technology” <https://research.ibm.com/blog/ibm-quantum-roadmap>

## **First principles study of structural, elastic and mechanical properties of Ti-(44-x)Al-5Zr-xNb alloys**

***Erdem Mermer***

*Gazi University- Department of Metallurgical and Materials Engineering, 06500, Ankara, Turkey,  
mermererdem84@gmail.com  
ORCID: 0000-0002-2540-1586*

***Hanifi Çinici***

*Gazi University-Department of Metallurgical and Materials Engineering, 06500, Ankara, Turkey,  
hcinici@gazi.edu.tr  
ORCID: 0000-0001-6983-0772*

***Gökay Uğur***

*Gazi University-Department of Physics, 06500, Ankara, Turkey,  
gokay@gazi.edu.tr  
ORCID: 0000-0003-4764-4113*

***Rahmi Ünal***

*Gazi University-Department of Mechanical Engineering, 06570, Ankara, Turkey,  
runal@gazi.edu.tr  
ORCID: 0000-0001-5379-5159*

*Cite this paper as: Mermer, E, Cinici, H, Ugur, G, Unal, R. First principles study of structural, elastic and mechanical properties of Ti-(44-x)Al-5Zr-xNb alloys. Int. Conf. Advanced. Mater. Sci. & Eng. HiTech. and Device Appl. Oct. 27-29 2022, Ankara, Turkey*

**Abstract.** In this work, structural, elastic and mechanical properties of Ti-(44-x)Al-5Zr-xNb alloys have been analyzed via first principle calculations based on density functional theory. Crystal structures of the alloys have been developed by Virtual crystal approximation (VCA) method. Niobium (Nb) has been doped up to 5 wt. % in increments of 1 wt. % to Ti-44Al-5Zr alloy. Lattice parameters, elastic constants and mechanical properties have been calculated and discussed. Calculated elastic constants and bulk moduli values imply that mechanical properties have been improved by doping Nb whereas ductility has been diminished when Nb doping concentration is greater than 2 wt. %.

**Keywords:** First-principles, virtual crystal approximation, elastic constants, Nb doped  
© 2022 Published by ICMATSE

Ti-Al alloys draw great attention due to low density, high melting point, high specific strength as well as oxidation resistance [1]–[4]. They are promising materials for aerospace and automobile industries. However, low ductility at room temperature prevents of extensive usage of Ti-Al alloys [5]. To solve this problem alloying studies with transition elements are performed. Theoretical approach is useful methodology to develop alloying and

investigate properties. In this study, first principles calculation is are performed utilizing Cambridge Sequential Total Energy Package (CASTEP) code [6]. TiAl<sub>2</sub> alloy with Zr addition has been chosen as starting point which was performed by our previous works. Ti-44Al-5Zr alloys have been doped with Nb concentration. DFT calculations have been performed to understand mechanical properties.

**Computational methodology.** DFT calculations have been done by Cambridge Sequential Total Energy Package (CASTEP) code [6]. Gradient approximation (GGA) of Perdew-Burke-Ernzerhof (PBE) [7] is utilized for electronic exchange-correlation. Ultrasoft pseudo-potentials is defined for Electron-core interactions [8]. The cut-off energy is determined as 500 eV and Monkhorst-Pack scheme [9] k-points in the Brillouin zone are decided as 6x18x18 after a series convergence tests. Full geometry optimization has been performed using Broyden-Fletcher-Goldfarb-Shanno (BFGS) [10]. Virtual Crystal Approximation (VCA) [11] is employed for simulating through the electron valence states  $3s^2 3p^6 3d^2 4s^2$  for Ti,  $3s^2 3p^1$  for Al and  $4s^2 4p^6 4d^2 5s^2$  for Zr. Geometrical model of Ti-(44-x)Al-5Zr-xNb alloy is shown in Figure 1.

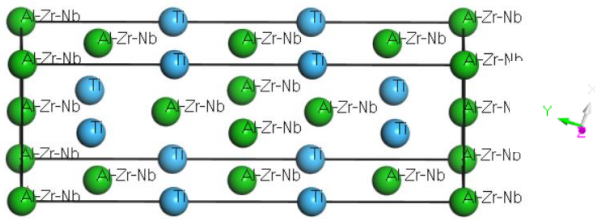


**Figure 1. VCA Model**

**Results and Discussion.** DFT calculations have been started with geometrical optimization. The crystal structure is based on  $TiAl_2$  intermetallic which is orthorhombic with the space group Cmmm (No.#65), Lattice parameters of Ti-(44-x)Al-5Zr-xNb alloys are shown in Table 1 and Figure 2.

**Table 1. Lattice parameters of Ti-(44-x)Al-5Zr-xNb alloys**

Property	Alloy Designation					
	Ti-(44-x)Al-5Zr-xNb					
	x=0	x=1	x=2	x=3	x=4	x=5
$a$ (Å)	12.4239	12.8206	13.2675	13.8548	14.1667	14.2642
$b$ (Å)	3.8141	3.7699	3.7228	3.6664	3.6245	3.6029
$c$ (Å)	3.8379	3.7635	3.6932	3.6167	3.5784	3.5590

The results imply that lattice parameter “a” is increased whereas lattice parameters “b” and “c” are slightly decreasing.

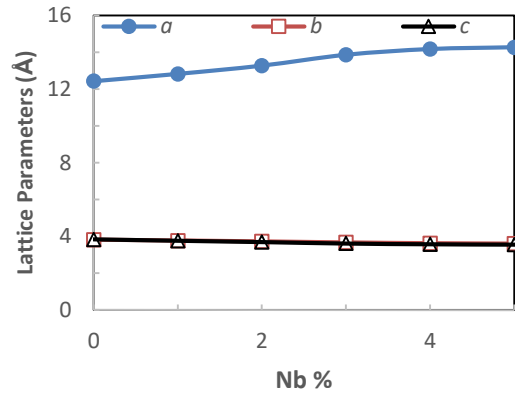


**Figure 2. Obtained lattice parameters of a Ti-(44-x)Al-5Zr-xNb alloys as a function of Nb concentration**

To understand Nb impact on mechanical properties of Ti-(44-x)Al-5Zr-xNb alloy, DFT calculations have been performed. There are nine independent elastic constants which are;  $C_{11}$ ,  $C_{12}$ ,  $C_{13}$ ,  $C_{22}$ ,  $C_{23}$ ,  $C_{33}$ ,  $C_{44}$ ,  $C_{55}$ ,  $C_{66}$ . Born’s theory [12] has been applied to understand mechanical stability of of Ti-(44-x)Al-5Zr-xNb alloy.

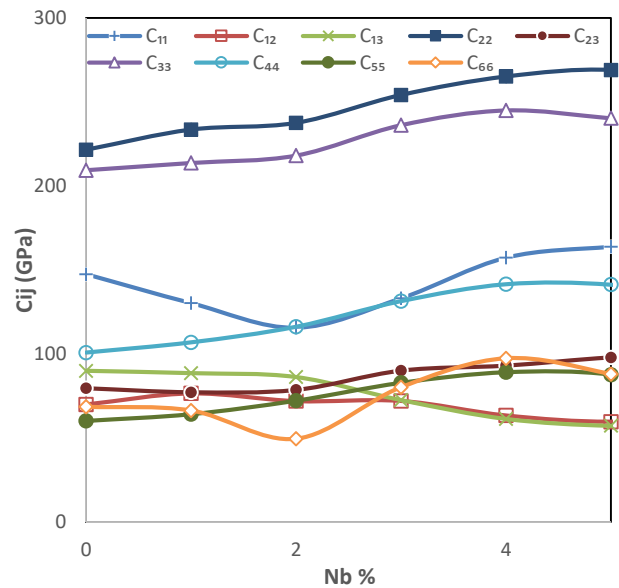


**Figure 3. Elastic constants of Ti-(44-x)Al-5Zr-xNb alloys**

The criteria for orthorhombic structure is;

$$C_{11} + C_{12} + C_{33} + 2C_{12} + 2C_{13} + 2C_{23} > 0, C_{11} + C_{22} > 2C_{12}, C_{11} + C_{33} > 2C_{13}, C_{22} + C_{33} > 2C_{23}, C_{ij} > 0 \quad (i=1-6)$$

One can see from Figure 3 and Table 2, of Ti-(44-x)Al-5Zr-xNb alloy is mechanically stable. As shown in

Figure 3, elastic constants values are strongly dependent on Nb content.

Bulk Modulus (B), Shear Modulus (G) and Young's Modulus (E) have been evaluated by Voight-Reuss-Hill (VRH) proposal [13] based on elastic constants:

$$B = (C_{11} + 2C_{12})/2$$

$$G = (G_R + G_V)/2$$

$$G_R = 5(C_{11} - C_{12})C_{44} / [4 C_{44} + 3 (C_{11} - C_{12})]$$

$$G_V = (C_{11} - C_{12} + 3 C_{44})/ 5$$

$$E = 9 BG / (3B + G)$$

$$\nu = (3B - 2G) / 2 (3B + G)$$

Although bulk modulus remains almost constant, shear and young moduli are increasing when Nb concentration is greater than 2 wt.% as illustrated in Figure 4. The physical approach of this situation is related to the atomic and electronic rearrangements during alloying.

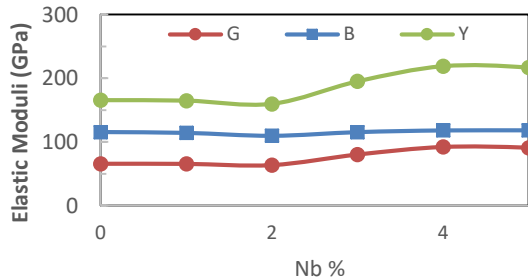


**Figure 4. Elastic moduli of Ti-(44-x)Al-5Zr-xNb alloys**

Elastic anisotropy is an important mechanical feature giving clue about phase transformations and dislocation dynamics [14]. Universal elastic anisotropy index ( $A^U$ ) is calculated by  $A^U = 5(G_V/G_R)/(B_V/B_R)-6$ . The material is supposed as anisotropic when  $A^U$  value is different from zero. Our computed values recommend that Ti-(44-x)Al-5Zr-xNb alloy is anisotropic as illustrated in Figure 5 (a).

It is generally accepted that ductility/brittleness is an essential parameter of an alloy intended to use in industry. Pugh's ratio (B/G) [15] is accepted as a sign for a material ductile-brittle property. If B/G ratio value is higher than 1.75 material is ductile otherwise brittle. It is understood from Figure 5 (b) that when Nb doping is greater than 1 wt.% concentration, ductility is decreased.

**Table 2.** Obtained elastic constants and other mechanical properties of Ti-(44-x)Al-5Zr-xNb alloys

Property	Alloy Designation					
	Ti-(44-x)Al-5Zr-xNb					
	x=0	x=1	x=2	x=3	x=4	x=5
C <sub>11</sub>	147.4	130.2	115.5	133.0	157.2	163.7
C <sub>12</sub>	69.9	76.5	71.9	72.0	63.3	59.6
C <sub>13</sub>	89.9	88.5	86.2	72.5	61.3	57.2
C <sub>22</sub>	221.4	233.4	237.4	254.0	265.0	268.9
C <sub>23</sub>	79.5	77.1	78.5	90.0	93.0	97.9
C <sub>33</sub>	209.3	213.6	218.0	236.1	244.9	240.2
C <sub>44</sub>	100.7	106.8	116.1	131.4	141.5	141.2
C <sub>55</sub>	60.1	64.1	72.1	82.7	89.0	87.6
C <sub>66</sub>	68.5	66.3	49.5	80.1	97.3	87.9
B	115.5	114.2	109.7	115.4	118.0	118.2
G	65.6	65.4	63.5	80.1	91.9	90.7
Y	165.5	164.8	159.7	195.0	218.9	216.7
B/G	1.76	1.75	1.73	1.44	1.28	1.30
$\nu$	0.26	0.26	0.26	0.22	0.19	0.19
A <sup>U</sup>	0.483	0.792	1.222	0.744	0.488	0.431
H <sub>Tian</sub>	9.4	9.4	9.3	13.5	17.0	16.6

Hardness is the ability of a material's resistance to plastic deformation. Hence, hardness values are calculated by Tian approach [16],  $H_v = 0.92k^{1.137} G^{0.708}$  where  $k = G/B$ . Figure 5 (c) shows hardness values of Ti-(44-x)Al-5Zr-xNb alloy. Nb doping higher than 2 wt. % enhances hardness. Higher hardness values correlate with diminishing of ductility.

Another important feature is Poisson's ratio which is defined as the ratio of transverse and longitudinal strains. Poisson's ratio value of metals and alloys are commonly between 0.25- 0.42 [17]. Poisson's ratio ( $\nu$ ) value higher than 0.26 is believed as ductile otherwise brittle. It is comprehended from Figure 5 (d) that  $\nu$  values are smaller than 0.26 when Nb concentration is higher than 2 wt. % which is consistent with ductility results explained above.

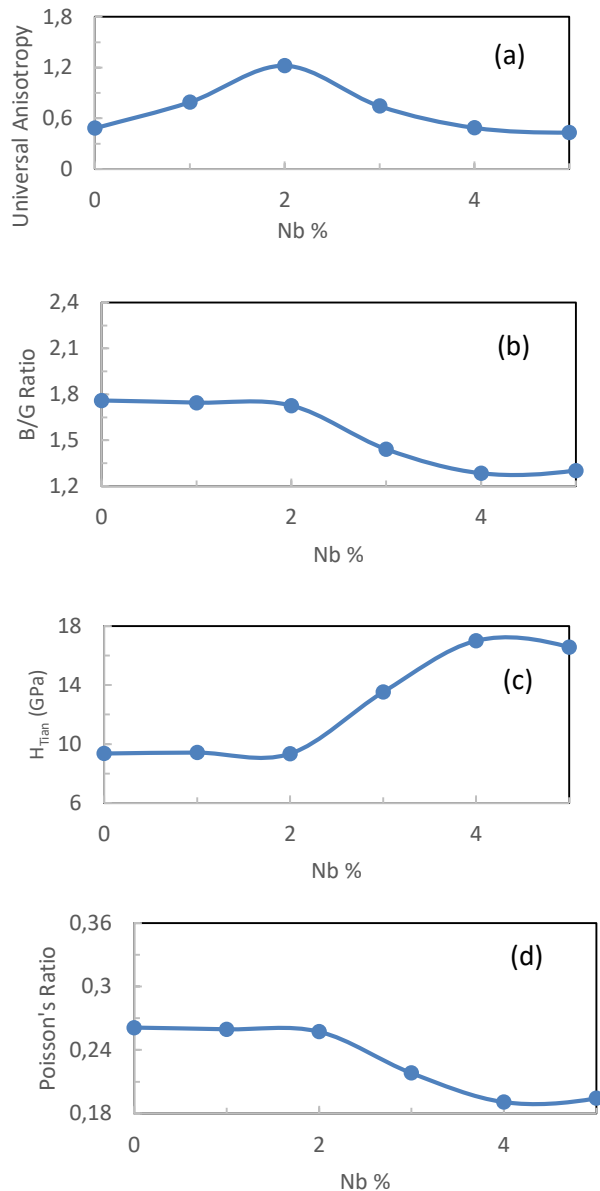


**Figure 5. a) Universal anisotropy b) Pugh (B/G) Ratio c)Hardness d)Poisson's ratio values of Ti-(44-x)Al-5Zr-xNb alloys**

#### References

- [1] Y. Song, Z. X. Guo, and R. Yang, "First principles studies of TiAl-based alloys," *J. Light Met.*, vol. 2, no. 3 SPEC., pp. 115–123, 2002, doi: 10.1016/S1471-5317(02)00038-X.
- [2] S. Banumathy, N. Sruti Neelam, V. Chandravanshi, A. Bhattacharjee, and K. R. Ravi, "The Effect of Nb addition on microstructure, oxidation behavior and strength of some  $\gamma$ -TiAl alloys," *Mater. Today Proc.*, vol. 5, no. 2, pp. 5514–5520, 2018, doi: 10.1016/j.matpr.2017.12.141.
- [3] O. Ouadah, G. Merad, and H. S. Abdelkader, "Effect of co-alloying elements on the structural stability, elastic, ductility and thermodynamic properties of TiAl intermetallic compound," *Solid State Commun.*, vol. 337, no. December 2020, pp. 1–9, 2021, doi: 10.1016/j.ssc.2021.114438.
- [4] K. Kothari, R. Radhakrishnan, and N. M. Wereley, "Advances in gamma titanium aluminides and their manufacturing techniques," *Progress in Aerospace Sciences*. 2012, doi: 10.1016/j.paerosci.2012.04.001.
- [5] M. Kanani, A. Hartmaier, and R. Janisch, "Interface properties in lamellar TiAl microstructures from density

**Conclusions.** Structural, elastic and mechanical properties of **Ti-(44-x)Al-5Zr-xNb** alloys have been investigated by DFT. We can summarize following results;

- 1- **Ti-(44-x)Al-5Zr-xNb** alloys are mechanically stable.
- 2- When Nb doping is higher than 1 wt.%, the alloys show brittle behavior
- 3- We have also computed other mechanical properties of **-(44-x)Al-5Zr-xNb** alloys. It is explored that more than 2 wt. % Nb addition has improved shear and young moduli values.

- functional theory," *Intermetallics*, vol. 54, pp. 154–163, 2014, doi: 10.1016/j.intermet.2014.06.001.
- [6] S. J. Clark *et al.*, "First principles methods using CASTEP," *Zeitschrift fur Krist.*, vol. 220, no. 5–6, pp. 567–570, 2005, doi: 10.1524/zkri.220.5.567.65075.
- [7] J. P. Perdew, K. Burke, and M. Ernzerhof, "Generalized Gradient Approximation Made Simple [Phys. Rev. Lett. 77, 3865 (1996)]," *Phys. Rev. Lett.*, 1997, doi: 10.1103/physrevlett.78.1396.
- [8] D. Vanderbilt, "Soft self-consistent pseudopotentials in a generalized eigenvalue formalism," *Phys. Rev. B*, 1990, doi: 10.1103/PhysRevB.41.7892.
- [9] Hendrik J Monkhorst and J. D. Pack, "Special points for Brillouin-zone integration Monkhorst and Pack," *Physical Review B*, vol. 13, no. 12, pp. 5188–5192, 1976, [Online]. Available: [http://prb.aps.org/pdf/PRB/v13/i12/p5188\\_1](http://prb.aps.org/pdf/PRB/v13/i12/p5188_1).
- [10] T. H. Fischer and J. Almlöf, "General methods for geometry and wave function optimization," *J. Phys. Chem.*, vol. 96, no. 24, pp. 9768–9774, 1992, doi: 10.1021/j100203a036.
- [11] L. Bellaïche and D. Vanderbilt, "Virtual crystal approximation revisited: Application to dielectric and piezoelectric properties of perovskites," *Phys. Rev. B - Condens. Matter Mater. Phys.*, vol. 61, no. 12, pp. 7877–7882, 2000, doi: 10.1103/PhysRevB.61.7877.
- [12] M. Born, K. Huang, and M. Lax, "Dynamical Theory of Crystal Lattices," *Am. J. Phys.*, 1955, doi: 10.1119/1.1934059.
- [13] D. A. Silverston, R. E. Siday, D. A. Silverston, F. C. Frank, and A. N. Stroh, "Related content The Elastic Behaviour of a Crystalline Aggregate," vol. 2, 1952.
- [14] S. I. Ranganathan and M. Ostoja-Starzewski, "Universal elastic anisotropy index," *Phys. Rev. Lett.*, vol. 101, no. 5, pp. 3–6, 2008, doi: 10.1103/PhysRevLett.101.055504.
- [15] S. F. Pugh, "XCII. Relations between the elastic moduli and the plastic properties of polycrystalline pure metals," *London, Edinburgh, Dublin Philos. Mag. J. Sci.*, 1954, doi: 10.1080/14786440808520496.
- [16] Y. Tian, B. Xu, and Z. Zhao, "Microscopic theory of hardness and design of novel superhard crystals," *Int. J. Refract. Met. Hard Mater.*, vol. 33, pp. 93–106, 2012, doi: 10.1016/j.ijrmhm.2012.02.021.
- [17] G. N. Greaves, A. L. Greer, R. S. Lakes, and T. Rouxel, "Poisson's ratio and modern materials," *Nat. Mater.*, vol. 10, no. 11, pp. 823–837, 2011, doi: 10.1038/nmat3134.

## The Use of Chitosan as a Corrosion Inhibitor with Graphene Oxide

**Narmina Guliyeva**

- 1) Azerbaijan State Oil and Industry University, 16/21 Azadlig Avenue, Baku, Azerbaijan  
 2) SRI - Geotechnological Problems of Oil, Gas and Chemistry, AZ1010, Baku, Azerbaijan

E-mail: [narmina.guliyeva@asoiu.edu.az](mailto:narmina.guliyeva@asoiu.edu.az)

ORCID: 0000-0002-9095-2982

**Elshan Aliyev**

SRI - Geotechnological Problems of Oil, Gas and Chemistry, AZ1010, Baku, Azerbaijan

E-mail: [elsan67@mail.ru](mailto:elsan67@mail.ru)

ORCID: 0000-0003-1840-4188

**Aynur Mammadova**

Azerbaijan State Oil and Industry University, 16/21 Azadlig Avenue, Baku, Azerbaijan

E-mail: [aynur.memmedova@asoiu.edu.az](mailto:aynur.memmedova@asoiu.edu.az)

ORCID: 0000-0002-4183-5528

**Elsun Azizov**

SRI - Geotechnological Problems of Oil, Gas and Chemistry, AZ1010, Baku, Azerbaijan

E-mail: [elsun418@gmail.com](mailto:elsun418@gmail.com)

ORCID: 0000-0003-4207-9143

*Narmina Guliyeva, Elshan Aliyev, Aynur Mammadova, Elsun Azizov. The Use of Chitosan as a Corrosion Inhibitor with Graphene Oxide. Int. Conf. Advanced. Mater. Sci.& Eng. HiTech. and Device Appl. Oct. 27-29 2022, Ankara, Turkey*

**Abstract.** Based on the results of the work done, it was determined that the inhibitory composition based on graphene oxide and chitosan provides anti-corrosion protection for St3 grade steel operated in an acidic environment, following the example of sea water. Gravimetric experiments were carried out according to standard procedures. Three parallel experiments were carried out, and for greater accuracy, an average value was taken to calculate the corrosion rate. The best results were obtained with the concentration of the composite mixture Graphene Oxide/Chitosan (GO/Chs) = 0.5/5. This is explained by the presence of large amounts of functional groups containing nitrogen and oxygen atoms.

**Key words:** graphene oxide, chitosan, corrosion, industry.

**Introduction.** Currently, the chemical industry suffers global losses from plant shutdowns and process shutdowns. It can be seen from the literature that when using corrosion inhibitors for low-carbon steel in an environment of nitrogen-containing organic substances, the floor. In the

present study, we studied the effect of chitosan on mild steel corrosion inhibition in a duplicated marine environment. Most of the organic corrosion inhibitors used today, for example, based on alkenylphenols, are not biodegradable, that is, they are not biodegradable and toxic to fauna and flora,

which is one of the main problems of the industry [1]. Since all over the world, all scientists are striving to develop biodegradable corrosion inhibitors, that is, related to "green chemistry", which implies their complete biodegradation without harm to the environment. Also, today they play a major role in the development of new ecological strategies and ecological approach [2].

One of the most common biodegradable materials is chitosan, which is derived from chitin and is natural in nature [2-4].

As you know, one of the newest materials that is taken into account all over the world is graphene oxide, it has a layered multilayer structure, which allows it to be used in all branches of science and is a good synthon for syntheses and structuring.

So today, graphene oxide is used to purify water and to create supramolecular ensembles for their use in the medical sector. The latest sensors based on graphene oxide and graphene are also being developed. It is known about antibacterial properties and functionalization of graphene oxide with organic molecules [6].

We have studied the combined use of graphene oxide with chitosan as a corrosion inhibitor.

Graphene oxide (GO) has a very complex chemical composition, Figure 1. It contains various functional groups such as carboxyl, hydroxyl, ketone, aldehyde in varying amounts depending on the oxidative process. Considering all the positive factors and the layered structure of graphene oxide, we decided to test its effect as a corrosion inhibitor together with chitosan [5].

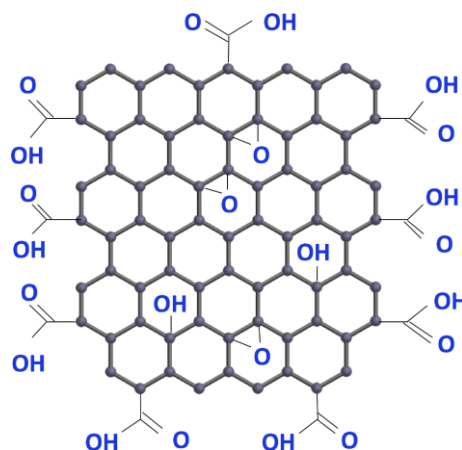


**Figure 1.** The structure of the surface layer of graphene oxide

**Experimental part.** Evaluation of the effectiveness of the inhibitory composition based on chitosan with graphene oxide is carried out on samples of stainless-steel grade St3, the data are presented in table 1.

Experimental gravimetric tests were carried out in a reaction beaker for corrosion testing with stirring at 800 rpm and a temperature of 80 degrees Celsius. Each calculated composition was used three times to avoid errors and the result was taken, which was reliably repeated in all three experiments, the duration of the tests was 24 hours, the temperature was 80°C.

Due to the simplicity and reliability of the gravimetric (weight loss) method, it is used to assess the effectiveness of inhibition of inhibitors.

Gravimetric experiments were carried out according to standard procedure. For a significant accuracy in calculating the corrosion rate, three parallel experiments were carried out and the average value was taken.

Corrosion rate calculation equation:

$$C_R = \frac{W}{At}$$

Where an is the total area of one mild steel sample, t is the immersion period, and w is the average weight loss of mild steel samples collected in three

parallel tests (3 h). The following formulae were used to determine the inhibition efficiency (%) and surface coverage area based on the calculated corrosion rate:

$$\eta\% = \frac{C_R - C_{R(i)}}{C_R} * 100$$

$$\theta = \frac{C_R - C_{R(i)}}{C_R}$$

Where  $C_R$  and  $C_{R(i)}$  are the corrosion rates ( $\text{mg cm}^{-2} \text{ h}^{-1}$ ) of mild steel in the absence and presence of inhibitors, respectively.

**Table 1.** Results of corrosion rate and protective effect

Composition of inhibiting composites by examples	Stainless-steel St3	
	Corrosion rate mm/year	Protective effect, %
GO/Chs = 0.5/5	0,0002	99,7
GO/Chs = 0.5/1	0,0031	97,9
GO/Chs = 0.5/0.5	0,0043	96,7
GO/Chs = 0.4/5	0,0032	97,1
GO/Chs = 0.4/1	0,0041	97,0
GO/Chs = 0.4/0.5	0,0031	96,5
GO/Chs = 0.3/5	0,0055	91,1
GO/Chs = 0.3/1	0,0063	90,2
GO/Chs = 0.3/0.5	0,0073	88,7

## References

1. Neeraj Kumar Gupta, Chandrabhan Verma, M.A. Quraishi, A.K. Mukherjee, Schiff's bases derived from l-lysine and aromatic aldehydes as green corrosion inhibitors for mild steel: Experimental and theoretical studies, Journal of Molecular Liquids, Volume 215, 2016, Pages 47-57, ISSN 0167-7322, <https://doi.org/10.1016/j.molliq.2015.12.027>.
2. N. L. Chen, P. P. Kong, H. X. Feng, Y. Y. Wang and D. Z. Bai, Journal of Bio- and Tribo-Corrosion, 2019, 5, 1.
3. G. Ćirić-Marjanović, Synth. Met., 2013, 177, 1.
4. R. E. Morsi, E. A. Khamis and A. M. Al-Sabagh, J. Taiwan Inst. Chem. Eng., 2016, 60, 573.
5. Y. Yi, G. Liu, Z. Jin and D. Feng, Int. J. Electrochem. Sci., 2013, 8, 3540.
6. Yoo, M. J.; Park, H. B. Effect of Hydrogen Peroxide on Properties of Graphene Oxide in Hummers Method. Carbon 2019, 141, 515–522. <https://doi.org/10.1016/j.carbon.2018.10.009>.

**Result and discussion.** According to the results of the work done, our inhibitory composition based on graphene oxide and chitosan provides anti-corrosion protection St3, which is an integral part and layout in a variety of technological equipment operated in an acidic environment, following the example of sea water. The obtained positive result is explained by the fact that chitosan has in its composition hydroxyl and amino groups rich in electrons, also, in turn, graphene oxide has a functional group containing an oxygen atom and due to which coordination bonds with the metal surface can be formed since there are free electron pairs of electrons.

**Conclusion.** We have determined that the composition based on graphene oxide and chitosan exhibits good anti-corrosion protection of steel grade St3 in an environment close to that of sea water. The experimental part includes three experiments carried out for each concentration and the final result was taken as an average value. A composite mixture of graphene oxide/chitosan (GO/Chs) with a concentration of = 0.5/5 showed the best result.

## The Use of Chitosan with Graphene Oxide to Create a Membrane for Water Purification

**Narmina Guliyeva**

1) Azerbaijan State Oil and Industry University, 16/21 Azadlig Avenue, Baku, Azerbaijan

2) SRI - Geotechnological Problems of Oil, Gas and Chemistry, AZ1010, Baku, Azerbaijan

E-mail: [narmina.guliyeva@asoju.edu.az](mailto:narmina.guliyeva@asoju.edu.az)

ORCID: 0000-0002-9095-2982

*Guliyeva Narmina. The use of chitosan with graphene oxide to create a membrane for water purification. Int. Conf. Advanced. Mater. Sci. & Eng. HiTech. and Device Appl. Oct. 27-29 2022, Ankara, Turkey*

**Abstract.** Composite materials Graphene Oxide/Chitosan (GO/Chs) and single-walled carbon nanotubes/chitosan (SwCNT/Chs) were used in the work carried out to purify the water of the Caspian Sea. In our study, the optimal conditions for obtaining graphene oxide by a new method were established, that is, to obtain a more functionalized graphene oxide, and the presence of nanolayers was confirmed by TEM results. Thus, the mechanism of formation and interaction of the composite mixture is shown. As a result of the experiments, we proved that GO/Chs purifies water better than SwCNT/Chs when using GO/Chs and SwCNT/Chs composite materials, and this is due to the layered structure of graphene oxide.

**Key words:** membrane, graphene oxide, chitosan, single-walled carbon nanotubes, water purification

**Introduction.** Studies of chitosan are carried out all over the world, and up to 70 areas of its practical application are currently known. The most important of them are directions [1] in the food industry, necessary for the production of dietary food, radionuclide purification of the body, simple and multicomponent supplements, in medicine and pharmaceuticals. To date, the protective properties of chitosan films in combination with others are known to protect apples, oranges, strawberries, blackberries, peaches, tomatoes, peppers, and chitosan coating causes some morphological structural changes in pathogens. Chitosan also belongs to the class of fibers that are not digested by the human body [2,3], which allows them to be used for weight loss and form a highly viscous solution in the acidic environment of the stomach. Chitosan is a good reagent for increasing the digestibility and effectiveness of hard-to-digest medicinal substances.

Chitosan is used in dentistry and for problems of the gastrointestinal tract, for cardiovascular diseases. In agriculture, chitosan is an indispensable reagent for obtaining a richer harvest, as it is a biostimulant that increases the yield of vegetables. Today, chitosan plays the main role in the field of biotechnology and ecology [4,5], since it is a biocompatible polymer of a natural nature; the use of chitosan in the sorption of heavy metals and radionuclides gives very good results.

Also, one should not forget about biodegradability, good adhesion and non-toxicity. Chitosan contains electron-rich hydroxyl and amino groups, the electron pairs of which form strong coordination bonds with the metal surface. This allows them to act as corrosion inhibitors [6].

Some researchers have described the effect of chitosan and its derivatives against the corrosion of metals in an acidic environment [6–8].

Today, the state of water resources and the oceans on our planet has deteriorated, and this problem plays a very important role in the future development and growth of life on the planet. Due to the fact that a large amount of oil refining waste and oil, oil products and other materials enter the rivers and seas. We must not forget that today the main sources of environmental pollution are industrial enterprises, without which it is impossible to imagine our world, thermal power plants for mankind and everyday life. With the development of science around the world, the application of nanotechnology has begun to solve the problem of sewage and sea treatment.

Various nano-structured membranes and complex compounds for the purification process, where an economic and environmental improvement of the process is achieved. Graphene oxide has a very complex structure [7,8]. It contains effective groups such as carboxyl, hydroxyl and alkyl groups, but despite all this, there is no formula. Carbon nanotubes each have a different effect on water treatment, and graphene oxide is the most suitable among them. Graphene retains the properties of carbon nanotubes and graphene oxide, it can be seen that graphene oxide has more functional groups.

### **Experimental part.**

**Materials:** Distilled water, filter paper, spatula, 250 ml chemical beaker, ice bath, sodium chloride (NaCl), sodium nitrate (NaNO<sub>3</sub>), potassium permanganate (KmnO<sub>4</sub>), sulfuric acid (H<sub>2</sub>SO<sub>4</sub>), H<sub>2</sub>O<sub>2</sub> - 30%.

**Structure Characteristics:** IR-Fourier spectrometer. FTIR spectra were recorded on a Varian 3600 spectrometer with KBr particles. At room temperature, the spectrum was recorded in the range 4000–400 cm<sup>-1</sup>. TEM analysis of nanoparticles was performed on a Field Emission SEM JEOL JSM-7600F instrument with an increased voltage of 15 kV.

**Synthesis of graphene oxide:** There are various methods for synthesizing GO nanoparticles in the laboratory. The most commonly used methods are the Hammer method, a modified and improved Hammer method by applying The production of membranes using graphene and carbon nanotubes is more expensive and takes a long time to synthesize. Graphene is mainly produced by the reduction of GO in the presence of hydrazine. In this case, we get graphene with a lower C/O ratio and a lower quality of layer functionality compared to GO [9,10]. Graphite is coated with sodium nitrate and sulfuric acid, then oxidized with potassium permanganate and hydrogen peroxide. The goal of oxidation is to create more functional groups that help attract ions.

**Water purification method:** A GO/Chs, SwCNT/Chs membrane is packed onto the Shottan filter and polluted water is filtered through it. The synthesized compositions were carried out on 10 samples to study the ability to purify water in the laboratory.

**Result and discussion.** By analyzing the graphene oxide nanoparticles, we obtained, we can see in the TEM and FTIR images that the obtained GO is suitable for creating a membrane that allows you to create a thin film layer and get results with chitosan for our water treatment.

The resulting GO/Chs composite showed a good result in the process of water purification. Hydroxyl and amine groups are controlled by chitosan electrons, since chitosan has an amino group and hydroxyl groups, and their influence has found its place. As can be seen from the results of TEM and XRD, the graphene oxide synthesized by us is a single layer and has good functionality.

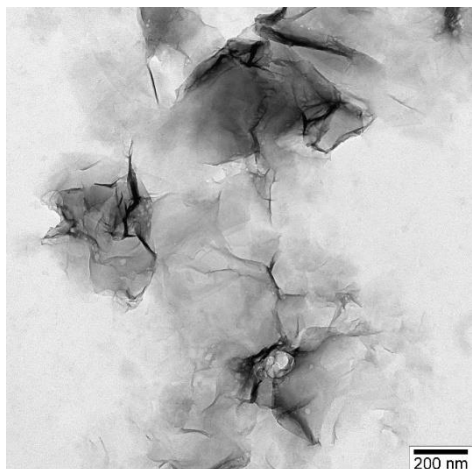


**Figure 1.** TEM image of graphene oxide

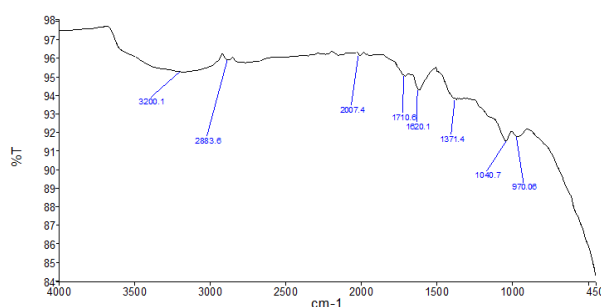


**Figure 2.** FTIR analysis of graphene oxide nanoparticles

**Conclusion.** Based on the results of our work, we can conclude that mechanical mixing of graphene oxide and chitosan to obtain new membranes for water purification is a good composite material. Graphene oxide, synthesized with the largest number of functional groups, gives the best result for water purification. The use of carbon nanotubes does not provide good results because there are no functional groups on the surface of carbon nanotubes.

#### References.

1. T. Peme, L. O. Olasunkanmi, I. Bahadur, A. S. Adekunle, M. M. Kabanda and E. E. Ebenso, *Molecules*, 2015, 20, 16004.
2. P. P. Deshpande, E. G. Jadhav, V. J. Gelling and D. Sazou, *J. Coat. Technol. Res.*, 2014, 11, 473.
3. N. A. Salahuddin, M. M. Ayad and M. E. Essa, *Int. J. Mater. Chem.*, 2015, 5, 54.
4. S. John, A. Joseph, A. J. Jose and B. Narayana, *Prog. Org. Coat.*, 2015, 84, 28.
5. S. A. Umoren and U. M. Eduok, *Carbohydr. Polym.*, 2016, 140, 314.
6. M. N. El-Haddad, *Int. J. Biol. Macromol.*, 2013, 55, 142.
7. Dreyer, D. R.; Park, S.; Bielawski, C. W.; Ruoff, R. S. *The Chemistry of Graphene Oxide*. *Chem. Soc. Rev.* 2010, 39 (1), 228–240. <https://doi.org/10.1039/B917103G>
8. Yoo, M. J.; Park, H. B. Effect of Hydrogen Peroxide on Properties of Graphene Oxide in Hummers Method. *Carbon* 2019, 141, 515–522. <https://doi.org/10.1016/j.carbon.2018.10.009>.
9. Guerrero-Contreras, J.; Caballero-Briones, F. Graphene Oxide Powders with Different Oxidation Degree, Prepared by Synthesis Variations of the Hummers Method. *Materials Chemistry and Physics* 2015, 153, 209–220. <https://doi.org/10.1016/j.matchemphys.2015.01.005>.
10. Yu, H.; Zhang, B.; Bulin, C.; Li, R.; Xing, R. High-Efficient Synthesis of Graphene Oxide Based on Improved Hummers Method. *Scientific Reports* 2016, 6 (1), 36143. <https://doi.org/10.1038/srep36143>.

## Utilization of biomass-based hard carbon in energy storage

Tolga Depci<sup>1</sup>, Yunus Onal<sup>2</sup>, Mustafa Goktan Aydin<sup>3</sup> Emine Yalman<sup>4</sup>

<sup>1,3,4</sup>Iskenderun Technical University- Department of Petroleum and Natural Gas Engineering,  
31200, Hatay, Turkiye

<sup>2</sup>Inonu University, Department of Chemical Engineering, 44280, Malatya, Turkiye

<sup>1</sup>[tolga.depci@iste.edu.tr](mailto:tolga.depci@iste.edu.tr) ORCID: 000-0001-9562-8068

<sup>2</sup>[yunus.onal@inonu.edu.tr](mailto:yunus.onal@inonu.edu.tr) ORCID: 0000-0001-6342-6816

<sup>3</sup>[goktan.aydin@iste.edu.tr](mailto:goktan.aydin@iste.edu.tr) ORCID: 0000-0001-5876-0705

<sup>4</sup>[emine.avci@iste.edu.tr](mailto:emine.avci@iste.edu.tr) ORCID: 0000-0002-1782-3543

*Cite this paper as: Depci, Tolga, Onal, Yunus, Aydin, Mustafa Goktan, Yalman, Emine. Utilization of biomass-based hard carbon in energy storage. Int. Conf. Advanced. Mater. Sci. & Eng. HiTech. and Device Appl. Oct. 27-29 2022, Ankara, Turkey*

**Abstract.** Due to the rapid developments in technology in recent years, the number of materials that are constantly used in daily life and that work with energy is increasing, and this causes the need for energy to rise day by day. The most suitable material to meet this need is batteries and similar systems. Moreover, the most suitable raw material for energy storage as a battery is biomass-based carbonized material (carbonized biomass, activated carbon, carbon black, graphene, hard carbon, etc.). Biomass, which is the only raw material of such materials, is one of the most abundant renewable energy sources in various wastes (agricultural, forest, urban) and organic material such as plants and trees sources. It is mainly composed of lignin, cellulose and hemicellulose, with minor amounts of protein, ash and pectin, and also has a carbon content that can 60% (in dry form). Thanks to these properties, biomass is one of the most popular raw materials for carbon production. Recently, a great attention has been paid to studies of carbonaceous materials derived from biomass, which can be an to graphite, and it is a field that has been studied extensively in the current literature to be used for energy storage in supercapacitors, sodium-ion, lithium-ion and potassium-ion batteries. In general, carbonaceous materials are produced from biomass by applying different methods such as carbonization, activation and surface modification. In this study, obtaining hard carbon (HC) from biomass, which is a very current topic in recent years, has been studied to be used in the field of energy storage. As a result, biomass-based hard carbon is considered a promising alternative in energy storage systems due to its low cost and environmentally friendly properties. It also provides a great advantage in terms of large-scale production and commercialization.

**Keywords:** Energy storage, hard carbon, biomass.

© 2022 Published by ICMATSE

### 1. Introduction

Population growth and rapid developments in technology have increased the need for energy. In order to meet this increasing energy need, countries have increased their consumption of fossil fuels including oil, natural gas and coal day by day with the effect of worldwide economic expansion [1, 2]. It is estimated by researchers that the energy consumed worldwide will nearly double in 2050 [3].

Providing a large part of the energy supply from fossil fuels has brought along many problems. The

decrease in fossil fuel resources and the damage caused by the fossil fuels used are the most important of these problems. In order to prevent these problems, researchers have focused their studies on new, clean and environmentally friendly energy sources that can meet the energy supply. Energy production from renewable sources, conversion and storage of the produced energy have become very valuable [4-7].

Researchers have focused on green, high efficiency and renewable energy studies as well as energy storage technologies. Among these energy storage

systems, electrochemical energy storage systems such as lithium ion batteries (LIBs), sodium ion batteries (SIBs), potassium ion batteries (KIBs), capacitors, supercapacitors have become popular and interesting study subjects with high potential [8, 9].

Today, lithium-ion batteries, which occupy an important place among energy storage systems, are widely used due to their high energy density, long cycle life and high electrochemical performance [10]. However, reasons such as the decrease in lithium resources in the world and the increase in costs have increased the efforts to develop alternative energy storage systems to lithium-ion batteries [11]. Sodium, which has almost similar physical and chemical properties with lithium, is used in studies. The high sodium reserves, the absence of supply problems and the low cost have made sodium a promising candidate as an alternative to lithium in energy storage systems [12, 13].

From the literature studies, it is seen that various anode materials are used and their performances are compared for the development and better performance of sodium ion batteries. When the studies are examined, it is seen that carbon-based materials [14-16], ti-based oxides [17], alloys [18] and some organic compounds [19] have been used as anode materials for sodium ion batteries. The fact that sodium ion batteries produced by using these anode materials cause problems such as low energy efficiency and structure instability has accelerated the search for anode materials.

Researchers have revealed that hard carbon (HC), which has an amorphous structure unlike graphite, has a high potential to be used as anode material in sodium ion batteries. In this context, instead of expensive inorganic materials for the synthesis of hard carbon, the use of biomass-based materials with abundant resources has increased.

Many different natural biomass sources have been used to obtain the hard carbons used. Corn stalks [20], sorghum stalks [21], pinecone [22],

mangosteen [23], argan shell [24], rice husk [25], dandelion [26], corn straw piths [27], ramie fiber [28], cotton [29], kelp [30], and coconut endocarp [31] were carbonized at different temperatures. Hard carbons with different morphological structures were obtained by the carbonization process. It has been revealed by researchers that the specific capacity of hard carbons is directly related to the temperature at which they are exposed to carbonization [32].

Potassium ion batteries, developed as an alternative to lithium-ion batteries, are one of the energy storage systems that researchers concentrate on [33]. Many anode materials are used in potassium ion batteries, just as in sodium ion batteries [34,35]. Recently, the use of hard carbons synthesized from different biomass sources at different temperatures as anode material in potassium ion batteries has increased. It has been observed that the amorphous structures of the hard carbons used increase the potassium ion storage capacity [36].

Hard carbon synthesized from biomass sources has also been used in other energy storage systems. In studies in the field of supercapacitors, it has been seen that biomass-derived hard carbon is used quite a lot. In the studies, easily synthesized, high performance and low cost biomass sources are used. Corn cob, banana stems are among the biomass sources used as anode material [37].

## 2. Methodology

In this study, a literature review was conducted using databases such as Web of Science and Scopus. Numerous studies over the last decade on the use of biomass-based hard carbon in energy storage systems have been collected and then summarized and analyzed. It is aimed to increase research studies on the subject by analyzing and researching current studies. All literature used in the study was given in the references section.

## 3. Applications of biomass-derived hard carbon in energy storage systems

### 3.1. Applications of biomass-derived hard carbon in lithium-ion batteries

It has been proven by researchers that hard carbon electrochemically provides promising performance in alkali metal ion batteries [38]. The specific

capacity of HC in LIBs can reach  $\approx 1000 \text{ mAh g}^{-1}$ . This capacity value is about 3 times higher than graphite. Also, speed performances of HC are better than graphite due to the amorphous nature of the structure [39]. In Table 1, the capacity values

**Table 1.** Applications of hard carbon in Lithium-ion battery [40]

Material	Precursor	Synthesis	Performance [ $\text{mAh g}^{-1}$ ] [rate, cycles]
HC1	Biomass (cotton)	Pyrolysis $800^\circ\text{C}$	248 [300 $\text{mAh g}^{-1}$ , 200]
HC2	Biomass (eucalytus trees)	Pyrolysis $1000^\circ\text{C}$	N/A
P- doped HC	Biomass (leaves)	Pyrolysis $500^\circ\text{C}$	190 [500 $\text{mAh g}^{-1}$ , 1000]
N-doped HC	Biomass (nanoshells)	Pyrolysis $850^\circ\text{C}$	723 [100 $\text{mAh g}^{-1}$ , 200]

HC: Hard Carbon

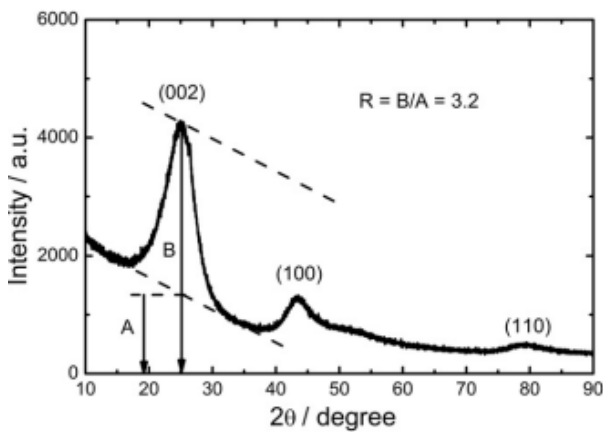


**Figure 1.** Hard karbon XRD pattern for lithium ion battery [41]

### 3.2. Applications of biomass based hard carbon in Na-ion batteries

In sodium ion batteries, which is another class of alkali metal ion batteries, biomass-sourced hard carbon is widely used as the anode material. In Table 2, the capacity values achieved by applying HCs produced from biomass to sodium ion batteries at different pyrolysis temperatures and in different forms were given. Fig. 2 shows the XRD of hard carbon obtained from Phenolic Resin at different temperatures, based on the study performed by Kamiyama et.al.(2020).

**Table 2.** Applications of hard carbon in sodium-ion battery of [40]

Material	Precursor	Synthesis	Performance [ $\text{mAh g}^{-1}$ ] [rate, cycles]
HC1	Biomass (shaddock peel)	Pyrolysis $1200^\circ\text{C}$	352 [50 $\text{mAh g}^{-1}$ , 200]
HC2	Biomass	Pyrolysis $1300^\circ\text{C}$	287 [200 $\text{mAh g}^{-1}$ , 1000]

HC3	Biomass	Pyrolysis 1400 °C	333 [33 mAh g <sup>-1</sup> , 100]
HC4	Biomass	Pyrolysis 1600 °C	290 [30 mAh g <sup>-1</sup> , 100]

### 3.3. Applications of biomass based hard carbon in K- ion batteries

Studies on potassium ion batteries, which are another class of alkali metal batteries considered as an alternative to lithium-ion batteries, have begun to increase today. Many anode materials have been used in studies to improve the performance of potassium ion batteries. Hard carbon obtained by

using biomass sources such as cotton [43], loofah [44], chitin [45], bamboo [46] has been applied in the field of potassium ion batteries as the anode material. In Table 3, two hard carbon results applied as biomass sourced anode material for potassium ion batteries were given and XRD pattern of hard carbon produced from biomass in potassium-ion battery can be seen in Fig.3.

**Table 3. Applications of hard carbon in potassium-ion battery [40, 42]**

Material	Precursor	Synthesis	Performance [mAh g <sup>-1</sup> ] [rate, cycles]
HC1	Biomass (phenolic resin)	Pyrolysis 1500 °C	336 [50 mAh g <sup>-1</sup> , 100]
HC2	Biomass	Pyrolysis 1200 °C	221 [100 mAh g <sup>-1</sup> , 150]

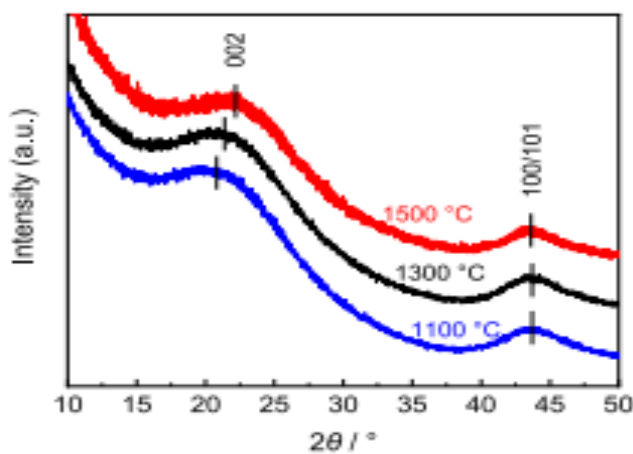


**Figure 2. Hard karbon XRD pattern sodium-ion battery [42]**

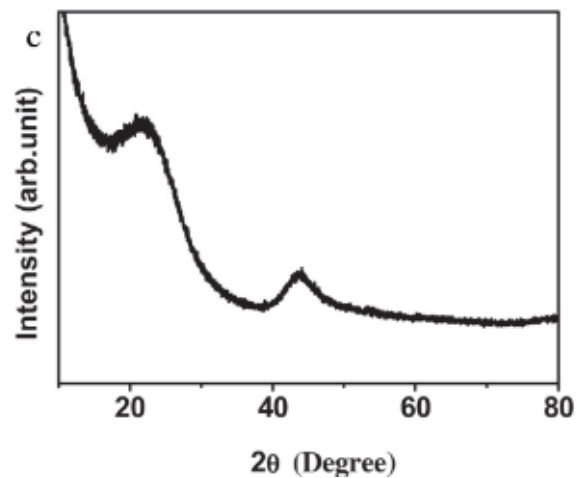


**Figure 3. Hard karbon XRD pattern for potassium-ion battery [41]**

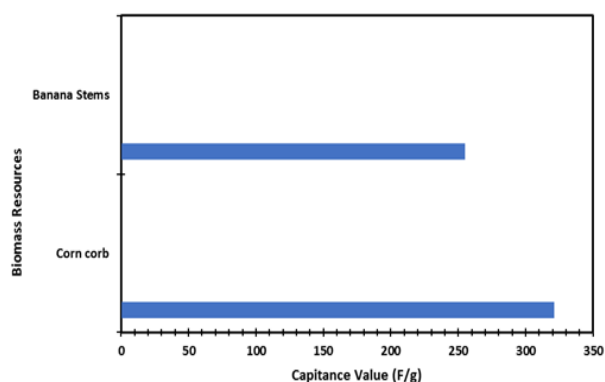


**Figure 4.** Applications of hard carbon in supercapacitor [37]

### 3.4. Applications of biomass based hard carbon in supercapacitor

In recent years, it is seen that the importance given to the biomass source has increased in the field of supercapacitors, as in other energy storage systems. When the studies are examined, it is seen that the researchers turn to products containing high amounts of cellulose and hemicellulose, such as corn cob and banana stems. These biomass

resources have attracted the attention of researchers because they are cost-effective, agricultural by-products and easy to supply. These studies also show promise in the use of natural carbon-based materials as a substitute for other materials for energy storage systems [37].

The capacitance value obtained from hard carbon activated with KOH applied in the supercapacitor area was shown in Fig. 4.

### 4. Conclusion

In this study, application of biomass-derived hard carbon was investigated in energy storage systems. Considering many parameters such as cost, supply and efficiency, it has been determined that hard carbon synthesized from biomass sources gives successful results when used as an anode material and is an open field for improvement.

### References

- Deng, J., Li, M., & Wang, Y. (2016). Biomass-derived carbon: synthesis and applications in energy storage and conversion. *Green chemistry*, 18(18), 4824-4854.
- Dai, L., Chang, D. W., Baek, J. B., & Lu, W. (2012). Carbon nanomaterials for advanced energy conversion and storage. *small*, 8(8), 1130-1166.
- T. G. Doung , "2002 Annual Progress Report for Energy Storage Research and Development", Freedom Car & Vehicle Technolo-gies Program, 2003 .
- Hu, B., Wang, K., Wu, L., Yu, S. H., Antonietti, M., & Titirici, M. M. (2010). Engineering carbon materials from the hydrothermal carbonization process of biomass. *Advanced materials*, 22(7), 813-828.
- Lai, X., Halpert, J. E., & Wang, D. (2012). Recent advances in micro-/nano-structured hollow spheres for energy applications: From simple to complex systems. *Energy & Environmental Science*, 5(2), 5604-5618.
- Titirici, M. M., & Antonietti, M. (2010). Chemistry and materials options of sustainable carbon materials made by hydrothermal carbonization. *Chemical Society Reviews*, 39(1), 103-116.
- Noked, M., Soffer, A., & Aurbach, D. (2011). The electrochemistry of activated carbonaceous materials: past, present, and future. *Journal of Solid State Electrochemistry*, 15(7), 1563-1578.
- Wang, J., Nie, P., Ding, B., Dong, S., Hao, X., Dou, H., & Zhang, X. (2017). Biomass derived carbon for energy storage devices. *Journal of materials chemistry a*, 5(6), 2411-2428.
- Yang, Z., Ren, J., Zhang, Z., Chen, X., Guan, G., Qiu, L., ... & Peng, H. (2015). Recent advancement of nanostructured carbon for energy applications. *Chemical reviews*, 115(11), 5159-5223.
- El Moctar, I., Ni, Q., Bai, Y., Wu, F., & Wu, C. (2018). Hard carbon anode materials for sodium-ion batteries. *Functional Materials Letters*, 11(06), 1830003.
- Zhao, J., Zhao, L., Chihara, K., Okada, S., Yamaki, J. I., Matsumoto, S., ... & Nakane, K. (2013). Electrochemical and thermal properties of hard carbon-type anodes for Na-ion batteries. *Journal of power sources*, 244, 752-757.
- Hasegawa, G., Kanamori, K., Kannari, N., Ozaki, J. I., Nakanishi, K., & Abe, T. (2015). Hard Carbon Anodes for Na-Ion Batteries: Toward a Practical Use. *ChemElectroChem*, 2(12), 1917-1920.

13. Liu, P., Li, Y., Hu, Y. S., Li, H., Chen, L., & Huang, X. (2016). A waste biomass derived hard carbon as a high-performance anode material for sodium-ion batteries. *Journal of Materials Chemistry A*, 4(34), 13046-13052.
14. Wang, Z., Qie, L., Yuan, L., Zhang, W., Hu, X., & Huang, Y. (2013). Functionalized N-doped interconnected carbon nanofibers as an anode material for sodium-ion storage with excellent performance. *Carbon*, 55, 328-334.
15. Jache, B., & Adelhelm, P. (2014). Use of graphite as a highly reversible electrode with superior cycle life for sodium-ion batteries by making use of co-intercalation phenomena. *Angewandte Chemie*, 126(38), 10333-10337.
16. Yang, J., Zhou, X., Wu, D., Zhao, X., & Zhou, Z. (2017). S-doped N-rich carbon nanosheets with expanded interlayer distance as anode materials for sodium-ion batteries. *Advanced Materials*, 29(6), 1604108.
17. Pan, H., Lu, X., Yu, X., Hu, Y. S., Li, H., Yang, X. Q., & Chen, L. (2013). Sodium storage and transport properties in layered Na<sub>2</sub>Ti<sub>3</sub>O<sub>7</sub> for room-temperature sodium-ion batteries. *Advanced Energy Materials*, 3(9), 1186-1194.
18. Wu, L., Hu, X., Qian, J., Pei, F., Wu, F., Mao, R., ... & Cao, Y. (2013). A Sn-SnS-C nanocomposite as anode host materials for Na-ion batteries. *Journal of Materials Chemistry A*, 1(24), 7181-7184.
19. Park, Y., Shin, D. S., Woo, S. H., Choi, N. S., Shin, K. H., Oh, S. M., ... & Hong, S. Y. (2012). Sodium terephthalate as an organic anode material for sodium ion batteries. *Advanced Materials*, 24(26), 3562-3567.
20. Wang, F., Cao, M., Qin, Y., Zhu, J., Wang, L., & Tang, Y. (2016). ZnO nanoparticle-decorated two-dimensional titanium carbide with enhanced supercapacitive performance. *RSC advances*, 6(92), 88934-88942.
21. Zhu, X., Jiang, X., Liu, X., Xiao, L., & Cao, Y. (2017). A green route to synthesize low-cost and high-performance hard carbon as promising sodium-ion battery anodes from sorghum stalk waste. *Green Energy & Environment*, 2(3), 310-315.
22. Zhang, T., Mao, J., Liu, X., Xuan, M., Bi, K., Zhang, X. L., ... & Shao, G. (2017). Pinecone biomass-derived hard carbon anodes for high-performance sodium-ion batteries. *RSC advances*, 7(66), 41504-41511.
23. Wang, K., Jin, Y., Sun, S., Huang, Y., Peng, J., Luo, J., ... & Han, J. (2017). Low-cost and high-performance hard carbon anode materials for sodium-ion batteries. *ACS omega*, 2(4), 1687-1695.
24. Dahbi, M., Nakano, T., Yabuuchi, N., Ishikawa, T., Kubota, K., Fukunishi, M., ... & Komaba, S. (2014). Sodium carboxymethyl cellulose as a potential binder for hard-carbon negative electrodes in sodium-ion batteries. *Electrochemistry communications*, 44, 66-69.
25. Rybarczyk, M. K., Li, Y., Qiao, M., Hu, Y. S., Titirici, M. M., & Lieder, M. (2019). Hard carbon derived from rice husk as low cost negative electrodes in Na-ion batteries. *Journal of Energy Chemistry*, 29, 17-22.
26. Wang, C., Huang, J., Qi, H., Cao, L., Xu, Z., Cheng, Y., ... & Li, J. (2017). Controlling pseudographitic domain dimension of dandelion derived biomass carbon for excellent sodium-ion storage. *Journal of power sources*, 358, 85-92.
27. Zhu, Y. E., Gu, H., Chen, Y. N., Yang, D., Wei, J., & Zhou, Z. (2018). Hard carbon derived from corn straw piths as anode materials for sodium ion batteries. *Ionics*, 24(4), 1075-1081.
28. Jiang, Q., Zhang, Z., Yin, S., Guo, Z., Wang, S., & Feng, C. (2016). Biomass carbon micro/nano-structures derived from ramie fibers and corncobs as anode materials for lithium-ion and sodium-ion batteries. *Applied Surface Science*, 379, 73-82.
29. Li, Y., Hu, Y. S., Titirici, M. M., Chen, L., & Huang, X. (2016). Hard carbon microtubes made from renewable cotton as high-performance anode material for sodium-ion batteries. *Advanced energy materials*, 6(18), 1600659.
30. Deng, J., Li, M., & Wang, Y. (2016). Biomass-derived carbon: synthesis and applications in energy storage and conversion. *Green chemistry*, 18(18), 4824-4854.
31. Feng Wu, Lu Liu, Yifei Yuan, Yu Li, Ying Bai, Tao Li, Jun Lu, and Chuan Wu. *ACS Applied Materials & Interfaces* (2018) 10 (32), 27030-27038
32. Ramos, A., Cameán, I., Cuesta, N., Antuña, C., & García, A. B. (2016). Expanded graphitic materials prepared from micro- and nanometric precursors as anodes for sodium-ion batteries. *Electrochimica Acta*, 187, 496-507.
33. Ren, X., Yu, D., Yuan, L., Bai, Y., Huang, K., Liu, J., & Feng, S. (2020). In situ exsolution of Ag from AgBiS<sub>2</sub> nanocrystal anode boosting high-performance potassium-ion batteries. *Journal of Materials Chemistry A*, 8(30), 15058-15065.
34. Peng, D., Chen, Y., Ma, H., Zhang, L., Hu, Y., Chen, X., ... & Ju, Z. (2020). Enhancing the cycling stability by tuning the chemical bonding between phosphorus and carbon nanotubes for potassium-ion battery anodes. *ACS applied materials & interfaces*, 12(33), 37275-37284.
35. Yu, A., Pan, Q., Zhang, M., Xie, D., & Tang, Y. (2020). Fast rate and long life potassium-ion based dual-ion battery through 3D porous organic negative electrode. *Advanced Functional Materials*, 30(24), 2001440.
36. Yang, M., Kong, Q., Feng, W., & Yao, W. (2021). N/O double-doped biomass hard carbon material realizes fast and stable potassium ion storage. *Carbon*, 176, 71-82.
37. Ghosh, S., Santhosh, R., Jeniffer, S., Raghavan, V., Jacob, G., Nanaji, K., ... & Grace, A. N. (2019). Natural biomass derived hard carbon and activated carbons as electrochemical supercapacitor electrodes. *Scientific reports*, 9(1), 1-15.
38. Al Hassan, M. R., Sen, A., Zaman, T., & Mostari, M. S. (2019). Emergence of graphene as a promising anode material for rechargeable batteries: a review. *Materials today chemistry*, 11, 225-243.
39. Hao, J., Wang, Y., Chi, C., Wang, J., Guo, Q., Yang, Y., ... & Zhao, J. (2018). Enhanced storage capability by biomass-derived porous carbon for lithium-ion and sodium-ion battery anodes. *Sustainable Energy & Fuels*, 2(10), 2358-2365.

40. Zhao, L. F., Hu, Z., Lai, W. H., Tao, Y., Peng, J., Miao, Z. C., ... & Dou, S. X. (2021). Hard carbon anodes: fundamental understanding and commercial perspectives for Na-ion batteries beyond Li-ion and K-ion counterparts. *Advanced Energy Materials*, 11(1), 2002704.
41. Ni, J., Huang, Y., & Gao, L. (2013). A high-performance hard carbon for Li-ion batteries and supercapacitors application. *Journal of Power Sources*, 223, 306-311.
42. Kamiyama, A., Kubota, K., Nakano, T., Fujimura, S., Shiraishi, S., Tsukada, H., & Komaba, S. (2019). High-capacity hard carbon synthesized from macroporous phenolic resin for sodium-ion and potassium-ion battery. *ACS Applied Energy Materials*, 3(1), 135-140.
43. Hao, R., Lan, H., Kuang, C., Wang, H., & Guo, L. (2018). Superior potassium storage in chitin-derived natural nitrogen-doped carbon nanofibers. *Carbon*, 128, 224-230.
44. Wu, Z., Wang, L., Huang, J., Zou, J., Chen, S., Cheng, H., ... & Niu, X. (2019). Loofah-derived carbon as an anode material for potassium ion and lithium ion batteries. *Electrochimica Acta*, 306, 446-453.
45. Wu, X., Chen, Y., Xing, Z., Lam, C. W. K., Pang, S. S., Zhang, W., & Ju, Z. (2019). Advanced carbon-based anodes for potassium-ion batteries. *Advanced Energy Materials*, 9(21), 1900343.
46. Zhang, G., Chen, Y., Chen, Y., & Guo, H. (2018). Activated biomass carbon made from bamboo as electrode material for supercapacitors. *Materials Research Bulletin*, 102, 391-398.

## An investigation of the biomass-derived carbon for next-generation energy storage systems

**Tolga Depci**

*Iskenderun Technical University, Department of Petroleum and Natural Gas Engineering, 31200,  
Hatay, Turkey  
tolga.depci@iste.edu.tr ORCID: 000-0001-9562-8068*

**Yunus Onal**

*Inonu University, Department of Chemical Engineering, 44280, Malatya, Turkey  
yunus.onal@inonu.edu.tr ORCID: 0000-0001-6342-6816*

**Emine Yalman**

*Iskenderun Technical University, Department of Petroleum and Natural Gas Engineering, 31200,  
Hatay, Turkey  
emine.avci@iste.edu.tr ORCID: 0000-0002-1782-3543*

**Ersin Bahceci**

*Iskenderun Technical University, Department of Metallurgy and Material Engineering, 31200, Hatay,  
Turkey  
ersin.bahceci@iste.edu.tr ORCID: 0000-0002-7719-6051*

*Cite this paper as: Depci, Tolga, Onal, Yunus, Yalman, Emine, Bahceci, Ersin. An investigation of the biomass-derived carbon for next-generation energy storage systems. Int. Conf. Advanced. Mater. Sci. & Eng. HiTech. and Device Appl. Oct. 27-29 2022, Ankara, Turkey*

**Abstract.** Today, number of portable electronic devices, communication devices, computer memory systems, medical devices, electric hybrid vehicles and sensors are constantly increasing. This situation causes the need energy storage systems which are high-tech devices. From this study, it is concluded that by converting biomass wastes into high-performance value-added carbon materials and using them in high-tech new generation energy storage systems, problems related to fossil fuels and cost of electrode material required for sustainable energy technology will decrease significantly.

**Keywords:** Biomass, carbon, next-generation energy storage.

© 2022 Published by ICMATSE

### 1. Introduction

Today, rapid industrialization, increasing trade, population and demands cause a rapid increase in consumption, and the need for energy is gradually increasing [1], [2]. With the beginning of industrialization, fossil fuels have been used as the basic resource in the world. Nevertheless, consumption of fossil resources causes environmental pollution and disrupts the structure of nature. Besides the negative effects of fossil resources on the environment, reserve amounts of

the fossil resources are limited and their formation takes a long time. Negotiations and agreements are made in the international arena to solve these problems. With the Paris Agreement (2015) [3], it is aimed to keep global warming to no more than 1.5 °C and lower carbon emissions to zero by 2050. In addition, due to the growing energy crisis and environmental problems of fossil resources, there is a great interest in clean renewable energy technologies, which are obtained by sustainable methods. In this context, it is foreseen that all vehicles in the European Union countries will consist

of electric vehicles until 2030. Our country has accepted this prediction until 2050. Other countries, especially Japan, attach great importance to the production and expansion of electric vehicle use. Although there is no problem in terms of vehicle production technologies in this transition, the most important problem is the necessity of long and sustainable energy storage systems.

Energy storage systems reduce the dependence on fossil fuels and the ratio between energy supply and demand, and therefore stability in the grids is ensured. As a result of the development and innovation of electronic technology, hybrid vehicles and electronic equipments such as laptops and mobile phones have been widely used. Rechargeable batteries (lithium-ion, sodium-ion, potassium-ion), supercapacitors, metal-air batteries, fuel cells are among the promising energy storage devices [2], [4], [5].

Carbon is one of the versatile elements found in nature in different allotropic forms such as amorphous carbon, graphite, and diamond. Carbon materials are used in many fields as electrodes for batteries and fuel cells, adsorbent and catalyst supports for water treatment.

Carbonaceous materials are considered as promising materials in energy storage and attract great attention by researchers [6]. Particularly, recently, carbon nanotube, fullerene and graphene that are the new carbon materials have been a focus area due to their suitable chemical structures and high electrochemical performances [2], [5]. However, these materials are produced from fossil sources and synthesized by methods that require quite a lot of energy [1]. In this respect, fossil resources are finite materials and can be both costly and environmentally harmful. Therefore, production of cheap, environmentally friendly and sustainable carbon materials is critical.

Electrochemical renewable energy technologies which can be seen in Fig.1 are considered as an alternative to address the challenges caused by fossil fuel. On the other hand, with the decrease in population density in rural areas due to the development of technology and industrialization, the amount of biomass is gradually increasing and approximately 130 billion tons of biomass waste is generated annually [7], [8]. The low utilization of this

large amount of biomass is still a serious problem. In addition, the carbon composition in the biomass content can be about 45-50% (as dry) that indicates that biomass is a carbon-rich raw material [4], [5]. Hence, utilization of carbon materials formed by biomass precursors that are renewable, sustainable, abundant and clean in next-generation energy storage systems is critical both in solving the energy crisis and in preventing environmental damage.

Fig. 1 shows the synthesis of carbon material from biomass by various techniques and next generation energy storage systems where it can be used.

In the study, state of art biomass derived carbon materials and their application in next generation energy storage systems were presented. To this end, many studies have been cited and evaluated in order to better understand the process of having superior properties.

## 2. Methodology

As a methodology, a literature review was carried out based on various data sets such as web of science and scopus. Since the subject of adapting carbonaceous materials obtained from biomass to new generation energy storage systems is quite up-to-date, the studies carried out especially in the last five years have been taken into consideration and extensive data from the raw material sources used to the production methods have been summarized and analyzed. In this context, many studies are cited and all relevant literature is listed in the reference section.

## 3. Biomass sources

Biomass is the organic matter mostly formed by the photosynthesis process necessary for the development and metabolic activities of plants. Biomass is the most common resource, particularly in developing countries.

Any organic matter derived by the process of photosynthesis is considered as biomass. Biomass resources are renewable energy sources and can be expressed as raw materials that can be used directly in energy production and transformed into products with high added value. Biomass resources are also generally plant or plant-based, unlike fossil resources, are readily available in nature and are formed by the function of photosynthesis through carbon dioxide and water. Since the carbon in the biomass is taken

as carbon dioxide (CO<sub>2</sub>) from the atmosphere through photosynthesis by plants, there is no additional CO<sub>2</sub> release to the atmosphere that occurs in fossil fuels when they are used [9].

Biomass sources consist of a wide variety of plant and animal materials. Biomass sources such as plant-based wastes (shrubs, algae, trees, crops), animal-based wastes (sewage, algae), urban and industrial wastes constitute sources which can be employed in energy production [9]. The resources are important energy precursors for both the world and our country, as they contribute to the protection of the environment and can be employed in energy production, as well as being easily cultivated and having a positive impact on socio-economic life, particularly in rural areas.

In addition to being chemically rich in carbon, biomass contains hydrogen, oxygen and nitrogen. Classification of biomass raw materials can be seen in Fig. 1.

#### 4. Synthesis methods

Various conversion methods are used for the use of biomass and other organic wastes for energy purposes. In the case of using pre-treated wastes as electricity, heat and light needs, the technologies applied are grouped into three main groups. These are thermochemical transformation, physico-chemical transformation and biochemical transformation. Today, most of the wastes used for energy purposes are converted into heat and electricity by thermochemical method.

Recently, important researches related to production of carbon materials, energy and fuel have been carried out by applying thermochemical conversion methods to biomass.

Activation, hydrothermal carbonization and template methods are generally used for production biomass derived carbon. These three methods were summarized below.

##### 4.1. Activation

Activated carbon is an artificial material that can be used in many applications from adsorbent to electrode material in energy storage. By improving the pore structure of this artificial material, its performance in these applications can be increased

and new application areas that can be used can be discovered. One of the most effective methods for this purpose is the activation process. The activated carbon is basically synthesized by physical and chemical methods [2].

##### 4.1.1. Physical activation

The physical activation process also takes place in two stages. These are carbonization (pyrolysis) and/or activation processes [10].

In the first stage, also known as carbonization, pyrolysis is first applied to the precursor material at medium temperature and in an inert atmosphere. Subsequently, the obtained carbonized product (char) is activated in the presence of various activating agents (CO<sub>2</sub> and steam) in order to obtain more porosity [1].

Specific surface area (SSA) and porosity of the product obtained are increased by the oxidizing gas used in physical activation by binding the functional groups to itself and removing these groups from the carbonaceous structure. The physical activation process, which usually takes place endothermically, varies according to the activation rate, activation temperature and activation materials.

##### 4.1.2. Chemical activation

H<sub>3</sub>PO<sub>4</sub>, ZnCl<sub>2</sub>, K<sub>2</sub>CO<sub>3</sub>, KOH, ve H<sub>2</sub>SO<sub>4</sub> are among the chemicals used to provide activation in chemical activation. kullanılan kimyasallar arasındadır [1], [6], [10]. Among them, KOH is the most widely used activating chemical due to its low activation temperature and high efficiency. These chemicals used affect the pore structure of the product and provide the formation of micropores.

Parameters such as the chemical substance used in the chemical activation method, the raw material, the rate of absorption of the chemical into the raw material, the applied carbonization and activation temperatures affect the product considerably.

Compared to physical activation, this form of activation has some advantages. These advantages are low activation temperature, shorter process time and high surface area.

### 4.2. Hydrothermal carbonization

Hydrothermal carbonization is an environmentally friendly, low-temperature thermochemical process that can convert organic materials into value-added products [11]. With the hydrothermal carbonization process, carbon materials possess high SSA can be obtained by various biomass precursors. For instance, Wang et al., (2022) [12] achieved a high Brunauer-Emmett-Teller (BET) surface area (2645.8 m<sup>2</sup>/g) from egg white.

Hydrothermal carbonization method in carbon production is considered as an alternative to physical and chemical activation methods due to its low cost, environmental friendliness and easy applicability [13]. However, compared to these methods, the SSA and porosity of the product obtained by hydrothermal carbonization method are lower.

### 4.3. Template method

This method is preferred in order to adjust the porosity of carbon derived from biomass. It is basically divided as hard template and soft template [2].

The practices of carbon from biomass for batteries of Li-ion, Na-ion and K-ion, supercapacitor, Li-S batteries, water splitting, fuel cells and microbial fuel cells were listed in Table 1-9, respectively.

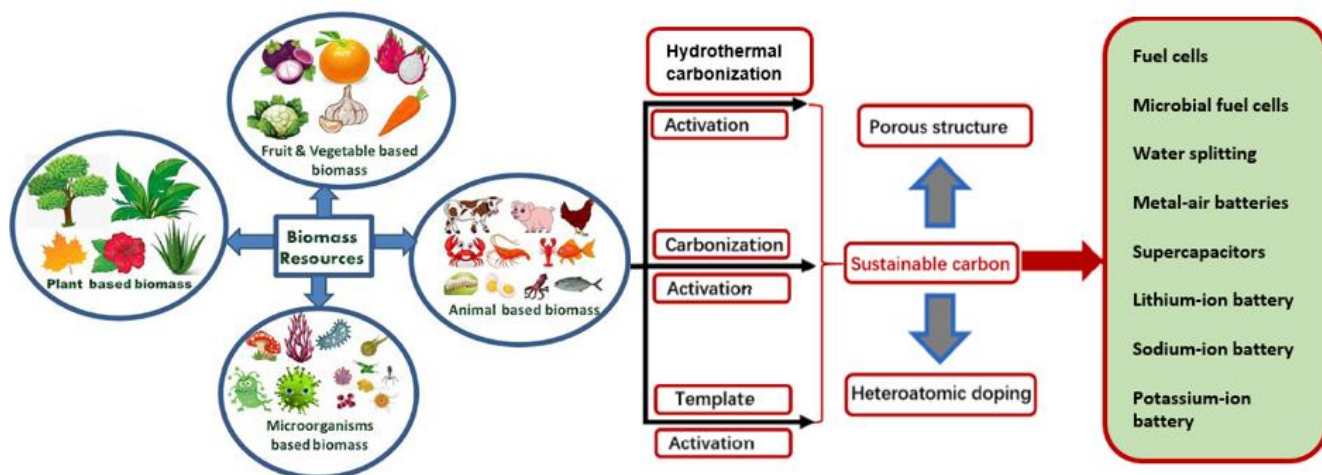


**Figure 1.** Diagram of biomass-based carbon in next generation energy storage systems and classification of biomass resources (Derived from [9] and [4]).

**Table 1.** Practices of carbon formed by biomass resources in Li-ion batteries

Source	Sample	Method	BET surface area (m <sup>2</sup> /g)	Electrolyte	Reversible capacity (mAh/g)	Current density (A/g)	Ref .
--------	--------	--------	--------------------------------------	-------------	-----------------------------	-----------------------	-------

Agaric	hollow hierarchical porous olive-like carbon (HHPOC)	self-templated strategy	856	1 M LiPF <sub>6</sub> (1:1 EC/DEC)	1121.8	0.1	[14]
Pollen	hierarchical N, P co-doped porous 3D-carbon	template assisted sol-gel method	69.6	1 M LiPF <sub>6</sub> (1:1:1 EC/DMC/EMC)	687.3 after 200 cycles	0.1	[15]
Chrysanthemum	hierarchically porous nitrogen-doped carbon	KOH activation	800	1 M LiPF <sub>6</sub> (1:1:1 EC/DMC)	975 100 cycles	0.1	[16]
Waste saccharomyces cerevisiae	N/O co-doped hard carbon	calcining and pickling	-	1 M LiPF <sub>6</sub> (1:1:1 EC/EMC/DEC)	307.4 after 500 cycles	1.0	[17]
Cattle bones	porous carbon	carbonization	2096	1 M LiPF <sub>6</sub> (1:1 EC/DEC)	1488 after 250 cycles	1.0	[18]
Bagasse	porous carbon	chemical activation	347	1.25 M LiPF <sub>6</sub> in EMC	325 after 100 cycles	0.1	[19]

**Table 1- (continued)**

Soda papermaking black liquor (SPBL)	graphene-like carbon sheet	Carbon thermal reduction technique assisted by hydrothermal method	258.70	1 M LiPF <sub>6</sub> (1: 1 EC/DEC/EMC)	750 after 1400 cycles	1.0	[20]
Drug residue	N/S dual-doped porous hard-carbon (N/S-PC)	simple heat treatment.	989.7	1.25 M LiPF <sub>6</sub> (1:1: 1 EC/DEC/DMC)	1060 after 50 cycles	0.1	[21]
Tannic acid	carbon superstructure material (PTA-700)	carbonization	361.36	1 M LiPF <sub>6</sub> (1:1: 1 EC/DEC/DMC)	535 after 100 cycles	0.1	[22]
Wood fiber	N-doped carbonized porous wood fiber (N-PCF-2)	Sacrificial template-assisted hydrothermal strategy	201.9	-	434 after 300 cycles	0.2	[23]

**Table 2. Practices of carbon formed by biomass resources in Na-ion batteries**

Source	Sample	Method	BET surface area (m <sup>2</sup> /g)	Electrolyte	Reversible capacity (mAh/g)	Current density (A/g)	Ref.
Agaric	hollow hierarchical porous olive-like carbon	self-templated strategy	856	1 M NaPF <sub>6</sub> in (1:1 EC/DEC)	386.8	0.1	[14]
Chrysanthemum	hierarchically porous nitrogen-doped carbon	KOH activation	800	1 M NaClO <sub>4</sub> (1:1: EC/DMC)	205 after 100 cycles	0.1	[16]
Onion peel	D hierarchical porous carbon nanosheet (HPCN)	Na <sub>2</sub> HPO <sub>4</sub> template-assisted activation method	756.5	1 M NaClO <sub>4</sub> (1:1: EC/DEC) with FEC (5 wt%)	333.8	0.05	[24]
Mango kernels	disordered carbon	carbonization	7.7	1 M NaClO <sub>4</sub> EC:PC/FEC (5wt%)	231 after 100 cycles	0.05	[25]
Camphor wood	hard carbon (CHC-0.25)	carbonization	3.74	1 M NaClO <sub>4</sub> (1:1: EC/DMC)	327.4	0.01	[26]

**Table 2 (continued)**

Drug residue	N/S dual-doped porous hard-carbon (N/S-PC)	simple heat treatment	989.7	1.25 M NaPF <sub>6</sub> (1:1 EC/DEC)	801	0.1	[21]
Spring onion peel	Sulphur-doped carbon nanosheets (S-CNS)	pyrolysis	230.97	1 M NaClO <sub>4</sub> (1:1: EC/DEC) with FEC (5 wt%)	605	0.05	[27]
Tannic acid	carbon superstructure material (PTA-700)	carbonization	361.36	1 M NaPF <sub>6</sub> in (1:1:1 EC/DEC/DMC)	114.0 after 3000 cycles	1.0	[22]
Pomelo peels	porous hard carbon	pyrolysis	1272	1 M NaClO <sub>4</sub> (1:1 EC:PC)	181	0.2	[28]
Argan shell	hard carbon	pyrolysis	2.6	1M NaPF <sub>6</sub> (1:1 EC/DEC)	300	0.025	[29]
Tea tomentia	N, P co-doped hard carbon (Tea-1100-NP)	carbonization and doped methods	39.78	1.0 M NaCF <sub>3</sub> SO <sub>3</sub> (DEGDME)	326.1	0.028	[30]
Wood fiber	N-doped carbonized porous wood fiber (N-PCF-2)	sacrificial template-assisted hydrothermal strategy	201.9	-	266 after 300 cycles	0.2	[31]
Sugarcane straw	porous carbon	direct-carbonization	218.0	1 M NaClO <sub>4</sub> (1:1 EC/PC)	189 after 50 cycles	0.1	[32]
Mangosteen epicarp	biowaste-sustained MoSe <sub>2</sub> composite (MoSe <sub>2</sub> /BC/CNTs)	hydrothermal process	289.035	1.0 M NaClO <sub>4</sub> (1:1:0.05 EC-DEC-FEC)	405.0 after 250 cycles	-	[33]
Onion waste	nitrogen-doped carbon spheres	hydrothermal and annealing process		1.0 M NaClO <sub>4</sub> (1:1 DEC/EC with 5% FEC)	152 after 200 cycles	0.05	[34]
Oak seeds	S/P co-doped hard carbon	one-step pyrolysis process	26.56	-	119.9 after 1000 cycles	1.0	[35]
Indonesian snake fruit peel	activated porous carbons (APC-1)	Pre carbonization and KOH-chemical activation	845	1 M NaClO <sub>4</sub> (PC with FEC (5%wt))	255 until 100 cycles	0.1	[36]

**Table 3. Practices of carbon formed by biomass resources in K-ion batteries**

Source	Sample	Method	BET surface area (m <sup>2</sup> /g)	Electrolyte	Reversible capacity (mAh/g)	Current density (A/g)	Ref.
Hemp	nano-phosphorus supported on biomass carbon ed P@ hemp-derived N-doped carbon (denoted as C-hemp/P) composite	carbonization	-	1 M KF <sub>6</sub> PO <sub>4</sub> (1:1 EC: DEC)	463	0.04	[40]
Bacterial cellulose	compressible, and hierarchical porous carbon	pyrolysis	778.75	1.0 M KPF <sub>6</sub> (4:3:2 in EC/DMC/EMC)	122	5.0	[41]
Potato	porous carbon	two-step carbonization	531.67	3M potassium bis(fluorosulfonyl) imide(KFSI) dissolved in dimethyl ether (DME)	248	0.1	[42]
Hemp core	fluorine-doped biomass carbon	modification	281.1	0.8 M KPF <sub>6</sub> (1:1 EC/DEC)	369.6 after 500 cycles	0.2	[43]

**Table 4. Practices of carbon formed by biomass resources in supercapacitor**

Source	Sample	Method	BET surface area (m <sup>2</sup> /g)	Electrolyte	Highest specific capacitance	Current density	Ref.
--------	--------	--------	--------------------------------------	-------------	------------------------------	-----------------	------

Egg white	graphene-like carbon	post-hydrothermal carbonization approach	2645.8	0.5 M H <sub>2</sub> SO <sub>4</sub>	528 mF·cm <sup>-2</sup>	1 mA·cm <sup>-2</sup>	[12]
Alginate	3D porous carbon	Template-assisted synthesis of porous carbon Covalent	902.841	6 M KOH	302 F g <sup>-1</sup>	0.5 A g <sup>-1</sup>	[44]
Banana tree leaves	S/N-doped porous carbon DAAQ-S/N-C-850	modification of organic small molecules with pseudocapacitive properties.	282.7	1 M H <sub>2</sub> SO <sub>4</sub>	355.3 F g <sup>-1</sup>	5 mV s <sup>-1</sup>	[45]
Tea leaf	activated biomass carbon (AC-KH)	chemical and thermal activation	45.73	3 M KOH	131.95 F g <sup>-1</sup>	0.5 A g <sup>-1</sup>	[46]
Sechium edule leaves	heteroatom-doped porous activated carbon nanoflakes SE-700	Facile methods of chemical activation and carbonization	475.87	0.5 M H <sub>2</sub> SO <sub>4</sub>	334 F g <sup>-1</sup>	1.0 A g <sup>-1</sup>	[47]
Sword bean shells	N and B co-doped hierarchical porous carbon BNAC-3	two-step of activation and hydrothermal post-treatment process	2471	6 M KOH	369 F g <sup>-1</sup>	1.0 A/g	[48]
Leonardite fulvic acid (LFA)	Dendritic like porous carbon aerogels PCAs2	solvent exchange method followed by an activation process	2807	6 M KOH	368 F g <sup>-1</sup>	0.05 A g <sup>-1</sup>	[49]
Pristine trees/shrubs	hierarchical porous hollow carbon nanospheres (HCNSs)	pyrolysis	1984	6 M KOH	225 F g <sup>-1</sup>	0.2 A g <sup>-1</sup>	[50]

**Table 4 (continued)**

Carrots	nitrogen enriched porous carbons (N-PC) N-PC-0.2	simple silica-activation process	1265	6 M KOH	268 F g <sup>-1</sup>	1.0 A g <sup>-1</sup>	[6]
Orange peel	activated carbon	KOH activation	2160	1 M H <sub>2</sub> SO <sub>4</sub>	460 F g <sup>-1</sup>	1.0 A g <sup>-1</sup>	[51]
Peanut shell	porous carbon	ZnCl <sub>2</sub> activation	1549	1M H <sub>2</sub> SO <sub>4</sub>	340 F g <sup>-1</sup>	1.0 A g <sup>-1</sup>	[52]
Cattail	porous carbon	carbonization and CO <sub>2</sub> activation.	441	6M KOH	126.5 F g <sup>-1</sup>	0.5 A g <sup>-1</sup>	[53]
Nori	N, O, S, Cl co-doped carbon	ZnCl <sub>2</sub> activation	639	6M KOH	220 F g <sup>-1</sup>	0.1 A g <sup>-1</sup>	[54]

**Table 5. Practices of carbon formed by biomass resources in Li-S batteries**

Source	Sample	Method	BET surface area (m <sup>2</sup> /g)	Specific capacity	Electrolyte	Ref.
Bean sprout stems	hierarchical porous carbon	KOH activation and carbonizing	451	980 mAh g <sup>-1</sup> at 0.1 C	1 M LiTFSI	[55]
Guar gum	nitrogen-doped ordered multi-hollow layered carbon	one-step carbonization.	299	1276.6 mAh g <sup>-1</sup> at 0.2 C	-	[56]

**Table 6. Practices of carbon formed by biomass resources for metal-air battery**

Source	Sample	Method	BET (m <sup>2</sup> /g)	Electrolyte	Onset Potential (V)	Current density (mA cm <sup>-2</sup> )	Ref.
Waste pine needle	microporous and defective carbon	hydrothermal method and NH <sub>3</sub> high-temperature activation	1840.51	0.1 M KOH	-0.04 V vs. Ag/AgCl	6.5	[57]

**Table 7. Summary of the practices of carbon formed by biomass resources in water splitting**

Source	Sample	Method	Solution	Current density	OER	HER	Ref.
Cotton fibers	Bifunctional electrocatalyst cobalt supported on biomass carbon tubes (CO/BCT)	Impregnation and subsequent carbonization process	1.0 M KOH	10 mA cm <sup>-2</sup>	330	74	[58]

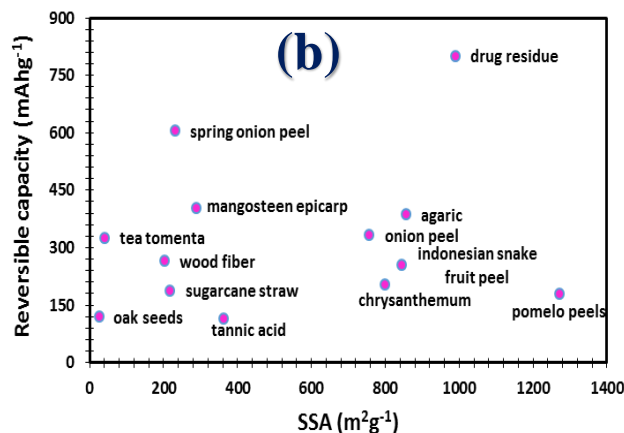
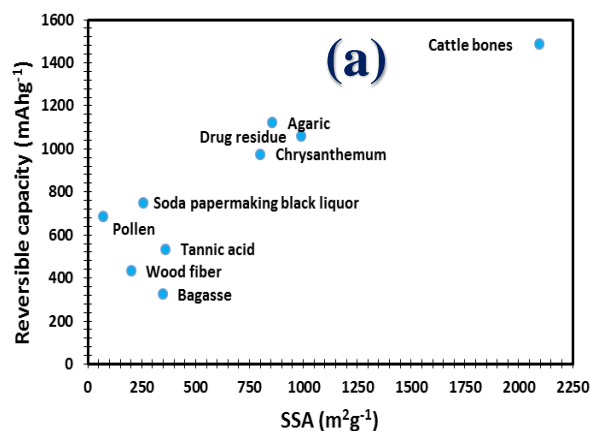
OER: Oxygen evolution reaction, HER: Hydrogen evolution reaction

**Table 8.** Practices of carbon formed by biomass resources in fuel cell

Source	Method	BET (m <sup>2</sup> /g)	Electrolyte	Onset potential (V)	Ref.
Okara	Pyrolysis	516.5	0.1M KOH	0.975 vs. RHE	[59]
Waste leather	Pyrolysis	2100	0.5M KOH	0.905 vs. RHE	[60]

**Table 9.** Practices of carbon formed by biomass resources in microbial fuel cell

Source	Sample	Method	BET (m <sup>2</sup> /g)	Onset potential (V)	Power density	Ref.
Egg	heteroatom-doped carbon nanosheets (EGC1-10-2)	g-C <sub>3</sub> N <sub>4</sub> Template	382.6230	+ 0.257 V vs. Ag/AgCl	737.1 mW m <sup>-2</sup>	[61]



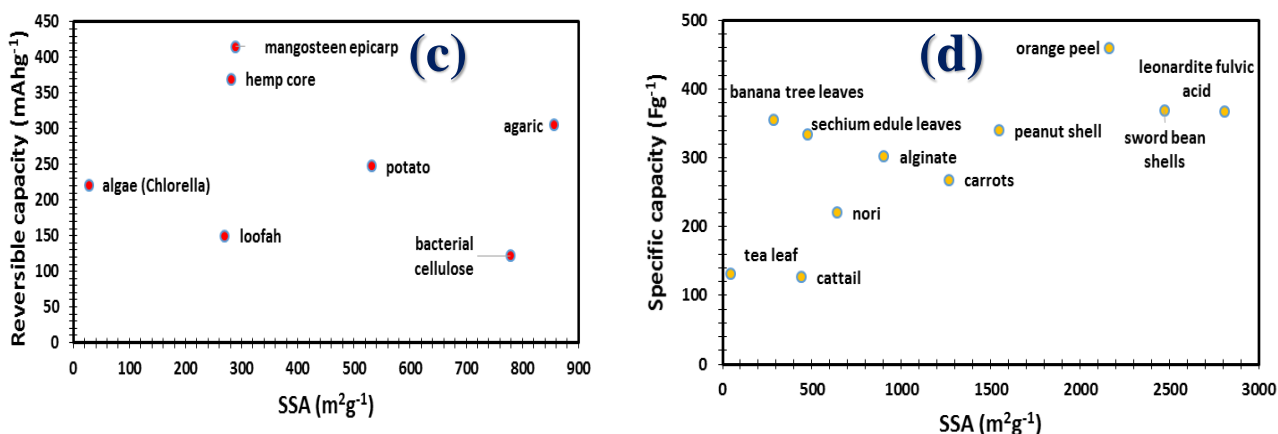
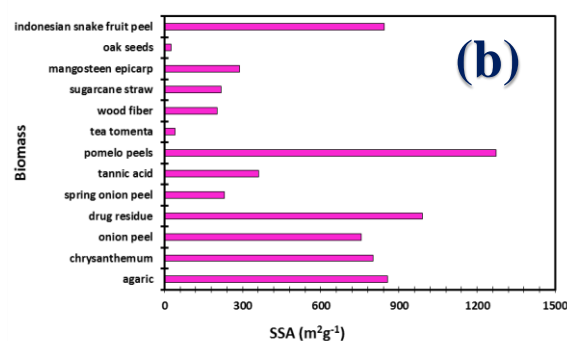
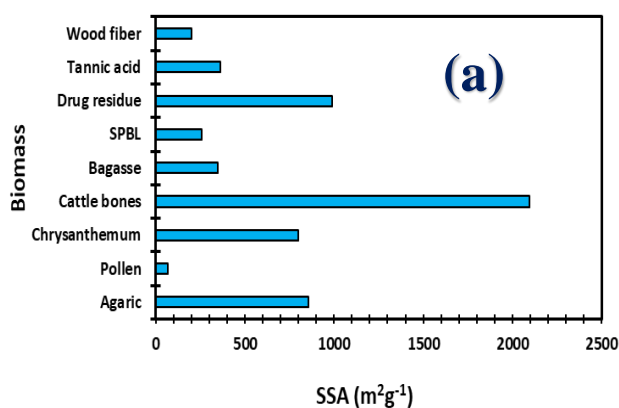


**Figure 2.** Surface area and capacity relationship of carbon material derived from biomass, battery Li-ion (a), Na-ion (b), K-ion (c) and supercapacitor (d).

From Fig. 3, it is seen that SSAs of materials obtained from various biomass sources for lithium-ion batteries can vary from 69.6 to 2096 (m<sup>2</sup>/g). SSAs varying from 2.6 to 1272 (m<sup>2</sup>/g) were obtained for Na-ion batteries. Surface areas for the K-ion battery ranged from 27.9 to 856 (m<sup>2</sup>/g). Unlike batteries, it is seen that higher surface area carbon from biomass are obtained in supercapacitors. A surface area of 45.73 to 2645.8 (m<sup>2</sup>/g) was obtained for the supercapacitor.

In the literature, it is seen that the capacity of energy storage devices is directly associated with the SSA of

the developed electrode material. Capacitance values corresponding to surface areas were plotted to reveal that the capacity of carbon formed by biomass is not only dependent on surface area. Results were given in Fig. 2 for batteries of Li-ion, Na-ion and K-ion and supercapacitors, respectively. From the figure, it is seen that the developed carbon material has no direct correlation on the obtained capacities that is also in line with the study carried out by Escobar et al., (2020) [62]. It is believed that the performance of the material based on many combined parameters such as pore structure, pore distribution, pore size and conductivity.



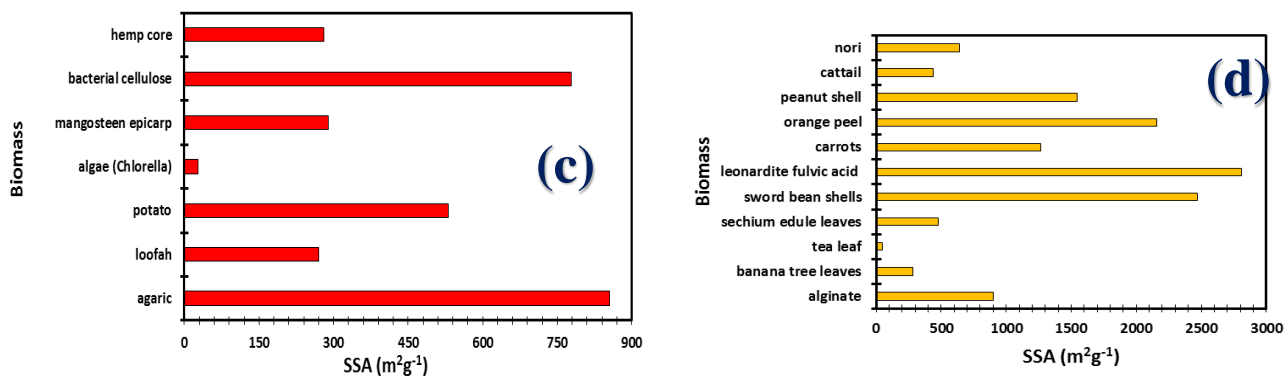


**Figure 3.** SSAs of carbon materials formed by various biomass sources, battery of Li-ion (a), Na-ion (b), K-ion (c) and supercapacitor (d).

## 5. Conclusions

In this study, applications of carbon produced from biomass cheap, renewable, sustainable and environmentally friendly in new generation energy storage systems has been analyzed. From the study, it was determined carbonaceous materials can be produced from many natural biomass materials and used in high performance in next generation energy storage systems. In addition, the applied production process and selection of raw materials significantly affect the chemical structure of the final product and its energy storage potential. By replacing the carbon materials traditionally used

in new generation energy storage systems with carbonaceous materials derived from biomass, it is expected to present a sustainable future and provide an advantage to the country's economy. Although many studies have been carried out on the subject so far, there have been some missing aspects. For instance, for future studies, it is necessary to determine the optimum composition biomass source and optimum production method, surface area and capacity to obtain carbon with high electrochemical performance from biomass. As a result, the authors believe that biomass-derived carbon could be applied in large-scale mass production of energy storage devices in the short term.

## References

- Zhu, Z., & Xu, Z. (2020). The rational design of biomass-derived carbon materials towards next-generation energy storage: A review. *Renewable and Sustainable Energy Reviews*, 134, 110308.
- Wang, J., Nie, P., Ding, B., Dong, S., Hao, X., Dou, H., & Zhang, X. (2017). Biomass derived carbon for energy storage devices. *Journal of materials chemistry a*, 5(6), 2411-2428.
- Jeong, D., Kim, J., Choi, D., & Park, E. (2022). Social networking services as new venue for public perceptions of energy issues: The case of Paris agreement. *Energy Strategy Reviews*, 39, 100758.
- M. Zhang, J. Zhang, S. Ran, W. Sun, Z. Zhu, Biomass-Derived Sustainable Carbon Materials in Energy Conversion and Storage Applications: Status and Opportunities. A mini review. *Electrochemistry Communications*, 107283 (2022).
- Deng, J., Li, M., & Wang, Y. (2016). Biomass-derived carbon: synthesis and applications in energy storage and conversion. *Green chemistry*, 18(18), 4824-4854.
- Du, J., Zhang, Y., Lv, H., & Chen, A. (2021). Silicate-assisted activation of biomass towards N-doped porous carbon sheets for supercapacitors. *Journal of Alloys and Compounds*, 853, 157091.
- Shen, F., Xiong, X., Fu, J., Yang, J., Qiu, M., Qi, X., & Tsang, D. C. (2020). Recent advances in mechanochemical production of chemicals and carbon materials from sustainable biomass resources. *Renewable and Sustainable Energy Reviews*, 130, 109944.
- Deng, B., Huang, Q., Zhang, W., Liu, J., Meng, Q., Zhu, Z., ... & Zhang, Y. (2021). Design high performance biomass-derived renewable carbon material for electric energy storage system. *Journal of Cleaner Production*, 309, 127391.
- Manasa, P., Sambasivam, S., & Ran, F. (2022). Recent progress on biomass waste derived activated carbon electrode materials for supercapacitors applications—A review. *Journal of Energy Storage*, 54, 105290.
- Saini, S., Chand, P., & Joshi, A. (2021). Biomass derived carbon for supercapacitor applications. *Journal of Energy Storage*, 39, 102646.

11. Shen, Y. (2020). A review on hydrothermal carbonization of biomass and plastic wastes to energy products. *Biomass and Bioenergy*, 134, 105479.
12. Wang, Y. F., Zou, S. J., Hu, W. P., Wu, F. F., Yang, J. X., Cen, Y. Y., ... & Huang, K. J. (2022). Biomass-derived graphene-like carbon nanoflakes for advanced supercapacitor and hydrogen evolution reaction. *Journal of Alloys and Compounds*, 167176.
13. Gao, Z., Zhang, Y., Song, N., & Li, X. (2017). Biomass-derived renewable carbon materials for electrochemical energy storage. *Materials Research Letters*, 5(2), 69-88.
14. Zhu, L., Zhang, Z., Luo, J., Zhang, H., Qu, Y., & Yang, Z. (2021). Self-templated synthesis of hollow hierarchical porous olive-like carbon toward universal high-performance alkali (Li, Na, K)-ion storage. *Carbon*, 174, 317-324.
15. Zhao, J., Wei, D., Zhang, X., Zhang, S., Zhang, C., & Yang, X. (2022). Biomass-derived hierarchical N, P codoped porous 3D-carbon framework@ TiO<sub>2</sub> hybrids as advanced anode for lithium ion batteries. *Journal of Colloid and Interface Science*, 606, 577-587.
16. Ou, J., Yang, L., & Zhang, Z. (2019). Chrysanthemum derived hierarchically porous nitrogen-doped carbon as high performance anode material for Lithium/Sodium ion batteries. *Powder Technology*, 344, 89-95.
17. Liu, G., Zhao, Y., Li, J., Zhang, T., Yang, M., Guo, D., ... & Liu, X. (2022). Hierarchical N/O co-doped hard carbon derived from waste *saccharomyces cerevisiae* for lithium storage. *Journal of Electroanalytical Chemistry*, 911, 116226.
18. Niu, J., Shao, R., Liang, J., Dou, M., Li, Z., Huang, Y., & Wang, F. (2017). Biomass-derived mesopore-dominant porous carbons with large specific surface area and high defect density as high performance electrode materials for Li-ion batteries and supercapacitors. *Nano energy*, 36, 322-330.
19. Wan, H., & Hu, X. (2019). From biomass-derived wastes (bagasse, wheat straw and shavings) to activated carbon with three-dimensional connected architecture and porous structure for Li-ion batteries. *Chemical Physics*, 521, 108-114.
20. Graphene-like carbon sheet/Fe<sub>3</sub>O<sub>4</sub> nanocomposites derived from soda papermaking black liquor for high performance lithium ion batteries
21. Wan, H., Shen, X., Jiang, H., Zhang, C., Jiang, K., Chen, T., ... & Chen, Y. (2021). Biomass-derived N/S dual-doped porous hard-carbon as high-capacity anodes for lithium/sodium ions batteries. *Energy*, 231, 121102.
22. Huang, G., Kong, Q., Yao, W., & Wang, Q. (2022). Poly tannic acid carbon rods as anode materials for high performance lithium and sodium ion batteries. *Journal of Colloid and Interface Science*.
23. Chen, Y., Wu, Y., Liao, Y., Zhang, Z., Luo, S., Li, L., ... & Qing, Y. (2022). Tuning carbonized wood fiber via sacrificial template-assisted hydrothermal synthesis for high-performance lithium/sodium-ion batteries. *Journal of Power Sources*, 546, 231993.
24. Sun, Y., Li, X., Zhang, Y., Li, Y., Zhao, G., & Chen, C. (2022). One-step production of capacitive-dominated carbon anode derived from biomass for sodium-ion batteries. *Inorganic Chemistry Communications*, 144, 109921.
25. Bhawana, K., Roy, A., Chakrabarty, N., Gautam, M., Dutta, D. P., & Mitra, S. (2022). Sodium-ion batteries: Chemistry of biomass derived disordered carbon in carbonate and ether-based electrolytes. *Electrochimica Acta*, 425, 140744.
26. Guo, S., Chen, Y., Tong, L., Cao, Y., Jiao, H., & Qiu, X. (2022). Biomass hard carbon of high initial coulombic efficiency for sodium-ion batteries: Preparation and application. *Electrochimica Acta*, 410, 140017.
27. Zhao, G., Yu, D., Zhang, H., Sun, F., Li, J., Zhu, L., ... & Sun, Y. (2020). Sulphur-doped carbon nanosheets derived from biomass as high-performance anode materials for sodium-ion batteries. *Nano Energy*, 67, 104219.
28. Hong, K. L., Qie, L., Zeng, R., Yi, Z. Q., Zhang, W., Wang, D., ... & Huang, Y. H. (2014). Biomass derived hard carbon used as a high performance anode material for sodium ion batteries. *Journal of materials chemistry a*, 2(32), 12733-12738.
29. Dahbi, M., Kiso, M., Kubota, K., Horiba, T., Chafik, T., Hida, K., ... & Komaba, S. (2017). Synthesis of hard carbon from argan shells for Na-ion batteries. *Journal of Materials Chemistry A*, 5(20), 9917-9928.
30. Wang, H., Chen, H., Chen, C., Li, M., Xie, Y., Zhang, X., ... & Lu, C. (2022). Tea-derived carbon materials as anode for high-performance sodium ion batteries. *Chinese Chemical Letters*.
31. Chen, Y., Wu, Y., Liao, Y., Zhang, Z., Luo, S., Li, L., ... & Qing, Y. (2022). Tuning carbonized wood fiber via sacrificial template-assisted hydrothermal synthesis for high-performance lithium/sodium-ion batteries. *Journal of Power Sources*, 546, 231993.
32. Kim, M., Fernando, J. F., Li, Z., Alowasheer, A., Ashok, A., Xin, R., ... & Li, J. (2022). Ultra-stable sodium ion storage of biomass porous carbon derived from sugarcane. *Chemical Engineering Journal*, 445, 136344.
33. Su, C., Ru, Q., Gao, Y., Shi, Z., Zheng, M., Chen, F., ... & Wei, L. (2021). Biowaste-sustained MoSe<sub>2</sub> composite as an efficient anode for sodium/potassium storage applications. *Journal of Alloys and Compounds*, 850, 156770.
34. Khan, M., Ahmad, N., Lu, K., Sun, Z., Wei, C., Zheng, X., & Yang, R. (2020). Nitrogen-doped carbon derived from onion waste as anode material for high performance sodium-ion battery. *Solid State Ionics*, 346, 115223.
35. Ding, J., Zhang, Y., Huang, Y., Wang, X., Sun, Y., Guo, Y., ... & Tang, X. (2021). Sulfur and phosphorus co-doped hard carbon derived from oak seeds enabled reversible sodium spheres filling and plating for ultra-stable sodium storage. *Journal of Alloys and Compounds*, 851, 156791.

36. Arie, A. A., Kristianto, H., Demir, E., & Cakan, R. D. (2018). Activated porous carbons derived from the Indonesian snake fruit peel as anode materials for sodium ion batteries. *Materials Chemistry and Physics*, 217, 254-261.
37. Wu, Z., Wang, L., Huang, J., Zou, J., Chen, S., Cheng, H., ... & Niu, X. (2019). Loofah-derived carbon as an anode material for potassium ion and lithium ion batteries. *Electrochimica Acta*, 306, 446-453.
38. Xu, L., Wang, Y., Lin, C., Xia, X., Chen, X., Xiong, P., ... & Zeng, L. (2022). Algal residues-engaged formation of novel WVO<sub>4</sub>/V<sub>3</sub>Se<sub>4</sub> hybrid nanostructure with carbon fiber confinement for enhanced long-term cycling stability in sodium/potassium storage. *Journal of Alloys and Compounds*, 892, 162177.
39. Sun, Y., Zhu, D., Liang, Z., Zhao, Y., Tian, W., Ren, X., ... & Tai, R. (2020). Facile renewable synthesis of nitrogen/oxygen co-doped graphene-like carbon nanocages as general lithium-ion and potassium-ion batteries anode. *Carbon*, 167, 685-695.
40. Wang, P., Gong, Z., Zhu, K., Ye, K., Yan, J., Yin, J., ... & Cao, D. (2020). Nano-phosphorus supported on biomass carbon by gas deposition as negative electrode material for potassium ion batteries. *Electrochimica Acta*, 362, 137153.
41. Li, H., Cheng, Z., Zhang, Q., Natan, A., Yang, Y., Cao, D., & Zhu, H. (2018). Bacterial-derived, compressible, and hierarchical porous carbon for high-performance potassium-ion batteries. *Nano letters*, 18(11), 7407-7413.
42. Cao, W., Zhang, E., Wang, J., Liu, Z., Ge, J., Yu, X., ... & Lu, B. (2019). Potato derived biomass porous carbon as anode for potassium ion batteries. *Electrochimica Acta*, 293, 364-370.
43. Wang, P., Gong, Z., Wang, D., Hu, R., Ye, K., Gao, Y., ... & Cao, D. (2021). Facile fabrication of F-doped biomass carbon as high-performance anode material for potassium-ion batteries. *Electrochimica Acta*, 389, 138799.
44. Xi, Y., Xiao, Z., Lv, H., Sun, H., Wang, X., Zhao, Z., ... & An, Q. (2022). Template-assisted synthesis of porous carbon derived from biomass for enhanced supercapacitor performance. *Diamond and Related Materials*, 128, 109219.
45. Xie, Y., Su, W., Zhang, H., Wang, X., Xiong, D., Chen, L., ... & He, M. (2022). 2, 6-diaminoanthraquinone-functionalized S, N-codoped graphitic biomass carbon as advanced electrode materials for supercapacitors. *Colloids and Surfaces A: Physicochemical and Engineering Aspects*, 130102.
46. Zhang, L., Wang, Y., Yang, S., Zhao, G., Han, L., Li, Y., & Zhu, G. (2022). Biomass-derived S, P, Cl tri-doped porous carbon for high-performance supercapacitor. *Diamond and Related Materials*, 126, 109061.
47. Jalalah, M., Rudra, S., Aljafari, B., Irfan, M., Almasabi, S. S., Alsuwian, T., ... & Harraz, F. A. (2022). Novel porous heteroatom-doped biomass activated carbon nanoflakes for efficient solid-state symmetric supercapacitor devices. *Journal of the Taiwan Institute of Chemical Engineers*, 132, 104148.
48. Luo, L., Luo, L., Deng, J., Chen, T., Du, G., Fan, M., & Zhao, W. (2021). High performance supercapacitor electrodes based on B/N Co-doped biomass porous carbon materials by KOH activation and hydrothermal treatment. *International Journal of Hydrogen Energy*, 46(63), 31927-31937.
49. Ma, Y. Z., Guo, Y., Zhou, C., & Wang, C. Y. (2016). Biomass-derived dendritic-like porous carbon aerogels for supercapacitors. *Electrochimica Acta*, 210, 897-904.
50. He, D., Gao, Y., Wang, Z., Yao, Y., Wu, L., Zhang, J., ... & Wang, M. X. (2021). One-step green fabrication of hierarchically porous hollow carbon nanospheres (HCNSs) from raw biomass: Formation mechanisms and supercapacitor applications. *Journal of Colloid and Interface Science*, 581, 238-250.
51. Subramani, K., Sudhan, N., Karnan, M., & Sathish, M. (2017). Orange peel derived activated carbon for fabrication of high-energy and high-rate supercapacitors. *ChemistrySelect*, 2(35), 11384-11392.
52. Xiao, Z., Chen, W., Liu, K., Cui, P., & Zhan, D. (2018). Porous biomass carbon derived from peanut shells as electrode materials with enhanced electrochemical performance for supercapacitors. *Int. J. Electrochem. Sci*, 13, 5370-5381.
53. Yu, M., Han, Y., Li, J., & Wang, L. (2017). CO<sub>2</sub>-activated porous carbon derived from cattail biomass for removal of malachite green dye and application as supercapacitors. *Chemical Engineering Journal*, 317, 493-502.
54. Wang, C., & Liu, T. (2017). Nori-based N, O, S, Cl co-doped carbon materials by chemical activation of ZnCl<sub>2</sub> for supercapacitor. *Journal of Alloys and Compounds*, 696, 42-50.
55. Lin, Y., He, S., Ouyang, Z., Li, J., Zhao, J., Xiao, Y., ... & Cheng, B. (2023). Synergistic engineering of cobalt selenide and biomass-derived S, N, P co-doped hierarchical porous carbon for modulation of stable Li-S batteries. *Journal of Materials Science & Technology*, 134, 11-21.
56. Xu, G., Gao, S., Song, X., Jiang, Y., & Zhang, X. (2022). Nitrogen-doped ordered multi-hollow layered carbon embedded with Mo<sub>2</sub>C as lithium polysulfide restrained cathode for Li-S batteries. *Applied Surface Science*, 574, 151634.
57. Wang, M., Lei, X., Hu, L., Zhang, P., Hu, H., & Fang, J. (2017). High-performance waste biomass-derived microporous carbon electrocatalyst with a towel-like surface for alkaline metal/air batteries. *Electrochimica Acta*, 250, 384-392.
58. Jiang, E., Song, N., Hong, S., Xiao, M., Zhu, D., Yan, Z., ... & Dong, H. (2022). Cobalt supported on biomass carbon tubes derived from cotton fibers towards high-efficient electrocatalytic overall water-splitting. *Electrochimica Acta*, 407, 139895.
59. Wang, R., Wang, H., Zhou, T., Key, J., Ma, Y., Zhang, Z., ... & Ji, S. (2015). The enhanced electrocatalytic activity of okara-derived N-doped mesoporous carbon for oxygen reduction reaction. *Journal of Power Sources*, 274, 741-747.

60. Alonso-Lemus, I. L., Rodriguez-Varela, F. J., Figueroa-Torres, M. Z., Sanchez-Castro, M. E., Hernandez-Ramírez, A., Lardizabal-Gutierrez, D., & Quintana-Owen, P. (2016). Novel self-nitrogen-doped porous carbon from waste leather as highly active metal-free electrocatalyst for the ORR. *International Journal of Hydrogen Energy*, 41(48), 23409-23416.
61. Lu, Y., Zhu, N., Yin, F., Yang, T., Wu, P., Dang, Z., ... & Wei, X. (2017). Biomass-derived heteroatoms-doped mesoporous carbon for efficient oxygen reduction in microbial fuel cells. *Biosensors and Bioelectronics*, 98, 350-356.
62. Escobar, B., Martínez-Casillas, D. C., Pérez-Salcedo, K. Y., Rosas, D., Morales, L., Liao, S. J., ... & Shi, X. (2021). Research progress on biomass-derived carbon electrode materials for electrochemical energy storage and conversion technologies. *International Journal of Hydrogen Energy*, 46(51), 26053-26073.

ICMATSE 2022

## Tuning the Properties of Spray-Deposited Zinc Oxide (ZnO) for Solar Cells and Optoelectronic Applications: A Review

*Shadia J. Ikhmayies*

*Jabal El-Hussain,, Amman 11121, Jordan, shadia\_ikhmayies@yahoo.com, ORCID: 0000-0002-2684-3300*

*Cite this paper as: Ikhmayies, S.J. Tuning the Properties of Spray-Deposited Zinc Oxide (ZnO) for Solar Cells and Optoelectronic Applications: A Review. Int. Conf. Advanced. Mater. Sci. & Eng. HiTech. and Device Appl. Oct. 27-29 2022, Ankara, Turkey*

**Abstract.** Zinc oxide (ZnO) is a very important transparent conducting oxide. It is a wide band gap II-VI compound semiconductor of several applications in solar cells and optoelectronic industry, especially in thin film form. Naturally ZnO has n-type conductivity due to native defects, but it can be doped to become p-type semiconductor. For these applications the high quality of the produced material and low cost production methods are required. The spray pyrolysis method is a low cost method that enables the production of large area and highly transparent undoped and intentionally doped thin films. Through this method, tuning the properties of the produced films is accessible through changing several deposition parameters such as substrate temperature, concentration of the precursor solution, types of the dopants and their concentrations, annealing, nozzle size, and nozzle to substrate distance, etc. A review of the methods used to tune the structural, morphological, optical, and electrical properties of spray-deposited ZnO thin films to be suitable for the different applications is performed. It is found that; structure, morphology, band gap, transmittance, resistivity, and other related properties of these films can be tuned to fit the requirement.

**Keywords:** Zinc oxide, Spray Pyrolysis, Solar Cells, Doping, Annealing.

© 2022 Published by ICMATSE

## Investigation of The Effect of Leaching Applied To Rice Hull Ash On Silica Content and BET Surface Area

**Oykum BASGOZ**

Mersin University-Department of Metallurgy and Materials Engineering, 33110, Mersin, Turkey,  
oykumbasgoz@mersin.edu.tr  
ORCID: 0000-0002-0479-2389

**Ali Oktay GUL**

İskenderun Technical University-Department of Metallurgy and Materials Engineering, 31200, Hatay,  
Turkey, aoktay.gul@iste.edu.tr  
ORCID: 0000-0002-4891-5280

**Ersin BAHCECI**

İskenderun Technical University-Department of Metallurgy and Materials Engineering, 31200, Hatay,  
Turkey, ersin.bahceci@iste.edu.tr  
ORCID: 0000-0002-7719-6051

**Tolga DEPCI**

İskenderun Technical University-Department of Petrol and Natural Gases Engineering, 31200, Hatay,  
Turkey, tolga.depci@iste.edu.tr  
ORCID: 0000-0001-9562-8068

**Omer GULER**

Munzur University-Rare Earth Elements Application and Research Center, 62000, Tunceli,  
omerguler@munzur.edu.tr  
ORCID: 0000-0003-4334-7314

**Abstract.** In this study, it was carried out to increase the SiO<sub>2</sub> amount and BET surface area value of RHA. In this context, leaching and calcination processes were applied to RHA. For the calcination process, the optimum temperature and time were determined by using two different techniques, directly and gradually. According to the XRF result, it was determined that the calcination process performed gradually was more successful. Leaching process was carried out using 0.5 M HCl and HNO<sub>3</sub> chemicals. At this stage, it is aimed to remove metallic impurities from the structure before the calcination process to obtain RHA synthesis with higher purity and silica content. Characterization studies were carried out with SEM, XRF and BET surface area analyzes. According to XRF analysis, the highest SiO<sub>2</sub> content and the highest BET surface area value were obtained as a result of leaching with 0.5 M HNO<sub>3</sub> and 0.5 HCl, respectively. This study showed that chemical pretreatments are necessary to obtain silica with high purity and high surface area. In addition, it has been observed that chemical pretreatments are necessary to remove metallic impurities. As a result of the pretreatment, the silica content of RHA increased from %92.075 to %99.13 and the BET surface area value increased from 247.9205 m<sup>2</sup>/g to 296.0692 m<sup>2</sup>/g. In addition, it has been determined that the RHA obtained from this Turkey has better properties compared to similar studies in the literature.

**Keywords:** Rice hull ash (RHA), Silica, Leaching, BET Surface Area.

## Introduction

Rice constitutes the main food source of almost more than half of the world's population (NGES, 2014) [1]. About 600 million tons of rice are produced globally each year. Approximately 20% of the total rice amount is rice hull. 1 ton of rice produces about 0.20 tons of hull, and each ton of rice hull produces about 0.18–0.20 tons of ash, depending on the climatic conditions of the rice field, rice varieties and geographical location. The chemical content of rice hull varies depending on the type of rice, the chemistry of the soil, the climatic conditions and the geographical location of the culture [2].

The rice hull can absorb water in varying amounts ranging from 5% to 16% of unit weight. The unit weight of rice hull is 83-125 kg/m<sup>3</sup>. The rice hull ash (RHA) is slowly entering the industry due to its high silica content. The properties of SiO<sub>2</sub> obtained from rice hull ash change according to the calcination temperature and time [3].

The rice hull ash (RHA) is formed as a result of the burning of rice hull. RHA, which is an agricultural waste, can cause air pollution if not used correctly due to its fine particle size.

The silica present in RH is predominantly dependent on the inorganic compound. However, a small amount of this silica is covalently bonded to the organic compound. The silica bonded to the organic compound is insoluble in alkali and withstands very high temperatures. Therefore, by exposure to RH combustion, the pure silica content can be separated from the organic part of RH [4, 5]. It is known that after the organic portion of RH is separated, the remaining inorganic portion is relatively pure.

Ash obtained at lower temperatures (773–873 K) contains amorphous silica. Amorphous silica is one of the industrial white minerals used together with tile clay, CaCO<sub>3</sub> and talc, which is used as a filler in paper, paint, rubber, fertilizer and pesticides. (Amorf silika, kağıt, boya, kauçuk, gübre ve böcek ilaçlarında, dolgu maddesi olarak kullanılan çini kili, CaCO<sub>3</sub> ve talk ile birlikte kullanılan endüstriyel beyaz minerallerden biridir.) Amorphous silica with high purity, small particle size and high surface area can be used as adsorbent or catalyzer. Acid washing of rice hull ensures that the hull contains high purity SiO<sub>2</sub> and has a high specific surface area [6].

In this context, in this study, different chemical pretreatments were applied to increase the SiO<sub>2</sub> content and surface area values of RHA. In addition, calcination processes were applied at different times and temperatures.

## Material and Method

The aim of this study is to determine the suitable temperature, time and washing conditions for the calcination process of rice hull. For this, different washing solutions were used together with the calcination process carried out under different temperatures and times. The rice hull Rice Hull (RH) was provided from "Tat Bakliyat" company located in Mersin, Turkey. In this study the chemicals of sodium hydroxide (NaOH) (Isolab Co.), hydrochloric acid (HCl) (Merck Co.) and nitric acid (Merck Co.) were used. The applied temperatures and times are given in Table 1.

**Table 1.** *The temperatures and times used in the calcination process applied to RHA.*

Calcination Method	Temperature (°C)	Time (dk)	Sample Codes
Direct	600	60	D6-60
Direct	600	120	D6-120
Direct	600	240	D6-240
Direct	600	600	D6-600
Gradual	600	60	K6-60
Gradual	600	120	K6-120
Gradual	600	180	K6-180
Gradual	600	240	K6-240

As can be seen in Table 1, the calcination process was carried out in two cases, direct and gradual. The samples were kept for 60 minutes at every 100 °C temperature increase before reaching 600 °C in the gradual calcination process. After the temperature reached 600 °C, the samples were kept for the times given in Table 5.2. In the directly applied calcination process, a classical calcination process was carried out by keeping it at the temperature and time given in Table 1.

First of all, the temperature and time with the highest SiO<sub>2</sub> content were determined. Then, RHA was leached with 0.5 M HNO<sub>3</sub> and 0.5 M HCl acids to examine the effects of acid leaching on the chemical and surface area of RHA before the calcination process at the determined temperature and time.

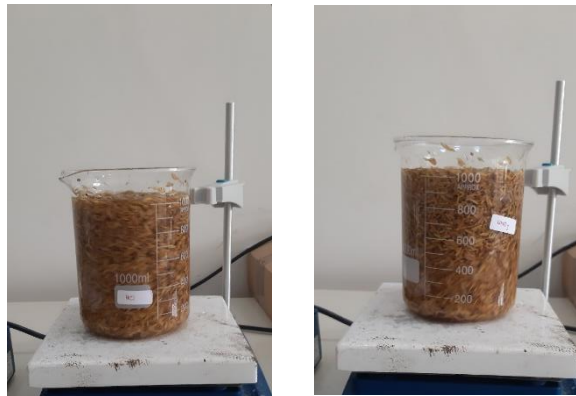


**Figure 2.** Images of rice hull treated with acid leaching (a) HCl and (b) HNO<sub>3</sub>

After the leaching process, it was gradually calcined at 600 °C for 4 hours. In order to examine the effect of acid leaching on metallic impurities and the amount of SiO<sub>2</sub>, XRF analysis was performed on the synthesized RHA samples. The result of XRF analysis is given in Table 4. In addition, the XRF result of RHA, which was washed with pure water without applying acid leaching, is given in Table 4. The flow chart of the chemical pretreatment applied to RH is given in Figure 3.

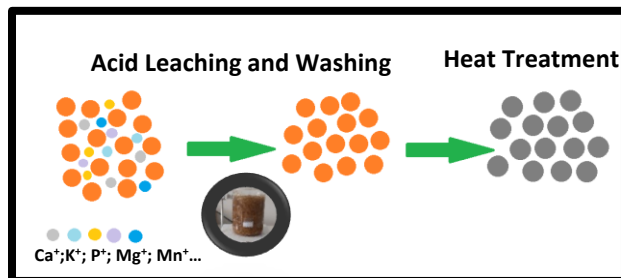


**Figure 3.** Chemical pretreatment for the production of high purity RHA.

The images of the rice hulls (RH) with acid leaching process are given in Figure 2. Pre-leaching of RH with acid or base solutions such as hydrochloric acid (HCl), nitric acid (HNO<sub>3</sub>), sulfuric acid (H<sub>2</sub>SO<sub>4</sub>) is carried out before the calcination process, which is carried out at temperatures between 500 °C and 1400 °C. Thus, most of the metallic impurities and organic substances, including hemicellulose, cellulose and lignin, are removed from the structure.

It has been proven by many researchers that HCl is the most effective leaching acid to obtain high purity amorphous silica with improved pozzolanic properties. After the RH leaching with HCl, harmful alkalis and other impurities such as aluminum oxide (Al<sub>2</sub>O<sub>3</sub>), iron (III) oxide (Fe<sub>2</sub>O<sub>3</sub>), calcium oxide (CaO), magnesium oxide (MgO) and potassium oxide (K<sub>2</sub>O) are removed from the structure [7].

### Characterization Studies

In order to examine the effect of calcination and washing processes applied to RHA; X-Ray Fluorescence Spectrometer (XRF) Rigaku ZSX Primus II, X-Ray Diffractometer (XRD) Rigaku SmartLab, Scanning Electron Microscope (SEM) and Thermo Fisher Scientific Apreo S SEM, Zeiss Supra 55 and Branuer, Emmet, and Teller (BET) Surface Area Measurement Micrometrics Surface Area and Porosity TriStar II analyzes were performed.

### Results and Discussion

In order to determine the calcination process method and time of RH with the highest SiO<sub>2</sub> content, direct and gradual heat treatments were applied at different times. The XRF analysis results for the determined times of the RHAs obtained after direct and gradual heat treatment are given in Table 3 and Table 4 respectively.

At this stage, a chemical pretreatment or washing process was not applied to the synthesized RHAs. According to the XRF analysis, it was decided to use the K6-240 sample of RHA synthesized in the next steps. Because the highest SiO<sub>2</sub> amount was determined in K6-240 sample. This sample contains 92.075% SiO<sub>2</sub>. In addition, it was determined that the amount of SiO<sub>2</sub> in all RHAs synthesized as a result of the gradual calcination process was higher than the RHAs obtained by the directly applied calcination process.

**Table 3.** XRF analysis results of RHAs obtained by direct heat treatment at different times

(% Mass)	D6-60	D6-120	D6-240	D6-600
Na <sub>2</sub> O	-	0.14	0.096	0.099
MgO	0.73	0.74	0.76	0.79
Al <sub>2</sub> O <sub>3</sub>	0.51	0.37	0.35	0.36
SiO <sub>2</sub>	84.03	85.46	90.10	89.80
P <sub>2</sub> O <sub>5</sub>	1.13	0.99	0.97	1.03
SO <sub>3</sub>	0.54	0.52	0.53	0.54
Cl	0.27	0.27	0.31	0.28
K <sub>2</sub> O	5.56	5.11	5.15	5.24
CaO	1.34	1.38	1.36	1.39
Cr <sub>2</sub> O <sub>3</sub>	-	-	-	-
MnO	-	-	0.15	0.16
Fe <sub>2</sub> O <sub>3</sub>	0.68	0.24	0.24	0.26
ZnO	0.08	0.019	0.014	0.015
A.Z	5.13	4.73	-	-

**Table 4.** XRF analysis results of RHAs obtained by gradual heat treatment at different times

(% Kütile)	K6-60	K6-120	K6-180	K6-240
Na <sub>2</sub> O	-	0.3578	0.3351	0.303
MgO	0.78	0.6277	0.6359	0.618
Al <sub>2</sub> O <sub>3</sub>	0.40	0.2365	0.2569	0.2466
SiO <sub>2</sub>	85.14	91.86	91.874	92.075
P <sub>2</sub> O <sub>5</sub>	1.03	0.5044	0.5653	0.5309
SO <sub>3</sub>	0.54	0.4618	0.4854	0.4753
Cl	0.27	0.199	0.2354	0.2092
K <sub>2</sub> O	5.02	2.9327	3.0076	2.9506
CaO	1.41	1.3307	1.4647	1.395
Cr <sub>2</sub> O <sub>3</sub>	-	0.1078	0.0685	0.0849
MnO	-	0.0694	0.0685	0.0662
Fe <sub>2</sub> O <sub>3</sub>	0.24	0.9174	0.7466	0.7884
ZnO	0.015	0.0077	0.0076	0.0074
A.Z	5.19	0.2983	0.2483	0.1829

SEM images of RH and RHA are given in Figure 4. The calcination process was applied to RH directly and gradually at different times. According to the XRF results given in Table 3 and Table 4, it was observed that the D6-600 and K6-240 coded samples had the highest SiO<sub>2</sub> content. SEM images of these samples at x500 and x1000 magnifications are given in Figure 2.

As can be seen from the SEM images given in Figure 4; According to the microstructure images given in c1 and c2, there is no obvious change in the surface morphology caused by the direct calcination process. It is seen that the SEM images given in a1 and a2 are quite similar.

However, it is seen that the gradual calcination process changes the surface morphology of RHA. In the microstructure images given in b1 and b2, it is seen that a highly porous structure has formed. The presence of the porous structure can be explained both by the nature of the original rice hull and the removal of volatile and organic elements (carbon) from the structure during the calcination process [8].

RHA, whose time and calcination method were determined for the synthesis of higher purity SiO<sub>2</sub>, was applied to the acid leaching process before being gradually calcined at 600 °C. Rice hull was leached for 24 hours with 0.5 M HNO<sub>3</sub> and 0.5 M HCl acids. After the leaching process, it was washed with distilled water until pH=7 in order to remove the acid from the rice hull.

It is clearly seen in the XRF analysis results given in Table 4 that acid leaching is an effective pre-

treatment for the removal of organic elements and metallic impurities in the waste. After leaching RH with HCl and HNO<sub>3</sub> acids, it was observed that harmful alkalis were removed from the RHA. Examples of these are impurities such as aluminum oxide (Al<sub>2</sub>O<sub>3</sub>), iron (III) oxide (Fe<sub>2</sub>O<sub>3</sub>), calcium oxide (CaO), magnesium oxide (MgO), and more importantly alkalis such as potassium oxide (K<sub>2</sub>O) and sodium (Na<sub>2</sub>O). As a result, it is seen that more pure SiO<sub>2</sub> is obtained. It has been observed that potassium in RH causes surface dissolution of RH and acts as a crystallizer for silica.

With the combustion of RH, organic substances are separated into their components and carbonization occurs and carbon is produced.

**Table 4.** XRF analysis results of RHAs that were leached and washed with pure water

Chemical Composition (%)	RHA Leached with HCl acid	RHA Leached with HNO <sub>3</sub>	RHA Washed with Pure Water
SiO <sub>2</sub>	98.53	99.18	97.57
SO <sub>3</sub>	0.399	0.0940	0.179
CaO	0.345	0.207	0.996
MgO	0.235	0.154	0.517
Na <sub>2</sub> O	0.124	0.0535	0.0452
Fe <sub>2</sub> O <sub>3</sub>	0.123	0.0618	0.1
Al <sub>2</sub> O <sub>3</sub>	0.085	0.0890	0.158
P <sub>2</sub> O <sub>5</sub>	0.0813	0.0663	0.183
K <sub>2</sub> O	0.0243	0.0183	0.168
BaO	0.0178	-	-
ZnO	0.0117	0.0136	0.0072
MnO	0.0054	0.0042	0.0449
Cl	0.0053	0.0155	0.014
Cr <sub>2</sub> O <sub>3</sub>	0.0037	0.0033	0.0037
NiO	0.0031	0.0035	0.0024
TiO <sub>2</sub>	0.0024	0.0027	0.0059
SrO	0.0022	0.0011	0.0045
Ta <sub>2</sub> O <sub>5</sub>	0.0016	-	-
CuO	0.0016	-	0.0039
PbO	0.0014	-	-

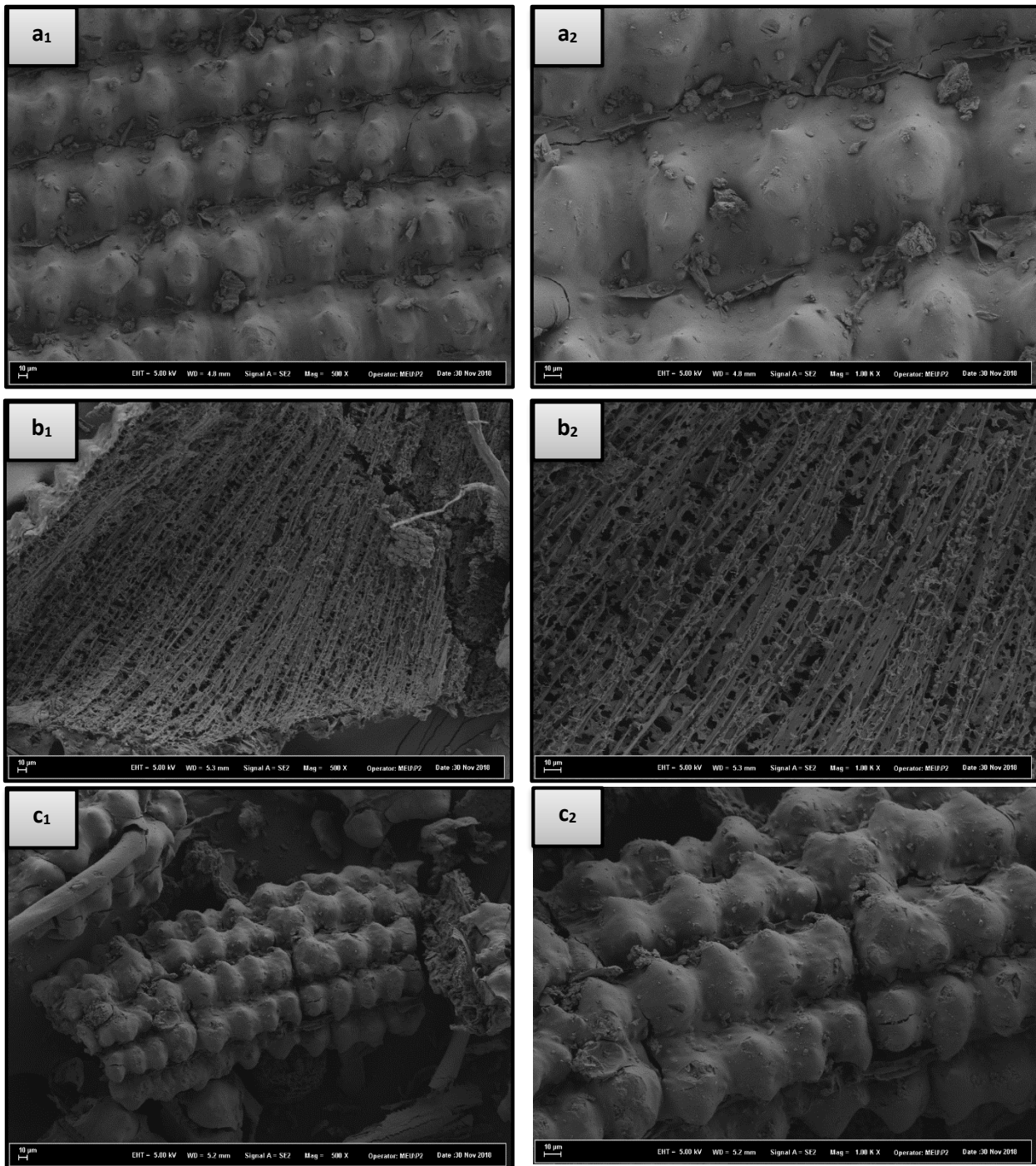


**Figure 4.** SEM images of RH and RHA **a1)** RH x500 before calcination, **a2)** RH x1000 before calcination, **b1)** K6-180 sample x500, **b2)** K6-180 sample x1000, **c1)** D6-600 sample x500, **c2)** D6- 600 samples x1000.

When the combustion temperature is constantly increased and sufficient oxygen is provided, carbon turns into carbon dioxide. When the combustion temperature is constantly increased and sufficient oxygen is provided, carbon turns into carbon dioxide. If the temperature is not sufficient for the potassium oxide ( $K_2O$ ) to be removed from the body of RH, unoxidized carbon is formed. This molten glass fraction blocks the contact surface with oxygen

and carbon dioxide and causes the crystallize of the molten surface silica. For this reason,  $K_2O$  is undesirable in the structure of the RHA [7]. According to the results of the XRF analysis given in Table 4, the  $Na_2O$  and  $K_2O$  content of the  $HNO_3$  leached RHA was 0.0535% and 0.0183%, respectively, while the  $Na_2O$  and  $K_2O$  content of the HCl leached RHA was 0.124% and 0.0243%, respectively. The amounts of  $Na_2O$  and  $K_2O$

contained in RHA washed only with pure water are 0.0452% and 0.168%, respectively. According to these results; The least amount of Na<sub>2</sub>O was seen in the washing process with distilled water, and the least amount of K<sub>2</sub>O was seen in the RHA leaching with HNO<sub>3</sub>.

Therefore, it is observed that leaching with HNO<sub>3</sub> contains higher purity SiO<sub>2</sub> compared to leaching with HCl. For this reason, it is seen that the leaching process with HNO<sub>3</sub> gives a more effective result. Figure 5 are shown the BET isotherm graphs of RHA leached with 0.5 M HNO<sub>3</sub>, 0.5M HCl acids and washed with distilled water before the calcination process. Surface area values are given in Table 5. As a result of the leaching process with HNO<sub>3</sub> and HCl acids, the BET surface area values are 264,8322 and 296,0692 m<sup>2</sup>/g, respectively. The lowest surface area was determined in RHA washed with distilled water and it was 247.9205 m<sup>2</sup>/g. Therefore, it is seen that the leaching process and acid type have a significant effect on the BET surface area. The effects of acid leaching performed in other studies on SiO<sub>2</sub> amount in RHA and BET surface area are given comparatively, in the table 6.5.

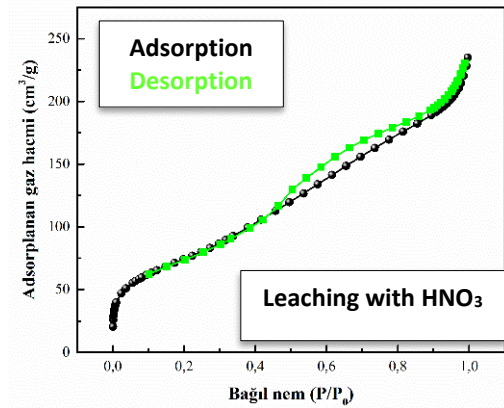


**Figure 5.** BET isotherm graphs of RHAs washed with pure water and chemically pre-treated

**Table 5.** BET surface area values of RHAs washed with pure water and chemically pre-treated

Applied Process	BET Surface Area (m <sup>2</sup> /g)
RHA leached with HNO <sub>3</sub>	264.8322
RHA leached with HCl	296.0692
RHA Washed with Distilled Water	247.9205

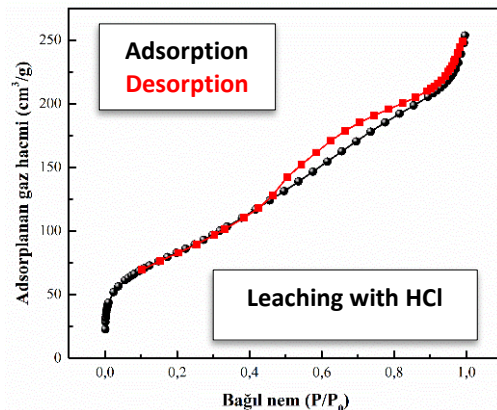
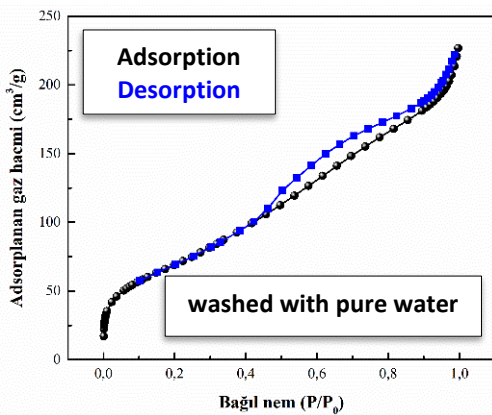


**Table 6.** The effect of acid leaching on SiO<sub>2</sub> amount and BET Surface Area in other studies.

Chemical Composition	BET surface area (m <sup>2</sup> /g)	SiO <sub>2</sub> (%)	Reference
No leaching	-	94.7	[9]
H <sub>2</sub> SO <sub>4</sub>	84.9	99.6	[9]
HCl	65.6	98.0	[9]
1-butyl-3-methylimidazole	185.1	99.5	[9]
Hydrogen sulphate (C <sub>8</sub> H <sub>16</sub> N <sub>2</sub> O <sub>4</sub> S)	70.6	98.0	[9]
No leaching	116	95.77	[10]
H <sub>2</sub> SO <sub>4</sub>	208	99.08	[10]
HCl	218	99.58	[10]
HCl	247.18	-	[11]
No leaching	-	97.25	[12]
Citric acid	-	99.5-	[12]
HNO <sub>3</sub>	264.8322	99.13	Present Study
HCl	296.0692	98.53	Present Study
No leaching	247.9205	97.57	Present Study

In this study, as seen in Table 6, the highest BET surface area value was obtained by leaching with the HCl. The presence of metallic impurities during the calcination process causes the formation of crystalline silica and thus a significant reduction in the surface area occurs. However, BET surface area values were higher in chemically pre-treated RHA since metal impurities were successfully removed from the structure. In addition, it is seen in this study that the highest amount of SiO<sub>2</sub> was obtained in the sample made with the HNO<sub>3</sub> leaching process.

These results indicate that chemical pretreatments are required to obtain silica with higher purity, higher surface area and partially/completely reduce metallic impurities rather than direct combustion.

According to XRF and BET surface area analysis, the highest SiO<sub>2</sub> content and the highest surface area value were obtained by leaching with 0.5 M HNO<sub>3</sub> and 0.5 M HCl, respectively. As a result of leaching with 0.5M HNO<sub>3</sub> and 0.5M HCl, a silica content difference of 0.6% was observed. However, according to the BET surface area analysis, the difference between the surface areas was higher. Therefore, the leaching with HCl was thought to be more effective than the leaching with HNO<sub>3</sub>. Figure 6 shows the SEM and XRD results of RHA leached with 0.5 M HCl.

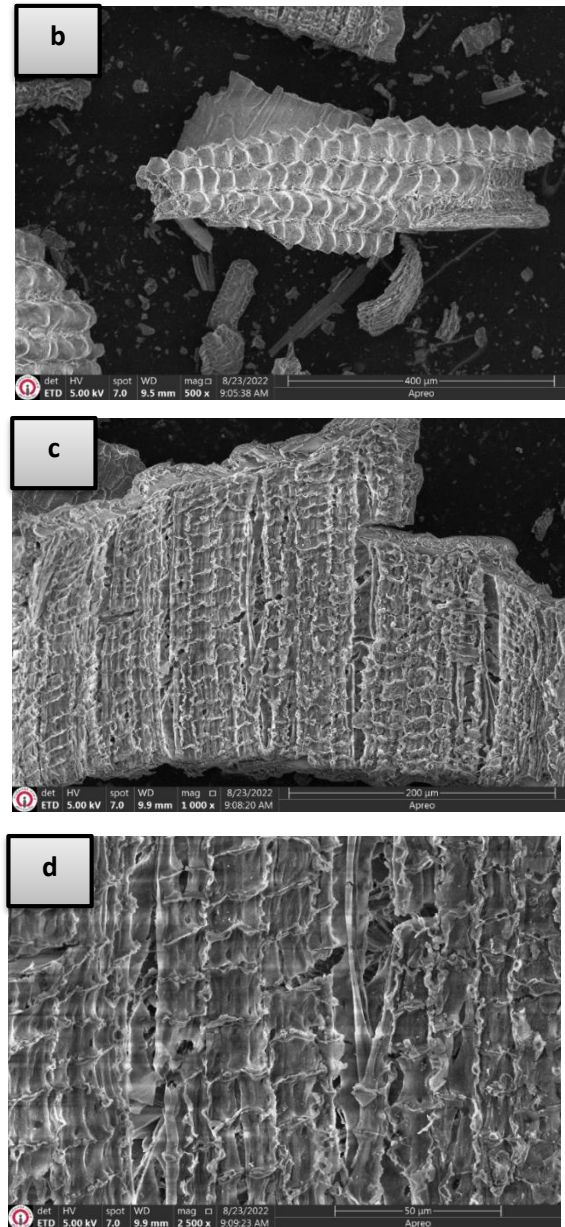
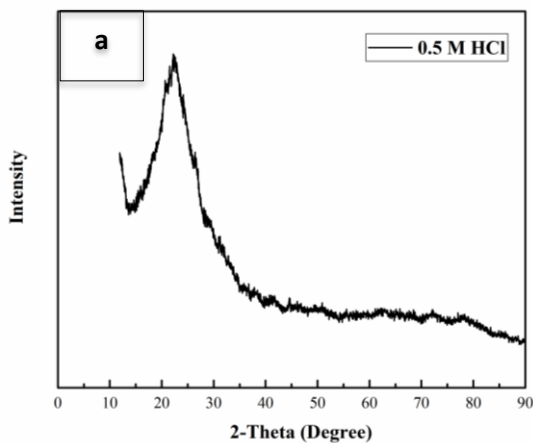


**Figure 6. (a)** XRD pattern of RHA, and SEM images of RHA leached with 0.5 M HCl at different magnifications **(b)** x500, **(c)** x1000 and **(d)** x1500

According to the XRD result given in Figure 6, it has been observed that the RHA obtained by chemical pretreatment with HCl has an amorphous structure. The peak point at  $2\theta=22^\circ$  indicates that only amorphous silica is formed [13]. According to the SEM image given in Figure 6, it was observed that the indentations in the outer shell of the leached RHA were smaller and angular compared to the non-leaching RHA. In addition to all these, it was observed that the leached RHA had larger pores.

Leaching process was carried out using 0.5 M HCl and HNO<sub>3</sub> chemicals. At this stage, it is aimed to remove metallic impurities from the structure before the calcination process. As a result, it was considered to obtain RHA synthesis with higher purity and silica content. For this, the K6-240 sample

was leached using HCl and HNO<sub>3</sub> chemicals. Characterization studies were carried out with SEM, XRF and BET surface area analyzes. According to the results of XRF analysis, the highest SiO<sub>2</sub> content and the highest BET surface area value were obtained as a result of leaching with 0.5 M HNO<sub>3</sub> and 0.5 HCl, respectively. This study showed that chemical pretreatments are necessary to obtain silica with high purity and high surface area. In addition, it has been observed that chemical pretreatments are necessary to remove metallic impurities. As a result of the pretreatment, the silica content of RHA increased from %92.075 to %99.13 and the BET surface area value increased from 247.9205 m<sup>2</sup>/g to 296.0692 m<sup>2</sup>/g.

## Conclusion

### References

1. S. A. Miller, P. R. Cunningham, J.T. Harvey, Rice-based ash in concrete: A review of past work and potential environmental sustainability, *Resour Conserv Recycl*, 146 (2019), pp. 416-430, [10.1016/j.resconrec.2019.03.041](https://doi.org/10.1016/j.resconrec.2019.03.041)
2. B. MistryBhavna, Properties and industrial applications of rice husk, *From the Desk of Editors*, 4 (2015), pp. 7-11
3. N. Phonphuak, P. Chindaprasirt, Types of waste, properties, and durability of pore-forming waste-based fired masonry bricks, *Eco-efficient masonry bricks and blocks*, (2015), pp. 103-127, [10.1016/B978-1-78242-305-8.00006-1](https://doi.org/10.1016/B978-1-78242-305-8.00006-1)
4. W. H. Kwan, Y. S. Wong, Acid leached rice husk ash (ARHA) in concrete: A review, *Mater Sci Energy Technol*, 3 (2020), pp. 501-507, [10.1016/j.mset.2020.05.001](https://doi.org/10.1016/j.mset.2020.05.001)
5. R. Prasad, M. Pandey, Rice husk ash as a renewable source for the production of value added silica gel and its application: an overview, *Bull Chem React*, 7.1 (2012), pp. 1-25, <http://bcrec.undip.ac.id>
6. Q. Feng et al., Study on the pozzolanic properties of rice husk ash by hydrochloric acid pretreatment, *Cem Concr Res*, 34.3 (2004), pp. 521-526, [10.1016/j.cemconres.2003.09.005](https://doi.org/10.1016/j.cemconres.2003.09.005)
7. J. M. Riego, Z. Sedin, J. Zaldívar, N. C. Marziano, C. Tortato, Sulfuric acid on silica-gel: an inexpensive catalyst for aromatic nitration, *Tetrahedron Lett*, 37.4 (1996), pp. 513-516, [10.1016/0040-4039\(95\)02174-4](https://doi.org/10.1016/0040-4039(95)02174-4)
8. F. Andreola, L. Luisa, L. Isabella, The environmental friendly route to obtain sodium silicate solution from rice husk ash: a comparative study with commercial silicates deflocculating agents, *Waste Biomass Valorization*, 11.11 (2020), pp. 6295-6305, [10.1007/s12649-019-00849-w](https://doi.org/10.1007/s12649-019-00849-w).pdf
9. J. H. Lee, J. H. Kwon, J. W. Lee, H. S. Lee, J. H. Chang, J. H., B. I. Sang, Preparation of high purity silica originated from rice husks by chemically removing metallic impurities, *J Ind Eng Chem*, 50 (2017), pp. 79-85, [10.1016/j.jiec.2017.01.033](https://doi.org/10.1016/j.jiec.2017.01.033)
10. R.A. Bakar, Y. Rosiyah, S.N. Gan, Production of high purity amorphous silica from rice husk, *Procedia chem*, 19 (2016), pp. 189-195, [10.1016/j.proche.2016.03.092](https://doi.org/10.1016/j.proche.2016.03.092)
11. S. Sankar, S.K. Sharma, N. Kaur, B. Lee, D.Y. Kim, S. Lee, H. Jung, Biogenerated silica nanoparticles synthesized from sticky, red, and brown rice husk ashes by a chemical method, *Ceram Int*, 42.4 (2016), pp. 4875-4885, [10.1016/j.ceramint.2015.11.172](https://doi.org/10.1016/j.ceramint.2015.11.172)
12. J. Umeda, K. Kondoh, High-purification of amorphous silica originated from rice husks by combination of polysaccharide hydrolysis and metallic impurities removal, *Ind Crops Prod*, 32.3 (2010), pp. 539-544.
13. L. Usgodaarachchi, C. Thambiliyagodage, R. Wijesekera, M. G. Bakker, Synthesis of mesoporous silica nanoparticles derived from rice husk and surface-controlled amine functionalization for efficient adsorption of methylene blue from aqueous solution. *Current Research in Green and Sustainable Chemistry*, 4 (2021), pp. 100116, [10.1016/j.crgsc.2021.100116](https://doi.org/10.1016/j.crgsc.2021.100116)

## Synthesis of Three-Dimensional Graphene Coated, Molybdenum Loaded Electrode as Microbial Fuel Cell Anode

*Habib Akyazi*

Gazi Üniversitesi- Kimya Mühendisliği Bölümü, 06570, Ankara, Türkiye, hakyazi@ankara.edu.tr  
ORCID: 0000-0002-3512-0438

*Çiğdem Güldür*

Gazi Üniversitesi- Kimya Mühendisliği Bölümü, 06570, Ankara, Türkiye, cguldur@gazi.edu.tr  
ORCID: 0000-0002-4404-6882

*Cite this paper as: Akyazi, H., Güldür, Ç. Synthesis of Three-Dimensional Graphene Coated, Molybdenum Loaded Electrode as Microbial Fuel Cell Anode. Int. Conf. Advanced. Mater. Sci. & Eng. HiTech. and Device Appl. Oct. 27-29 2022, Ankara, Turkey*

**Abstract.** Microbial fuel cells (MFCs) are chemical reactors that can convert the chemical energy stored in the bonds of organic compounds into electrical energy through the catalytic reactions of microorganisms in an anaerobic environment. With these cells, while electrical energy is produced, waste water treatment can be done simultaneously. The wastewater treatment systems used today are quite costly. For this reason, it is necessary to use MFC systems, which consume less energy, do not produce sludge and provide efficiency by using the energy they produce, as a wastewater treatment process and improve their performance. In this study, anode electrodes were synthesized with different synthesis methods in order to be used at the anode cell, which is a defining element of Microbial Fuel Cells (MFC), and the most suitable method for the synthesis process was determined. For this purpose, first a three-dimensional graphene foam with a macroporous structure (250-500  $\mu\text{m}$ ) was synthesized. Then, different molybdenum (Mo) loading methods were studied to increase the adhesion of electroactive species to the surface. In total, seven samples were prepared and the characterization of the samples was made with EDS analysis and SEM images. According to the data obtained, it was concluded that the best result was in the NK/rGO/Mo/EG sample loaded with 84.39% molybdenum.

**Keywords:** Microbial Fuel Cell, Anode Electrode Synthesis Graphene Synthesis, Molybdenum Loading

© 2022 Published by ICMATSE

### 1. INTRODUCTION

Microbial fuel cells (MFCs) are defined as chemical reactors which can convert the chemical energy stored within the chemical bonds in organic compounds to electrical energy using catalytic reactions of microorganisms in anaerobic conditions [1–10]. By using microbial fuel cells, electrical energy generation and wastewater treatment can be achieved simultaneously [3,11–20]. As a result of chemical decomposition of organic material by microorganisms, electrons and protons are generated along with carbon dioxide and water at the anode [21–25]. Electrons absorbed by the anode and the protons are transferred to the cathode through electrical circuit and the electrolyte solution, respectively [6,26–29]. As a consequence, the oxygen reduction reaction is completed at the cathode by consumption of the electrons and protons [27,30,31]. MFCs are advantageous compared with the conventional treatment processes, because conventional processes typically use aerobic

microorganisms and the wastewater needs to be aerated on a regular basis for the continuation of their biological activities [29,32,33]. This process considerably increases the cost of treatment [34,35]. Also, these processes generate waste sludge [19,36], which is difficult to be disposed of due to environmental and political factors [35,37]. Therefore, applications of MFC systems which require less energy, generate no sludge and provide energy efficiency by using the generated electrical energy as a wastewater treatment process has a great importance [19,35,38]. These systems should be further developed as a contributor to the national economy, in order to reduce the cost of currently used wastewater treatment processes and to benefit from, or reduce the harmful environmental effects of the municipal wastewaters which have great energy potential in terms of biologically decomposable organic matter (biomass) [17,35]. In this study, anode electrodes were synthesized to improve the anode cell performance which is a definitive element of the MFC technology. The

material used at the anode directly affects the accumulation of microorganisms at the anode, oxidation of the substrate and the transfer of electrons [39–41]. Therefore, anode electrode were prepared by synthesizing three dimensional and macroporous (250-500  $\mu\text{m}$ ) graphene foam and by depositing molybdenum (Mo) on the graphen foam to increase the accumulation of the electroactive species on the surface [42], with the aim of developing a bio-compatible anode material with high electrical conductivity and a suitable porous medium facilitating the growth and accumulation of microorganisms [43,44]. In the synthesis of graphene foam, graphite oxide will be reduced to graphene oxide on three dimensional nickel foam, generating multiple conductive paths will be generated at the anode thanks to the macroporous network [5,45,46]. Consequently, development of microbial colonization, efficient electron transfer and ion diffusion, and thanks to multimodal porous structure, prevention of the detachment of electroactive bacteria will be possible [47,48]. In the next phase of the anode electrode preparation, the as-synthesized graphene foam was loaded by molybdenum (Mo) nanoparticles for the electroactive species to form a robust biofilm layer on the anode surface [42]. For this purpose, different molybdenum (Mo) loading methods were studied to increase the adhesion of electroactive species to the surface [49–51]. In total, seven samples were prepared and the characterization of the samples was made with EDS analysis and SEM images.

## 2. MATERIALS AND METHOD

### 2.1. Anode Electrode Synthesis

Since different graphene and molybdenum loading methods are used in the literature for anode electrode synthesis, studies were carried out on the determination of the loading method in this study. Graphene loadings on nickel foam were loaded with the Hummers method used by Wang et al., (2013) [5] and the effect of hydrogen ( $\text{H}_2$ ) gas on molybdenum loading was also investigated. Ethylene Glycol (EG) was used as a dispersing agent in some studies in molybdenum loadings [49,50], while EG was not used in some studies [52]. In our study, two different loading methods were used to determine which method was better, and it was concluded that the loadings made using EG loaded higher Mo and the surface morphology was more homogeneous. All of the syntheses were made using the hydrothermal synthesis method and 80% of the autoclave volume was filled with solution [53]. In our study, seven different anode electrode samples were prepared

and the prepared samples were characterized. The syntheses of the mentioned anode electrode samples are given in Figure 1.

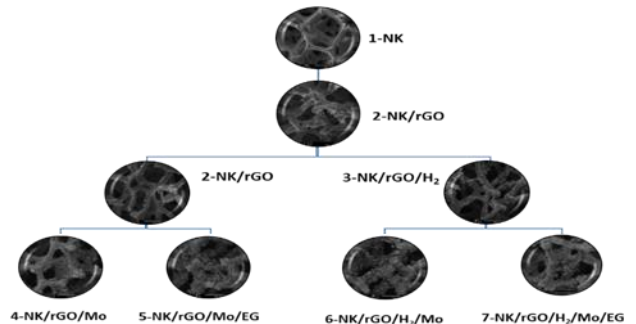


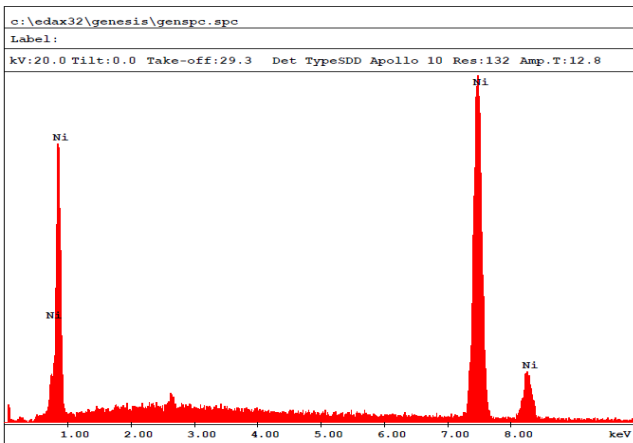
**Figure 1.** Anode Electrode Synthesis Steps

Here, nickel foam treated as sample number 1, sample number 2; GO reduced nickel foam (NK/rGO), sample 3; By passing  $\text{H}_2$  gas at 400  $^\circ\text{C}$  over GO reduced nickel foam (NK/rGO/ $\text{H}_2$ ), sample number 4; By loading Mo on sample number 2 (NK/rGO/Mo), sample number 5; By adding Mo salt and EG on sample number 2 (NK/rGO/Mo/EG), sample number 6; By loading Mo on the 3rd sample (NK/rGO/ $\text{H}_2$ /Mo) and the 7th sample; It was synthesized by adding Mo salt and EG (NK/rGO/ $\text{H}_2$ /Mo/EG) to the sample number 3, and in the final stage, samples 4, 5, 6 and 7 were prepared by heat treatment with Argon gas at 500  $^\circ\text{C}$  in a horizontal furnace for 2 hours.

## 3. RESULTS AND DISCUSSION

The anode material is one of the critical materials affecting the performance of MFCs, and the pore size is essential for the growth of bacteria at the anode. Three-dimensional macroporous graphene has a large surface area due to its structure and this feature facilitates the adhesion of electroactive bacteria species on the surface. Therefore, in this study, three-dimensional macroporous (250-500  $\mu\text{m}$ ) graphene foam was synthesized as the anode material since its surface structure is suitable for the adhesion of bacteria, has high electrical conductivity, and can easily transfer the electrons produced by bacteria. Characterization of the samples was made with EDS analysis and Scanning Electron Microscope (SEM) images. The abundance of Mo element in the samples was determined by EDS analysis and the suitability of the synthesis was checked. Micro-scale imaging of the samples was performed with SEM images. The morphology and texture of the samples were examined in the images, and the state of coating the nickel foam with graphene and the loading state of Mo nanoparticles on the surface were examined. The EDS analyzes of the synthesized samples are given in Figure 2-6, and the SEM images are given in Figure 7-13. EDS analysis only shows the abundance of metals.

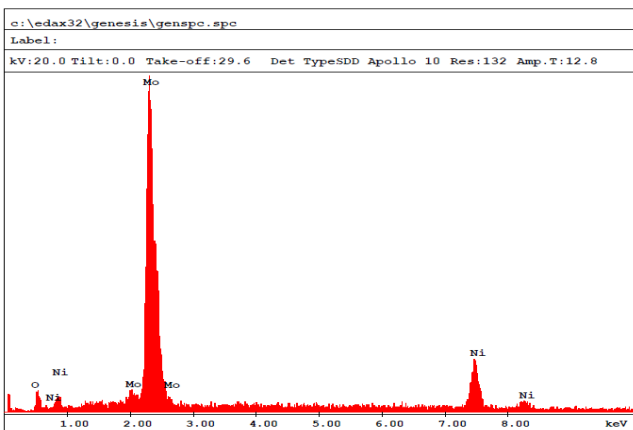
Therefore, molybdenum loading is not observed in the 1st, 2nd and 3rd (Figure 2) samples, which were not loaded with Mo. When the EDS analysis Sample 4 (NK/rGO/Mo-Figure 3), Sample 5 (NK/rGO/Mo/EG-Figure 4), Sample 6 (NK/rGO/H<sub>2</sub>/Mo-Figure 5), and Sample 7 (NK/rGO/H<sub>2</sub>/Mo/EG-Figure 6) were examined, it was observed that 75.57%, 84.39%, 76.18% and 83.37% Mo by mass were loaded on the graphene-coated Nickel Foam, respectively. Based on these results, it was concluded that the best Mo loading method was the path followed for the synthesis of sample 5.



EDAX ZAF Quantification (Standardless)  
Element Normalized  
SEC Table : Default

Element	Wt %	At %	Z	A	F
NiK	100.00	100.00	1.0000	1.0000	1.0000
Total	100.00	100.00			

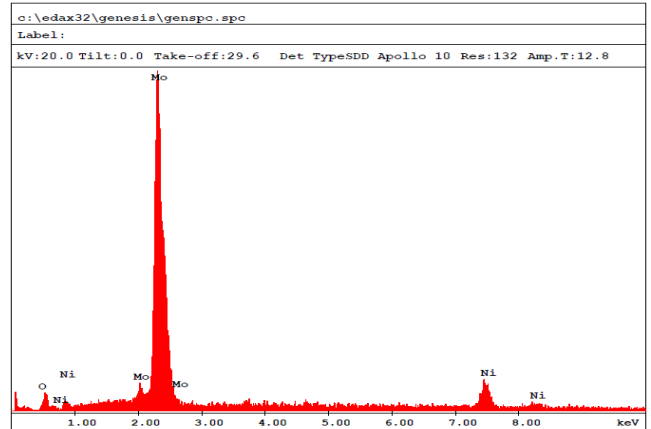
**Figure 2. Nickel Foam EDS Analysis**



EDAX ZAF Quantification (Standardless)  
Element Normalized  
SEC Table : Default

Element	Wt %	At %	Z	A	F
MoL	75.57	65.44	0.9678	0.9037	1.0000
NiK	24.43	34.56	1.0930	0.9545	1.0000
Total	100.00	100.00			

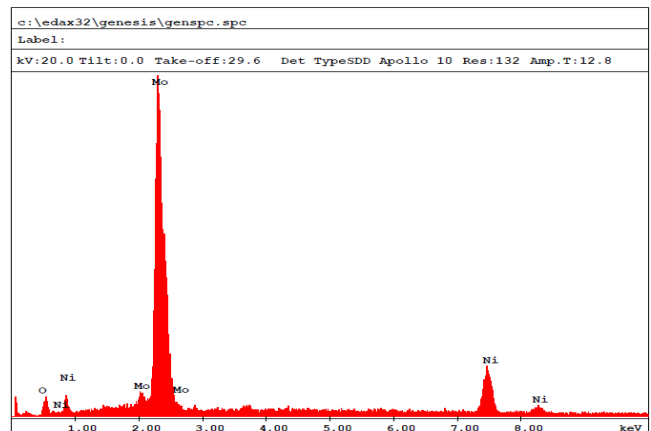
**Figure 3. NK/rGO/Mo EDS Analysis**



EDAX ZAF Quantification (Standardless)  
Element Normalized  
SEC Table : Default

Element	Wt %	At %	Z	A	F
MoL	84.39	76.78	0.9791	0.9369	1.0000
NiK	15.61	23.22	1.1056	0.9492	1.0000
Total	100.00	100.00			

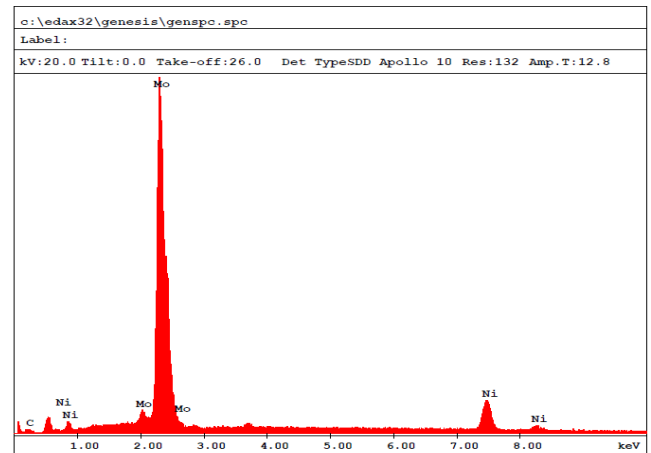
**Figure 4. NK/rGO/Mo/EG EDS Analysis**



EDAX ZAF Quantification (Standardless)  
Element Normalized  
SEC Table : Default

Element	Wt %	At %	Z	A	F
MoL	76.18	66.18	0.9686	0.9059	1.0000
NiK	23.82	33.82	1.0939	0.9541	1.0000
Total	100.00	100.00			

**Figure 5. NK/rGO/H<sub>2</sub>/Mo EDS Analysis**



EDAX ZAF Quantification (Standardless)  
Element Normalized  
SEC Table : Default

Element	Wt %	At %	Z	A	F
MoL	83.37	75.42	0.9778	0.9264	1.0000
NiK	16.63	24.58	1.1042	0.9439	1.0000
Total	100.00	100.00			

**Figure 6. NK/rGO/H<sub>2</sub>/Mo/EG EDS Analysis**

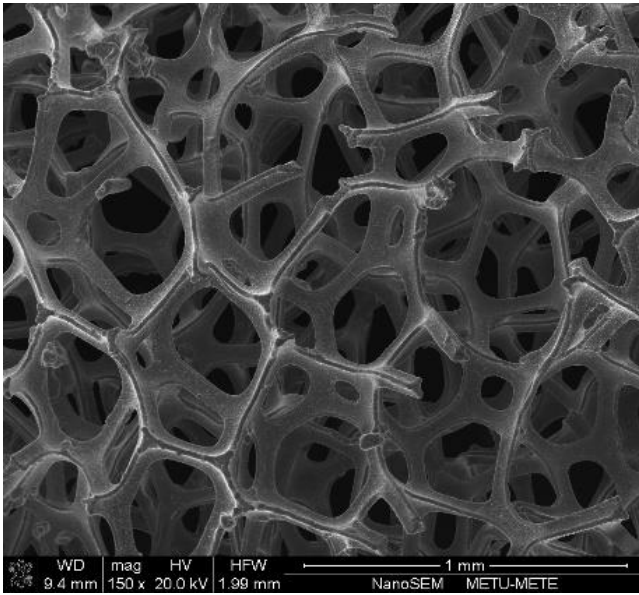


**Figure 7. Nickel Foam SEM Image (1 mm)**

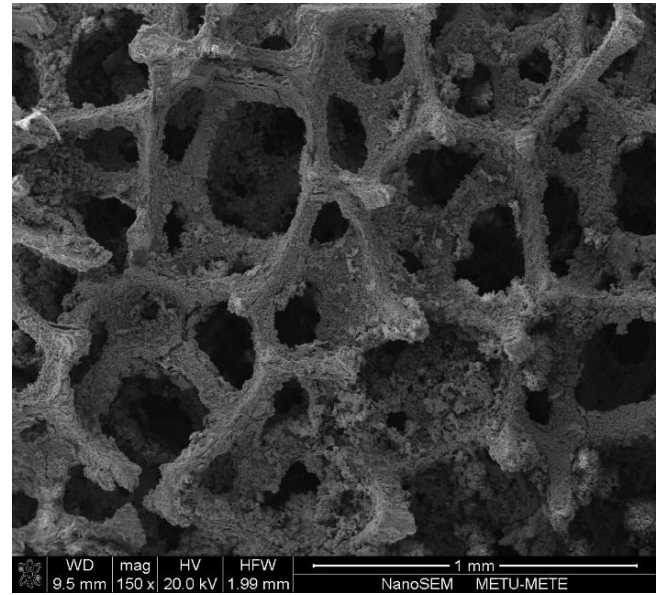


**Figure 10. NK/rGO/Mo SEM Image (1 mm)**

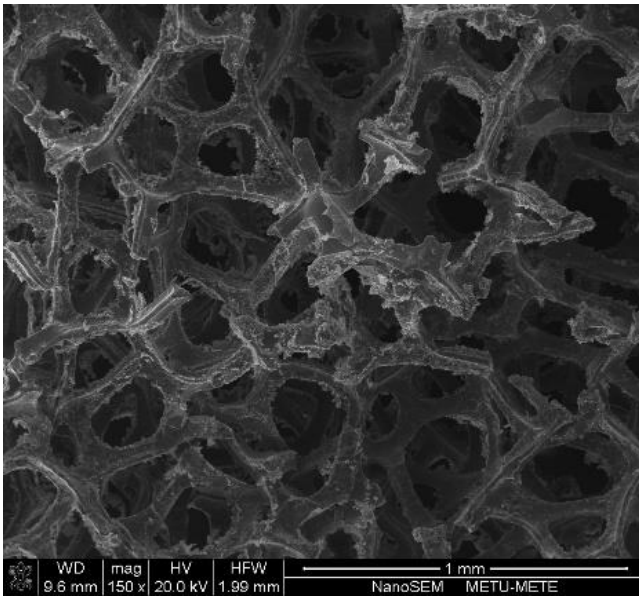


**Figure 8. NK/rGO SEM Image (1 mm)**

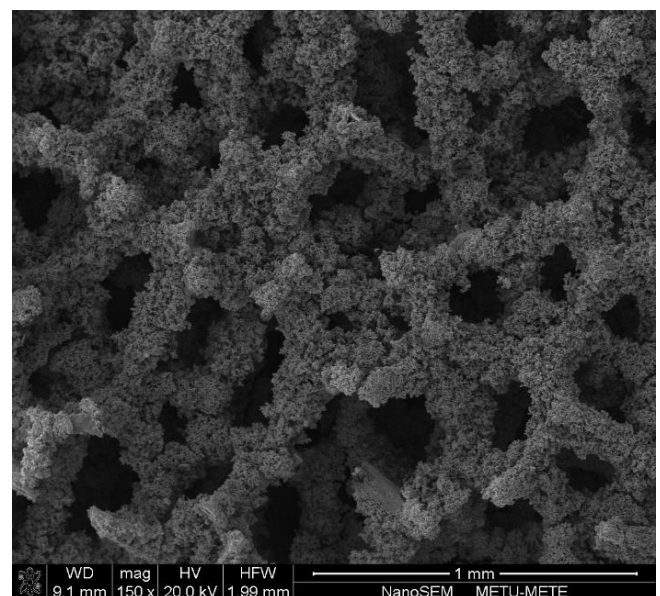


**Figure 11. NK/rGO/Mo/EG SEM Image (1 mm)**

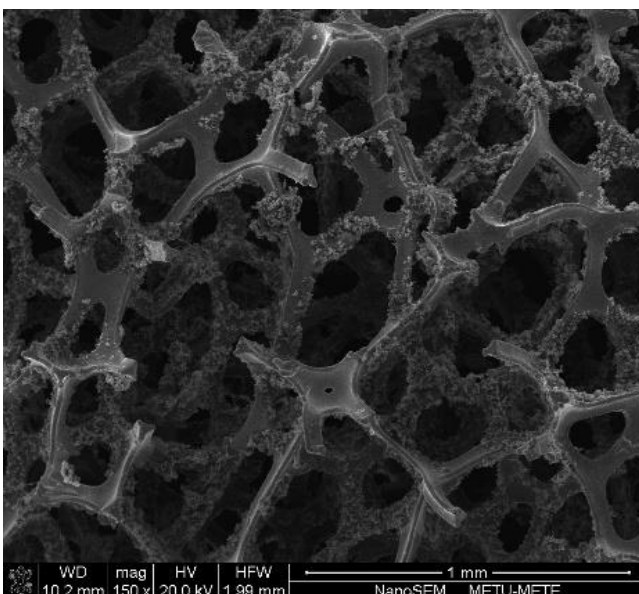


**Figure 9. NK/rGO/H<sub>2</sub> SEM Image (1 mm)**

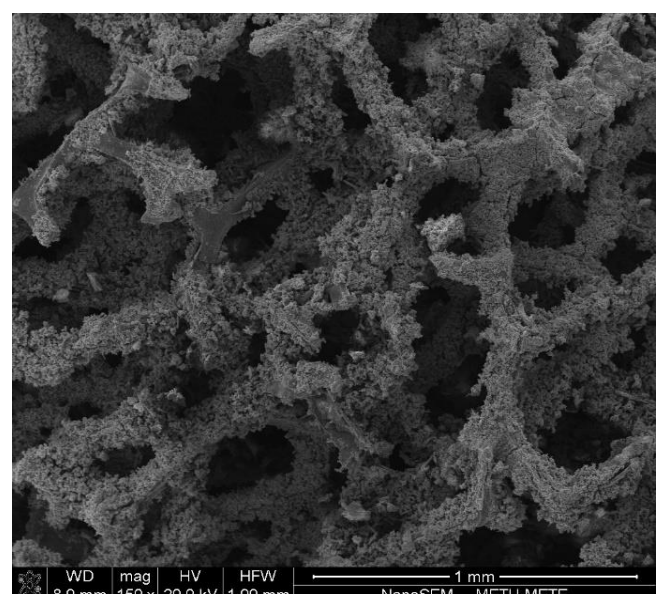


**Figure 12. NK/rGO/H<sub>2</sub>/Mo SEM Image (1 mm)**

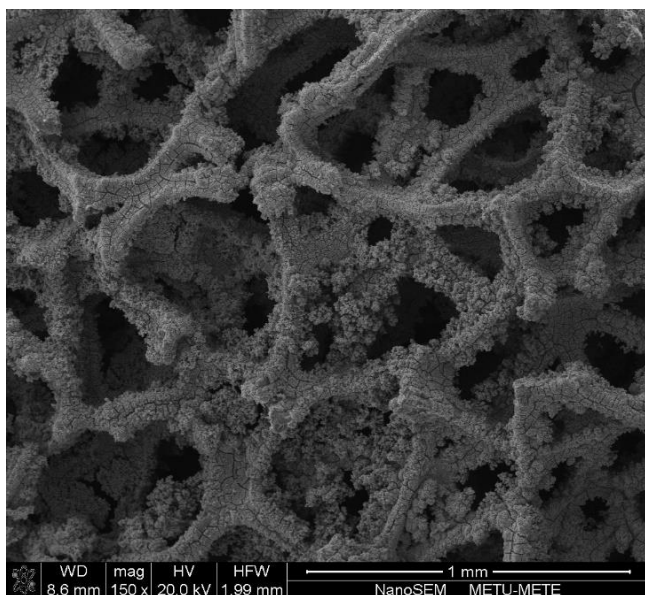


**Figure 13.** NK/rGO/H<sub>2</sub>/Mo/EG SEM Image (1 mm)

#### 4. CONCLUSION

The selection of the anode electrode and the material from which it is produced is the most critical issue in MFC performance. According to the literature review, graphene-coated three-dimensional and macroporous anode materials are suitable electrodes for MFCs as they are biocompatible for microorganisms and facilitate the transfer of electrons. In our study, seven samples were prepared to determine the experimental method to be followed in the synthesis of the anode electrode. When the EDS analyzes and SEM images of the prepared samples are examined in terms of Mo loading; It is seen that in the samples 5 and 7 using Ethylene Glycol (EG), more efficiency is obtained than the samples that are not used, and the best result is in the sample number 5, in which 84.39% molybdenum is loaded. In addition, when the SEM images of the samples are examined, it can be concluded that the most homogeneous surface morphology is in the 5th sample.

#### REFERENCES

1. Wang H, Ren ZJ. A comprehensive review of microbial electrochemical systems as a platform technology. *Biotechnol. Adv.* [Internet]. 31(8), 1796–1807 (2013). Available from: <http://dx.doi.org/10.1016/j.biotechadv.2013.10.001>.
2. Zhou M, Chi M, Luo J, He H, Jin T. An overview of electrode materials in microbial fuel cells. *J. Power Sources* [Internet]. 196(10), 4427–4435 (2011). Available from: <http://dx.doi.org/10.1016/j.jpowsour.2011.01.012>.
3. Du Z, Li H, Gu T. A state of the art review on microbial fuel cells: A promising technology for wastewater treatment and bioenergy. *Biotechnol. Adv.* 25(5), 464–482 (2007).
4. Guo K, Hassett DJ, Gu T. Microbial fuel cells: Electricity generation from organic wastes by microbes. .
5. Wang H, Wang G, Ling Y, *et al.* High power density microbial fuel cell with flexible 3D graphene-nickel foam as anode. *Nanoscale.* 5(21), 10283–10290 (2013).
6. Bruce E. Logan, Bert Hamelers, René Rozendal, Uwe Shroder, Jurg Keller, Stefano Freguia, Peter Aelterman WV and KR. Critical Review Microbial Fuel Cells : Methodology and Technology. *Environ. Sci. Technol.* [Internet]. 40(17), 5181–5192 (2006). Available from: <http://pubs.acs.org/doi/abs/10.1021/es0605016>.
7. Schröder U. Anodic electron transfer mechanisms in microbial fuel cells and their energy efficiency. *Phys. Chem. Chem. Phys.* 9(21), 2619–2629 (2007).
8. Jiawei Y, Shaoan C. Effects of using anode biofilm and cathode biofilm bacteria as inoculum on the start-up, electricity generation, and microbial community of air-cathode single-chamber microbial fuel cells. *Polish J. Environ. Stud.* 28(2), 693–700 (2019).
9. Aldrovandi A, Marsili E, Stante L, Paganin P, Tabacchioni S, Giordano A. Sustainable power production in a membrane-less and mediator-less synthetic wastewater microbial fuel cell. *Bioresour. Technol.* [Internet]. 100(13), 3252–3260 (2009). Available from: <http://dx.doi.org/10.1016/j.biortech.2009.01.041>.
10. Tee PF, Abdullah MO, Tan IAW, Amin MAM, Nolasco-Hipolito C, Bujang K. Effects of temperature on wastewater treatment in an affordable microbial fuel cell-adsorption hybrid system. *J. Environ. Chem. Eng.* [Internet]. 5(1), 178–188 (2017). Available from: <http://dx.doi.org/10.1016/j.jece.2016.11.040>.
11. Jorge AB, Hazael R. Use of *Shewanella oneidensis* for Energy Conversion in Microbial Fuel Cells. *Macromol. Chem. Phys.* 217(13), 1431–1438 (2016).
12. Hu J, Zhang Q, Lee DJ, Ngo HH. Feasible use of microbial fuel cells for pollution treatment. *Renew. Energy* [Internet]. 129, 824–829 (2018). Available from: <https://doi.org/10.1016/j.renew.2017.02.001>.
13. Lorenzo M Di, Scott K, Curtis TP, Head IM. Effect of increasing anode surface area on the performance of a single chamber microbial fuel cell. 156, 40–48 (2010).
14. Karuppiah T, Pugazhendi A, Subramanian S, Jamal MT, Jeyakumar RB. Deriving electricity from dye processing wastewater using single chamber microbial fuel cell with carbon brush anode and platinum nano coated air cathode. *3 Biotech* [Internet]. 8(10), 0 (2018). Available from: <http://dx.doi.org/10.1007/s13205-018-1462-1>.
15. Gude VG. Wastewater treatment in microbial fuel cells - An overview. *J. Clean. Prod.* [Internet]. 122, 287–307 (2016). Available from: <http://dx.doi.org/10.1016/j.jclepro.2016.02.022>.

16. Sevda S, Dominguez-Benetton X, Vanbroekhoven K, De Wever H, Sreerishnan TR, Pant D. High strength wastewater treatment accompanied by power generation using air cathode microbial fuel cell. *Appl. Energy* [Internet]. 105, 194–206 (2013). Available from: <http://dx.doi.org/10.1016/j.apenergy.2012.12.037>.
17. Liu H, Ramnarayanan R, Logan BE. Production of Electricity during Wastewater Treatment Using a Single Chamber Microbial Fuel Cell. *Environ. Sci. Technol.* 38 (7), 2281–2285 (2004).
18. Daniel DK, Das Mankidy B, Ambarish K, Manogari R. Construction and operation of a microbial fuel cell for electricity generation from wastewater. *Int. J. Hydrogen Energy* [Internet]. 34(17), 7555–7560 (2009). Available from: <http://dx.doi.org/10.1016/j.ijhydene.2009.06.012>.
19. Asai Y, Miyahara M, Kouzuma A, Watanabe K. Comparative evaluation of wastewater-treatment microbial fuel cells in terms of organics removal, waste-sludge production, and electricity generation. *Bioresour. Bioprocess.* 4(1) (2017).
20. Ahn Y, Logan BE. Domestic wastewater treatment using multi-electrode continuous flow MFCs with a separator electrode assembly design. *Appl. Microbiol. Biotechnol.* 97(1), 409–416 (2013).
21. Wang H, Qian F, Li Y. Solar-assisted microbial fuel cells for bioelectricity and chemical fuel generation. *Nano Energy* [Internet]. 8, 264–273 (2014). Available from: <http://dx.doi.org/10.1016/j.nanoen.2014.06.004>.
22. Santoro C, Agrios A, Pasaogullari U, Li B. Effects of gas diffusion layer (GDL) and micro porous layer (MPL) on cathode performance in microbial fuel cells (MFCs). *Int. J. Hydrogen Energy* [Internet]. 36(20), 13096–13104 (2011). Available from: <http://dx.doi.org/10.1016/j.ijhydene.2011.07.030>.
23. Rahimnejad M, Adhami A, Darvari S, Zirepour A, Oh SE. Microbial fuel cell as new technology for bioelectricity generation: A review. *Alexandria Eng. J.* [Internet]. 54(3), 745–756 (2015). Available from: <http://dx.doi.org/10.1016/j.aej.2015.03.031>.
24. Jiang D, Curtis M, Troop E, et al. A pilot-scale study on utilizing multi-anode/cathode microbial fuel cells (MAC MFCs) to enhance the power production in wastewater treatment. *Int. J. Hydrogen Energy* [Internet]. 36(1), 876–884 (2011). Available from: <http://dx.doi.org/10.1016/j.ijhydene.2010.08.074>.
25. Erable B, Duțeanua NM, Ghangrekar MM, Dumas C, Scott K. Application of electro-active biofilms. *Biofouling.* 26(1), 57–71 (2010).
26. Zhang Y. Energy Recovery from Waste Streams with Microbial Fuel Cell (MFC)-based Technologies. .
27. Fan Y, Hu H, Liu H. Enhanced Coulombic efficiency and power density of air-cathode microbial fuel cells with an improved cell configuration. *J. Power Sources.* 171(2), 348–354 (2007).
28. Liu H, Cheng S, Logan BE. Production of electricity from acetate or butyrate using a single-chamber microbial fuel cell. *Environ. Sci. Technol.* 39(2), 658–662 (2005).
29. Watanabe K. Recent Developments in Microbial Fuel Cell Technologies for Sustainable Bioenergy. *J. Biosci. Bioeng.* [Internet]. 106(6), 528–536 (2008). Available from: <http://dx.doi.org/10.1263/jbb.106.528>.
30. Prathiba S, Kumar PS, Vo D-VN. Recent advancements in microbial fuel cells: A review on its electron transfer mechanisms, microbial community, types of substrates and design for bio-electrochemical treatment. *Chemosphere* [Internet]. 286(P3), 131856 (2021). Available from: <https://doi.org/10.1016/j.chemosphere.2021.131856>.
31. Chen J, Hu Y, Zhang L, Huang W, Sun J. Bacterial community shift and improved performance induced by in situ preparing dual graphene modified bioelectrode in microbial fuel cell. *Bioresour. Technol.* [Internet]. 238, 273–280 (2017). Available from: <http://dx.doi.org/10.1016/j.biortech.2017.04.044>.
32. Arceivala SJ, Asolekar SR. Wastewater Treatment for Pollution Control. .
33. Rosso D, Larson LE, Stenstrom MK. Aeration of large-scale municipal wastewater treatment plants: State of the art. *Water Sci. Technol.* 57(7), 973–978 (2008).
34. Mizuta K, Shimada M. Benchmarking energy consumption in municipal wastewater treatment plants in Japan. *Water Sci. Technol.* 62(10), 2256–2262 (2010).
35. Li WW, Yu HQ, He Z. Towards sustainable wastewater treatment by using microbial fuel cells-centered technologies. *Energy Environ. Sci.* 7(3), 911–924 (2014).
36. HALL JE. Sewage Sludge Production, Treatment and Disposal in the European Union. *Water Environ. J.* 9(4), 335–343 (1995).
37. Trapero JR, Horcajada L, Linares JJ, Lobato J. Is microbial fuel cell technology ready? An economic answer towards industrial commercialization. *Appl. Energy* [Internet]. 185, 698–707 (2017). Available from: <http://dx.doi.org/10.1016/j.apenergy.2016.10.109>.
38. Zou L, Huang Y, Wu X, Long Z er. Synergistically promoting microbial biofilm growth and interfacial bioelectrocatalysis by molybdenum carbide nanoparticles functionalized graphene anode for bioelectricity production. *J. Power Sources* [Internet]. 413(October 2018), 174–181 (2019). Available from: <https://doi.org/10.1016/j.jpowsour.2018.12.041>.
39. Qiao Y, Li CM, Bao SJ, Bao QL. Carbon nanotube/polyaniline composite as anode material for microbial fuel cells. *J. Power Sources.* 170(1), 79–84 (2007).
40. Karthikeyan R, Wang B, Xuan J, Wong JWC, Lee PKH, Leung MKH. Interfacial electron transfer and bioelectrocatalysis of carbonized plant material as effective anode of microbial fuel cell. *Electrochim. Acta* [Internet]. 157, 314–323 (2015). Available from: <http://dx.doi.org/10.1016/j.electacta.2015.01.029>.
41. Yaqoob AA, Ibrahim MNM, Rodríguez-Couto S. Development and modification of materials to build cost-effective anodes for microbial fuel cells (MFCs): An overview. *Biochem. Eng. J.* [Internet]. 164(June), 107779 (2020). Available

from: <https://doi.org/10.1016/j.bej.2020.107779>.

42. Yamashita T, Yokoyama H. Molybdenum anode: A novel electrode for enhanced power generation in microbial fuel cells, identified via extensive screening of metal electrodes. *Biotechnol. Biofuels* [Internet]. 11(1), 1–13 (2018). Available from: <https://doi.org/10.1186/s13068-018-1046-7>.
43. Chen J, Hu Y, Tan X, Zhang L, Huang W, Sun J. Enhanced performance of microbial fuel cell with in situ preparing dual graphene modified bioelectrode. *Bioresour. Technol.* [Internet]. 241, 735–742 (2017). Available from: <http://dx.doi.org/10.1016/j.biortech.2017.06.020>.
44. Chong P, Erable B, Bergel A. Effect of pore size on the current produced by 3-dimensional porous microbial anodes: A critical review. *Bioresour. Technol.* [Internet]. 289(February), 121641 (2019). Available from: <https://doi.org/10.1016/j.biortech.2019.121641>.
45. Ren H, Tian H, Gardner CL, Ren TL, Chae J. A miniaturized microbial fuel cell with three-dimensional graphene macroporous scaffold anode demonstrating a record power density of over 10000 W m<sup>-3</sup>. *Nanoscale*. 8(6), 3539–3547 (2016).
46. Chen W, Huang YX, Li DB, Yu HQ, Yan L. Preparation of a macroporous flexible three dimensional graphene sponge using an ice-template as the anode material for microbial fuel cells. *RSC Adv*. 4(41), 21619–21624 (2014).
47. Chen M, Zeng Y, Zhao Y, *et al.* Monolithic three-dimensional graphene frameworks derived from inexpensive graphite paper as advanced anodes for microbial fuel cells. *J. Mater. Chem. A*. 4(17), 6342–6349 (2016).
48. Zhang K, Ma Z, Song H, Zhang M, Xu H, Zhao N. Macroporous carbon foam with high conductivity as an efficient anode for microbial fuel cells. *Int. J. Hydrogen Energy* [Internet]. 45(21), 12121–12129 (2020). Available from: <https://doi.org/10.1016/j.ijhydene.2020.02.123>.
49. Chiang TH, Yeh HC. The Synthesis of  $\alpha$ -MoO<sub>3</sub> by ethylene glycol. *Materials (Basel)*. 6(10), 4609–4625 (2013).
50. Wu JZ, Li XY, Zhu YR, Yi TF, Zhang JH, Xie Y. Facile synthesis of MoO<sub>2</sub>/CNTs composites for high-performance supercapacitor electrodes. *Ceram. Int.* [Internet]. 42(7), 9250–9256 (2016). Available from: <http://dx.doi.org/10.1016/j.ceramint.2016.03.027>.
51. Xu Y, Yi R, Yuan B, *et al.* High capacity MoO<sub>2</sub>/graphite oxide composite anode for lithium-ion batteries. *J. Phys. Chem. Lett.* 3(3), 309–314 (2012).
52. Ren J, Ren RP, Lv YK. A flexible 3D graphene@CNT@MoS<sub>2</sub> hybrid foam anode for high-performance lithium-ion battery. *Chem. Eng. J.* 353(May), 419–424 (2018).
53. Ay B. Dikarboksilik Asit Grupları İçeren Geçiş Metal komplekslerinin Hidrotermal Sentezi, UV Etkileşimlerinin ve Katalitik Aktivitelerinin İncelenmesi. (2011).

## **Characterization of Radar Absorption Performance of Polyurethane Paint Combined With Different Reinforcements**

***Ipek ALISKIN***

*Iskenderun Technical University-Department of Metallurgy and Materials Engineering, 31200, Hatay, Turkey  
ipekaliskin.lee20@iste.edu.tr  
ORCID: 0000-0003-1141-3196*

***Ali Oktay GUL***

*Iskenderun Technical University-Department of Metallurgy and Materials Engineering, 31200, Hatay, Turkey  
ISTE Center for Science and Technology Studies and Research (ISTE-CSTSR), 31200, Hatay, Turkey,  
aoktay.gul@iste.edu.tr  
ORCID: 0000-0002-4891-5280*

***Ersin BAHCECI***

*Iskenderun Technical University-Department of Metallurgy and Materials Engineering, 31200, Hatay, Turkey  
ISTE Center for Science and Technology Studies and Research (ISTE-CSTSR), 31200, Hatay, Turkey,  
ersin.bahceci@iste.edu.tr  
ORCID: 0000-0002-7719-6051*

*Cite this paper as: Ipek ALISKIN, Ali Oktay GUL, Ersin BAHCECI. Characterization of Radar Absorption Performance of Polyurethane Paint Combined With Different Reinforcements. Int. Conf. Advanced. Mater. Sci. & Eng. HiTech.and Device Appl.Oct. 27-29 2022, Ankara, Turkey*

**Abstract.** It is aimed to produce polyurethane paint with absorbent reinforcing element on aluminum plates and to examine the magnetic permeability properties. Materials with low visibility or invisibility properties are widely used in military aircraft. First of all, absorbing nano powders with polyurethane paint and then applying to surfaces were investigated for absorbing radar waves. The homogeneous mixture was prepared by adding 5 %, 10 %, 15 % (C, MnO<sub>2</sub>, C+MnO<sub>2</sub> and Fe) powders by weight to the polyurethane paint. Then, spray coating (painting) method was applied to the aluminum plate surfaces with different thicknesses (approximately 43, 51,32 and 68 microns). Network Analyzer was used for the transmission and reflection values of the coated plates. TGA/DSC analysis and SEM characterization method were used to determine the physical and mechanical properties of the mixed polyurethane paint. It was determined that a single coat of 10 % C and 5 % MnO<sub>2</sub> reinforced paint application had better absorption properties at values between 70 % and 99 % in the X band. However, it was observed that the paint retained its properties with multi-layer painting. It has been determined that the paint is distributed homogeneously on the surfaces in general, there is no change in the chemical properties of the paint and it wets the reinforcement.

**Keywords:** : Radar Absorption Materials (RAM), Polyurethane, Nano Powders, Spray Coating Method  
© 2022 Published by ICMATSE

### **Introduction**

With the presence of "low visibility" materials in military warfare systems, it becomes difficult to detect targets such as air and sea vehicles with infrared, radar and other detection methods [1,2]. In particular, the improvement of the undetected feature in aircraft, the materials used and the geometric shape are known as the most important factors affecting low visibility [3]. Materials interact

with radar waves hitting them in ways such as reflection, transmission, and absorption. Absorption coatings are used to reduce or prevent these interactions. The use of radar absorbing materials ensures that the electromagnetic wave sent by the radar is absorbed by the target and minimized [4-6]. The development of radar absorption materials (RAM) has significant capabilities in reducing radar detection of military targets to meet electromagnetic (EM) absorption requirements. RAMs absorb and

weaken electromagnetic waves by converting electromagnetic energy into heat or other energy forms to reduce incoming wave reflection and transmission [4]. The interest in RAMs has increased due to the fact that they absorb radar waves and effectively prevent backscattering. The features such as exhibiting powerful microwave properties in a wide frequency band, thin and low density especially in terms of energy saving, and easy application during emergency operation are specific features of excellent RAMs. As a result of the increasing interest in such materials, various studies are continuing to develop new radar absorber materials with magnetic and dielectric loss [7].

In general, metals are used effectively for protective purposes. However, it is not preferred to be used alone due to the specific properties of metals such as low elastic properties, high density, corrosion tendency. In addition, electromagnetic signals are almost completely reflected from the metal plate surface [8,9]. Therefore, it is difficult for a single material to meet the technical requirements for radar protection applications. As a result, the coatings that provide absorption of radio waves are preferred. These coatings are composed of conductive reinforcement element and insulating polymer matrix. While electrical conductivity is achieved by combining some of the ferromagnetic and dielectric components, matrices can be formed from polymers with low density and easily processed [5, 10].

In the applications of absorption materials, materials such as polyurethane (PU) with protective properties are used as matrix material [11]. In order to increase the performance of the shielding material, magnetite ferrite is used together with dielectric materials. In recent years, nano-sized materials have been added to dielectric materials in order to increase the efficiency of radar wave absorption and improve their properties [12-14]. Nano-sized materials used in RAMs show the ability to absorb more radar waves. These structures are also preferred due to their low density and fine structure. Materials such as carbon (C), manganese oxide ( $MnO_2$ ), iron (Fe) etc. can be given as examples of radar absorption reinforcement materials.

Carbon allotropes are widely used in RAMs due to their high electrical conductivity and low density. Carbon reinforced composites improve radar absorption performance by providing strong impedance adaptation [4, 15]. In the literature, it is known that polyurethane and carbon fiber/polyurethane radar absorber coating are

produced as carbon fiber and matrix [16]. Nanostructured manganese oxides, which are transition metal oxides, have attracted great attention due to their advantages such as easy synthesis, thermal stability, energy storage and molecular absorption. The studies show that manganese oxides with strong dielectric loss mechanism can be used as high performance radar absorption materials [17]. In addition to all these, maximum absorption of electromagnetic energy is obtained by the inclusion of magnetic additives [18]. The electromagnetic wave can be weakened by the dielectric or magnetic loss mechanism by homogeneously dispersing the absorber materials and additives in the main polymer matrix [19]. The combination of dielectric and magnetic loss materials has been reported to be an effective design to achieve excellent impedance adaptation and high microwave absorption [19,20]. It has attracted attention whether the performance of these structures can be increased when they are combined. It is a desired feature to increase the visibility properties without a negative change in the mechanical properties of the matrix material.

In this study, Carbon (C), Manganese dioxide ( $MnO_2$ ) and (C+  $MnO_2$ ) were added to the polyurethane (PU) two-component paint at the rates of 5%, 10%, 15% by weight. Reinforced paints (C,  $MnO_2$  and C+  $MnO_2$ ) were coated on Al plate surfaces by spray method. In addition, in order to examine the effect of Iron (Fe), after the reinforced coatings, 10 wt% Fe powder content painting was carried out as the last layer. Thus, the effects of reinforcement materials on the radar wave absorption properties of Al plates were investigated. In addition, the synergistic effect was investigated by using (C+ $MnO_2$ ) supplement together in the study.

## Materials and Method

In this study, two-component polyurethane (PU) paint (Sahika Group), Carbon(C) (99.99 % purity,),  $MnO_2$  and Fe powders were used. 5%, 10% and 15% by weight of C,  $MnO_2$  and (C+ $MnO_2$ ) powders were added to the paint. The paint is applied in a single layer on the Al plate surface. The mixing ratios and plate codes of the powders used are given in Table 1.

A second coating was applied to the Al plate surface. The average coating thickness after the second coating on the Al plate surface is 50.0  $\mu m$ . The mixing ratios and plate codes of the powders reinforced to the paint applied to the second layer on the Al plate surface are given in the Table 2.

**Table 1.** *Mixing ratios and plate codes of the powders used in different proportions into the paint applied in a single layer on the Al surface.*

	<b>Carbon Amount</b>	<b>MnO<sub>2</sub> Amount</b>	<b>(C+MnO<sub>2</sub>) Amount</b>	<b>Fe Amount</b>
<b>1. Mixing Wt. (%)</b>	5	5	5	-
<b>Sample Code</b>	1C5	1M5	1C5M5	-
<b>2. Mixing Wt. (%)</b>	10	10	10	10
<b>Sample Code</b>	1C10	1M10	1C10M5	1F10
<b>3. Mixing Wt. (%)</b>	15	15	15	-
<b>Sample Code</b>	1C15	1M15	1C15M5	-

After coating with the addition of C, MnO<sub>2</sub>, (C+MnO<sub>2</sub>), Fe-containing dyeing was performed as the last layer. Fe powder used at a rate of 10% by weight was dispersed in 6 g thinner. The prepared solution Interactions between component A and component B were investigated by performing Thermo gravimetric analysis / Differential Scanning Calorimetry (TGA/DSC) (Hitachi/Next STA 300) analysis in Iskenderun Technical University Science Technology and Research Center (ISTE BTM). Microstructure images of the reinforcement materials and PU paint were characterized using

Scanning Electron Microscopy (SEM) (Thermo Fisher Scientific Apreo S SEM). The wave absorption ability of the coated Al plates obtained at different concentrations was examined in the Network Analyzer (Agilent 2-Port PNA-L) in ISTE BTM with an operating frequency varying between 3-18 GHz. The measurement values of reflection (S<sub>11</sub>) and transmission (S<sub>12</sub>) were measured. The absorption values of the composite coatings were calculated as shown in the following equation [21];

$$A(\omega) = 1 - R(\omega) - T(\omega) \quad (1)$$

Here in R(ω) represents reflection and T(ω) transmission coefficients. These scattering parameters can be defined as follows:

$$R(\omega) = |S_{11}|^2 \quad (2)$$

$$T(\omega) = |S_{21}|^2 \quad (3)$$

In order to obtain a homogeneous mixture using the turbula shaker-mixer containing the ball for 1 hour. The average thickness of the last coating with Fe powder is 68 μm.

was supplemented with the dye mixture obtained by using 40 g of component A and 4 g of component B.

**Table 2.** *Mixing ratios and plate codes of the powders used in different proportions into the paint applied on the Al surface with a second layer*

<b>Amount of the reinforcement (wt. %)</b>	<b>1. Layer</b>	<b>2. Layer</b>	<b>Plate Code</b>
5	C	MnO <sub>2</sub>	1C52M5
	MnO <sub>2</sub>	C	1M52C5
	C+ MnO <sub>2</sub>	C	1C5M52C5
	C	MnO <sub>2</sub>	1C102M10
10	MnO <sub>2</sub>	C	1M102C10
	C+ MnO <sub>2</sub>	C	1C10M52C10
	C	Fe	1C102F10
	MnO <sub>2</sub>	Fe	1M102F10
15	C+ MnO <sub>2</sub>	Fe	1C10M52F10
	C	MnO <sub>2</sub>	1C152M15
	MnO <sub>2</sub>	C	1M152C15
	C+ MnO <sub>2</sub>	C	1C15M52C15

## Results and Discussion

The microstructure images of the reinforcement materials were characterized by SEM. The SEM images of Fe, C and used as reinforcement materials are given in Figure 2.a, Figure 2.b and Figure 2.c, respectively. In the SEM image given in Figure 2.a, it is seen that the morphology of Fe powders is needle-like, long, sharp-edged and indented. As seen in Figure 2.b, sharp-edged C powders were used. In the

SEM image given in Figure 2.c, it is seen that the morphology of the mixture  $MnO_2$  is in spherical form and in the size range of approximately 1-50  $\mu m$ . SEM images show that the morphologies of Fe, C and  $MnO_2$  used as reinforcement materials are different. It has been observed that the effects of reinforced powders in different forms are positive on absorption.

In Figure 3, the SEM microstructure image of the pure paint is given. When the SEM images of the pure paint were examined in Figure 3, it was observed that component A and component B agglomerated in the solvent. In addition, the presence of regional remains is observed. For this reason, attention was paid to the mixing process in order to ensure that the mixture of the paint was homogeneous. After homogeneous mixing, it was determined that the paint wetted the reinforcement materials sufficiently.

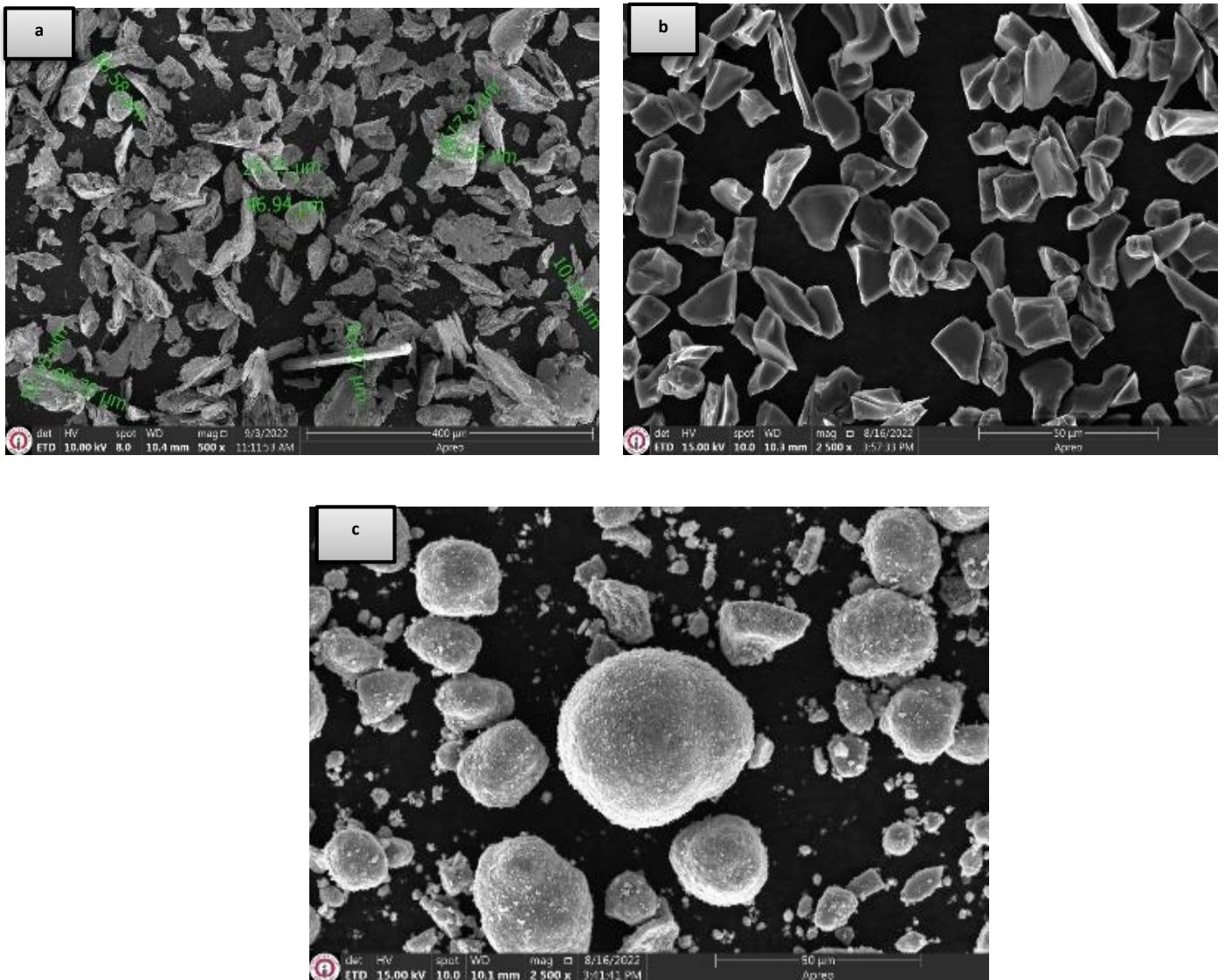


**Figure 2.** SEM images of reinforced powders a) Fe powders, b) C powders, c)  $MnO_2$  powders.

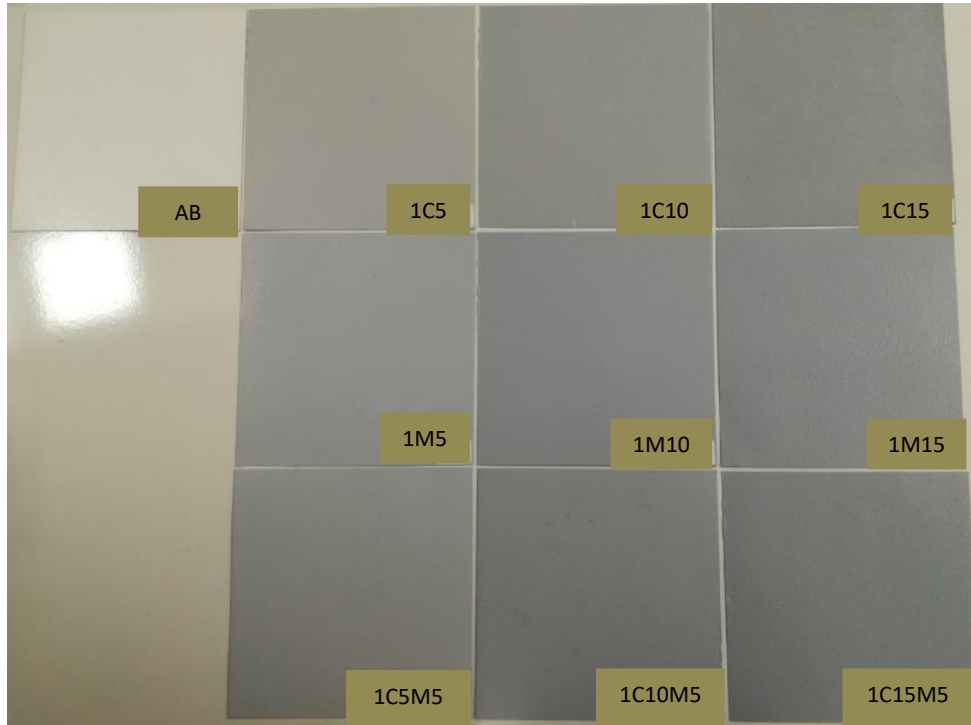


Figure 1. Images of the Al plates with a single layer coating.

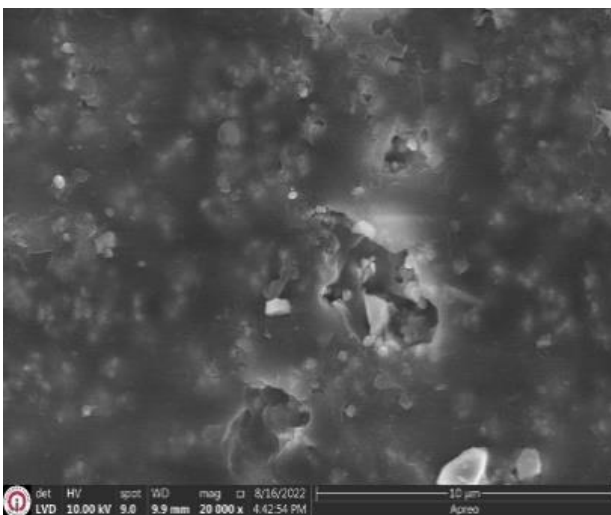
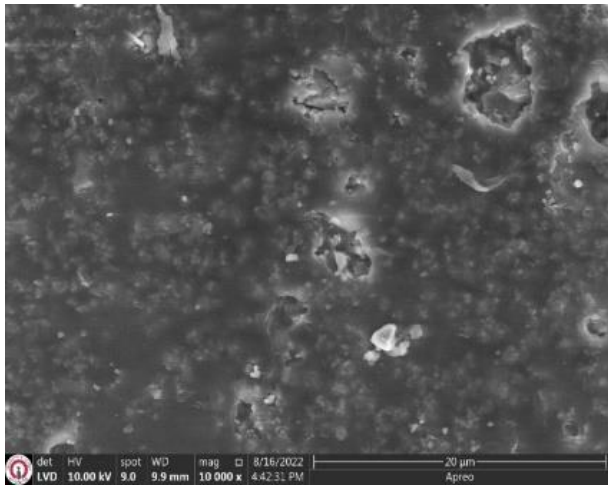


Figure 3. SEM image of the pure paint.

The thermal properties of component A and component A+B were investigated using Thermogravimetric analysis (TGA) and Differential Scanning Calorimetry (DSC). In Figure 4, the TGA-DSC analysis result of component A is given together (simultaneously).

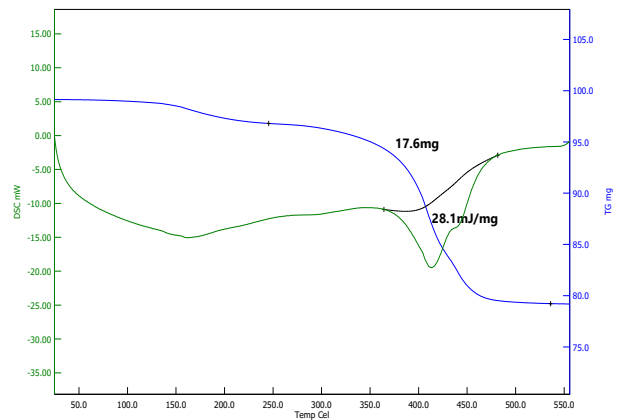
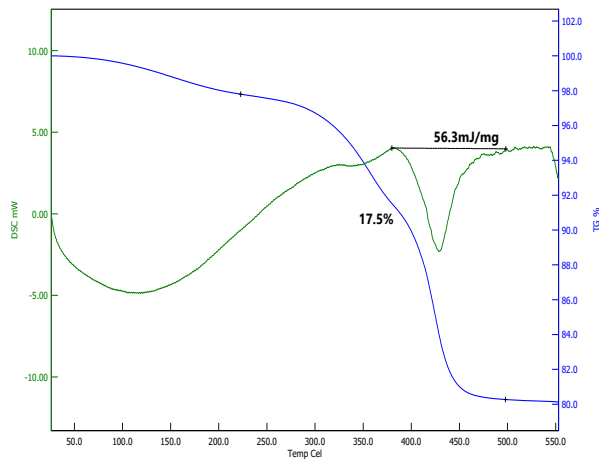


Figure 4. TGA-DSC analysis result of Component A.

According to the result of TG analysis carried out to examine the thermal stability of component A, it is seen that the mass loss increases as the temperature increases. The 17.6% mass loss seen in the TGA curve represents the volatile compounds moving away from the structure. In Figure 4, it was determined that the volatile matter was removed in the temperature range of 350-400 °C.

In the DSC analysis, which expresses the change in structure with the increase in temperature, the samples were heated to 550 °C in a nitrogen atmosphere at a rate of 10 °C/min. According to the DSC analysis results, the soft segment glass transition temperature ( $T_g$ ) and the hard segment melting temperature ( $T_e$ ) were observed in the sample, respectively. An exothermic peak was observed in the DSC curve in the temperature range of 400-425°C. It was also observed that the enthalpy value was 28.1 mJ/mg. TGA-DSC analysis result of Component A+B is shown in Figure 5.



**Figure 5.** TGA-DSC analysis result of component A+B mixture.

According to the TGA graph given in Figure 5, the mass loss of 17.5% was observed with the increase in temperature. Desorption of component A+B or volatile compounds separated from the structure is the cause of this mass loss. It was observed that mass loss continued from 250 °C to 450 °C in the TG curve of the component A+B mixture.

As seen in the DSC curve, the peak occurring between 390°C and 490°C was observed to be exothermic. In addition, the reaction enthalpy was found to be 56.3 mJ/mg. It was determined that the B supplement to component A increased the melting temperature.

In the results of the examination, it was thought that the chemical change of the aliphatic paint would

positively affect its low invisibility feature. It has been understood that the paint dries quickly even at ambient temperatures after it is applied to the floor and can operate at 60°C service temperatures.

In Figure 6, figure 7 and figure 8, Network Analysis obtained by applying single and double layers of polyurethane paint prepared with reinforcing powders on the aluminum plate surface are shown.

In Figure 6, the absorption results obtained by applying a single layer of polyurethane paint prepared with C and  $MnO_2$  reinforcing powders to the aluminum plate surface are given. As seen in the figure above the highest absorption values were obtained using 1C10 sample at certain frequency bands. In this test, the calibration was carried out by using metallic plate and air. Metallic plate provide full reflection which was used to normalize the reflection parameter while air was used for full transmission which was used to normalize the transmission parameter. Both transmission and reflection parameters were used to determined the absorption behavior. In this graph on the other hand, sample title 1M5 provided the best absorption behavior at X-band while the other samples had lower absorption rates.

In this graph (Figure 7.), although 1C102M10 provided high absorption behavior particularly at 8.7 GHz and 9.75 GHz, 1C152M15 sample also provided better absorption when wideband is required.

For the case when the second layer is applied, 1C15M52C15 sample provided the best absorption behavior compared to the other samples. The absorption also has a relatively higher band than the other particularly at around 9.2 GHz.

In this measurement, the red line (for Figure 8.) corresponding to 1C102F10 provided the top results at 3 frequency bands where the absorption reached to almost 99%. While the others remained lower values.

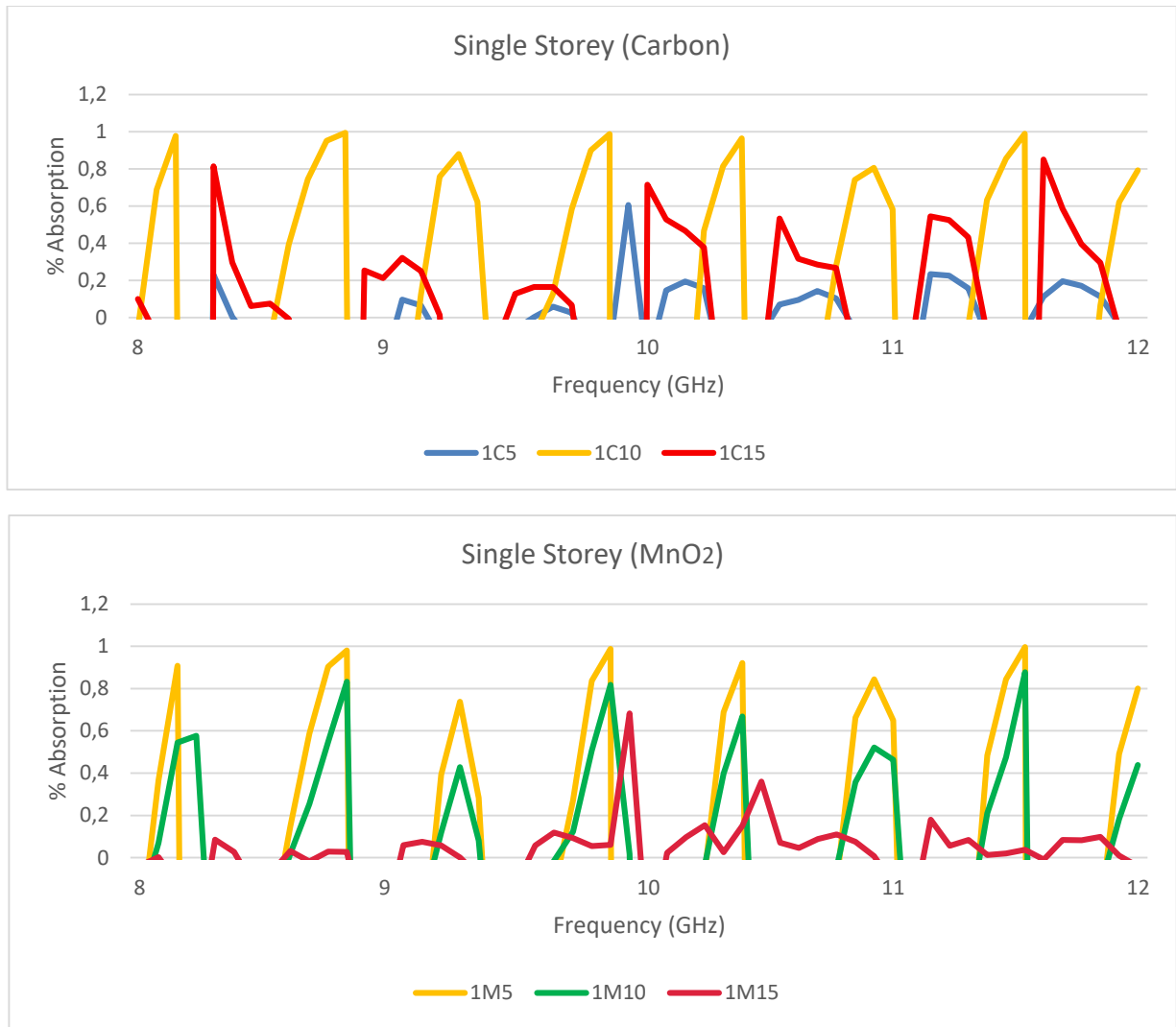


**Figure 6.** Absorption results obtained by applying a single layer of polyurethane paint prepared with C and MnO<sub>2</sub> reinforcing powders to the aluminum plate surface.

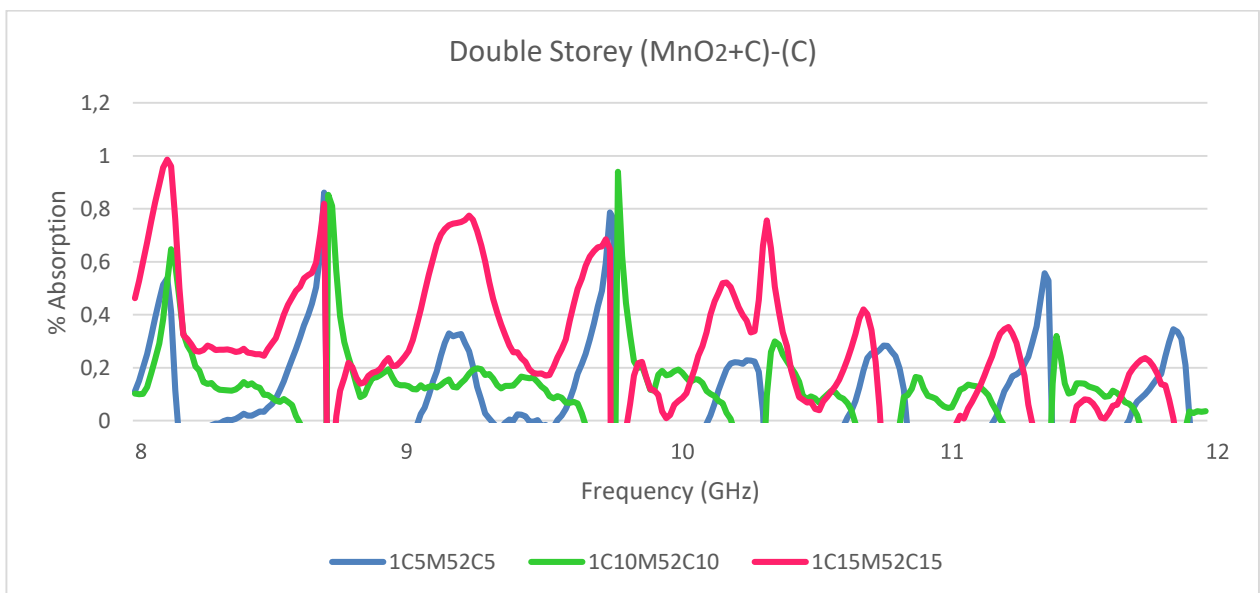
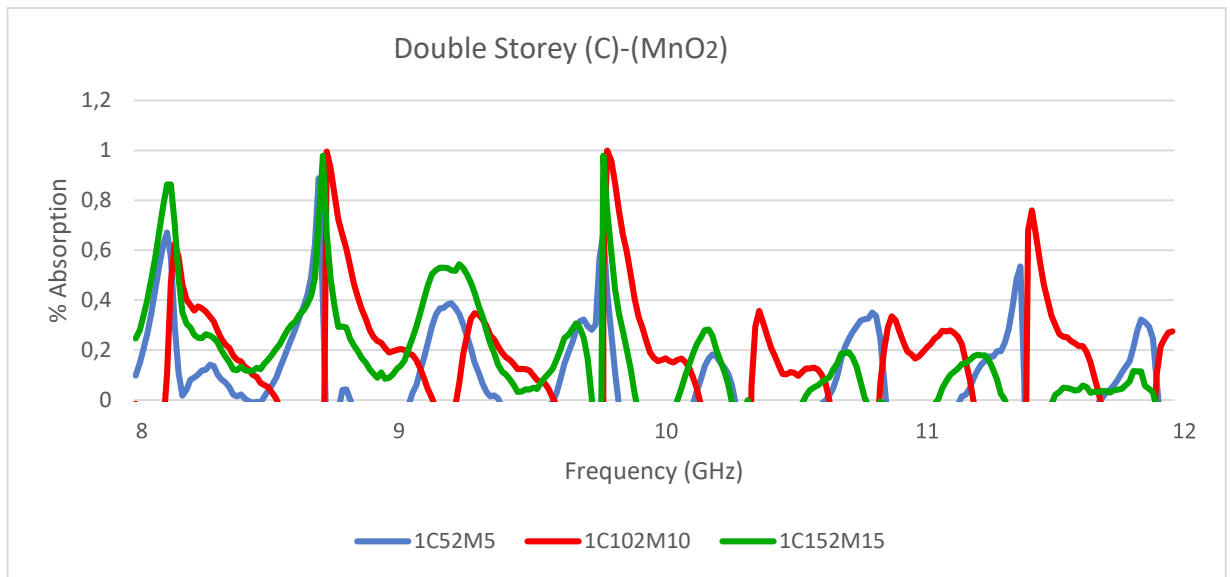
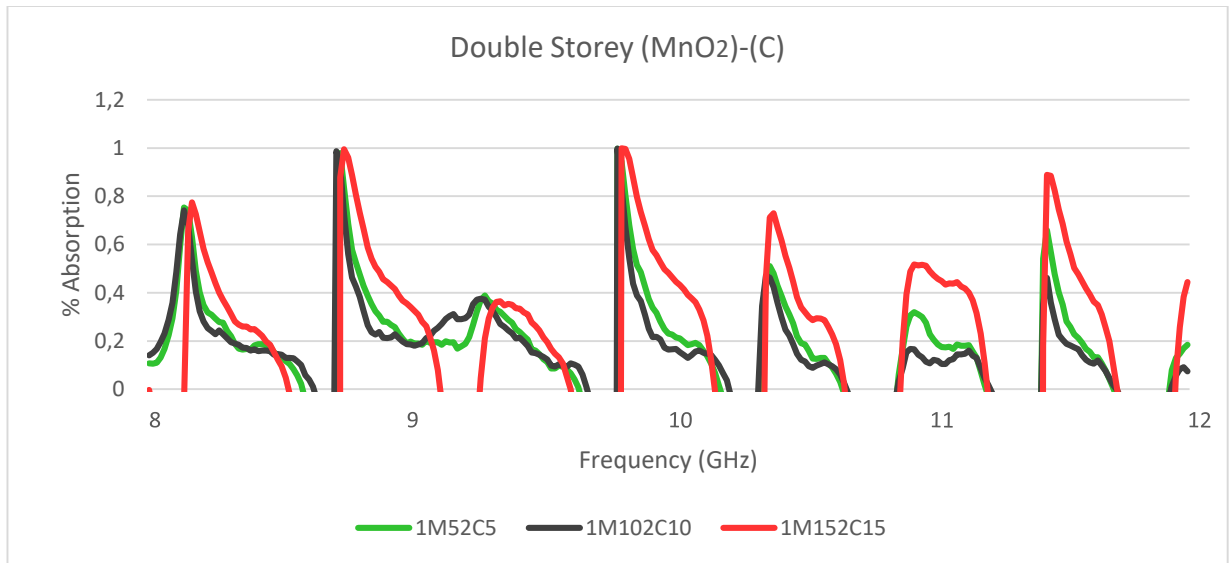


**Figure 7.** Absorption results obtained as a result of the second layer application.

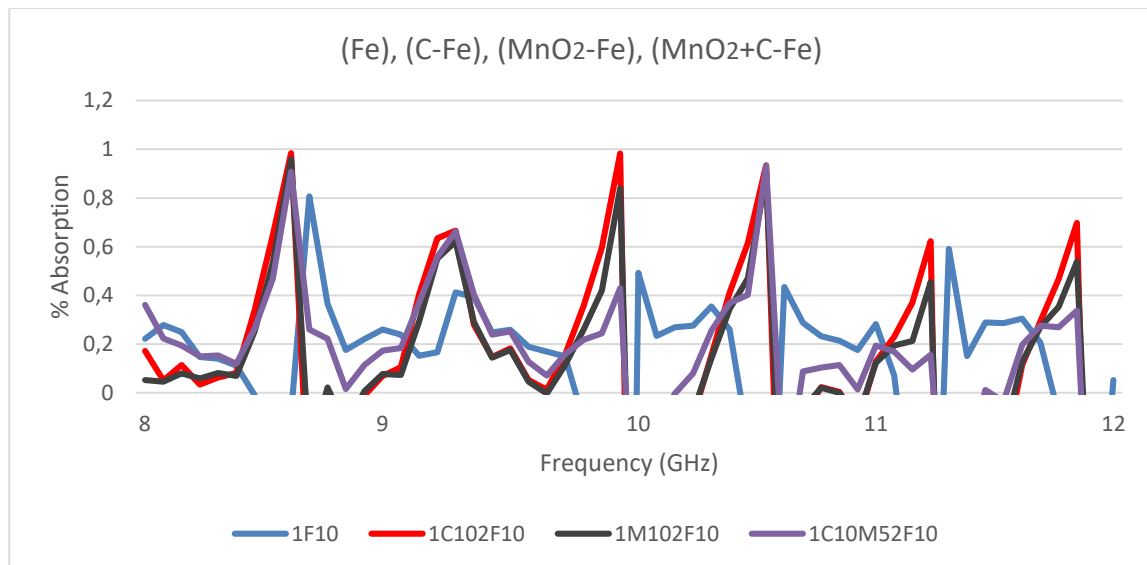


**Figure 8.** Absorption results obtained as a result of the application of 10% C, MnO<sub>2</sub>, C+ MnO<sub>2</sub> powders as the first layer and the polyurethane paint prepared with 10% Fe powder as the second layer.

## Conclusion

The following results were obtained after the application of composite paint.

The paint was applied by mixing the reinforcement elements homogeneously in the paint. It can be used as an ideal shape due to the fact that the reinforcement elements are morphologically suitable and the adhesion (increasing the surface area) surface increases in the paint. Appropriate surface roughness has been obtained due to the high adhesion of the paint thickness.

It has been determined by chemical analysis that the paint can be used at ambient temperatures such as 60°C. It has been observed that the paint application temperature is important in terms of the rapid

removal of the components from the environment as a result of the reaction of the material.

While the best absorption was obtained in the reinforcement material at 10% C and 5% MnO<sub>2</sub> concentrations applied in a single layer, it was 70-99% in the X band. However, It was determined that the second layer applied C and MnO<sub>2</sub> reinforcement had lower damping values in the wide band. The damping value of the sample dyed with C as the first layer and Fe as the second layer was measured as approximately 99%. However, at high frequencies (11-12 GHz), damping values of approximately 50-70% were obtained. The low damping values show promise for the use of samples as radome dyes. As a result, according to the frequency values studied, the desired damping values can be obtained by using different layer numbers and the same concentrations of Fe powder.

## References

1. G. Jayalakshmi, A. Inamdar, A. Anand ve B. Kandasubramanian, «Polymer matrix composites as broadband radar absorbing structures for stealth aircrafts,» *Journal of Applied Polymer Science*, cilt 136, no. 14, p. 47241, 2019.
2. H. Ahmad, A. Tariq, A. Shehzad, M. Faheem, M. Shafiq, I. Rashid, A. Afzal, A. Munir, M. Riaz, H. Haider, A. Afzal, M. Qadir ve Z. Khaliq, «Stealth technology: Methods and composite materials—A review,» *Polymer Composites*, cilt 40, no. 12, pp. 4457-4472, 2019.
3. A. Teber, I. Unver, H. Kavas, B. Aktas ve R. Bansal, «Knitted radar absorbing materials (RAM) based on nickel–cobalt magnetic materials,» cilt 406, pp. 228-232, 2016.
4. C. Kim ve M. Kim, «Intrinsically conducting polymer (ICP) coated aramid fiber reinforced composites for broadband radar absorbing structures (RAS),» *Composites Science and Technology*, cilt 211, p. 108827, 2021.
5. Z. Fan, G. Luo, Z. Zhang, L. Zhou ve F. Wei, «Electromagnetic and microwave absorbing properties of multi-walled carbon nanotubes/polymer composites,» *Materials Science and Engineering: B*, cilt 132, no. 1-2, pp. 85-89, 2006.
6. A. Kolanowska, D. Janas, A. Herman, R. Jędrzyśiak, T. Giżewski ve S. Boncel, «From blackness to invisibility – Carbon nanotubes role in the attenuation of and shielding from radio waves for stealth technology,» *Carbon*, cilt 126, pp. 31-52, 2018.
7. Y. Wang, T. Li, L. Zhao, Z. Hu ve Y. Gu, «Research Progress on Nanostructured Radar Absorbing Materials,» *Energy and Power Engineering*, cilt 3, pp. 580-584, 2011.

8. R. Bhattacharyya, O. Prakash, S. Roy, A. P. Singh, T. K. Bhattacharya, P. Maiti, S. Bhattacharyya ve S. Das, «Graphene oxide-ferrite hybrid framework as enhanced broadband absorption in gigahertz frequencies,» *Scientific Reports*, cilt 9, no. 12111, 2019.
9. Z. Zeng, M. Chen, Jin H., W. Li, X. Xue, L. Zhou, Y. Pei, H. Zhang ve z. Zhang, «Thin and flexible multi-walled carbon nanotube/waterborne polyurethane composites with high-performance electromagnetic interference shielding,» *Carbon*, cilt 96, pp. 768-777, 2016.
10. A. Kolanowska, D. Janas, A. P. Herman, R. G. Jędrzyśiak, T. Giżewski ve S. Boncel, «From blackness to invisibility – Carbon nanotubes role in the attenuation of and shielding from radio waves for stealth technology,» *Carbon*, cilt 126, pp. 31-52, 2018.
11. L. Huang, Y. Duan, J. Liu, Y. Zeng, G. Ma, H. Pang ve W. Zhang, «Bionic composite metamaterials for harvesting of microwave and integration of multifunctionality,» *Composites Science and Technology*, cilt 204, p. 108640, 2021.
12. M. Ahmad, G. Arezoo, F. Reza ve K. Maryam, «Synthesis and Optimization of Thermoplastic Polyurethane/Polyaniline/Ferrite Cobalt Composite as an Effective Absorber in X-Band Region,» *Polymer Science, Series A*, cilt 62, p. pages744–757, 2020.
13. S. S. Jehangir, M. I. Hussein, I. J. Rajmohan, Y. Haik, Q. Clément ve N. Vukadinovic, «Polyurethane-Based Functionalized CNT Composites as Absorbers for Microwave Applications,» %1 içinde *2019 IEEE MTT-S International Microwave Workshop Series on Advanced Materials and Processes for RF and THz Applications (IMWS-AMP)*, 2019.
14. S. S. Jehangir, M. I. Hussein, I. J. Rajmohan, Y. Haik, Q. Clément ve N. Vukadinovic, «Polyurethane-Based Functionalized CNT Composites as Absorbers for Microwave Applications,» %1 içinde *2019 IEEE MTT-S International Microwave Workshop Series on Advanced Materials and Processes for RF and THz Applications (IMWS-AMP)*, 2019.
15. H. Pang, Y. Duan, Y. Huang, L. Song, J. Liu, T. Zhang, X. Yang, J. Liu, X. Ma, J. Di ve X. Liu, «Research advances in composition, structure and mechanisms of microwave absorbing materials,» *Composites Part B: Engineering*, cilt 224, p. 109173, 2021.
16. Z. H. Liu, R. Tao, P. Luo, X. Shu ve G. D. Ban, «Preparation and microwave absorbing property of carbon fiber/polyurethane radar absorbing coating,» *RSC advances*, cilt 7, no. 73, pp. 46060-46068, 2017.
17. M. Zhou, X. Zhang, J. Wei, S. Zhao, L. Wang ve B. Feng, «Morphology-Controlled Synthesis and Novel Microwave Absorption Properties of Hollow Urchinlike R-MnO<sub>2</sub> Nanostructures,» *The Journal of Physical Chemistry C*, cilt 115, no. 5, p. 1398–1402, 2011.
18. B. Belaabed, J. J. Wojkiewicz, S. Lamouri, N. El Kamchi ve T. Lasri, «Synthesis and characterization of hybrid conducting composites based on polyaniline/magnetite fillers with improved microwave absorption properties,» *Journal of Alloys and Compounds*, cilt 527, pp. 137-144, 2012.
19. M. Jafarian, S. S. S. Afghahi, Y. Atassi ve M. Salehi, «Enhanced microwave absorption characteristics of nanocomposite based on hollow carbonyl iron microspheres and polyaniline decorated with MWCNTs,» *Journal of Magnetism and Magnetic Materials*, cilt 462, pp. 153-159, 2018.
20. A. Afzali, V. Mottaghitalab, S. S. S. Afghahi, M. Jafarian ve Y. Atassi, «Electromagnetic properties of absorber fabric coated with BaFe<sub>12</sub>O<sub>19</sub>/MWCNTs/PANi nanocomposite in X and Ku bands frequency,» *Journal of Magnetism and Magnetic Materials*, cilt 442, pp. 224-230, 2017.
21. M. Ç. Ayan, S. Kiriş, A. Yapıcı, M. Karaaslan, O. Akgöl, O. Altıntaş ve E. Ünal, «Investigation of cotton fabric composites as a natural radar-absorbing material,» *Aircraft Engineering and Aerospace Technology*, cilt 92, no. 8, p. 1275–1280, 2020.

## **Advanced Materials and Manufacturing Concepts for Next-Generation Aircraft Development Programs**

***Mete Bakir***

*Turkish Aerospace – Materials Engineering Department, 06980, Ankara, Turkey,  
mete.bakir@tai.com.tr*

*Ankara Yildirim Beyazit University – Mechanical Engineering Department, 06010, Ankara, Turkey  
ORCID: 0000-0002-5044-3104*

*Cite this paper as: Bakir, M. Advanced Materials and Manufacturing Concepts for  
Next-Generation Aircraft Development Programs.Int. Conf. Advanced. Mater. Sci. & Eng. HiTech.and Device  
Appl.Oct. 27-29 2022,Ankara, Turkey*

**Abstract.** A well-engineered airframe incorporates advanced structural materials and functional material technologies to demonstrate the utmost operational and performance capability for civilian and military purposes. Over the last decade, Turkish Aerospace has undertaken the indigenous design and development responsibility for various multi-role next-generation air platforms. This article provides an overview of the ongoing efforts to realize advanced material and manufacturing concepts on these air platforms. The most recent and innovative research efforts are explained in the realm of material and manufacturing systems to pinpoint critical technologies to be implemented in the downstream air platform programs. The development and qualification projects managed by Turkish Aerospace, in collaboration with leading international and national research institutes and industrial partners, in part to advance the current status of structural assemblies as well as including additional functionalities on the air platforms are presented.

**Keywords:** *aerospace industry; advanced materials; manufacturing technologies.*

© 2022 Published by ICMATSE

### **INTRODUCTION**

Turkish Aerospace was established on June 28, 1973, under the Ministry of Industry and Technology to reduce Turkey's foreign dependence on the defense industry. Turkish Aerospace completed the manufacture of F-16 aircraft, integration of on-board systems, and flight tests between 1984-2009 as a Turkish-U.S. joint investment company. In 2005, Turkish Aerospace was restructured as a solely Turkish company to widen its activities to become a technology center for the development, manufacture, and system integration aerospace industry in Turkey. Turkish Aerospace is among the top hundred global players in the aerospace industry. Turkish Aerospace concurrently leads several indigenous design and development projects, including the Turkish Fighter Jet (TF-X), Advanced Jet Trainer and Light Attack Aircraft (HURJET), and Multirole Heavy Combat Helicopter (ATAK-II) [1].

TF-X is a 5+ generation jet fighter possessing the critical capabilities of increased situational awareness, sensor fusion, and low observability with the support of Artificial Intelligence. HÜRJET is a single-engine, tandem-seat with modern avionics and high-performance features to fulfill a critical role in state-of-the-art pilot training through its superior performance characteristics. ATAK-II will be a combat helicopter

that can successfully perform its missions in harsh geographical and environmental conditions, with increased payload capacity and modern avionic systems alongside high performance and low maintenance cost [1].

At Turkish Aerospace, the Materials Engineering Department, with 30+ years of experience, operates under the Test and Verification Directorate in Engineering Executive Vice Presidency, with engineering offices and laboratory facilities located in Kahramankazan, Ankara. The core competencies of the Materials Engineering Department include Metallic Materials (titanium, aluminum alloys, steel), Composite Materials (thermosets, thermoplastics), Assembly Technologies (mechanical, welding, adhesives), Additive Manufacturing (metals, plastics), Surface Technologies (corrosion prevention, sealants, paints), Special Processes (process and part qualification), Calibration (dimension, force, temperature, pressure, electronics), and Test and Characterization (mechanical, chemical, NDT, failure) (Figure 1).



**Figure 3** Turkish Aerospace Mechanical Testing Laboratory

This paper demonstrates the recent technology development efforts in Materials Engineering Department at Turkish Aerospace, in collaboration with national and international universities and research centers. Digital Twin-based mechanical testing tools, fire retardant composites, fiber-metal laminated composites, and electromagnetic materials are investigated. The results shall shed light on the development of novel airframe architectures.

## MATERIALS AND METHODS

Fatigue tests of aerospace-grade Al-7050 specimens were carried out according to ASTM E466-21 standard, under load controlled testing conditions. The specimens were loaded using a periodic sinusoidal function. The fatigue tests were carried out at room temperature, with a ratio of  $R = -1$  and a limit life of 106. The fatigue life is predicted using an in-house developed digital twin model, with an Artificial Neural Network for modeling fatigue behavior since weight and bias parameters of neurons can be utilized conveniently for a Transfer Learning.

Aerospace-grade woven carbon fibers, fiber glasses, modified thermosetting resins, nanomaterial-based inclusions, hardeners, and release agents were used in a wet layup process to develop fire-retardant composites. UL-94 tests were conducted with a Bunsen burner flame to characterize the flame interaction performances of the fire retardant composites.

Fiber metal laminated composite is 4A-3/2-0.4 Glare, with three layers of metal and two stacking plies in the form of "0/90/0" with S2 Glass UD prepreg. The thickness of each prepreg used is nominally 0.13 mm. The total thickness value is 2 mm, the Aluminum type

is the 2024-T3, and the resin type is the FM 94 Epoxy Adhesive.

Electromagnetic tests are conducted in a free-space setup and one sample holder, where antennas are connected to a vector network analyzer. The sample is placed into the holder, and scattering parameters, also known as S-parameters, are measured. Permittivity and permeability values can then be calculated from S-parameters.

## RESULTS AND DISCUSSION

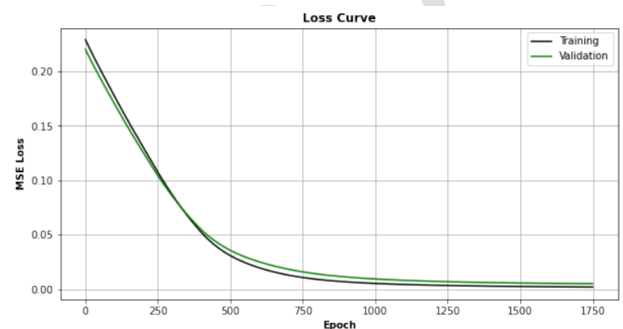


**Figure 2** Loss curve of AI-2050 with Transfer Learning training

Mechanical testing is critical for civilian and military certification processes in the aerospace industry. The calculation of fatigue strength is essential but also time-consuming and expensive to conduct fatigue tests. Thus, the test loads can be potentially reduced by exploring Machine Learning with a Digital Twin approach. In a recent collaboration with the National Center for Supercomputing Applications (NCSA) and TOBB University of Economics and Technology, Turkish Aerospace developed a machine learning reinforced digital material testing platform. The Digital Twin framework employs Machine Learning techniques, including Transfer Learning (TL). A proof-of-concept study using Al-7050 specimens showed that the fatigue test load can be reduced to 40% with only minimum error. Only a 0.27% error is observed using 30% training, 10% validation, and 60% test data. Figure 2 shows the comparison of training and validation data on loss curves. The outcomes of this study are expected to shorten aircraft design lifecycles for fatigue-critical parts [2].



**Figure 3** Specimens with Cu film using resin, solvent, and boric acid.

Although having excellent strength, stiffness, corrosion resistance, and creep properties, fiber-reinforced polymer composites are vulnerable to fire and lightning strike damages. Metallic skins minimize these damages but come along with a weight penalty and can corrode in the extended service life. Yet, the thermal and electrical conductivities of composites can be improved by using thin Ti and Cu films for higher corrosion and fire resistance without adding much weight. The joint research effort in collaboration with Wichita State University resulted in fire-retardant fiber-reinforced composites utilizing modified thermoset resins and Ti and Cu metallic thin films (Figure 3). The mechanical, chemical, and thermal studies highlighted that the modified robust resins and electronically conductive metallic films can help to increase flame retardancy and improve mechanical performance. Additionally, the presence of nanomaterial-based inclusions within the resin formulation was observed to contribute to the flame retardance performance [3].

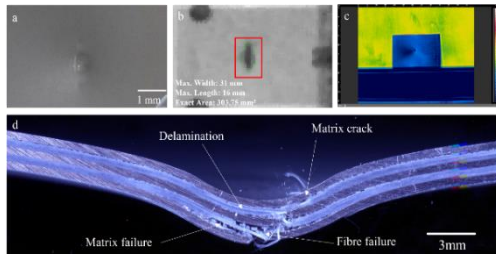


**Figure 4** Low-velocity impacted fiber metal laminate composite panel with 60J impact energy at 90°C. Damaged pattern results are (a) Damaged pattern (b) Ultrasonic C scanning (c) Thermography (d) Macrostructure scanning.

Metal alloys have widespread use in the aerospace industry, including but not limited to aluminum, titanium, and magnesium. The metal alloys can attain high strength by heat treatments and are amenable to machining. Fiber metal laminates have emerged by composing a hybrid structure to combine the advantages of both metals and polymer composites. Fiber metal laminates can inhibit the progression of fatigue damage through fiber reinforcement; the mechanism is due to the fatigue resistance of fiber-reinforced composites and the crack-bridging effect of the fibers. In addition, the low impact resistance of fiber-reinforced composites can be supported by the aluminum layers in the fiber metal laminate structure. Turkish Aerospace and Ankara Yildirim Beyazit University have investigated the low-velocity impact performance of fiber metal laminates through testing and simulations at different temperatures and impact energies. The results demonstrated that aluminum absorbs more energy at elevated temperatures, therefore upper prepreg layers were not damaged at lower temperatures (Figure 4). At room temperature

upper and lower prepreg layers had delamination, with inter-laminar delamination and intra-laminar damaged matrix cracks and fiber failures [4].

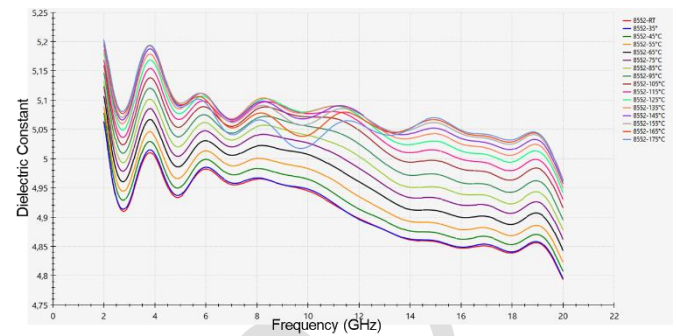


**Figure 5** Dielectric constant of silica fiber reinforced polymer composite between 2-20 GHz range at various temperatures.

In an aircraft, the signal exchange process takes place through the functional radome structures. It is of utmost importance to minimize pollution and noise in the signal exchange process. Thus highly permeable materials are desired in radome structures. Also, the radome structures are exposed to the drag resistance by which the skin temperature can drastically increase. In collaboration with Ankara Yildirim Beyazit University and Bilkent University, silica fiber-reinforced polymer composites were electromagnetically characterized at various temperatures, designating the operational window of an aircraft. Not drastically, but significant changes were observed in the dielectric constant ranging from room temperature to 175°C (Figure 5). The results highlighted that the electromagnetic analysis of high-temperature exposing parts shall take the changes in dielectric constant into account.

## CONCLUSION

Turkish Aerospace is concurrently developing various indigenous multi-role next-generation air platforms. The Materials Engineering Department is sought to realize advanced material and manufacturing concepts on these air platforms. Through joint research with national and international universities and research centers, the Materials Engineering Department developed Digital Twin-based mechanical testing tools, fire retardant composites, fiber-metal laminated composites, and electromagnetic materials over the last year. With these new concepts, the operational and performance capabilities of the airplatform are expected to improve.

## ACKNOWLEDGMENTS

The experimental analyses and simulation studies are partially carried out at National Center for Supercomputing Applications, Wichita State University and Materials Testing and Characterization

Laboratories at Turkish Aerospace. The findings, conclusions, and recommendations expressed in this manuscript are those of the authors; shall not be related to university, research center, or company per se.

## REFERENCES

- [1] <https://www.tusas.com/en/corporate/about-us>
- [2] M. Kahya, C. Soyleyici, M. Bakir and H.O. Unver, "A Digital Twin Framework for Mechanical Testing Powered by Machine Learning," Proceedings of the ASME 2022 International Mechanical Engineering Congress and Exposition IMECE2022 October 30–November 3, 2022, Columbus, OH.
- [3] M.S. Murad, E. Asmatulu, O. Er, M. Gursoy, B. Safaker, E. Bahceci, M. Bakir and R. Asmatulu, "Improving Flame Retardancy of Fiber Reinforced Composites via Modified Fire-Resistant Resins and Metallic Thin Film Coatings" The CAMX Composites and Advanced Materials Expo, October 17-20, 2022, Anaheim, CA.
- [4] Z. P. Chow, Z. Ahmad, K. J. Wong and S. S. Abdullah, "Experimental and Numerical Analyses of Temperature Effect on Glare Panels under Quasi-Static Perforation. Composite Structures, 275, 114434 (2021)

## Development and Characterization Of 3d Printed Frequency Selective Surface Structures in Aerospace Applications

**Omer Ziyaeddin Alaboyun**

TUSAŞ, Ankara, Türkiye,  
[omer.alaboyun@tai.com.tr](mailto:omer.alaboyun@tai.com.tr)  
ORCID: 0000-0001-7387-150X

**Mete Bakir**

TUSAŞ, Ankara, Türkiye,  
[mete.bakir@tai.com.tr](mailto:mete.bakir@tai.com.tr)  
ORCID: 0000-0002-5044-3104

**Oguzhan Akgol**

Iskenderun Technical University, Hatay, Türkiye,  
[oguzhan.akgol@iste.edu.tr](mailto:oguzhan.akgol@iste.edu.tr)  
ORCID: 0000-0002-1423-1569

*Cite this paper as: Alaboyun, O.Z, Bakir, M., Akgol, O., Development and Characterization Of 3d Printed Frequency Selective Surface Structures in Aerospace Applications.Int. Conf. Advanced. Mater. Sci.& Eng. HiTech.and Device Appl.Oct. 27-29 2022,Ankara, Turkey*

**Abstract.** In this study, a frequency selective surface (FSS) combined with metamaterial structure (MTM) is developed and investigated using 3D printed materials as substrate layers. The samples manufactured with 3D printing technology are in the dimensions of fitting a waveguide measurement setup (in Ku band) which provides electromagnetic permittivity ( $\epsilon$ ) and permeability ( $\mu$ ) values of the samples. Samples with three different raster orientations are used and their performances are compared to obtain the highest efficiency. The FSS structure is designed to provide band-pass behavior at  $f=6$  GHz while the MTM structure integrated on the top layer of the structure allows an EM absorption behavior. FSS structure is optimized in a way to increase the bonding between 3D printed layers. In order to show the performance of the proposed design, an antenna operating at  $f=6$  GHz is designed and simulated using the proposed design as a radome. The proposed design does not alter the working performance of the antenna while improving the Radar Cross Section (RCS) value. The designed structure is tested for various angles of incidence. Due to the nature of the design, it can be adjusted to any desired frequency for filtering and the absorption response. Thanks to the 3D printing technology, wideband or multiband absorption behaviors along with band-pass response can be easily and cost efficiently obtained not only on flat surfaces but also on any non-planar surfaces which is a significant challenge in radome designs in aerospace industry.

**Keywords:** 3D Printing, frequency selective surface, metamaterials, RCS reduction, RF/EM Absorber  
© 2022 Published by ICMATSE

### INTRODUCTION

With the developing technology, the use of 3D printed materials increasing day by day from agriculture to aerospace applications. As a result of these new 3D printing technologies, many types of materials can be fabricated within the field of material science with different methods of 3D printing, such as Fused Deposition Modeling (FDM), Selective Laser Sintering (SLS), Stereo Lithographic Apparatus (SLA), and etc... Every single 3D printed fabrication depends upon additively manufacturing

processes. Models are being created in computer aided design tools and produced these models by 3D printers.

There are numerous materials (filaments) used by 3D printers including ASA, Polycarbonate, Nylon 6, ABS, PLA, ULTEM 9085/1010. In recent years, 3D printing technology started to be used in material engineering as well due to its fast production and lower cost in various fields [1]. A promising study

field is the use of 3D printers to manufacture MTM absorbers for electromagnetic application, despite the fact that numerous approaches have been examined in diverse studies. 3D printing can definitely be preferred and used including the design of metamaterials along with frequency selective surfaces mentioned by S. Ghosh and S. Lim as in [2]. These types of structures are preferred to reduce Radar Cross Section (RCS) in Aerospace [3]. 3D printing allows layer by layer fabrication of structures from a computer aided model. This technology enables parts to be created with difficult geometries. Fused deposition modeling (FDM) is the most popular and handy additively manufacturing method. It offers one of the most cost-efficient ways of 3D printing [4]. Solid objects are created by melting a polymer filament which is deposited through a nozzle tip one layer on top of another. In [5], a manufactured FSS when compared to the identical design that was fully metallized, the resonant frequency was dramatically reduced and the angle of incidence performance was improved by partially metallizing 3-D printed structures [6]. Electromagnetic band gap (EBG) structures have been utilized frequently to enhance the performance of antenna [7]-[9]. For more efficient antenna in terms of matching and directivity, they can serve as high impedance surfaces. There have been suggestions for small coplanar waveguide (CPW) antennas that use commercial laminates [7] and textile materials [8].

In this letter, the samples with three different raster orientations ([0° 90°] crossply, [-45° +45°] crossply, [Perimetric] orientation) are fabricated by STRATASYS F900 brand 3D printer. The printed parts' electromagnetic performances are measured using waveguide measurement setup operating between 12-18 GHz. This study focuses not only on using FSS for providing band-pass filter response but also on reducing RCS by adding a metamaterial layer with help of 3D printed substrates.

## MATERIALS AND METHODS

In this study, it was aimed to use 3D printed materials as the substrate for the combination of metamaterials and FSS structures. For this purpose, three samples with different configurations were manufactured using a 3D printer. ULTEM 9085

flame retardant 3D printing filament was used. The full name of the filament is given as "ULTEM 9085 resin black, 92 cu in - Plus". The configurations are; 0°/90° crossply orientation, -45°/45° crossply orientation and perimetric orientation as shown in the figure below (Figure 1). There are certain parameters that need to be mentioned such as T16 nozzle tip is used and its raster width is 0.508 mm and layer height is 0.254 mm. The enclosed 3D printing platform's ambient temperature is 180 °C while filament is melted and deposited from the nozzle tip at 430 °C temperature.

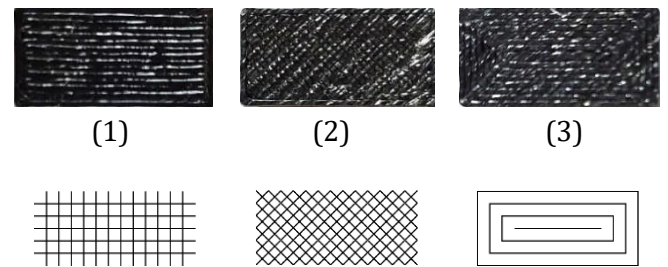


**Figure 4** 3D printed actual samples with three different configurations

**Table 1** Samples with different raster orientations

Samples	3D Printing Orientations
1	0° / 90° Cross-ply
2	-45° / +45° Cross-ply
3	Perimetric Orientation

The sizes of the samples chosen according to sample holder dimensions so that they can be used in electromagnetic waveguide measurement system in order to find their electromagnetic characteristics. This type of setup is used to obtain electrical permittivity and magnetic permeability values of the manufactured materials with various configurations. In waveguide test setup, there are two waveguides and one sample holder connected to a vector network analyzer (VNA). The sample is placed into the sample holder and scattering parameters, also known as S-parameters, are measured. Permittivity and permeability values can then be calculated from S-parameters using Nicholson Ross Weir method (NRW) [10-11]. In this method, some auxiliary terms are introduced as shown in the following equations.

$$X = \frac{S_{11}^2 - S_{21}^2 + 1}{2S_{11}}, \Gamma = X \pm \sqrt{X^2 - 1} \quad \text{and}$$

$$T = \frac{S_{11} + S_{21} - \Gamma}{1 - (S_{11} + S_{21})\Gamma}, \frac{1}{\Lambda^2} = - \left[ \frac{1}{2\pi L} \ln(T) \right]^2$$

After obtaining  $X$  and  $T$ , permittivity and permeability values can be calculated by the following equations;

$$\mu_r^* = \frac{2\pi}{\Lambda \sqrt{k_0^2 - k_c^2}} \left( \frac{1+\Gamma}{1-\Gamma} \right) \text{ and } \varepsilon_r^* = \frac{1}{\mu_r^* k_0^2} \left( \frac{4\pi^2}{\Lambda^2} + k_c^2 \right)$$

The wave guide measurement setup used in this study to determine the scattering parameters and the electrical permittivity and magnetic permeability parameters is shown in the figure below (Figure 2).

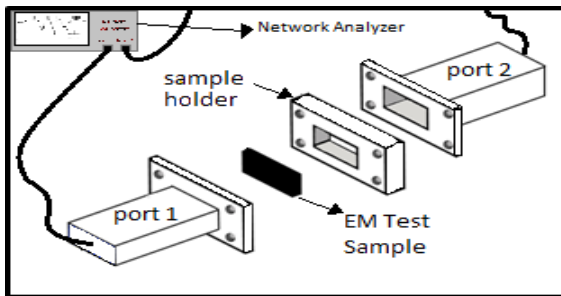


**Figure 5** Waveguide measurement setup and electromagnetic test sample

Once the electrical permittivity and magnetic permeability values are calculated, the corresponding material can be transferred into the computer environment. The next step is the design of frequency selective surface (FSS) and the metamaterial structure. In this study, we have designed a circular FSS providing a band-pass filtering property. The shape and dimensions of this structure can be seen in the following figure (Figure 3). The dimensions of the structure were chosen so that the filtering behavior occurs at around  $f=12$  GHz. For the metamaterial part, we have used circular split ring resonators (CSRR) with the dimensions providing absorption behavior in the range of  $f=15-20$  GHz. The detailed dimensions of the CSRR FSS can also be seen in the following figure (Figure 3).

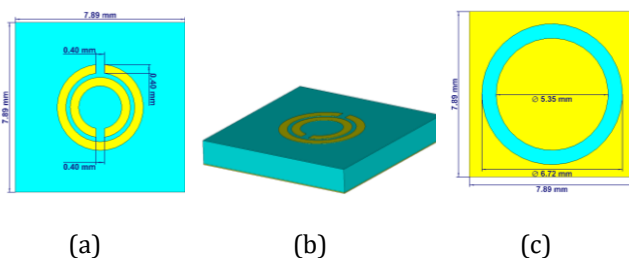


**Figure 6** Copper CSRR (a) as the top layer, perspective of the structure (b) and copper circular FSS (c) at the bottom layer.

The structure is composed of three layers including FSS layer at the bottom, dielectric layer at the middle section and MTM layer at the top layer of the structure. FSS cell is simply a ring removed from a copper ground with the dimensions of  $R_1=6.72$  mm and  $R_2=5.35$  mm where  $R_1$  refers to the outer diameter while  $R_2$  is the inner diameter. This is designed so that it reflects all the signals but signals having frequencies at about 12 GHz will only pass through. FSS structure acts as a band-pass filter operating at that certain frequency point. On the other hand, MTM structure integrated on top of the structure is composed of a split ring resonator as seen in the figure above (Figure-3). The thickness of the substrate was chosen as 1.6 mm while the copper thickness is 0.035 mm.

In terms of absorption perspective, we should note that absorption is directly related to transmission and reflection. The following equation summarizes these relations between them.

$$A(w) = 1 - R(w) - T(w)$$

Here,  $A(w)$  is the frequency related absorption,  $R(w)$  and  $T(w)$  are the frequency dependent reflection and transmission behaviors, respectively. In addition, reflection and transmission behavior can be written as  $R(w) = |S_{11}|^2$  and  $T(w) = |S_{21}|^2$  respectively using scattering parameters. In order to have high absorption, reflection and transmission must be minimized. In most absorber studies, transmission response is minimized and even eliminated by placing a metal ground plane at the back of the structures. In our case, this task is performed by the copper sections of FSS part placed at the bottom layer of the structure.

## RESULTS AND DISCUSSION

The combinations of FSS and MTM structure using three different 3D printed substrates are tested and the resulting reflection, transmission and absorption graphs are drawn in this section. In the first case, Sample-1 was used as the substrate and the obtained graphs are shown below in Figure 4. As seen in the figure, band-pass behavior is present at around  $f=12$  GHz while the reflection and

transmission stay low after  $f=15$  GHz resulting a good absorption behavior.

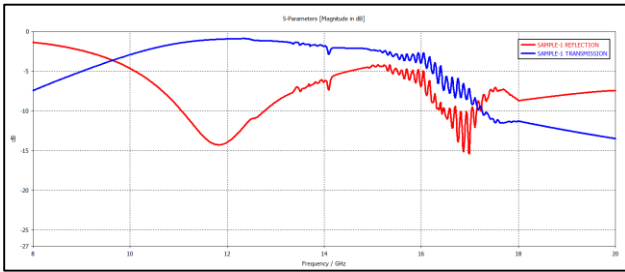


**Figure 7** Reflection and transmission of the structure for Sample-1 (Amplitude in dB vs Frequency in GHz)

The same approach was applied to all three samples and the reflection along with transmission behaviors are given in Figure 5 and 6 for the second and third samples, respectively. One can see from the figures that filtering operation works well at  $f=12$  GHz with reflection magnitudes of approximately -12.5 dB for both cases. In addition, the transmission values are very close to 0 dB at  $f=12$  GHz, meaning that there is no electromagnetic wave transmission between two ports at this frequency point. Besides, the absorption behavior can also be seen at higher frequencies, similar to Sample-1.

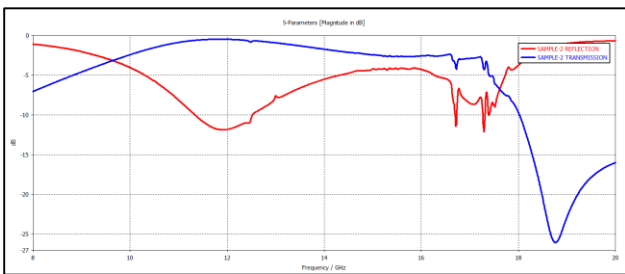


**Figure 8** Reflection and Transmission of the structure for Sample-2

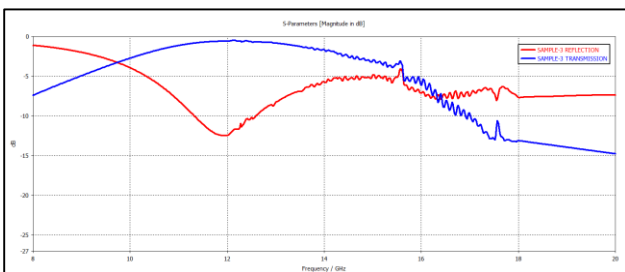


**Figure 9** Reflection and Transmission of the structure for Sample-3

For a better understanding, the absorption graphs have been drawn for all three cases in terms of frequency bands (Figure 7-9). In figures below, x-axis refers frequency in GHz while the y-axis represents absorption level (where 1 stands for

100% absorption). In Figure 7 and Figure 9, the absorption values are very close to 80% where as in Figure 8 the absorption value is almost 70% top as expected from the reflection and transmission graphics for all three samples.

As a result, samples with  $0^\circ / 90^\circ$  cross-ply and perimetric orientation provided higher absorption values for higher frequencies (smaller wavelength). However, the sample with  $-45^\circ/+45^\circ$  cross-ply orientation shows slightly less absorption behavior compared to the other samples.

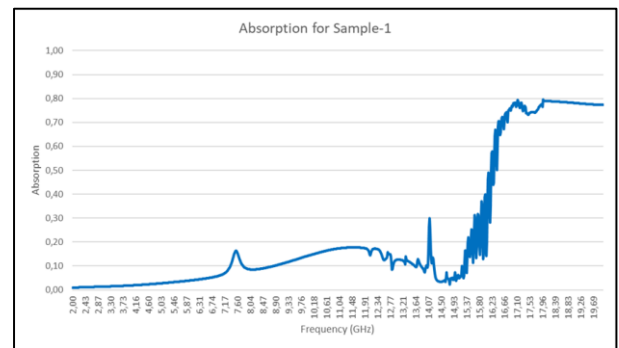


**Figure 10** Absorption of MTM+FSS structure for the Sample-1 with respect to wavelength

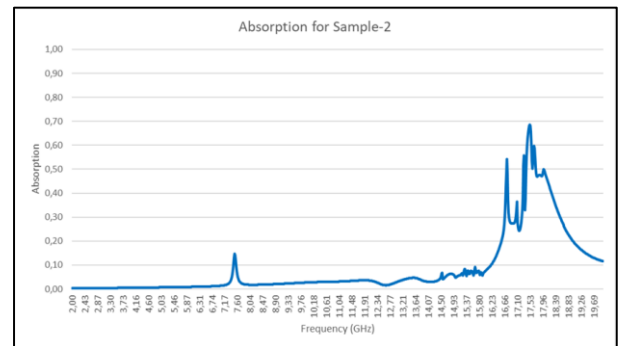


**Figure 11** Absorption of MTM+FSS structure for the Sample-2 with respect to wavelength

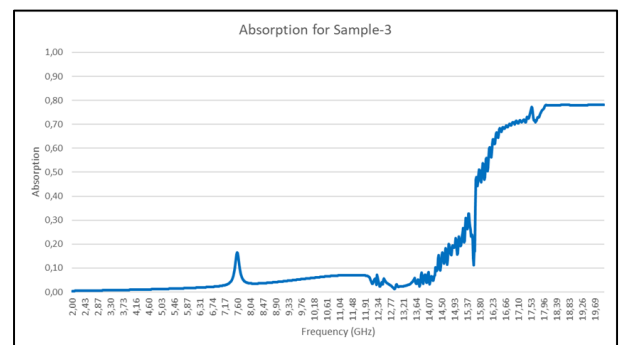


**Figure 12** Absorption of MTM+FSS structure for the Sample-3 with respect to wavelength

## CONCLUSION

In conclusion, the idea of using metamaterials with frequency selective surfaces worked well in the structure we designed in this study. Normally, an FSS structure built for a band-pass behavior allow signals at a certain frequency band while reflecting the rest of the signals in different frequencies. With the combination we suggested in this paper, high frequencies are absorbed with the help of metamaterial split ring resonator structure placed on the other side of the structure. This can be seen both from the absorption graphs and from the transmission/reflection graphs. It is obvious that absorbing signals rather than reflecting back fully will significantly reduce the radar cross section of

the structure. Finally, it can be said that this structure and approach can be used safely and easily particularly in antenna radomes to reduce RCS in various applications. The challenging part of this study will be the application of this structure on non-planar surfaces which will be the future study on this subject.

## ACKNOWLEDGMENTS

The experimental analyses and simulation studies are carried out at Electromagnetic and Optical Characterization Laboratory at Turkish Aerospace. The findings, conclusions, and recommendations expressed in this manuscript are those of the authors; shall not be related to company per se.

## REFERENCES

- [5] Lee, J.Y., An, J., Chua, C.K., "Fundamentals and applications of 3D printing for novel materials", *Applied Materials Today*, Vol 7, Pages 120–133, 2017
- [6] S. Ghosh and S. Lim, "A Miniaturized Bandpass Frequency Selective Surface Exploiting Three-Dimensional Printing Technique," in *IEEE Antennas and Wireless Propagation Letters*, vol. 18, no. 7, pp. 1322-1326, July 2019, doi: 10.1109/LAWP.2019.2915048.
- [7] Ren LS, Jiao YC, Zhao JJ, et al. RCS reduction for a FSS-backed reflectarray using a ring element. *Prog Electromagnet Res Lett*. 2011 ;26:115– 123.
- [8] Jun, S. and Sanz-Izquierdo, Benito and Parker, Edward A. (2016) 3D printing technique for the development of non-planar electromagnetic bandgap structures for antenna applications. *Electronics Letters*, 52 (3). pp. 175-176. ISSN 0013-5194.
- [9] Sanz-Izquierdo, B. and Parker, E.A.: 'Frequency Selective Surfaces Formed by Partially Metalising 3D Printed Shapes', in *Antennas and Propagation (EuCAP)*, 2015 9th European Conference on, (2015).
- [10] Sanz-Izquierdo, B. and Parker, E.A.: '3-D Printing of Elements in Frequency Selective Arrays', *IEEE Trans. Antennas Propag.*, 2014, 62, (12), pp. 6060-6066.
- [11] Sievenpiper, D., Zhang, L.J., Broas, R.F.J., Alexopolous, N.G., and Yablonovitch, E.: 'High-Impedance Electromagnetic Surfaces with a Forbidden Frequency Band', *IEEE Trans. Antennas Propag.*, 1999, 47, (11), pp. 2059-2074.
- [12] Shaozhen, Z. and Langley, R.: 'Dual-Band Wearable Textile Antenna on an Ebg Substrate', *IEEE Trans. Antennas Propag.*, 2009, 57, (4), pp.926-935. Kim, S., Yu-Jiun, R., Hoseon, L., Rida, A., Nikolaou, S., and Tentzeris, M.M.: 'Monopole Antenna with Inkjet-Printed Ebg Array on Paper Substrate for Wearable Applications', *IEEE Antennas Wireless Propag. Lett*, 2012, 11, pp. 663-666.
- [13] Bin, L., Sanz-Izquierdo, B., Parker, E.A., and Batchelor, J.C.: 'A Frequency and Polarization Reconfigurable Circularly Polarized Antenna Using Active Ebg Structure for Satellite Navigation', *IEEE Trans. Antennas Propag.*, 2015, 63, (1), pp. 33-40.
- [14] Nicolson, A.M.; Ross, G.F. Measurement of the Intrinsic Properties of Materials by Time-Domain Techniques. *IEEE Trans. Instrum. Meas.* 1970, 19, 377–382.
- [15] Weir, W.B. Automatic measurement of complex dielectric constant and permeability at microwave frequencies. *Proc. IEEE* 1974, 62, 33–36

## Processing and material design approaches for advanced oxide thermoelectrics: representative cases

**Andrei V. Kovalevsky, Gabriel Constantinescu, Diogo Lopes, Tiago Paulino, Kiryl V. Zakharchuk,**

*CICECO – Aveiro Institute of Materials, Department of Materials and Ceramic Engineering, University  
of Aveiro, 3810-193 Aveiro, Portugal.*

*e-mails: [akavaleuski@ua.pt](mailto:akavaleuski@ua.pt); [gabriel.constantinescu@ua.pt](mailto:gabriel.constantinescu@ua.pt); [djlopes@ua.pt](mailto:djlopes@ua.pt); [paulino@ua.pt](mailto:paulino@ua.pt);  
[k.zakharchuk@ua.pt](mailto:k.zakharchuk@ua.pt).*

*ORCID: 0000-0001-5814-9797, 0000-0002-1614-1962, 0000-0002-1087-9990, 0000-0001-9868-687X,  
0000-0002-5109-5359*

**Nuno M. Ferreira, Florinda M. Costa,**

*i3N, Physics Department, University of Aveiro, 3810-193 Aveiro, Portugal*

*e-mails: [flor@ua.pt](mailto:flor@ua.pt), [nmferreira@ua.pt](mailto:nmferreira@ua.pt).*

*ORCID: 0000-0002-4398-9256, 0000-0001-8729-714X*

**Wenjie Xie, Anke Weidenkaff.**

*Materials and Resources, Techn. Universität Darmstadt, Alarich-Weiss Str.2, DE-64287 Darmstadt,  
Germany*

*e-mails: [wenjie.xie@mr.tu-darmstadt.de](mailto:wenjie.xie@mr.tu-darmstadt.de), [anke.weidenkaff@mr.tu-darmstadt.de](mailto:anke.weidenkaff@mr.tu-darmstadt.de).*

*ORCID: 0000-0003-1826-7574, 0000-0002-7021-1765*

*Cite this paper as Kovalevsky, AV, Constantinescu, G, Lopes, D, Paulino, T, Zakharchuk, KV, Ferreira, NM,  
Costa, FM, Xie, W, Weidenkaff, A. Processing and material design approaches for advanced oxide  
thermoelectrics: representative cases. Int. Conf. Advanced. Mater. Sci. & Eng. HiTech. and Device Appl. Oct. 27-  
29 2022, Ankara, Turkey.*

**Abstract.** Oxide materials are currently considered a promising alternative to traditional thermoelectrics. Moderate charge carrier mobility stemming from strong covalent and ionic bonding, combined with relatively high thermal conductivity, represent known disadvantages of these materials for thermoelectric applications. However, oxides offer a possibility to operate at high temperatures, resulting in a higher Carnot efficiency. In addition, their known structural and microstructural versatility can open new horizons for thermoelectric applications. This work reviews some representative cases of engineering the composition and microstructure of a series of selected oxides towards high thermoelectric performance. The selected approaches will include laser processing, in situ formed composites, defects tailoring and aluminothermy-boosted sintering, also taking into account the unique redox-tuning capabilities of oxides. Representative examples will include ceramic materials based on SrTiO<sub>3</sub>, ZnO, CaMnO<sub>3</sub> and Ca<sub>3</sub>Co<sub>4</sub>O<sub>9</sub>.

**Keywords:** thermoelectrics, energy conversion, electroceramics, oxides.

© 2022 Published by ICMATSE

The UN 2030 Agenda goals give particular emphasis to the growing need for low-carbon and energy-efficient technologies. Significant efficiency savings can be thus achieved by recovering useful energy from waste heat. A promising solution is direct thermal to electrical energy conversion based on the Seebeck effect and using thermoelectric materials. Thermoelectric technology offers a short route to power generation and is self-sufficient to enable mobile or remote applications [1]. The efficiency of

a thermoelectric generator is directly linked to the performance of the semiconducting materials from which it was composed. Different material families have promising thermoelectric properties [1,2], with the focus given to oxides when considering high-temperature applications, owing to their stability in air at elevated temperatures and abundance. The results presented in this work was obtained for bulk ceramic thermoelectric materials. Detailed structural, microstructural, electrical and thermal

characterization (Fig. 1) was performed to obtain new guidelines for processing and design of performing oxide thermoelectrics. Laser floating zone (LFZ) method was demonstrated as a suitable method for processing ceramics with good thermoelectric properties, although the equilibration of the phase composition after growth represents a challenge [3].

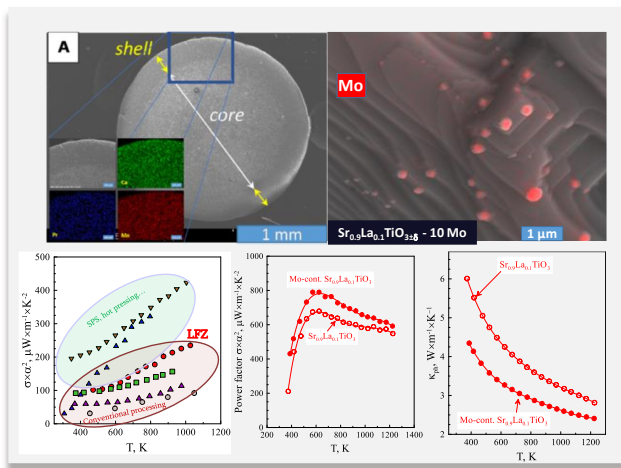


**Figure 1.** Representative microstructures and thermoelectric performance of some laser-processed ceramics and in-situ formed composites.

The thermoelectric properties of oxides can be tuned and enhanced by redox-sensitive additions, as exemplified by the cases of Sr(La)TiO<sub>3</sub> – MoO<sub>3</sub> composites [4] and Ca<sub>3</sub>Co<sub>4</sub>O<sub>9</sub> containing metallic Co addition [5]. Aluminothermy reaction can be used to promote the donor doping of ZnO-based thermoelectrics, leading to an enhancement of the electrical performance. These and some other approaches are discussed in the present work.

## References

1. R. Freer, A.V. Powell, Realising the potential of thermoelectric technology: a roadmap, *J Mater Chem C*, 8 (2020), pp. 441-463, 10.1039/c9tc05710b.
2. X.-L. Shi, J. Zou, Z.-G. Chen, Advanced thermoelectric design: from materials and structures to devices, *Chem Rev*, 120 (2020), pp. 7399–7515, 10.1021/acs.chemrev.0c00026.
3. F.P. Carreira, N.M. Ferreira, A.V. Kovalevsky, Laser processing as a tool for designing donor-substituted calcium-manganite-based thermoelectrics, *J Alloys and Compounds*, 829 (2020), p. 154466, 10.1016/j.jallcom.2020.154466.
4. A.V. Kovalevsky, K.V. Zakharchuk, M.H. Aguirre, W. Xie, S.G. Patrício, N.M. Ferreira, D. Lopes, S.A. Sergiienko, G. Constantinescu, S.M. Mikhalev, A. Weidenkaff, J.R. Frade, Redox engineering of strontium titanate-based thermoelectrics, *J Mater Chem A*, 8 (2020), pp. 7317-7330, 10.1039/c9ta13824b.
5. G. Constantinescu, A.R. Sarabando, Sh. Rasekh, D. Lopes, S. Sergiienko, P. Amirkhizi, J.R. Frade, A.V. Kovalevsky, Redox-promoted tailoring of the high-temperature electrical performance in Ca<sub>3</sub>Co<sub>4</sub>O<sub>9</sub> materials by metallic cobalt addition, *Materials*, 13 (2020), p. 1060.

## Microstructural and Mechanical Effects of Intercritical Annealing on Mid-Mn Steels

**Mehmet Eroglu**

*Firat University-Metallurgy and Materials Engineering, 23000, Elazig, Turkey, meroglu@firat.edu.tr*  
ORCID: 0000-0002-5097-1943

**Fatih Demir**

*Batman University-Mechanical Engineering, 72000, Batman, Turkey, fatihdemir23@hotmail.com*  
ORCID: 0000-0003-3239-4641

*Cite this paper as: Eroglu, M, Demir, F. Microstructural and Mechanical Effects of Intercritical Annealing on Mid-Mn Steels. Int. Conf. Advanced. Mater. Sci. & Eng. HiTech.and Device Appl.Oct. 27-29 2022,Ankara, Turkey*

**Abstract.** Since the last century, the priorities of the automotive industry have changed, and factors such as fuel consumption and passenger safety have been decisive in the design of automobiles. This has led to the development of advanced high-strength steels with high strength and enhanced elongation. Safety rules and renewed demands have increased the need for new AHSS types over time and forced the steel industry to produce new generation AHSS. One of these new types of AHSS is medium manganese steels. In this study, the effect of intercritical annealing on the microstructure and mechanical properties of 0.16C-5.5Mn mid-Mn steel was investigated. The 0.16C-5.5Mn steel plate manufactured by casting has been thinned into sheet form by hot press and hot forging method. Then, intercritical (675°C) and conventional (800°C) annealing processes were applied to the samples. Microstructures were observed with optical microscopy (OM) and scanning electron microscopy (SEM), and volume fractions of retained austenite were calculated by X-ray diffraction (XRD). The mechanical behavior of 0.16C-5.5Mn steel was investigated by tensile and hardness tests, and the fracture behavior was examined with SEM micrographs. The findings revealed that the intercritical annealing improves the strength-elongation combination in 0.16C–5.5Mn steel. The fracture surface images showed that the cooling rate had an effect on the fracture behavior.

**Keywords:** Mid-Mn, Intercritical Annealing, AHSS

© 2022 Published by ICMATSE

### 1. Introduction

The current demands, safety requirements, and the requirement for thinner panel thickness to provide the prescribed stiffness for the automotive industry have created the need for special combinations of strength and elongation. These requirements are summarized by the term "Advanced High-Strength Steels (AHSS)", which generally means yield strength above 280 - 300 MPa and tensile strength above 590 - 600 MPa with improved elongation. While the main category of AHSSs is DP steels, the requirements of the automotive industry have led to the development of new special microstructures from high-strength steel sheets to meet specific demands for certain safety conditions. The first of these are TRIP steels, which show transformation-induced plasticity with an extremely high hardening ratio up to the limit of uniform elongation, which can help provide extremely high energy absorption in collisions [1].

The general trend followed by the steel industry in automobile production is to achieve higher strength values with the same level of formability as an existing type of high strength steel (HSS) or AHSS. The evolution of existing high and ultra high strength formable steels has spawned new types of so-called "Third Generation" steels that have essentially high strength at significantly higher elongation and approach the values of high Mn TWIP steels. The sustainability of the steel industry and the place of AHSS in the automotive industry make these new generation steels extremely important. It should be noted that the strength and elongation combinations expected from the third generation AHSS consider the yield strength along with the tensile strength as the strength criterion. Extensibility includes uniform elongation with total elongation, as well as hole expansion. Several new steel grades have been developed that exhibit extremely high combinations of these parameters

and have attracted the attention of both researchers and industry [2]. One of the promising steel types with combinations of properties attributable to the Third Generation are medium manganese steels with a relatively high but still moderate concentration of Mn content (4-10%) [3, 4].

In this study, the effect of annealing conditions on the microstructure and mechanical properties of medium manganese steels is discussed. With the help of different analyzes and mechanical tests, the effects of annealing parameters on the phases forming the microstructure and accordingly the changes in the strength-elongation combination were investigated. The role of cooling rate on fracture behavior was investigated with SEM images taken from rupture surfaces.

## 2. Material and Method

Medium manganese steel plates used in this study were manufactured by casting. 5 mm thick sheets were obtained by hot forging method from these 45 mm thick plates. The chemical composition of the medium manganese 0.16C-5.5Mn steel is given in Table 1.

**Table 1.** Chemical composition of 0.16C-5.5Mn steel

Chemical Composition (wt.%)					
C	Mn	Si	Mo	Ni	Al
0.16	5.54	0.3	0.26	0.12	0.11

Samples taken from 0.16C-5.5Mn steel were first normalized at 900 °C. Then, different heat treatment cycles were applied to the samples in the critical temperature range ( $Ac_1 < T_A < Ac_3$ ) and above the critical temperature range ( $T_A > Ac_3$ ). These cycles are shown schematically in Figure 1.

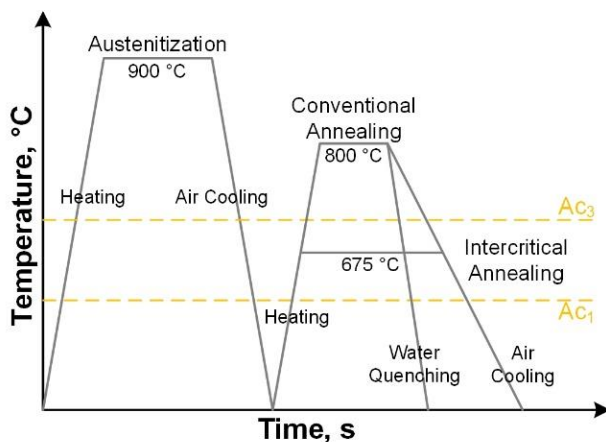


**Figure 1.** Annealing cycles

The heat treatment parameters of the samples annealed under different conditions are given in Table 2.

**Table 2.** Annealing conditions

Sample	Annealing Conditions		
	Temperature (°C)	Time (min)	Cooling Media
S1	675	30	Air
S2	800	30	Air
S3	675	30	Water
S4	800	30	Water

The annealed samples were sanded and polished for metallographic examinations and etched with 2% nital solution. Afterwards, optical microscopy (OM) and scanning electron microscopy (SEM) images were taken from the samples. In addition, phase analyzes were performed with Rigaku brand MiniFlex II model XRD analyzer. Tensile and hardness tests were applied to the samples in order to see the effect of annealing conditions on the mechanical properties of 0.16C-5.5Mn steel.

## 3. Results and Discussion

OM and SEM micrographs of 0.16C-5.5Mn samples annealed under different conditions are given in Figure 2 and Figure 3, respectively.

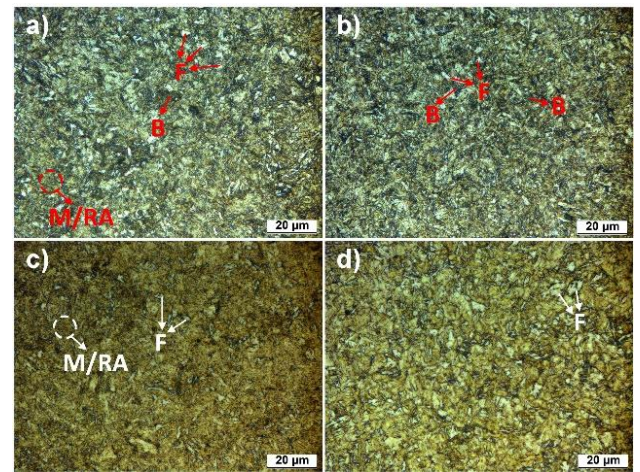


**Figure 2.** OM micrographs of 0.16C-5.5Mn samples; a) S1, b) S2, c) S3, d) S4

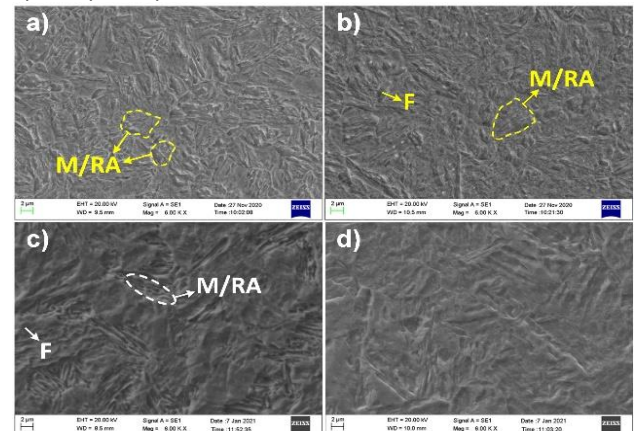


**Figure 3.** SEM micrographs of 0.16C-5.5Mn samples; a) S1, b) S2, c) S3, d) S4

When the OM images given in Figure 2 are examined, it is seen that the microstructure of 0.16C-5.5Mn steel consists of martensite (M) matrix and ferrite (F), bainite (B) and retained austenite (RA) phases. It was observed that the presence of the ferrite phase in the microstructure decreased with the annealing temperature exceeding the  $A_{c3}$  temperature, and there was some coarsening in the size of the ferrite grains [5]. It was determined that both ferrite and bainite phase fractions decreased in the water quenched samples. Increasing the cooling rate resulted in lath-shaped M/RA [6]. In particular, the layered M/RA structure can be seen more clearly in the SEM images of the water quenched samples (Figure 3c).

Retained austenite phase observed in SEM micrographs was also detected in XRD patterns (Figure 4).

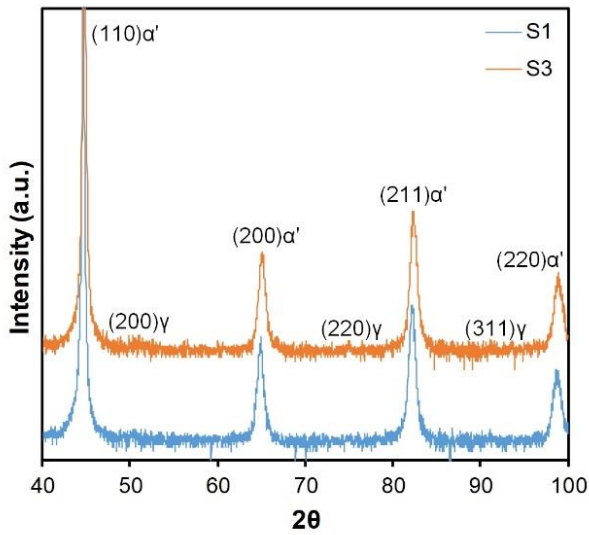


**Figure 4.** XRD graphs of samples S1 and S3

The volume fractions of the retained austenite phase were calculated with the help of the data of the martensite ( $\alpha'$ ) and residual austenite ( $\gamma$ ) phase peaks. The change in the volume fraction of retained austenite is given in Figure 5.

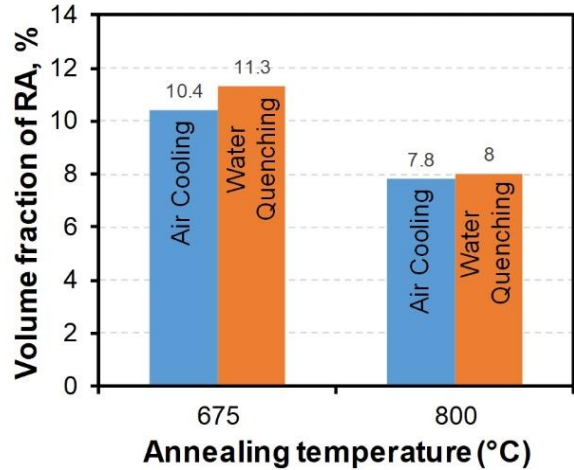


**Figure 5.** Volume fractions of RA

When the retained austenite phase fractions given in Figure 5 are examined, it is seen that the intercritical annealing applied between  $A_{c1}$  and  $A_{c3}$  temperatures increases the volume fraction of the retained austenite phase. This can be attributed to the fact that the critical austenite phase between  $A_{c1}$ - $A_{c3}$  temperatures is more enhanced in terms of Mn and C than the austenite phase above  $A_{c3}$  temperature [7, 8].

The effect of annealing parameters on the retained austenite phase fraction and phase distributions in the microstructure was also determinative on the stress-strain behavior of 0.16C-5.5Mn steel (Figure 6).

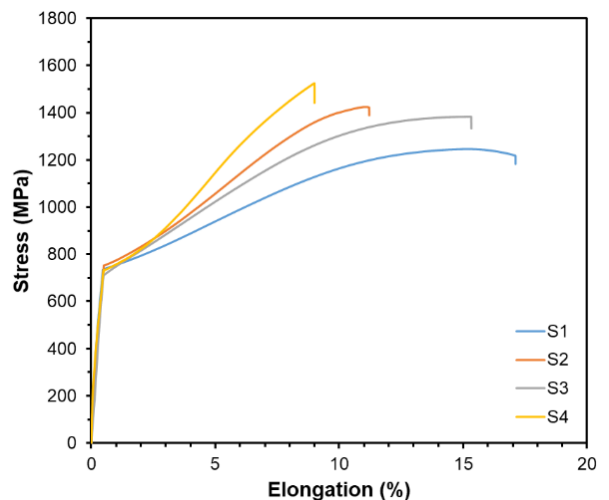


**Figure 6.** Stress-elongation graphs of samples

When the stress-strain graphs of the samples were examined, it was observed that the samples annealed in the full-austenite region reached higher strength values, while the elongation ability of the samples annealed in the critical temperature range was observed to be improved. The increase in cooling rate increased the strength values of the

samples, but negatively affected the total elongation. The mechanical properties of the samples after the mechanical tests are given in Table 3.

**Table 3.** Mechanical test results of the samples

Sample	TS (MPa)	TE (%)	TSxTE (GPa.%)	Hardness (HRC)
S1	1246	17.1	21.3	43.4
S2	1424	11.2	15.9	45.3
S3	1383	15.3	21.2	45.4
S4	1525	9	13.7	47.2

When the tensile strength-total elongation combinations (TSxTE) of the samples were examined, it was determined that the TSxTE combination of S1 and S3 samples annealed in the critical temperature range reached higher values (Table 3). The results obtained from the hardness tests showed that the increase in both the annealing temperature and the cooling rate increased the hardness values. This improvement seen in the TSxTE combination was made possible by the microstructure provided by the intercritical annealing process [9].

When the SEM images taken from the fracture surfaces of the samples were examined, it was observed that the samples exhibited mixed-type fracture behavior. Higher annealing temperature and cooling rate increased the efficiency of the brittle fracture mechanism (Figure 7).

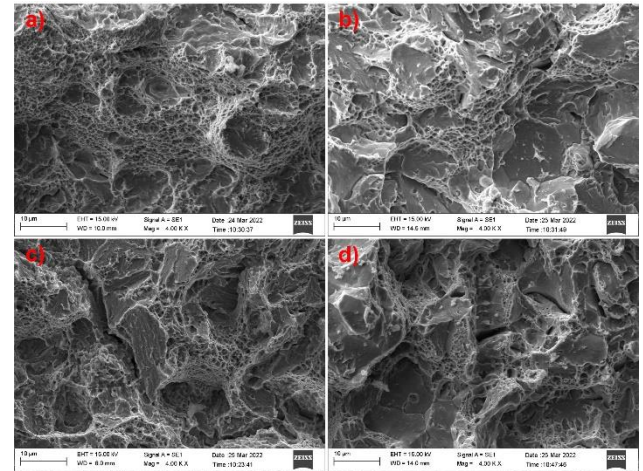


**Figure 7.** SEM images of the fracture surfaces; a) S1, b) S2, c) S3, d) S4

#### 4. Conclusion

In this study, the effects of intercritical annealing on the microstructure and mechanical properties of 0.16C-5.5Mn steel were investigated and the following results were obtained.

- The microstructure of 0.16C-5.5Mn steel consists of martensite matrix and phases of ferrite, bainite and retained austenite. Intercritical annealing increased the amount of retained austenite in the microstructure.
- Annealing in the critical temperature range has improved the TSxTE combination of 0.16C-5.5Mn steel.
- It has been determined that the fracture behavior of 0.16C-5.5Mn steel is dominated by mixed-type fracture.

#### Acknowledgements

This study was carried out with support from the Scientific Research Projects Unit of the Firat University (Project No: MF.19.49)

#### References

1. N. Fonstein, Evolution of Strength of Automotive Steels to Meet Customer Challenges, In Advanced High Strength Sheet Steels: Physical Metallurgy, Design, Processing, and Properties, (2015), pp. 1–16, Springer, London, doi:10.1007/978-3-319-19165-2
2. D.K. Matlock, J.G. Speer, Design Consideration for the next Generation of Advanced High Strength Sheet Steels, In The 3rd International Conference on Advanced Structural Steels, (2006), pp. 774–781, Gyeongju, Korea
3. A. Arlazarov, A. Hazotte, O. Bouaziz, M. Gouné, F. Kegel, Characterization of microstructure formation and mechanical behaviour of an advanced Medium-Mn steel, In Conf. Proc. Materials Science & Technology, (2012), pp. 1124–1131, MS&T, Pittsburgh
4. Y.K. Lee, J. Han, Current opinion in medium manganese steel, Materials Science and Technology, 31(7) (2015), pp. 843–856, 10.1179/1743284714y.0000000722
5. G. Speich, V. Demarest, R. Miller, Formation of Austenite During Intercritical Annealing of Dual-Phase Steels, Metallurgical and Materials Transactions A, 12(8) (1981), pp. 1419–28
6. G. Thomas, J.Y. Koo, Developments in Strong, Ductile Duplex Ferritic - Martensitic Steels, In Conference of Structure and Properties of Dual-Phase Steels, Symposium at the AIME Annual Meeting, (1981), pp. 183–201, New Orleans, LA, USA
7. A.M. Streicher, J.G. Speer, D.K. Matlock, Forming response of retained austenite in a C-Si-Mn high strength TRIP sheet steel, Steel Research, 73(6-7) (2002), pp. 287–293, 10.1002/srin.200200210

8. K. Sugimoto, M. Kobayashi, A. Nagasaka, S. Hashimoto, Warm stretch-formability of TRIP-aided dual-phase sheet steels, *ISIJ international*, 35(11) (1995), pp. 1407-1414, 10.2355/isijinternational.35.1407
9. N. Fonstein, *Advanced High Strength Sheet Steels: Physical Metallurgy, Design, Processing, and Properties*, Springer, London, 10.1007/978-3-319-19165-2

## THE PREPARATION OF Al<sub>2</sub>O<sub>3</sub>-Ag CORE-SHELL MICROSPHERES BY USING SEED MEDIATED GROWTH ELECTROLESS PLATING

**Meryem BOZKAYA**

Gazi University- Advanced Technologies, 06500, Ankara, Turkey, meryem.bozkaya@gazi.edu.tr  
ORCID: 0000-0001-5711-9369

**Hakan ATEŞ**

Gazi University- Metallurgical and Materials Engineering, 06500, Ankara, Turkey, hates@gazi.edu.tr  
ORCID: 0000-0002-5132-4107

**Ramazan KARSLIOĞLU**

Ankara Yıldırım Beyazıt University- Metallurgical and Materials Engineering, 06500, Ankara, Turkey,  
rkarslioglu@ybu.edu.tr  
ORCID: 0000-0001-5490-3449

*Cite this paper as: Bozkaya, M, Ateş, H and Karslıoğlu, R. The preparation of Al<sub>2</sub>O<sub>3</sub>-Ag Core-shell Microspheres by using seed mediated electroless plating. Int. Conf. Advanced. Mater. Sci. & Eng. HiTech. and Device Appl. Oct. 27-29 2022, Ankara, Turkey*

**Abstract.** In this study, Al<sub>2</sub>O<sub>3</sub>@Ag Core@shell microspheres were synthesized via seed mediated electroless plating method. Polyvinylpyrrolidone (PVP) was used to control uniform shell synthesis. Moreover, the influence of the PVP content and Ag powder concentration during the synthesis of Ag shell was investigated by scanning electron microscopy (SEM) and energy dispersive spectroscopy (EDS). The results show that silver powder concentration and adding PVP during shell synthesis are important parameters in terms of obtaining homogeneous and uniform silver shell synthesis.

**Keywords:** core-shell, Al<sub>2</sub>O<sub>3</sub>-Ag, electroless plating,  
© 2022 Published by ICMATSE

### INTRODUCTION

Recently, the core-shell microspheres are intriguing materials due to excellent properties such as, mechanical stability, good electric-magnetic properties and thermal conductivity [1,2]. Especially, ceramic core like silica, polystyrene and noble metal shell such as gold and silver has an important role to apply surface enhanced raman scattering, plasmon resonance frequency applications and so on [3,4]. So, there exist many way to synthesis core-shell microspheres, such as layer-by-layer method [5], electroless plating [6], chemical deposition [7], and sonochemical approach [8]. Electroless plating of core-shell structures have attracted method due to excellent advantages such as cheap, fast production,

easily scalable and modifying. In terms of last two decades research about the ceramic-

metal core-shell microspheres have devoted high demand in photonics, optoelectronics, biosensing and surface-enhanced raman scattering (SERS) [9]. Especially when the literature is examined for silica core-silver shell synthesis, Liz-Marzan and co-workers have shown that SiO<sub>2</sub>@Ag core-shell were synthesized successfully without the activated agent like palladium or gold with the help of decorating silver atoms [10]. After that Liu and co-workers obtained homogenous and monodisperse SiO<sub>2</sub>@Ag core shell by adding PVP to stabilize and control full covered silver shell process [11]. Although there are many studies in the literature for silver shell synthesis

on ceramic core, it is seen that alumina core silver shell growth with electroless coating method is rarely studied. In this paper, Al<sub>2</sub>O<sub>3</sub>-Ag core-shell microspheres were synthesized via seed mediated electroless plating method. Polyvinylpyrrolidone (PVP) was used to control uniform shell synthesis. We characterized each samples by field emission scanning electron microscopy (FESEM) and energy dispersive spectroscopy (EDS). The results show that with the process of as-seed mediated silver nuclei and adding PVP during the complete silver shell synthesis are important parameters in terms of obtaining homogeneous and uniform silver shell synthesis.

## EXPERIMENTAL

### Materials

Polyvinylpyrrolidone (PVP, k30), silver nitrate (AgNO<sub>3</sub>, %99.8), formaldehyde (HCHO, 37%), Ammonia solution (28%), hydrochloric acid (HCl, %25) and SnCl<sub>2</sub>·2H<sub>2</sub>O and DIW were used to growth Al<sub>2</sub>O<sub>3</sub>-Ag core-shell.

### Pre-treatment of Al<sub>2</sub>O<sub>3</sub> powders

The chosen Al<sub>2</sub>O<sub>3</sub> powders has an average size 40µm. The first step 0.5 gr Al<sub>2</sub>O<sub>3</sub> powders were cleaned with 100 ml acetone through the 15 min. After that the cleaning Al<sub>2</sub>O<sub>3</sub> were washed by DIW a few times and finally were collected with the help of filtrate process to sensitize immediately pre-treating Al<sub>2</sub>O<sub>3</sub> powders.

### Sensitization process of Al<sub>2</sub>O<sub>3</sub> powders

Pre-treating Al<sub>2</sub>O<sub>3</sub> powders were immersed 100 ml DIW and were added 3gr. SnCl<sub>2</sub> to sensitize. Moreover, to avoid hydrolyzation of SnCl<sub>2</sub> were used 10 ml HCl. The process lasted for 30min in 30°C under the magnetic stirring to 400 rpm. When the process was finished, The sensitized Al<sub>2</sub>O<sub>3</sub> powders were separated the solution and were cleaned a few times to remove unabsorbed SnCl<sub>2</sub>.

### Decorating silver nuclei of Al<sub>2</sub>O<sub>3</sub> core and process of the Al<sub>2</sub>O<sub>3</sub>-Ag core-shell synthesis

0.35 M AgNO<sub>3</sub> and sensitized Al<sub>2</sub>O<sub>3</sub> were added ammonical solution for 20 min. Then, The Al<sub>2</sub>O<sub>3</sub> powders were collected again and were dispersed a few times with DIW. To obtain a homogeneous and uniform silver shell, sequentially decorated alumina, 0.025M AgNO<sub>3</sub>, 0.1 gr. PVP and 3 ml of

formaldehyde were added while mixing with a 400 rpm magnetic stirrer. Then 40 ml of ammonia was added to activate the silver shell synthesis reaction. This process continued until the solution turned a deep black color. After the samples were washed, they were dried at 80C for 6 hours. The synthesized samples were characterized FESEM and EDS.

## RESULTS AND DISCUSSION

Elemental and morphology analysis of Al<sub>2</sub>O<sub>3</sub>-Ag core-shell samples were characterized with a SEM Hitachi SU5000 FESEM which is the accelerating voltage was set to 10 kV with a working distance of approximately 6 mm.

Electroless plating method has consist of autocatalytic process without electrical energy. So, It has commonly used to grow silver shell onto ceramic cores due to excellent advantages like large scale product, more modifyng, cheap and fast process without the low vacuum. Despite all these advantages, there are many sensitive parameters for the core-shell synthesis to be homogeneous and controlled. These parameters are value of pH, type and amount of the reactants, temperature Sensitization process and amount of catalytic agents [3,10].

The silver shell can not directly synthesis on Al<sub>2</sub>O<sub>3</sub> cores that has chemical inertness nature. So, Al<sub>2</sub>O<sub>3</sub> should be sensitiized with the SnCl<sub>2</sub> and HCl solution. Thus, as-sensitized Al<sub>2</sub>O<sub>3</sub> has suitable for the Ag ions seed process to obtain and uniform silver shell.

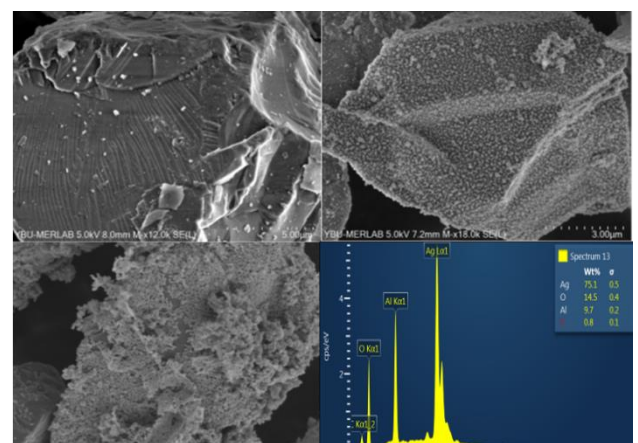


Figure.1. SEM images of Al<sub>2</sub>O<sub>3</sub>-Ag core-shell a) Decorated Al core, b) bu adding 0.1 PVP growth core-shell, c) growth core-shell without PVP, d) EDS images of core-shell.

In order to obtained uniform and dense Al<sub>2</sub>O<sub>3</sub>-Ag core-shell, dielectric core should be activated with the help of diverse metal catalyst such as Palladium,

gold etc. However, mentioned of these metal catalytics are quite expensive. On the other hand, activating the sensitized Al<sub>2</sub>O<sub>3</sub> core with silver atoms acting as seed mediated is highly effective in homogeneous synthesis of silver shell. This reaction occurs that;



To synthesis fully covered silver shell onto Al<sub>2</sub>O<sub>3</sub> core, the ratio of Sn/Ag have been optimized as 3gr SnCl<sub>2</sub> and 0.35M AgNO<sub>3</sub>, respectively. Figure 1.a. shows that Ag decorated Al<sub>2</sub>O<sub>3</sub> core, silver nuclei form on the core is occurred pretty homogenous which is supported the formation of the uniform silver shell.

To obtain uniform and full covered Al<sub>2</sub>O<sub>3</sub>-Ag core-shell to the other parameters are quite significant, as well. For instance, the pH of the solution must be critical for formaldehyde to activate silver ions. This value is set to 13. When the pH value is below 13, the formaldehyde-silver interaction will be weak, which results in agglomeration in the formation of silver shell.

Although the pH value is optimal, the cores interact with each other during shell formation and the homogeneous and fully covered shell structure is disrupted, resulting in the formation of agglomerated or uncoated regions. Various polymer surfactants are used to prevent this. PVP is widely used among these

polymer surfactants. Adding some pvp during the shell formation process ensures that the formed shell is homogeneous and uniform. Figure 1.b. and 1.c. indicated that Sem images of Al<sub>2</sub>O<sub>3</sub>-Ag core shell without PVP and PVP, respectively. While agglomeration occurs in the Al<sub>2</sub>O<sub>3</sub>-Ag core shell synthesized without using PVP (Fig.1.b.), the agglomeration is prevented by the addition of PVP. Thus, the core-shell structure formed is fully covered and homogeneous (Fig.1.c.). The EDS imaging of Al<sub>2</sub>O<sub>3</sub>-Ag core shell supported to the results as well.

## CONCLUSION

In our study show that homogeneous and uniform silver shell synthesis was successful by adding PVP. In silver shell synthesis without the addition of PVP, silver ions interact with each other to form a heterogeneous and agglomerated shell structure. This results were indicated that the PVP addition protects the shell structure by preventing silver ions from interacting with each other. In addition, silver decoration was used instead of expensive activating precursors such as palladium. In this way, more cheaper and homogenous silver shell was synthesized on the alumina core.

## Acknowledgement

The first author is supported by the Council of Higher Education as a scholarship student of YÖK 100/2000 Priority Areas/Micro-Nanotechnology field.

## References

1. Liu, T., Li, D., Yang, D., & Jiang, M. (2011). An improved seed-mediated growth method to coat complete silver shells onto silica spheres for surface-enhanced Raman scattering. *Colloids and Surfaces A: Physicochemical and Engineering Aspects*, 387(1-3), 17-22.
2. Chen, D., Liu, H. Y., Liu, J. S., Ren, X. L., Meng, X. W., Wu, W., & Tang, F. Q. (2008). A general method for synthesis continuous silver nanoshells on dielectric colloids. *Thin Solid Films*, 516(18), 6371-6376.
3. Choe, W. G., & Park, O. O. (2014). Morphology control and temporal growth of a continuous silver shell on core-shell spheres. *CrystEngComm*, 16(23), 5142-5149.
4. Zhu, M., Qian, G., Hong, Z., Wang, Z., Fan, X., & Wang, M. (2005). Preparation and characterization of silica-silver core-shell structural submicrometer spheres. *Journal of Physics and Chemistry of Solids*, 66(5), 748-752.
5. Beygi, H., Sajjadi, S. A., Zebarjad, S. M., & Babakhani, A. (2011). Preparation of Al<sub>2</sub>O<sub>3</sub>/Cu core-shell structural composites by electroless plating and determination of optimum bath composition using Taguchi experimental design. In *18th International Conference on Composite Materials, Jeju Island, Korea*.
6. Uysal, M., Karslioglu, R., Alp, A., & Akbulut, H. (2013). The preparation of core-shell Al<sub>2</sub>O<sub>3</sub>/Ni composite powders by electroless plating. *Ceramics international*, 39(5), 5485-5493.
7. Y. Kobayashi, V. Salgueirino-Maceira, L.M. Liz-Marzan, Deposition of silver nanoparticles on silica spheres by pretreatment steps in electroless plating, *Chem. Mater.* 13 (2001) 1630-1633.
8. J.B. Jackson, N.J. Halas, Silver nanoshells: variations in morphologies and optical properties, *J. Phys. Chem. B* 105 (2001) 2743-2746.
9. Z.J. Jiang, C.Y. Liu, Y. Liu, Z.Y. Zhang, Y.J. Li, Fabrication of silver nanoshell on functionalized silica sphere through layer-by-layer technique, *Chem. Lett.* 32 (2003) 668-669.
10. J.B. Jackson, N.J. Halas, Silver nanoshells: variations in morphologies and optical properties, *J. Phys. Chem. B* 105 (2001) 2743-2746.

11. J.C. Flores, V. Torres, M. Popa, D. Crespo, J.M. Calderón-Moreno, Variations in morphologies of silver nanoshells on silica spheres, *Colloids Surf. A: Physicochem. Eng. Aspects* 330 (2008) 86–90.

## Laser Technologies to fabricate Large Scale Bi-2212 Superconducting Plates

**C. Özçelik**

*Instituto de Nanociencia y Materiales de Aragón, INMA (CSIC-Universidad de Zaragoza), María de Luna, 3,  
50018 Zaragoza, Spain, ozcelik@unizar.es  
ORCID: 0000-0002-8100-6417*

**H. Amaveda**

*Instituto de Nanociencia y Materiales de Aragón, INMA (CSIC-Universidad de Zaragoza), María de Luna, 3,  
50018 Zaragoza, Spain, hippo@unizar.es  
ORCID: 0000-0003-2212-447X*

**M. Mora**

*Instituto de Nanociencia y Materiales de Aragón, INMA (CSIC-Universidad de Zaragoza), María de Luna, 3,  
50018 Zaragoza, Spain, mmora@unizar.es  
ORCID: 000-0003-4839-5286*

**E. Martínez**

*Instituto de Nanociencia y Materiales de Aragón, INMA (CSIC-Universidad de Zaragoza), María de Luna, 3,  
50018 Zaragoza, Spain, elenamar@unizar.es  
ORCID: 000-003-4839-5286*

**B. Özçelik**

*Department of Physics, Faculty of Sciences and Letters, Çukurova University, Adana, Turkey, ozcelik@cu.edu.tr  
ORCID: 0000-0002-8767-1426*

**G.F. de la Fuente**

*Instituto de Nanociencia y Materiales de Aragón, INMA (CSIC-Universidad de Zaragoza), María de Luna, 3,  
50018 Zaragoza, Spain, german.delafuente.leis@csic.es  
ORCID: 0000-0002-0500-1745*

**L. A. Angurel**

*Instituto de Nanociencia y Materiales de Aragón, INMA (CSIC-Universidad de Zaragoza), María de Luna, 3,  
50018 Zaragoza, Spain, angurel@unizar.es  
ORCID: 0000-0001-5685-2366*

*Cite this paper as: Ozçelik, C, Amaveda, H, Mora, M, Martínez, E, Ozçelik, B, de la Fuente, GF, Angurel, LA. Laser Technologies to fabricate Large Scale Bi-2212 Superconducting Plates. Int. Conf. Advanced. Mater. Sci. & Eng. HiTech.and Device Appl.Oct. 27-29 2022,Ankara, Turkey*

**Abstract.** Due to the properties anisotropy exhibited by high temperature ( $HT_c$ ) superconductors, develop adqate processing technologies is a major challenge. Recently, the laser induced solidification techniques have been using to improve the microstructure of  $HT_c$  superconductors namely,  $\text{Bi}_2\text{Sr}_2\text{CaCu}_2\text{O}_{8+x}$  (Bi-2212),  $\text{REBa}_2\text{Cu}_3\text{O}_{7-x}$  (RE-123, RE=Y,Gd). Different laser technologies have been used to fabricate well-textured samples and to machine them without generating cracks. Texture has been controlled using a Laser Zone Melting (LZM) technique while the sample is at thigh temperature in a system calle Laser Furnace. This tecniue can be considered as a modification of the laser line scanning protocol. A very flat solidification front has been obtained in samples up to 100 mm wide. We have fabricated Bi-2212 superconducting samples up to 10cm x 10cm size. The flatness reached in the solidification front allows obtaining misorientation angles lower than  $15^\circ$  in the full width of the sample. The transport properties of these superconducting materials have been correlated with

the level of texture and the thickness of the textured region reached during the laser process. It can be argued that the size of the plate samples is adequate to design several electrical circuits adapted for different applications.

**Keywords:** Laser Zone Melting, Bi2212 Plate, SEM-EDX.

**Acknowledgements**

*Work funded by the Spanish MCIN/AEI/10.13039/501100011033 (project PID2020-113034RB-I00) and by Gobierno de Aragón (research group T54\_20R). B. O. acknowledges to the Scientific and Technological Research Council of Turkey (TUBITAK) for a grant via 2219-Science Fellowships and Grant Programmes Department, with the project number:1059B192000390. Authors also would like to acknowledge the use of Servicio General de Apoyo a la Investigación-SAI, Universidad de Zaragoza*

© 2022 Published by ICMATSE

## **Fabrication of spinel ferrite nanoparticles via laser ablation**

**B. Özçelik**

*Department of Physics, Faculty of Sciences and Letters, Çukurova University, Adana, Turkey, ozcelik@cu.edu.tr  
ORCID: 0000-0002-8767-1426*

**H. Amaveda**

*Instituto de Nanociencia y Materiales de Aragón, INMA (CSIC-Universidad de Zaragoza), María de Luna, 3,  
50018 Zaragoza, Spain, hippo@unizar.es  
ORCID: 0000-0003-2212-447X*

**L. A. Angurel**

*Instituto de Nanociencia y Materiales de Aragón, INMA (CSIC-Universidad de Zaragoza), María de Luna, 3,  
50018 Zaragoza, Spain, angurel@unizar.es  
ORCID: 0000-0001-5685-2366*

**G.F. de la Fuente**

*Instituto de Nanociencia y Materiales de Aragón, INMA (CSIC-Universidad de Zaragoza), María de Luna, 3,  
50018 Zaragoza, Spain, german.delafuente.leis@csic.es  
ORCID: 0000-0002-0500-1745*

*Cite this paper as: Ozçelik, B, Amaveda, H, Mora, de la Fuente, GF, Angurel, LA. Fabrication of spinel ferrite nanoparticles via laser ablation. Int. Conf. Advanced. Mater. Sci. & Eng. HiTech.and Device Appl.Oct. 27-29 2022,Ankara, Turkey*

**Abstract:** Transition metal ferrite ceramics present very interesting magnetic properties, and are presently being considered in nanometric grain sizes for a number of applications in bioscience. Depending on the preferred transition metal for usage, these ferrite ceramics show stable melt behavior. Thus, they become ideal candidate materials for laser melt processing. Laser Zone Melting process provides many advantages, although until recently it was not possible to process large areas under controlled solidification conditions. These are necessary to exert a good degree of microstructure control. An effective solution to achieve a satisfactory directional solidification interface is found using Laser Line Scanning [1,2], where an instantaneous melting line is obtained on a substrate with a planar geometry. The resulting sharp melt-solid interface provides controlled microstructures and a stable melt on a moving material. In this particular case, the movable material is the preferred transition metal ferrite ceramic compact. Laser Line Scanning generates a dense compact on the machined surface that may be suitable for the subsequent production of nanoparticles with controlled properties via Laser Ablation. The purpose of present research is to focus on the evaluation of the microstructural and magnetic properties of nanoparticles of Mn ferrite spinel material fabricated via Laser ablation process.

**Keywords:** Subnanosecond Laser Ablation, Nanoparticles, Spinel ferrites.

[1] V. Lennikov et al., J.of Superconductivity and Novel Magn. **26** (2013) 947-952.

[2] B. Özçelik et al., Journal of Materiomics **6** (2020) 661-670.

**Acknowledgements:** B. Özçelik acknowledges to the Scientific and Technological Research Council of Turkey (TUBITAK) for a grant via 2219-Science Fellowships and Grant Programmes Department, with the project number:1059B192000390. Work funded by the Spanish MCIN/AEI/10.13039/501100011033 (project PID2020-113034RB-I00) and by Gobierno de Aragón (research group T54\_20R). Authors also would like to acknowledge the use of Servicio General de Apoyo a la Investigación-SAI, Universidad de Zaragoza.

© 2022 Published by ICMATSE

## Hybrid Terminal Block Design With Two Different Connection Types

**Burak Karaca**

*ONKA Elektrik Malz.San. ve Tic.Ltd.Şti.- R&D and Design Department, 41400, Kocaeli, Türkiye,  
burak.karaca@onka.com.tr  
ORCID: 0000-0001-5635-9459*

**Orhan Kara**

*ONKA Elektrik Malz.San. ve Tic.Ltd.Şti.- R&D and Design Department, 41400, Kocaeli, Türkiye,  
orhan.kara@onka.com.tr  
ORCID: 0000-0002-0544-5821*

**Aydın Şık**

*Gazi University - Faculty of Architecture, Department of Industrial Design, 06500, Ankara, Türkiye,  
aydins@gazi.edu.tr  
ORCID: 0000-0002-8977-9094*

### Abstract.

Terminal blocks are widely used in the manufacturing, construction and transportation industries today. They are the most preferred products for securely connecting two or more conductors in application areas. According to the usage areas of the terminals; There are many types such as row terminals, metal terminals, terminal blocks. Terminal blocks are terminals that are generally used in electrical panels by arranging them side by side on EN Norm Rails, the dimensions of which are internationally standardized. A rail terminal basically consists of conductive busbar, insulating body and connection mechanism parts. There are many connection mechanisms (screw pressure, spring pressure, push-in connection, lug connection, etc.) available to connect the conductors with the conductor busbar. Each of these mechanisms is used in different places and has various advantages and disadvantages compared to each other.

In the study, by designing the terminal block with push-in connection on the left and screw connection on the right, the installation time of the applicator was shortened and it was ensured that he could interfere with the conductors whenever needed. By design, the conductor is mounted on the screw-connected side of the terminal block, parallel to the ground, while the spring-connected side is mounted at 90 degrees from the ground. This provides ergonomics and convenience in the assembly of cables coming from different directions in the panel. The product designed as closed on both sides; slots are designed for snap-on labels on the right and left, and a strip label can be used on it. This has also increased the level of security.

**Keywords:** Terminals, Terminal blocks, Design, Screw connection, Spring connection, Conductor

© 2022 Published by ICMATSE

### Introduction

Terminals; Today, it is widely used in the manufacturing, construction and transportation sectors. They are the most preferred products for securely connecting two or more conductors in application areas.

According to the usage areas of the terminals; There are many types such as strip terminals, metal terminals, terminal blocks.

Terminal blocks are terminals that are generally used in electrical panels by arranging them side by side on DIN Norm Rails, the dimensions of which have been made internationally standard. A terminal block basically consists of conductive bar, insulating body and connection mechanism parts. There are many connection mechanisms (screw pressure, spring pressure, lug connection, etc.) available to connect the conductors with the conductive bar. Each of these mechanisms is used in different places and has various advantages and

disadvantages compared to each other. Screw pressure (Fig. 1) ; The conductors are connected parallel to the ground. There is a 180 degree angle between each other. The screw must be tightened with a certain torque to prevent loosening. It takes a lot of time to tighten the screws or unscrew them when needed.

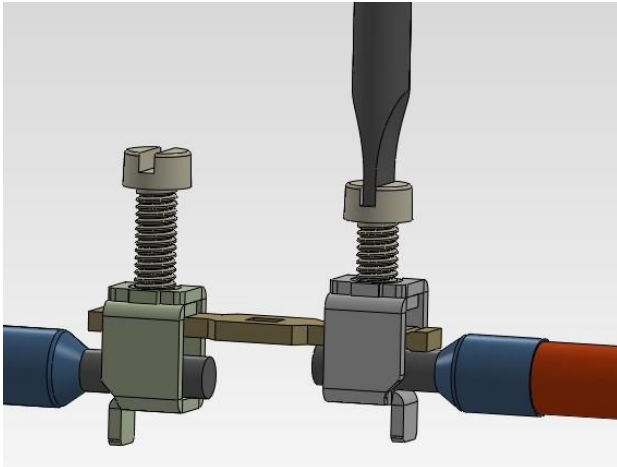


**Figure 1.** *Screw pressure connection*

Spring pressure (Fig. 2) (Push-in type); There is a 90 degree angle between the conductors and the ground and the conductors are parallel to each other. No tools or screws are required. Removing and replacing the conductor when needed is simple and fast.

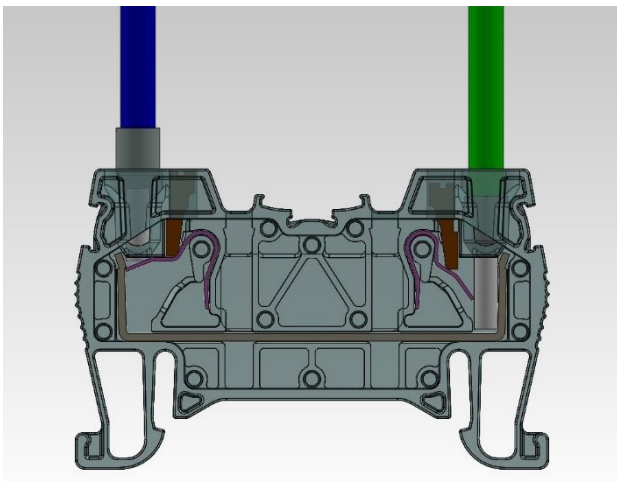


**Figure 2.** *Spring pressure connection*

### Design

Within the scope of this study, a new terminal block was designed by combining the technical features of two different connection types in a single terminal block (Fig. 3).

The left side of the terminal block is designed with push-in connection and the right side is designed with screw connection, and the angle between conductor input slots is preferred to be 90 degrees. The product is designed to be closed on both sides, as in other ONKA products. This feature increases the insulation resistance.

3 slots have been added for labeling, on the right, on the left and on the top. 2 slots have been added for jumper bridging.

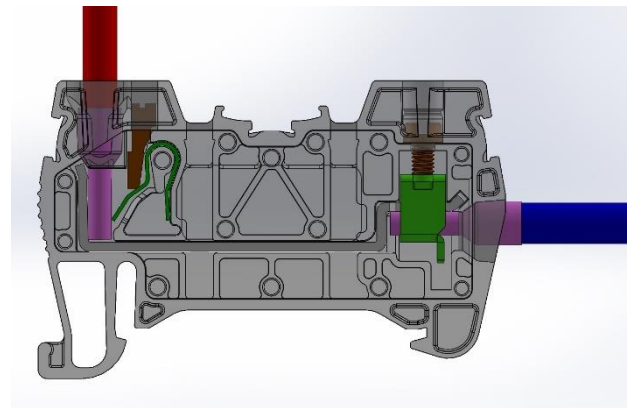


**Figure 3.** *Hybrid connection*

### Material/Method

Polyamide 6.6, which can meet the insulation, non-flammability and flexibility conditions at the same time, was chosen as the material for the body and cover.

Plastic injection method is used for body and cover production, therefore, 2 molds with 4-cavity were designed and manufactured within ONKA.

Conductive bar material has been determined as copper and will be produced with an eccentric press. For this, a press mold has been designed and manufactured within ONKA.

Existing parts of other terminal bars were used for the connection mechanism parts of the Hybrid terminal bar.

### Results And Discussion

In control cabinet assembly, wiring is the longest and most costly process.

Within the scope of our project; By designing the terminal block with push-in connection on the left and screw connection on the right, the assembly

time of the applicator is approximately 40% has been shortened.

By design, the conductor is mounted on the screw-connected side of the terminal block parallel to the

ground, while the spring-connected side is mounted at 90 degrees from the ground. This provides ergonomics and convenience in the assembly of cables coming from different directions in the panel. The compact design and front connection enable wiring in a confined space.

The product designed as closed on both sides; slots are designed for snap-on labels on the right and left, and a strip label can be used on it. This is important for increasing the level of security.

#### References

1. IEC 60947-7-1:2009, Low-voltage switchgear and controlgear -- Part 7-1: Ancillary equipment - Terminal blocks for copper conductors
2. IEC 60079-7:2015, Explosive atmospheres - Part 7: Equipment protection by increased safety "e"

With the completion of our project, the goal of bringing a product, which has no example in Turkey but is frequently preferred by domestic companies, to the domestic market and to increase competition in the foreign market, has been realized.

#### Acknowledgements

The authors thanks to Prof. Dr. Aydın Şık for for his support and advice.

## Exciton optoelectronics in two-dimensional monolayer interfaces

**Chandan Biswas**

Center for Integrated Nanostructure Physics, Institute for Basic Science, Sungkyunkwan University,  
Suwon, Republic of Korea,  
[chandan@skku.edu](mailto:chandan@skku.edu)

**Abstract.** Unusually high exciton binding energies in two-dimensional (2D) materials exhibit stable excitonic many-body effects and provide opportunities for exploring exciton optoelectronic devices at room temperature. Many-body neutral excitons, trions, bi-excitons, and defect-induced excitons are rarely realized in bulk materials at room temperature. Here we investigate different excitonic states invoked by the crystal defects in monolayer tungsten disulfide ( $WS_2$ ) at the substrate interface. This was achieved by carrier screening engineering with photogenerated carrier modulation, external doping, and substrate scattering. Defect-induced trions strongly coupled with inherent  $SiO_2$  hole-traps under high photocarrier densities and become more prominent in rhenium-doped  $WS_2$ . The absence of defect-induced trion peaks was confirmed using a trap-free hexagonal boron nitride substrate, regardless of power density. Furthermore, excitonic solar cell properties were investigated in graphene/n-Si Schottky Ideal diode structure by minimizing trap charge density in the graphene-Si interface. We controlled the doping methods to increase the conductivity of graphene that transforms nonlinear kink photodiodes with low FF and solar cell efficiency toward trap-free nearly ideal diode photovoltaic  $I$ - $V$ . The solar cell efficiency obtained with our strategy is around 13.6% and suggests the possibility to reach the theoretical limit of 19%.

**Keywords:** exciton binding energy, defect-induced B-trion, neutral-to-trion conversion, space charge current, Schottky solar cell

© 2022 Published by ICMATSE

We demonstrate a clear signature of defect-induced A-trions and B-trions in monolayer  $WS_2$  *via* carrier screening engineering. Here, carrier screening was performed in three separate ways – i) photo-generated carrier modulation, ii) impurity (rhenium) doping, and iii) reduction of the substrate-induced hole trap effect. These effects were employed to distinguish A and B-exciton charge-state properties from their neutral state. Defect-induced trions prevailed on  $SiO_2/Si$  substrates and became more dominant in rhenium-doped  $WS_2$  (Re- $WS_2$ ), whereas they disappeared on hexagonal boron nitride (h-BN) substrates. PL and STS investigations were utilized to obtain the binding energy of the trions, and defect-induced trions compared with the neutral exciton species. Our results demonstrate i) the identification of defect-induced A and B trions and their BE modulation *via* carrier screening engineering, ii) observation of two distinct screening regimes triggered by neutral-to-trion conversion, and iii) spatial BE distributions of many-body exciton species on the micrometer scale.

Furthermore, we have systematically demonstrated the effect of conductivity improvements of Gr using homogeneous doping throughout the junction region in the Gr/n-Si Schottky diode to realize the linear  $I$ - $V$  characteristics. Ionic-liquid electrolyte gate was used to facilitate high conductivity of Gr (two orders of magnitude improvement over the pristine sample) together with homogenous doping distribution to achieve a solar cell efficiency of 13.6%. This efficiency without interface engineering and antireflection coating is highest among doped Gr. We further studied the charge trapping and recombination processes in different  $I$ - $V$  regions of Gr/n-Si solar cells by diode modeling with the shunt resistance and space-charge-limited-current analysis in the injection region. Our findings suggest that the trapped charges at the native oxides layer can be compensated by homogeneous Gr doping. This is deemed necessary to improve the overall device performance and for commercialization prospective of Gr/n-Si Schottky solar cell.

### References

1. Riya Sebait, Chandan Biswas, Bumsub Song, Changwon Seo, Young Hee Lee, Identifying Defect-Induced Trion in Monolayer  $WS_2$  via Carrier Screening Engineering, *ACS Nano*, 1, 15.2 (2021), 2849–57, 10.1021/acsnano.0c08828

2. Subash Adhikari, Chandan Biswas, Manh-Ha Doan, Sungtae Kim, Chandramouli Kulshreshtha, Young Hee Lee, Minimizing Trap Charge Density towards an Ideal Diode in Graphene–Silicon Schottky Solar Cell, ACS Applied Materials & Interfaces, 2, 11.1 (2019), 880–88, 10.1021/acsami.8b18140

## **Study of the effect of pressure and temperature on the microstructure and thermoelectric performances of hot-pressed Sr-doped $\text{Ca}_3\text{Co}_4\text{O}_9$**

**A. Sotelo<sup>a</sup>, M. A. Madre<sup>a</sup>, O. J. Dura<sup>b</sup>, G. García<sup>c</sup>, S. Marinel<sup>d</sup>, P. Martinez-Filgueira<sup>c</sup>, M. A. Torres<sup>a</sup>**

<sup>a</sup>*Instituto de Nanociencia y Materiales de Aragón (INMA), CSIC-Universidad de Zaragoza, 50018 Zaragoza (Spain)*

<sup>b</sup>*Departamento de Física Aplicada (Universidad de Castilla-La Mancha), 13071 Ciudad Real (Spain)*

<sup>c</sup>*CS Centro Stirling S. Coop., Avda. Alava 3, 20550 Aretxabaleta (Spain)*

<sup>d</sup>*Normandie Univ, ENSICAEN, UNICAEN, CNRS, CRISMAT, 14000 Caen (France)*

[asotelo@unizar.es](mailto:asotelo@unizar.es) ORCID: 0000-0001-7056-0546

*Cite this paper as: Sotelo A, Madre MA, Dura OJ, García G, Marinel S, Martinez-Filgueira P, Torres MA. Study of the effect of pressure and temperature on the microstructure and thermoelectric performances of hot-pressed Sr-doped  $\text{Ca}_3\text{Co}_4\text{O}_9$ . Int. Conf. Advanced. Mater. Sci. & Eng. HiTech. and Device Appl. Oct. 27-29 2022, Ankara, Turkey*

**Abstract:** Pressure and temperature are the main factors influencing the microstructure of hot-pressed materials which can, in turn, affect the electric performances of these materials. In this work, the effect of different pressures and temperatures on the microstructure and thermoelectric performances of Sr-doped  $\text{Ca}_3\text{Co}_4\text{O}_9$  materials is explored. Samples were prepared using attrition milled precursors, which reduced the particle sizes, and increased their reactivity, drastically decreasing the processing time. Consequently, it has been found that calcination to decompose Ca and Sr carbonates can be performed in only one step at 850°C for 1h. After uniaxial cold pressing in form of discs under 200MPa, they were hot-pressed using temperatures between 800 and 900°C and pressures from 51 to 71MPa, for only 1h. Out-of-plane X-ray diffraction showed that all samples are formed by the thermoelectric phase, with a good grain orientation, improved with T, and P, as demonstrated by the calculated Lotgering factor. Scanning Electron Microscopy has shown that grain sizes and orientation are enhanced with T, and P. Moreover, density determined through Archimedes's method follows the same trend. All these structural and microstructural characteristics are reflected in the three-point flexural strength and microhardness values. Electrical resistivity is decreased when temperature and/or pressure, are increased. The minimum electrical resistivity, 6.4mΩ cm at 800°C, has been determined in samples processed at 900°C and 71MPa, which is about the best reported values in the literature. On the other hand, contrarily to the typical behavior observed in these types of materials, they also displayed the highest S values, 182μV/K at 800°C, which are similar to the best reported values for high density textured materials. However, total thermal conductivity values do not follow a regular evolution with the hot-pressing conditions, probably associated to the presence of internal stresses; anyhow, the lowest values at 800°C were determined in samples processed at 800°C and 51MPa (1.51W/K m) or 900°C and 61MPa (1.53W/K m). Consequently, the highest ZT values have been determined in samples processed at 900°C and 61MPa (0.35) which is higher than the best reported values in literature for bulk textured samples, to the best of our knowledge.

**Keyword:** Thermoelectric, Power factor, Seebeck coefficient,

© 2022 Published by ICMATSE

## Laser Zone Melting Process for fabricating MnFe<sub>2</sub>O<sub>4</sub> spinel ferrites

**L. A. Angurel**

*Instituto de Nanociencia y Materiales de Aragón, INMA (CSIC-Universidad de Zaragoza), María de Luna, 3,  
50018 Zaragoza, Spain, angurel@unizar.es  
ORCID: 0000-0001-5685-2366*

**B. Özçelik**

*Department of Physics, Faculty of Sciences and Letters, Çukurova University, Adana, Turkey,  
ozcelik@cu.edu.tr  
ORCID: 0000-0002-8767-1426*

**H. Amaveda**

*Instituto de Nanociencia y Materiales de Aragón, INMA (CSIC-Universidad de Zaragoza), María de Luna, 3,  
50018 Zaragoza, Spain, hippo@unizar.es  
ORCID: 0000-0003-2212-447X*

**G.F. de la Fuente**

*Instituto de Nanociencia y Materiales de Aragón, INMA (CSIC-Universidad de Zaragoza), María de Luna, 3,  
50018 Zaragoza, Spain, german.delafuente.leis@csic.es  
ORCID: 0000-0002-0500-1745*

*Cite this paper as: Angurel, LA, Özçelik, B, Amaveda, H, Mora, de la Fuente, GF. Laser Zone Melting Process for fabricating MnFe<sub>2</sub>O<sub>4</sub> spinel ferrites. Int. Conf. Advanced. Mater. Sci. & Eng. HiTech.and Device Appl.Oct. 27-29 2022,Ankara, Turkey*

**Abstract.** The Laser Furnace (LF) technology has been used to produce uniform, dense MnFe<sub>2</sub>O<sub>4</sub> spinel disks from a mixture of Fe and Mn oxides for controlled synthesis of spinel nanoparticles via Laser Ablation. Application of a CO<sub>2</sub> laser in Line Scan mode onto a sample with the desired stoichiometry, enabled melt processing above 1580°C at its outer surface layer. In this process, a combination of a laser system and a continuous roller furnace operating at a maximum volume temperature of 1000°C is used. Such combination helps avoid excessive thermal stress, crack formation and catastrophic failure of these magnetic ceramic monoliths. Higher energy incubation values yield increased molten volumes and a thicker resolidified surface layer with a dense microstructure. Despite the high solidification rates imposed, MnFe<sub>2</sub>O<sub>4</sub> spinel is the main phase obtained according to X-Ray Diffraction (XRD), Scanning Electron Microscopy (SEM) and magnetization studies. LF processed samples exhibit a reduction of the coercive fields and an increase of the saturation magnetization values, evidence for soft ferromagnetism and characteristic of the magnetic behavior associated with this spinel. This work demonstrates the convenience of the LF method for preparation of uniform, dense targets for Laser Ablation and other evaporation based techniques used in the fabrication of nanoparticles.

**Keywords:** Laser Furnace, Laser Zone Melting, Spinel ferrites.

### Acknowledgements

*B. Özçelik acknowledges to the Scientific and Technological Research Council of Turkey (TUBITAK) for a grant via 2219-Science Fellowships and Grant Programmes Department, with the project number:1059B192000390. Work funded by the Spanish MCIN/AEI/10.13039/501100011033 (project PID2020-113034RB-I00) and by Gobierno de Aragón (research group T54\_20R). Authors also would like to acknowledge the use of Servicio General de Apoyo a la Investigación-SAI, Universidad de Zaragoza.*

## The investigation of Pd<sub>2</sub>Si/n-Si(111) Schottky barrier diodes (SBDs) from $C - V - T$ and $G/\omega - V - T$ measurements on the basis the generalized model

*Izzat Afandiyeva*

*Baku State University, Institute for Physics Problem, AZ 1148 Baku , Azerbaijan  
afandiyeva@mail.ru*

**Abstract.** In this study, both the capacitance-voltage ( $C - V$ ) and conductance-voltage ( $G/\omega - V$ ) characteristics of Pd<sub>2</sub>Si/n-Si(111) SBDs have been investigated in the wide temperature range of 79-360 K and  $\pm 1V$  for 500 kHz. On the basis of the temperature dependent characteristics potential barrier height ( $\Phi_B$ ), the doping concentration of donor atoms ( $N_D$ ), the Fermi energy level ( $V_n$ ), series resistance ( $R_s$ ), distribution of applied bias voltage and the role of surface states were analyzed. The value of  $\Phi_B$  was irregular changed between 0.46 and 0.69 eV with temperature. Such behavior in  $\Phi_B$  with temperature was attributed to the influence of surface states and electrons exchanging between surface states and semiconductor or metal under temperature and voltage effects. In addition, it has been taken into account the generalized model of the metal-semiconductor (MS) contact/SD with a thin dielectric interlayer. The distribution of applied voltage ( $V$ ) between this dielectric interlayer ( $V_1$ ) and depletion layer ( $V_2$ ), the recharging potential of surface states ( $V_1^i$ ) have been investigated based on this model. The voltage dependent profile of  $R_s$  was obtained by using Nicollian and Brews method for each temperature.

**Keywords:** Pd<sub>2</sub>Si/n-Si(111) Schottky barrier diode (SBDs); basic electrical parameters; surface states and series resistance

2022 Published by ICMATSE

### 1.Introduction

This presented work is devoted to the study of the electro-physical parameters of Pd<sub>2</sub>Si/n-Si(111) SBDs, which create a basis for understanding the physics of the functioning of electronic devices. The great interest shown in Pd<sub>2</sub>Si/n-Si(111) SBD based on Schottky barriers is caused by the formation of palladium silicide (Pd<sub>2</sub>Si) [1-7]. Palladium reacts with silicon to form silicide's at very low temperatures (about 473 K). The activation energy ( $E_a$ ) for this process is in the range of 1,1-1,5 eV. A characteristic feature of Pd<sub>2</sub>Si is a very loose structure, which facilitates the diffusion process. Palladium silicide (Pd<sub>2</sub>Si) also characterized by volume diffusion. Therefore, the activation energy and the diffusion mechanism do not change up to 973K [5]. In these structures (Pd<sub>2</sub>Si/n-Si(111)) the formation of the potential barrier of the space-charge region in the semiconductor caused to the electronic properties of the surface of the semiconductor and localized

states in the band gap of semiconductor. The of current transport/conduction mechanisms in these structures depend on the space charge region parameters of the semiconductor and the transition layer at the interface.

The particular interest is the study of multicomponent metallization on a semiconductor. The specific purpose of the selection of multicomponent metallization is to protect silicon from diffusion of aluminum, which is usually used as an ohmic contact. Defects, arising as a result of the chemical interaction of Pd with silicon can play a significant role in electronic phenomena in diode structures, affect the properties of Schottky barriers, change the distribution profiles of carrier concentration in the near-contact region. In addition, a decrease in the geometric dimensions of the diodes increases the likelihood of fluctuations in the parameters. The choice of contact structures of small sizes, the study of fluctuations of parameters, the identification of legitimacy in their occurrence

and alternation are of interest for creating multifunction devices with well-known characteristics.

All these factors determined the reason for this investigation of Pd<sub>2</sub>Si/n-Si(111) SBDs. Firstly, palladium was deposited on a silicon surface by thermal spraying, because the used technological method does not violate the initial properties of substrate surface. Secondly, the formation of a silicide film on the surface of silicon shifts the interface into a semiconductor. Thirdly, to prevent the penetration of aluminum, as a diffusion barrier was used an amorphous alloy TiW. Besides, we investigated small diodes, areas of which about 10<sup>-6</sup> cm<sup>2</sup>.

It should be noted, that a choice of a semiconductor substrate is determined by the choice of the semiconductor itself also by the crystalline orientation of its slice [8-11]. The selected silicon in the (111) direction has the smallest work function. In addition, all the minima of the conduction band in this direction make the same contribution to the current; the effective Richardson constant reaches its maximum value. The above characteristics can determine the homogeneous surface of the natural cleavage, the highest potential barrier and current stability. In addition, due to the silicon band gap, it is possible to create elements based on it that are resistant to elevated temperature [12-14].

The main aim of this study is two-fold: first, the study of the temperature influence on the functionality of Pd<sub>2</sub>Si/n-Si (111) SBDs. Second, the analyze of the identified physical phenomena for the manufacture of new multifunctional devices.

## 2. Materials and Methods

For manufacturing of Pd<sub>2</sub>Si/n-Si(111) SBDs the simplest, most rational methods have been chosen. As a semiconductor substrate a 2 inch(=2,5 cm) diametr n-type silicon single crystal (P doped) wafer with a resistivity of 0.7 Ohm-cm, 3.5 μm thickness and a surface orientation of (111) was used. The diode matrix contained 14 SBDs, the areas of which

varied from 1 × 10<sup>-6</sup> cm<sup>2</sup> to 14 × 10<sup>-6</sup> cm<sup>2</sup> [8, 11-15].

Investigated diodes was fabricated by using the modern method planar technology based on the method of photolithography, which traditionally used for the fabricating of a small sizes diodes. Prior to the deposition of the metal film, the silicon (n-Si) substrate was cleaned in a mix of a peroxide – ammoniac solution for 10 minutes using two stages of chemical purification. Then, the substrate was washed for a long time in deionized water until the resistivity of water became 18 MΩcm. The dielectric mask (SiO<sub>2</sub>) was obtained by thermal oxidation at a temperature of 1320 K in O<sub>2</sub>+H<sub>2</sub>+HCl vapors. Prior to the deposition of palladium, the silicon wafers were annealed in a system chamber at a vacuum of 6 × 10<sup>-5</sup> Torr and a temperature of 573 K for 300 seconds. The palladium film was applied by thermal spraying. For fabrication a homogeneous Pd<sub>2</sub>Si film the wafer (Pd<sub>2</sub>Si/n-Si(111)) was annealed at 6 × 10<sup>-5</sup> Torr at 773K for 10 minutes. Then, the structure was annealed in a special ampoule with the furnace at 783K for 30 minutes in atmosphere of the gases N<sub>2</sub> and H<sub>2</sub>. To prevent the penetration of Al to Pd<sub>2</sub>Si the amorphous TiW alloy was deposited between Al and Pd<sub>2</sub>Si as diffusion barrier [27-29]. All processes were carried out in a clean room of class 100 [8,11-16].

The capacitance-voltage (*C* – *V*) and conductance –voltage (*G*/*ω* – *V*) characteristics of the fabricated Pd<sub>2</sub>Si/n-Si(111) SBDs were measured in the temperature range of 79 K-360 K by using a HP 4192A LF impedance analyzer. Small sinusoidal test signal of 20 mV<sub>p-p</sub> (500 kHz) was applied from the external pulse generator. The temperature dependence measurements were performed in a Janes VPF-475 cryostat with a Lake Shore model 321 auto-tuning temperature controllers in a vacuum at about 5 × 10<sup>-4</sup> Torr. All measurements were carried out with the help of a microcomputer through an IEEE-488 ac/dc converter card. In this paper the results of measurements of diode with the area of 8 × 10<sup>-6</sup> cm<sup>2</sup> are presented.

### 3.Results and discussion

By the using of a small sinusoidal test *ac* signal with 20 mV peak to peak amplitude at 500 kHz a set of capacitance-voltage ( $C - V$ ) and conductance-voltage ( $G/\omega - V$ ) characteristics of  $\text{Pd}_2\text{Si}/\text{n-Si}(111)$  Schottky barrier diode (SBD) was measured in the temperature range of 79K-360K and voltage  $\pm 1$  V and given in Fig.1 and Fig.2, respectively. This is very important to get more information on the conduction mechanisms and the formation of barrier height (BH) between metal and semiconductor. Because, when these measurements were carried out only at one or narrow voltage and temperature range cannot supply enough information on them.

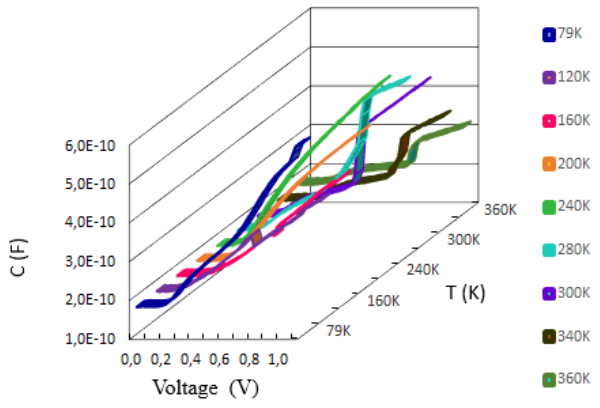


Fig.1. The measured  $C - V$  characteristics of  $\text{Pd}_2\text{Si}/\text{n-Si}(111)$  SBD at various temperatures.

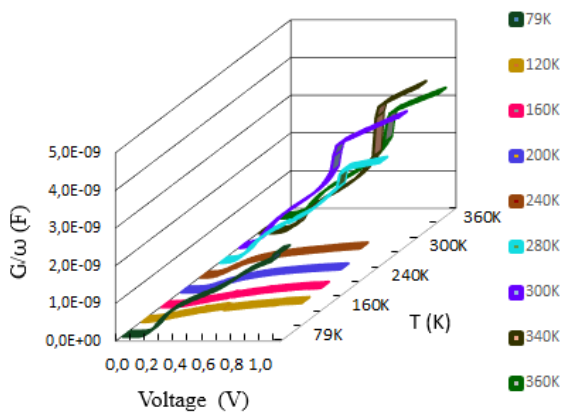


Fig.2. The measured  $G/\omega - V$  characteristics of  $\text{Pd}_2\text{Si}/\text{n-Si}(111)$  SBD at various temperatures

As can be seen from these figures, dependences of  $C - V$  and  $G/\omega - V$

characteristics of  $\text{Pd}_2\text{Si}/\text{n-Si}(111)$  diode on temperature are different for different regions of temperature. One of the reasons for such temperature dependence is the existence of surface states and their life-times ( $\tau$ ) recharging [13,17,18].

In the present paper on the basis of the measured  $C - V$  characteristics for various temperature in order to assess the values of the  $V_n$ ,  $N_d$  and  $\Phi_B$  and factors affecting the parameters of  $\text{Pd}_2\text{Si}/\text{n-Si}(111)$  SBD the reverse bias  $(A/C)^2 - V$  plots have been obtained for each temperature (Fig.3).

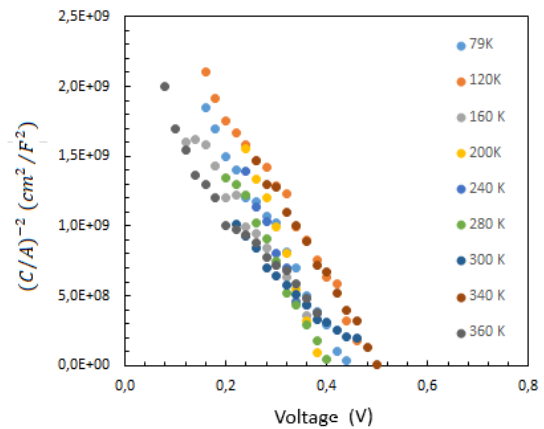


Fig.3. The  $(C/A)^{-2} - V$  characteristics of  $\text{Pd}_2\text{Si}/\text{n-Si}(111)$  SBD at various temperatures.

These plots have a large linear region with different slopes and intercept points. Therefore, the values of  $V_n$  and  $N_D$  were calculated from the intercept and slope of this plot for each temperature. The value of  $N_D$  was calculated by using following relation [11,12]:

$$\frac{d(A/C^2)}{dV} = \frac{2}{\epsilon_s \epsilon_0 q N_D} \quad (1)$$

where  $\epsilon_s$  and  $\epsilon_0$  are the permittivity of the semiconductor (11,8 for Si) and the permittivity of free space charge ( $\epsilon_0 = 8.85 \times 10^{-14}$  F/cm), respectively.  $N_D$  is the doping concentration of n-type semiconductor Si,  $A$  is the diode contact area [12,13,17-21].

The experimental value of  $N_d$  was calculated by using Eq. 2 for each temperature (Fig.

$$N_d = \frac{2dV}{\epsilon_s \epsilon_0 q d(A/C^2)} \quad (2)$$

The value of  $\Phi_B$  of Pd<sub>2</sub>Si/n-Si(111) SBD has been also calculated using the intercept voltage  $(A/C)^2 - V$  plot as function of the temperature by using the following equation [12,15,17-24]:

$$\Phi_B = q(V_0 + V_n) \quad (3)$$

where  $V_0$  is diffusion potential, which has been determined from intersection of linear part of  $(A/C)^2 - V$  characteristics with  $V$  axis.

The values of  $V_n$ , according to Ref.[15], has been obtained as

$$V_n = \frac{kT}{q} \ln \left( \frac{N_c}{N_D} \right) \quad (4)$$

with

$$N_c = 4,82 \times 10^{15} T^{3/2} \left( \frac{m_e^*}{m_0} \right)^{3/2} \quad (5)$$

where  $N_c$  is the effective density of states in non-degenerated Si conductance band,  $m_e^* = 1,09m_0$  is the effective mass of the density of states of silicon [17,18]. The obtained temperature dependent experimental values of  $V_0$ ,  $N_D$ ,  $V_n$ , and  $\Phi_B$  from the reverse bias  $(A/C)^2 - V$  plot for 500 kHz are tabulated in Table 1 for various temperatures.

As is seen in Table 1 and Fig.4. potential barrier height of Pd<sub>2</sub>Si/n-Si(111) Schottky barrier diode irregularly depends on temperature. It should be noted, that the true value of the potential BH does not depend in a similar way on temperature.

Tabl.1

T (K)	$V_0$ , (V)	$N_D \times 10^{16}$ (cm <sup>-3</sup> )	$N_c \times 10^{18}$ (cm <sup>-3</sup> )	$V_n$ (meV)	$\Phi_B$ (eV)
79	0.43	3.75	3.85	3.15	0.46
120	0.50	3.70	7.21	5.45	0.55
160	0.48	3.74	1.11	7.85	0.56
200	0.43	3.39	1.55	10.3	0.53
240	0.39	3.84	2.04	13.0	0.52
280	0.42	3.69	2.57	15.8	0.58
300	0.46	3.75	2.85	17.2	0.64
340	0.52	4.99	3.44	19.2	0.69
360	0.43	2.59	3.74	22.6	0.66

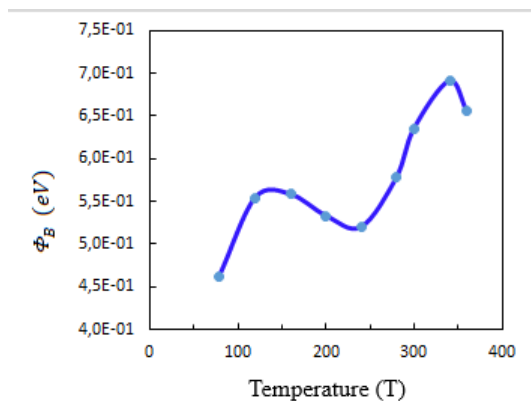


Fig.4. The dependence of Pd<sub>2</sub>Si/n-Si(111) SBD potential barrier height on the temperature.

The value of  $R_s$  is also more effective on the  $C - V$  and  $G/\omega - V$  characteristics especially at accumulation region and also it may be more dependent both on the temperature and frequency. Therefore, the value of  $R_s$  were calculated by using Nicollian and Brews [25] method for each temperature as function of applied bias voltage by using following relation:

$$R_s = G_{ma} (G_{ma}^2 + (\omega C_{ma})^2)^{-1} \quad (6)$$

Where  $C_m$  and  $G_m$  are measured capacitance and conductance respectively,  $\omega$  is angular frequency ( $\omega = 2\pi f$ ). As is shown in Fig.5 the  $R_s - V$  plot has a peak for each temperature. However, the position of peaks shifts change

irregularly with increasing of temperature. This behavior implies the existence of surface states and their recharging. Moreover, it is known that the processes of transfer and accumulation of charges are temperature activated processes.

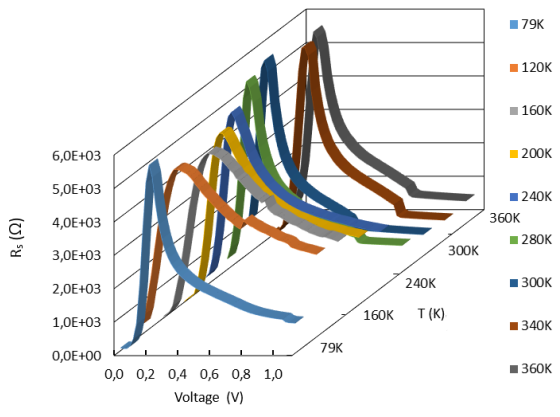


Fig.5. The dependence of series resistance of Pd<sub>2</sub>Si/n-Si(111) SBD on voltage at different temperatures.

It is known, that the electronic processes of real physical contact models are much more complicated than for an idealized model. This complexity is determined by two factors: the presence of a dielectric gap and the presence of surface states, which are actively involved in electronic processes. The charge of the space charge region is compensated by the charge of the metal, as well as the charge of the surface states [13,17,18,26]. It should be noted, that silicon, being a covalent semiconductor, characterized by a high density of surface states. Between the current and voltage there is a phase shift caused by recharging of the surface states. When a charge is exchanged between the surface level and the conduction band the recharging time of surface state is defined as

$$\tau_i \approx 10^{-11} \exp\left(\frac{E_i - E_c}{kT}\right) \quad (7)$$

where  $E_i$  is the energy level of surface state,  $E_c$  is the bottom of the conduction band. If  $E_i - E_c = 0,3$  eV then  $\tau_i = 10^{-6}$  sec that is, surface states can play a significant role at frequencies  $f \leq 10^6$  Hz. In this case, this behavior of  $C - V$  and  $G/\omega - V$  characteristics measured at 500kHz at various

temperatures can be explained by the contribute of surface states [18].

On the other hand is known, that the crystal lattice of Si(111) contains deformed hexagonal voids, areas of which are about  $14,6 \times 10^{-2} \text{ nm}^2$  [14]. In addition, the formation of metal film on the surface of Si depends on the ratio of crystallographic parameters of the contacting materials [27]. In our previous paper [15], we studied the temperature dependence of  $C - V$  and  $G/\omega - V$  characteristics of PtSi/n-Si(111) SBD measured at the frequency of 500 kHz and small  $ac$  signal ( $20 \text{ mV}_{p-p}$ ). Taking into account the big value of apparent doping concentration ( $N_{Dapp}$  is about  $10^{18} - 10^{19} \text{ cm}^{-3}$ ), the mismatch of the lattice parameters of PtSi and Si is about 9% and the non-ideality dependences of characteristics on temperature and voltage, the obtained result has been attributed to formation of self-assembled local patches.

However, due to the mismatch of the lattice parameters of Si and Pd<sub>2</sub>Si is very small (2%), the appearance of quantum wells is excluded. Therefore, the temperature dependence of a parameters of Pd<sub>2</sub>Si/n-Si(111) SD, can be explained by the presence of a thin dielectric gap and the enhanced role of surface electronic states at the interface. The nonlinear dependences  $(A/C)^2 - V$  characteristics on temperature confirmed the contribution of surface states [28].

The basic model of a SBD takes into account the presence of a thin dielectric gap between the metal and the semiconductor (Fig.6).

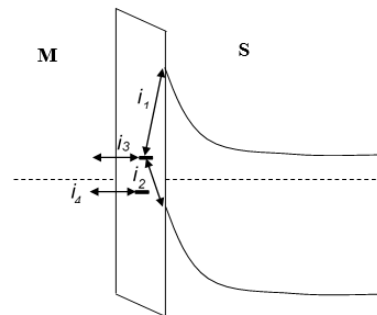


Fig.6. General model of metal-semiconductor contact with a Schottky barrier.

The applied voltage is distributed between the thin dielectric gap and the space charge region [13,17,18]:

$$V = V_1 + V_2 \quad (8)$$

where  $V_1$  and  $V_2$  are voltages in thin dielectric gap and space charge region, respectively. In this case, capacitance of structure determined as

$$C = \frac{C_1 C_2}{C_1 + C_2} \quad (9)$$

where  $C_1$  and  $C_2$  are capacitances of thin dielectric layer and space charge region, respectively. In accordance with the general model, the figure shows the possible paths of current passage through surface states ( $i_1$ - $i_4$ ).

To study of distribution of voltage in space charge region, dielectric gap and potential of recharging of surface states the  $C - V$  characteristics at 5 MHz has been measured. It was revealed, that at high voltages the capacitance is independent of voltage, due to the interface states cannot follow the ac-signal. This behavior can be explained by the fact that the interface states at 5 MHz do not contribute to the capacitance, practically.

On the basis of measurement  $C - V$  characteristics of Pd<sub>2</sub>Si/n-Si(111) SBD one can determine the distribution of voltage in space charge region ( $V_2$ ) and potential of recharging of surface states ( $V_1^i$ ) (Fig.7, Fig.8) [13,18,29]:

$$V_2 = \frac{\Phi_B}{e} \left( \frac{1}{C_0} - \frac{1}{C_1} \right)^{-2} \left( \frac{1}{C_0} - \frac{1}{C} \right) \left( \frac{1}{C_0} + \frac{1}{C} - \frac{2}{C_1} \right) \quad (10)$$

where  $\Phi_B$  is potential barrier,  $C_1$  is maximal capacitance,  $C_0$  is the capacitance at  $V=0$  ( $T=300K$ ).

The potential of recharging of surface states ( $V_1^i$ ) has been obtained as [13,18,29]:

$$\pm V_1^i = V - \frac{\Phi_0}{e} \left( \frac{1}{C_0} - \frac{1}{C_1} \right)^{-2} \left[ \left( \frac{1}{C_0} \right)^2 - \left( \frac{1}{C} \right)^2 \right] \quad (11)$$

It should be noted that by the sign of  $V_1^i$  it is possible to determine the mechanism of the predominant exchange of surface states. Analysis of the dependence  $V_1^i$  on  $V_1$  and  $V_2$  for Pd<sub>2</sub>Si/n-Si(111) SBD revealed that it is possible to overfill of surface states by electrons exchange with metal and semiconductor. According to a method presented by V.I.Strikha et.al [13,18,29], the value of  $V_1^i$  at the voltage from 0 V to 0,3 V can be attributed to electron exchange between surface states and conductance band.

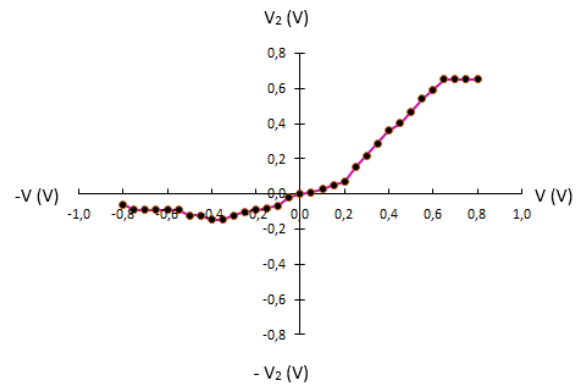


Fig.7. The dependence of  $V_2$  on voltage  $V$  at 300 K.

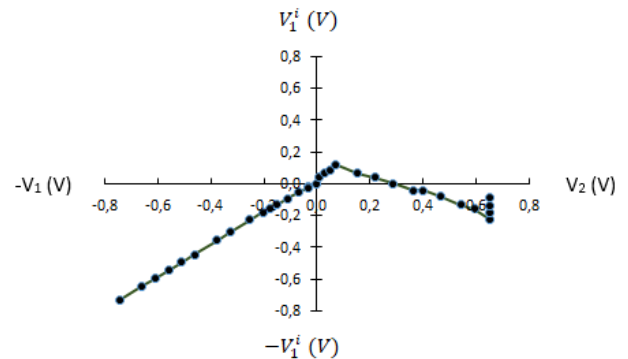


Fig.8. The dependence of surface states recharging potential ( $V_1^i$ ) on  $V_1$  and  $V_2$ .

Voltage from 0 V to 0,3 V can be attributed to electron exchange between 1) surface states - metal (0-0,1V) , 2) exchange between conductance band-surface states increases (0,1-0,3V) , 3)  $V > 0,3$  V exchange between conductance band and surface states.

At the reverse voltage the value of surface states recharging potential ( $V_1^i$ ) connected with an exchange between metal and surface states.

The observed changes of investigated parameters ( $\Phi_B$ ,  $N_D$ ,  $V_n$  and  $R_s$ ) with temperature can be attributed to the influence of surface states under temperature and voltage of electric field. The deviation of the parameter values from the true values is due to the recharging of the surface states and the exchange of electrons: the surface state - semiconductor or the surface state - metal.

In very recently, similar results on the temperature dependent  $C - V$  and  $G/\omega - V$  characteristics were also reported in the literature as [ 30-34].

#### 4. Conclusion

A set of capacitance-voltage ( $C - V$ ) and conductance-voltage ( $G/\omega - V$ ) characteristics of Pd<sub>2</sub>Si/n-Si(111) Schottky barrier diode with the using of a small sinusoidal test *ac* signal of 20 mV peak to peak amplitude at 500 kHz were measured in the

temperature range 79-360K to get more information on their conduction mechanisms and BH. On the basis of measured characteristics the values of  $V_0$ ,  $\Phi_B$ ,  $N_D$ ,  $V_n$  and  $R_s$  have been investigated as function of temperature and applied bias voltage. Obtained result was attributed to the presence of dielectric gap between metal and semiconductor and recharging of surface states. Taking into account  $C - V$  characteristics the distribution of the potential and surface states recharging potential ( $V_1^i$ ) have been calculated. It was revealed that there is electron exchange between surface states and metal or semiconductor. The voltage dependent profile of  $R_s$  was also obtained from Nicollian and Brews method for each temperature as function. In conclusion, the observed changes of investigated parameters with temperature can be attributed to the influence of surface states under temperature and voltage of electric field.

#### References

- [1]. Kircher C J. Metallurgical properties and electrical characteristics of palladium silicide-silicon contact. *Solid State Electron*, 1971, 14(6): 507
- [2]. Shepela A. The specific contact resistance of Pd<sub>2</sub>Si contacts on *n*- and *p*-Si. *Solid State Electron*, 1973, 16(4): 477
- [3]. Wittmer M, Smith D L, Lew P W and Nicolet M-A. Electrical characteristics of palladium silicide. *Solid-State Electron*, 1978, 21(3): 573
- [4]. Pellegrini B. Current-voltage characteristics of silicon metallic-silicide interfaces. *Solid State Electron*, 1975, 18: 417
- [5]. Poate J M, Tu K N, Mayer J W. *Thin films – Interdiffusion and Reactions*. New York: Wiley-Interscience, 1978
- [6]. Ho P S, Rubloff G W, Lewis J E, et al. Chemical bonding and electronic structure of Pd<sub>2</sub>Si. *Physical Review B* 22, 1980, 10: 4784
- [7]. Murarka S P, *Silicides for VLSI: Application*. New York: Academic Press, 1983
- [8]. Afandiyeva I M, Askerov S G, Abdullayeva L K, et al. The obtaining of Al-Ti<sub>10</sub>W<sub>90</sub>-Si(n) Schottky diodes and investigation of their interface surface states density. *Solid State Electron*, 2007, 51: 1096.
- [9]. Sakurai Y, Takeda Y, Ikeda S, et al. Electrical resistivity and its thermal coefficient of TiW alloy thin films prepared by two different sputtering systems. *Phys Status Solidi C*, 2014, 11(9/10): 1423.
- [10]. Kwak J S, Kang K M, Park M J, et al. Improved thermal stability of GaN-based flip-chip light emitting diodes with TiW based diffusion barrier. *Sci . Adv. Mater*, 2014, 6 (10): 2249
- [11]. Dökme I, Altındal Ş, Afandiyeva I M. The distribution of the barrier height in Al-TiW-Pd<sub>2</sub>Si/n-Si Schottky diodes from I-V-T measurements. *Semiconductor science and technology*, 2008, 23: 035003
- [12]. Sze S.M, *Physics of Semiconductor Devices*. New York: John Wiley and Sons, 1981

- [13]. Strikha V I. Theoretical bases of metal–semiconductor contact work. Kiev: Naukova Dumka, 1974 (in Russian)
- [14]. Shaskolskaya M P. Crystallography. Moscow: Visshaya shkola, 1984
- [15]. Afandiyeva I M, Altındal Ş, Abdullayeva L K, et al. Self-assembled patches in PtSi/n-Si(111) diodes. *Journal of Semiconductors*, 2018, 39(5): 054002-1
- [16]. Afandiyeva I M, Dökme I, Altındal Ş, et.al. The frequency and voltage dependent electrical characteristics of Al-TiW-Pd<sub>2</sub>Si/nSi(111) structure using I-V, C-V and G/ω-V measurements. *Microelectronic engineering*, 2008, 85:365
- [17]. Buzanyova E V. Microstructures of integrated electronics. Moscow: Radio i svyaz, 1990
- [18]. Strikha V I, Buzanyova E V, Radziyevskiy I.A. Semiconductor devices with the Schottky barrier, Moskow: Sovetskoye radio, 1974
- [19]. Soltanovich O A, Shmidt N M, Yakimov E B. Frequency and temperature dependences of capacitance–voltage characteristics of InGaN/GaN light-emitting structures with multiple quantum wells. *Semiconductors*, 2011, 45(2): 221.
- [20]. Moloi S J, McPherso M. Capacitance–voltage behaviour of Schottky diodes fabricated on p-type silicon for radiation-hard detectors. *Radiation Physics and chemistry*, 2013, 85:73
- [21]. Yahiya I S, Zahran H Y, Alamri F H., Aslam M. Microelectronic properties of the organic Schottky diode with pyronin-Y: Admittance spectroscopy, and negative capacitance. *Physica B: Condensed Matter*, 2018, 543: 46
- [22]. Yildirim N, Ejderha K, Turut A. On temperature-dependent experimental I-V and C-V data of Ni/n-GaN Schottky contacts. *Journal of Applied Physics*, 2010, 108(11):114506
- [23]. Lintu Rajan, Periasamy C, Vineet Sahula. Electrical characterization of Au/ZnO thin film Schottky diode on silicon substrate. *Perspectives in Science*, 2016, 8: 66
- [24]. Yuksel O F, Tuğluoğlu N, Gülveren B, Şafak H, Kuş M. Electrical properties of Au/perylene-monoimide/p-Si Schottky diode. *Journal of Alloys and Compounds*, 2013, 577: 30
- [25]. Nicollian E H, Brews J R, *MOS Physics and Technology*, New York: Wiley, 1982
- [26]. Bardeen J. Surface states and rectification at a metal-semiconductor contact. *Phys. Rev*, 1947, 71(10): 717
- [27]. Krylov P N. Physical models of thermo-processed contact metal–semiconductors. *Journal of Udmurt University, Fizika*, 2006, 4: 125 [in Russian].
- [28]. Murygin V I, Fattakhdinov A U, Loktev D A, et al. Anomal dependences of diode barrier capacitance on bias voltage and temperature. *Fizika I tekhnika poluprovodnikov*, 2007, 41(10):1207
- [29]. Strikha V I, Panichevskaya VI, Buzanyova E V. On the determination of the energy spectrum of surface electronic states in a metal-semiconductor contact with a Schottky barrier. *Izvestiya visshikh uchebnikh zavedeniy. Fizika*, 1973, 11: 40
- [30]. Güçlü Ç Ş, Özdemir A F, Karabulut A., Kökce A, Altındal Ş, [Investigation of temperature dependent negative capacitance in the forward bias CV characteristics of \(Au/Ti\)/Al<sub>2</sub>O<sub>3</sub>/n-GaAs Schottky barrier diodes \(SBDs\)](#). *Materials Science in Semiconductor Processing*, 2019, 89: 26
- [31]. Demir G E, Yücedağ İ, Azizian-Kalandaragh Y, Altındal Ş. [Temperature and interfacial layer effects on the electrical and dielectric properties of Al/\(CdS-PVA\)/p-Si \(MPS\) structures](#). *Journal of Electronic Materials*, 2018, 47:6600
- [32]. Baraz N, Yücedağ İ, Azizian-Kalandaragh Y, Altındal Ş. [Determining electrical and dielectric parameters of Al/ZnS-PVA/p-Si \(MPS\) structures in wide range of temperature and voltage](#). *Journal of Materials Science: Materials in Electronics*, 2018, 29:12735
- [33]. Demirezen S, Orak I, Azizian-Kalandaragh Y, Altındal Ş. [Series resistance and interface states effects on the C–V and G/w–V characteristics in Au/\(Co<sub>3</sub>O<sub>4</sub>-doped PVA\)/n-Si structures at room temperature](#). *Journal of Materials Science: Materials in Electronics*, 2017, 28:12967

- [34]. Gümüş A, Ersöz G, Yücedağ İ, Bayrakdar S, Altındal Ş, [Comparative study of the temperature-dependent dielectric properties of Au/PPy/n-Si \(MPS\)-type Schottky barrier diodes](#). Journal of the Korean Physical Society, 2015, 67: 889.

## Microfluidic Human Placenta DNA purification using superparamagnetic microbeads

**Güneş Kibar**

Adana A. T. Sci. & Tech. Uni., Material Sci. & Eng. Dept. 01250, Adana, Türkiye,  
gkibar@atu.edu.tr  
ORCID: 0000-0002-2586-6770

**Serkan Doğanay**

İzmir Katip Çelebi Uni., Mechatronics Eng. Dept., 35620, İzmir, Türkiye,  
serkan.doganay@ikcu.edu.tr  
ORCID: 0000-0002-3237-693X

**Mikail Yıldız**

Tekgen Health Service Inc., 34775, İstanbul, Türkiye, mikail@tekgen.com.tr

**Barbaros Çetin**

İ.D. Bilkent University, Mech. Eng. Dept., 06800, Ankara, Türkiye, barbaros.cetin@bilkent.edu.tr  
ORCID: 0000-0001-9824-4000

*Cite this paper as: Güneş Kibar, Serkan Doğanay, Mikail Yıldız, Barbaros Çetin, Microfluidic Human Placenta DNA purification using superparamagnetic microbeads, .Int. Conf. Advanced. Mater. Sci. & Eng. HiTech. and Device Appl. Oct. 02-04 2020, Ankara, Turkey*

**Abstract.** In this study, we purified the Human Placenta DNA using superparamagnetic microbeads in PDMS based microfluidic chip with 3D printed magnetic platform. Unlike packed column-based chromatographic systems, microbeads could move inside the microchannel in either the same or opposite direction of the magnetic field. The magnetic field was analyzed using COMSOL. Nanodrop readings gave the purification results to obtain the adsorption curve. The developed system could be an alternative to chromatographic separations with rapid analysis time and no-requiring high-pressure equipment.

**Keywords:** Human DNA purification, microbeads, microfluidics, superparamagnetic, high-throughput  
© 2022 Published by ICMATSE

DNA (Deoxyribonucleic acid) is a valuable substance for biochemistry, microbiology, genetics, and forensic science [1]. There are many techniques to purify DNA, such as spin columns and high-pressure liquid chromatography (HPLC). Compared to commercial static bench-top analysis, we propose a miniature device with a PDMS-based microfluidic chip to purify DNA using superparamagnetic microbeads. The novel magnetic platform provides a rapid adsorption-desorption rate and enables to study of 10 $\mu$ L sample volume.

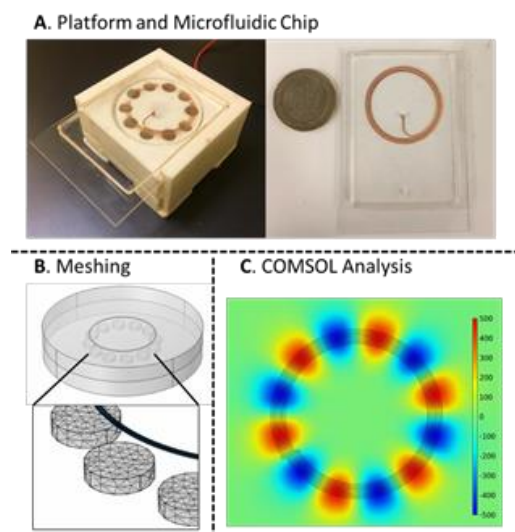


**Figure 1.** 3D printed-magnetic microfluidic platform and COMSOL Multiphysics meshing model and analysis

The platform was 3D printed and assembled with permanent magnets on a brushless motor moving compartment (in Fig 1-A) [2]. COMSOL Multiphysics was used to develop a 3D time-dependent model to evaluate the rotational effect of the magnets. The free tetrahedral mesh structure was employed (in Fig 1-B). Each magnet was modeled by using its remanent flux density. Then, the generated magnetic flux density in the channel was determined by Gauss' Law for magnetism (in Fig 1-C). The PDMS-microfluidic chip was designed as spirals placed over the moving compartment with dimensions of 200 $\mu$ m x 400 $\mu$ m and 0.42m in length. The superparamagnetic silica microbeads were loaded in PDMS based-microfluidic chip.

The superparamagnetic silica microbeads were synthesized using a multi-step polymerization technique [3]. The silica beads were grown on magnetic carboxyl functional polymeric beads and then calcinated to remove the polymeric part.

The microbeads were obtained around 8 $\mu$ m monodisperse in size with superparamagnetic character (in Fig 2-A). The microbeads were used for human placenta DNA (Sigma-D3035) with 20 $\mu$ L/min adsorption and 10 $\mu$ L/min desorption flow rate.

For this purpose, different amounts of DNA were loaded into the microfluidic chip. First, microbeads washed with adsorption buffer (6M Guanidium HCL-Tris Buffer pH:6.0). Then known amount human placenta DNA sample (0.6mg to 250mg) loaded with adsorption buffer. Then, microbeads were washed with 4:1 (v:v) isopropanol/water. Final step, DNA was collected using elution buffer (10mM tris buffer pH:9). The adsorbed DNA concentration ( $Q_{DNA}$  [ng DNA/mg dry particles]) was analyzed by Nanodrop (Thermo Fisher Scientific ND 2000,USA).

$$(Eq 1) \quad Q_{DNA} = (C_o V_o - C_f V_f) / M_p$$

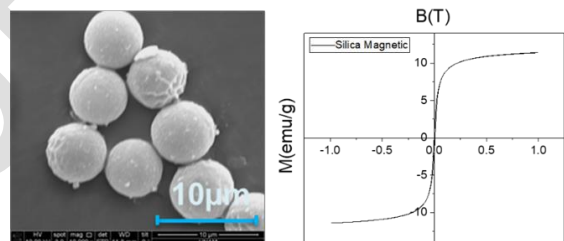
where  $C_o$  is initial DNA concentration (ng DNA/ $\mu$ L medium);  $V_o$  is the volume of the adsorption buffer ( $\mu$ L);  $C_f$  is the final DNA concentration (ng DNA/ $\mu$ L medium),  $V_f$  is the volume of the collected desorption buffer ( $\mu$ L) and  $M_p$  is the amount of particle (mg). The isolation experiments were carried out with 3 independents replicated for each concentration.

The adsorption curve was obtained to determine the maximum adsorption capacity (in Fig 2-B). The maximum adsorption capacity was approximately 100mg/mg particle from experimental data. The desorption yield was 40% for adsorbed-DNA on the microbeads.

The high-throughput with small amount of sample volume and fast processing time are favorable properties compare to similar material and techniques in the literature [4]. Due to the motion of the microbeads in the microfluidic channel, the diffusion barrier observed in packed systems was diminished in our proposed model. This motion effect could increase the adsorption yield of the microbeads.

This new device could be promising tool for the detection or purification of specific targets and biological samples such as exosomes, cffDNA, mRNA, bacteria and viruses with the proper surface modification of the superparamagnetic microbeads.

A. Superparamagnetic Silica Microbeads



B. Adsorption Curve

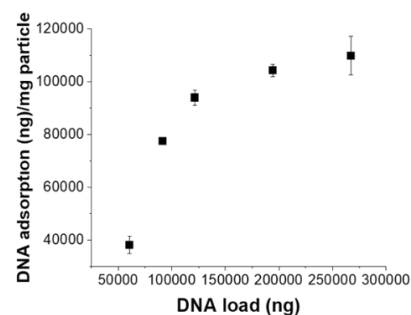


**Figure 2.** Superparamagnetic silica microbeads and adsorption curve

**Acknowledgments:** This study is financially supported by the Turkish Scientific and Technology Research Council, under Grant No. TEYDEB- 1170524.

#### References

1. Changzheng Wu, Feng Feng and Yi Xie, Design of vanadium oxide structures with controllable electrical properties for energy applications, Chem. Soc. Rev., 2013, **42**, 5157, \* DOI: 10.1039/c3cs35508j
2. Sihai, Chan; Characterization of nanostructured VO<sub>2</sub> thin films grown by magnetron controlled sputtering deposition and post annealing method, Optics Express, Vol 17, (2009).

ICMATSE 2022

## Superconducting Base Elements for Artificial Neural Network

**Anatolie Sidorenko<sup>1,2\*</sup>, Nikolai Klenov<sup>3</sup>, Igor Soloviev<sup>3</sup>, Sergey Bakurskiy<sup>3</sup>, Vladimir Boian<sup>1</sup>, Cezar Casian Malcoci<sup>1</sup>, Roman Morari<sup>1</sup>, Yurii Savva<sup>2</sup>, Alexander Vakhrushev<sup>2,4</sup>**

<sup>1</sup>Institute of Electronic Engineering and Nanotechnologies, Academiei str., 3/3, MD-2028, Chisinau, Moldova;

<sup>2</sup>I.S. Turgenev Orel State University Komsomolskaya str. 95, 302026, Orel, Russia;

<sup>3</sup>M.V. Lomonosov Moscow State University, Skobeltsyn Institute of Nuclear Physics, Moscow, 119991, Russia;

<sup>4</sup>Nanotechnology and Microsystems Department, Izhevsk State Technical University, Izhevsk 426069, Russia;

Radical reducing of energy consumption becomes the important goal in the advance of supercomputers. The Artificial Neural Networks (ANN) based on superconducting spintronic elements seems to be the most promising solution. Superconducting ANN needs elaboration of two main elements – nonlinear one (neuron) [1] and linear connecting element (synapse) [2]. Results of our theoretical and experimental study of the proximity effect in a stack-like superconductor/ferromagnet (S/F) superlattice with Co-ferromagnetic layers of different thicknesses and coercive fields, and Nb-superconducting layers of constant thickness equal to coherence length of niobium are presented.

It was designed and investigated superconducting spin-valves as artificial neuron and kinetic conducting element, based on layered hybrid S/F nanostructure, serves as synapse.

We present results of our theoretical and experimental study of the proximity effect in a stack-like superconductor/ferromagnet (S/F) superlattice with Co-ferromagnetic layers of different thicknesses and coercive fields, and Nb-superconducting layers of constant thickness equal to coherence length of niobium.

The layered nanostructures Nb/Co demonstrate change of the superconducting order parameter in thin s-films due to switching from the parallel to the antiparallel alignment of neighboring F-layers. We argue that such superlattices can be used as tunable kinetic inductors for ANN synapses design.

The study was financially supported by the Russian Science Foundation Grant (RSF) No. 20-62-47009 “Physical and engineering basis of computers non-von Neumann architecture based on superconducting spintronics”, and partially by the Moldova State Program Project «Nanostructuri și nanomateriale funcționale pentru industrie și agricultură» no. 20.80009.5007.11.

### References

1. N. Klenov, Y. Khaydukov, S. Bakurskiy, R. Morari, I. Soloviev, V. Boian, T. Keller, M. Kupriyanov, A. Sidorenko, B. Keimer, Periodic Co/Nb pseudo spin valve for cryogenic memory, *Beilstein J. Nanotechnol.* 10 (2019) 833–839. <https://doi.org/10.3762/bjnano.10.83>.
2. S. Bakurskiy, M. Kupriyanov, N. Klenov, I. Soloviev, A. Schegolev, R. Morari, Yu. Khaydukov, A. Sidorenko. Controlling the proximity effect in a Co/Nb multilayer: the properties of electronic transport. *Beilstein J. Nanotechnol.* 2020, 11, 1336–1345. <https://doi.org/10.3762/bjnano.11.118>

## Direct and Continuous Routes for the Synthesis of Complex Advanced Functional Ceramic Materials

*Prof Jawwad A. Darr*

*University College London, Department of Chemistry Faculty of Maths & Physical Sciences, London,  
UK, j.a.darr@ucl.ac.uk*

ORCID: 0000-0002-7950-8602

*Cite this paper as: Darr J.A. Direct and Continuous Routes for the Synthesis of  
Complex Advanced Functional Ceramic Materials. Int. Conf. Advanced. Mater. Sci. & Eng. HiTech.and Device  
Appl.Oct. 27-29 2022,Ankara, Turkey*

**Abstract.** Laboratory scale Continuous Hydrothermal Flow Synthesis (CHFS) systems for the controlled synthesis of inorganic nanoparticles (diameter <100 nm) have many potential commercial applications from catalysts to sunscreens and battery materials to fuel cell components. CHFS systems offer many advantages over batch processes: it is a green technology (using supercritical water as the reagent at >374°C and 22.1 MPa), and uses inexpensive precursors (e.g. metal nitrate salts), and parameters such as  $T$ ,  $P$ , etc. can be controlled independently for the synthesis of high-quality, technologically-important functional nanomaterials in a single step (or fewer steps than conventionally used). ***The Clean Materials Technology Group at UCL, now use CHFS made intimately mixed metal oxide precipitates as precursors to the direct synthesis of “difficult to make” solid-state phases using only a single heat treatment step and no grinding (i.e., “Bake Without the Shake!”).*** This approach can be used for rapid materials discovery and also to manufacture materials using continuous, low energy manufacturing methods which are inherently scalable. As well as the use of CHFS for battery materials discovery, the talk will discuss the design and operation of a scaled-up CHFS Pilot Plant capable of Kg/h synthesis of nanoceramics as well as future directions for the CHFS technology. A review article on the topic has been published and gives an excellent overview on the technology, see Darr JA, et al. “*Continuous Hydrothermal Synthesis of Inorganic Nanoparticles: Applications and Future Directions*”, ACS Chem. Rev. **2017**, 117 (17), 11125–11238

**Keywords:** Functional Ceramic Materials  
© 2022 Published by ICMATSE



Figure 1. Lab view

## Coating glass polycapillary optic with luminescent silicon nanoparticle to enhance the optical characteristics in the EUV/X-ray regime

**Jiacheng Xu**

University of Illinois at Urbana-Champaign, Department of Physics, Urbana, Illinois 61801

**Dmitry Gorin**

Skolkovo Institute of ST, Center of Photonics & Quantum Materials (CPQM), Moscow, Russia  
ORCID: 0000-0001-8760-615X

**Julia Skibina**

Saratov State University and SPE Nanostructured Glass Technology Ltd., Saratov, Russia  
ORCID: xxxx-xxxx-xxxx-xxxx

**Ammar M. Nayfeh**

Khalifa University, Masdar Institute, Abu Dhabi, UAE  
ORCID: 0000-0002-5207-244X

**Mete Bakir**

Yildirim Beyazit University, Mechanical Engineering, Ankara, TÜRKİYE  
ORCID: 0000-0002-5044-3104

**Ersin Bahceci**

Iskenderun Technical University, Department of Metallurgical and Materials Engineering, Hatay, Turkey  
ersin.bahceci@iste.edu.tr ORCID: 0000-0002-7719-6051

**Hakan Ates**

Gazi University, Department of Metallurgical and Materials Engineering, Ankara, Turkey  
[hates@gazi.edu.tr](mailto:hates@gazi.edu.tr), ORCID: 0000-0002-5132-4107

**Munir H. Nayfeh**

University of Illinois at Urbana-Champaign, Department of Physics, Urbana, Illinois 61801  
[M-nayfeh@illinois.edu](mailto:M-nayfeh@illinois.edu), ORCID: 0000-0002-1459-4976

*Cite this paper as: Xu, J., Gorin, D., Skibina J., Nayfeh, A. M., Bakir, M., Bahceci, E., Ates, H., Nayfeh, M.h., Coating glass polycapillary optic with luminescent silicon nanoparticle to enhance the optical characteristics in the EUV/X-ray regime .Int. Conf. Advanced. Mater. Sci. & Eng. HiTech.and Device Appl.Oct. 27-29 2022,Ankara, Turkey*

**Abstract** The refractive index  $n$  at the high-frequency limit of scattering electromagnetic waves (x-ray/EUV) from matter is complex with dependence on the frequencies of the incident photon and the plasmon of the material, with its real part is ever so slightly less than one  $\leq 1$ . Such high frequency when propagating at grazing incidence from vacuum to matter suffers total external reflection. Arrays of curved and tapered glass capillary (polycapillary optic) utilize this effect to collect X-ray tube output, guide and focuses it onto smaller areas with flux that is orders of magnitude greater than what can be achieved by mechanically collimated systems. We examine the feasibility of internal surface doping, which may produce a thin silicon coating that assumes the shape of the polycapillary. We show that unlike static incubation or drying in a colloid of 2.85-nm silicon nanoparticles, slow self-assembly via dynamic circulation of the colloid through the capillary over extended time produces homogenous coating to reduce roughness. Optical, luminescence and SEM imaging and spectroscopy show uniform silicon-coated polycapillary that is optically active in the UV. Silicon coatings promise larger critical angles for x-ray propagation over what glass provides, which provide higher focusing power. The use of ultrasmall nanoparticles (2.85-nm diameter) ensures reduced losses to roughness-related scattering with uncompromised transmission intensity, which may increase the spatial resolution and speed of imaging and diagnostics.

**Keywords:** Polycapillary, luminescent, silicon, nanoparticle.  
© 2022 Published by ICMATSE

## I. Introduction

As electronics and electronic components continue to get smaller and more complex, metal finishes on these components need to be plated on smaller features - as thinner layers - and controlled to tighter tolerances to arrive at the thinnest coating without premature failure and damage, and avoiding thicker plating resulting in material waste, mechanical fit and costly scrap or rework. X-ray fluorescence (XRF) is a widely used technique for measuring coating thickness and composition because it is non-destructive, fast and straightforward to use [1]. To measure coatings on small features, traditional XRF instruments use mechanical collimation (metal irises) to reduce the beam size of the X-ray tube to fractions of a millimeter. Because of the sizable divergence of the incoming x-ray, most of the x-ray are blocked as the iris allows only the X-rays aligned with the opening to pass through.

Recently, an approach that uses a polycapillary optic [2-4] which is made up of arrays of thousands of small hollow glass tubes that are curved and tapered has been developed for focusing X-rays. In the device, x-rays are guided through the tubes by multiple reflection, similar to the way light is guided in fiber optic technology. The basic principle however is based on the fact that the refractive index of vacuum is larger than that of matter in the deep UV and x-ray regime. At their entrance, the polycapillary is typically matched to the output a micro-spot of an x-ray tube to enhance collection, overlapping or focusing / merging them onto smaller areas with flux that is orders of magnitude greater than that of a mechanically collimated system. Moreover, because they are based on reflection, not diffraction, they are achromatic, appropriate for broadband applications, including white beam synchrotron focusing and collection of astronomical signals

Though the output come from the incoherent overlap of the beams from thousands of channels drawing from large divergent sources such as conventional X ray tubes, the procedure has

enabled measurement of smaller features and thinner coatings and, can potentially be designed to measure nanometer-scale coatings. Yet, the attributes of this phenomenon has not been fully realized or exploited, especially with regard to the reduction of the diameter of the output beam,

To keep up with the miniaturization trend of the metal-silicon devices as well as their sub features, progress must be achieved in enhancing the intensity as well as the beam size of the x-ray used. Beam sizes of less than 30  $\mu\text{m}$ , is required to make it possible to measure present-day ultra-fine features on microelectronics, advanced circuit boards, connectors, lead frames and wafers. It is imperative to develop systems with tighter focusing while allowing collection of greater radiation, which improves precision and speed.

In this paper, we examine the use of silicon in polycapillary applications to achieve a larger critical angle hence a larger focusing power. So far, silicon dioxide (glass Pyrex) has been the main material in use. Since it is not possible to make tubes of silicon we examine the possibility of using monodispersed silicon nanoparticles [5-8] to perform surface doping of the glass capillary. Because ultrasmall silicon nanoparticles are strongly luminescent, the procedure effectively promises to produce a fused silica capillary column system with a luminescent functionality. But it is not clear if surface doping is capable of producing a "silicon" coating that assumes the shape of the capillary, and whether the glass polycapillary system can act as a template to support structure to produce a thin silicon polycapillary system. Moreover, it is not clear if the nano solid coating can act as a continuous silicon layer, nor it is feasible to get a smooth nano solid with minimal agglomeration and reduced roughness, since surface roughness results in a reduction in the reflected intensity, due to scattering, which may offset the focusing gain.

## II. Experimental:

The polycapillary is produced from borosilicate optical glass for commercial use at SPE Nanostructured Glass Technology Ltd, Saratov, Russian Federation [9-10]. Manufacturing is based on classical micro- and nanocapillary glass technology. First, precision, thin-walled, round glass capillaries are stacked in a bundle, for example in the shape of a hexagon. The capillaries are heated to the temperature of glass softening and drawn to create hexagonal polycapillary structures. Several of these are then assembled into a hexagonal package and

drawn again. The procedure is repeated until the desired variable periodicity of air channels is achieved. If several capillaries are removed or replaced one in the center of an initial package, one can create a core made of glass or air in the final structure. This technology allows the manufacturing of micro- and nanostructured PCFs from different types of glass and produce PCFs with a great variety of configurations, stacking types (hexagonal, squared, and triangular, among others), and defect-arrangement topologies. **Figure 1** shows an SEM image of the capillary bundle systems. It shows that the diameter of the individual tube is about 38  $\mu\text{m}$ , with a density of  $\sim 250/\text{cm}$  or  $6.25 \times 10^4/\text{cm}^2$

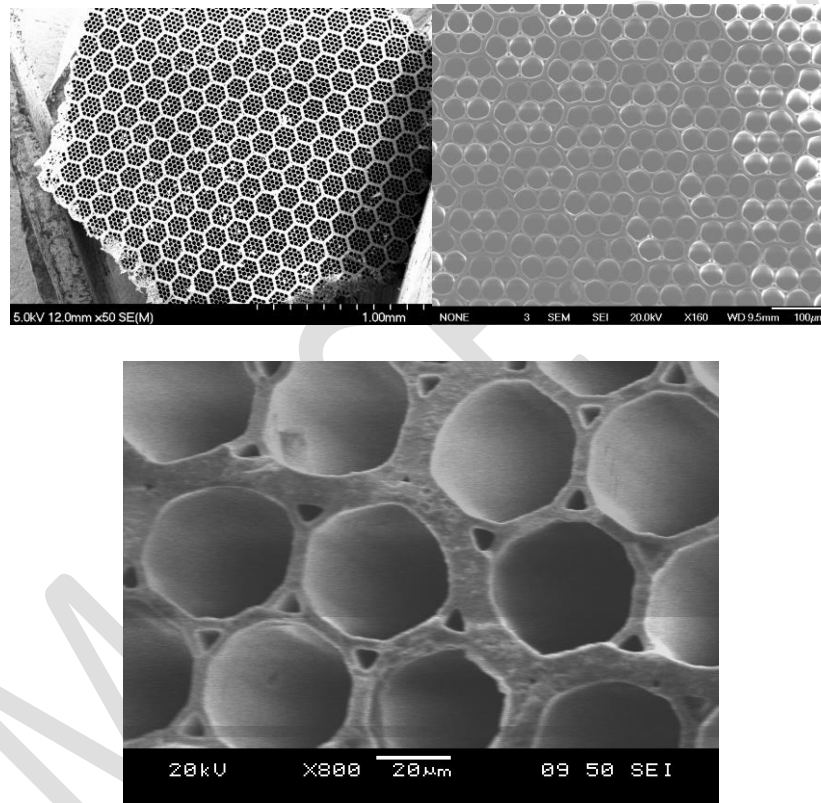


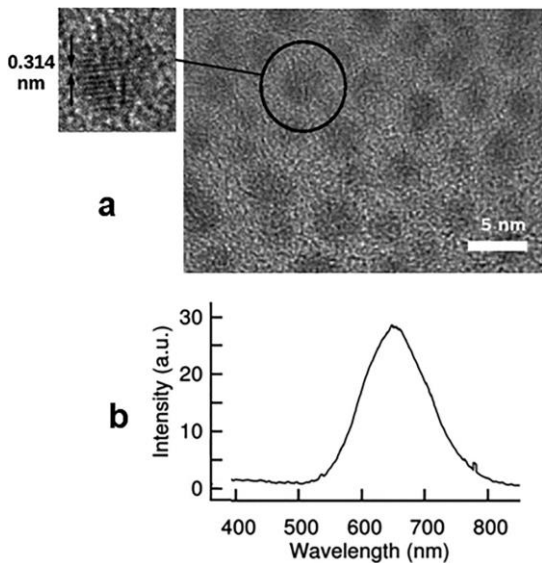
**Figure 1** SEM images of the capillary bundle systems. The diameter of the individual tubes is about 38  $\mu\text{m}$ , with a density of  $\sim 250/\text{cm}$  or  $6.25 \times 10^4/\text{cm}^2$

The nanoparticles are prepared from Si wafers by chemical etching in  $\text{HF}/\text{H}_2\text{O}_2$  using electrical or hexachloroplatinic acid catalyst with reproducibility in size, shape and characteristics [11-13]. Generally, we produce a set of discrete size  $\text{Si}_n\text{H}_x$  particles of 1.0 ( $\text{Si}_{29}\text{H}_{24}$ ), 1.67 ( $\text{Si}_{123}$ ), 2.15, and 2.95-nm diameter, with confinement bandgaps of 3.44, 2.65, 2.39 and 2.0 eV. The particles have hydrogenated reconstructed surfaces consisting of network of bulk-like  $(2 \times 1)$  reconstruction Si-Si dimers on (001) facets [14-15]. **Figure 2a** gives a transmission electron microscope (TEM) image of 3-nm particles placed on a graphite substrate, resolving the characteristic atomic planes. To obtain the luminescence spectra,

we excite particle colloids by 365-, 300-, or 254-nm incoherent light. For detection, we use a fiber optic spectrometer, equipped with optical fibers to extract the emission and a holographic grating. The spectrum was taken by a fiber optics grating detector made by Ocean Optics HR2000. It is a near-infrared grating with a groove density of 600/mm with a blaze wavelength of 0.4  $\mu\text{m}$  and with best efficiency in the range of 0.25–0.80  $\mu\text{m}$ . The luminescence spectrum of a colloid with a peak at 2.9-nm Si nanoparticles dispersed in isopropanol alcohol under UV-excitation at 300 nm is a wide band over the range of 550–750 nm with a band maximum at 620 nm as shown in **Figure 2b**. Unlike direct-bandgap

nanoparticles, which emit sharp lines, indirect-bandgap nanoparticles emit broad bands due to structural relaxation [5-8].

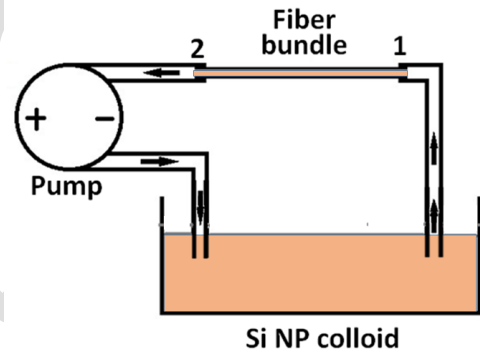
The 1-nm particle is small enough to be amenable to first principle atomistic simulation. The simulated prototype is found to have a molecular structure of  $Si_{29}H_{24}$  with the formed novel dimers affording strong luminescence and optical monitoring [16-17]



**Figure 2** Characteristics of 3-nm silicon nanoparticles (a) high resolution transmission electron microscope (HTEM) image of 3-nm particles placed on a graphite substrate, resolving the characteristic atomic planes. (b) luminescence spectrum of a colloid of the nanoparticles dispersed in isopropanol alcohol under UV-excitation at 300 nm using an incoherent Hg UV discharge tube, showing a wide band over the range of 550–750 nm with a band maximum at 620 nm.

Several procedures were used to coat the interior wall of the capillary, including incubation, static fill / dry of the capillary system, as well as dynamic deposition procedure. The latter is depicted in **Figure 3**. It uses a pump to circulate the colloid through the polycapillary as shown. We use a voltage of 8V, but actually, it is ok to use 4-12V difference. The adjoined point 1 and 2 are sealed and the fiber is held

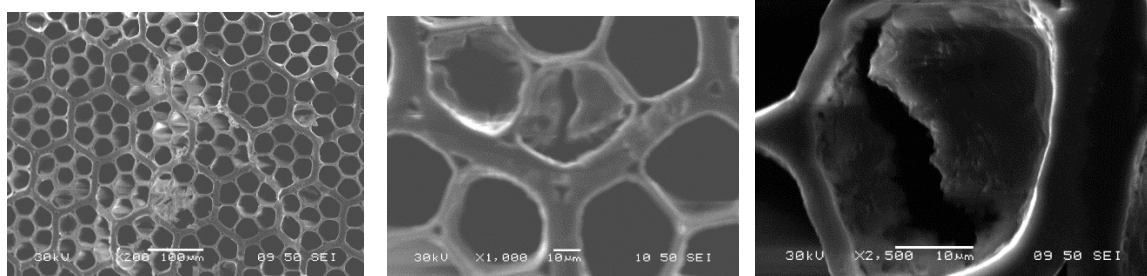
horizontally to avoid the effect of gravity. The colloid is diluted to slow down the deposition and with a small sticking factor, the deposition rate is slowed down enough to allow dynamic equilibrium to take place. Circulation of the colloid required over 24 hours to achieve appropriate thicknesses. The slow rate and longtime allowed for self-assembly allows ample time for the nanoparticles to find the equilibrium positions that among other things minimizes the roughness of the surface. The nano particle will uniformly stick to the inner side of the fiber automatically as the solution flows across the fiber. This process takes time, so we will leave the system running for 80 hours (running time is changeable, depend on how thick coating is required.). After 80 hours, take out the fiber. As shown, below, during the circulation, the flow at two end of fiber is not steady, which may lead to an uneven coating at two ends. Thus, we will cut its two ends and only use the middle fiber for test.



**Figure 3** Procedures to coat the interior wall of the polycapillary system. It is a dynamic deposition procedure that uses a pump to circulate the colloid through the polycapillary over several hours to achieve appropriate thicknesses

**III. Results:**

We incubated a polycapillary in a colloid until the liquid dried up. **Figure 4** gives an SEM image of the bundle after the treatment. It shows that the capillaries are clogged to different degrees, with some sections are completely clogged. The deposition in the interior is most likely inhomogeneous and not uniform.



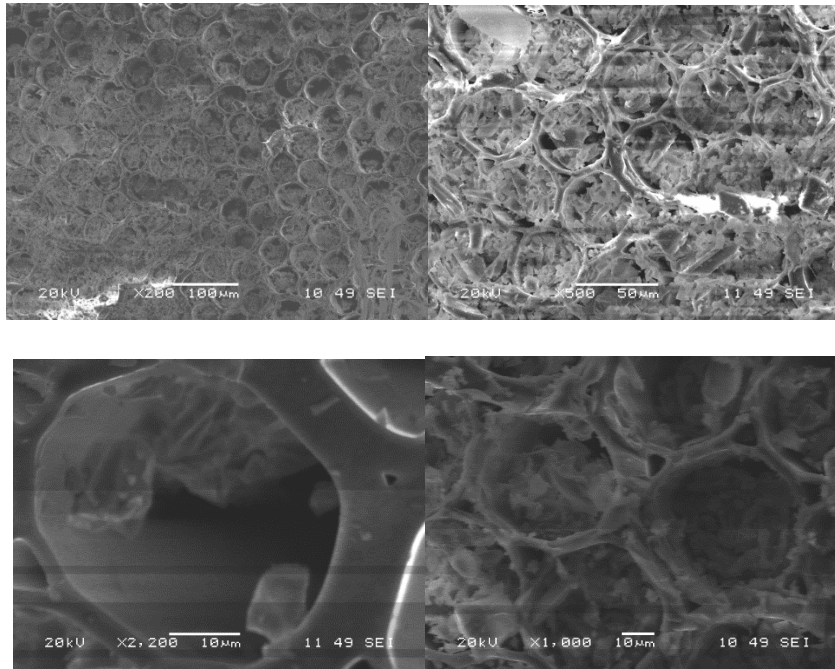


**Figure 4** SEM image of the bundle after the treatment. The capillaries are clogged to different degrees at the opening, with some sections are completely clogged. The deposition in the interior is uniform.

More uniform coating is achieved by the circulation system. **Figure 5a-b** gives SEM scan for a treated poly capillary using the circulation system as was described above in Figure 3. In Figure 5b we show the SEM image of a control untreated sample. We can see there is no

obvious difference under SEM for coated and uncoated fiber. Thus, it indicates that the silicon is uniformly coated to the inner wall. (The crack at the edge is due to cutting the fiber. We can see there is no obvious difference under SEM for coated and uncoated fiber.

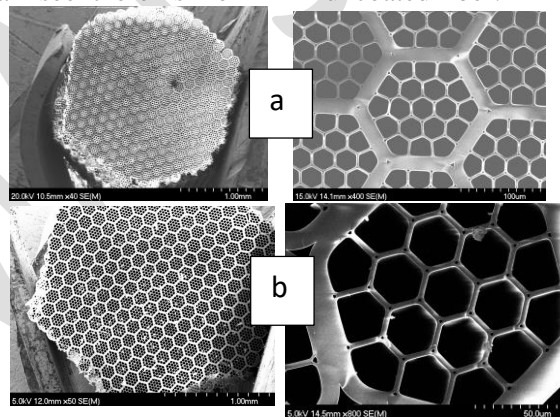


**Figure 5 (a)** SEM scan for a treated poly capillary using the circulation system after cutting a small section at the opening. **(b)** SEM image of a control untreated sample (uncoated poly capillary). We can see there is no obvious difference between coated and uncoated fiber. Thus, it indicates that the silicon is uniformly coated to the inner wall. (The crack at the edge is due to cutting the fiber.)

**Figure 6** gives luminescent photos of the bundles using excitation at wavelength of 300 nm. In each frame, the left bundle is uncoated fiber and the right one is coated fiber. It is clear to the naked eye that compared to the uncoated

one, the treated fibers turn to pink/red, indicating the presence of the nanoparticles. This conclusion can be confirmed further by recording the photo-luminescence spectra.

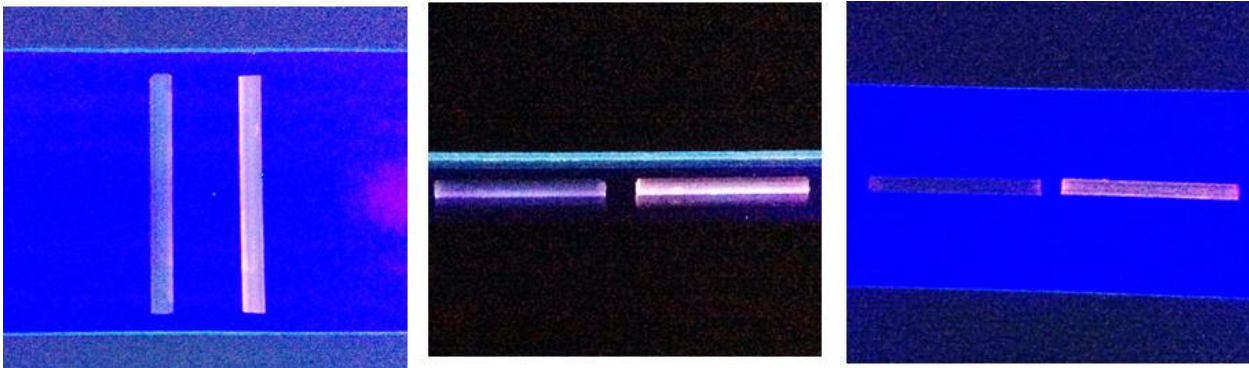


**Figure 6** luminescent photos of the coated and uncoated bundles using excitation at wavelength of 300 nm. In each frame, the left bundle is uncoated fiber and the right one is coated fiber. It is clear to the naked eye that compared to the uncoated one, the treated fibers turn to pink/red, indicating the presence of the nanoparticles. This conclusion can be confirmed further by recording the photo luminescence spectra.

We recorded the luminescent spectrum of the capillaries using the configuration shown in **Figure 7a** in which the detector was placed at one end of the poly capillary, while the excitation is carried out using a 300nm UV shining from the side. For comparison, and to be used as a background signal we present the spectrum of a control sample (uncoated (3 tests are made)). This is shown in **Figure 7b** (shown in black). The spectrum is basically the emission spectra characteristic of optical glass. The emission spectrum has typical local peaks in the blue and in the green part of the spectrum at  $\sim 435$  and  $\sim 525$  as well as a band in the deep infrared at 680 nm at the edge of the sensitivity of the eye. The spectrum of coated fiber (average of 5 tests made) is shown in **Figure 7b** in red. **Figure 7b** also shows the difference of the spectra of the coated and uncoated (shown in blue) to subtract out the emission from the glass. The difference spectrum is dominated by a red band extending over the range 550-720nm with a maximum at  $\sim 610$  nm. This band is characteristic of the emission of the silicon nanoparticles colloid with a slight blue shift from 650 nm to 610 nm. This points to the presence of a silicon nanoparticle coating inside the capillary. With the SEM and luminescence measurements, it might be concluded that the silicon nanoparticles are uniformly coating the inner wall. (The crack at the edge is due to cutting the fiber)

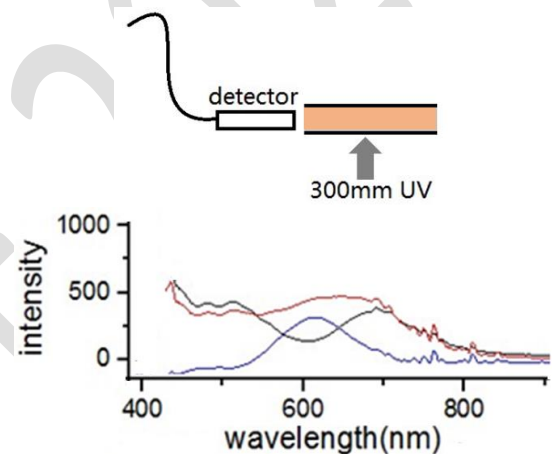


**Figure 7** luminescent spectrum of coated and uncoated capillaries. **(a)** normal configuration used for emission in which the detector was placed at one end of the poly capillary, while the excitation is carried out using a 300nm UV shining from the side. **(b)** The emission spectrum of coated fiber (average of 5 tests made) is shown in red. Background spectrum of a control sample (shown in black) (uncoated (3 tests are made)). It is basically the emission spectra characteristic of optical glass. The difference of the spectra of the coated and uncoated (shown in blue).

As to the nature of the silicon nanoparticle attachment to the glass wall, namely physical Vs. chemical, we note that of Optical glass is known to absorb in the region of 550 nm to 630 nm with band head at 600 nm due to defect absorbing around 2 eV. The defect is the non-bridging oxygen hole center, NBOHC ( $\equiv\text{Si}-\text{O}\cdot$ ), as well as the peroxy radical, POR ( $\equiv\text{Si}-\text{O}-\text{O}\cdot$ ), [18-19] and the self-trapped holes, STH ( $\equiv\text{Si}-$

O<sup>-</sup>-Si≡) [20-22]. Because the nanoparticles are hydrogen terminated (Si-H), those defect sites with a variety of charge states are amenable to hydrogen bonding type reactions and bonding attachments. Such chemical attachment may be responsible for the blue shift in the emission spectra of the colloid and the thin films from 650 nm to 610 nm.

#### IV. Analysis

##### Critical Angle

Visible light can be totally reflected when travelling from a denser medium into a less dense medium (e.g. light traveling in glass towards a glass-air interface will be totally reflected when the incident angle (measured from the normal to the interface) is less than ~40°). This is due to the fact that at visible wavelengths the refractive index of denser matter is larger than that less dense matter. This phenomenon is utilized to trap (stop escape/transmission) light in glass/plastic fibers embedded in material of lower refractive index. A critical incidence angle  $\theta_c$  is defined as a parameter for which  $\sin \theta_c = n_e/n_m$ , where  $n_e$  and  $n_m$  are the refractive indices of the environment and medium respectively,

X-rays interact rather weakly with matter (e.g., absorption lengths are on the order of millimeters). Hence, x-ray refractive indices are extremely close to 1, with critical angles very small (as measured from the tangent to the interface) or 90 degrees as measured from the normal to the interface [23]. Moreover, the refractive index and hence the critical angle depends on the x-ray energy and the material, but is typically on the order of 0.1° to 0.5°. In other words, for x-rays, the beam can be totally reflected when travelling from a less dense medium into a denser medium (e.g. x-rays traveling in vacuum towards a vacuum-silicon interface will be totally reflected if the grazing-incidence angle is less than ~0.2°). For example, EM waves at extreme UV or x-ray wavelengths propagating in a cavity pipe in a certain material suffers this phenomenon. Because the dip below vacuum is very small, the critical angle for such situation is large ~ 90 such that the phenomenon requires nearly grazing angle incidence. In this case, it is more convenient to utilize the angle  $\alpha_c$  with respect to the tangent to the interface

instead with respect to the normal to the interface, namely  $\alpha_c = 90 - \theta_c$ .

We start with Snell's law  $n_1 \sin \theta = n_2 \sin \theta'$ , where  $\theta$  and  $\theta'$  are the incident and refracted angles with respect to the normal to the capillary surface. Using the angles with respect to the tangent to the surface  $\alpha = 90 - \theta$  and  $\alpha' = 90 - \theta'$ , we get  $n_1 \cos \alpha = n_2 \cos \alpha'$ . In vacuum ( $n_1 = 1$ ):  $\cos \alpha = n_2 \cos \alpha'$ . We now get an approximate expression for the critical angle  $\alpha_c$  for grazing angle propagation,  $\alpha' \sim 0^\circ$  or  $\cos \alpha' \sim 1$ . Thus  $\cos \alpha_c = n_2$ . The real part of  $n_2$  may then be written as  $1 - \delta_2$ . In fact, from the detailed analysis of Maxwell's equations and the resulting Fresnel relations the refractive index of the material is a complex quantity in this limit. Hence one can cast that the complex refractive index for x-rays is given by  $n = 1 - \delta + i\beta$ , where  $\beta$  represents the imaginary part. The real part  $1 - \delta$  is given by the high-frequency limit of scattering an electromagnetic wave from matter  $n = 1 - \omega_p^2 / \omega^2$  where  $\omega$  and  $\omega_p$  are frequency of the x-ray photon and the plasma frequency of the material, respectively [6]. Note that the real part of  $n$  is ever so slightly less than one. This means that for propagation of high frequency EM waves (x-rays for example) from vacuum to matter at grazing incidence angle (angle of incidence is nearly 90) there will be total external reflection. The critical angle from the tangent to the surface can be obtained (approximated) by expanding  $\cos \alpha_c = n_2$  for small angles. The result is  $\alpha_c = \sqrt{2\delta}$ .

The critical angle for a lens containing an array of glass microcapillaries of borosilicate glass were calculated to be 0.927, 0.489, 0.239, 0.150, 0.119, and 0.079 for 2, 4, 8, 12, 16, 24 keV energies respectively [24]. Another interesting material is silicon. Pure silicon is a material has been known to be well suited for refractive lenses operating at high X-ray energies (> 50 keV), particularly if implemented in a single-crystal form to minimize small-angle scattering. For silicon similar calculations give critical angles of 0.824, 0.451, 0.224, 0.149, 0.112, 0.07426 degrees for 2, 4, 8, 12, 16, 24 keV energies respectively [24]. It is interesting to note that at 10keV, the critical angle for carbon is 0.173 compared to 0.180 for silicon. Metal, such as copper and gold (Cu and Au) exhibit significantly larger angles at 0.326 and 0.443 degrees [25]

In polycapillary optics, the formation of the focal spot can be well described as a superposition of beams from individual capillaries. The lateral dimensions of the focal spot are of an order of  $2f \theta_c$ , where  $\theta_c$  is the critical angle for total external reflection ( $\theta_c = 30 \text{ mrad} / E(\text{keV})$ ), and  $f$  is the focal length determined by the bending radius of capillaries [Reviews]. The special bending of capillaries is able to focus x-rays into an intense micro spot. Thus, it is clear that using silicon as the reflecting surface provides more focusing power.

For glass, the refractive index dips below one at  $\sim 195\text{nm}$ , which is considered to be in the UVA region. In general, the UV covers the wavelength range 400-100 nm and is divided into three bands: UVA (400-315 nm), UVB (315-280 nm), and UVC (280-100 nm). They differ in their biological activity and the extent to which they can penetrate the skin. The shorter the wavelength, the more harmful the UV radiation. However, shorter wavelength UV radiation is less able to penetrate the skin. Extreme UV radiation has the shortest wavelength range and highest energies of the regions of the ultraviolet spectrum, and lies on the border between UV and X-ray radiation. Extreme UV radiation spans the 10 to 30 nm wavelength range. Wavelengths in the range 11–14 nm are in the extreme ultraviolet (EUV) or soft x-ray portion of the electromagnetic spectrum.

Note that at wavelengths  $< 50 \text{ nm}$ , all materials have indices of refraction  $\approx 1$ . Thus, it is difficult to create a highly reflective interface. At EUV wavelengths, it has proven possible to make mirrors with moderate reflectivity, in the range of 60–70%, using multilayers. Multilayer reflectors are made by depositing alternating layers of high- $Z$  and low- $Z$  materials, giving a small but effective difference between refractive indices at each interface. By making the periodicity  $d$  of the multilayer stack satisfy the Bragg condition, the net effect of small reflectivity at each interface is moderately high reflectivity overall when the stack has enough layers.

For silicon the refractive index dips to 0.951 at a wavelength of 190 nm [26-28].

### Nano solid film

The thickness of the nanolayer is important for the functioning of prospective devices. The question is whether a thin film of nanoparticles would act as a thin layer of silicon. The nature of the wave scattered at or below the critical angle  $\alpha < \alpha_c$  is such that the refracted wave cannot propagate into the material; instead there will be an evanescent wave travelling parallel to the surface, with exponentially decaying amplitude away toward the interior of the material.  $k_{zc}$  ( $\text{\AA}^{-1}$ ) is found to be  $\sim 0.0159$ . Hence, the depth of penetration of the incident wave is 63  $\text{\AA}$ , limited to about 100  $\text{\AA}$ . This is equivalent to  $\sim 3\text{-}4$  monolayers of 3-nm particles. With a self-assembly of the red nanoparticles and from the strength of the emission band and that the red is seen with the naked eye we expect this to Hence the depth of penetration of the incident wave is 63  $\text{\AA}$ , limited to about 100  $\text{\AA}$ . With nanoparticles of  $\sim 3 \text{ nm}$  diameter, one need  $\sim 5$  monolayers to isolate propagation in the underlying glass [29]

### Charging characteristics

The ionization levels of silicon atoms is 8.15, 16.2, 33.5, 45, 167, 205, 246, 303, 351, 401, 476, 523, 2437, and 2672 eV. The corresponding excitation wavelengths of the first five are 152, 76, 38, 27.5, and 7.4 nm. On the other hand, bulk silicon work function is 4.60 – 4.85 eV depending on the crystal orientation. It is to be noted that the demarcation of this phenomenon in silicon occurs at excitation with UV radiation of a photon energy of  $\sim 6.5 \text{ eV}$  corresponding to a wavelength of 191 nm. At this wavelength the refractive index dips just below 1.0 to 0.951. For silicon the refractive index dips to 0.951 at a wavelength of 190 nm [26-28]

For an  $n$ -electron system, the electron affinity (adding an electron) and ionization (removing an electron) energies can be expressed in terms of the ground-state total energies  $E$  of the  $n$ ,  $(n+1)$ , and  $(n-1)$  electron systems as follows

$$I = E(n-1) - E(n) \quad A = E(n) - E(n+1)$$

Calculation of the charging energies of  $\text{Si}_{29}\text{H}_{24}$  was done at the UHF-DFT level using the B3LYP functional with the TURBOMOLE quantum computational package [30-31]. The TZVP basis was used which is a triple split

valence basis with polarization functions added for each atom. The electronic density used for the density functional calculations is built from an unrestricted Hartree-Fock (UHF) type Slater determinant. The silicon particle ionization energy and electron affinity are found to be 7.29 eV and 1.46 eV respectively. This is much closer to the atomic values of silicon (8.15 eV and 1.38 eV respectively) than to the crystalline bulk silicon values of 4.05 eV and 5.17 eV. This further demonstrates the silicon nanoparticle is most appropriately discussed in the molecular regime than approximations from the crystalline condensed matter regime.

#### Ionization and affinities (for 2.8 nm diameter)

The ionization energies  $I$  and electron affinities  $A$  for hydrogenated Si nanoparticles as a function of the nanocrystal's radius  $R$  was calculated using real-space *ab initio* pseudopotentials constructed within the local-density approximation [32]. At small values of  $R$ , the electron affinities are small in comparison with the ionization energies. Small affinity values are consistent with a weak localization of the lowest unoccupied state. As radius increases, the ionization energy gradually decreases whereas the affinity energy increases. With size, the ionization and affinity scale with radius  $R$  of the nanocrystal as  $R^{-\sigma}$ , where  $\sigma = 1.1 \pm 0.2$ . This is much slower than what has been calculated using the effective-mass theory, namely for this latter the scaling factor  $l$  is found to be 2. The size dependence has been attributed to spatial quantum confinement. The strong size dependence characteristic remains significantly different from corresponding bulk values even for the largest nanocrystals studied (2.8 nm across). For 2.8 nm, the affinity rises to 3 eV, while the ionization drops to 6 eV.

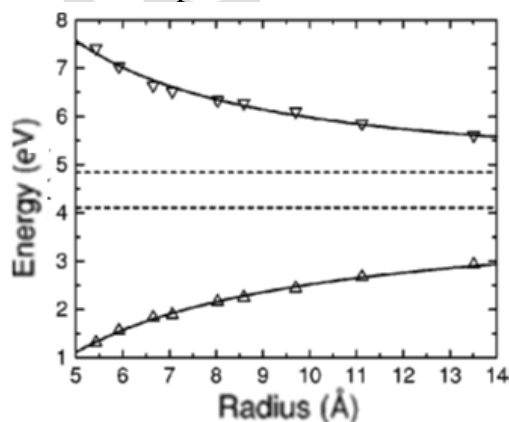


**Figure 8** Ionization energy (top) and electron affinity (bottom) of Si nanocrystals as functions of nanocrystal's radius  $R$ . The results are calculated using real-space *ab initio* pseudopotentials constructed within the local-density approximation. Solid lines are the best fits to the calculated data. Straight dashed lines correspond to bulk values of ionization energy (4.8 eV) and affinity at 4.1 eV for Si.

Silicon Size	Ionization (eV)	Electron Affinity (eV)
1 nm	7.29	1.43
2.8 nm	5.50	2.95
Bulk	4.80	4.10

The charge characteristics of the 2.85 nm particles approach that of bulk but slightly remain somewhat different from corresponding bulk values. However, previous measurements showed that the refractive index of the 2.8 nm particle is approaching that of bulk. With close packing due to the very slow self-assembly provided by the dynamic flow arrangement, we believe that those parameters may serve as a good indicator and trend. Moreover, these differences in the ionization of the outer electrons, would not factor in for deeper electron processes under short wavelength of deep UV or x-ray, where transitions in individual atoms dominate. For instance in studies of bulk silicon resonant absorption edges within the range of energy values studied, such as in the range of 0.5-1.2 keV, experiments and calculations show that the drop in the refractive index follows a  $\lambda^2$ -dependent curve and the absorption  $\beta$  follows a  $\lambda^3$ -dependent curve [33]. In other words, the quantities in the range  $\delta$  can be represented by the equation  $\delta = 2.84 \times 10^{-6} \lambda^2 A^{-2}$ . This may be related to the real part of the silicon "atomic scattering factor"  $f_{si}$ , which takes the value of  $f_{si} = 12.6$ . On the other hand, classically,  $f$  is the number of electrons (per atom) with binding energy less than the incident photon energy (12 in the case of silicon at these photon energies) [33-34].

#### Loss due to roughness of the nanofilm

As to the surface quality and the degree of scattering and losses. A vector scattering model for uncorrelated roughness, as described by

Vidal and Vincent [35], has been used to introduce a parameter  $\sigma$  which represents the root-mean-square roughness of a surface. This model of roughness assumes that the departures of the interface from an ideal planar boundary can be described by a normal distribution in the first approximation. Shadowing and multiple-scattering effects are neglected. This model of roughness is valid for all values of  $\sigma/\lambda$ , provided the wavelength is such that surface plasmon phenomena can be ignored. Under these assumptions, It has been calculated that the effect of the surface roughness parameter  $\sigma$  is to decrease the reflected intensity by a factor which increases with grazing-incidence angle  $\theta$ . Hence,  $\sigma$  can be determined from scans of  $R$  vs the grazing angle  $\theta$  with the wavelength held fixed. At the critical angle, the critical reflectivity coefficient  $r_c$  drops proportional to the factor [33]:

$$r_c \sim \text{EXP} \sim [-(2\pi/\lambda) \sigma]^2 = \text{EXP} [-k\sigma]^2$$

Using 195nm for the wavelength of the incident radiation and taking the size of a single particle for  $\sigma$ , this factor is 0.99, indicating only a loss of 1%. For wavelengths of 10nm, we get a factor of 0.018, indicating a loss of 82%.

## V. Other Applications

Finally, poly capillary x-ray optics have found potential application in many different fields, including anti-scatter and magnification in mammography, radiography, x-ray fluorescence, x-ray lithography, and x-ray diffraction techniques. In x-ray diffraction, an optic is used to collect divergent x-rays from a point source and redirect them into a quasi-parallel, or slightly focused beam. Monolithic poly capillary optics have been developed recently for macromolecular crystallography and have already shown considerable gains in diffracted beam intensity over pinhole collimation.

Poly capillary x-ray optics have found potential application in many different fields, including anti scatter and magnification in mammography, radiography, x-ray fluorescence, x-ray lithography, and x-ray diffraction techniques.

Polycapillary optics are well suited for clinical, *in situ*, or laboratory-based applications such as X ray fluorescence and X ray diffraction, especially on small samples [26, 27]. A new tool combining local XRF and scanning probe microscopy is finally proposed. Moreover, a confocal-type XRF based on polycapillary has been developed. A polycapillary lens is used to tightly focus the primary X-ray beam of a low power rhodium X-ray source, while the fluorescence signal is collected by a SDD detector through a cylindrical monicapillary. Capillary radii ranging from 50  $\mu\text{m}$  down to 5  $\mu\text{m}$  were used.

In x-ray diffraction, an optic is used to collect divergent x-rays from a point source and redirect them into a quasi-parallel, or slightly focused beam. In fact, monolithic polycapillary optics have been developed recently for macromolecular crystallography and have already shown considerable gains in diffracted beam intensity over pinhole collimation.

## VI. Conclusion

We examine the use of a glass polycapillary system as a template and support structure to produce a silicon polycapillary system. We perform surface doping using self -assembly silicon nanoparticles, which produces a silicon coating that assumes the shape of the polycapillary. The silicon polycapillary is optically active in the UV. We produced novel fused silica capillary columns with optical functionality. Silicon provides a larger critical angle for x-ray proportion over what glass provides which may increase the efficiency of focusing of x-rays.

**References**

1. Coating Thickness Determination Using X-ray Fluorescence Spectroscopy: Monte Carlo Simulations as an Alternative to the Use of Standards, Walter Giurlani, Enrico Berretti, Massimo Innocenti and Alessandro Lavacchi, *Coatings* (2019), 9, 79 3 of 11.
2. MacDonald, Carolyn A. (2010). "Focusing Polycapillary Optics and Their Applications". *X-Ray Optics and Instrumentation*. **2010**: 1–17. Bibcode:2010XROI.2010E..11M. doi:10.1155/2010/867049. Carolyn A. MacDonald, Focusing Polycapillary Optics and Their Applications, X-Ray Optics and Instrumentation Volume 2010, Article ID 867049, 17 pages doi:10.1155/2010/867049 Hindawi Publishing Corporation
3. POLYCAPILLARY OPTICS FOR ANGULAR FILTERING OF X-RAYS AND NEUTRONS IN TWO DIMENSIONS, W.M. Gibson T, H. Huang Y, J. Nicolich, P. Klein, and C.A. MacDonald, *Advances in X-ray Analysis*, Volume 45. 313 (2002)
4. Paul shields, D. Gibson, W. Gibson, N. Gao, H. Huang, and I. Ponomarev, overview of polycapillary x-ray optics Powder diffraction, V17 70, (2002)
5. M. H. Nayfeh, *Fundamentals and applications of nano silicon in plasmonics and fullerenes: current and future trends* Elsevier Publishing, (2018)
6. M. Nayfeh, in *Optics in Our Time*, M. Alamri, M. M. El Gomati, and M. S. Zubairy, ed Springer (2016).
7. M. H. Nayfeh and L. Mitas, in *Nanosilicon*, V. Kumar, ed. Elsevir, 1 (2007).
8. M.I Baratron, ed., *Synthesis, Functionalization, and Surface Treatment of Nanoparticles* American Scientific Publishers, (2002).
9. SPE Nanostructured Glass Technology Ltd., Saratov, Russia: <http://ngt2005.narod.ru>
10. J. S. Skibina et al., Technologies of manufacturing polycapillary optics for X-ray engineering, *J. X-Ray Sci. Technol.* 13 (4), p. 161, 2005.
11. O. Ackakir, J. Therrien, G. Belomoin, N. Barry, J. Muller, E. Gratton, and M. Nayfeh, *Appl. Phys. Lett.* 76, 1857 (2000).
12. G. Belomoin, J. Therrien, A. Smith, S. Rao, R. Twesten, S. Chaieb, M. H. Nayfeh, L. Wagner, and L. Mitas, *Appl. Phys. Lett.*, 80, 841 (2002).
13. D. Nielsen, L. AbuHassan, M. Alchihabi, A. Al-Muhanna, J. Host, and M. H. Nayfeh, *J. Appl. Phys* 101, 114302 (2007).
14. L. Mitas, J. Therrien, R. Twesten, G. Belomoin, and M. H. Nayfeh, *Appl. Phys. Lett.*, 78, 1918 (2001).
15. G. Belomoin, E. Rogozhina, J. Therrien, P. V. Braun, L. Abuhassan, M. H. Nayfeh, L. Wagner, and L. Mitas, *Phys. Rev. B*, 65, 193406 (2002).
16. G. Allan, C. Delerue, and M. Lannoo, *Phys. Rev. Lett.* 76, 2961 (1996).
17. M. Nayfeh, N. Rigakis, and Z. Yamani, *Phys. Rev. B* 56, 2079 (1997).ero
18. Origin of the visible absorption in radiation-resistant optical fibers, A. Morana,1,2 M. Cannas,2 S. Girard,1 A. Boukenter,1 L. Vaccaro,2 J. P'erisse,3 J.-R. Mac'e,4 Y. Ouerdanel and R. Boscaino2 *Optical Materials Express* 3(10):1769-1776 (2013) DOI: [10.1364/OME.3.001769](https://doi.org/10.1364/OME.3.001769)
19. D. L. Griscom and M. Mizuguchi, "Determination of the visible range optical absorption spectrum of peroxy radicals in gamma-irradiated fused silica," *J. Non-Cryst. Solids* **239**, 66–77 (1998).
20. D. L. Griscom, "γ-Ray-induced visible/infrared optical absorption bands in pure and F-doped silica-core fibers: are they due to self-trapped holes?," *J. Non-Cryst. Solids* **349**, 139–147 (2004).
21. Y. Sasajima and K. Tanimura, "Optical transitions of self-trapped holes in amorphous SiO<sub>2</sub>," *Phys. Rev. B* **68**, 014204 (2003).
22. S. Girard, D.L. Griscom, J. Baggio, B. Brichard, and F. Berghmans, "Transient optical absorption in pulsed-X-ray-irradiated pure-silica-core optical fibers: Influence of self-trapped holes," *J. Non-Cryst. Solids* **352**, 2637– 2642 (2006).
23. E. Spiller, "*X-Ray Optics*". *Encyclopedia of Optical Engineering*. Taylor & Francis. Bibcode:2003eoe..book....D. doi:10.1081/E-EOE-120009497 (inactive 2020-12-07) (2003) close to 1
24. [http://gisaxs.com/index.php/Critical\\_angle#Examples](http://gisaxs.com/index.php/Critical_angle#Examples)
25. <https://www.classe.cornell.edu/~dms79/refl/X-rayScattering.html>
- a. <https://refractiveindex.info/?shelf=main&book=Si&page=Pierce> RefractiveIndex.INFO website: © 2008-2020 Mikhail Polyanskiy
26. D. T. Pierce and W. E. Spicer, Electronic structure of amorphous Si from photoemission and optical studies, *Phys. Rev. B* 5, 3017-3029 (1972).
27. Handbook of Optical Constants of Solids, Edward D. Palik, ed. Academic Press, Boston, 1985 (ref. 2 provides numerical values for the graphical data reported in ref. 1)
28. X-ray Scattering at Grazing Incidence, Detlef Smilgies, <https://www.classe.cornell.edu/~dms79/refl/X-rayScattering.html>
29. K. A. Mantey, *Structure, electronic levels, and ionic interactions of 1 nm silicon particles* [https://www.ideals.illinois.edu/bitstream/handle/2142/26172/Mantey\\_Kevin.pdf?...1](https://www.ideals.illinois.edu/bitstream/handle/2142/26172/Mantey_Kevin.pdf?...1) by KA Mantey, University of Illinois at Urbana-Champaign (2011)
30. Iron oxide–Si nanoparticle magnetic core–shell induced by the interaction of d-orbitals of Fe<sup>2+</sup> with reconstructed Si dimer-like defects, Noha Elhalawany, Kevin Mantey, Tuan Hoang, Ersin Bahceci, Jiacheng Xu, Hakan Ates, Dmitry Gorin, Zain Yamani, and Munir H. Nayfeh, *AIP Advances* 10, 055221 (2020); <https://doi.org/10.1063/1.5144880>

31. Electron affinities and ionization energies in Si and Ge nanocrystals, Dmitriy V. Melnikov and James R. Chelikowsky, **PHYSICAL REVIEW B** **69**, 113305 (2004)
32. X-RAY REFRACTIVE INDEX OF SILICON IN THE RANGE 400 TO 1100 eV, S. C. WORONICK, W. NG, A. KROL and Y. H. Kao, *J. Phys. Chem. Solids* Vol. 53, No. 10, pp. 1265-1268. (1992)
33. The silicon-metal system at the nano scale, Munir Nayfeh, H. M. Nayfeh, A. M. Nayfeh, O. M. Nayfeh, Elsevier, (In press) (2022)
34. Metallic multilayers for x rays using classical thin-film theory, B. Vidal and P. Vincent, **Applied Optics**, Vol. 23, Issue 11, pp. 1794-1801 (1984) <https://doi.org/10.1364/AO.23.001794>

## **EFFECTS OF UNDERCUT DEPTH AND LENGTH ON WELD STATIC STRESS CONSANTRATION AND DUCTILITY**

**Memduh KURTULMUŞ**

*Marmara University - Faculty of Applied Sciences, 34722, Istanbul, Turkey,  
memduhk@marmara.edu.tr  
ORCID: 0000-0001-6525-232X*

**Ezgi DOĞAN**

*Marmara University- Institute of Pure and Applied Sciences, 34722, Istanbul, Turkey,  
ezgi.dogan@marun.edu.tr  
ORCID: 0000-0003-0207-7178*

*Cite this paper as: Kurtulmus, M, Dogan, E. Effects Of Undercut Depth And Length On Weld Static Stress  
Consantraion And Ductility. Int. Conf. Advanced. Mater. Sci. & Eng. HiTech.and Device Appl.Oct. 27-29  
2022,Ankara, Turkey*

**Abstract.** Undercutting is a welding defect that appears as a groove in the base metal directly along the edges of the weld metal. It is inevitable in fillet and butt joints if improper welding parameters are used in the operation. It is a discontinuity in the welding which produces stress concentration and lowers the strength of the weld. The stress concentration factor of an undercut is due to reinforcement angle, undercut width, undercut depth and undercut root radius.

In this study 20 mm thick mild steel plates were welded by gas metal arc welding process. Before welding a 30° single bevel groove angle was obtained by milling on the longitudinal side of a test plate. Two plates were welded with one pass. After welding the weldment was tested with radiographic NDT process. A defect free weldment was obtained. Then standard tensile test samples were machined from the weldment. A groove was drilled in the heat affected zone, adjacent to the weld metal boundary on every tensile test sample. Each groove resembled an undercut. The length, root radius and depth of grooves were varied. Then samples were broken on a tensile test machine. From the test results the static stress concentration factor of each groove was calculated. The effects of groove geometry on stress concentration factors and mechanical properties were determined.

**Keywords:** Welding defects, Undercut, Undercut geometry, Static stress concentration factor  
© 2022 Published by ICMATSE

### **Introduction**

Recent manufacturers have to constantly improve their production without sacrificing the quality of their products in order to cope with the competition of their competitors. They can achieve improvement in their production by increasing the speed of their production and reducing their costs. Industrial branches such as steel construction, shipbuilding, automotive, petrochemical, space, pressure vessels, nuclear energy units and electronics widely use welding methods. In the welding methods applied in these business lines, reductions in production costs are realized by increasing the resource efficiency [1]. Undercuts are a weld discontinuity seen in fusion welds. These discontinuities are generally grooves and notches that occur in areas close to the joining of the weld seam and the weld base metal (at the seam toe end) and parallel to the weld seam. Since

these areas cannot be filled with liquid weld metal during solidification, undercuts are formed. The undercut error in the X butt weld joint made with the submerged arc welding method is shown in Figure 1 [2].

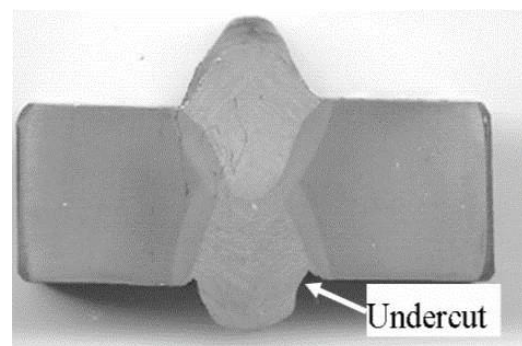


**Figure 1.** Typical undercut [2].

Undercut defect occurs under extremely high welding current and/or welding at extremely high welding speed [3]. This welding defect occurs different from gas arc welding [4-6], TIG welding [7,8], laser welding [9,10], submerged arc welding [2,11], MMA arc welding [12] and electron beam welding [13] methods in industrial applications. It is seen in Figure 2 that the arc welding faults are basically divided into two main groups as discontinuous and continuous [14]. In discontinuous faults, the defect section changes along the seam.

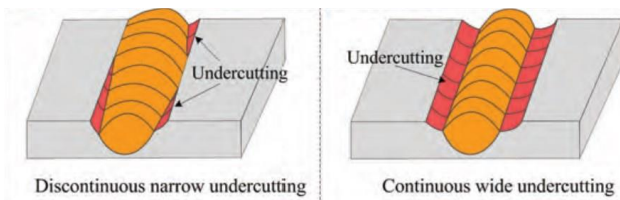


**Figure 2.** Two types of undercutting defects in GMAW [14].

Local stress concentration occurs in the cross-sectional changes of welded and non-welded metal parts and around any discontinuities in the section [15]. Since the undercuts also have a kind of notch effect, stress concentration occurs at the bottom of the undercut [16]. Local stress concentrations reduce the static and dynamic strength of the workpiece or welded part. Undercuts significantly reduce the fatigue strength of the welded part [17]. The maximum stresses are determined in the notches and discontinuities of the objects under static load, using the calculations made using the theory of elasticity and the measurements made using the photoelasticity technique [15]. In addition, if there were no notches or discontinuities, the stress that would occur in that section is calculated. This stress is called the nominal stress of the workpiece. By dividing the maximum stress by the nominal stress, the stress concentration coefficient (stress concentration factor),  $K$ , is found for the static force in that object [16].

In this study, the stress concentration coefficient ( $K$ ) around the combustion trough was found by dividing the tensile strength of the sample containing the combustion trough defect by the tensile strength of the faultless sample. In addition, the effect of notch geometry on ductility was investigated.

### Material and Methods

Two pieces 1000x300x20 mm St-37 unalloyed steel plates were used in the experimental studies. Half-V welding groove with 30° angle was opened on the long side of the plates. 60° butt weld joint was made

on the plates in horizontal position. Welds were made by automatic CO<sub>2</sub> shielded gas metal arc (MAG) method. ER 70S-6 welding wires are used in welding processes. Before the root pass is made, the workpieces are inverted to ensure that the parts remain within 180° after welding. Cracks were checked by applying penetrating liquid test after each welding process. After the cover pass, radiographic examination was performed on the workpiece. An error-free resource was obtained.

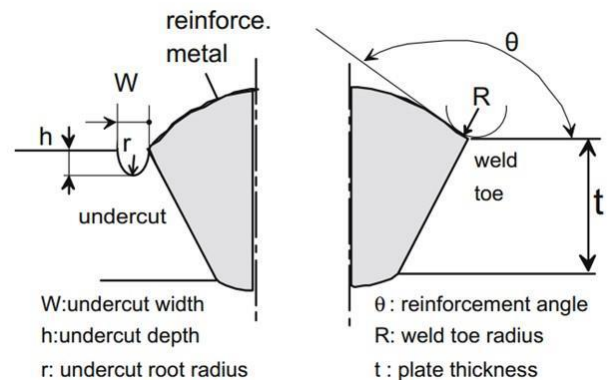


**Figure 3.** Characteristic parameters of a butt weld undercut defect [18].

After removing the 75 mm wide parts from both sides of the welded part by laser cutting, tensile test specimens were cut in the direction perpendicular to the welding progress direction. Tensile tests were prepared in accordance with the ASTM standard [21]. In the plunge erosion bench, the notch of the undercut shown in Figure 3 was made at the foot end of the weld seam. The width ( $W$ ) of each notch was kept constant at 1 mm and the root radius ( $r$ ) at 0.5 mm. There are 3 tensile specimens for each notch condition and for the non-notch welded condition. Tensile tests were carried out on a 50 ton electronically controlled hydraulic pulling machine. By taking the average of the test results of 3 samples belonging to each experimental group, the mechanical properties of that group were determined. Then, the tensile strength of each unnotched test specimen was divided by the tensile strength of each test group, and the stress concentration coefficient ( $K$ ) of each test group was calculated.

### Results

The tensile test results and the static stress coefficient ( $K$ ) values calculated using these results are shown in Table 1. Using these results, the graphs in 6, 7, 8, 9 and 10 were drawn.

**Table 1.** The tensile test results and the calculated K coefficient values

Specimen No.	Tensile Strength, MPa	% Elongation	Calculated K coefficient
1	551	30,1	1,00
2	507	28,4	1,08
3	501	24,3	1,10
4	492	17,9	1,12
5	498	19,2	1,11
6	487	16,5	1,13
7	466	9,8	1,18
8	497	18,2	1,11
9	464	14,3	1,19
10	422	8,0	1,31

### Discussion

As the seam depth increases, the weld tensile strength decreases depending on the undercut length. As the notch depth and length increase, the decrease in strength occurs more. The negative effect of notch depth on strength becomes evident depending on the length of the undercut. In samples with fixed notch length, the tensile strength decreases significantly as the notch depth increases.

### Conclusion

#### References

1. N.T. Nguyen, D. Weckman, D. Johnson, H. Kerr, High Speed Fusion Weld Bead Defects, *Sci and Tech of Weld and Join*, 11(2006), pp. 618-633, 10.1179/174329306X128464.
2. Y. Yang, The Effect of Submerged Arc Welding Parameters on the Properties of Pressure Vessel and Wind Turbine Tower Steels, MSc. Thesis, Saskatchewan University, Canada, 2008.
3. R. Zong, J. Chen, G. Wu, G. Padhy, Influence of Shielding Gas on Undercutting Formation in Gas Metal Arc Welding, *J of Mat Proc Tech*, 234(2016), pp. 169-176, 10.1016/j.jmatprotec.2016.03.020.
4. W. Xu, C. Wu, D. Zou, Predicting of bead undercut defects in high-speed gas metal arc welding (GMAW), *Fron Mat Sci in China*, 2(2008), pp. 402-408, 10.1007/s11706-008-0065-x.
5. Y. Hu, J. Xue, C. Dong, L. Jin, Z. Zhang. Effect of Additional Shielding Gas on Welding Seam Formation during Twin Wire DP-MIG High-Speed Welding, *App Sci*, 8(2018), pp. 1-13, 10.3390/app8091658.
6. N. Khalid, P. Zamanhuri, F. Baharin, A Study of Weld Defects of Gas Metal Arc Welding with Different Shielding Gases, *J of Eng and App Sci*, 12(2017), pp. 2006-2011,
7. X. Meng, G. Qin, X. Bai, Z. Zou, Numerical analysis of undercut defect mechanism in high speed gas tungsten arc welding, *J of Mat Proc Tech*, 236(2016), pp. 225-234, 10.1016/j.jmatprotec.2016.05.020
8. X. Meng, G. Qin, X. Bai, Z. Zou, Sensitivity of driving forces on molten pool behavior and defect formation in high-speed gas tungsten arc welding, *Int J of Heat and Mass Trans*, 107(2017), pp. 1119-1128, 10.1016/j.jmrt.2021.06.042.
9. J. Frostevarg, A. Kaplan, Undercuts in laser arc hybrid welding, *Phys Proc*, 56(2014), pp. 663-672, 10.1016/j.phpro.2014.08.071.
10. J. Karlsson, P. Norman, A. Kaplan, P. Rubin, J. Lamas, A. Yanez, Observations of the Mechanisms Causing Two Kinds of Undercut During Laser Hybrid Arc Welding, *App Surf Sci*, 257(2011), pp. 7501-7506, 10.1016/j.apsusc.2011.03.068.
11. J. Nowacki, P. Rybicki, The influence of welding heat input on submerged arc welded duplex steel joints imperfections, *J of Mat Proc Tech*, 164-165(2005), pp. 1082-1088, 10.1016/j.jmatprotec.2005.02.079.

When the depth of the undercut is increased from 1 mm to 2 mm in each notch length, a large decrease in ductility is observed. However, when the depth of the undercut is increased from 2 mm to 3 mm, there is a slight decrease in ductility. The loss of ductility in the workpiece depending on the seam depth is seen in Figure 10. While the % elongation value of the workpiece decreases significantly between 1-2 mm notch depth, ductility loss occurs at a much smaller rate between 2-3 mm seam depth. If it is compared the strength and ductility losses caused by notches in the workpiece, it is seen that the ductility loss rate is larger. For example, in the tensile sample of the fault (sample No. 1), the tensile strength is 551 MPa and the total elongation is 31%. The tensile strength is 422 MPa and the ductility is 8% in the sample (sample No. 10) containing a 3 mm deep and 20 mm long undercut. While there is a 23% loss in strength, the ductility loss rate is 74%. This result shows that the undercut causes embrittlement of the workpiece. Embrittlement increases further as the bottom radius of the combustion chute decreases. Due to this embrittlement, the fatigue resistance of the workpiece is significantly weakened.

12. S. Garg, I. Kakkar, A. Pandey, M. Gupta, N. Kishors, Effect of Different Coating Composition's Rutile-type Welding Electrodes on Undercut Defect in Manual Electric Arc Welding, *Int J of Mech Eng and Res*, 3(2013), pp. 381-388.
13. A. Kaur, Electron Beam Diagnosis for Weld Quality Assurance, PHd. Thesis, Brunel University, London, 2016.
14. R. Zong, J. Chen, C. Wu, M. Chen , Undercutting Formation Mechanism in Gas Metal Arc Welding, *Weld J*, 95(2016), pp. 174-184, 2016.
15. R. Juvinall, K. Marshek, *Fundamentals of Machine Component Design*, John Wiley and Sons, New York, 1991.
16. J. Shigley, *Mechanical Engineering Design*, McGraw-Hill Book Company, New York, 1986.

## ACTIVATING FLUX GAS METAL ARC WELDING PROCESS

**Memduh KURTULMUS**

*Marmara University - Faculty of Applied Sciences, 34722, Istanbul, Turkey,  
memduhk@marmara.edu.tr  
ORCID: 0000-0001-6525-232X*

**Ezgi DOGAN**

*Marmara University- Institute of Pure and Applied Sciences, 34722, Istanbul, Turkey,  
ezgi.dogan@marun.edu.tr  
ORCID: 0000-0003-0207-7178*

*Cite this paper as: Kurtulmus, M, Dogan, E. Activating Flux Gas Metal Arc Welding Process. Int. Conf. Advanced. Mater. Sci. & Eng. HiTech.and Device Appl.Oct. 27-29 2022,Ankara, Turkey*

**Abstract.** A more efficient and economical method of improving the productivity of gas metal arc welding process is using activating fluxes in welding. The activating fluxes which consist of halogens and oxides have a positive effect on electric arc formation and droplet transfer of electrode metal to the liquid metal pool. Activated Flux Gas Metal Arc (A-MIG) welding can increase the joint penetration, weld depth/width ratio and weld area. In this review paper, the effects of A-MIG welding on weld bead shape in mild steels, austenitic stainless steels, aluminum and magnesium alloys are examined. The effects of this welding process on weld mechanical properties weld distortions are explained.

**Keywords:** MIG welding, A-MIG welding, MIG activating fluxes

© 2022 Published by ICMATSE

### Introduction

Welding is an important processing operation in manufacturing and production enterprises. The gas metal arc welding (GMAW) has the advantages of high efficiency, good weld quality, low production cost and easy to realize automation in manufacturing, therefore it has been widely used in the industry. Modern manufacturing industries are facing an intense market competition. Thus, there is an urgent need to substantially improve production efficiency. The GMAW has to increase welding speed in order to enhance market competitiveness and reduce production costs. However, if the welding speed is increased beyond a certain level, the weld formation quality will get worse and welding defects occur [1]. In recent years, a clear trend towards higher productivity and better quality has been leading to the development of many variants of the GMAW process. Pulsed gas metal arc welding (P-GMAW) is a highly controlled variant of axial spray transfer, in which the welding current is cycled between a high peak current level to a low background current level. Metal transfer occurs during the high energy peak level in the form of a single molten droplet. One of the advantages of P-

GMAW is to weld with a higher welding speed than classic GMAW [2].

For the welding of thick and large metal specimens, a novel process, namely double electrode or tandem gas metal arc welding (DE-GMAW), was developed at the University of Kentucky [3]. The uniqueness of this process lies in its strong penetration capability and deposition rate achieving high productivity with low cost and high durability [4]. A higher welding speed than the P-GMAW was obtained in this process.

Little work has been done on using activated flux in GMAW method [5-20]. The aim of this paper is to summarize the findings of activated flux GMAW research studies. The effects of activated flux on gas metal arc welding process were explained in the following chapter.

### Material and Methods

The main effect of activated fluxes in GMAW process is to enhance the penetration depth of a weld bead. The fluxes also affects other properties during a

welding operation. These effects are explained below.

The fluxes positively alter the efficiency of heating of metal by electric arc and current density in GMAW [16,17]. The heat effective coefficient of usefulness of electric arc or the part of electric arc energy which is spent on metal melting increases in activated gas metal arc welding (A-MIG) operation than the conventional MIG welding. Therefore a deeper weld is obtained in A-MIG welding at a constant arc energy. Hence, arc activation, which increases the penetration by several times when compared to the conventional welding method, enables the reduction of drive energy while welding the metal of the same thickness. Also, the activation increases the speed of heating of welding joint metal and heat affected zone [16].

One of the most characteristic phenomena of gas metal arc welding is molten droplets transferring across the arc from the wire electrode to the liquid weld pool. Different transfer behavior, referred to as “droplet transfer mode”, can be observed [21]. Droplet transfer mode is influenced by growth time, dimension and detachment frequency of the droplets. The main parameters affecting droplet formation are wire composition and diameter, shielding gas composition, electric polarity, arc length and welding current level [22].

Figure 1 shows the variation tendencies of the welding current without and with activating fluxes with the time lapse during MIG welding AZ61 magnesium alloy plates with and without KCl, TiO<sub>2</sub> and CaCl<sub>2</sub> activating fluxes. It can be seen that the change of the welding current of single MIG welding is comparatively stationary and the average current value is kept up by 184 Amperes. The KCl flux not only makes the fluctuation of the current become intense but also increases the average welding current value by 17 Amperes in comparison with single MIG welding. When the CaCl<sub>2</sub> flux is used, the average current value is reduced to 175 Amperes, and the variation trend of the current is erratic. With respect to the TiO<sub>2</sub> flux, the welding current is almost the same as that of single MIG welding. Since the arc voltage is maintained at 23 volts in this study and the change in the arc conductivity will lead to an inverse change in arc resistance, it is concluded that the arc conductivity is proportional to the welding current on the basis of the Ohm’s law. The arc conductivity may be altered when the activating fluxes are added.

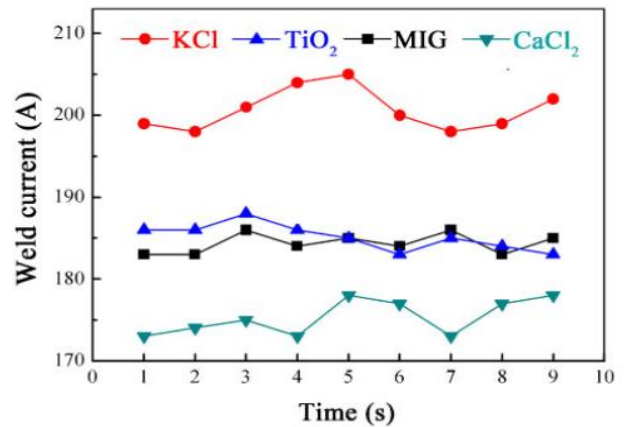


Figure 1. Variation tendency of welding current in MIG welding of AZ61 magnesium plates without and with activating fluxes (10).

The typical MIG and A-MIG weld cross sections of austenitic stainless steels are shown in Figure 2 [1]. The width and penetration depth is bigger in the A-MIG weld. The penetration depth increased 1.31% in A-MIG welding. The weld depth/width ratio is also increased in A-MIG weld. The weld depth/width ratio is 0.20 in the MIG weld and 0.40 in the A-MIG weld. Each flux has a characteristic effect on weld geometry. Similar high penetration depths were obtained [18] in austenitic stainless steels A-MIG welding applications.

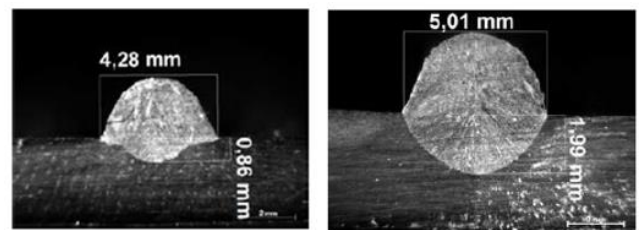


Figure 2. Macro section of weld bead produced with (a) MIG and (b) A-MIG welding of CrNi18-10 austenitic stainless steels [18].

## Results

These welds were produced on AISI 304L austenitic stainless steel plates. The Ar-2.5% CO<sub>2</sub> shielding gas was consumed during welding. A-MIG welds were done with SiO<sub>2</sub> flux.

The first line welds were produced with 160 Amperes, the middle line welds were welded with 200 Amperes and the bottom line welds were produced with 230 Amperes. At every welding current A-MIG weld has a deeper weld than the MIG weld. This result matches with the main purpose of using activating flux in welding. At 200 and 230 Amperes weldings finger shaped penetration occurred. This geometry proves that spray transfer mode happened in these welds [25]. At welding with 160 Amperes no finger shaped penetration occurred. That shows that globular transfer mode happened [25]. Both MIG and A-MIG processes have the same metal transfer mode. The weld with decreased with spray transfer mode. The width increased parallel to the welding current. The penetration depth and weld width increased with a rise in welding current because of high energy inputs. The effect of welding current on penetration can be described either with penetration depth or weld depth/weld width ratio in MIG and A-MIG welding operations.

#### Discussion

Welding joins metals by melting and fusing the base metals being joined; usually with the addition of a filler metal. Due to the localized heating, the temperature distribution in the weldment is non uniform. The top face of the weld usually shrinks more than the root. If the stresses produced from thermal expansion and contraction exceed the yield strength of the base metal, an angular geometry: deep and narrow welds resulting in lower angular distortion.

#### References

1. N.T. Nguyen, D. Weckman, D. Johnson, H. Kerr, High Speed Fusion Weld Bead Defects, *Sci and Tech of Weld and Join*, 11(2006), pp. 618-633, 10.1179/174329306X128464.
2. B. Mvola, P. Kah, J. Martikainen, E. Hiltunen, Applications and Benefits of Adaptive Pulsed GMAW, *Mechanika*, 19(2013), pp. 694-701, 10.5755/j01.mech.19.6.6003.
3. K. Li, Y. Zhang, Metal Transfer in Double-Electrode Gas Metal Arc Welding. *J of Manf Sci and Eng*, 129(2007), pp. 991-999, 10.1115/1.2769729.
4. T. Ueyama, T. Ohnawa, K. Yamazaki, M. Tanaka, M. Ushio, K. Nakata, High-Speed Welding of Steel Sheets by the Tandem Pulsed Gas Metal Arc Welding System, *Transactions of JWRI*, 34(2005), pp. 11-18.
5. M. Kurtulmus, A. Yukler, D. Ezgi, Activated Flux TIG Welding Of Non-Ferrous Metals, *Ind J of Chem Tech*, 26(2019), pp. 164-169.
6. H. Huang, Research on the Activating Flux Gas Tungsten Arc Welding and Plasma Arc Welding for Stainless Steel, *Met and Mat Int*, 16(2010), pp. 819-825, 10.1007/s12540-010-1020-9.
7. R. Kaul, Effect of active flux addition on laser welding of austenitic stainless steel, *Sci and Tech of Weld and Join*, 12(2007), pp. 127-137, 10.1179/174329307X159793.
8. R. Zhang, D. Fan, S. Katayama, Electron Beam Welding with Activating Flux, *Trans of Jap Weld Res Inst*, 35(2006), pp. 19-22.

distortion is experienced in a butt joint [29]. MIG with Fe<sub>2</sub>O<sub>3</sub>, SiO<sub>2</sub> and MgCO<sub>3</sub> as flux reduced the angular distortion of the weldment. It is of interest to note that the value of the angular distortion of the weldment depended on the relative penetration depth of the welds. The weld depth was equal to the plate thickness (full penetration); essentially, the plate was heated more evenly in its thickness, thus reducing bending. Consequently, angular distortion was reduced.

#### Conclusion

This paper explains the welding activating flux affects on weld bead geometry and mechanical properties of A-MIG welding process of metals. The following results were obtained from the literature review:

1. The weld penetration depth and weld width size of a A-MIG weld depends on the chemical composition of the flux.
2. Flux mixtures give better results than mono fluxes.
3. A-MIG process gives small penetration depth advantages in mild steels, aluminum and magnesium alloys.
4. High cooling rates in A-MIG welds cause higher tensile strength and hardness.
5. The angular distortion of the weldment was reduced by the flux aided MIG. The angular distortion is associated with weld bead

9. H. Huang, Effects of activating flux on the welded joint characteristics in gas metal arc welding, *Mat and Des*, 31(2010), pp. 2488-2495, 10.1016/j.matdes.2009.11.043.
10. Y. Ruan, X. Qiu, W. Gong, D. Sun, Y. Li, Mechanical properties and microstructures of 6082-T6 joint welded by twin wire metal inert gas arc welding with the SiO<sub>2</sub> flux, *Mat and Des*, 35(2012), pp. 20-24, 10.1016/j.matdes.2011.09.002.
11. S. G. Parshin, Using ultrafine particles of activating fluxes for increasing the productivity of MIG/MAG welding of steels, *Weld Int*, 26(2012), pp. 800-804, 10.1080/09507116.2011.653165.
12. Z. Zhang, Q. Cao, Study on metal transfer behaviour in metal inert gas arc welding with activating flux for magnesium alloy, *Sci and Tech of Weld and Join*, 17(2012), pp. 550-555, 10.1179/1362171812Y.0000000046.
13. S.G. Parshin, Increasing the productivity of MIG welding aluminium alloys by adding ultrafine particles of activating fluxes, *Weld Int*, 27(2013), pp. 735-739, 10.1080/09507116.2012.753284.
14. H. Lin, J. Yan, Optimization of weld bead geometry in the activated GMA welding process via a grey-based Taguchi method, *J of Mech Sci and Tech*, 28(2014), pp. 3249-3254, 10.1007/s12206-014-0735-9.
15. T.M. Patel, K.R. Patel, Parametric Optimization of Gas Metal Arc Welding Process Using Activated Flux for SS 304 by Taguchi Method, *Int J of Adv Sci and Tech Res*, 4(2015), pp. 683-690.
16. O. Savytsky, The Influence of Electric Arc Activation on the Speed of Heating and the Structure of Metal in Welds, *Ther Sci*, 20(2016), pp. 239-246.
17. O.M. Savytsky, M.M. Savytsky, D. Bajic, Efficiency of the application of activating fluxes in shielded arc welding, *Tehn Vjes*, 24(2017), pp.975-980.
18. H. Lin, Applying gray fuzzy logic to decide the weight ratio of activating flux during activated MIG aluminum alloy butt-joint welding, *Int J of Adv Manf Tech*, 92(2017), pp. 471-479, 10.1007/s00170-017-0161-0.
19. B. Varbai, R. Kormos, K. Majlinger, Effects of Active Fluxes in Gas Metal Arc Welding, *Per Poly*, 61(2017), pp. 68-73, 10.3311/PPme.9756.
20. R.M. Saidov, Study of influence of physical and chemical properties of oxides fluxes on the weld formation during MIG welding of stainless steel, *Comp Nanotech*, 3(2017), 52-58.
21. P. Chaudhari, P. Patel, J. Patel, Evaluation of MIG welding process parameter using Activated Flux on SS316L by AHP-MOORA method, *Mat Today Proc*, 5(2018), pp. 5208-5220.
22. A. Kulkarni, K. Madavi, Effect of Oxygen Content Chemical on the Gas Metal Arc Welding, *Int J of Sci Res in Sci and Tech*, 4(2018), pp. 360-365, 10.3390/cryst12020176.

## Enhanced VGG16 Deep Learning Network for Classification of Deformation Rate from Microstructure Images

**Selim Özdem**

Hitit University- Alaca Avni Çelik Vocational School, 19600, Alaca-Corum, Turkey,  
selimozdem@gmail.com  
ORCID: 0000-0002-5633-9543

**İlhami Muharrem Orak**

Karabük University- Faculty of Engineering, Computer Engineering Department, 78050, Karabük,  
Turkey, imorak@karabuk.edu.tr  
ORCID: 0000-0002-7219-4209

*Cite this paper as: Özdem, S, Orak, İM. Enhanced VGG16 Deep Learning Network for Classification of Deformation Rate from Microstructure Images. Int. Conf. Advanced. Mater. Sci. & Eng. HiTech. and Device Appl. Oct. 27-29 2022, Ankara, Turkey*

**Abstract.** The promising outputs obtained in image recognition and classification studies have revealed the great potential of deep learning in microscopic analysis in materials science. Microstructures provide significant data about the features of the material they belong to. The phase structures visible in the material microstructure give clues about the deformation rate of the material, which the naked eye cannot notice. In this study, S235JR structural steel was deformed at different rates via a tensile test in the laboratory environment before metallographic processes. In the next step, a data set belonging to five classes and images of microstructure were obtained via an optical microscope. The deep learning model developed by preprocessing was determined on the data set containing 10000 images of S235JR structural steel, contributing to the literature. The novelty of the model created using VGG16 is to adjust the network architecture to fit the microstructure images. The dataset is trained to classify images through their microstructure and then to estimate the accuracy. As a result, the classification success was over 92%.

**Keywords:** Deep learning, VGG16, S235 JR structural steel, deformation rate  
© 2022 Published by ICMATSE

## Introduction

The life of a material depends on many factors, such as usage time, structure, components during production, temperature and pressure values of the environment in which it is used, and the load it is exposed to [1]. Therefore, there is a significant relationship between the deformation rate of the material and the material life, and even the damage caused by some deformations is irreversible [2, 3].

The steel used as a building material is a material that is frequently mentioned in the construction industry [4]. Structural steels are used in areas such as railways, bridges, breakwater structures, industrial buildings, shipbuilding, power poles, oil and offshore gas platforms, multi-purpose social facilities, commercial structures, and roofs that do not load the building [5, 6]. This study's preference for structural steel is its widespread use and the lack of data set at the microstructure level considering its deformation. It is inevitable for structural steel to have defects in its structure due to effects such as compression, stress, and wear [7]. Rollers used in rolling mills are used to shape iron and steel by applying loads of tons and are subject to wear over time [8]. The barrels of firearms are subject to strong wear because of pressure and temperature. By examining the microstructures of the materials used in these examples, the deformation rates can be deduced [9, 10]. The internal structure of a material can be understood by analyzing its microstructure. Microstructural classification is mostly done manually by experts with a subjective view resulting in different interpretations regarding personal differences. The microstructure studies in the literature have taken into account technical properties mostly over phase structures in the field of materials science such as strength, flexibility, weld structure, damaged area detection [6, 11-13].

With the development of artificial intelligence technologies, significant progress has been achieved in the recognition and classification of microstructure images. The success of the Support Vector Machine [14] classifier, one of the Machine Learning [15] algorithms, has an important role in recognizing the microstructure features and the morphological model [16, 17]. Machine learning algorithms require a feature extraction process through traditional methods [18]. Gola et al. [19] obtained the microstructure images of martensite, perlite, and bainite phase steel plates with LOM

and SEM instruments and performed a phase classification study using the Support Vector Machine technique. Moreover, these methods require carefully designed manual feature extractors that depend heavily on expert knowledge and limit their performance in actual production.

Recently, Deep Learning approaches, which is more advanced and more successful than machine learning techniques, have been applied in classification, segmentation, and analysis of microstructure images. Extracting meaningful information with the help of deep learning networks by processing the features of microstructure images of materials provides a significant contribution to the field [20]. While feature extraction from images is done manually in Machine Learning algorithms, it is a great advantage that it is done automatically by Deep Learning algorithms in high-level grades [21]. Microstructure classification and defect analysis are feasible using deep learning methods [22]. Warmuzek et al. [23] prepared a dataset consisting of microstructure images of multi-alloyed iron and aluminum casting materials. They tested this dataset using a new CNN-based DenseNet201, InceptionResNetV2, InceptionV3, VGG16, VGG19, and Xception deep learning architectures detecting Twigg, petal, polyhedron, sphere, dendrite, needle, and Chinese script phases. The highest success rate (94.3%) was achieved using DenseNet201 architecture. It was observed that the data set was not balanced, and there were changing amount of data between 256 and 356 in the classes. Azimi et al. [24] studied microstructural classification. In their study, they mentioned the success of deep learning methods in computerized vision applications and suggested Deep Learning methods for microstructural classification in some microstructured component samples of low-carbon steel. Pixel-based segmentation was performed using a Maximum Voting Scheme with a Fully Convolutional Neural Network. With the system they established, they achieved a success rate of 93.94%. Ren et al. [25] conducted a study on the surface defects of steels and developed the Fast R-CNN (Fast Regional Based Convolutional Neural Network) model. They achieved defect-detection with an accuracy of 98.32% at an average speed of 0.05s per image. They created a surface defect dataset consisting of 4655 images from 6 classes such as scrapes, scratches, wrinkles, burrs, inclusion (the material included from the outside) and nano-oxide layer.

Yingying et al. [26] detected defects on tunnel surfaces by developing a new Mask R-CNN method. In addition, they designed an algorithm at the end of the network to improve the accuracy focusing on the edge information of the network, and enabling the creation of feature maps of the image. These studies contribute to the field of materials science and do not provide information about the deformation rate.

Hosseini-Toudeshky et al. [27] applied tensile tests at different rates to DP600 dual-phase steel samples, prepared large and small deformation simulations from the microstructure images of the deformed samples, and compared them with Light Optical Microscopy (LOM) and Scanning Electron Microscopy (SEM) images using Finite Element method. This study is about the deformation rate, and current deep learning techniques have not been studied.

### Experimental procedure

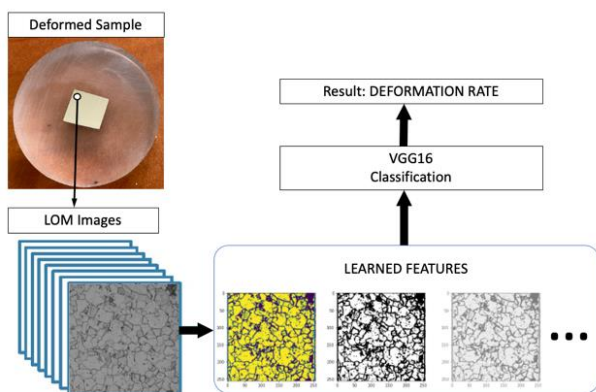


**Figure 1.** Classification of deformation rate via VGG16 deep learning network

In this study, S235 JR structural steel samples, whose technical specifications are given in Table 1 and shown in Figure 2, were obtained. The area to be deformed was determined to be 10 cm long. This area is numbered from 1 to 10 at equal intervals. These samples were deformed by tensile tests in the laboratory environment. The region with the highest deformation was measured with a caliper, and the region with the highest elongation (the region with the lowest cross-section) was determined. The region was cut and separated from the main sample (Figure 5).

**Table 1.** Technical properties of S235 JR construction steel

Material	Yield Strength (MPa)	Tensile Strength (MPa)	Elongation (%)
S235JR	235	340-470	25

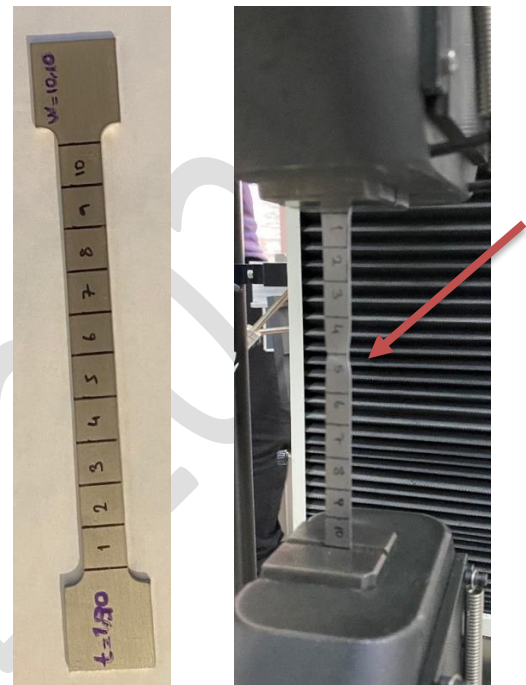


**Figure 2.** S235 JR Construction Steel sample prepared for tensile test

The samples were prepared according to the TS EN ISO 4136 standard for the tensile test, and then the tensile elongation diagrams were obtained by pulling at a speed of 1mm/min with the INSTON model tensile test instrument (100 kN in capacity). It is known that the total elongation rate of S235 JR structural steel is 25-26%, according to the catalog information. Accordingly, based on the length of the sample, tensile tests were performed at approximately 25% (7mm), 50% (14mm), and 75% (21mm) ratios. Raw and plucked samples were also included in the analysis. Thus, five classes were established. At the end of the test, the elongation rate at break was approximately 26-27%. This result is consistent with the data in the catalog of S235JR steel. The graphics on the Stress-Deformation Rate of the tests are given in Figure 3.

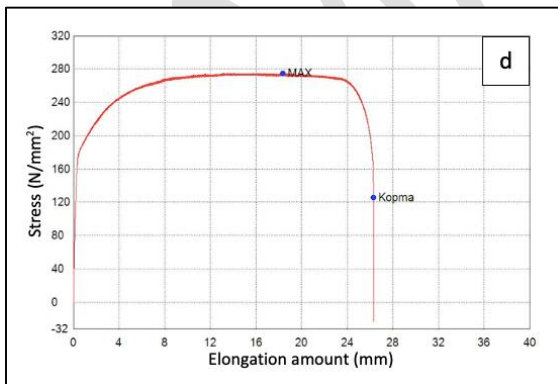
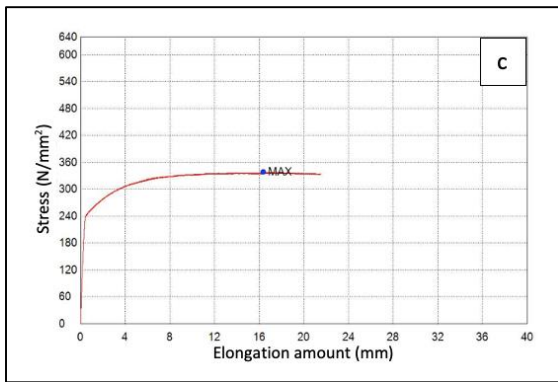
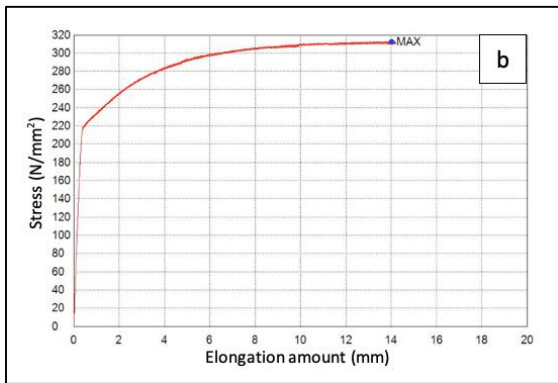
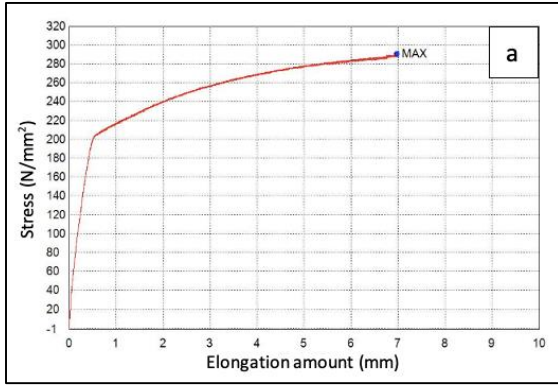


**Figure 3.** Tensile and shear test, a) Deformation Rate (7 mm); b) Deformation Rate (14 mm); c) Deformation Rate (21 mm); d) Deformation (26 mm- Fracture)

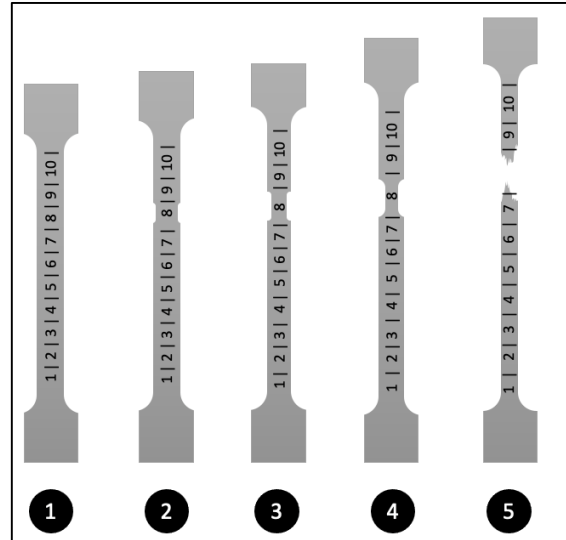


**Figure 4.** Formation of classes according to Deformation Rates 1: Raw sample, 2: 7mm drawn sample, 3: 14mm drawn sample, 4:21mm extruded sample, 5: Broken sample

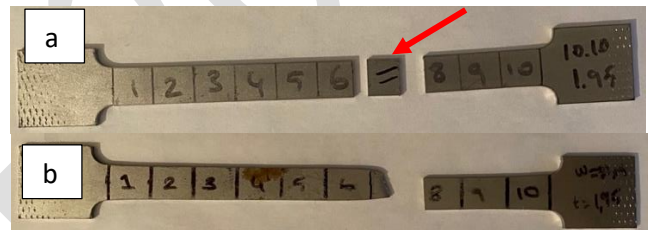


**Figure 4.** a) 7 mm drawn sample, b) After the shear test

In order to reach the microstructure images of the deformed samples, the classical metallographic stages (cutting, bagalizacion (Figure 6), coarse-fine sanding, polishing, 2% Nital etching) were applied with respect to rules in materials science. Microstructure images were obtained via the Nikon Eclipse LV150N LOM instrument shown in Figure 7.



**Figure 5.** Bagalizacion process

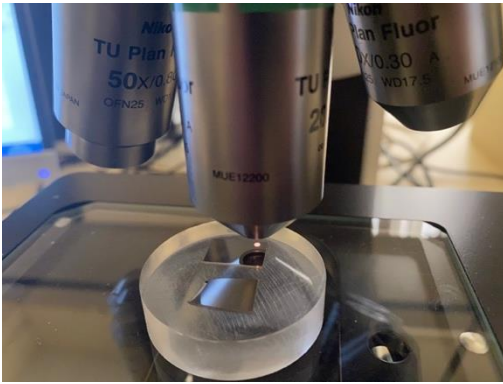


**Figure 6.** Microstructure image by LOM

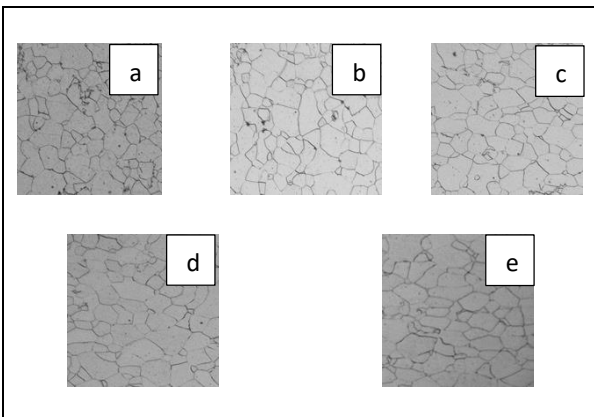


**Figure 8.** Data set categories; a) Raw sample with no deformation, b) 7mm drawn sample, c) 14mm drawn sample, d) 21mm drawn sample, e) Sample broken by tensile test

Microstructure images were classified into five categories, and two thousand images were obtained from each category with 256x256 pixel dimensions (Table 2). Contribution to the literature was provided with a total of ten thousand images.

**Table 2.** Categories and number of images of the original data set created

Category	Label	Image Size	Number of Images
Crude Sample	0		2000
Drawn Sample 7 mm	1	256x256 px	2000
Drawn Sample 14 mm	2		2000
Drawn Sample 21 mm	3		2000

Broken Sample	4	2000
---------------	---	------

**Total: 10000 images**

### Applied VGG16 Model

VGG16 is the most common and successful CNN model used in VGG-Net in image classification problems [28]. Transfer Learning is frequently used in classification problems in Convolutional Neural Network (CNN) models. Instead of training a neural network with random initial values, transfer learning and pre-trained weights are used [29]. In this study, the VGG16 model having classical convolutional neural network architectures was established that was previously trained on the ImageNet image set exploiting the transfer learning method and the features were obtained by using the pre-trained weights of the model.

Images (80% and 20% of the 10000) in the data set were used for training and testing, respectively. Images (8000 in number) were used for training the network. Test data were achieved using 2000 images. The VGG-16 network consists of 16 convolutional layers and has a small 3x3 receptive field. Moreover, it has a Max pooling layer of 2x2 and thus has a total of 5 such layers. Following the last Max pooling layer, there are three fully connected layers. In this study, the training speed of the network increased by 54% by reducing the output parameters with a decrease in the number of fully connected layers to 2. No significant difference in classification success was observed compared to the standard VGG16 model.

### Results and discussion

In the first stage of the study, data were classified into five categories. The classification success rate was found to be 92% (Figure 9). Here, the success of distinguishing images obtained from the broken sample (labeled as 4) and the sample elongated 21mm (labeled as 3) from each other was lower than the ones in other categories. Therefore, the classification process was repeated over four categories, excluding the broken sample category. The success rate was determined as 97%.

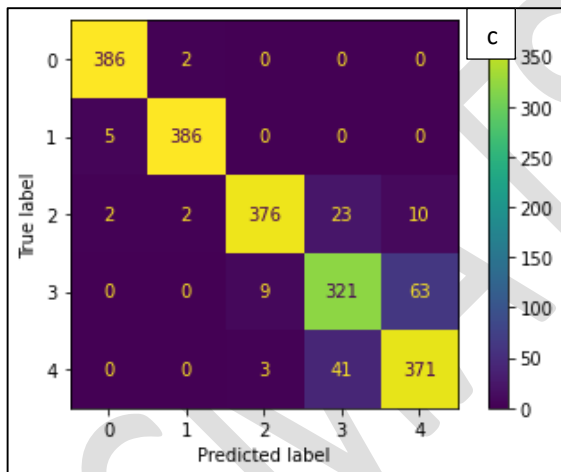
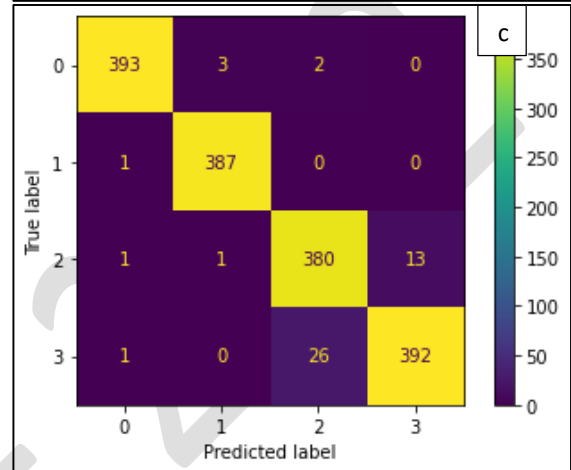
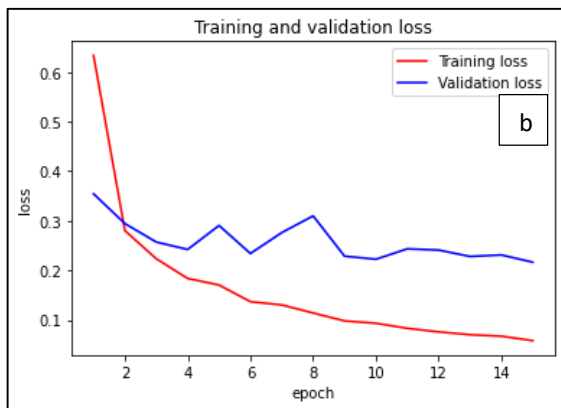
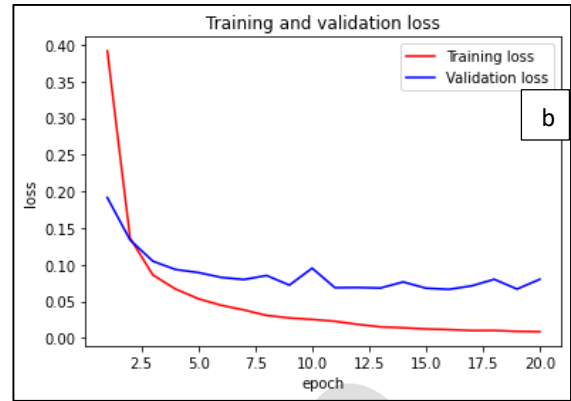
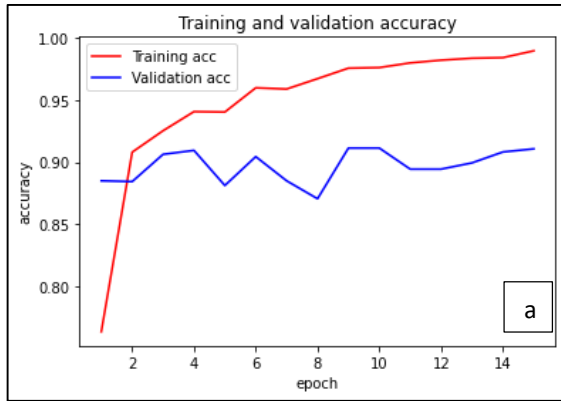


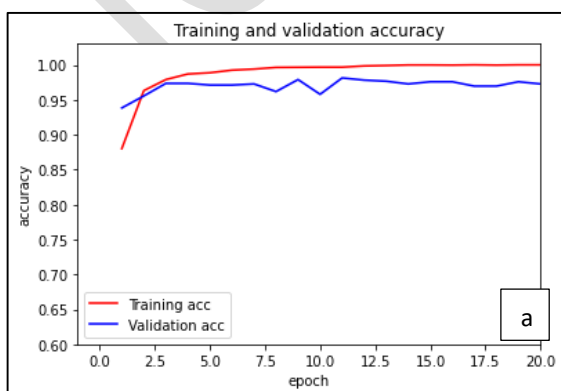
**Figure 9.** Classification by deformation rate for five categories; a) Training and validation accuracy, b) Training and validation loss, c) Confusion Matrix

**Figure 10.** Classification by deformation rate for four categories (Raw Sample, 7mm – 14mm – 21mm elongated sample); a) Training and validation accuracy graphic, b) Training and validation loss graphic, c) Confusion Matrix

### Conclusion

In this paper, automatic classification results of S235 JR structural steel, which has been deformed in the laboratory environment and divided into five categories with the VGG16 deep learning network, are published. Deformation rates were labeled, divided into five categories, and 10000 data sets were added to the literature. The training time was shortened by 54% in the data classification by adjusting the VGG16 model. It is thought that an important gap in metallurgical and materials engineering has been eliminated by achieving a success rate of 92% in the data classification process in 5 categories and a success rate of 97% in the classification of 4 categories.

In future studies, it is aimed to improve the network and increase the success rate. It has been concluded that the success rate in especially five categories should be increased. The data needs to be tested in different deep-learning networks. It is thought to carry out studies on which network the microstructure images are best classified.



The numerical calculations reported in this paper were fully/partially performed at TUBITAK

ULAKBIM, High Performance and Grid Computing Center (TRUBA resources)

## References

1. Dieter, G.E. and D.J. Bacon, *Mechanical metallurgy*. Vol. 3. 1976: McGraw-hill New York.
2. Kachanov, L., *Introduction to continuum damage mechanics*. Vol. 10. 1986: Springer Science & Business Media.
3. Chaboche, J.-L., *Continuum damage mechanics: Part II—Damage growth, crack initiation, and crack growth*. 1988.
4. Şık, A., *MIG/MAG kaynak yöntemi ile birleştirilen çelik malzemelerde ilave tel türleri ve koruyucu gaz karışımlarının eğmeli yorulma ömürlerine etkilerinin araştırılması*. Gazi Üniversitesi Mühendislik Mimarlık Fakültesi Dergisi, 2007. 22(4): p. 769-777.
5. Aydın, Ş., *YAPI ÇELİĞİNİN (St52-3) MIG/MAG KAYNAĞINDA GAZ KARIŞIMLARININ ÇEKME DAYANIMI ÖZELLİKLERİNE ETKİSİ*. Trakya Univ J Sci, 2006. 7(1): p. 9-15.
6. Huang, X., et al., *Surface damage detection for steel wire ropes using deep learning and computer vision techniques*. Measurement, 2020. 161: p. 107843.
7. Yu, H., Y. Guo, and X. Lai, *Rate-dependent behavior and constitutive model of DP600 steel at strain rate from 10<sup>-4</sup> to 10<sup>3</sup> s<sup>-1</sup>*. Materials & Design, 2009. 30(7): p. 2501-2505.
8. Bulzak, T., et al., *Internal crack formation in cross wedge rolling: Fundamentals and rolling methods*. Journal of Materials Processing Technology, 2022. 307: p. 117681.
9. Chaboche, J.-L., *Continuum damage mechanics: Part I—General concepts*. 1988.
10. Chaboche, J.-L., *Continuous damage mechanics—a tool to describe phenomena before crack initiation*. Nuclear Engineering and Design, 1981. 64(2): p. 233-247.
11. Iren, D., et al., *Aachen-Heerlen annotated steel microstructure dataset*. Scientific Data, 2021. 8(1): p. 140.
12. Cameron, B.C. and C.C. Tasan, *Towards physical insights on microstructural damage nucleation from data analytics*. Computational Materials Science, 2022. 202: p. 110627.
13. Shen, M., et al., *Multi defect detection and analysis of electron microscopy images with deep learning*. Computational Materials Science, 2021. 199: p. 110576.
14. Noble, W.S., *What is a support vector machine?* Nature Biotechnology, 2006. 24(12): p. 1565-1567.
15. Mitchell, T.M. and T.M. Mitchell, *Machine learning*. Vol. 1. 1997: McGraw-hill New York.
16. DeCost, B.L. and E.A. Holm, *A computer vision approach for automated analysis and classification of microstructural image data*. Computational Materials Science, 2015. 110: p. 126-133.
17. Iacoviello, F., et al., *Classification of ductile cast iron specimens based on image analysis and support vector machine*. Procedia Structural Integrity, 2017. 3: p. 283-290.
18. Sabnis, H., J. Angel Arul Jothi, and A.M. Deva Prasad. *Microstructure Image Classification of Metals Using Texture Features and Machine Learning*. 2022. Cham: Springer International Publishing.
19. Gola, J., et al., *Advanced microstructure classification by data mining methods*. Computational Materials Science, 2018. 148: p. 324-335.
20. Kondo, R., et al., *Microstructure recognition using convolutional neural networks for prediction of ionic conductivity in ceramics*. Acta Materialia, 2017. 141: p. 29-38.
21. LeCun, Y., Y. Bengio, and G. Hinton, *Deep learning*. nature, 2015. 521(7553): p. 436-444.
22. Tsopanidis, S., R.H. Moreno, and S. Osovski, *Toward quantitative fractography using convolutional neural networks*. Engineering Fracture Mechanics, 2020. 231: p. 106992.
23. Warmuzek, M., M. Żelawski, and T. Jałocha, *Application of the convolutional neural network for recognition of the metal alloys microstructure constituents based on their morphological characteristics*. Computational Materials Science, 2021. 199: p. 110722.
24. Azimi, S.M., et al., *Advanced steel microstructural classification by deep learning methods*. Scientific reports, 2018. 8(1): p. 2128.
25. Ren, Q., J. Geng, and J. Li. *Slighter Faster R-CNN for real-time detection of steel strip surface defects*. in *2018 Chinese Automation Congress (CAC)*. 2018. IEEE.
26. Xu, Y., et al., *Automatic defect detection and segmentation of tunnel surface using modified Mask R-CNN*. Measurement, 2021. 178: p. 109316.
27. Hosseini-Toudeshky, H., et al., *Microstructural deformation pattern and mechanical behavior analyses of DP600 dual phase steel*. Materials Science and Engineering: A, 2014. 600: p. 108-121.
28. Simonyan, K. and A. Zisserman, *Very deep convolutional networks for large-scale image recognition*. arXiv preprint arXiv:1409.1556, 2014.
29. Torrey, L. and J. Shavlik, *Transfer learning*, in *Handbook of research on machine learning applications and trends: algorithms, methods, and techniques*. 2010, IGI global. p. 242-264.

## Thermodynamic Properties of Half –Heusler Semiconductor RhTiSb Compound

**İlknur Kars Durukan**

Gazi University, Ankara, Turkey, [ilknurdurukan@gazi.edu.tr](mailto:ilknurdurukan@gazi.edu.tr)  
ORCID: 0000-0001-5697-0530

**Yasemin Oztekin Ciftci**

Gazi University- Physics Department, 06500, Ankara, Turkey, [yasemin@gazi.edu.tr](mailto:yasemin@gazi.edu.tr)  
ORCID: 0000-0001-1796-0270

*Cite this paper as: Durukan Kars İlknur. Oztekin Ciftci Yasemin Thermodynamic Properties of Half –Heusler Semiconductor RhTiSb Compound, .Int. Conf. Advanced. Mater. Sci. & Eng. HiTech.and Device Appl.Oct. 27-29 2022,Ankara, Turkey*

**Abstract.** A appropriate semiconductor provide a significant advantage to the technology and industry because to the fact that better, available, and tunable materials is important. Between the various materials in use as semiconductor devices, the half-Heusler alloys have proved to be promising contribution on the possibilities of tuning the various properties to meet the desired demand. These kind of compounds have extraordinary electronic, elastic, optical, thermodynamical and thermoelectric properties. Under the extreme conditions of temperature and pressure the fundamental properties of the various properties of materials may change as compared to the ambient condition. Therefore, the knowledge of thermodynamical properties under the variation of temperature and pressure acts as an extremely helpful tool for their technological applications in extreme conditions. The temperature- and pressure- dependent thermodynamical functions such as specific heat at constant volume, entropy, volume, thermal expansion coefficient, Debye temperature, gruniesen parameters have been investigated using quasi-harmonic Debye approximation The thermodynamic parameters are determined in the pressure range from 0 to 20 GPa and temperature range from 0 to 1000 K.

**Keywords:** DFT, RhTiSb, thermodynamic properties  
© 2022 Published by ICMATSE

### Introduction

Population growth all over the world has brought along the development of industry and the ever-increasing need for energy. The increase in energy demand and the decrease in fossil fuels as a result of excessive use led the scientific world to alternative energy sources. In addition, the waste of energy in the form of unusable heat has brought energy savings to the fore. In addition to all these, greenhouse gases are formed by the use of fossil fuels and these gases seriously increase air pollution. Generating electricity by utilizing waste heat has made thermoelectric materials popular. Most of the work has been done on thermoelectric materials, especially lanthanide and transition metal-containing compounds[1–4]. In these studies, Heusler compounds with thermoelectric properties have received great attention.

The first study with Heusler compounds was made by Friedrich Heusler in 1903 with the compound  $\text{Cu}_2\text{MnSn}$ [5]. The crystal structures of Heusler compounds are studied under two headings. The

chemical formulations of these structures, named as Full Heusler and Half Heusler, are  $\text{X}_2\text{YZ}$  and  $\text{XYZ}$ , respectively. Compounds attracted great attention after the discovery of half-heusler compounds, where the components are not magnetic but the compound is magnetic[6]. Many semi-heusler compounds with a valence electron number (VEC) of 18 in the unit cell have a band gap and show promising thermoelectric properties with high thermopower and high electrical conductivity.

Thermodynamic properties are defined as characteristic features of a system capable of specifying the system's state . Half-Heuslers (HH) alloys are ternary compounds and have cubic  $\text{MgAgAs}$  structure. These kind of compounds have extraordinary electronic, elastic, optical, thermodynamical and thermoelectric properties[7,8]

In this study, the effect of temperature and pressure changes on the thermodynamic properties of RhTiSb semi-heusler compound was investigated.

### Calculation Methods

In this computational work, to investigate the thermodynamic properties of RhTiSb, as a first step, a set of total energy calculation versus primitive cell volume (E-V) was carried out, in the static approximation. The results are then fitted with a numerical EOS in order to determine its structural parameters at  $P = 0$  and  $T = 0$ , and to derive the macroscopic properties as a function of pressure and temperatures from standard thermodynamic relations based on quasi-harmonic Debye Model [9–12] using GIBBS program [13]. All calculations based on geometric optimization were calculated using the DFT method [14–16] using the Vienna ab initio simulation package program (VASP) [15, 17, 18].

### Results and Discussion

The crystal structure of RhTiSb intermetallic compound is cubic, with the space group F-43m (No.216). The unit cell of RhTiSb is shown in Fig. 1. There are three atoms in the unit cell where the Wyckoff atomic positions are occupied by 4b site (0.5, 0.5, 0.5), 4c site (0.25, 0.25, 0.25), and 4a site (0.0, 0.0, 0.0) for Rh, Sb, and Ti, respectively [47].

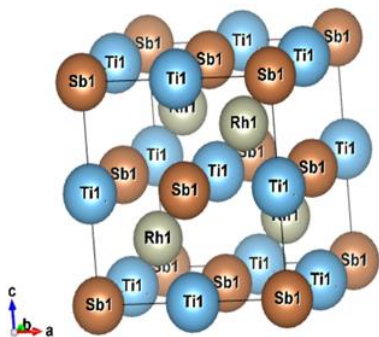


**Figure. 1.** The unit cell of RhTiSb

The total energy as a function of volumes for RhTiSb is plotted in Fig. 2.

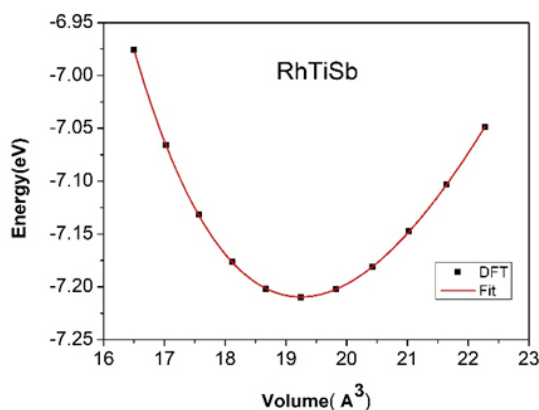


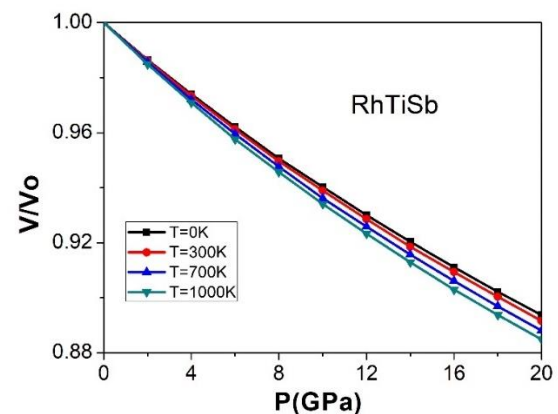
**Figure.2.** Energy-volume curves of the RhTiSb

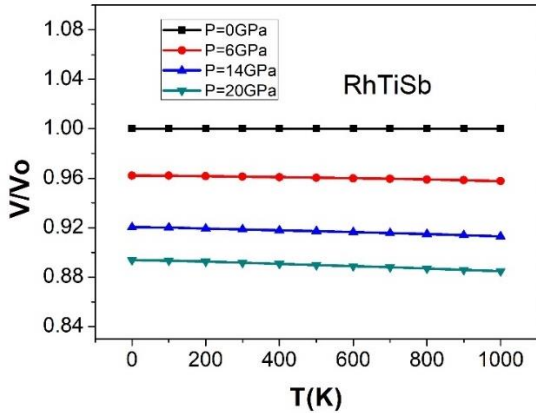
The calculated total energies are adapted to the Birch equation of states [35] to determine equation of state (EoS) parameters such as equilibrium lattice constant ( $a_0$ ), mass modulus (B), pressure derivative (B'), and volume. The calculated data are presented in Table 1 and compared with the literature.

**Table .1** Structural parameters of the RhTiSb

RhTiSb	a(Å)	B(GPa)	B'(GPa)
This study	6.14	141.46	4.68
TiRhSb	6.14	142.43	4.15

The thermodynamic properties of the material under different temperatures and pressures are very valuable for industrial applications. The pressure range in which the thermodynamic properties are determined is 0-20 GPa, and the temperature range is 0-1000K. The variation between normalized volume and pressure at different temperatures is presented in Fig. 3a, and the variation between volume and temperature at different pressures is presented in Fig. 3b. For a given pressure, the volume was determined to be nearly constant with rising temperature. On the other hand, for a given temperature, the cell combining the volumes decreases with increasing pressure. This result is expected, because generally the material expands at higher temperature. Also, the volume change with temperature is stronger at low pressure than at high pressure. With an increase in pressure, the relative volume simply decreases for all different series of temperatures as the material is compressed at higher pressure.

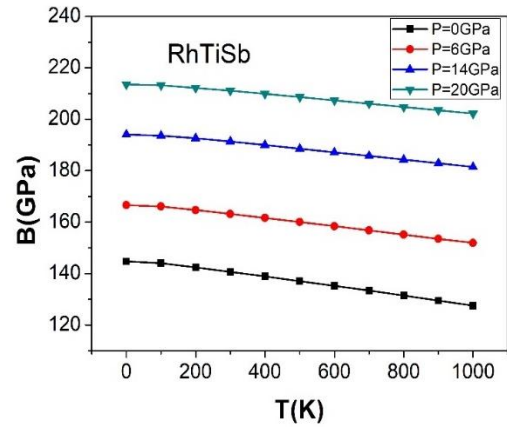
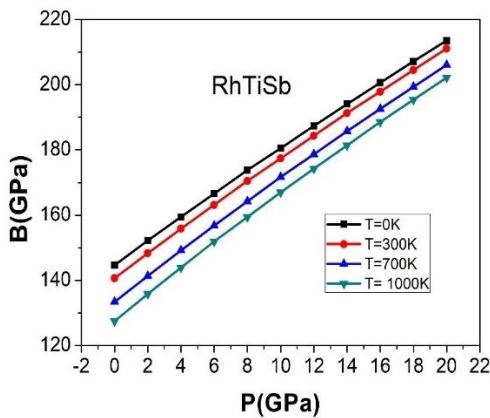




**Figure.3** Normalized volume versus a) temperature at different pressure b) pressure at different temperatures for RhTiSb compound

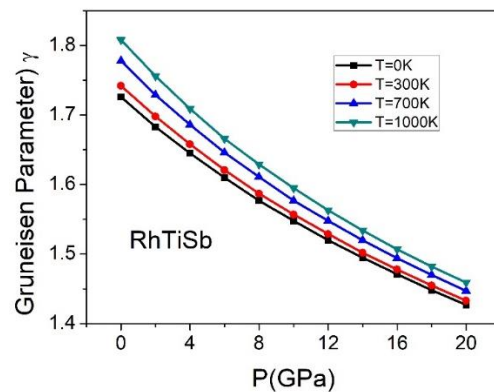
In order to obtain an indication of the variation of the hardness of the investigated RhTiSb Half-heusler compounds with temperature and pressure, the variation of the mass modulus of the compound with temperature and pressure is presented in Fig.4. As seen in Fig.4a, between 0 K and 100 K, there is a negligible dependence of the bulk modulus on temperature, but above 100 K, there is a linear decrease of the bulk modulus with temperature. In addition, at room temperature the bulk modulus reaches 144.69 GPa at zero pressure for the RhTiSb compound.

In Fig. 4b, the Bulk modulus values increased with the increase in pressure at constant temperature. It can be noticed that the volume modulus is an important parameter to define the resistance to volume change under compression.



**Figure.4.** Bulk modulus versus a) temperature at different pressures b) pressure at different temperatures for RhTiSb compound

Gruneisen parameter ( $\gamma$ ) is a crucial parameter and a dimensionless quantity to describe the thermomechanical properties and anharmonic correlation in vibrating lattices. The variation of the  $\gamma$  with the temperature at different sets of pressures is depicted in Fig. 5(a). It is observed that  $\gamma$  increases slowly with an increase in temperature at different pressures, while  $\gamma$  decreases rapidly as pressure increases at different temperature values. However, the influence of pressure is more significant than that of the temperature. The value of  $\gamma$  of RhTiSb compound is 1.726 at zero pressure and temperature, but this value reduces to 1.427 at zero temperature and 20 GPa, resulting in decreasing anharmonicity in the lattice. A high value of  $\gamma$  indicates high anharmonicity in the compound, which results in poor lattice thermal conductivity. At room temperature, the value of  $\gamma$  is 1.742 at zero pressure.



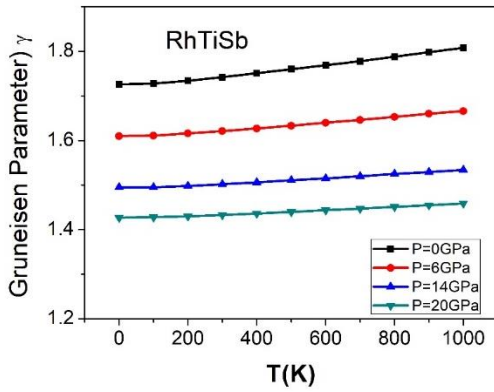


**Figure. 5.** Gruneisen parameter versus a) temperature at different pressures b) pressure at different temperatures for RhTiSb compound

Debye temperature ( $\theta_D$ ) is also one of the thermodynamic parameters that characterize the strength of the covalent bond and is related to elasticity and heat capacity of the material[19]. The evolution of Debye temperature as a function of temperature (K) at different pressures and pressure at different temperature are presented in Fig. 6.  $\theta_D$  exhibits a negligible change in the temperature domain 0 – 100 K and, thereafter, decreases with increasing temperature for all sets of pressure. Clearly,  $\theta_D$  decreases very slowly at higher pressure. We observed that,  $\theta_D$  exhibits a quasi-linear rising variance with pressure at a constant temperature. Furthermore, it is also clear that the effect of pressure on  $\theta_D$  is more important than the temperature. The computed value of  $\theta_D$  is found to be 331.34 K at 0 K and 0 GPa.

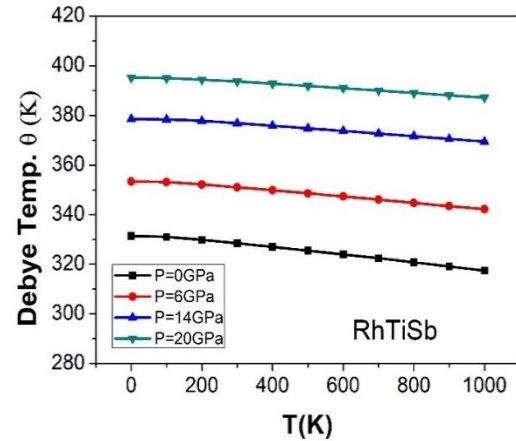
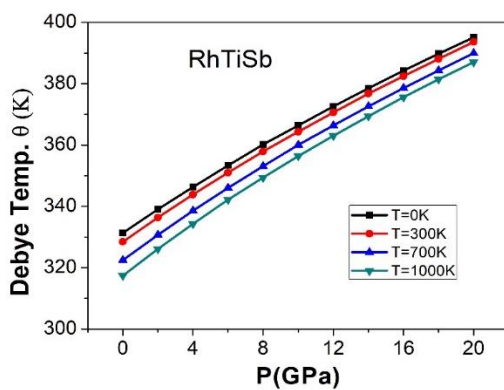


**Figure. 6.** Debye temperature versus a) temperature at different pressures b) pressure at different temperatures for RhTiSb compound

Specific heat at constant volume ( $C_V$ ), which is another thermodynamic property related to the lattice vibration, internal energy, phase transition, and many other physical variables of the materials. The variation of the  $C_V$  as a function of temperature at different pressures is displayed in Fig. 7. For a constant pressure, it is noticed that at 0 K, the  $C_V$  is zero which means the absence of lattice vibrations. Initially,  $C_V$  increases linearly with the rise in temperature following the Debye  $T^3$ [16] law, thereafter, reveals constant variation with temperature and converges to the Dulong and Petit's limit ( $\sim 75K$ ), which is the behavior of all solid materials. At low pressure, the value of  $C_V$  is larger than high pressure. At room temperature and 0GPa  $C_V$  is obtained as 70.53 J/mol.K.

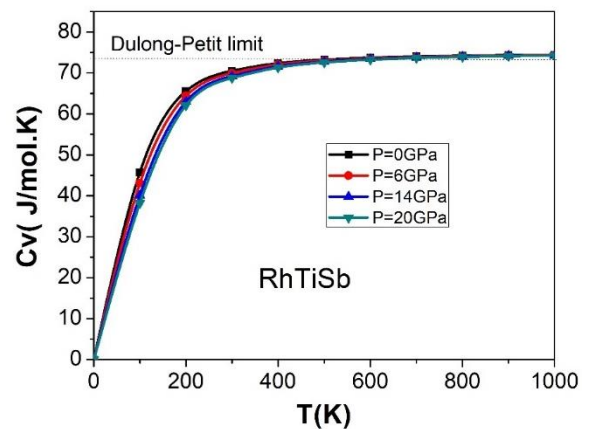


**Figure. 7.** Specific heat coefficient versus temperature at different for RhTiSb compound

### Conclusion

Thermodynamic properties of RhTiSb Semi-heusler compound in the pressure range of 0-20 GPa and temperature of 0-1000 K were investigated with the

GIBBS code. The bulk modulus at room temperature for the RhTiSb compound was determined to be 144.69 GPa at zero pressure. The bulk modulus is important in determining the compressibility of the material. The anharmonic decreases with the

increase in pressure. This indicates an increase in thermal conductivity. The Debye temperature was found to be 331.34 K at zero pressure and zero temperature.

## References

1. F. Benzoudji, O. M. Abid, T. Seddik, A. Yakoubi, R. Khenata, and H. Meradji, Insight into the structural , elastic , electronic , thermoelectric , thermodynamic and optical properties of MRhSb ( M = Ti , Zr , Hf ) half-Heuslers from ab initio calculations, vol. 59, no. April, pp. 434–448, 2019, doi: 10.1016/j.cjph.2019.04.009.
2. K. A. Gschneidner *et al.*, Influence of the electronic structure on the ductile behavior of B2 CsCl-type AB intermetallics, *Acta Materialia*, vol. 57, no. 19, pp. 5876–5881, 2009, doi: 10.1016/j.actamat.2009.08.012.
3. T. Kanemitsu, H. Muta, K. Kurosaki, and S. Yamanaka, Transport properties of niobium doped MNiSn (M-Ti, zr), *International Conference on Thermoelectrics, ICT, Proceedings*, vol. 59, no. 13, pp. 531–534, 2006, doi: 10.1109/ICT.2006.331350.
4. P. Larson, S. D. Mahanti, S. Sportouch, and M. G. Kanatzidis, Electronic structure of rare-earth nickel pnictides: Narrow-gap thermoelectric materials, *Physical Review B - Condensed Matter and Materials Physics*, vol. 59, no. 24, pp. 15660–15668, 1999, doi: 10.1103/physrevb.59.15660.
5. F. Shi, M. S. Si, J. Xie, K. Mi, C. Xiao, and Q. Luo, Hybrid density functional study of bandgaps for 27 new proposed half-Heusler semiconductors, *Journal of Applied Physics*, vol. 122, no. 21, 2017, doi: 10.1063/1.4998145.
6. I. Kars Durukan and Y. Oztekin Ciftci, First-principles calculations of vibrational and optical properties of half-Heusler NaScSi, *Indian Journal of Physics*, 2020, doi: 10.1007/s12648-020-01887-0.
7. I. Kars Durukan and Y. Öztekin Çiftci, The Effect of Pressure on Elastic Anisotropy, Vibration and Optical Properties of a AgScSi Compound, *Journal of Electronic Materials*, vol. 48, no. 6, pp. 4050–4056, 2019, doi: 10.1007/s11664-019-07167-w.
8. D. R. Jaishi, S. Bati, N. Sharma, B. Karki, B. P. Belbase, and M. P. Ghimire, Rhodium based half-Heusler alloys as possible optoelectronic and thermoelectric materials, pp. 1–10, 2021.
9. X. Zeng, R. Peng, Y. Yu, Z. Hu, Y. Wen, and L. Song, Pressure effect on elastic constants and related properties of Ti3Al intermetallic compound: A first-principles study, *Materials*, vol. 11, no. 10, 2018, doi: 10.3390/ma11102015.
10. F. Peng, H. Z. Fu, and X. D. Yang, Transition phase and thermodynamic properties of PtC from first-principles calculations, *Solid State Communications*, vol. 145, no. 3, pp. 91–94, 2008, doi: 10.1016/j.ssc.2007.10.030.
11. F. Peng, H. Fu, and X. Yang, Ab initio study of phase transition and thermodynamic properties of PtN, *Physica B: Condensed Matter*, vol. 403, no. 17, pp. 2851–2855, 2008, doi: 10.1016/j.physb.2008.02.022.
12. F. Peng, H. Z. Fu, and X. L. Cheng, First-principles calculations of thermodynamic properties of TiB2 at high pressure, *Physica B: Condensed Matter*, vol. 400, no. 1–2, pp. 83–87, 2007, doi: 10.1016/j.physb.2007.06.020.
13. M. A. Blanco, E. Francisco, and V. Luaña, GIBBS: Isothermal-isobaric thermodynamics of solids from energy curves using a quasi-harmonic Debye model, *Computer Physics Communications*, vol. 158, no. 1, pp. 57–72, 2004, doi: 10.1016/j.comphy.2003.12.001.
14. N. Mehmood, R. Ahmad, and G. Murtaza, Ab Initio Investigations of Structural, Elastic, Mechanical, Electronic, Magnetic, and Optical Properties of Half-Heusler Compounds RhCrZ (Z = Si, Ge), *Journal of Superconductivity and Novel Magnetism*, vol. 30, no. 9, pp. 2481–2488, 2017, doi: 10.1007/s10948-017-4051-3.
15. G. Kresse and J. Hafner, Ab initio molecular dynamics for liquid metals, *Physical Review B*, vol. 47, no. 1, pp. 558–561, 1993, doi: 10.1103/PhysRevB.47.558.
16. I. K. Durukan and Y. O. Ciftci, Ab-initio study on physical properties of intermetallic LiPb compound, *Journal of Computational Science*, vol. 54, no. May, p. 101428, 2021, doi: 10.1016/j.jocs.2021.101428.
17. G. Kresse and J. Hafner, Ab initio molecular-dynamics simulation of the liquid-metalamorphous- semiconductor transition in germanium, *Physical Review B*, vol. 49, no. 20, pp. 14251–14269, 1994, doi: 10.1103/PhysRevB.49.14251.
18. G. Kresse and J. Furthmüller, Efficiency of ab-initio total energy calculations for metals and semiconductors using a plane-wave basis set, *Computational Materials Science*, vol. 6, no. 1, pp. 15–50, 1996, doi: 10.1016/0927-0256(96)00008-0.
19. O. Sahnoun, H. Bouhani-Benziane, M. Sahnoun, M. Driz, and C. Daul, Ab initio study of structural, electronic and thermodynamic properties of tungstate double perovskites Ba2MWO6 (M = Mg, Ni, Zn), *Computational Materials Science*, vol. 77, no. April 2018, pp. 316–321, 2013, doi: 10.1016/j.commatsci.2013.04.053.

## Laser Induced Reverse Transfer

**F. Rey-García**

UA de Microóptica y Óptica GRIN, Facultade de Óptica e Optometría, Universidad de Santiago de Compostela, c/Campus Sur s/n, 15782 Santiago de Compostela, Spain  
ORCID: 0000-0002-3083-9355

**C. Bao**

UA de Microóptica y Óptica GRIN, Facultade de Óptica e Optometría, Universidad de Santiago de Compostela, c/Campus Sur s/n, 15782 Santiago de Compostela, Spain  
ORCID: 0000-0002-0602-800X

**L. A. Angurel**

Instituto de Nanociencia y Materiales de Aragón, INMA (CSIC-Universidad de Zaragoza), María de Luna, 3,  
50018 Zaragoza, Spain, [angurel@unizar.es](mailto:angurel@unizar.es)  
ORCID: 0000-0001-5685-2366

**G.F. de la Fuente**

Instituto de Nanociencia y Materiales de Aragón, INMA (CSIC-Universidad de Zaragoza), María de Luna, 3,  
50018 Zaragoza, Spain, [german.delafuente.leis@csic.es](mailto:german.delafuente.leis@csic.es)  
ORCID: 0000-0002-0500-1745

*Cite this paper as: F. Rey-García, C. Bao, L. A. Angurel, G. F. de la Fuente Laser Induced Reverse Transfer. Int. Conf. Advanced. Mater. Sci. & Eng. HiTech.and Device Appl.Oct. 27-29 2022,Ankara, Turkey*

**Abstract:** Laser irradiation of transparent substrates in front of an absorbing target results in ablation of the target material and the consequent coating on the back of such substrate [1-4]. The use of pulsed near-IR lasers is reviewed in this talk, with particular attention to coatings or surface modification produced on glass substrates. This method enables the fabrication of thin coatings on glass at low cost and without the need for vacuum or chemicals. It is thus attractive from the environmental and efficiency points of view.

This relatively new fabrication method will be briefly presented and overviewed, and a number of examples analyzed in relation to the coatings obtained and types of lasers used.

**Keywords:** Laser Ablation, Surface Modification.

© 2022 Published by ICMATSE

[1] R. Rangel-Rojo et al., Opt. Express. **14** (2006) 8765-8771.

[2] A. Castelo et al., Optics Commun. **273** (2007) 193-199.

[3] F. Rey-García et al., Appl. Surf. Sci. **307** (2014) 645-653.

[4] R. Molina et al., Appl. Surf. Sci. **556** (2021) 149673.

**Acknowledgements:** Work funded by EU project SPRINT (H2020-FETOPEN 801464), the Spanish MCIN/AEI/10.13039/501100011033 (project PID2020-113034RB-I00) and by Gobierno de Aragón (research group T54\_20R).

## In Situ SEM Scratch Testing to Evaluate Wear Mechanisms of TiC-Ti6Al4V Nanocomposites Manufactured by Selective Laser Melting

**Beverley J Inkson**

*The University of Sheffield, Department of Materials Science and Engineering, S1 3JD, Sheffield,  
United Kingdom, [beverley.inkson@sheffield.ac.uk](mailto:beverley.inkson@sheffield.ac.uk)  
ORCID: 0000-0002-2631-9090*

**İdris Tuğrul Gülenç**

*The University of Sheffield, Department of Materials Science and Engineering, S1 3JD, Sheffield,  
United Kingdom, [i.t.gulenc@sheffield.ac.uk](mailto:i.t.gulenc@sheffield.ac.uk)  
ORCID: 0000-0001-5163-9478*

**Shaumik Lenka**

*The University of Sheffield, Department of Materials Science and Engineering, S1 3JD, Sheffield,  
United Kingdom, [shaumiklenka17@gmail.com](mailto:shaumiklenka17@gmail.com)  
ORCID: 0000-0003-2753-120X*

*Cite this paper as: Inkson, BJ, Gülenç, İT, Lenka, S, In Situ SEM Scratch Testing to Evaluate Wear Mechanisms of TiC-Ti6Al4V Nanocomposites Manufactured by Selective Laser Melting. Int. Conf. Advanced Mater. Sci. & Eng. HiTech. and Device Appl. Oct. 27-29 2022, Ankara, Turkey*

**Abstract.** Ball-on-disk and reciprocating wear tests are common methodologies to evaluate the friction and wear properties of metallic alloys and composites. However, it can be a challenge to fully understand time-dependent wear mechanisms by post-mortem examination of wear tracks, particularly at the micro-nano scale. Here, scratch tests are carried out in situ in a scanning electron microscope (SEM) to enable real-time imaging of microstructural evolution during scratch tests. In this talk, in situ SEM tribology is applied to evaluate the wear mechanism of novel Ti6Al4V-TiC nanocomposites. In situ nano-TiC reinforced Ti6Al4V matrix composites and plain Ti6Al4V alloys were manufactured using selective laser melting (SLM). The tribological properties of these alloys were quantified using dry reciprocating wear tests and in situ SEM scratch tests. Post mortem optical profilometry of the wear tracks showed that despite their higher hardness, in situ TiC reinforced composites had a higher wear rate compared to the parent Ti6Al4V matrix. In situ SEM scratch tests revealed that nano-sized TiC particles dissociate from the Ti6Al4V matrix under frictional forces and cause a higher wear rate despite their positive contribution to improved part hardness.

**Keywords:** (Calibri, 10 punto, 3-up to 5 should be given)

© 2022 Published by ICMATSE

## In situ X-ray Microscopy tensile testing of Ti6Al4V Parts Manufactured by Selective Laser Melting

***İdris Tuğrul Gülenç***

*The University of Sheffield, Department of Materials Science and Engineering, S1 3JD, Sheffield,  
United Kingdom, i.t.gulenc@sheffield.ac.uk  
ORCID: 0000-0001-5163-9478*

***Hongbo Shi***

*The University of Sheffield, Department of Materials Science and Engineering, S1 3JD, Sheffield,  
United Kingdom, hshi24@sheffield.ac.uk  
ORCID: 0000-0002-0276-3154*

***Ria Mitchell***

*The University of Sheffield, Department of Materials Science and Engineering, S1 3JD, Sheffield,  
United Kingdom, r.mitchell@sheffield.ac.uk  
ORCID: 0000-0002-6328-3998*

***Beverley J Inkson***

*The University of Sheffield, Department of Materials Science and Engineering, S1 3JD, Sheffield,  
United Kingdom, beverley.inkson@sheffield.ac.uk  
ORCID: 0000-0002-2631-9090*

*Cite this paper as: Gülenç, İT, Shi, H, Mitchell, R, Inkson, BJ. In situ X-ray Microscopy tensile testing of Ti6Al4V Parts Manufactured by Selective Laser Melting. Int. Conf. Advanced. Mater. Sci. & Eng. HiTech. and Device Appl. Oct. 27-29 2022, Ankara, Turkey*

**Abstract** Additive Manufacturing (AM) can offer advantages over conventional manufacturing methods such as complex geometries and unique microstructures. However, the porosity of AM parts can deteriorate their mechanical properties and limit their applications. To evaluate the effect of internal pores on mechanical properties, here we apply in situ tensile loading of AM parts inside an X-ray microscope (XRM). In situ XRM mechanical testing enables 3D quantification of internal pores under increasing load, including their shape, 3D distribution and movement under compressive loading.

This talk will discuss the opportunities, capabilities and limitations of in situ XRM microscopy to evaluate the behaviour of porosity within additively manufactured Ti6Al4V components under load. Ti6Al4V parts were manufactured by selective laser melting (SLM) using a high energy density to generate keyhole pores within dog bone shape test pieces specific to the in situ XRM mechanical test rig. Samples were imaged using XRM under increasing tensile load conditions. The changes in pore morphology, position, movement and combination of the pores within the sample, has been evaluated. While the load stayed within the elastic zone, no observable change of pores was detected. However plastic deformation of the Ti6Al4V part changed porosity distribution and shape, with merging and deformation of small pores occurring inhomogeneously throughout the 3D volume.

**Keywords:** (Calibri, 10 punto, 3-up to 5 should be given)

© 2022 Published by ICMATSE

## **A review of the microstructural evolution of the parts which produced with wire arc additive manufacturing technique**

**Adem KAYADELEN**

*Gazi University, Advanced Technologies Department, 06500, Ankara, Turkiye, adem.kayadelen@gazi.edu.tr,  
ORCID: 0000-0002-4982-7215*

**Oguzhan YILMAZ**

*Advanced Manufacturing Technologies Research Group (AMTRG), Faculty of Engineering, Gazi University, Celal Bayar Boulevard, 06570, Maltepe, Ankara, Turkiye, Gazi University Welding and Joining Technologies Research and Application Center 06500, Ankara Turkiye  
oguzhanyilmaz@gazi.edu.tr  
ORCID: 0000-0002-2641-2324*

**Hakan ATES**

*Gazi University, Department of Metallurgical and Materials Engineering, 06500, Ankara, Turkiye Gazi University Welding and Joining Technologies Research and Application Center 06500, Ankara Turkiye  
hates@gazi.edu.tr, ORCID: 0000-0002-5132-4107*

*Cite this paper as: Kayadelen A., Yilmaz, O. Ates H., A review of the microstructural evolution of the parts which produced with wire arc additive manufacturing technique, Int. Conf. Advanced. Mater. Sci. & Eng. HiTech. and. Device. Appl. Pct. 27-29 2022, Ankara, Turkey*

**Abstract.** Wire arc additive manufacturing, which is a sub-branch of metal additive manufacturing, is a production method in which wire is used as raw material and arc energy is used as energy source. The deposition rate in WAAM production technique is higher than other metal additive manufacturing methods. In addition, large parts can be produced in WAAM compared to other metal AM methods. Due to these positive aspects, WAAM has been the focus of attention of researchers. Researchers are working on the mechanical properties of the produced parts as well as the development of the production technique. In this study, -in scope of WAAM- the materials that produced with various welding types and wires were examined. The studies conducted in the review focused on the microstructure formations that directly affect the mechanical properties. In this context, what kinds of microstructures are formed in various parameters (especially at different heat inputs) have been compiled. The properties of each material group were evaluated within itself. Thus, the effect and contribution of the changes in the parameters used in production in the same material group on the microstructure were reviewed by literatures.

**Keywords:** wire, arc, additive, microstructure

© 2022 Published by ICMATSE

**1. Introduction.** Additive Manufacturing is defined in the ASTM F2792 standard as, "The process of joining materials to make objects from 3D model data, usually layer-upon-layer, as opposed to subtractive manufacturing methodologies".[1] Wire Arc Additive Manufacturing is the sub-branch of AM.[2] Parts can be produced in WAAM using MIG, MAG and PAW welding methods and different welding wires.[3] Additionally Cold Metal

Transfer (CMT) is also used in WAAM.[4] WAAM is preferred due to low instrument price and high deposition rates according to other AM methods. But the parts that produced with WAAM has disadvantages like surface roughness. The usage of WAAM has been proved on steels[7], aluminum[29], titanium[21]. Beside mechanical properties of parts which produced with WAAM, improving of the production parameters are

examined by Researchers. These examinations still ongoing.[5] In WAAM, there are many challenges like, especially, heat accumulation and the intricate thermal conditions. Because of microstructure get effected to the heat

**2. Metals and welding methods used in WAAM**  
Weldability is the keyword for the WAAM. For this reason, which metal has the welding ability, that metal can be used in WAAM. [15] In WAAM welding wires are deposited layer by layer. Additionally different arc welding types

accumulation and cooling rates, heating and cooling conditions directly affect mechanical properties.[6] So microstructural analysis are vital importance in the scope of the WAAM.

convenient for WAAM.[2] GTAW, GMAW and PAW are the most frequently preferred methods. [4] WAAM consist of a robot, welding equipment as shown in (Fig. 1), rotating table and robo-controller.[26]

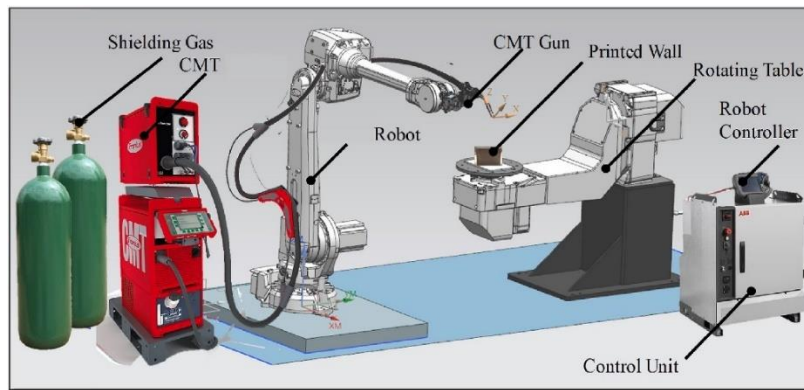


Figure 1. General WAAM presentation (WAAM-CMT) (26)

**2.1. Steel-base**

Xu et al. studied on maraging steel that produced with WAAM-PAW. MARVAL 18S of diameter 1,2 mm. wire used. One of the two samples prepared for microstructural examination was set as produced and the other was set as heat treated. The heat treatment applied as recommend ASM metal handbook grade 250 maraging steels. As-

produced microstructures from samples taken by transverse cross-sectioned are shown in Fig 2. According to the Xu et al. as-produced parts have non-uniform structure and heat treated parts have uniform microstructure. Thus, the mechanical properties (especially hardness) does not uniform at as-deposited part. [7]

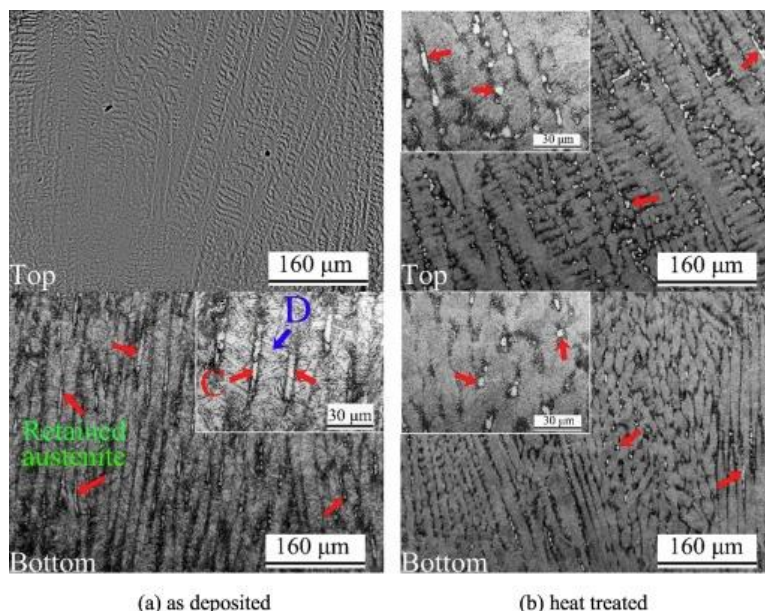


Figure 2. Microstructure of the maraging steel (fabricated by WAAM). (7)

According to Ge et al. conducted researches on 2Cr13 steel at different times.[8],[9] WAAM-CMT was used in these studies. Both

researches had same production parameters.(Table 1) And another study of the 2Cr13 was given to the Table 1, sample 3.

Table 1. WAAM-CMT Deposition Parameters [8-9]

Depositing parameters for 2Cr13	Sample 1 [8]	Sample 2 [9]	Sample 3 (17)
Depositing Speed	0.4 m/min	0.4 m/min	0,3 m/min
Depositing Voltage	12.9 V	12.9 V	16 V
Depositing Current	96 A	96 A	186 A
Wire Feed Speed	5.2 m/min	5.2 m/min	6 m/min
Wire Feed Angle	90°	90°	No value
Dwelling Time	120 s	120 s	120 s

Fig 3. shows that the surface morphology of the polish but unetched samples.As shown of the Fig 3. there are only pores in the several ranges but the metallurgical bonding

was obtained with CMT. Gu et al. also reported that the first layer relatively had bigger pores because of the high cooling rates.[8]

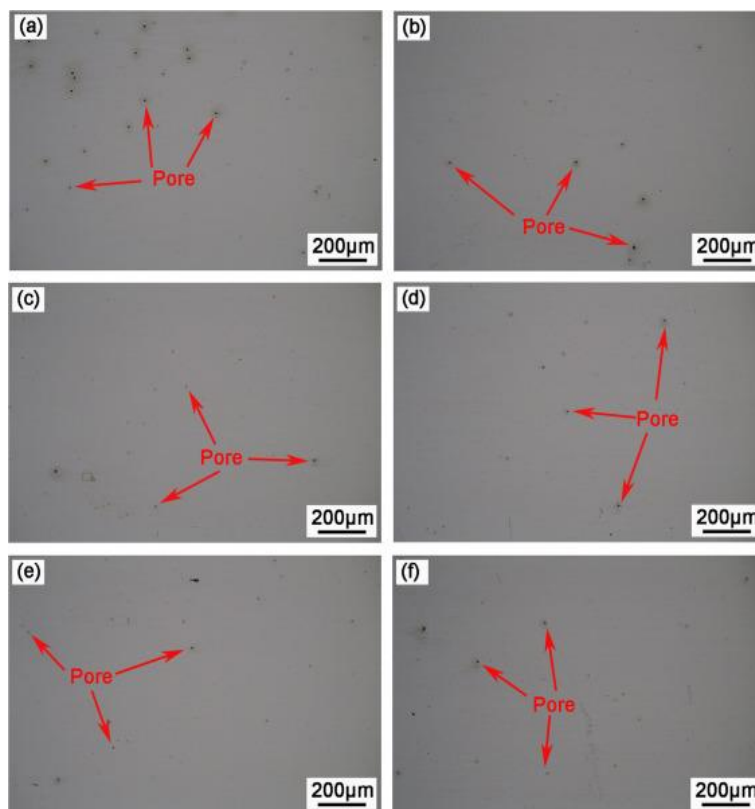


Figure. 3. X-Y plane of 2Cr13 AM part (optical micrograph): (a) 01st layer; (b) 05th layer; (c) 10th layer; (d) 15th layer; (e) 20th layer; (f) 25th layer.[8]

Fig 4. 2Cr13 steel commonly contains martensitic microstructure. As is known in the layer deposition technique, the heat accumulation of the upper layer affects the lower layer. So presence of ferrite in the middle region shown in Fig 4. Presence of ferrite could be effect of the in-situ heat

treatment. As known in the layer by layer deposition technique, heat accumulation of the upper layer affected the lower layer. Ge et al. reported that equiaxed ferrite grains were observed inner region and top layer had needle-like martensitic structure. [9]

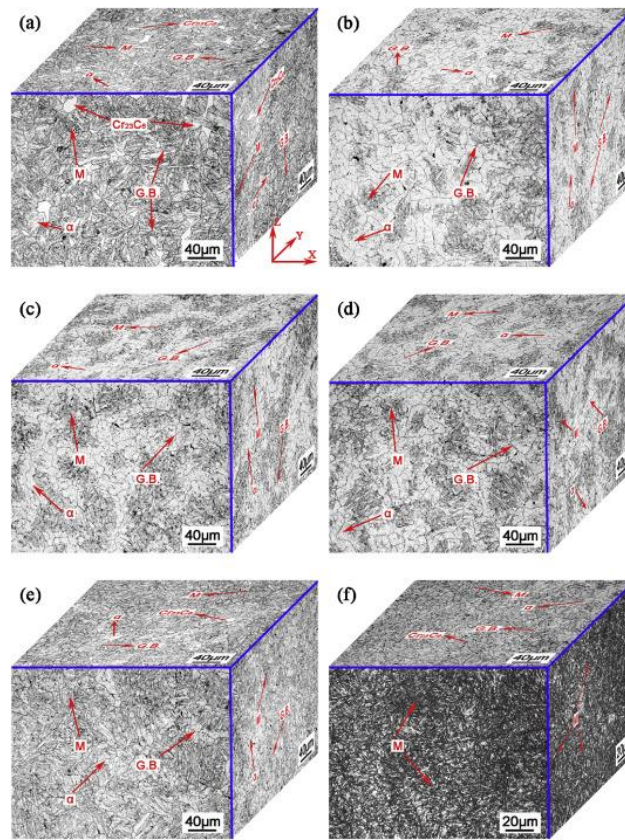


Figure 4. 3D microstructures of 2Cr13 WAAM part: (a) 01 st layer; (b) 05 th layer; (c) 10 th layer; (d) 15 th layer; (e) 20 th layer; (f) 25 th layer[9]

According to the Lyu et al. different martensitic structure depends on interpass temperature. As seen in Figure 5, the reason for the hardness differences in Zone 1 and Zone 2 is the effect of interpass

temperature differences on the start and finish temperatures of the martensite phase. [17]

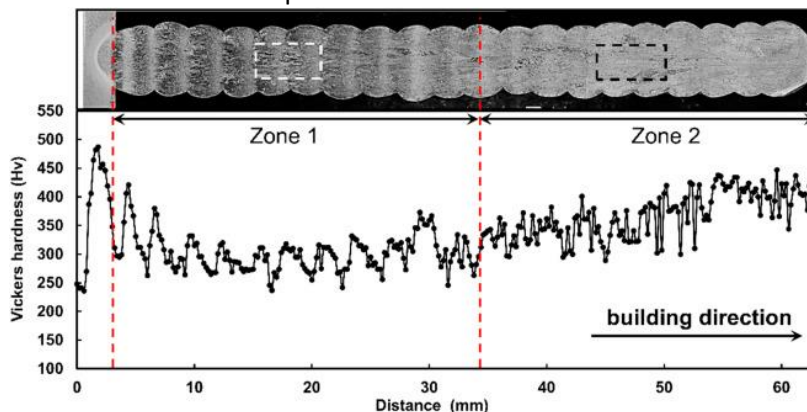


Figure 5. Cross-section perpendicular to the deposition direction with hardness profile measured at the centerline of the cross section toward the building direction.[17]

Lyu et al. also reported that hardness differences between Zone 1 and Zone 2 created preferential place for crack beginning and the mechanical properties behaviour become anisotropic. [17]

Wang et al.[10], Caballero et al.[12], van Nuland et al. [18], Wang et al.[19] and Hadjipantelis et al.[20] worked on stainless steels.

*Table 2. Parameters at different works. [10], [12], [18], [19], [20]*

	[10]	[12]	[18]	[19]	[20]
Method	WAAM-CMT	WAAM-CMT	WAAM-GMAW (Robotic)	WAAM-CMT	WAAM-CMT
Material	316L , 1,2 mm diameter	17-4PH, 1,2 mm diameter	316L	316L, 1 mm diameter	308LSi, 1 and 1,2 mm diameter
Current (A)	135-140	No value	160	150	100-140
Voltage (V)	22,1-19,5	No value	20,5	14,1	18-21
Wire Feed Speed (mm/min)	4500	6000		1100	4000-8000-5700
Travel/Deposition/Scanning Speed (mm/min)	600	372		700	900-1800-780
Dwell Time (s)	20	0		20	30

Wang et al. [19] examined the anisotropy of microstructure and corrosion resistance of 316L stainless steel (SS). van Nuland et al. and Wang et al.[10] worked on 316L SS too. Van Nuland et al. analyzed the crystal plasticity with the help of finite element simulation and correlation between mechanical properties and microstructure. Wang et al. [10] examined the correlation

between arc mode and microstructure. Caballero et al. examined the effect of different processing conditions on microstructure and mechanical properties. Hadjipantelis et al. described the anisotropic material response of WAAMed elements. Parameters that used seen in Tab. 2. Examination of the WAAMed stainless steels conclusion has been shown in Tab. 3

Table 3. Reported Conclusions about stainless steel parts that produced with WAAM

Wang et al. [10]	Spedpulse and speedarc WAAM methods relatively stable methods. It is observed that in the top layer, secondary dendrite arms larger than bottom layer. Mechanical parameters strongly depend on production parameters such as heat input.
Caballero et al.[12]	As deposited WAAM parts have partially heterogeneous microstructure composition. After heat treatment, these heterogeneity can be eliminated. Retained austenite and quantity and shape of the martensite depend on heat input and cooling rate. Mechanical properties strongly depend on retained austenite and martensite quantity.
van Nuland et al. [18]	Modelling and simulation methods are usefull for WAAM. The grain geometry obtained with Voronoi grain geometry methods. Grain orientations that effected macroscopic anisotropy is shown and verified with modelling and simulation.
Wang et al.[19]	Relationships between microstructure and corrosion resistance were examined. In WAAMed parts corrosion resistance depended on microstructural orientation. Due to different layers had different cooling rates, ferrite austenite transformation would be changed. So ferrite or austenite content were changed. Depending on the content of the austenite and ferrite phases, the corrosion resistance varies according to the content of these two structures.
Hadjipantelis et al.[20]	Material behaviors were demonstrated on thin-walled as-built WAAMed parts. Anisotropy was examined elastic and inelastic ranges. According to the paper acquired information of the simulation reasonable. Simulation of the anisotropy to the WAAM is usefull methods.

Zhang et al. studied the microstructure and tensile properties on Cr-Mn (HNS0.99) steel. Production parameters is shown in Tab 4. [11] In this study CMT-WAAM system was

used and wire feed speed was 6 m/mm. Also annealing process were added to the experimental procedure.

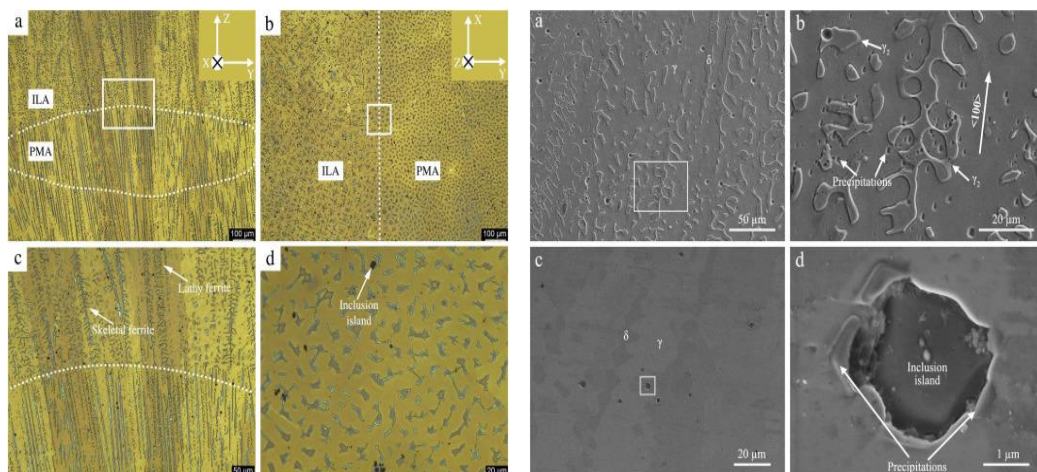


Figure. 6. Microstructures of HNS0.99 steel that build by WAAM-CMT. Left side As-built and right side T2-1050 (a-c) and T2-1100 (b-d) annealed heat treatment. ILA: Inter-layer area, PMA:Partial melting area. [11]

Zhang et al. were reported that in the inner-layer area two types of ferrite. First one was skeletal and the second one was lathy form. Ferrite forms can be seen in Fig 6. Left hand side. The precipitation forms can be seen in Fig 6 right hand side. According to the Zahang et al. Horizontal deposited as built parts had 860,6 Mpa UTS, T2-1050 annealed parts had 892,2 Mpa UTS and T2-1100 annealed parts had 663,5 Mpa UTS.

Another work was performed on high strength-low alloy steel which produce with WAAM-MIG (robotic).[13] Effect of thermal cycles on microstructure and mechanical properties were examined. Formed ferrites were acicular and quasi-polygonal ferrites. According to the Rodrigues et al., because of the reheat conditions and thermal accumulation the grain size would become coarser along the building direction. This situation has effected hardness and tensile properties directly.

Due to anisotropic behaviour of the WAAM, many paper focused to this phenomena. Jinguo et al.[14] investigated pore

distribution, microstructural progress and mechanical performances of H13 steel parts that manufactured with WAAM-CMT. Vahedi et al. compared the microstructures of steel plates that produced by conventional rolling and WAAM-CMT . [15] ER70S welding wire was used. After the fabrication with both methods, as-built parts were compared in terms of mechanical properties, heat treatments were applied on parts. The results are in line with the results of the studies on steels above. [15] An another work , ER70S-6 mild steel was used in WAAM-GMAW Robotic system.[16] Aldalur et al. revealed that the different deposition strategy created different thermal cycles. Therefore heat input is variable. The microstructure of the walls that deposited with oscillated and overlapped deposition strategy are totally different. In the overlapped depositions strategy has bigger heat input. So grain size is larger than oscillated strategy. As a result of grain size differences mechanical properties are different too. [16]

## 2.2. Titanium-based

Titanium-based alloys are often preferred especially aerospace applications due to its specific strength. Because of conventional methods like subtractive manufacturing (SM) suffer high raw materials costs, additive manufacturing methods preferable for production of titanium-based alloys. In addition that, in AM, buy-to-fly ratio lower than SM.[2] Ti-6Al-4V alloy is the most widely studied alloy in the scope of WAAM.[22], [23], [24] Wu et al. examined effects of heat accumulation on microstructure and

mechanical properties of Ti6Al4V.[22] Another Ti-6Al-4V work performed by Wang et al. In this paper grain morphology and texture characterization of WAAMed Ti-6Al-4V was revealed.[23] McAndrew et al. studied on microstructural refinement Ti6Al4V parts that produced with WAAM. [24] Fatigue crack growth has a critical role on aerospace and it was reviewed in WAAMed Ti6Al4V by Xie et al. [27] Deposition parameters of WAAMed Ti6Al4V shown Table 4.

Table 4. Deposition parameters of Ti6Al4V parts.[22][23][24]

	[22]	[23]	[24]
Method	WAAM-GTAW	WAAM-GTAW	WAAM-GTAW
Material	Ti6Al4V, 1,2 mm diameter	Ti6Al4V, 1,2 mm diameter	Ti6Al4V, 1,2 mm diameter

Current (A)	110	120-140	200-190
Voltage (V)	12	14	No value
Wire Feed Speed (mm/min)	1000	2000	2200-2400
Travel/Deposition/Scanning Speed (mm/min)	95	250-350	200
Dwell Time (s)	125	20	No value

According to the Wu et al. heat accumulation has an important role in the WAAM. Grain size, microstructure, phases are affected from heat accumulation. Different layers had different phase distribution and grain size, as seen in Fig. 7. First deposited layers contacted with substrate. Due to this situation, the first few layers have a high cooling rate. As a result of high cooling rates, a structure was formed with long orthogonally martensite. (Fig. 7a) As a result of cooling rates

slowed from down to up, heat is accumulated in the wall. Middle region is formed with fully lamellar  $\alpha$ . (Fig. 7 b-c) At the top of the wall, large colonies of  $\alpha$  which are decorated with prior  $\beta$  grains are formed. (Fig. 7 d-f). In Fig. 7 b-c section, equiaxed grains can be seen. Differences in phases and grain size in different layers affect mechanical properties directly. [22]

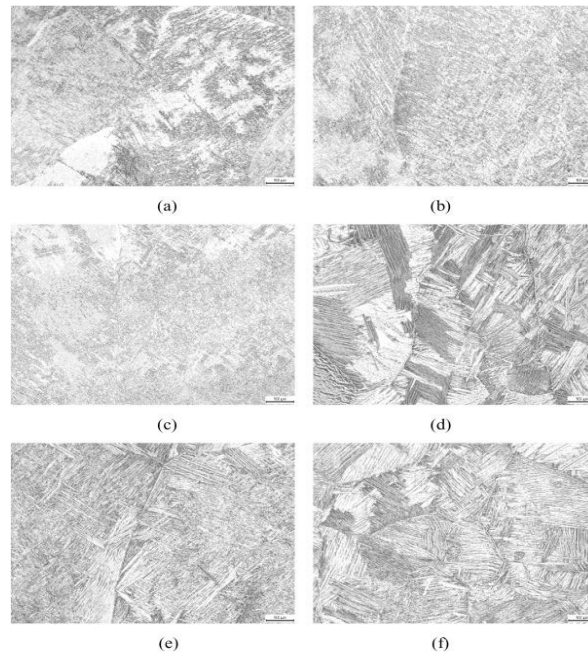
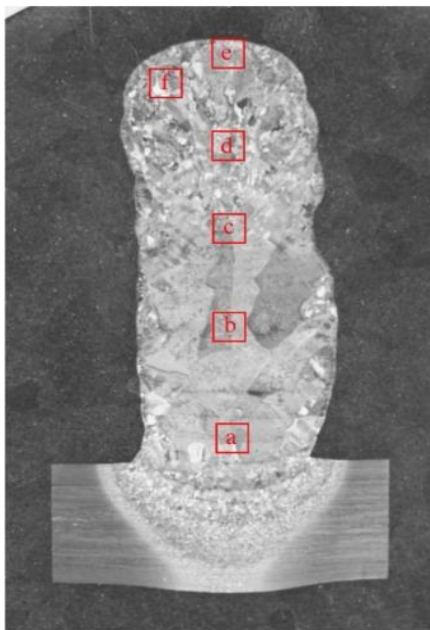


Figure 7. Cross-sectional macro (left hand side) and microphotograph (right hand side) of the Ti6Al4V wall [22]

Wang et al. reported that average equiaxed  $\beta$  grains size increased with current and decreased with wire feed and travel velocity. According to the paper, in fact, main reason

of equiaxed formation depends on heat input that is affected by travel speed, welding current and welding voltage. [23]

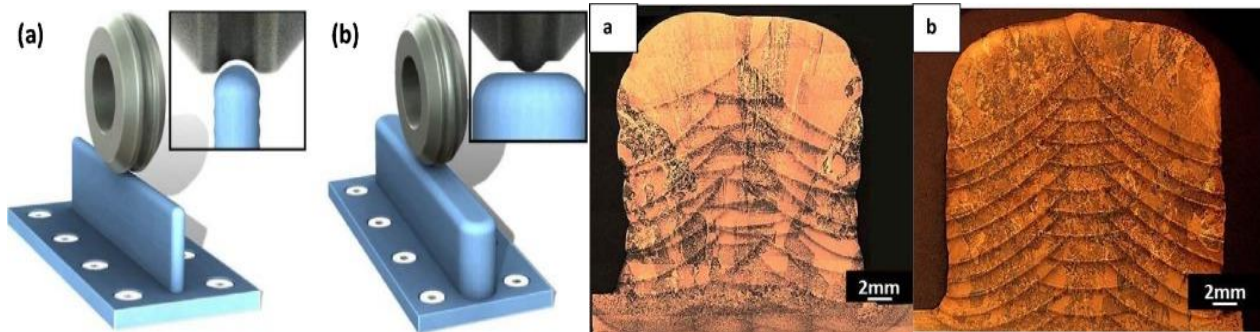


Figure 8. Schematic diagram of the rolling methods and microphotographs (Left a: vertical rolling, left b: inverted profiled rolling) (Right a: non-rolled, right b: rolled) [24]

McAndrew et al. added an extra methods into the WAAM. According to the study, rolling can be used after the wall produced to refine the microstructure. Rolling types and created microstructure seen in Fig 8. As a result of paper, grain refinement were achieved with rolling and rolling type and applied forces were produced more refinement.[24] Wang et al. conducted a work about characterization of WAAMed titanium aluminide. In this paper WAAM-GTAW system was used and wire feed speed ranging between 650-1050 mm/min, travel speed was 100 mm/min. Also current was 120 A. As result of Al percentage changed, phase constitution varied. Due to increasing Al content, hardness of the parts that produced increased. [21] According to the Bermingham et al. refinement of the titanium alloys that produced with WAAM can achieve as a result

of create heterogenous nucleation. It has been reported that grain refiners can be added to the structure to support heterogeneous nucleation. Adding La<sub>2</sub>O<sub>3</sub> to the structure provided %85 refinement of the grain structure. [25] Due to increase welding current, heat input increase. So grain size directly affected from this situation. Li et al. worked on reducing arc heat input to obtain equiaxed and fine grains. Ti-6.5Al-3.5Mo-1.5Zr-0.3Si welding wire was heated before the process. Thus, welding current can be reduced. The microstructure of the parts that manufactured with non-heated wire were coarse columnar  $\beta$  grains. But the using heat-wire achieved to decrease size of the columnar grains sharply. (Fig 9.) [26]

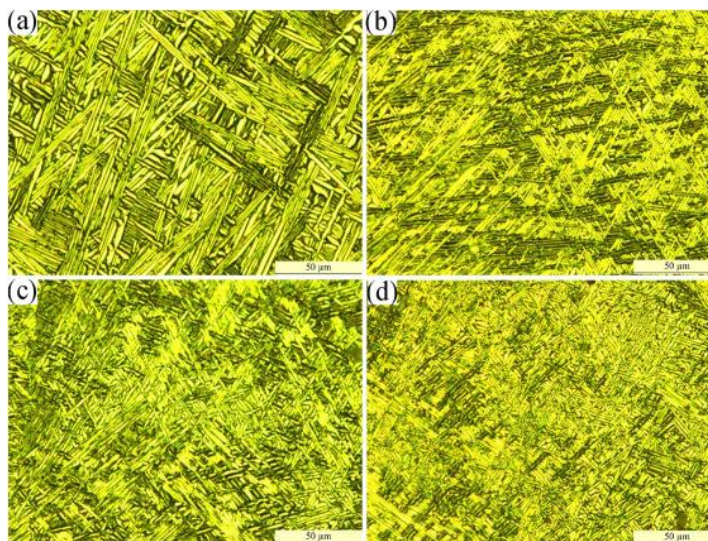


Figure 9. Microphotograph of the parts that heat and non-heat Wire(AAM)Ed (From b to c, heating of the wire increasing. a is non-heated wire) [26]

### 2.3. Aluminum-based

In recent years, because of energy saving, lightweight alloys gained more importance. Not only space and aeronautical but also marine, military, automotive industries have attractive attention on the lightweight alloys. For these reasons Al-based alloys are investigated by researchers of many countries. In contrast of Ti-based alloys that have been fabricated tungsten inert gas WAAM (TIG-WAAM) method, Al-based alloys have been fabricated with cold metal transfer waam (CMT-WAAM). As with other metals heat input important in Al-based alloys. As result, using the CMT-WAAM technique for Al-

alloys is reasonable. As known, CMT is developed on low heat input. So CMT-WAAM is preferable for Al Alloys. [29] [33] Also other welding methods like MIG and TIG were investigated for production of Al-Alloys.[29][31][32]

Researches about Al-based alloys which produced with AM techniques that performed 2018-2022 is given in Tab. 5. Different methods, different heat input (as a result of different deposition parameters) values and different alloys are showed that Al is widely investigated in scope of WAAM.

*Table 5. Deposition parameters of different works that performed on Al-base alloys[27][28][29][30][31][32][33]*

Research	Material	Method	WFS-TS (mm/m)	Dwell Time (s)	Post Treatment
Gu et al. [27]	ER5087 (1,2 mm)	CMT	6000-600	120	Rolling
Zhang et al. [28]	ER5183 (1,2 mm)	VP-CMT	7200-500	120	As-built
Li et al.[29]	ER5356 (1,2 mm)	Rob-MIG	TS: 200-400 (25 times)	300	As-built
Campatelli et al.[30]	ER4043 (1,2 mm)	CMT/ CMT mix	1800/6000 - 300	25/140	As-built
Li et al.[31]	Al-6.2Zn-2.2Mg (1,2 mm)	Rob-MIG	TS: 200-350 (16 times)	600	As-built
Dong et al.[32]	ER7055	Rob-TIG	1300-100	Variable	As-built
Fang et al.[33]	ER2319 (1,2 mm)	CMT	7000-500	Depend on post-treatment	Hammering

Gu et al. designed a hybrid system. After deposition of each layer rolling process was performed. Thus pores formation and grain refinement situations could be observed. In Fig.10 a belongs to as deposited layer. As

shown in Fig.10 pores gradually reduced under increasing rolling loads. And also grains are refined gradually under increasing rolling loads.[27]

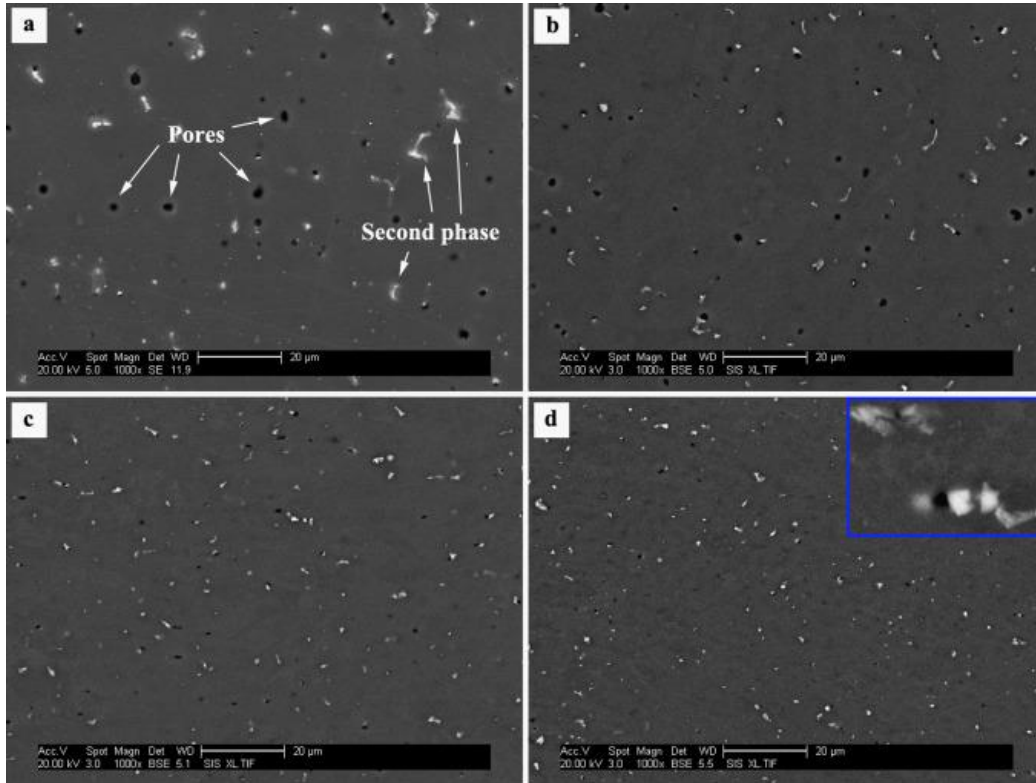


Figure 10. SEM images for deposited part (a: as deposited, b-d: interlayer rolled( (b: 15kN, c:30 kN and d:45 kN) [27]

Fang et al. designed other hybrid system. A hammering system was produced and used with CMT-WAAM system. Like system was designed by Gu et al., after deposition of each layer hammering process was

performed. As seen in Fig 11. Microstructures of the WAAMed and hammered samples are inhomogenous. Coarse grain formation decreased with increased of deformation.[33]

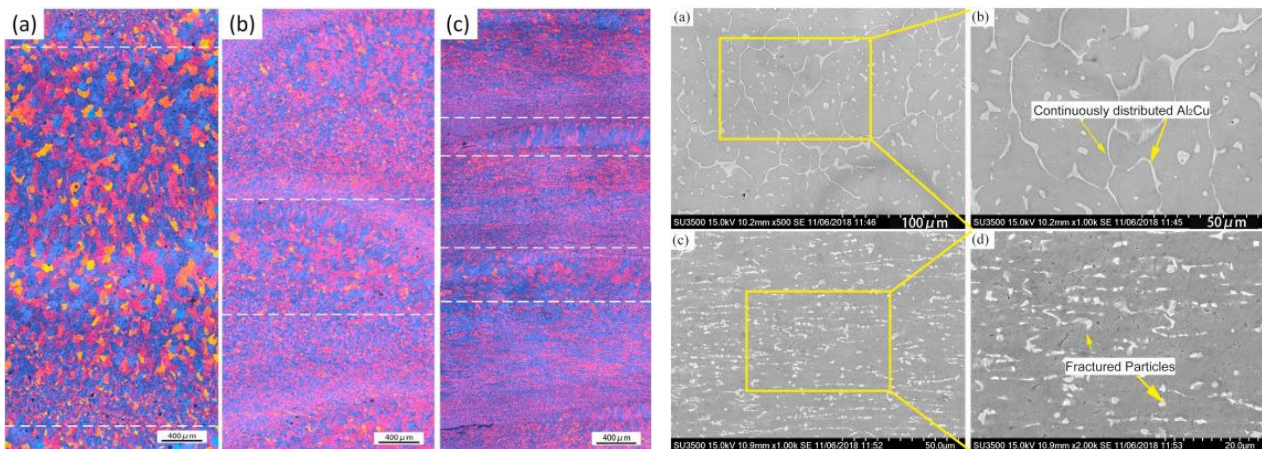


Figure 11. Microphotos of parts different deformation ratios (left a:%0; b: %21,8; c:%50,8) and distributions of the Al<sub>2</sub>Cu particles in  $\alpha$ -Al (a-b as-deposited and c-d %50,8 hammered)[33]

In terms of heat accumulation, number of layers in AM has important case. Deposited layers heat will not affect the layers that deposited before. So phase transformations and grain distribution will not affect from the additional heat input. Therefore Zhang et al. deposited nine walls which had different thickness. The walls thickness was ranged between 1-layer and 9-layers. Zhang et al. reported that bottom layers in different

groups had nearly similar microstructural evolution. When new layer is deposited, local thermal cycling is occurred by additional heat. This situation is caused grain coarsening (Fig 12.). And also additional heat is created new thermal gradient. According to the paper, after 7th layer, microstructure of the down layers will become more stable.[28]

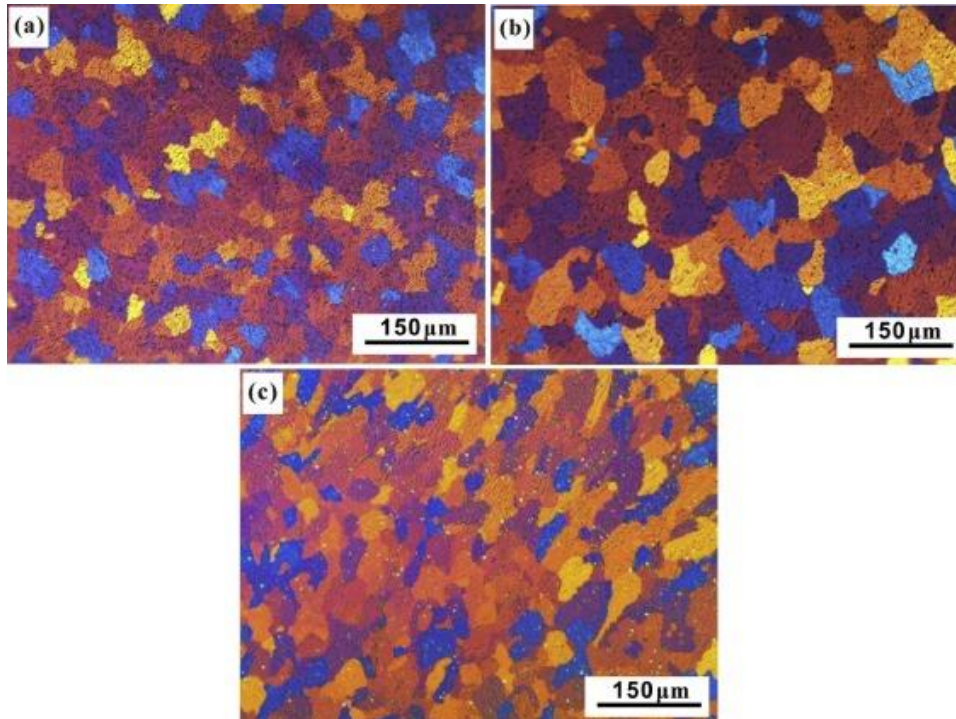


Figure 12. Grain morphologies of the bottom layers. (a: sample 1, b:sample 3 and c:sample 6)[28]

Li et al. researched the effects of shielding gas. N<sub>2</sub> and Ar shielding gas was chosen and studied in the same deposition parameters. According to the paper when N<sub>2</sub> shielding gas is used, it is observed that bead height was higher and bead width was narrower and surface roughness was rougher. Yield strength and ultimate tensile strength of the samples was more effective when Ar shielding gas was used. Although hardness value higher when N<sub>2</sub> is used, hardness more uniform when Ar is used. [29]

Comparative works are often used and it is very useful to investigation. Campatelli et al. researched to the effects of the various CMT modes. Deposition parameters can be seen in Tab. 5. Two different CMT modes were chosen: CMT and CMT mix drive. According to the results of this paper CMT-mD technique more energy-saver methods than CMT. And also reported that, although CMT

mode is resulted less uniform microstructure, there was no significant differences in mechanical properties. [30]

Li et al. deposited 16 different single layer to investigate weld bead formation with using different heat input. Heat input was ranged between 4243-2868 J/cm, 1 to 16 bead. According to Li et al. heat input is increased the number of ripples on the weld bead decreased.[31] To change and control interlayer temperature was tried to another paper. In this paper three sample walls were deposited with 100, 200 and 300 °C interlayer temperature with high 10.61, 11.76 and 14.50 mm. and investigated hardness distribution, texture and microstructure formation and precipitation. [32] Dong et al. reported that the precipitation and hardness was increased when interlayer temperature was increased. Texture formations was affected with

interlayer temperature. According to the Dong et al. when interlayer temperatures was increased, aspect ratio of columnar

grains that lied on  $\langle 011 \rangle$  and  $\langle 001 \rangle$  directions was decreased as seen in Fig 13.[32]

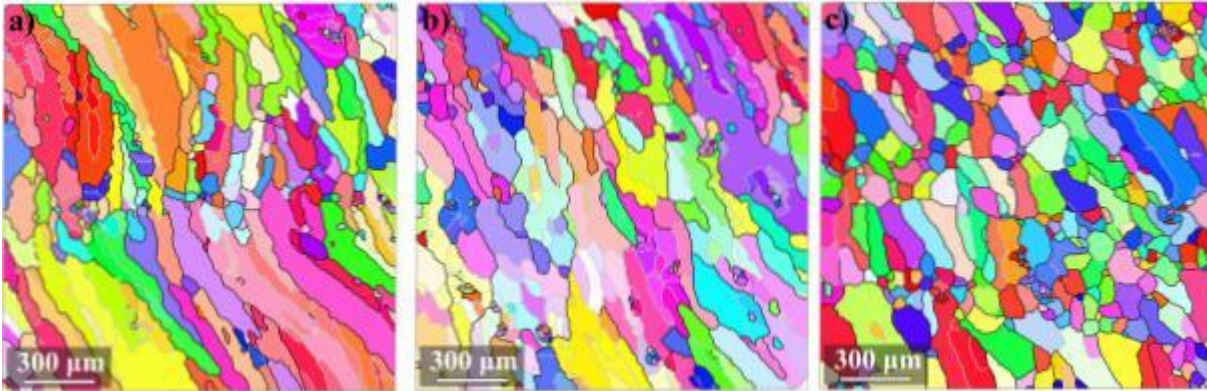


Figure 13. Texture and grain morphologies [32]

### 3. Conclusion

In this study, the production of iron-based, titanium-based and aluminum-based alloys within the scope of wire arc additive manufacturing technology was reviewed. This examination is limited to the examination of the microstructure, which directly affects the mechanical properties. In WAAM, parts are produced layer by layer. The properties of the parts that produced with this manufacturing method require the correct selection of welding parameters, regardless of which material type is used. When the studies were reviewed, the following conclusions were reached.

1. The basic parameters used in WAAM are wire feed speed, welding speed, interlayer dwell time.

2. Various and detailed studies have been carried out on deposition parameters in various material groups. In these studies, wire feeding speed and welding speed, which change the heat input (due to current and voltage), are used as variable parameters.

3. Microstructure formations were observed in the direction of cooling and deposition in all steel, titanium and aluminum alloys. The formation of the microstructure towards the cooling direction makes the mechanical properties anisotropic.

4. Post-production processes are in the fields of interest. In particular, studies have been carried out on post-manufacturing mechanical processes. In these studies, it was observed that the mechanical properties were improved by microstructure

manipulation. However, post-production processes increase the overall duration of production.

5. It is generally appropriate to determine which welding type will be used according to the melting temperature of the material. For example, TIG is frequently used in titanium-based alloys and CMT is frequently used in aluminum-based alloys.

6. Microstructure and pattern formation are directly affected by heat input and heat accumulation. For this reason, researchers have been working on kinetic data with various simulation methods. In these studies, the phenomenon of "columnar to equiaxed transition" (CET) has an important role. Microstructures of the the final parts that produced are not fully equiaxed or fully columnar as obtained by simulations. Because the lower regions are close to the substrate, they are the regions where cooling takes place quickly and they cool quickly. This rapid cooling usually produces a columnar grain structure. The middle regions are the regions where heat is accumulated depending on the number of layers and the equiaxed grains are more.

7. The grain sizes of the formed grains vary according to the cooling rate. Depending on the heat input, there is a finer grain structure in the parts with the heat input that preferred close to the optimum in the same regions.

8. The phases to be formed vary depending on the chemical composition and cooling rates.

9. When the welding parameters are set correctly in WAAM, the pore structure is not a problem regardless of which material is used.

### References

1. ASTM. ASTM F2792-12a, Standard Terminology for Additive Manufacturing Technologies; Technical Report 2; ASTM International: West Conshohocken, PA, USA, 2012.
2. S. W. Williams, F. Martina, A. C. Addison, J. Ding, G. Pardal & P. Colegrove (2016) Wire + Arc Additive Manufacturing, *Materials Science and Technology*, 32:7, 641-647, DOI: 10.1179/1743284715Y.0000000073
3. Yunpeng Nie, Peilei Zhang, Xi Wu, Guojin Li, Hua Yan & Zhishui Yu (2018): Rapid prototyping of 4043 Al-alloy parts by cold metal transfer, *Science and Technology of Welding and Joining*, DOI: 10.1080/13621718.2018.1438236
4. S. Selvi, A. Vishvakshana, E. Rajasekar (2018): Cold metal transfer (CMT) technology-An overview, *Defence Technology*, DOI: 10.1016/j.dt.2017.08.002
5. Jianglong Gao, Minjie Gao, Shouliang Yang, Jing Baic, Yuchun Zhai, Jialuo Ding (2020): Microstructure, defects, and mechanical properties of wire + arc additively manufactured Al\Cu4.3-Mg1.5 alloy, *Materials and Design*, DOI: 10.1016/j.matdes.2019.108357
6. Davoud Jafari, Tom H.J. Vaneker, Ian Gibson (2021) : Wire and arc additive manufacturing: Opportunities and challenges to control the quality and accuracy of manufactured parts, *Materials and Design*, DOI: 10.1016/j.matdes.2021.109471
7. Xu, X., Ganguly, S., Ding, J., Guo, S., Williams, S., & Martina, F. (2018). Microstructural evolution and mechanical properties of maraging steel produced by wire + arc additive manufacture process. *Materials Characterization*, 143, 152–162. <https://doi.org/10.1016/j.matchar.2017.12.002>
8. Ge, J., Lin, J., Chen, Y., Lei, Y., & Fu, H. (2018). Characterization of wire arc additive manufacturing 2Cr13 part: Process stability, microstructural evolution, and tensile properties. *Journal of Alloys and Compounds*, 748, 911–921. <https://doi.org/10.1016/j.jallcom.2018.03.222>
9. Ge, J., Lin, J., Lei, Y., & Fu, H. (2018). Location-related thermal history, microstructure, and mechanical properties of arc additively manufactured 2Cr13 steel using cold metal transfer welding. *Materials Science and Engineering: A*, 715, 144–153. <https://doi.org/10.1016/j.msea.2017.12.076>
10. Wang, L., Xue, J., & Wang, Q. (2019). Correlation between arc mode, microstructure, and mechanical properties during wire arc additive manufacturing of 316L stainless steel. *Materials Science and Engineering: A*, 751, 183–190. <https://doi.org/10.1016/j.msea.2019.02.078>
11. Zhang, X., Zhou, Q., Wang, K., Peng, Y., Ding, J., Kong, J., & Williams, S. (2019). Study on microstructure and tensile properties of high nitrogen Cr-Mn steel processed by CMT wire and arc additive manufacturing. *Materials & Design*, 166, 107611. <https://doi.org/10.1016/j.matdes.2019.107611>
12. Caballero, A., Ding, J., Ganguly, S., & Williams, S. (2019). Wire + Arc Additive Manufacture of 17-4 PH stainless steel: Effect of different processing conditions on microstructure, hardness, and tensile strength. *Journal of Materials Processing Technology*, 268, 54–62. <https://doi.org/10.1016/j.jmatprotec.2019.01.007>
13. Rodrigues, T. A., Duarte, V., Avila, J. A., Santos, T. G., Miranda, R. M., & Oliveira, J. P. (2019). Wire and arc additive manufacturing of HSLA steel: Effect of thermal cycles on microstructure and mechanical properties. *Additive Manufacturing*, 27, 440–450. <https://doi.org/10.1016/j.addma.2019.03.029>
14. Ge, J., Ma, T., Chen, Y., Jin, T., Fu, H., Xiao, R., Lei, Y., & Lin, J. (2019). Wire-arc additive manufacturing H13 part: 3D pore distribution, microstructural evolution, and mechanical performances. *Journal of Alloys and Compounds*, 783, 145–155. <https://doi.org/10.1016/j.jallcom.2018.12.274>
15. Vahedi Nemani, A., Ghaffari, M., & Nasiri, A. (2020). Comparison of microstructural characteristics and mechanical properties of shipbuilding steel plates fabricated by conventional rolling versus wire arc additive manufacturing. *Additive Manufacturing*, 32, 101086. <https://doi.org/10.1016/j.addma.2020.101086>
16. Aldalur, E., Veiga, F., Suárez, A., Bilbao, J., & Lamikiz, A. (2020). High deposition wire arc additive manufacturing of mild steel: Strategies and heat input effect on microstructure and mechanical properties. *Journal of Manufacturing Processes*, 58, 615–626. <https://doi.org/10.1016/j.jmapro.2020.08.060>
17. Lyu, Z., Sato, Y. S., Tokita, S., Zhao, Y., Jia, J., & Wu, A. (2021). Microstructural distribution and anisotropic tensile behavior in a 2Cr13 martensitic stainless steel thin wall fabricated by wire arc additive manufacturing. *Materials Today Communications*, 29, 102870. <https://doi.org/10.1016/j.mtcomm.2021.102870>

18. van Nuland, T. F. W., van Dommelen, J. A. W., & Geers, M. G. D. (2021). Microstructural modeling of anisotropic plasticity in large scale additively manufactured 316L stainless steel. *Mechanics of Materials*, 153, 103664. <https://doi.org/10.1016/j.mechmat.2020.103664>
19. Wang, C., Zhu, P., Wang, F., Lu, Y. H., & Shoji, T. (2022). Anisotropy of microstructure and corrosion resistance of 316L stainless steel fabricated by wire and arc additive manufacturing. *Corrosion Science*, 206, 110549. <https://doi.org/10.1016/j.corsci.2022.110549>
20. Hadjipantelis, N., Weber, B., Buchanan, C., & Gardner, L. (2022). Description of anisotropic material response of wire and arc additively manufactured thin-walled stainless steel elements. *Thin-Walled Structures*, 171, 108634. <https://doi.org/10.1016/j.tws.2021.108634>
21. Wang, J., Pan, Z., Ma, Y., Lu, Y., Shen, C., Cuiuri, D., & Li, H. (2018). Characterization of wire arc additively manufactured titanium aluminide functionally graded material: Microstructure, mechanical properties and oxidation behaviour. *Materials Science and Engineering: A*, 734, 110–119. <https://doi.org/10.1016/j.msea.2018.07.097>
22. Wu, B., Pan, Z., Ding, D., Cuiuri, D., & Li, H. (2018). Effects of heat accumulation on microstructure and mechanical properties of Ti6Al4V alloy deposited by wire arc additive manufacturing. *Additive Manufacturing*, 23, 151–160. <https://doi.org/10.1016/j.addma.2018.08.004>
23. Wang, J., Lin, X., Wang, J., Yang, H., Zhou, Y., Wang, C., Li, Q., & Huang, W. (2018). Grain morphology evolution and texture characterization of wire and arc additive manufactured Ti-6Al-4V. *Journal of Alloys and Compounds*, 768, 97–113. <https://doi.org/10.1016/j.jallcom.2018.07.235>
24. McAndrew, A. R., Alvarez Rosales, M., Colegrove, P. A., Hönnige, J. R., Ho, A., Fayolle, R., Eytayo, K., Stan, I., Sukrongpang, P., Crochemore, A., & Pinter, Z. (2018). Interpass rolling of Ti-6Al-4V wire + arc additively manufactured features for microstructural refinement. *Additive Manufacturing*, 21, 340–349. <https://doi.org/10.1016/j.addma.2018.03.006>
25. Bermingham, M. J., StJohn, D. H., Krynen, J., Tedman-Jones, S., & Dargusch, M. S. (2019). Promoting the columnar to equiaxed transition and grain refinement of titanium alloys during additive manufacturing. *Acta Materialia*, 168, 261–274. <https://doi.org/10.1016/j.actamat.2019.02.020>
26. Li, Z., Liu, C., Xu, T., Ji, L., Wang, D., Lu, J., Ma, S., & Fan, H. (2019). Reducing arc heat input and obtaining equiaxed grains by hot-wire method during arc additive manufacturing titanium alloy. *Materials Science and Engineering: A*, 742, 287–294. <https://doi.org/10.1016/j.msea.2018.11.022>
27. Gu, J., Wang, X., Bai, J., Ding, J., Williams, S., Zhai, Y., & Liu, K. (2018). Deformation microstructures and strengthening mechanisms for the wire+arc additively manufactured Al-Mg4.5Mn alloy with inter-layer rolling. *Materials Science and Engineering: A*, 712, 292–301. <https://doi.org/10.1016/j.msea.2017.11.113>
28. Zhang, B., Wang, C., Wang, Z., Zhang, L., & Gao, Q. (2019). Microstructure and properties of Al alloy ER5183 deposited by variable polarity cold metal transfer. *Journal of Materials Processing Technology*, 267, 167–176. <https://doi.org/10.1016/j.jmatprotec.2018.12.011>
29. Li, S., Zhang, L.-J., Ning, J., Wang, X., Zhang, G.-F., Zhang, J.-X., Na, S.-J., & Fatemeh, B. (2020). Comparative study on the microstructures and properties of wire+arc additively manufactured 5356 aluminium alloy with argon and nitrogen as the shielding gas. *Additive Manufacturing*, 34, 101206. <https://doi.org/10.1016/j.addma.2020.101206>
30. Campatelli, G., Campanella, D., Barcellona, A., Fratini, L., Grossi, N., & Ingarao, G. (2020). Microstructural, mechanical and energy demand characterization of alternative WAAM techniques for Al-alloy parts production. *CIRP Journal of Manufacturing Science and Technology*, 31, 492–499. <https://doi.org/10.1016/j.cirpj.2020.08.001>
31. Li, S., Zhang, L.-J., Ning, J., Wang, X., Zhang, G.-F., Zhang, J.-X., & Na, S.-J. (2020). Microstructures and mechanical properties of Al–Zn–Mg aluminium alloy samples produced by wire + arc additive manufacturing. *Journal of Materials Research and Technology*, 9(6), 13770–13780. <https://doi.org/10.1016/j.jmrt.2020.09.114>
32. Dong, B., Cai, X., Xia, Y., Lin, S., Fan, C., & Chen, F. (2021). Effects of interlayer temperature on the microstructures of wire arc additive manufactured Al-Zn-Mg-Cu alloy: Insights into texture responses and dynamic precipitation behaviors. *Additive Manufacturing*, 48, 102453. <https://doi.org/10.1016/j.addma.2021.102453>
33. Microstructure evolution of wire-arc additively manufactured 2319 aluminum alloy with interlayer hammering. *Materials Science and Engineering: A*, 800, 140168. <https://doi.org/10.1016/j.msea.2020.140168>

## Electrodeposition of Dense Lithium and Sodium Battery Cathodes for Solid-State Batteries

**Paul V. Braun**

*Department of Materials Science and Engineering, University of Illinois Urbana-Champaign, Urbana,  
IL 61801, USA pbraun@illinois.edu  
ORCID: 0000-0003-4079-8160*

*Cite this paper as: Braun, PV. Electrodeposition of Dense Lithium and Sodium Battery Cathodes for Solid-State Batteries. Int. Conf. Advanced. Mater. Sci. & Eng. HiTech. and Device Appl. Oct. 27-29 2022, Ankara, Turkey*

**Abstract.** Conventional Li-ion batteries are formed using slurry-cast electrodes whose random nature and porosity limits both energy density and rate performance. Slurry-cast electrodes also are generally incompatible with solid-state batteries unless the slurry contains solid electrolyte particles in addition to active material. While such composite electrodes, consisting of a mixture of active material, solid electrolyte, and potentially conductive additives are under active investigation, such designs exhibit power and energy limitations due to the tortuosity of the ion and electron conduction pathways. I will present our work on the molten salt electrodeposition of thick and nearly dense Na and Li-based cathodes on metallic current collectors, including cathodes based on LiCoO<sub>2</sub>, NaCoO<sub>2</sub>, LiMn<sub>2</sub>O<sub>4</sub>, and Al-doped LiCoO<sub>2</sub> which overcomes some of these challenges. The capacities are near-theoretical, and the crystallinities and electrochemical performance are comparable, or in some cases, even better than powders synthesized at much higher temperatures. A very attractive element of the electrodeposition process is control of the crystallographic orientation of the deposited film. For example, the crystallography can be oriented such that the fast electron and ion conduction directions are perpendicular to the substrate. Finally, I will discuss solid-state batteries built these electrodes and how the crystallography of the electrode | solid-electrolyte interface impacts interfacial reactions, rate performance, and cycle life.

**Keywords:** energy storage, batteries, electrodeposition  
© 2022 Published by ICMATSE

## The role of defects on structural and optical properties of ZnO nanorods synthesized by a hydrothermal route at various growth times and temperatures

**Şefda Kaya**

Central Research Laboratory, Kastamonu University, 37100, Kastamonu, Turkey,  
seydanurkaya@kastamonu.edu.tr  
ORCID: 0000-0002-6894-9082

**Ozgür Öztürk**

Department of Electric and Electronics Engineering, Faculty of Engineering and Architecture,  
Kastamonu University, 37100, Kastamonu, Turkey, oozturk@kastamonu.edu.tr  
ORCID:0000-0002-0391-5551

**A. T. Tasci**

Department of Electric and Electronics Engineering, Faculty of Engineering and Architecture,  
Kastamonu University, 37100, Kastamonu, Turkey, atasci@kastamonu.edu.tr  
ORCID:0000-0001-9450-6499

**F. Bulut**

Scientific and Technological Research Applications and Research Center, 57100, Sinop, Turkey,  
fatihbulut@sinop.edu.tr  
ORCID:0000-0001-5335-2307

**D. Akcan**

Bahcesehir University, Faculty of Engineering and Natural Sciences, Department of Mechatronic  
Engineering, 34349, Besiktas, Istanbul, Turkey, [dogan.akcan@eng.bau.edu.tr](mailto:dogan.akcan@eng.bau.edu.tr)  
ORCID:0000-0002-9293-7372

**L. Arda**

Bahcesehir University, Faculty of Engineering and Natural Sciences, Department of Mechatronic  
Engineering, 34349, Besiktas, Istanbul, Turkey, [lutfi.arda@eng.bau.edu.tr](mailto:lutfi.arda@eng.bau.edu.tr)  
ORCID:0000-0003-0722-3891

*Cite this paper as: Kaya S. et al, The role of defects on structural and optical properties of ZnO nanorods synthesized by a hydrothermal route at various growth times and temperatures, Int. Conf. Advanced. Mater. Sci. & Eng. HiTech. and Device Appl. Oct. 27-29 2022, Ankara, Turkey*

### Abstract

Zinc oxide (ZnO) nanorod arrays were manufactured by a hydrothermal route at various growth times (3, 4, and 5 hours) and temperatures (90, 120, and 150 °C). X-ray diffraction, SEM, energy-dispersive X-ray spectroscopy, UV-Vis spectrophotometry, and photoluminescence spectrophotometry were performed to analyze the role of defects on structural and optical properties of ZnO nanorods. All samples showed a typical ZnO wurtzite crystal structure.

There were no contamination and secondary phases in the X-ray diffraction patterns. At a growth temperature of 150 °C, perfect hexagonally shaped nanorods transformed into pyramid-like nanorods. The average optical transmittance and energy band values were obtained to be higher at relatively low growth time (3h) and temperature (90°C). A photoluminescence spectrophotometer was also employed to investigate the deficiency type and density, and crystal quality of ZnO nanorods. The broad visible emission band (including yellow-orange and red emissions) was detected. The yellow-orange and red emissions might be accredited to the double charged oxygen vacancy ( $V_o^{++}$ ) and oxygen interstitials ( $O_i$ ) which were strongly dependent on the growth time and temperature.

Depending on the results, these nanorods with manipulated optical properties could be an ideal candidate for the application in UV light emission.

*Keywords:* ZnO nanorods, hydrothermal route, optical transmittance, photoluminescence properties.

## Introduction

Among the metal oxide semiconductors such as  $\text{SnO}_2$ ,  $\text{In}_2\text{O}_3$ ,  $\text{WO}_3$ , and  $\text{TiO}_2$ , ZnO having 3.37 eV bandgap and 60 meV exciton binding energy has received considerable attention as a promising material in various applications including optoelectronic devices, nano-electromechanical (NEMs) systems, nanogenerators, and nanosensors [1-3]. ZnO is also a visual transparent conductive oxide (TCO) that is widely used in touch screens, flat-panel displays (FPDs), thin-film transistors (TFTs), organic light-emitting diodes (OLEDs), liquid crystal displays (LCDs), surface acoustic wave (SAW) devices and solar cells [4–10]. In addition to the superior physical properties of ZnO, it is also an environmentally friendly, biocompatible, non-toxic material, and its natural abundance, low-cost, and easy synthesis methods make this material suitable for large-scale production. Although various methods exist to obtain one dimensional (1D) ZnO nanostructures such as vapor-liquid-solid (VLS) growth, metal-organic chemical vapor deposition (MOCVD), and pulsed laser deposition (PLD), solution-based synthesis is one of the most reasonable ways because of its simplicity, simple equipment, and low-temperature requirement.

Among the solution-based synthesis, the hydrothermal route is widely used to fabricate ZnO nanorods with a variety of morphologies such as flower-like, pencil-like, and pyramid-like [11]. In this method, there are many synthesis parameters, including seed deposition, growth temperature, growth time, pH, and molarity, which are important in governing the structural properties of the films. The structural properties of ZnO thin films strongly depend on the crystal quality of this compound and affect the optoelectronic characteristics in surface engineering applications [12]. Moreover, in the hydrothermal route, it is expected to manipulate the optical properties of ZnO nanorods by changing only the synthesis parameters without annealing or adding any impurity to the crystal structure [13].

In this study, therefore, we focused on the relationship between the synthesis parameters (temperature and growth time) and the role of defects on structural optical properties. We synthesized ZnO nanorods using a hydrothermal route at various temperatures and growth times. The defect density of ZnO nanorods manufactured by the hydrothermal route is investigated by

Gaussian decomposition of the photoluminescence (PL) spectrum.

We also investigated the changes systematically in the optical properties concerning the structural and defects evolution of this compound. We observed that optical properties, including visible transmittance, the bandgap is easily organized by changing hydrothermal growth time and temperature.

## 2. Material and methods

ZnO nanorods were prepared by a hydrothermal route. All chemicals used in the experiment were acquired from Sigma-Aldrich and were used with no further purification. Glass substrates were employed for the growth of ZnO nanorod arrays. Figure 1 exhibits the production process for ZnO nanorods. First, an ultrasonic bath was used to clean glass substrates in ethanol and deionized (DI) water for 15 min and they were dried at 70 °C. The sol-gel method was used to prepare the solution for the seed layer. Zinc acetate dihydrate ( $\text{Zn}(\text{CH}_3\text{COO})_2 \cdot 2\text{H}_2\text{O}$ ) was used as a precursor material. Methanol was used as a solvent, and monoethanolamine was used as a sol-stabilizer. Then, the resultant was placed on the glass substrates by dip-coating technique. After 5-dipping, coated substrates were heat-treated at 600°C for 30 min to achieve proper crystal orientation as given in references [14-18].

In a typical synthesis of ZnO nanorods using the hydrothermal route, 0.1 M of zinc acetate dehydrate [ $\text{Zn}(\text{CH}_3\text{COO})_2$ ] and 0.1 M of hexamethylenetetramine (HMTA,  $\text{C}_6\text{H}_{12}\text{N}_4$ ) were used as the precursors. All the precursors were dissolved entirely in distilled water and stirred to form a transparent solution at room temperature. The mixture was transferred to a Teflon-lined stainless steel autoclave of 50 mL capacity and the substrates were vertically dipped into the solution. ZnO nanorods were produced at different reaction times as 3h, 4h, 5h (at 90 °C) and different reaction temperatures as 90 °C, 120 °C, 150 °C (for 3 hours). Finally, DI water was used to wash the substrates which were dried in a vacuum furnace at 60 °C overnight.

XRD—Bruker D8 Advance X-ray diffraction analyses were performed to characterize the crystal structure. SEM—FEI Quanta FEG 250 Scanning electron microscopy was used to investigate surface

morphology. EDX–EDAX Energy-dispersive X-ray spectroscopy mapping analysis was carried out to determine the elemental compositions. Shimadzu - UV Pharmaspec 1700 UV- Vis spectrophotometry measurements were carried out to analyze optical transmittance. Horiba- FluoroMax-4 photoluminescence spectrophotometer was used to examine the luminescence properties of all the samples.

### 3. Results and discussion

Figure 2 shows the XRD spectra of ZnO nanorods. All the diffraction peaks [(001), (002), and (004)] and their positions correspond to a typical ZnO wurtzite crystal structure. Secondary phases of impurity peaks were not detected in the diffraction patterns. A sharp (002) peak was detected for all ZnO nanorods, confirming the preferential orientation of the grains along the c-axis which is orthogonal to the substrate. Also, Figure 2 displays that the intensity of (002) peaks increased with an increase in growth time and temperature. This can be credited to a better crystallinity of the films. The crystallographic parameters found from the diffraction pattern are given in Table 1. Besides, using the SEM images, Table 2 shows that as the growth time and temperature of the NRs increase, their diameters and lengths increase, consequently the volumes of NRs also increase. The *c* lattice parameter of the samples was calculated from the (002) diffraction by the following expression

$$\frac{1}{d^2} = \frac{4(h^2 + hk + k^2)}{3a^2} + \frac{l^2}{c^2} \quad (1)$$

where *d* is the distance of crystalline planes for Miller indices (*hkl*), *a* and *c* are the lattice parameters for hexagonal structure.

The *c* lattice parameter decreased from 5,195 Å to 5.192 Å as growth time increased from 3h to 5 h, confirming a slight reduction in *c* values with increasing growth time (inset of Fig. 2(a)). Similarly, with the increase in the growth temperature from 90 °C to 150 °C, this value decreased from 5.195 Å to 5.180 Å (inset of Fig. 2(b)). This reduction in the *c* lattice parameters can be associated with compressive stress, which occurs owing to increased temperature and growth time [19]. Besides, as shown in Table 1, (002) peaks of the samples shifted towards higher *2θ* angles as the temperature and growth time increased. In a crystal

structure, the compressive stress occurring in the direction parallel to the surface may affect the lattice properties in the direction perpendicular to the surface, which appears with a shifting of diffraction peaks [20, 21]. The stress (*σ*) of lattice along the *c*-axis for the hexagonal crystal structure was calculated from the following expression [17]

$$\sigma = \left[ \frac{2C_{13}^2 - C_{33}C_{11} - C_{33}C_{12}}{C_{13}} \right] \frac{C_0 - C}{C_0} \sigma \left( N/m^2 \right) = -453.6 \frac{(C_0 - C)}{C_0} \quad (2)$$

where *C<sub>ij</sub>* is the elastic stiffness constant of ZnO, while *C<sub>11</sub>* = 209.7 Gpa, *C<sub>12</sub>* = 121.1 Gpa, *C<sub>33</sub>* = 210.9 Gpa, *C<sub>13</sub>* = 105.1 Gpa, *c* is the lattice parameter obtained from the XRD data, and *c<sub>0</sub>* is the strain-free lattice parameter (*c<sub>0</sub>* = 5.205 Å) computed from bulk ZnO [22, 23]. Table 1 illustrates the calculated stress values which are all negative of the samples indicating that the stress on the *c*-axis is compressive [24]. The compressive stress increased considerably from -0,871 GPa to -1,132 GPa, as the growth time increased. Although no change was observed in the stress values of ZnO nanorods for the temperature of 90 °C and 120 °C, when the growth temperature reached 150 °C, it was found to be -2.17 GPa. As mentioned before, a seed layer is coated on the substrate before the hydrothermal growth to prevent the lattice mismatch between the substrate and nanorods, which creates various structural defects on the film surface. Despite this, unhindered thermal and lattice mismatch strain could be responsible for the residual compressive stress in the crystal structure of ZnO [24, 25]. Table 1 displays full-width half maximum (FWHM) values of (002) and the shrinkage of the width of the peaks as the growth time and temperature increase, indicating a particle size increase [26].

Fig. 3 (a) - (d) illustrates the surface morphology of the ZnO nanorods. The SEM images reveal that all ZnO nanorods are grown perpendicular to the substrate. A perfect hexagonal structure is observed for the nanorods grown at different times, as can be seen in Fig. 3 (a) - (c). Note that the hexagonal structure starts to deteriorate resulting in secondary nucleation on the top of the rods, as growth temperature increases from 90 °C to 120 °C (Fig. 3 (e)). When the temperature reaches 150 °C,

pyramid-like structures are formed (Fig. 3 (f)). As it is well known, ZnO consists of polar and non-polar crystal planes, which affect the growth habit of 1D nanostructure such as nanorods [3]. Also, we can conclude that temperature has a strong effect on the axial and lateral growth rate of crystal planes. The difference in the growth velocity between these polar and non-polar planes could be responsible for pyramid-like structures.

Table 2 illustrates that using SEM images given in Figs. 3a-f we calculated the diameters and length of the NRs having 88 nm and 1275 nm, respectively, at 3h growth time and 150°C temperature. As the temperature and growth time increase, the diameters and lengths of NRs increase as shown in Table 2. The results are consistent with the studies of our previous work [27] and in the literature [28, 29].

In our earlier work, we examined the change of morphological properties of ZnO nanorods produced at various growth times and temperatures in detail [27].

Figure 4 shows the elemental distribution of the elements and Fig. 5 shows the EDX mapping spectra and elemental distribution rates of ZnO nanorods grown at 90 °C for 3 h. The purple, yellow and green phases correspond to Zn, O, and Si, respectively. According to the mapping results, the sample contains only two elements, Zn and O confirming that no elemental impurity is observed. Silicon peak appearing in the spectrum comes from the glass substrate. Also, it can be said that elemental distribution is quite homogeneous in ZnO nanorod arrays. According to the data given in Fig. 5, the elemental concentrations for Zn and O are 77.33 and 18.67 at weight %, respectively, while they are 46.83 and 47.46 at atomic %.

The optical transmittance spectra of ZnO nanorods are given in Fig. 6 (a) and (b). As can be seen from the figures, all the samples exhibit high transmittance in the visible (Vis) region and low transmittance in the ultraviolet (UV) region, which is a typical feature of ZnO [30]. The values of average optical transmittance are given in Table 3. According to the table, for the sample grown for 3 hours, the average optical transmittance corresponds to about 86 %, indicating that the film is transparent in the visible region (400-800 nm). This relatively high optical transmittance in the visible region decreases as growth time increases to 5 hours. The decrease in transmittance with the increase in growth time was

observed quite frequently in previous studies [31, 32]. According to Fig. 6 (b), for the sample grown at 90 °C, the average optical transmittance in the visible region is about to 86 %, which decreases to about 62 % as the growth temperature increases to 150 °C.

Many parameters affect the optical transmittance characteristics of one-dimensional ZnO nanostructures. The most crucial ones can be given as surface roughness, film thickness, crystal defects, oxygen vacancies, and impurities [33]. In our study, as shown in Tables 2 and 3, optical transmittance values depend on NRs' diameters and lengths. The average optical transmittance and band gap values decreased as the diameters and lengths of NRs increased, consequently, the volumes of NRs increased. Thus, the decrease in transmission may be related to the higher ZnO NRs' volume and the higher number of defects, and the increase in film thickness which is consistent with earlier reports [31,34]. Besides, it has been shown both theoretically and experimentally that the surface roughness has a significant effect on the optical transmittance of the thin films [35, 36]. Thus, it can be said that multiple random optical scattering on rough surfaces may result in lower transmittance in ZnO nanorods. The increment in both thickness and roughness of ZnO nanorods with increasing temperature and growth time was reported in our previous study [27]. Moreover, from a transmittance spectrum, the following equation gives

$$T = (1 - R)^2 \exp(-\alpha d) \quad (3)$$

the absorption coefficient  $\alpha$  where the transmittance is  $T$ , the reflectance is  $R$ , the thickness of the films is  $d$ . In the direct-transition-type semiconductors such as ZnO, we use  $\alpha$  to determine the energy band gap by applying the Tauc's plot method [37] as

$$E_g)^{1/2} \quad \alpha h\nu = (h\nu - E_g)^{1/2} \quad (4)$$

where the absorption coefficient is  $\alpha$ , Planck's constant is  $h$ , the transition frequency is  $\nu$  and  $E_g$  is the bandgap. The insets in Figures 6 a-b display the Tauc plots of the ZnO nanorods. The approximate  $E_g$  values of ZnO nanorods from the plots are given in Table 3. A reduction is observed in  $E_g$  values for all

the samples with increasing temperature and growth time. According to the previous reports, many factors affect the bandgap of ZnO, including residual strain, crystal defects, carrier concentration, and grain size confinement [38-41]. Thus, larger grain sizes of ZnO nanorods may be responsible for the decrease in energy band values due to the quantum size effect [42].

To study the crystal quality, defect type, and defect density of semiconductor materials, the photoluminescence spectra are widely used. Therefore, photoluminescence measurements are performed to analyze the effect of growth time and temperature on the photoluminescence properties of ZnO nanorods. Xenon arc-lamp is used as the light source and ZnO nanorods are excited at 365 nm. Figures 7 a-b display the fitted photoluminescence spectra of ZnO nanorods produced at various growth times and temperatures, respectively. There are two dominant emissions; sharp ultraviolet emission peak, and broad visible emission band, which correspond to the typical n-type ZnO semiconductor. Ultraviolet emission is responsible for the crystallization quality and the defect quantity of ZnO. And visible region emission is in charge of originating from defects. Besides, a few weak peaks were observed between 450 nm and 500 nm, which came from the use of the Xenon lamp [43, 44].

In the UV region, a sharp transition peak corresponding to band edge emission was observed at around 392-395 nm for ZnO nanorods. This emission in the UV region generally was attributed to the near band edge (NBE) transition as a common optical property of a wide bandgap of ZnO. NBE emission originated from the excitonic transitions between electrons and holes, in the conduction band and the valance band, respectively [45]. The stronger ultraviolet emission is observed in ZnO with higher crystallization quality and lesser defect. At the growth time of 4h, ZnO nanorods exhibited the lowest NBE emission, while a significant increase in this emission was observed with the growth time of 3 and 5 h (Fig. 7 (a)). The highest UV emission was observed at the growth temperature of 150°C while the lowest one was obtained at 120°C (Fig. 7 (b)). Thus, the growth time and temperature increments improved the crystallization quality of the ZnO nanorods.

The second dominant broad emission band is a visible region. The deep-level (DL) emission (a.k.a. visible emission) is assigned to impurities or defects including oxygen vacancies ( $V_o$ ), zinc interstitial

( $Zn_i$ ), zinc vacancies ( $V_{zn}$ ), oxygen antisite ( $O_{zn}$ ) and oxygen interstitial ( $O_i$ ) in ZnO crystal structure [45, 46]. These defects are divided into two parts; zinc interstitial ( $Zn_i$ ), and oxygen vacancies ( $V_o$ ), are donor and zinc vacancies ( $V_{zn}$ ), oxygen interstitial ( $O_i$ ) and oxygen antisite ( $O_{zn}$ ) are acceptors.

A decrease in DL peak intensities was observed as the growth time and temperature increased. This result can be attributed to reduced defects in the ZnO crystal structure, which is also supported by the XRD analysis. However, as seen in Figs 7(a)-(b), it is very difficult to get information about how the defects change in the visible region. Therefore, a detailed examination of the origin of the defects in the visible region is required. In the literature, the visible emissions of ZnO, originating from defects, were extensively studied by the researchers, the underlying mechanisms were still not fully identified. Therefore, the photoluminescence spectra were subjected to Gaussian decomposition to the subpeaks according to their origination.

The photoluminescence spectra of the ZnO nanorods were employed using Gauss decomposition to determine the luminescence measurements in detail. "Fityk" software was used to obtain Gaussian decomposition. The following function was used to determine the spectrum curves model in Gauss decomposition

$$f(\lambda) = ae^{-(\lambda-b)^2/2c^2} \quad (5)$$

and depicted in Figures 8 and 9.

As seen in Figures 8 and 9, the nine fundamental Gaussian decompositions of photoluminescence spectra were displayed versus emission wavelength for various growth times and temperatures. The peak labels with areas, positions center and FWHM of these curves varied according to the various growth times and growth temperatures of ZnO nanorods as indicated in Tables 4 and 5. These peaks belonged to various emissions; two ultraviolet emissions (Peaks 1 and 2), one violet emission (Peak 3), two blue emissions (Peak 4 and Peak 5), two yellow-orange emissions (Peaks 6 and 7), and two red emissions (Peaks 8 and 9) as shown in Figs. 8 and 9 and Tables 4 and 5. There were two dominant emission peaks one of which was the ultraviolet (Peaks 1 and 2) and the other the visible region (Peaks 6, 7, 8, and 9). Also, a few weak peaks were detected between 450 nm and 500 nm two blue emissions (Peaks 4 and 5), which came from the use of a Xenon lamp [43, 44].

In Tables 4 and 5, the emission regions could be explained as the following: Ultraviolet emissions from 360 to 390 nm could be attributed to the NBE of ZnO as an indication of the excitonic characteristic; violet-blue emissions (390–492 nm) might be credited to the transition of electrons from zinc interstitials ( $Zn_i$ ) to the valance band; yellow-orange emissions (560–620 nm) could be because of the double-charged oxygen vacancy ( $V_o^{++}$ ), the red emission (620–690 nm) and (690–750 nm) might be ascribed to oxygen interstitials ( $O_i$ ) and oxygen vacancies ( $V_o$ ), respectively [46-51].

A fluctuation was detected for Peak 1, Peak 2, and Peak 3 intensities the samples produced at various growth times as shown in Fig. 8. That is to say, Peak 1 and 2 have the highest intensities for the growth time of 3h while the lowest intensity was observed for the growth time of 4h. Accordingly, exciton transitions were observed to be more frequent for the growth time of 3h compared to the growth time of 4h. On the other hand, Peak 3 emission corresponding to ( $Zn_i$ )  $\rightarrow$  ( $V_B$ ) transitions increased in 4h and decreased in 5h [39, 40]. Similarly, the same fluctuation was perceived for Peak 1, Peak 2, and Peak 3 for the samples produced at the various growth temperatures. Depending on the peak areas given in Table 5, the highest excitonic transitions (Peak 1 and Peak 2) were observed for the sample produced at 90°C while the lowest one was observed for 120°C. The same behavior was observed for Peak 3 corresponding to ( $Zn_i$ )  $\rightarrow$  ( $V_B$ ) transitions.

Moreover, the second dominant and broad visible region (DL emission) consists of yellow-orange and red emission peaks for all ZnO nanorods in the wavelength range of 580–690 nm as illustrated in Figs. 8 and 9. In the yellow-orange region, a decrease was observed in the height of Peak 6 while an increase was observed for Peak 7 attributing to fluctuations in this region. Yellow-orange emission has been associated with double charged oxygen vacancies ( $V_o^{++}$ ) [47-51]. A fluctuation was also detected for the red emission peaks, namely, the emission intensity of Peak 7 increased when the growth time increased, whereas that of Peak 8 and Peak 9 increased at the growth time of 4h and then decreased at 5h. Depending on the spectra, it could be said that there is an increase in the red emission intensity up to 4h. These imply that as the double charged oxygen vacancy ( $V_o^{++}$ ) (donor) decreased whereas oxygen interstitials ( $O_i$ ) (acceptor) increased in ZnO nanorods grown at different times. It is stated in [52] that the ratio of PL intensities is the same as the ratio of defect concentrations.

Because of that, the decreasing tendency of the intensity of the shoulder region of PL spectrums designates that growth time and temperature reduce defect concentration in the crystal.

For the various growth temperatures, ZnO nanorods exhibit different emission behaviors in the yellow-orange region, namely, for Peak 6, a gradual decrease was observed with the increase in growth temperature. On the other hand, Peak 7 decreased significantly with increasing temperature from 90°C to 120°C but increased sharply at the temperature of 150 °C. Accordingly, it can be said that oxygen vacancies displayed a noteworthy decline when the growth temperature reaches 150°C.

With the increase in temperature from 90°C to 150°C, the intensity of Peak 8 decreased gradually as can be seen in Table 5. Nevertheless, a decrease was observed at 120°C whereas an increase was observed at 150°C for the emission intensity of Peak 9 confirming a fluctuation in emission characteristics of ZnO nanorods, as well. However, it means that the oxygen interstitials ( $O_i$ ) decreased at 120°C while increased at 150°C in the crystal structure.

Thus, it can be said that growth temperature plays a crucial role in reducing oxygen defects in ZnO nanorods. This outcome is also in excellent agreement with the XRD spectrums. Generally, crystal structure defects are detected repeatedly in 1D ZnO nanostructures produced by hydrothermal synthesis using low growth temperatures. Accordingly, we can conclude that the responses in the hydrothermal method may cause the double charged oxygen vacancies/oxygen interstitials and thus affect the luminescence properties of ZnO nanorods [53-55]. So, ZnO nanorods should be fabricated by choosing the appropriate surge time and temperature according to the defect ( $V_o$ - donor or  $O_i$ - acceptor) depending on the usage place.

#### 4. Conclusion

On glass substrates, ZnO nanorods were produced effectively by a hydrothermal route. The special effects of surge time and temperature on structural and optical properties of ZnO nanorods were examined at length. X-ray diffraction findings established that all the ZnO nanorods had a typical hexagonal wurtzite crystal structure without secondary phases. Improvement was observed in the crystal quality of the films as the surge time and temperature increase. Further, there was no elemental impurity phase, which was proved by elemental mapping analyzes. We obtained pyramid-like ZnO nanorods at the growth of a temperature of 150 °C. Thus, it could be concluded that surge

temperature had a robust influence on the form of the rods. The average optical transmittance and band gap values decreased as surge time and temperature increased. With a rise in surge time, the double charged oxygen vacancies ( $V_o^{++}$ ) (donor) decreases whereas oxygen interstitials ( $O_i$ ) (acceptor) increases. However, growth temperature decreases ( $V_o^{++}$ ) (donor) and increases ( $O_i$ ) (acceptor). The simple and inexpensive hydrothermal route could be used to obtain ZnO nanorods with good crystal quality. These ZnO nanorods with enhanced UV light emission property and tunable bandgap and defect (double-charged

oxygen vacancy/oxygen interstitials) characteristics could be a promising material for nanoscale optoelectronic devices.

### Acknowledgments

This work was supported by the Scientific Research Projects Coordination Department of Kastamonu University (Project No: KU-BAP01/2017-35, KU-BAP01/2017-17 and KU-BAP01/2018-19) and Research Fund of Bahcesehir University, Istanbul, Turkey (Project No: BAP-2021.01.27 and BAP.2019-01.04).

### References

- [1] Z.L. Wang, J. Phys. Condens. Matter. 16, R829 (2004).
- [2] M. Tosun et al., J. Mol. Struct. 1212,128071(2020).
- [3] Ü. Özgür et al., J. Appl. Phys. 98, 1 (2005).
- [4] H. Wei et al., Mater. Sci. Eng. A. 393, 80 (2005).
- [5] J. Liu et al., Compos. Part B Eng. 99, 366 (2016).
- [6] H. Hosono et al., Thin Solid Films. 515, 6000 (2007).
- [7] C. Madhu et al., Journal of Elec Materi 47, 7409 (2018).
- [8] D. Thomas et al., Journal of Elec Materi 48, 4726 (2019).
- [9] M. Law et al., Nat. Mater. 4, 455 (2005).
- [10] Y. Liu et al., J. Nanomater. 2013, 1 (2013).
- [11] B. Liu et al., J. Am. Chem. Soc. 125, 4430 (2003).
- [12] O.A. Gorlenko et al., Precis. Eng. 3,105 (1981).
- [13] Chu-Chi Ting et al., Thin Solid Films, Volume 518, Issue 15, 4156 (2010).
- [14] A. Goktas, Journal of Alloys and Compounds 735, 2038 (2018).
- [15] E. Asikuzun et al., Journal of Molecular Structure 1165, 1 (2018),
- [16] D. Akcan et al., Journal of Alloys and Compounds 797, 253 (2019).
- [17] M. Tosun et al., Ceramics International 45(13), 16234 (2019).
- [18] D. Akcan et al., Journal of Molecular Structure 1161, 299 (2018).
- [19] M. Riaz et al., Nanotechnology. 19, 415708 (2008).
- [20] R. Lohmann et al., Mater. Sci. Eng. A. 139, 259 (1991).
- [21] S.S. Lin et al., Surf. Coatings Technol. 176, 173 (2004).
- [22] M.K. Puchert et al., J. Vac. Sci. Technol. A. 14, 2220 (1996).
- [23] P. Paufler et al., Cryst. Res. Technol. 18, 1318 (1983).
- [24] C. Li et al., Appl. Surf. Sci. 253, 4000 (2007).
- [25] O.F. Farhat et al., Beilstein J. Nanotechnol. 6, 720 (2015).
- [26] K. Kulkarni et al., Thin Solid Films, Volume 345, Issue 2, 273 (1999).
- [27] S. Kaya et al., Ceramics International, Volume 46, Issue 10, Part A, 15183 (2020).
- [28] M. Kamruzzaman et al., Crystallogr Reports 63, 456 (2018).
- [29] G. Amin et al., J Nanomater 2011,1(2011).
- [30] A. Abdulrahman et al., Dig. J. Nanomater. Biostructures. 12, 1001 (2017).
- [31] S. Lin et al., Nanoscale Res. Lett. 8 (2013)
- [32] M.F. Malek et al., Jpn. J. Appl. Phys. 55 (2015)
- [33] S.H. Mohamed et al., J. Phys. Chem. Solids. 67, 2351 (2006).
- [34] M.F. Malek et al., AIP Conf. Proc. 1733, 20014 (2016).
- [35] M.M. Wind et al., Phys. A Stat. Mech. Its Appl. 125, 75 (1984).
- [36] C.Y. Tsay et al., Thin Solid Films. 517, 1032 (2008).
- [37] L.M. Salinger, The Physics of Thin Film Optical Spectra, Springer-Verlag, Berlin/Heidelberg, 2005.
- [38] V. Srikant et al., J. Appl. Phys. 81, 6357 (1997).
- [39] B.Z. Dong et al., J. Appl. Phys. 101, 33713 (2007).
- [40] K. Sakai et al., J. Appl. Phys. 99 (2006).
- [41] B.L. Zhu et al., Jpn. J. Appl. Phys. 45, 7860 (2006).
- [42] Y.J. Xing et al., Appl. Phys. Lett. 83, 1689 (2003).
- [43] T. Premkumar et al., ACS Appl. Mater. Interfaces. 2, 2863 (2010).
- [44] S. Sahoo et al., J. Phys. Chem. C. 113, 16927 (2009).

- [45] F. Wen et al., Solid State Commun. 135, 34 (2005).  
 [46] D. Motaung et al., MaterialsLetters. (139), 475 (2015).  
 [47] S. D. Senol et al., J. Alloy. Comp. 822,153514 (2020).  
 [48] D.E Motaung et al., ACS Appl. Mater. Interfaces 6 (12), 8981 (2014) .  
 [49] X.F. Liu et al., Materials Letters, 92,405 (2013).  
 [50] A.B. Djuriscic et al., Adv Funct Mater, 14, 856 (2004).  
 [51] B. Panigrahy et al., Adv Funct Mater, 20(7):1161 (2010).  
 [52] M.A. Reshchikov et al., Sci. Rep. 7, 1 (2017).  
 [53] S.-H. Jeong et al., Appl. Phys. Lett. 82, 2625 (2003).  
 [54] M. Fang et al., Mater. Sci. Semicond. Process. 57, 233 (2017).  
 [55] L.H. Quang et al., J. Cryst. Growth. 287, 157 (2006).

**Table 1.** Crystallographic parameters and grain size of ZnO nanorods were obtained from the diffraction patterns.

<i>Sample</i>	<i>2θ at (002) plane (°)</i>	<i>FWHM of peak (002) (°)</i>	<i>Grain size (nm)</i>	<i>c lattice paramete r (Å)</i>	<i>Stress (σ) (GPa)</i>
<i>3h</i>	34,46	0.199	42.95	5,195	-0,871
<i>4h</i>	34,47	0,156	54.79	5,194	-0,958
<i>5h</i>	34,48	0,169	50.57	5,192	-1,132
<i>90 °C</i>	34,46	0.199	42.95	5,195	-0,871
<i>120 °C</i>	34,46	0,164	52.11	5,195	-0,871
<i>150 °C</i>	34,63	0,167	51.20	5,180	-2,17

**Table 2.** Diameter, length, and aspect ratio for ZnO NRs at various growth times and temperatures.

<i>Sample</i>	<i>Diameter (nm)</i>	<i>Length (nm)</i>	<i>Aspect ratio</i>
<i>3h</i>	59	512.7	8.68
<i>4h</i>	72	586.9	8.15
<i>5h</i>	97	673.4	6.94
<i>90 °C</i>	59	512.7	8.68
<i>120 °C</i>	74	664.2	8.97
<i>150 °C</i>	88	1275	14.48

**Table 3.** Average optical transmittance and band gap values of ZnO nanorods.

Sample	Transmittance (%)	Band Gap (eV)
3h	86	3.25
4h	72	3.18
5h	69	3.11
90 °C	86	3.25
120 °C	73	3.19
150 °C	62	3.03

**Table 4.** Comparison of peak center, FWHM, and area of photoluminescence emission values of the ZnO nanorods at various growth times.

Peak Label	3h		4h		5h		Emission Range	Emission Origin	
	Peak FWHM (nm)	Peak Area (a.u)	Peak FWHM (nm)	Peak Area (a.u)	Peak FWHM (nm)	Peak Area (a.u)			
Peak 1 (392.17 nm)	19,91	3 080 040	15,85	1 121 260	17,83	1 146 340	Ultraviolet	Exciton	NBE Emission
Peak 2 (401.51 nm)	32,99	3 745 650	33,53	2 732 490	36,92	2 120 730	Ultraviolet	Exciton	
Peak 3 (415.02 nm)	124,94	14 979 800	164,69	16 110 200	214,30	14 439 200	Violet	(Zn <sub>i</sub> ) → (V <sub>B</sub> )	
Peak 4 (451.33 nm)	5,368	36 558	5,29	27 096	6,73	3 0585,5	Blue	Xenon lamp	DL Emission
Peak 5 (467.94 nm)	10,04	202 941	8,96	132 936	9,26	111 974	Blue	Xenon lamp	
Peak 6 (580.97 nm)	169,64	42 578 000	107,46	8 196 370	93,18	515 8150	Yellow-Orange	(V <sub>o</sub> <sup>++</sup> )	
Peak 7 (619.18 nm)	22,07	164 716	34,87	432 891	40,34	666 220	Yellow-Orange	(V <sub>o</sub> <sup>++</sup> )	
Peak 8 (651.08 nm)	21,53	244 956	35,69	357 028	33,02	289 594	Red	(O <sub>i</sub> )	DL Emission
Peak 9 (669.35 nm)	41,27	843 875	90,13	4 300 870	85,03	3 960 580	Red	(O <sub>i</sub> )	

**Table 5.** Comparison of peak center, FWHM, and area of photoluminescence emission values of the ZnO nanorods at various growth temperatures.

Peak Label	90°C		120°C		150°C		Emission Range	Emission Origin	
	Peak FWHM (nm)	Peak Area (a.u)	Peak FWHM (nm)	Peak Area (a.u)	Peak FWHM (nm)	Peak Area (a.u)			
Peak 1 (392.17 nm)	19,91	3 080 040	20,50	875 093	21,03	1 171 400	Ultraviolet	Exciton	NBE Emission
Peak 2 (401.51 nm)	32,99	3 745 650	30,70	1 162 870	45,62	1 598 260	Ultraviolet	Exciton	

Peak 3 (415.02 nm)	124,94	14 979 800	100,74	4 136 750	210,11	7 314 880	Violet	$(Zn_i) \rightarrow (V_B)$	DL Emission
Peak 4 (451.33 nm)	5,368	36 558	4,06	2 432,7	14,86	53 205,7	Blue	Xenon lamp	
Peak 5 (467.94 nm)	10,04	202 941	8,206	33 533,7	11,05	79 236	Blue	Xenon lamp	
Peak 6 (580.97 nm)	169,64	42 578 000	193,39	8 526 450	117,21	3 923 950	Yellow-Orange	$(V_o^{++})$	
Peak 7 (619.18 nm)	22,07	164 716	21,96	1,4	16,29	20 235,9	Yellow-Orange	$(V_o^{++})$	
Peak 8 (651.08 nm)	21,53	244 956	19,84	50 416,4	22,90	5,09	Red	$(O_i)$	
Peak 9 (669.35 nm)	41,27	843 875	22,20	41 887	89,10	1 648 260	Red	$(O_i)$	

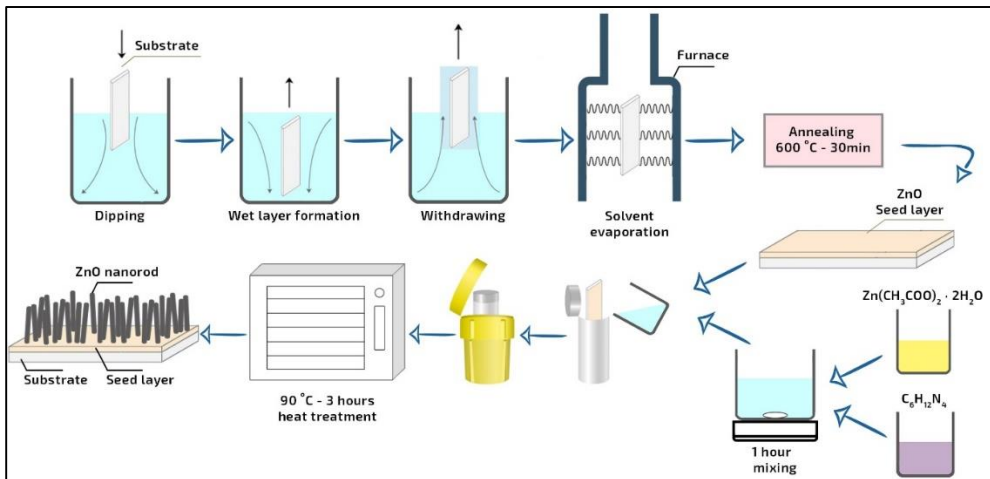


**Fig. 1.** Schematic diagram of the production process of ZnO nanorods.

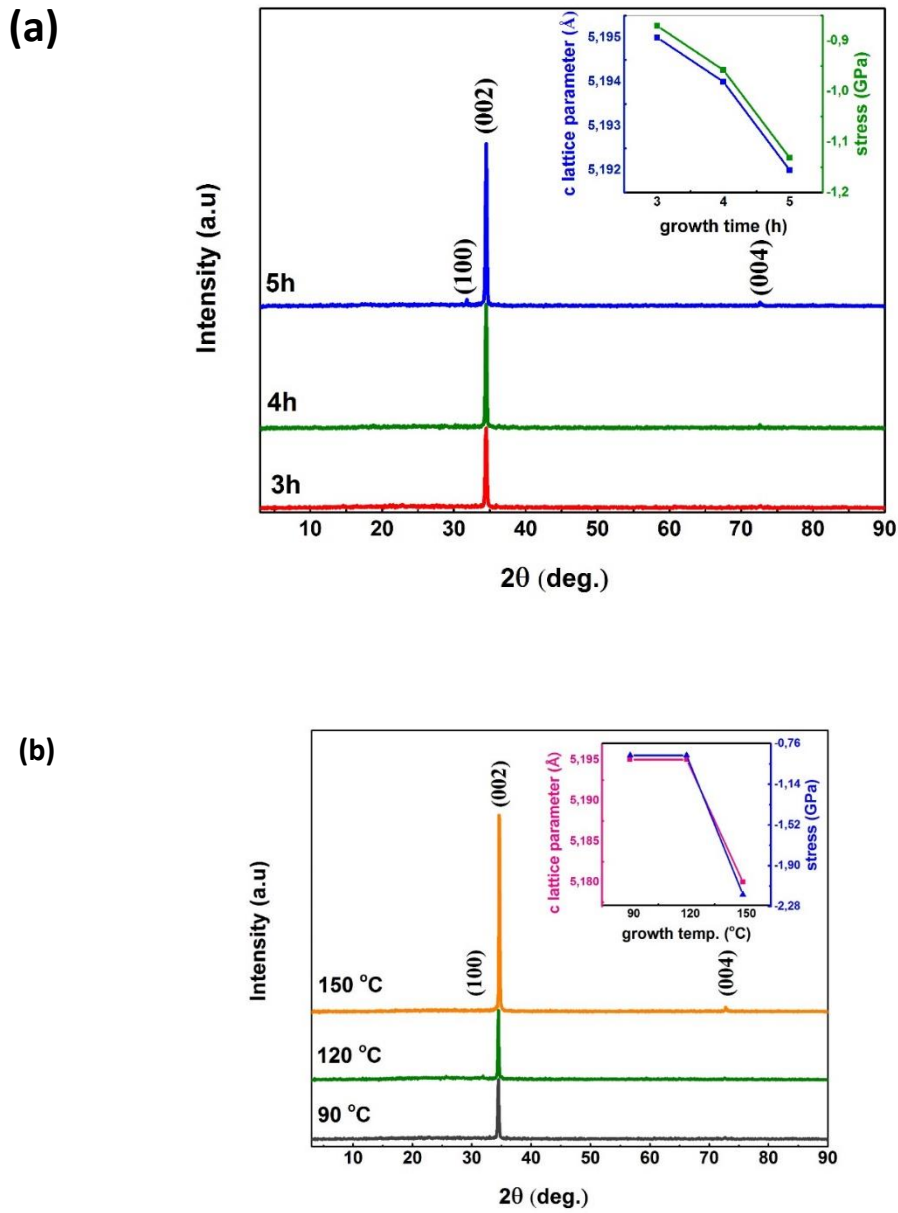


**Fig. 2.** Diffraction patterns of ZnO nanorods produced at (a) various growth temperatures, (b) various growth times. The insets show the plot of the variation of the c lattice parameter for growth parameters (time and temperature).

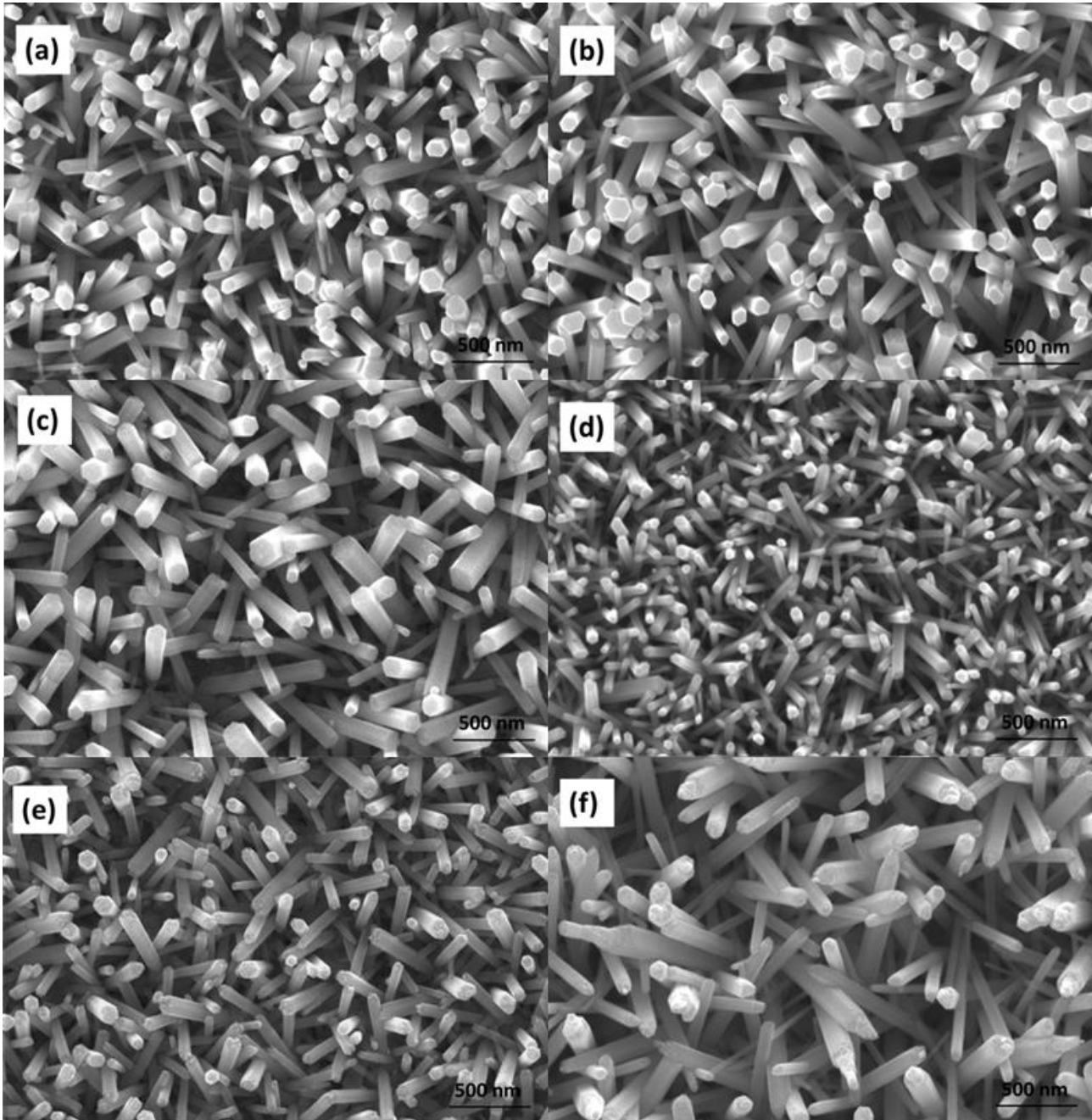


**Fig. 3.** SEM images of ZnO nanorods produced at various growth times as (a) 3h, (b) 4h, (c) 5h at 90 °C and growth temperatures as (d) 90 °C, (e) 120 °C, (f) 150 °C in 3h growth time.

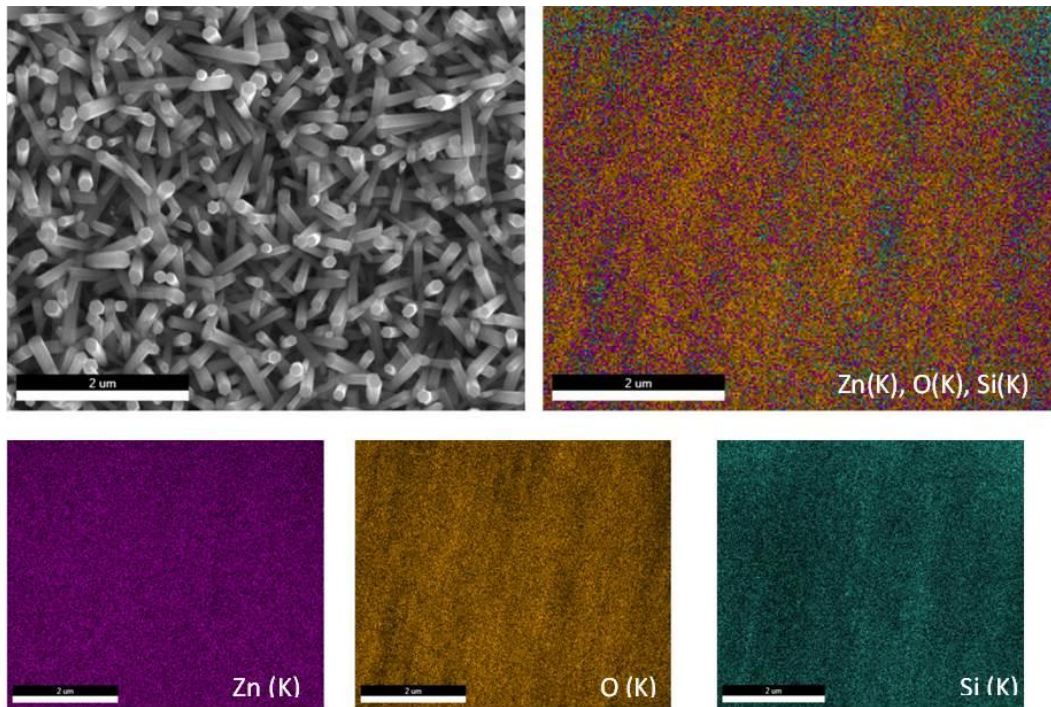


Fig. 4. EDX mapping images of ZnO nanorods grown at 90 °C for 3 h.

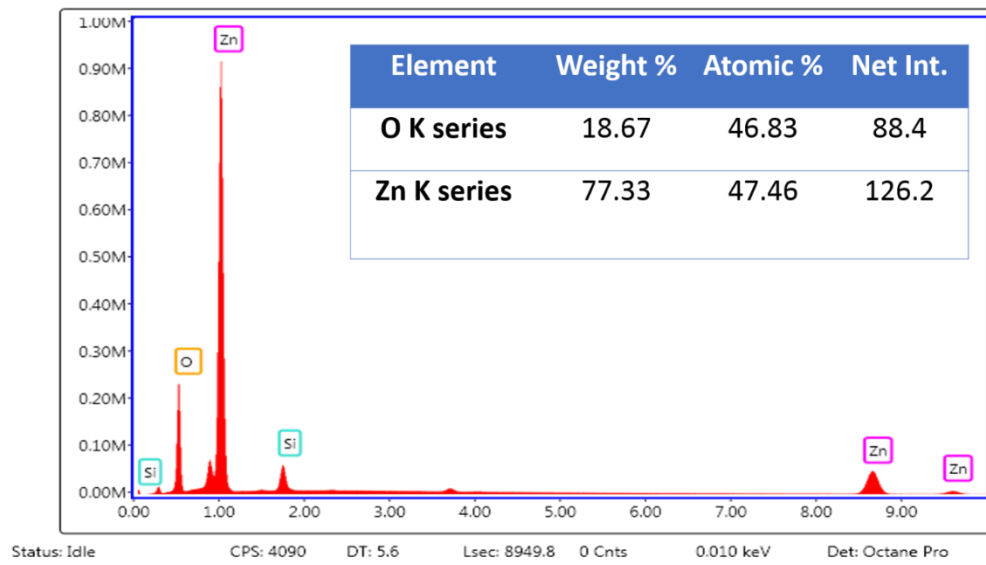
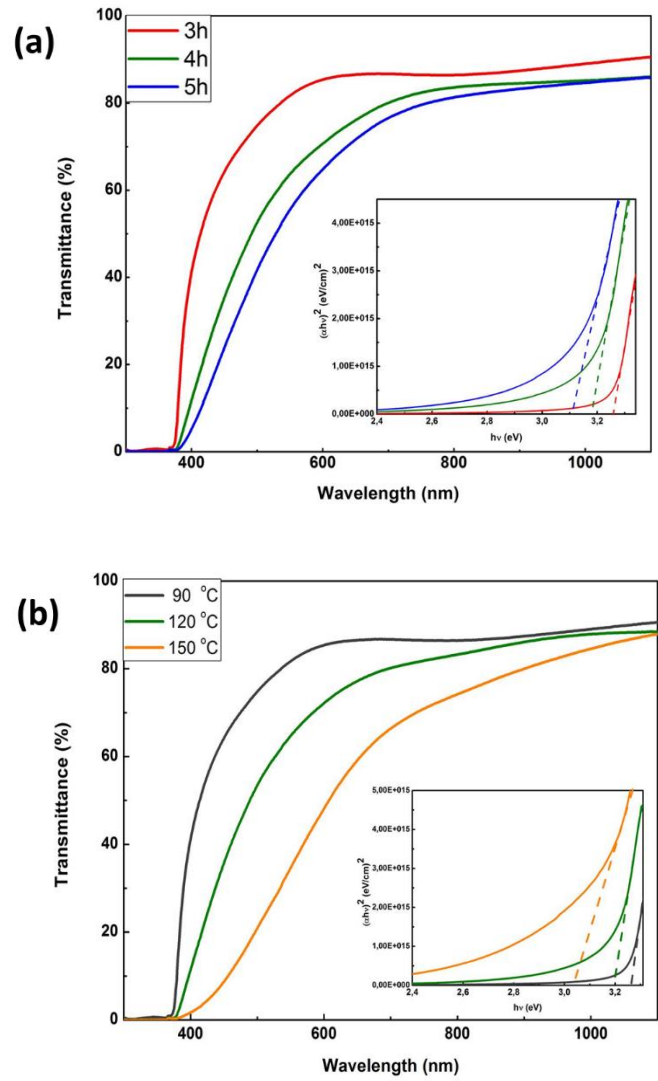
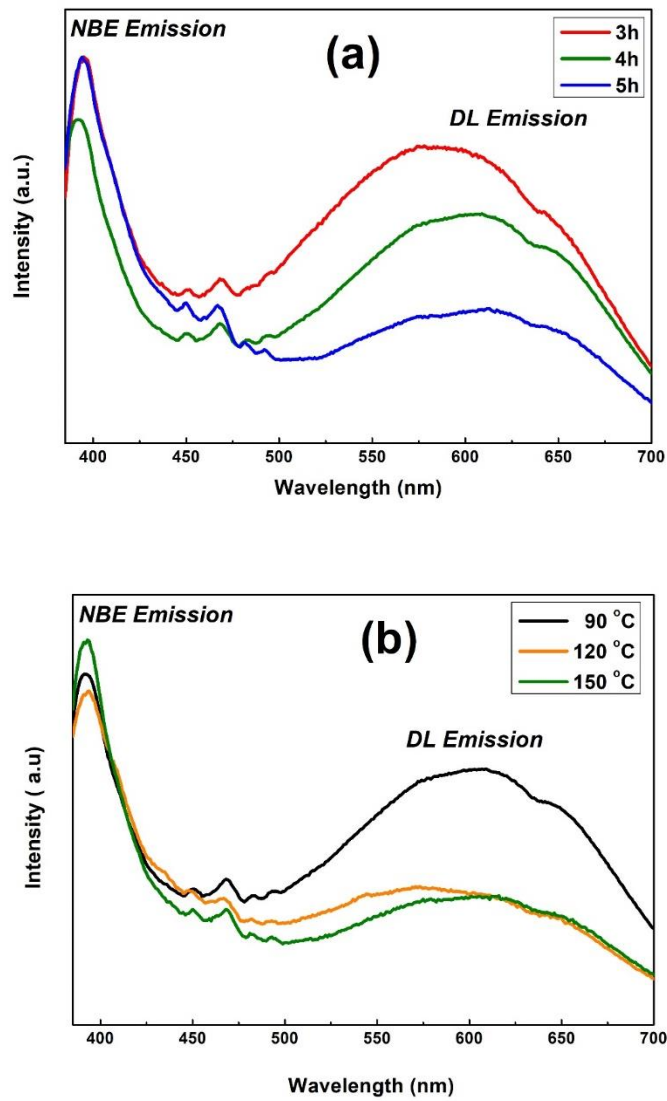


Fig. 5. The EDX mapping spectra and elemental distributions rates of ZnO nanorods grown at 90 °C for 3 h.



**Fig. 6.** Transmittance spectra and Tauc plot (shown in inset) of ZnO nanorods produced at (a) various growth times and (b) various growth temperatures.



**Fig. 7.** Photoluminescence e spectra of ZnO nanorods produced at (a) various growth times and (b) various growth temperatures.

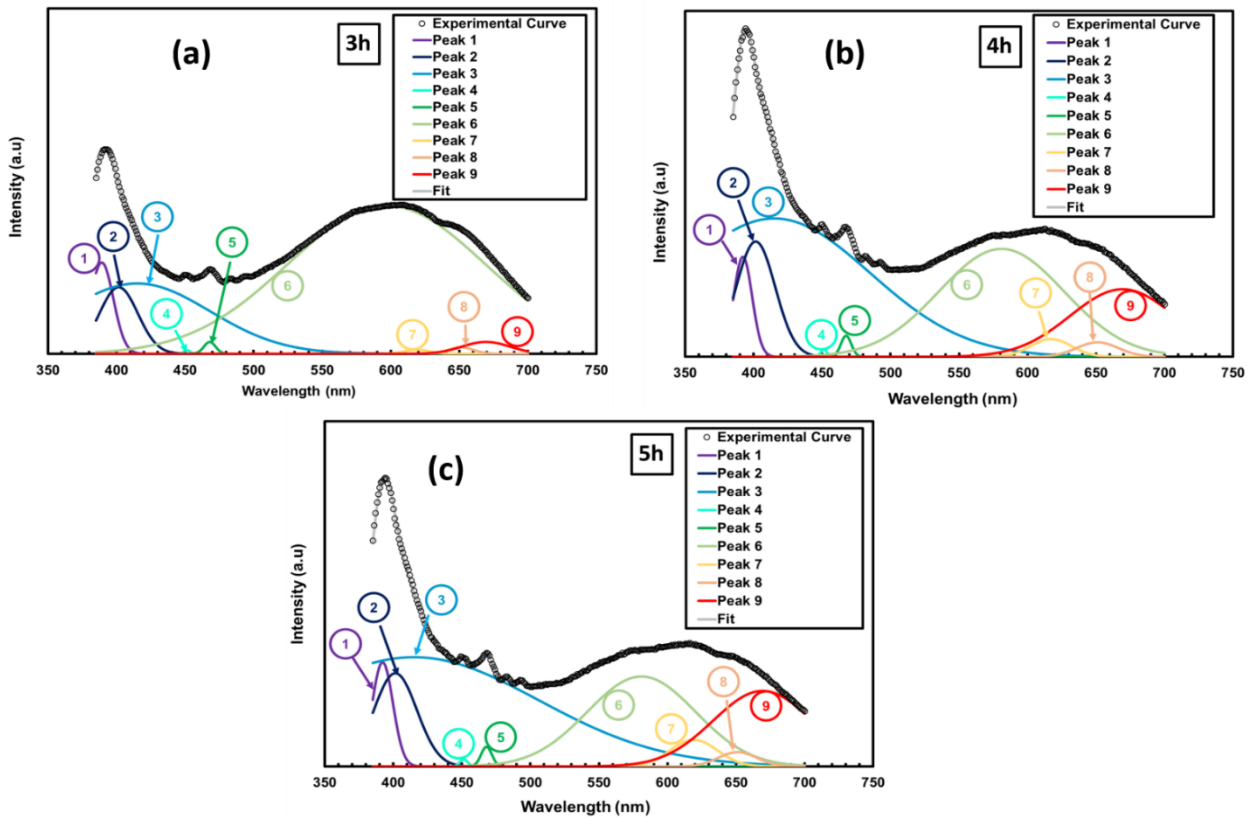


**Fig. 8.** Gaussian decompositions of photoluminescence spectra of the ZnO nanorods at various growth times a) 3h, b) 4h, and c) 5h at 90°C.

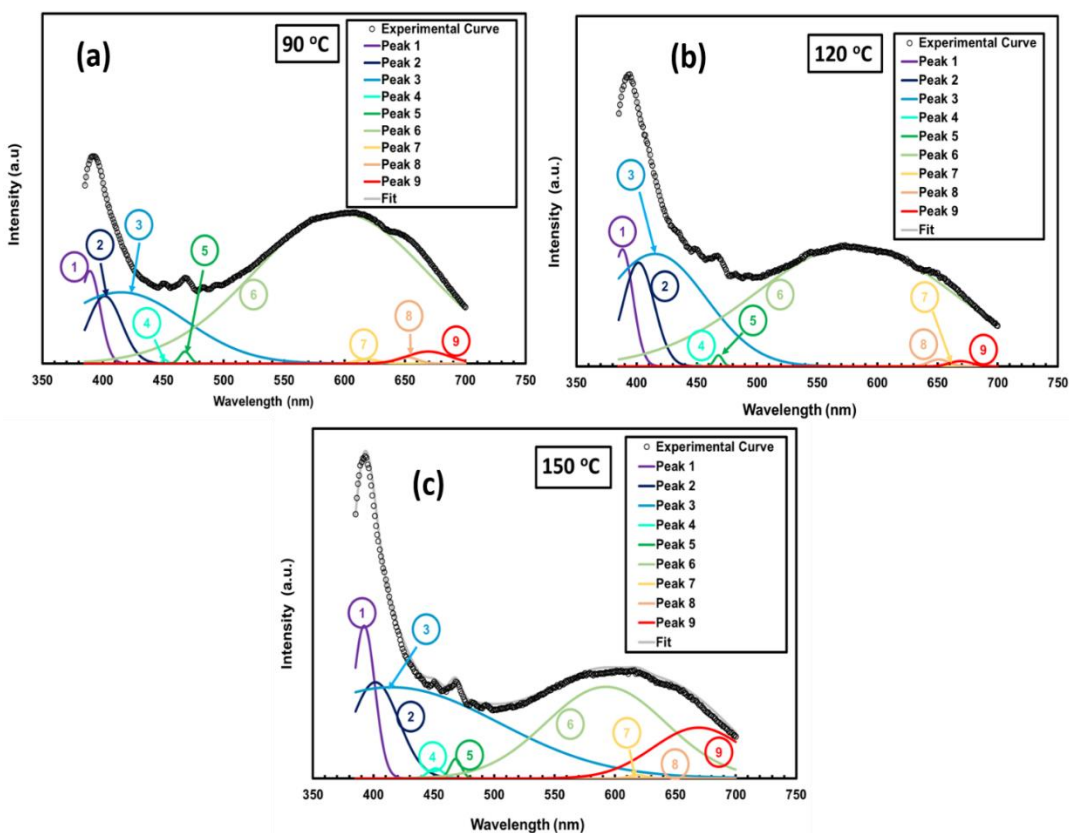


**Fig. 9.** Gaussian decompositions of photoluminescence spectra of the ZnO nanorods at various growth temperatures a) 90°C, b) 120°C and c) 150°C in 3h growth time.

## **Carbide-Free Bainitic Steels-A Short Review**

**Omer SAHIN**

*Department of Metallurgical and Materials Engineering, Faculty of Technology, Gazi University,  
Teknikokullar, Ankara, 06560, Turkey  
ORCID:0000-0002-2446-2512*

**Volkan KILICLI**

*Department of Metallurgical and Materials Engineering, Faculty of Technology, Gazi University,  
Teknikokullar, Ankara, 06560, Turkey  
ORCID: 0000-0002-0456-5987*

*Cite this paper as: Sahin, O,Kilicli, V. Carbide-Free Bainitic Steels-A Short Review.Int. Conf. Advanced. Mater. Sci. & Eng. HiTech.and Device Appl.Oct. 27-29 2022,Ankara, Turkey*

### **Abstract.**

In this study, carbide-free bainitic steels (CFBS) developed in recent years were investigated by making a short literature survey. In the presented study, the chemical composition, production, microstructure and mechanical properties of CFBS's were given and the transformation mechanisms were investigated. CFBSs can be produced with high mechanical properties (strength, hardness, fracture toughness, etc.) without the need to add expensive alloying elements and without the need for mechanical processes (rolling, forging, etc.). As it is known, advanced high strength steels are produced by thermomechanical rolling processes in large and complex rolling lines. In addition, strict process controls are needed in the production of these steels. Therefore, the cost of advanced high-strength steels is relatively high compared to other steel products. CFBSs, which can be produced at low cost thanks to their well-known heat treatment process, have great importance in science and industry as they are an alternative to reduce to cost of a steels such as 3rd generation advanced high strength steels, armor steels and maraging steels.

**Keywords:** Bainite, High silicon cast steel, Carbide-Free Bainite, Nano-Bainite, Austenitizing, Austempering  
© 2022 Published by ICMATSE

### **1. Introduction**

Carbide-free bainitic steels (CFBS) have been developed in recent years and are a new type of advanced high-strength steel. They have microstructures of ultra thin carbon-rich stable austenite and bainitic ferrite plates. CFBSs can be produced at low cost by heat treatment processes, without the need for expensive alloying elements and complex mechanical processes. Due to its superior mechanical properties (high strength, high hardness and high fracture toughness), it is an alternative to all steels requiring high strength in the machinery, automotive, defense and aerospace industries.[1-7]

### **2. Carbide-Free Bainite Steels**

Structures consisting of very thin bainitic ferrite plates 20-40 nm thick in a carbon-rich austenitic matrix are called "carbide-free bainite" (Figure 1). [8]. [9-11]. CFBSs can have high strength, ductility and even acceptable toughness values. It is

noteworthy that high toughness values are obtained that cannot be ignored at low temperatures.[9, 12]. Caballero ve Bhadeshia [13] reported that they obtained carbide-free bainitic steel for the first time in 2004 in their study titled "Very strong bainite". In their study, bainite formation was obtained in a high carbon and high silicon steel with a minimum transformation temperature of 125 °C. Although the bainite layers formed are very thin, they show high strength and acceptable ductility. It is noteworthy that the extremely fine bainite structure formed is 19 times lower in cost compared to maraging steels and shows similar toughness and strength[12]. It is reported that CFBS perform quite well as armor steel due to their high mechanical properties. [14, 15].

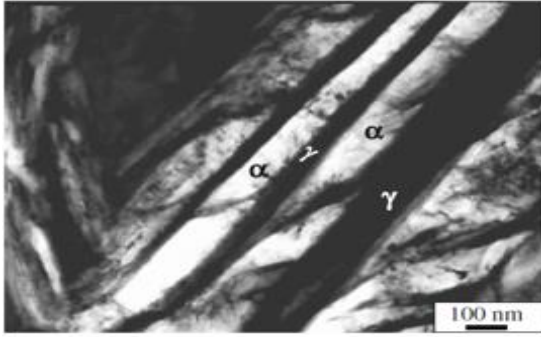


**Figure 1.** Bright field TEM microstructures of nano bainitic steel ( $\alpha$ : bainitic ferrite and  $\gamma$ : carbon-rich stable austenite) [16].

### 2.1. CFBS Chemical Composition

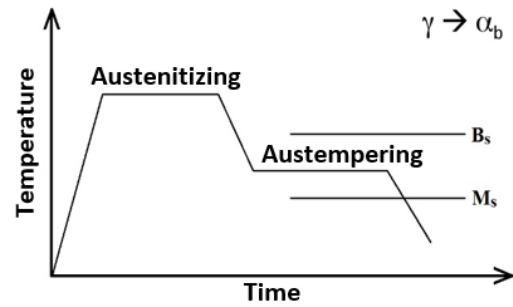
To produce CFBS, the steel must contain C (0.22 - 1.00 %), Mn (0.28 - 2.00 %), Si (1.5 - 3.00 %) and Cr (0.4 - 2.40). The amount of Si in the steel is vital for the production of CFBS and plays a critical role in the phase transformation. In steels containing more than 1.5% by weight of silicon, cementite precipitation is suppressed during isothermal holding, and thus carbide precipitation is hardly observed. [17-27]. The amount of silicon in steel plays an important role in enriching the austenite with carbon. In Table 1, the chemical composition ranges of the steels obtained with nano bainitic microstructure in the literature are given.

Table 1. Typical chemical composition range of CFBS [?]

Element	wt. (%)
C	0,22-1,00
Mn	0,28-2,00
Si	1,5-3,00
Cr	0,4-2.40
Mo	0,01-1,00
Al	0,1-1,00
Co	1,00-1,60
V	0,01-0,1

### 2.2. Heat Treatment for CFBS Production

The production of carbide-free bainite in alloy steels containing at least 1.5% Si by weight is possible with simple heat treatment cycles. In general, CFBS can be produced by isothermal holding just above the  $M_s$  temperature ( $M_s+10^\circ\text{C}$ ) after austenitization (Figure 2). Although different heat treatment cycles are required for each steel, the desired microstructure is obtained as a result of austenitizing at  $900^\circ\text{C}$  for 30 minutes on average, and then isothermal waiting at  $200^\circ\text{C}$  for a long time. [28].



**Figure 2.** Heat treatment cycle for CFBS transformation [28]

### 2.3. Mechanical Properties of Carbide-Free Bainitic Steels

CFBSs can have very high strength and acceptable toughness values. The high mechanical properties are attributed to the 20-40 nm thick bainitic ferrite and high carbon retain austenite laths in the form of nano-sized films in the microstructure of CFBSs [9]. When the studies in the literature are examined, according to the heat treatment and chemical composition parameters (the steels used in the studies have high carbon (0.77-1.02% by weight) and high silicon ( $\text{Si} > 1.5\%$ )) mechanical properties of CFBSs vary between, yield strength between 1400-2000 MPa, tensile strength between 1700-2500 MPa and hardness 600-650 HV. [29-35]

It is noteworthy that CFBSs exhibit toughness values that cannot non-negligible at low temperatures [9]. In addition, it has been determined that the wear resistance of KIBCs is superior to bainitic steels of similar hardness [36].

### 3. Conclusion

Microstructures consisting of very thin bainitic ferrite plates 20-40 nm thick in a carbon-rich austenitic matrix are called "carbide-free bainite".

CFBSs can be produced at low cost by heat treatment processes, without the need for expensive alloying elements and complex mechanical processes.

This structure, which can be obtained in high carbon steels containing minimum 1.5% silicon by weight, has 19 times lower cost compared to maraging steels and shows similar toughness (30-40 MPa  $m^{1/2}$ ) and strength (2500 MPa tensile strength, %5-%30 elongation, 700 HV hardness) draws attention.

Carbide-free bainitic steels are promising for industrial applications due to their high mechanical properties and being economical

CFBSs are a strong alternative to 3rd AHSS with the lowest cost.

## References

1. Murathan, O.F. and V. Kilicli, *Nano Bainitic Steels*. Journal of Polytechnic-Politeknik Dergisi, 2016. **19**(2): p. 115-128.
2. Tenaglia, N.E., R.E. Boeri, and A.D. Basso, *Mechanical properties of a carbide-free bainitic cast steel with dispersed free ferrite*. Materials Science and Technology, 2020. **36**(1): p. 108-117.
3. Tenaglia, N.E., et al., *Development of ultra-high strength carbide-free bainitic cast steels*. International Journal of Cast Metals Research, 2020. **33**(6): p. 258-265.
4. Tenaglia, N.E., et al., *Macro and microstructural characterisation of high Si cast steels - Study of microsegregation patterns*. International Journal of Cast Metals Research, 2017. **30**(2): p. 103-111.
5. Garcia-Mateo, C., C. FG, and B. HKDH, *Development of hard bainite*. ISIJ international, 2003. **43**(8): p. 1238-1243.
6. Bhadeshia, H.K.D.H. and D.V. Edmonds, *Bainite in silicon steels: new composition–property approach Part 1*. Metal Science, 1983. **17**(9): p. 411-419.
7. Santacruz-Londoño, A.F., et al., *Microstructural and mechanical characterization of a nanostructured bainitic cast steel*. Metals, 2020. **10**(5): p. 612.
8. Caballero, F.G., M.K. Miller, and C. Garcia-Mateo, *Carbon supersaturation of ferrite in a nanocrystalline bainitic steel*. Acta Materialia, 2010. **58**(7): p. 2338-2343.
9. Bhadeshia, H.K., *The first bulk nanostructured metal*. Sci Technol Adv Mater, 2013. **14**(1): p. 014202.
10. Rogal, L., et al., *Feasibility study for thixoforming nanostructured bainitic steels*. Materials Science and Engineering a-Structural Materials Properties Microstructure and Processing, 2016. **651**: p. 708-719.
11. Edmonds, D., D. Matlock, and J.G. Speer, *The recent development of steels with carbide-free acicular microstructures containing retained austenite*. La Metallurgia Italiana, 2011. **1**: p. 41-49.
12. Caballero, F.G., et al., *Very strong low temperature bainite*. Materials Science and Technology, 2013. **18**(3): p. 279-284.
13. Caballero, F.G. and H.K.D.H. Bhadeshia, *Very strong bainite*. Current Opinion in Solid State and Materials Science, 2004. **8**(3-4): p. 251-257.
14. Burian, W., et al., *Nanostructured bainite-austenite steel for armours construction*. Archives of Metallurgy and Materials, 2014. **59**(3): p. 1211-1216.
15. Burian, W., et al., *Protection effectiveness of perforated plates made of high strength steel*. International Journal of Impact Engineering, 2019. **126**: p. 27-39.
16. Garcia-Mateo, C., et al., *On measurement of carbon content in retained austenite in a nanostructured bainitic steel*. Journal of Materials Science, 2011. **47**(2): p. 1004-1010.
17. Bhadeshia, H.K.D.H., *Bainite in steels: theory and practice*. 2019: CRC Press.
18. Bhadeshia, H. and R. Honeycombe, *Steels: microstructure and properties*. 2017: Butterworth-Heinemann.
19. da Cruz Junior, J.A. and D.B. Santos, *Effect of tempering temperature on isothermal decomposition product formed below Ms*. Journal of Materials Research and Technology, 2013. **2**(2): p. 93-99.
20. Hofer, C., et al., *Structural characterization of "carbide-free" bainite in a Fe–0.2C–1.5Si–2.5Mn steel*. Materials Characterization, 2015. **102**: p. 85-91.
21. Zhang, X., et al., *Mechanical Behavior of Carbide-free Medium Carbon Bainitic Steels*. Metallurgical and Materials Transactions A, 2013. **45**(3): p. 1352-1361.
22. Timokhina, I.B., et al., *Nanoscale microstructural characterization of a nanobainitic steel*. Acta Materialia, 2011. **59**(14): p. 5511-5522.
23. Rakha, K., et al., *On low temperature bainite transformation characteristics using in-situ neutron diffraction and atom probe tomography*. Materials Science and Engineering: A, 2014. **589**: p. 303-309.
24. Martis, C.J., et al., *The static and dynamic mechanical properties of a new low-carbon, low-alloy austempered steel*. Materials Science and Engineering: A, 2014. **589**: p. 280-287.
25. Long, X.Y., et al., *Carbide-free bainite in medium carbon steel*. Materials & Design, 2014. **64**: p. 237-245.
26. Jezierska, E., J. Dworecka, and K. Rozniatowski, *Nanobainitic Structure Recognition and Characterization Using Transmission Electron Microscopy/ Rozpoznawanie I Charakteryzacja Struktury Nanobainitycznej Za Pomocą Transmisyjnej Mikroskopii Elektronowej*. Archives of Metallurgy and Materials, 2014. **59**(4): p. 1633-1636.
27. Mandal, D., et al., *Effect of austempering treatment on microstructure and mechanical properties of high-Si steel*. Journal of Materials Science, 2009. **44**(4): p. 1069-1075.
28. Garcia-Mateo, C., et al., *Nanostructured steel industrialisation: plausible reality*. Materials Science and Technology, 2013. **30**(9): p. 1071-1078.

29. Caballero, F. and H. Bhadeshia, *Very strong bainite*. Current opinion in solid state and materials science, 2004. **8**(3-4): p. 251-257.
30. Caballero, F.G., et al., *Toughness deterioration in advanced high strength bainitic steels*. Materials Science and Engineering: A, 2009. **525**(1): p. 87-95.
31. Garcia-Mateo, C., et al., *Tensile behaviour of a nanocrystalline bainitic steel containing 3 wt% silicon*. Materials Science and Engineering: A, 2012. **549**: p. 185-192.
32. Avishan, B., et al., *Strengthening and mechanical stability mechanisms in nanostructured bainite*. Journal of Materials Science, 2013. **48**(18): p. 6121-6132.
33. Sidhu, G., et al., *Characterization of Isothermally Heat-Treated High Carbon Nanobainitic Steels*. Journal of Materials Engineering and Performance, 2013. **22**(10): p. 3070-3076.
34. Weber, A., et al. *Mechanical properties of low-alloy-steels with bainitic microstructures and varying carbon content*. in *1st International Conference on Materials, Processing and Product Engineering (MPPE)*. 2015. Leoben, AUSTRIA.
35. Zhu, K.Y., C. Mager, and M.X. Huang, *Effect of substitution of Si by Al on the microstructure and mechanical properties of bainitic transformation-induced plasticity steels*. Journal of Materials Science & Technology, 2017. **33**(12): p. 1475-1486.
36. Leiro, A., et al., *Wear of nano-structured carbide-free bainitic steels under dry rolling–sliding conditions*. Wear, 2013. **298-299**: p. 42-47.

## DEVELOPMENT OF CONTINUOUS COLOR COATING LINE FOR STEEL & ALUMINUM STRIP

**Emrullah ÇAYIR, Mehmet YAVUZ, Fevzi ÖZÇELİK, Abdülkadir ÖZÇELİK, Mehmet UÇKAN**

*Teknoplan Engineering, Automation, Machinery & Software Ltd. ,  
Kdz.Eregli-Zonguldak, Türkiye,  
teknoplan@teknoplan.com.tr*

**İlhami Muharrem ORAK**

*Karabük University -Computer Engineering Faculty  
Karabük, Türkiye,  
imorak@karabuk.edu.tr*

**Ali Yavuz GÜNDOĞDU**

*AYG Engineering & Consultancy  
Kdz.Eregli-Zonguldak, Türkiye,  
aliyundogdu@gmail.com*

**Abstract.** For the first time in Turkey, continuous color coating line has been successfully developed by Teknoplan and group company NTS for paint coating both steel strip and aluminum strips. All design parameters have been determined by Teknoplan by considering the strip type, quality, thickness, width and production capacity according to the customer demands. The line has been taken into operation with all units in customer production area in Ankara in 2022. The production of the line is monitored and controlled operators with the Scada screens. In addition we have level-2 software to integrate with ERP systems and to direct the control system of the line to follow the products, to collect the data of the product and the line. By integrating tension leveler system to the line quality of strip is upgraded from A2 quality (due to wavy surface form) to A1 quality. Regeneratif thermal oxidizer (RTO) system, recuperator and heat exchanger systems have been designed to recover exhaust gas energy, to increase thermal efficiency, to decrease production cost from energy and also to prevent air pollution caused by solvents and volatilities.

**Keywords:** Continuous Color Coating Line.

### 1. INTRODUCTION

Color coated sheets are generally used for corrosion protection and for decorative purposes. The areas where painted sheets are used are quite wide. Therefore, demand for color coating strips or sheets in Turkey and in the World is increasing year by year.

The type of products typically made from coated sheets or coils are as follows:

- Roofing & wall cladding
- Guttering
- Fences & walls
- Whitegoods (appliances)

- Garage doors,
- Cool room panels
- Control panels
- Roofing tiles
- Housings & casings
- Industrial furniture & racking
- Office furniture

The types of metals to be coated include:

- Steel strips,
- Galvanized steel strips,
- Aluminum strips,
- Steel/Aluminium composites

The color coating line includes many complex processes. It is very important to produce in a quality and efficient manner on the coating line. The quality and synchronization of the processes of line are very important.

TEKNOPLAN has successfully developed Turkey's first domestic continuous color coating line (CCCL) in a complete manner and taken into commercial operation in a company in Ankara as a turnkey basis in 2022. The line has been specially designed for continuous color coating both steel strip and aluminum strips. Design parameters of the color coating line have been determined by considering strip type, quality, strip sizes and production capacity according to the customer demand.

In addition to mechanical systems, the automation of the line has also been designed by Teknoplana. The production of the line is monitored and controlled by operators with scada screens. We have developed level-2 software to integrate with ERP systems and to direct the control system of the line to follow the products, to collect the data of the product and the line.

#### Continuous Color Coating Line Design Data:

- Material: Steel & galvanized or aluminum strips.
- Coating: PVC, Epoxy, Regular Modified Polyester (RMP), Silicon Modified Polyester (SMP), Super Durable Polyester (SDP), Poly Vinylidene Fluoride (PVDF), etc.
- Annual Capacity :120.000 tpy
- Line Speed (max) : 75 mpm
- Line direction : From left to right
- Line length :150 meters
- Strip length in the line : 450 meters
- Strip Thickness : 0,20 mm to 1,30 mm
- Strip Width : 600 mm to 1300 mm
- Input Coil Weight (max) : 20 tonnes
- Input Coil Inner Diameter : 508 – 610 mm
- Input Coil Outer Diameter : 1800 mm
- Output Coil Weight (max) : 20 tonnes
- Output Coil Inner Diameter : 508 – 610 mm
- Output Coil Outer Diameter : 1800 mm

## 2. CONTINUOUS COLOR COATING PROCESSES

There are several processes and systems in CCCL. Synchronization of the systems of line are very important for efficient operation of the line.

The continuous color coating line includes following processes or systems:

- Entry Coil Saddels (4 sets)
- Entry Coil cars (2 sets)
- Uncoilers (2 sets)
- Peelers (2 sets)
- Pinch Rolls (6 sets)
- Conveyors
- Double cut shears
- Scrap removal system
- Stitcher- strip joiner
- Bridle units (6 sets)
- Entry loop
- Central position control units (6 sets)
- Alkali cleaning unit
- Rinsing Unit
- Drying unit (3 sets)
- Deflector roll units (12 set)
- Tension leveler
- Chemical coater
- Chemical drying oven
- Prime coater
- Prime coating dry oven
- Final coater
- Final coating dry oven
- Air cooling system (2 sets)
- Quench tanks systems (2 sets)
- Squeezing roll units (22 sets)
- Master bridle unit
- Exit loop unit
- Exit shear units
- Exit scrap removal systems
- Edge position control system (EPC)
- Recoiler with belt wrapper & support arm
- Exit Coil Saddels (2 sets)
- Exit Coil car
- RTO (Regneratif thermal oxidizer)
- Auxiliary Facilities
  - Hydraulic Syatems
  - Pneumatic System
  - Natural gas system
  - Heat recovery systems (Recuperator & heat exchangers)
  - Cooling system & towers
  - Water circulation systems
  - Water treatment systems

Configuration of Teknoplana Continuous color coating line is given in (Fig. 1).

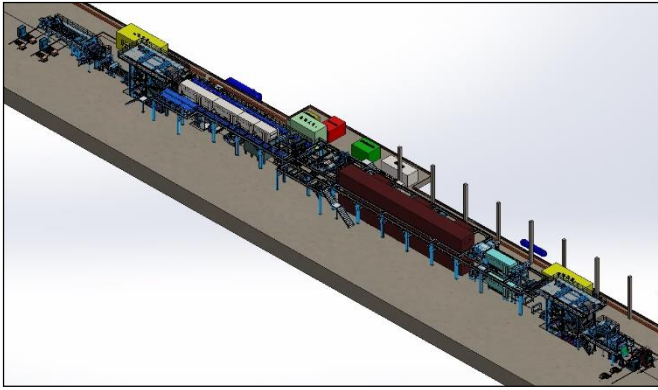


Figure 1: Teknoplan CCCL 3 Dimensional Model

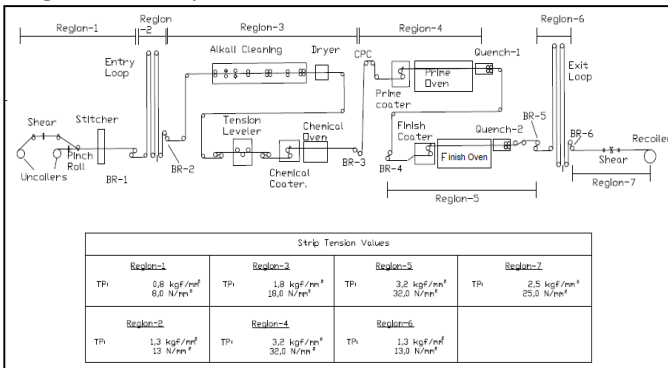


Figure 2. Flow process of Teknoplan CCCL Line.

All systems are important and critical in terms of production efficiency and quality production in the continuous color coating line. In the following sections, technical information is given about the coaters and tension leveler system, which are especially of critical importance in terms of quality and developed and designed by Teknoplan.

### 3. COATER MACHINES

Coaters used in steel strip coating lines are very important systems which significantly influence the quality of coated products. These machines are used to coat the metal strip with desired quality paint.

According to the line design coater can be S type or U type configuration. In the Teknoplan design for this Project, "S type" coaters have been designed and developed in order to optimize the line configuration.

The types of coaters in the CCCL line are as follows:

1. Chemical coater
2. Prime coater
3. Final coater

Schematic appearance of S Wrap type coating is given in (Fig. 3) and Teknoplan coater model is given in (Fig. 4).

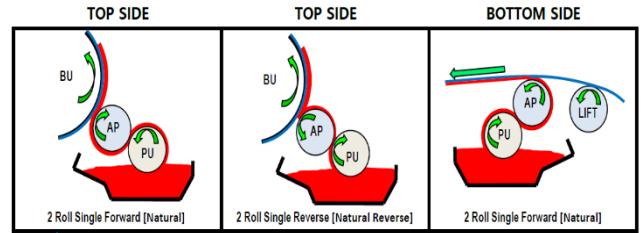


Figure 3. Appearance of "S Wrap Type" Coating

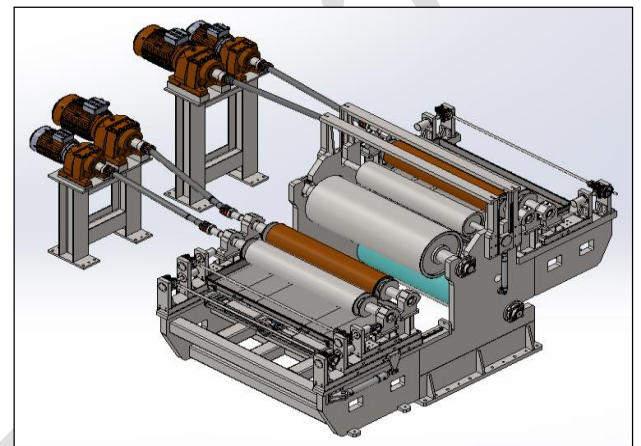


Figure 4. Model for Teknoplan coater

Table 1. Chemical Coating Thickness Values

Description		Paint Coating Thickness	
Chemical Coater	Top	1 ~ 2 μm	25-30 mg/m <sup>2</sup> wet
	Bottom	1 ~ 2 μm	25-30 mg/m <sup>2</sup> wet

Table 2. Typical coating thickness values

Paint coating: Epoxy, Polyester, PVDF

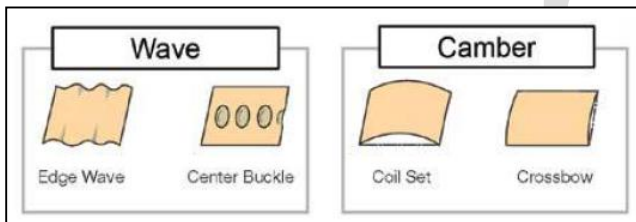
Description		Paint Coating Thickness (μm)	Gravity
Prime Coater	Top	3 ~ 7	1,12
	Bottom	3 ~ 7	1,12
Finish Coater	Top	5~20	1,12
	Bottom	3 ~ 7	1,12

Table 3. Coaters roll specifications

Roll description	Roll diameter (mm)	Barrel length (mm)	Lining Material	Lining Thickness	Hardness
Applicator Roll	Ø300	1500	Polyurethane (PU)	15 mm	52 HSA
Metering Roll	Ø300	1500	Polyurethane (PU)	15 mm	52 HSA
Back-up Roll	Ø600	1600	Hard Chromated Steel.	70 micron	HRC 63
Pick-up Roll	Ø300	1500	Hard Chromated Steel.	40 micron	HRC 63
Lift Roll	Ø300	1500	Hard Chromated Steel.	40 micron	HRC 63
Turn Around Roll	Ø500	1500	Polyurethane (PU)	15 mm	85 HSA

#### 4. TENSION LEVELER

In the cold rolling process, dead flat strip material can not be produced due to a variety of rolling conditions and material characteristics. In order to eliminate wave form shape of the strip permanently, tension leveler is necessary system.



**Figure 5.** Types of defects occurring in the sheets.

Tension Leveling is the process of pulling the strip beyond its yield point to permanently change the shape of the strip and make it flat. Tension levelling is an effective tension-assisted levelling method. The coil is put under significant tension between pull and drag bridles placed before and after the specially designed roller levelling device (Figure 6). With tension levelling, all parts of the metal are pulled past the yield point, top to bottom, edge to edge. The full cross section is elongated a fraction of a percent. All the previous history of trapped stress is deleted. The material should be dead flat and relatively free of internal stresses.

If the strip has an edge wave, the concept is to stretch the shorter fibers in the center of the strip so that they will match up in length with the longer fibers from the edge wave.

Conversely, if the strip has a full center, the concept is to stretch the edges of the strip to match up in length with the center buckle. If the strip is consistent in length across the width of the strip, you have created flat steel. The tension leveling process is a combination of elongating the strip and bending the fibers over a series of work rolls. Tension leveling will eliminate edge wave and center buckle as well as correct excessive crossbow and coil set.

Tension levelling usually is restricted to gauge thicknesses of metal. Because of the massive equipment and horsepower required, this process usually is not practical for thicker, hot-rolled plate coils. However, more and more service centres are using tension levelling lines to process cold-rolled steel and aluminium products.

In order to eliminate wave form shape of the strip permanently, tension leveler has been designed, developed and integrated to continuous color coating line by Teknoplan and group company NST. (Fig.6).

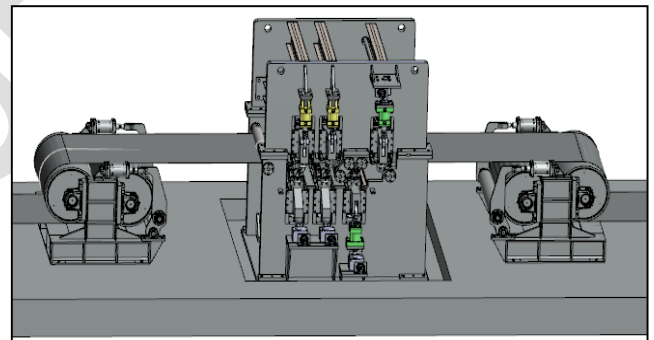


**Figure 6.** Teknoplan tension leveler model

Tension and as result of elongation generated by means of drive control of bridle rolls system. Tension leveller has been installed after cleaning unit and before chemical coater in the color coating line.

Tension leveler includes the following systems:

- Entry bridle unit with 2 rolls.
- Delivery bridle unit with 2 rolls.
- Anticrossbow roll & cassettes unit
- Anticoil set roll & cassette unit
- Tension leveler body
- Tension leveler electric & automation systems
- Hydraulic & pneumatic syatems
- Tension leveler casette quick change systems

Wavy edges, centre buckle, long bow and cross bow problems can be removed from strip. (Fig. 7)

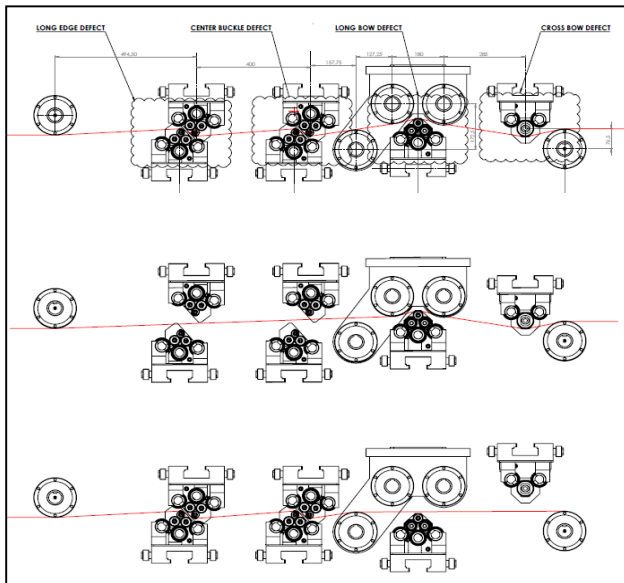


**Figure 7.** Strip flow schema thru tension leveler.

## 5. AUTOMATION OF THE LINE

Level 1 automation equipment part of the continuous coil color coating line has been designed as two panel rooms. 500 kW smart line modules with regeneration feature were used in both panel rooms. Coil openers, loop motors, bridle motors, tension leveler entry and delivery bridle motors are fed by this regen unit.

Motors such as coaters motors, oven circulation motors, exhaust fans, RTO supply fan that only require speed control are controlled by AC/AC drivers. Fixed speed motors are controlled from MCC panel.

-In addition, three drying ovens are automated. There is one zone in the chemical drying, three zones in the prime oven, and four drying zones in the final oven. The heat and negative pressures of each zone of the ovens can be continuously at real time monitored on the SCADA screen.

Another feature of the line is that the solvent gas released in the prime and final ovens is burned in the unit of RTO. The clean air is heated thru recuperator and given to the ovens. Temperature of each zone is automatically controlled by measuring zone temperature. Operation and temperature of the RTO is also controlled automatically.

in the ovens, the percent of the solvent is measured by LEL (Lower explosive limit) meter. There are two limits for the LEL meter. These are alarm limit and stop limit. If the solvent percentage reach the level of alarm limit, gives an audible and visual alarm signals. If the level of the solvent reaches to the dangerous set point, the line automatically is stopped.

One of the most important points in level 1 automation of the color coating line, there are 9 different tension zones and these tension values remain constant at all speeds and can be adjusted according to the material properties. Tension values for each tension zones can be set from the main control scada system. Tension zones (regions) of the line is given in (Fig.2).

Time duration of removal product coil from the line is very important. Because removal time duration determines also the line speed. Removal time of the coil with the set weight from the recoiler are automatic. The product coil is removed by coil car. During the removal time of the coil, the incoming coated coil strip material is accumulated in the exit loop and the line speed in the region of coaters, ovens and quench continues at the set speed as constant.

At the entry side of the line, the new coil is given or fed to the line automatically. For continuous operation of the line, new coil front end and rear end of the previous coil is joined mechanically at the stitcher (joiner) unit. During the joining time, the entry loop (accumulator) level decreases without losing its tension according to the line speed and ensures the continuity of the line after the entry loop as a set constant speed. After the joining of the strips are completed, the entry loop starts to accumulate the strip to full the loop capacity. All these processes are performed automatically by level 1 system.

In order to keep the strip in the center of the along the line, 6 central position control units (CPC) have been placed in the line. During the strip moving, the position of the strip is continuously measured by transmitter and receiver. If the strip slides from center of the line to the side, by proportional hydraulic valve system, strip is moved to the center of the line automatically.

For the recoiling unit, EPC (Edge position control) system is integrated to the recoiling (tension reel)

unit. Edge Position Control System (EPC) is to control material's edge and let the edge position be the same position in the production process of material. It can be operated automatically without the operator's manual controlling if during operation as an interlocking system is imbedded



**Figure 8.** Main Control Screen of the CCCL.

## 6. CONCLUSION

TEKNOPLAN has successfully developed Turkey's first domestic continuous color coating line (CCCL) in a complete manner and taken into commercial operation in 2022. All mechanical and automation systems have been designed by Teknoplan. There are several processes in CCCL lines and each process in the line is very important for the quality and productivity of view. In this paper especially importance of the tension leveler system and coater machines are explained.

Teknoplan has integrated tension leveler system to increase coating and strip quality. In Teknoplan design, tension leveller has been installed after cleaning unit and before chemical coater in the line. We have observed that by using tension leveler in the color coating line, coating quality has been increased and also product quality has been upgraded from A2 quality to A1 quality.

In near future, tension leveler system may/must be necessary for the color coating line. For the initial design of the color coating line, a suitable place should be left for the tension leveler system. A place before chemical coater and after cleaning (degreasing) unit is suitable. For the first stage at the beginning of the line if tension leveler isn't put, after after certain amount production, then it should be decided to integrate tension leveler system.

Homogeneity and tolerances of coating thickness are very important for the production quality and also cost. Coaters have been designed to optimize customer requirements. Prime & Final coaters have been designed  $\pm 2$  micron coating sensitivity. Mechanism and automation of the coaters have been designed in order to optimize the product quality, cost and the line practical operation.

All of the main electric motors used in the production line operate with driver control. Some motors operate in regen mode while the others operating in load mode. There are 7 tension zones in the line. These tensions are sensitively adjusted by the automation and drive control units according to the line speed.

Natural gas is used as fuel in prime and final coating drying ovens. Since there is a solvent in the paint coating, it cannot be directly thrown into the atmosphere in terms of environmental legislation. RTO system has been developed to recover the energy of solvents by burning them and to release flue gas in accordance with environmental legislation. Recuperator and economizer systems were designed after the RTO system, both to benefit from the energy of solvents and to recover the energies of the furnace chimney.

Approximately 200 °C hot air produced by using the exhaust gases in the recuperator is used for heating the furnaces. The hot water coming from the economizer is used for heating the cleaning circulation tanks.

With the energy recovery units made in this way, approximately 1,5 MW of energy is recovered. Energy recovery systems are considered as systems that pay for themselves within 2 years. We strongly recommend the establishment of energy recovery systems in such production lines in terms of environmental legislation, efficient use of energy and reducing production costs.

This project will positively affect to develop the new production lines. Success of the project has encouraged our company and other domestic companies to develop new domestic production lines. As a Teknoplan and NST group companies, we have started to develop new first domestic HCl pickling line with all units for the steel strip.

**ACKNOWLEDGEMENTS**

Thanks to the all Teknoplan and NST group people for the development works of the continuous color

coating line. Special thanks to supervisor Mr.Cuneyt Tezer, to our customer Ankara Ünallar Metal people and to our all suppliers

**REFERENCES**

1. Hiroyuki Uematsu, Keizo Abe, Development of Tension Leveler for Advanced High Strength Steel, at AISTech 2016-The Iron & Steel Technology Conference and Exposition, Pittsburgh, Pa., USA.
2. Xiaowen Hao, Ruixin Li, Jiao Wang, X. Yang, Numerical simulation of a regenerative thermal oxidizer for volatile organic compounds treatment, Environmental Engineering Research 2018; 23(4): 397-405.
3. John L., Amanda Baynham, Incinerators and Oxidizers, U.S. Environmental Protection Agency Research Triangle Park, NC 27711, November 2017.
4. A.W.Hassel., K.Bruder.,etc., New Aproaches in Electrolytic Cleaning of Cold Rolled Steel Sheet. European Commission. European Research Area. 2011-132 pp. ISSN 1831-9424.

ICMATSE 2022

## 2D MoS<sub>2</sub> Nanoparticle Based Solar Cell on Si

**Ammar Nayfeh**

Khalifa University, EECS 127788, UAE Abu Dhabi, UAE,  
ammarnayfeh@ku.ac.ae  
ORCID: 0000-0002-5207-244X

*Cite this paper as: Nayfeh, A MoS<sub>2</sub> Nanoparticle Based Solar Cell on Si  
.Int. Conf. Advanced. Mater. Sci. & Eng. HiTech.and Device Appl.Oct. 27-29 2022,Ankara, Turkey*

**Abstract.** In this work the performance of MoS<sub>2</sub> Nanoparticle/Si solar cell is studied. The MoS<sub>2</sub> nanoparticles (NPs) was synthesized through a chemical exfoliation method, and it was drop casted on a Si substrate, and it was characterized using SEM, and AFM, it was observed that MoS<sub>2</sub> NPs gives a good coverage of the substrate. The synthesized MoS<sub>2</sub> NPs was used to fabricate a MoS<sub>2</sub> NPs/Si solar cell, and the performance of this solar cell was tested under AM1.5G. Also the MoS<sub>2</sub> Si photodiode shows increased responsivity compared to Si alone. Moreover, it was concluded that the MoS<sub>2</sub> NPs can absorb a significant amount of photons making them suitable for future low cost solar cells.

**Keywords:**

© 2022 Published by ICMATSE

Molybdenum Disulfide (MoS<sub>2</sub>) is one of widely studied layered two-dimensional transition metal dichalcogenides (2-D TMDs) materials, it has unique electronic, optical, and attractive semiconducting properties, in addition, it is abundant in the nature MoS<sub>2</sub> nanoparticles synthesized using a chemical exfoliation method was used to fabricate [1-8] MoS<sub>2</sub> NPs/p-Si photodiode, to synthesize the MoS<sub>2</sub> NPs, a 0.5 g of the MoS<sub>2</sub> powder was dispersed in a 50 mL of N-Methyl-2-pyrrolidone (NMP), then it is sonicated in an ice bath using a probe sonicator, followed by two stage centrifugation steps, finally NMP was

removed, and the MoS<sub>2</sub> NPs was filtered and re-dispersed in a 50 mL of IPA. A photo of the fabricated solar cell is shown in figure 1 (a), and figure 2 (b) shows the final device. To test the performance of the fabricated solar cell, a solar simulator (Sol3a 94123A) was used. Figure 6 shows the measured J-V curve characteristics under 1sun, A.M. 1.5G of the solar with open circuit voltage ( $V_{OC}$ ) is 0.25 V. The obtained J-V curve has shown a solar cell function and proof of concept using MoS<sub>2</sub> nano particles to make the junction. The low current is due to thin metal and no optimized interface.

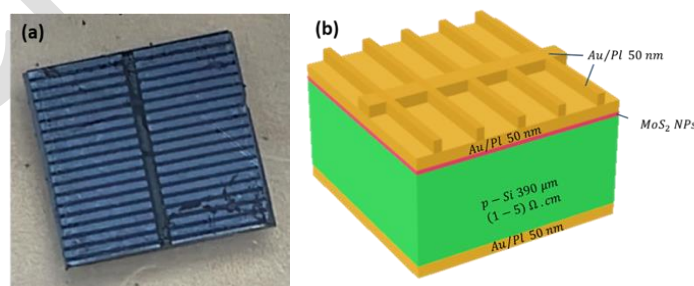


**Figure 13 (a) The fabricated MoS<sub>2</sub> NPs/p-Si Solar Cell, (b) Schematic of the final structure of the fabricated MoS<sub>2</sub> NPs/p-Si Solar Cell.**

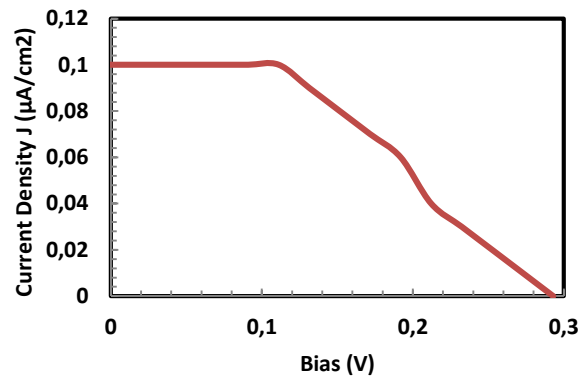


**Figure 2. The J-V characteristics of the MoS<sub>2</sub> NPs/p-Si solar cell under 1 Sun, A.M. 1.5G.**

### References

- [1] R. Singh, V. Rangari, Sanagapalli, V. Jayaraman, S. Mahendra, V. Singh, "Nano-structured CdTe, CdS and TiO<sub>2</sub> for thin film solar cell applications," *Solar Energy Materials and Solar Cells*, vol. 82, no. 1-2, pp. 315–330, 2004.
- [2] K. L. Chopra, P. D. Paulson, and V. Dutta, "Thin-film solar cells: an overview," *Progress in Photovoltaics: Research and Applications*, vol. 12, no. 23, pp. 69–92, 2004.
- [3] L. Wang, L. Huang, W. C. Tan, X. Feng, L. Chen, X. Huang, and K.-W. Ang, "2D Photovoltaic Devices: Progress and Prospects," *Small Methods*, vol. 2, no. 3, p. 1700294, 2018.
- [4] S. Das, D. Pandey, J. Thomas, and T. Roy, "The Role of Graphene and Other 2D Materials in Solar Photovoltaics," *Advanced Materials*, vol. 31, no. 1, p. 1802722, 2018.
- [5] D. Bhattacharya, S. Mukherjee, R. K. Mitra, and S. K. Ray, "Size-dependent optical properties of MoS<sub>2</sub> nanoparticles and their photo-catalytic applications," *Nanotechnology*, vol. 31, no. 14, p. 145701, 2020.
- [6] Z. He and W. Que, "Molybdenum disulfide nanomaterials: Structures, properties, synthesis and recent progress on hydrogen evolution reaction," *Applied Materials Today*, vol. 3, pp. 23–56, 2016.
- [7] C. P. Veeramalai, F. Li, Y. Liu, Z. Xu, T. Guo, and T. W. Kim, "Enhanced field emission properties of molybdenum disulfide few layer nanosheets synthesized by hydrothermal method," *Applied Surface Science*, vol. 389, pp. 1017–1022, 2016.
- [8] W. Alnaqbi, J. M. Ashraf, A. Rezk, S. Abdul Hadi, A. Alhammadi, and A. Nayfeh, "Absorption in the UV-vis region from chemically exfoliated mos<sub>2</sub> nanoparticles for solar applications," *2021 IEEE 48th Photovoltaic Specialists Conference (PVSC)*, 2021.

## Solar Energy Forecasting Using Machine Learning Models

**Yusuf Gencer**

*Istanbul Technical University, Faculty of Science and Letters, Physics Engineering Department, 34469 Maslak-Istanbul, Turkey,  
[gencery17@itu.edu.tr](mailto:gencery17@itu.edu.tr)  
ORCID: 0000-0001-7339-2066*

**Zuhal ER**

*Istanbul Technical University, Maritime Faculty (,and, Faculty of Science and Letters),  
34469 Maslak-Istanbul, Turkey,  
[erzuh@itu.edu.tr](mailto:erzuh@itu.edu.tr)  
ORCID: 0000-0002-9737-1435*

*Cite this paper as: Gencer, Y, Er, Z.. Solar Energy Forecasting Using Machine Learning Models.Int. Conf. Advanced. Mater. Sci.& Eng. HiTech.and Device Appl.Oct. 27-29 2022,Ankara, Turkey*

**Abstract.** In this paper, photovoltaic (PV) system production data and wheather data given enercast GmbH were analyzed by using Python codes on Jupyternotebook. These analyzed data showed the irregular energy production of PV systems described in the literature review section. In this study, the annual energy production amount from day to day has illustrated by the graph. As can be seen in the graph, the production amount of energy of each day is different from each other. Some of the days too much energy is produced meanwhile some days less energy is produced. Furthermore, the data which were provided by Enercast has been tried to obtain the best estimation result by applying machine learning techniques. Since, another graph emerges when the daily average of PV system energy production data is analyzed. It has been observed that while less energy is produced in the morning and evening hours, maximum energy is produced in the afternoon. This is due to the way it comes to the panel. When the PV system production data is analyzed on a monthly basis, it can be seen that more energy is produced in summer than in winter. This is due to the fact that the angle of incidence of the sun and the duration of sunshine are different in summer and winter. The nRMSE value of simple artificial neural network (ANN) is 8.33%. Although this closely matched the structure of the data, it was unable to accurately forecast the value of the power generated. Another approach which is time interval selection method was applied to dataset. Weather parameters exhibit different behavior at each time interval during the day. Thanks to this method, each interval is passed through the ANN model separately, increasing the predictive power. The ANN model includes only one hidden layer and containing 16 neurons. The solar model has a 7.29% nRMSE value. It is nearly flawless at forecasting when the panels will start producing and can predict the output during the day.

**Keywords:** Solar Energy Production Forecast, Machine Learning, Artificial Neural Networks

© 2020 Published by ICMATSE

### Introduction

The production of PV panels has increased every year due to the demand of PV. The biggest reason for this is that the use of fossil fuels increases global warming and air and water pollution with the released gases. To reverse this situation, some states financially support people who want to use renewable energy. Another major reason is that there is no other cost other than the PV panel cost. Because these panels provide enough profit to cover their own costs within a few years after installation and can produce energy for many years. Because of the enhanced efficiency of

solar energy generation and distribution, local residents have taken on the role of energy generators, even receiving credit for electricity provided to the grid under the net-metering policy[1]. All continents contributed significantly to global growth in 2020, with an expected 20 countries adding at least 1 GW of new solar PV capacity, up from 18 countries in 2019 [2, 20,21] .

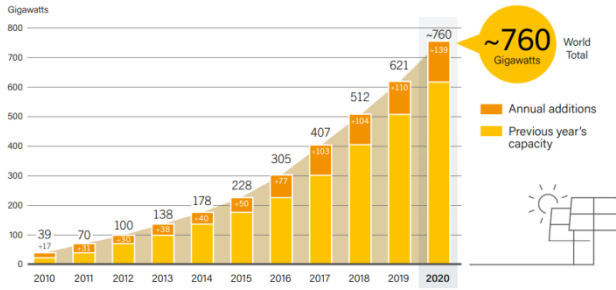


**Figure 1.** Solar photovoltaics global capacity from 2010-2020 [2].

### Objectives

A 24-hour solar energy forecast will be made using the weather and solar energy production data provided by enercast. Estimation will be made using machine learning methods and python software language. Five different machine learning methods were reviewed to make the best solar energy prediction. ANN was chosen as the best method among them. The selection of this methods was made by examining the methods that gave the best results in the researches. These are Bayesian neural network (BNN), ANN, Long Short-term Memory (LSTM), Long and Short-term Time Series Network (LSTNet), Recurrent Neural Network (RNN) [3-19].

### Current Progress

This study is carried out jointly with enercast GmbH. The provided data by enercast will be tried to obtain the best estimation result by applying the machine learning techniques mentioned in the literature review section. At this stage, the effects of weather parameters on the production data were examined in separate correlation graphs. It has been seen that the humidity value has a negative and high value correlation with the production data. Also day length values were also added to the data set and its share in the prediction was observed and it was determined that it increased the predictive power. In this study, the ML models mentioned were examined in the light of the information obtained from the articles in the reference section, and the study was carried out only on the ANN model. Other ML models will be studied in the future.

### Examining The Data

PV system production and wheather data which was taken from enercast analyzed by using Python codes on Jupyternotebook. These analyzed data showed the irregular energy production of PV systems described in the literature review section. Figure 2 shows the 4 years of production from day to day. As it can be seen in this graph, the energy production amount of each day is different from each other and some days too much energy is produced while some days too less energy is produced.

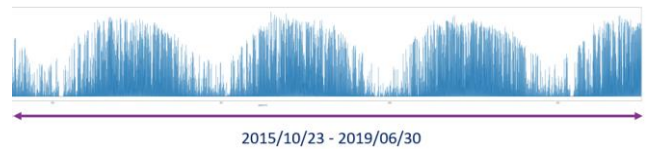


**Figure 2.** Solar energy production.

### ANN Method

The code was build and executed on Jupyter Notebook. Firstly, the weather parameters were adjusted to be hourly totals. Then, the Global Horizontal Irradiance (GHI) and cloud cover were combined with the solar energy production data. As it can be seen in Figure 3, the data set was divided into train and test. Following that, the ANN model was used. The nRMSE value for this model was 8.33 %. Other weather parameters were added and put into the model again. These parameters are humidity, pressure, wind speed, snowdepth. In this case, the total number of inputs became 8. When all weather parameters were used, the error rate nRMSE value of the model was reduced to 7.90%. Figure 4 shows the prediction ratio of the two models against the actual production data. As it can be seen in this chart, the nRMSE value of 7.90% predicts production at night in the green line. The reason is the GHI data is also 0 at night, but other weather parameters behave like they do during production hours. To solve this situation, the method of dividing the day into time intervals has been developed.

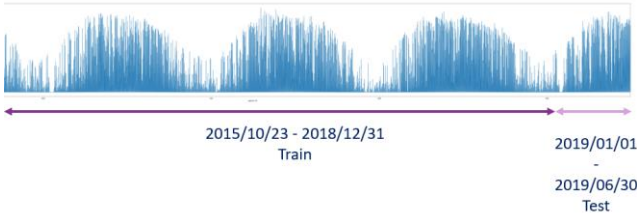


**Figure 3.** Train test split.

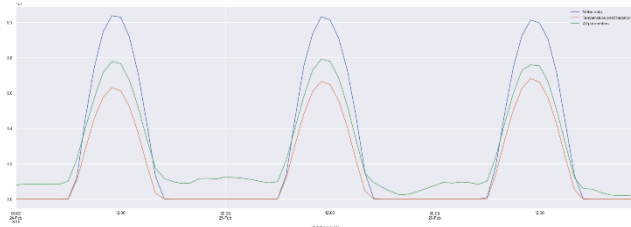


**Figure 4.** ANN results of different weather parameters (Orange: 8.33%, Green: 7.90%, Blue: Meterdata ).

### Time Intervals Selection

In this method, the hours of the day are dynamically divided into 6 time slots. In order to divide it into time intervals, first of all, the sunrise, solar noon and sunset data at the location of the production data were extracted and the data was divided with the help of the code written based on these data. Figure 5 shows the time intervals.

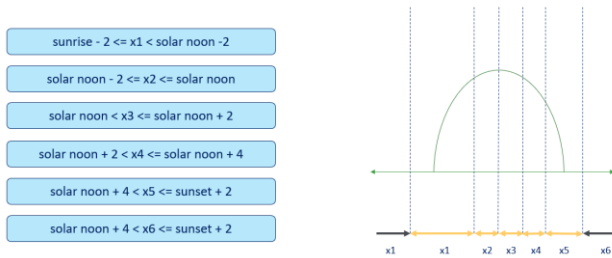


**Figure 5.** Time intervals selection.

### ANN Method With Time Intervals

Each selected time interval was passed through the ANN model separately and the prediction results were obtained. These results were combined and brought into a whole again. Thanks to this method, the abnormal production estimation at night was eliminated and the intraday production estimation gave better results. Deep neural network was used in this interval as learning at night is more difficult. Figure 6 shows the working principle of this system. Thanks to this method applied, the nRMSE value was reduced to 7.29%. In the correlation analysis, based

on the large negative ratio between the humidity data and the production data, the results obtained by including and without including the humidity data were observed, and the share of humidity data in reducing the error rate was proven.

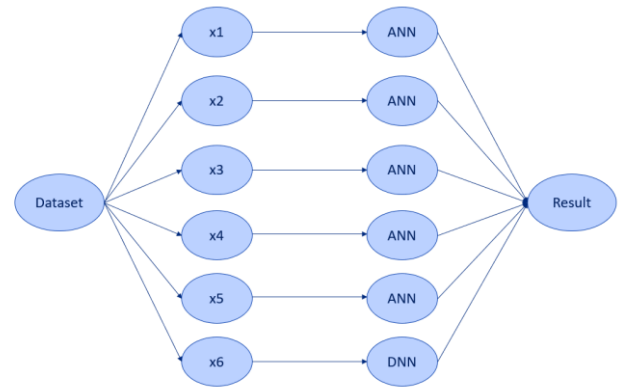


**Figure 6.** Time intervals ANN method.

### Results

Results were observed with 3 different datasets in the division method into time intervals. The nRMSE value obtained using all weather parameters was 7.29%, the nRMSE value obtained using only temperature and GHI was 8.28%, and the nRMSE value obtained using all weather parameters excluding humidity was 7.50%. Figure 7 shows these three different results.

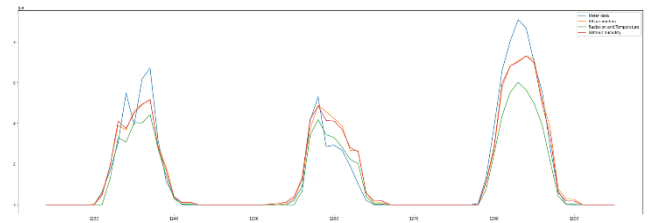


**Figure 7.** ANN method with time intervals results (Orange: 7.29%, Green: 8.28%, Red: 7.50%, Blue: Meterdata)

### Conclusion

Light is required in order to produce electrical energy in PV panels. In this context, the GHI value is directly related to the energy production value. For this reason, when the GHI is low, the energy production is low and the energy production is maximum at the noon hours of the GHI. Since the temperature of the panels also affects the efficiency in energy production, the weather temperature has a great effect on the production data. However, other weather parameters also have a small effect

individually, but when taken as a whole, they significantly affect the production data forecast. In the method of dividing the day into time intervals, the error rate was significantly reduced. It has been

observed that every hour of the day has different characteristics and better results are obtained by teaching it separately in machine learning.

## References

- [1] Ramirez, J., Soto, E. A., Wollega, E., & Bosman, L. B. (2020). Using Machine Learning to Assess Solar Energy Grid Disturbances. Paper presented at the Third International Conference on Industrial & Mechanical Engineering and Operations Management (IMEOM), Detroit, USA.
- [2] H. E. Murdock, D. Gibb, T. André, F. Appavou, A. Brown, B. Epp, B. Kondev, A. McCrone, E. Musolino, L. Ranalder, et al., "Renewables 2019 Global Status Report", 2019.
- [3] "Why (and how) Microgrid Technology is a good power source," The Pew Charitable Trusts. [Online]. Available: <https://www.pewtrusts.org/en/research-and-analysis/issue-briefs/2016/02/why-and-how-microgrid-technology-is-a-good-power-source>. [Accessed: 26-Feb-2016].
- [4] Agoua, X. G., Girard, R., & Kariniotakis, G. (2018). Short-term spatio-temporal forecasting of photovoltaic power production. *IEEE Transactions on Sustainable Energy*, 9(2), 538–546. <https://doi.org/10.1109/tste.2017.2747765>
- [5] C. Chen, S. Duan, T. Cai, and B. Liu, "Online 24-H solar power forecasting based on weather type classification using artificial neural network," *Solar Energy*, vol. 85, no. 11, pp. 2856–2870, 2011.
- [6] Tuohy, A., Zack, J., Haupt, S. E., Sharp, J., Ahlstrom, M., Dise, S., Gemit, E., Mohrlen, C., Lange, M., Casado, M. G., Black, J., Marquis, M., & Collier, C. (2015). Solar forecasting: Methods, challenges, and performance. *IEEE Power and Energy Magazine*, 13(6), 50–59. <https://doi.org/10.1109/mpe.2015.2461351>
- [7] P. Bacher, H. Madsen, and H. A. Nielsen, "Online short-term solar power forecasting," *Solar Energy*, vol. 83, no. 10, pp. 1772–1783, Oct. 2009.
- [8] Muhammad Qamar Raza, Mithulananthan Nadarajah, and Chandima Ekanayake. On recent advances in PV output power forecast. 2016. DOI: 10.1016/j.solener.2016.06.073.
- [9] Antonanzas, J., Osorio, N., Escobar, R., Urraca, R., Martinez-de-Pison, F. J., & Antonanzas-Torres, F. (2016). Review of Photovoltaic Power Forecasting. *Solar Energy*, 136, 78–111. <https://doi.org/10.1016/j.solener.2016.06.069>
- [10] Schmidt, T., Calais, M., Roy, E., Burton, A., Heinemann, D., Kilper, T., & Carter, C. (2017). Short-term solar forecasting based on Sky images to enable higher PV generation in remote electricity networks. *Renewable Energy and Environmental Sustainability*, 2, 23. <https://doi.org/10.1051/rees/2017028>
- [11] Jang, H. S., Bae, K. Y., Park, H.-S., & Sung, D. K. (2016). Solar power prediction based on satellite images and support vector machine. *IEEE Transactions on Sustainable Energy*, 7(3), 1255–1263. <https://doi.org/10.1109/tste.2016.2535466>
- [12] Wan, C., Zhao, J., Song, Y., Xu, Z., Lin, J., & Hu, Z. (2015). Photovoltaic and solar power forecasting for Smart Grid Energy Management. *CSEE Journal of Power and Energy Systems*, 1(4), 38–46. <https://doi.org/10.17775/cseejpes.2015.00046>
- [13] Rodríguez, F., Fleetwood, A., Galarza, A., & Fontán, L. (2018). Predicting solar energy generation through artificial neural networks using weather forecasts for microgrid control. *Renewable Energy*, 126, 855–864. <https://doi.org/10.1016/j.renene.2018.03.070>
- [14] Mishra, S., & Palanisamy, P. (2018). Multi-time-horizon solar forecasting using recurrent neural network. *2018 IEEE Energy Conversion Congress and Exposition (ECCE)*. <https://doi.org/10.1109/ecce.2018.8558187>
- [15] Li, Wang, Zhang, Xin, & Liu. (2019). Recurrent neural networks based photovoltaic power forecasting approach. *Energies*, 12(13), 2538. <https://doi.org/10.3390/en12132538>
- [16] Chen, H., & Chang, X. (2021). Photovoltaic Power Prediction of LSTM model based on Pearson Feature Selection. *Energy Reports*, 7, 1047–1054. <https://doi.org/10.1016/j.egyr.2021.09.167>
- [17] Lai, G., Chang, W.-C., Yang, Y., & Liu, H. (2018). Modeling long- and short-term temporal patterns with deep neural networks. *The 41st International ACM SIGIR Conference on Research & Development in Information Retrieval*. <https://doi.org/10.1145/3209978>.
- [18] Regunath, G. (2021, December 16). Understanding the difference between AI, ML, and DL: Using an incredibly simple example. *Advancing Analytics*. Retrieved June 20, 2022, from <https://www.advancinganalytics.co.uk/blog/2021/12/15/understanding-the-difference-between-ai-ml-and-dl-using-an-incredibly-simple-example>
- [19] Correspondent, T. G. (2020, December 4). Understanding the difference between AI, ML, and DL. *TechGig*. Retrieved June 20, 2022, from <https://content.techgig.com/technology/understanding-the-difference-between-ai-ml-and-dl/articleshow/75493798.cms>
- [20] H.Miray Yakisan, Zuhail Er. (November 2020). A Study For Smart Solar Solar Systems Managing By Artificial Intelligence Conference: EURASIAN SCIENCE TECH, DOI:10.13140/RG.2.2.16296.80644
- [21] Zuhail Er, Defne Eryilmaz, Kerem Horzum. (2 November 2018). Predicting The Efficiency Of Sun Tracking Systems Over Fixed Panels By Making Use Of A Simulation Driven By A Convolutional Neural Network And Genetic Algorithm, The 33rd Sisecam Glass Symposium, <https://www.camsempozyumu.com/sites/catalogs/en/General%20Documents/Bildiriler%20Kitab%C4%B1/33.pdf>

## Presentation Real time microstructural control for product quality and new steel grade development using electromagnetic sensors

*Claire Davis*

*University of Warwick, Thermo-mechanical Processing Advanced Manufacturing & Materials Centre*

ORCID: xxxx-xxxx-xxxx-xxxx

*Cite this paper as: Davis, C. Presentation Real time microstructural control for product quality and new steel grade development using electromagnetic sensors. Int. Conf. Advanced. Mater. Sci. & Eng. HiTech. and Device Appl. Oct. 27-29 2022, Ankara, Turkey*

**Abstract.** The ability to measure microstructure (and properties) in real time during steel processing is highly desirable. Electromagnetic (EM) sensors are being used on-line during steel processing for quality control, for example in cold strip mills with the sensor signals being correlated to mechanical properties. This allows strip quality to be monitored along length, matched to specification and the option for feedback control. More recent innovation is the use of EM sensors for microstructural characterization during hot strip processing, specifically for quantification of phase transformation during cooling on the run out table after hot rolling. There is potential for EM sensors (and other sensor technologies) to be used for real time microstructure control in other process scenarios. For this to occur it is important that the sensitivities of EM signals to different microstructural features and external factors such as temperature, stress and sample/product geometry are understood, and where possible modelled. This talk will include discussion on: the application of EM sensors for steel microstructure and property monitoring; the fundamental principles and models linking the EM signals to microstructure; and opportunities for future use of EM sensors for real-time microstructural monitoring and hence future steel grade development.

## Boron R&D Activities and TENMAK BOREN

**Abdulkerim YORUKOGLU**

*TENMAK BOREN Boron Research Institute, 06530 Ankara, Turkey,  
kerimyor@gazi.edu.tr  
ORCID: 0000-0003-3194-3901*

*Cite this paper as: Yorukoglu, A. Boron R&D Activities and TENMAK BOREN .Int. Conf. Advanced. Mater. Sci. & Eng. HiTech.and Device Appl.Oct. 27-29 2022,Ankara, Turkey*

**Abstract.** With globalization, we can summarize all kinds of activities of countries as interacting internationally. With globalization, events, activities, interactions, scales gain an international character beyond national borders. The economic performance of a country can be measured by the sum of the competitiveness of institutions and organizations. R&D is one of the most important activities required for innovation in the world . In the first quarter of the current century, there are intense and well-fictionalized research and development studies behind the rapidly advancing technology, product development and innovative approaches. In parallel with these, the application areas of boron minerals and products used in a wide and various fields are increasing day by day. Since boron is used more or less in more than 250 areas, it is known as the “Salt of the Industry” and offers a wide range of uses in the sector. Boron is frequently used in chemistry, materials, automotive, construction, nuclear energy, defense industry, cleaning and detergent, glass, ceramics, health, agriculture, aerospace and aircraft, military vehicles, fuels, electronics and communications, polymeric materials, nanotechnologies and metallurgy and many chemicals and products are still developed. Besides the reserve and market conditions of boron in the world and in our country, in order to increase the economic contribution based on boron in our country, researches are presented to develop high value added boron products and technologies and to spread their usage areas with researches in this field.

**Keywords:** Boron, Boron materials, BOREN, R&D  
© 2022 Published by ICMATSE

Boron minerals are natural compounds containing different proportions of boron oxide (B<sub>2</sub>O<sub>3</sub>) in their structures. There are more than 230 boron minerals in nature, and tincal, colemanite, ulexite and kernite are the most common commercially [1]. The chemical formulas and B<sub>2</sub>O<sub>3</sub> contents of the main boron minerals with commercial value are given in Table 1.

**Table 1. Commercial Boron Minerals.**

MINERAL	FORMULA	B <sub>2</sub> O <sub>3</sub> CONTENT (% by weight)
<b>Colemanite</b>	Ca <sub>2</sub> B <sub>6</sub> O <sub>11</sub> .5H <sub>2</sub> O	50,8
<b>Ulexite</b>	NaCaB <sub>5</sub> O <sub>9</sub> .8H <sub>2</sub> O	43,0
<b>Tinkal</b>	Na <sub>2</sub> B <sub>4</sub> O <sub>7</sub> .10H <sub>2</sub> O	36,5
<b>Kernit</b>	Na <sub>2</sub> B <sub>14</sub> O <sub>7</sub> .4H <sub>2</sub> O	51,0
<b>Pandermite</b>	Ca <sub>4</sub> B <sub>10</sub> O <sub>9</sub> .7H <sub>2</sub> O	49,8
<b>Hydroboracite</b>	CaMgB <sub>6</sub> O <sub>11</sub> .6H <sub>2</sub> O	50,5

Boron; It has many known effects such as strength enhancer, heat insulator, flame retardant-smoke

suppressor, antimicrobial agent, radiation and defense armor, energy carrier-storage, plant nutrient and cleaner.

Since its establishment in 2003 by Turkish Energy, Nuclear and Mineral Research Agency Boron Research Institute (TENMAK BOREN), a total of 348 projects have been supported and the work of 25 projects continues.As a result of these projects, 31 patent certificates were obtained and 16 products were commercialized.

By the TENMAK BOREN, which aims to produce economic value based on knowledge and technology from boron ore, which is an important national resource; Boron Coating, Boron Materials, Boron Biotechnology, Organobor and Polymer and Boron Composite Materials Research Laboratories have been established.

**References**

1. Boron Sector Report-2021, Eti Mine (2022).  
<https://www.etimaden.gov.tr/storage/pages/June2022/2021%20YILI%20BOR%20SEKT%C3%96R%20RAPORU.pdf>

## **Development of a New Lining Material with Boron Addition**

**Sırma Nur DINLER**

*Gazi University- Department of Metallurgical and Materials Engineering,, Ankara, Türkiye,  
sirmanur.dinler@gazi.edu.tr  
ORCID: 0000-0002-4631-7340*

**Sedat SURDEM**

*Gazi Üniversitesi- Graduate School of Natural and Applied Sciences, 06500, Ankara, Türkiye,  
sedatsurdem@gazi.edu.tr  
ORCID: 0000-0001-8220-7934*

**Hakan ATES**

*Gazi University- Department of Metallurgical and Materials Engineering, 06500, Ankara, Türkiye,  
hates@gazi.edu.tr  
ORCID: 0000-0002-5132-4107*

*Cite this paper as: Dinler, S, Surdem, S, Ates H.,. Development of a New Material with Boron Addition.Int.  
Conf. Advanced. Mater. Sci. & Eng. HiTech.and Device Appl.Oct. 27-29 2022,Ankara, Turkey*

**Abstract.** In this study, it is aimed to develop a new brake lining material that does not harm human health and the environment, has a stable friction coefficient, can be used in passenger cars, and includes the economic and technological evaluation of valuable boron reserves in Turkey. Produced by powder metallurgy; rockwool, graphite, phenolic resin, barite, cashew, hexagonal boron nitride (h-BN) content of the lining material in varying proportions (0.5%, 1%, 3%), in different sizes (1-3  $\mu\text{m}$  and 1-10  $\mu\text{m}$ ) boron carbide ( $\text{B}_4\text{C}$ ) is added. Mixing, sintering and all production processes of the powders were carried out in METISAFE lining R&D laboratories. The samples were subjected to pin-on disc wear test after their production. Test; 20 s braking and 90 s no-load time were performed as 15 periods. According to the test results; While 0.5% and 1% additions of 1-10  $\mu\text{m}$  boron carbide improved the wear properties of the material, a slight decrease in properties was observed as a result of the addition of 3%. In the lining samples produced by adding 1-3  $\mu\text{m}$  boron carbide, the wear properties were improved in all of the additives at 0.5%, 1%, and 3%. When comparing the dimensions, it has been observed that 1-10  $\mu\text{m}$  boron carbide doping provides more improvement in wear properties than 1-3  $\mu\text{m}$ . With this study, it is expected to add a new one to the usage areas of boron reserves in Turkey, to obtain a product that will add added value to Turkey and to shed light on the next studies to be made on this subject.

**Keywords:** Brake Pad, Boron Carbide, Tribology, Powder Metallurgy

© 2022 Published by ICMATSE

### **1. Introduction**

With the effect of developing technology, the need for a good braking system has emerged with the increase in speed, load and engine power in the transportation industry. In order to achieve a safe braking performance in brake systems, the friction materials of the brake system are the most important criteria [1].

Brake system friction materials are expected to show a stable friction coefficient and low wear rate against various effects (operating speed, pressure,

temperature, environmental conditions). The friction material must also be compatible with the disc. This harmony will reduce factors such as vibration, excessive wear and noise. These requirements, which are required from friction materials, should be cost-effective and in a way that causes the least damage to the environment [2]. For this reason, many different components such as polymers, ceramics and metals are used in friction materials. With the use of various compositions with different properties, brake pads are seen as one of the most complex composite

materials [3]. Brake pads convert the kinetic energy of the car into heat energy by friction in the contact area [4]. The performance of brake pads depends on various factors such as driving conditions, pad composition, production parameters. In recent years, the development of brake pads with different compositions with appropriate performance, considering the need for balanced friction, low noise and environmental factors, has caused academic interest. Turkey has the largest boron reserves in the world with a rate of 63% [5]. Boron compounds have a strategic importance for Turkey [6]. Boron; It has various industrial uses such as detergent, pharmaceutical industry, agriculture, energy storage, metallurgy. Boron carbide ( $B_4C$ ), one of the valuable compounds of boron, has superior properties such as high temperature stability and high hardness. In the light of these superior properties, it was thought that it would be appropriate to use boron carbide as a friction material.

In this study, the usability of  $B_4C$  as a brake friction material was investigated by conducting experimental studies. Samples were produced and tests were carried out by using three different amounts of  $B_4C$  (0.5%, 1% and 3% by mass) and in different sizes (1-3  $\mu m$  and 1-10  $\mu m$ ).

## 2. Methodology

Sample composition was determined according to studies in the literature [7,8,9,10]. As indicated in Table 1, rock wool was used as reinforcement, phenolic resin as binder, barite as filling material, hexagonal boron nitride and  $B_4C$  as friction modifier. In addition to the studies in the literature, 0.5%, 1%, 3%  $B_4C$  by mass was used. Boron carbide was added in two different sizes as 1-3  $\mu m$  and 1-10  $\mu m$ .

**Table 1.** Compositions of the friction composite materials

Component	Ingrediens
<b>Reinforcement</b>	Rockwool
<b>Binder</b>	Phenolic resin
<b>Space filler</b>	Barite
<b>Friction modifier</b>	h-BN, boron carbide
<b>Others</b>	Graphite, CNSL

The samples were produced by powder metallurgy method. The powders were measured in the desired proportions and added to the mixer. It was mixed in

the mixer until it became homogeneous. The mixture was added to the pin-on disc sample mold at 80°C in Figure 1, and the temperature was increased to 150°C and cured for 15 minutes. The sample obtained in 20x15 dimensions seen in Figure 2 was cured at 200°C for 20 minutes. Three different amounts (0,5%, 1% and 3% by mass) and two different sizes (1-3  $\mu m$  and 1-10  $\mu m$ ) boron carbide doped samples were produced. In order to see the effect of boron carbide, a raw sample without boron carbide addition was also produced.



**Figure 1.** Pin-on disc sample mold



**Figure 2.** Produced samples

The samples placed in the pin-on disc tribology test device as in Figure 3 were passed through the acclimatization process for full contact with the disc. Afterwards, the samples weighed on precision scales were placed back in the device and tests were carried out for 15 periods, including 90 seconds of idling and 20 seconds of braking. At the end of the test, the samples were weighed again on sensitive scales and the wear amounts were determined.



**Figure 3.** Pin-on disc tribology tester

### 3. Results and discussion

The data obtained as a result of the pin-on disc tribology test are shown in Figure 4. According to the test results, 0.5% and 1% additions of boron carbide in 1-10  $\mu\text{m}$  size increased the wear value of the material from 0.026 to 0.029 and then to 0.073, resulting in an improvement in wear properties. When boron carbide was increased above 3%, a slight decrease in wear was observed compared to the addition of 1% boron carbide. The friction coefficient value did not show a big change in 0.5% boron carbide addition, but increased from 0.15 to 0.19 in 1% boron carbide addition. The wear properties of the samples produced by adding 1-3  $\mu\text{m}$  boron carbide were improved by 0.5%, 1%, and 3% with each addition. The friction coefficient value decreased compared to the raw sample.

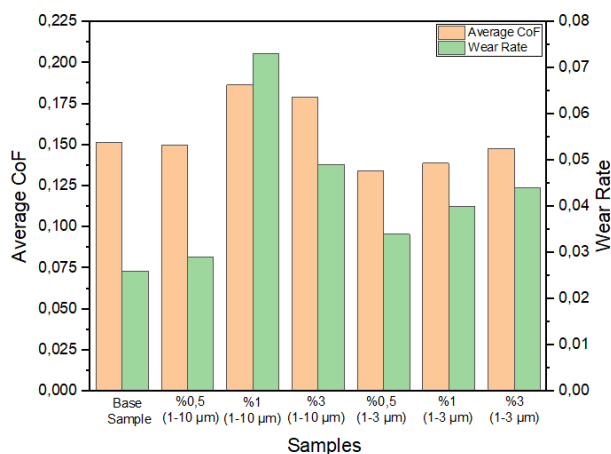


**Figure 4.** Variation of average CoF and wear rate of the samples

When the dimensions are compared, it is seen that 1-10  $\mu\text{m}$  boron carbide additive provides more improvement in wear properties than 1-3  $\mu\text{m}$ .

### 4. Conclusions

### 6. References

1. Cho, M.H., Kim, S.J., Kim, D., & Jang, H.K. (2005). Effects of ingredients on tribological characteristics of a brake lining: an experimental case study. *Wear*, 258, 1682-1687.
2. Hee, K., & Filip, P. (2005). Performance of ceramic enhanced phenolic matrix brake lining materials for automotive brake linings. *Wear*, 259, 1088-1096.
3. Kim, S.J., Kim, K.S., & Jang, H.K. (2003). Optimization of manufacturing parameters for a brake lining using Taguchi method. *Journal of Materials Processing Technology*, 136, 202-208.
4. Ertan, R., & Yavuz, N. (2010). An experimental study on the effects of manufacturing parameters on the tribological properties of brake lining materials. *Wear*, 268, 1524-1532.
5. Sokmen, N., & Buyukakinci, B.Y. (2018). THE USAGE OF BORON/ BORON COMPOUNDS IN THE TEXTILE INDUSTRY AND ITS SITUATION IN TURKEY. *CBU International Conference Proceedings*.
6. Yiğitbaşıoğlu, H. (2004). TÜRKİYE İÇİN ÖNEMLİ BİR MADEN BOR An Important Ore for Turkey Boron.

In this study, the usability of boron carbide as brake pad material and the effect of boron carbide size on brake pad properties were investigated. Samples were prepared by using three different amounts of boron carbide, 1-10  $\mu\text{m}$  and 1-3  $\mu\text{m}$  in size, 0.5%, 1%, and 3%. The samples were tested in a pin-on disc tribology test device and the results obtained from the tests are as follows;

- Among the 1-10  $\mu\text{m}$  sized samples, the sample with 1% boron carbide additive has the highest wear value with 0.073, and the sample with 0.5% boron carbide additive has the lowest wear value with 0.029.
- Among the 1-3  $\mu\text{m}$  sized samples, the 3% boron carbide added sample has the highest wear value with 0.044, and the 0.5% boron carbide added sample has the lowest wear value with 0.034.
- Increasing boron carbide grain size resulted in further improvement in wear properties.
- The friction coefficient decreased when the boron carbide grain size decreased.
- During the pin-on disc tribology test, it was determined that the 1-3  $\mu\text{m}$  1% boron carbide added sample produced more noise compared to the other samples. From this situation, it can be concluded that the brake pad in this composition will work noisily.

With this study, it is expected to add a new one to the usage areas of boron reserves in Turkey, to obtain a product that will add added value to Turkey and to shed light on the studies to be done on this subject from now on.

### 5. Acknowledgments

The authors thank Metisafe Co., Ankara, Turkey, and TENMAK BOREN, Ankara, Turkey, for their support.

7. Yanar, H., Purcek, G., Demirtas, M., & Ayar, H.H. (2022). Effect of hexagonal boron nitride (h-BN) addition on friction behavior of low-steel composite brake pad material for railway applications. *Tribology International*.
8. Sugözü, B., Buldum, B.B., & Sugözü, İ. (2018). ÜLEKSİT VE BORAKS İÇEREN FREN SÜRTÜNME MALZEMELERİNİN TRIBOLOJİK ÖZELLİKLERİ.
9. Eriksson, M., & Jacobson, S. (2000). Tribological surfaces of organic brake pads. *Tribology International*, 33, 817-827.
10. Baklouti, M., Cristol, A., Desplanques, Y., & Elleuch, R. (2015). Impact of the glass fibers addition on tribological behavior and braking performances of organic matrix composites for brake lining. *Wear*, 507-514.

## Design, Fabrication and Characterization of Tunable Metamaterials

**Buse Budak**

*Gazi University, Metallurgical and Materials Engineering, 06500, Ankara Turkiye*

*Bilkent University, Nanotam, Ankara Turkiye*

[buse.budak@bilkent.edu.tr](mailto:buse.budak@bilkent.edu.tr)

ORCID: 0000-0001-5905-4570

**Hakan Ates**

*Gazi University, Metallurgical and Materials Engineering, 06500, Ankara Turkiye*

[hates@gazi.edu.tr](mailto:hates@gazi.edu.tr)

ORCID: 0000-0002-5132-4107

**Mutlu Gokkavas**

*Bilkent University, Nanotam, Ankara Turkiye*

[gokkavas@bilkent.edu.tr](mailto:gokkavas@bilkent.edu.tr)

ORCID: 0000-0002-9244-4201

**Seval Donertas**

*Bilkent University, Nanotam, Ankara Turkiye*

[donertas@bilkent.edu.tr](mailto:donertas@bilkent.edu.tr)

ORCID: 0000-0002-3550-1281

**Ekmel Ozbay**

*Bilkent University, Nanotam, Ankara Turkiye*

[ozbay@bilkent.edu.tr](mailto:ozbay@bilkent.edu.tr)

ORCID: 0000-0003-2953-1828

*Cite this paper as: Budak,B., Ates, H., Gokkavas, M., Donertas, S., Ozbay, E., Design, Fabrication and Characterization of Tunable Metamaterials .Int. Conf. Advanced. Mater. Sci.& Eng. HiTech.and Device Appl.Oct. 27-29 2022,Ankara, Turkey*

**Abstract.** Unique metamaterial structures tailored to work in the terahertz range combined with high quality vanadium (VO<sub>2</sub>) thin films was investigated in order to develop fast modulators. THz modulators, the goal is to develop devices which have excellent electrical characteristics and that also can be modulated by applying an electrical or optical signal. The metal insulator transition for vanadium will be triggered using optical and electrical techniques, resulting in a rapid phase change this will allow the vanadium based metamaterial devices to modulate the THz radiation at high rates. To ensure that these devices work well in the THz region the frequency tunable metamaterial structures as well as the resonant features have to be optimized. The electrical parameters of vanadium dioxide thin films have been studied for the phase change behavior by RF-MS and post-annealing practice. It is examined as it were in two extraordinary administrations: hot and cold states and in the alteration temperatures, where VO<sub>2</sub> acts like an inherent metamaterial with blended metallic shield character. In this extend of metallic and insulating inclusions are temperature adjusted and therefore a gradual change in optical parameters can be achieved.

**Keywords:** Tunable, metamaterials, design, fabrication characterization

© 2022 Published by ICMATSE

Metal-based metamaterials are artificial structures consist of arrays of metallic components with subwavelength dimensions embedded in a dielectric background. These structures have developed taking after their beginning presentation [1]. It is serious issue for special surface recurrence applications [2] and change optics, e.g. cloaking [3], negative file materials and super-lensing [4]. Metamaterials have controlled electromagnetic properties.

New metamaterials can do incredible work, (memory effects with negative refractive index etc.) It gives energizing capacities such as high-resolution imaging, change optics or intangibility [5,6]. Split-ring resonators (SRRs) are a vital components of metamaterial generation due to their ease of manufacture and demonstrating. All SRR structures have capacitance (c) and inductance (L) due to loading. Capacitance and inductance material detects selectors and determines the resonant frequency [2]. Dynamic metamaterials which are designed and fabricated by integrating metal-based metamaterial and materials with tunable electrical or optical properties, show greater control over their resonant responses [7]. This metamaterial is a composite structure consisting of metallic elements on a dielectric substrate in shape [8-10]. As an alternative geometry reported in [1] for the active split-ring resonator (SRR) metamaterials, self-aligned, hybrid Ag/VO<sub>2</sub> SRR bi-layers were designed and fabricated to tune the metamaterial response in the near-IR by controlling the resonator geometry with the phase transition of VO<sub>2</sub>[11]. As of now, a part of investigate endeavors are situated towards dynamic, controllable metamaterials having nonlinear properties [8,112] by utilizing dynamic alteration of the shapes of their unit cells or of the encompassing environment, through outside boosts [8,9].

On the other hand, active metamaterials which are designed and fabricated by integrating metal-based metamaterial and appear assist control over their resonant reactions. THz investigate and innovation pull in an expansive portion of this inquire about exertion in arrange to neutralize the confinements of

normal materials with craved electromagnetic properties in this portion of the recurrence range. By changing the capacitance in the SRR gap using an optically tunable semiconductor, it is possible to switch the resonances from the first mode to the second one [5]. As an alternative geometry reported in [5] for the active SRR metamaterials, self-aligned, hybrid Ag/vanadium oxide and SRR bi-layers were designed and fabricated to tune the metamaterial reaction within the near -IR by controlling the resonator shape with the stage move of VO<sub>2</sub> [6]. Vanadium oxide could be a promising candidate that shows a emotional alter in its mixed refractive record emerging from a basic stage move from protection mono clinic to metallic rutile upon either coordinate heating or optical pumping [13,14]. Here, using measured values of DC resistance, carrier density and carrier mass of our fabricated VO<sub>2</sub> sample, we design active SRR metamaterials operating at mid-IR. The top view of our design is schematically outlined within the inset of Fig. 1.

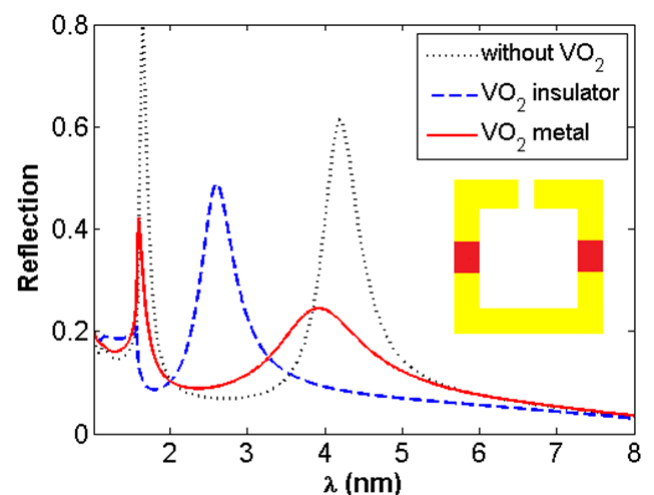


**Fig. 1:** Reflection of the considered gold SRR array for the absence (dotted-black) and presence of VO<sub>2</sub> (dashed blue insulator phase and solid-red metal phase). The inset schematically shows the unit cell of the considered structures. Width of the gap and the arms of SRR is 100 nm, length of the arms is 460 nm, unit cell dimension is 900x900 nm<sup>2</sup>, and the thickness of gold is 70 nm. The incident plane wave in the simulation is normally incident to the array with the electric field perpendicular to the SRR arms.

As expected, the SRR array without the presence of VO<sub>2</sub> exhibits two sharp peaks in the reflection spectrum corresponding to the electric and magnetic resonances. Once we consider VO<sub>2</sub> in its insulator phase (T=20 °C), the resonances of the dashed-blue curve are weakened and blue-shifted, as compared to those of dotted-black curves. On the other hand, in case of increasing temperature to 80 °C and changing the phase of VO<sub>2</sub> to metal, it is seen from the solid-red curve illustrated in Fig. 1 that red-shift of those resonances can be observed in comparison with those observed in the insulator phase. In spite of the fact that the VO<sub>2</sub> move is commonly controlled through warm inners, it has additionally been appeared that the VO<sub>2</sub> move may be actuated and controlled through optical suggests by utilizing either determined wave excitation [15,16] or beat excitation [17, 18].

### CONCLUSION

To summarize, the SRR array structures without absence and presence of VO<sub>2</sub> have been designed and simulated. Once we consider VO<sub>2</sub> in its insulator phase (T=20 °C), the resonances of the dashed-blue curve are weakened and blue-shifted, as compared to those of dotted-black curves. On the other hand, in case of increasing temperature to 80 °C and changing the phase of VO<sub>2</sub> to metal, it is seen from solid-red curve illustrated in Fig. 1(b). Considering deposition of VO<sub>2</sub>; VO<sub>2</sub> thin film with 80 nm thickness has been deposited onto a c-plane sapphire wafer under nonreactive environment. According to Ar and O<sub>2</sub> gas ratio optimization during annealing, resistance change has been analyzed. It has been confirmed that O<sub>2</sub> gas ratio has an important effect on the electrical

### References

1. V. G. Veselago, "The electrodynamics of substances with simultaneously negative values of permittivity and permeability," *Sov. Phys. Usp.* 10, 504–509 (1968).
2. S. Linden, C. Enkrich, M. Wegener, J. F. Zhou, T. Koschny, and C. M. Soukoulis, "Magnetic response of metamaterials at 100 terahertz," *Science* 306 (5700), 1351–1353 (2004).
3. W. S. Cai, U. K. Chettiar, A. V. Kildishev, and V. M. Shalaev, "Optical cloaking with metamaterials," *Nat. Photonics* 1(4), 224–227 (2007).
4. K. Aydina, I. Bulu, and E. Ozbay, "Subwavelength resolution with a negative-index metamaterial superlens," *Appl. Phys. Lett.* 90, 254102 (2007).

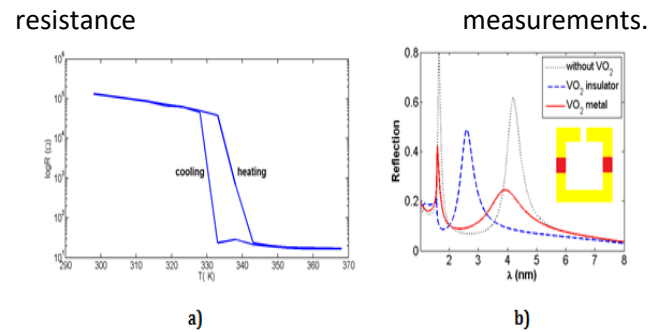


**Fig. 2.** (a) Hysteresis loop for electrical resistance (b) Reflection of the considered gold SRR array for the absence (dotted-black) and presence of VO<sub>2</sub> (dashed blue insulator phase and solid-red metal phase).

Electrical resistance depends on temperature. This is demonstrated four-probe measurements. For example, maximum electrical resistance change; transition temperature is nearly 340 K and max./min. resistance ratio is in the order of nearly 1.5E+3 and graph has been observed. Four-probe measurement results are shown in Fig. 2(a). Using measured value of DC resistance of fabricated VO<sub>2</sub> sample, active SRR metamaterials operating at mid-IR have been designed. Designed structure is schematically illustrated in Fig. 2(b).

The oxidation state of the sputtered films tried to be controlled by optimizing O<sub>2</sub> ratio of the post annealing atmosphere. The absence of O<sub>2</sub> in the annealing atmosphere prohibits obtaining a phase change thin film. In the case of the presence of O<sub>2</sub>, 5% seems to be the optimum ratio for getting a phase change film with high max/min resistance ratio. With increase in O<sub>2</sub> ratio, phase change still can be observed but max/min resistance ratio gets worse. But when O<sub>2</sub> ratio in the annealing atmosphere reaches to 20%; phase change cannot be observed.

5. Nian-Hai Shen, Maria Massaouti, Mutlu Gokkavas, Jean-Michel Manceau, Ekmel Ozbay, Maria Kafesaki, Thomas Koschny, Stelios Tzortzakis, and Costas M. Soukoulis, "Optically Implemented Broadband Blueshift Switch in the Terahertz Regime," *Phys. Rev. Lett.* 106, 037403 (2011).
6. Matthew J. Dicken, Koray Aydin, Imogen M. Pryce, Luke A. Sweatlock, Elizabeth M. Boyd, Sameer Walavalkar, James Ma, and Harry A. Atwater, "Frequency tunable near-infrared metamaterials based on VO<sub>2</sub> phase transition," *Opt. Exp.* 19, 18330 (2009).
7. Peng Zhou and G.G. Zheng "Active control of broadband perfect absorption with phase changing materials-cooperated symmetry-broken nanodisks" *Optik* 217 164842 (2020)
8. B. Pendry, A. Holden, D. Robbins, and W. Stewart, "Magnetism from conductors and enhanced nonlinear phenomena," *IEEE Trans. Microw. Theory Tech.*, vol. 47, no. 11, pp. 2075-2084, 1999.
9. D. R. Smith, W. Padilla, D. C. Vier, S. C. Nemat-Nasser and Schultz, S. "Composite medium with simultaneously negative permeability and permittivity," *Phys. Rev. Lett.* Vol. 84, pp. 4184-4187, 2000.
10. H. T. Chen, W. 1 Padilla, J. M. O. Zide, A. C. Gossard, A. 1 Taylor, and R. D. Averitt, "Active terahertz metamaterial devices," *Nature* vol. 444, pp. 597-600, 2006.
11. Matthew J. Dicken et al "Frequency tunable near-infrared metamaterials based on VO<sub>2</sub> phase transition" *OPTICS EXPRESS* vol. 17, Issue 20, pp. 18330-18339 (2009)
12. H.-T. Chen, W. 1 Padilla, R. D. Averitt, A. C. Gossard, C. Highstrete, M. Lee, J. F. O'Hara, and A. J. Taylor, "Electromagnetic Metamaterials for Terahertz Applications," *Terahertz Science and Technology*, vol. 1, no. 1, pp. 42-50, March 2008
13. S. Zhang, W. Fan, N. C. Panoiu, K. 1 Malloy, R. M. Osgood, and S. R. 1. Brueck, "Experimental demonstration of nearinfrared negative-index metamaterials," *Phys. Rev. Lett.*, vol. 95, pp. 137404, 2005.
14. N. Zheludev, "The Road Ahead for Metamaterials ", *Science*, vol. 328, pp. 5582-5583, April 2010
15. T. Ben-Messaoud, G. Landry, J. P. Gariépy, B. Ramamoorthy, P. V. Ashrit, and A. Haché, "High contrast optical switching in vanadium dioxide thin films," *Opt. Commun.* 281(24), 6024-6027 (2008).
16. S. Bonora, U. Bortolozzo, S. Residori, R. Balu, and P. V. Ashrit, "Mid-IR to near-IR image conversion by thermally induced optical switching in Vanadium Dioxide," *Opt. Lett.* 35(2), 103-105 (2010).
17. A. Cavalleri, C. Tóth, C. W. Siders, J. A. Squier, F. Ráksi, P. Forget, and J. C. Kieffer, "Femtosecond structural dynamics in VO<sub>2</sub> during an ultrafast solid-solid phase transition," *Phys. Rev. Lett.* 87(23), 237401 (2001).
18. M. F. Becker, A. B. Buckman, R. M. Walser, T. Lépine, P. Georges, and A. Brun, "Femtosecond laser excitation of the semiconductor-metal phase transition in VO<sub>2</sub>," *J. Appl. Phys.* 65(12), 1507-1509 (2000).

## **Highly efficient Cr(VI) removal from aqueous solution by SnO<sub>2</sub> loaded wild plumb kernel shell biochar composite**

**Md Mehedi Hasan**

*Konya Technical University, Faculty of Engineering and Natural Sciences, Department of Metallurgical and Materials Engineering, Konya, Turkey,  
mehedihasan98609@gmail.com  
ORCID: 0000-0002-1451-9650*

**Elif Gezgin**

*Konya Technical University, Faculty of Engineering and Natural Sciences, Department of Chemical Engineering, Konya, Turkey,  
elfgezginci@gmail.com  
ORCID: 0000-0003-0645-3038*

**Ozlem Altintas Yildirim**

*Konya Technical University, Faculty of Engineering and Natural Sciences, Department of Metallurgical and Materials Engineering, Konya, Turkey.  
Nanotechnology and Advanced Materials Development, Application and Research Center, Konya Technical University, Konya, Turkey,  
oayildirim@ktun.edu.tr  
ORCID: 0000-0001-7867-7992*

**Erol Pehlivan**

*Konya Technical University, Faculty of Engineering and Natural Sciences, Department of Chemical Engineering, Konya, Turkey,  
epehlivan@gmail.com  
ORCID: 0000-0003-3960-6790*

**Abstract.** Wastes like Cr (VI) contribute more and more each year to the contamination of underground and surface natural spring waters increases every year. The mixing of Cr (VI) into drinking water and daily use water has become a global public health problem. There is currently intense interest in eliminating Cr (VI) contamination in the water. Biochar-nanostructure composites have drawn attention as promising removal agents for their high catalytic and adsorption activity, low cost, and environmental friendliness. In this study, a novel composite of wild plumb kernel shell (WPKS) biochar (BC) loaded with SnO<sub>2</sub> nanoparticles (SnO<sub>2</sub>/BC) was successfully prepared for the highly effective removal of Cr (VI) from aqueous solution under UV-light irradiation. The composite sample was structurally, morphologically and optically characterized by XRD, SEM and UV-visible spectroscopy analysis. Cr (VI) removal was investigated with an aqueous solution containing 5, 10 and 25ppm Cr (VI). Furthermore, Cr (VI) removal was also examined with 20, 30, and 40mg composite addition into an aqueous solution. The results indicated that superior Cr (VI) removal efficiency (~100%) for SnO<sub>2</sub>/BC nanocomposite had been achieved after 135 minutes of UV-light illumination with 30mg composite addition into 10 ppm Cr (VI) containing aqueous solution. This study shows that the prepared SnO<sub>2</sub>/BC nanocomposite structure exhibits highly efficient Cr (VI) removal capacity from an aqueous solution.

**Keywords:** Biochar, SnO<sub>2</sub> nanoparticles, Cr (VI) removal, Adsorption, Photocatalysis

© 2022 Published by ICMATSE

### **1. Introduction**

Water is the most significant and crucial resource on Earth, however, anthropogenic activities seriously pollute it. Increased levels and varieties of metal effluents from urban and industrial rivers are contaminating the water and threatening human

health [1]. Heavy metals must be removed from water since they are among the many harmful substances found in wastewater produced by industrial activity. Due to its activity, solubility, and transformation in water, chromium has been recognized as one of the most dangerous metal

pollutants in wastewater. There are several applications for Cr (VI), and it is frequently used in numerous industrial processes. Metallurgy, electroplating, dyeing, tanneries, fertilizer production, and fungicide production are the main ones. Highly soluble Cr (VI) is released into aquatic habitats because of these activities [2, 3].

Chromium (Cr) can be found in two different forms quite commonly in the wastewater environment. Both trivalent chromium (Cr (III)) and chromium (Cr (VI)) are used to denote it; Cr (VI) is approximately 300 times more harmful than Cr (III) and may transmit in the long-distance watery medium due to its vast bioavailability and high-water solubility [4]. Depending on the potential and pH of the medium, it can be found in a variety of forms. There are primarily two very soluble forms of Cr (VI) ( $\text{CrO}_4^{2-}$  and  $\text{Cr}_2\text{O}_7^{2-}$ ), which are much more poisonous and damaging than Cr (III) [3].

New studies on the production of low-carbon, environmentally friendly water cleaning products from carbon-containing biomass, an environmentally sustainable, consistent, and widely available resource, have gained popularity around the world. Biochar, an incredibly carbon-rich substance, can be produced by heating organic biomass, naturally occurring plant wastes, or plant byproducts under nitrogen atmospheres, which may have very low oxygen levels, in enclosed furnaces or reactors. Biochar (BC) is a carbohydrate-rich material produced by the pyrolysis of natural biomass with short heat excursions at acceptable low temperatures (600-700°C) [5]. Polysaccharides and other cellulosic components of biomass are converted into carbon-rich solids at high temperatures in a closed system. Biochar has a sizable surface area since so many micropores were created on the surface of the solid biomass during the pyrolysis process. Depending on the production conditions, the application of biochar, which has varied pore sizes and shapes, as an adsorbent in the retention of hazardous ions in water, significantly affects the adsorption capacity. BC possesses rich surface functional groups (C=O, C-O, COOH, COO<sup>-</sup>, -OH, etc.), a sizable surface area, controllable physicochemical properties, and the benefits of a simple raw material supply.

The multiple methods used to remove Cr (VI) from wastewater include adsorption, biological degradation, flocculation/coagulation, electro-dialysis, nano-filtration, photochemical degradation, chemical precipitation, reverse osmosis, membrane filtering, and oxidative degradation [6-8]. Adsorption is one of them, and it's frequently used for removing Cr (VI) in developing countries due to its improved

effectiveness, nontoxicity, consistency, and affordability [3].

The use of metal reduction by photocatalysis is a non-toxic, environmentally friendly, and energy-efficient technological solution for the issue of water-based hazardous materials [9]. The photocatalytic systems don't require reactive oxygen species and are safe for the environment. By using photocatalysis, the n-type semiconductor compound  $\text{SnO}_2$  has successfully removed contaminants.  $\text{SnO}_2$  has many advantages, including high photosensitivity, nontoxicity, relatively inexpensive, chemical resistance, and high electron mobility [10]. Cr (VI), whose content in the aqueous phase has greatly increased, can be controlled well as an alternative by photocatalytic reduction technique. It focuses on lighting an energetic semiconductor photon that generates electron-hole ( $e^-/h^+$ ) pairs causing photo-redox reactions where Cr (VI) is reduced to a less damaging state, particularly Cr (III) [11].

Metal oxide/biochar composites have extensive implications in the adsorption and photocatalytic degradation of the hazardous Cr (VI) from aqueous solution. The photocatalytic activity of  $\text{SnO}_2/\text{BC}$  is significantly influenced by their production processes. The increased photocatalytic performance of the  $\text{SnO}_2/\text{BC}$  composite, which may be employed to treat Cr (VI), is the main emphasis of this study. The first reports of photocatalytic reduction of Cr (VI)-Cr (III) in the presence of  $\text{SnO}_2/\text{BC}$  nanocomposite were generated with this research. The BC was produced by heating Wild Plum Kernel Shell (WPKS) in a nitrogen atmosphere in a furnace. The influence of key process variables, such as contact time and amount of  $\text{SnO}_2/\text{BC}$ , and Cr (VI) concentration was examined for Cr (VI) removal. The rate of Cr (VI) degradation and adsorption from aqueous solution were assessed.

## 2. Materials and Methods

### 2.1. Materials

BC is prepared from the wild plum (*Prunus domestica*) kernel shells. Tin (IV) chloride pentahydrate ( $\text{SnCl}_4 \cdot 5\text{H}_2\text{O}$ , 98.0%) and pure ethanol ( $\text{C}_2\text{H}_5\text{OH}$ ) were obtained from Sigma-Aldrich.

### 2.2. Synthesis of $\text{SnO}_2$ nanoparticles

Hydrothermal synthesis was used to produce  $\text{SnO}_2$  nanoparticles. First, 100 mL of DI-water was combined with 2.14 g of  $\text{SnCl}_4 \cdot 5\text{H}_2\text{O}$  and magnetically agitated for one hour to produce a tin salt solution. After vigorously swirling the mixture, 2M aqueous NaOH solution was gradually added until the pH

reached 9.0. Then, the solution was conditioned by refluxing for 60 minutes at room temperature. Following that, 40 mL of ethanol was introduced to the final solution and stirred for further one hour. A 150 mL Teflon container with a 75% fill level was used to deliver the concentrated white solution. The container was then heated to 180 °C for one day. Then, the white nanoparticles were separated and cleaned with 100% ethanol. The resultant white particulates have undergone a 5-hour, 100 °C oven drying process. The finished white SnO<sub>2</sub> nanoparticles from the hydrothermal synthesis method were pulverized in an agate mortar.

### 2.3. Fabrication of SnO<sub>2</sub>/BC composite

Biochar and SnO<sub>2</sub> nanoparticles that had been produced under the proper experimental conditions were used to construct the SnO<sub>2</sub>/BC composite. The composite was produced by combining WPKS (2.0 g) and previously manufactured SnO<sub>2</sub> nanoparticles (0.1 g). This composite powder was put into a tube furnace and heated to 450 °C before remaining at that temperature for an additional hour in an atmosphere of argon. After 2 hours, the tube furnace cooled to room temperature, and samples of the black nanocomposite had been formed.

### 2.4. Characterization

Using Cu-K radiation and the Bruker D8 Advanced X-ray Diffraction (XRD) equipment, the phase analysis of the produced samples was examined ( $\lambda = 1.5406 \text{ \AA}$ ) at the  $20^\circ \leq 2\theta \leq 70^\circ$  boundary values. An energy step size of 0.1 eV was used to record the XRD spectra. Using a ZEISS EVO LS10 type scanning electron microscope (SEM), the samples' microstructure was evaluated. Using a Cary 5000 UV-Vis spectrophotometer, the absorption spectra of samples were obtained to analyze the optical characteristics.

### 2.5. Evaluation of photocatalytic activity

Monitoring the degradation of Cr (VI) under UV light irradiation and using six 8-watt Osram UV-C lamps as the UV light supply allowed to assess the photocatalytic activity of SnO<sub>2</sub>/BC composite. For each measurement, the sample material was added to the aqueous Cr (VI) solution that had been made with a contaminant model at a concentration of 5, 10 and 25 ppm. The initial pH of Cr (VI) solutions was adjusted to 2.0, 7.0 and 10.0 adding 0.1 M HCl and 0.1 M NaOH solution. 5 mL of the Cr (VI) sample was obtained from the mother solution at intervals of 15 min irradiation, and it was instantly centrifuged at 10,000 rpm for 5 min to separate starting samples.

Then, on the centrifuged solutions, the highest absorption band ( $\sim 350 \text{ nm}$  for Cr (VI)) was detected using a UV-Vis spectrophotometer. To maintain a constant concentration during all measurements, the measured Cr (VI) solution and centrifuged solid samples were transferred back into suspension.

## 3. Results and Discussion

### 3.1. Structural Analyses

The determination of the phases of the produced nanostructures was investigated using XRD studies. Fig. 1 and 2 display the XRD patterns of the nano SnO<sub>2</sub> and SnO<sub>2</sub>/BC composites. The XRD pattern of the SnO<sub>2</sub> sample shows broad peaks that formed at 26.66°, 33.95°, 38.11°, 51.73°, and 62.26°, respectively, corresponding to the (110), (101), (200), (211), and (310) planes of the tetragonal crystal structure of SnO<sub>2</sub> (JCPDS card no: 41-1445). The average crystallite size of the produced SnO<sub>2</sub> nanostructures was calculated using the Debye-Scherrer equation to be 2.9 nm.

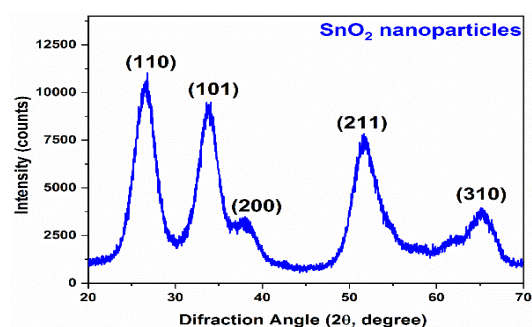


**Figure 1.** XRD phase diagram of hydrothermally synthesized SnO<sub>2</sub> nanoparticles.

Fig. 2 shows XRD phase diagram of SnO<sub>2</sub>/BC nanocomposites. Apart from characteristic SnO<sub>2</sub> peaks, XRD pattern exhibits various additional peaks indicated the formation of mineral crystals and other inorganic materials. Strong peaks appeared at  $2\theta = 29.1^\circ, 36.0^\circ, 39.5^\circ, 43.3^\circ$  and  $47.5^\circ$  can be indexed with pyrophyllite, chlorite, barite and hydrobiotite minerals [12]

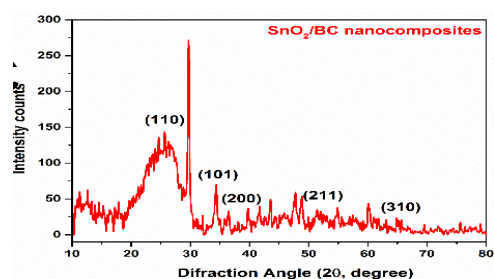


**Figure 2.** XRD phase diagram of SnO<sub>2</sub>/BC nanocomposites.

### 3.2. Morphological Analyses

Exploring morphological and microstructural details was done using SEM micrographs of the SnO<sub>2</sub>/BC composite. Both composite structures, as represented in Figs. 3(a) and (b), maintain their porous biochar framework with substantial specific surfaces. The pores in the biochar may allow SnO<sub>2</sub> nanoparticles to pass through the network.

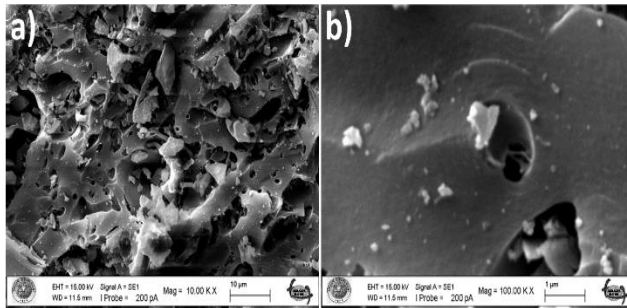


Figure 3. Low and high magnification SEM micrographs of SnO<sub>2</sub>/BC nanocomposites.

### 3.3. Photocatalytic properties

The photocatalytic performance of SnO<sub>2</sub>/BC composite was analyzed using Cr (VI) absorbance under UV light irradiation. Fig. 4 shows with a rise in starting concentration, the reduction efficiency of Cr (VI) steadily declines.

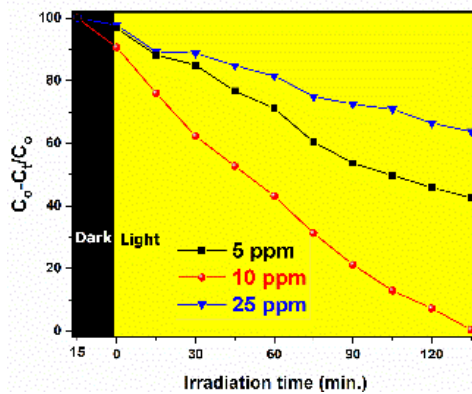
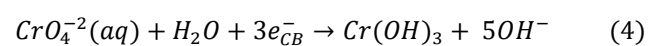
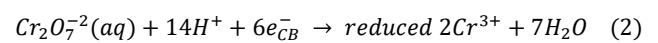
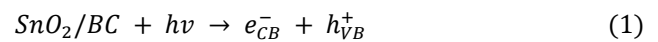


Figure 4. Effect of initial Cr (VI) concentration on the removal activity of SnO<sub>2</sub>@Biochar nanocomposites as a function of time.

Hetero-systems are preferred for photocatalytic degradation due to their huge surface area and interactive effects [13], and they offer significant advantages for energy transfer because they make it easier to separate charge carriers and conduct via interconnected microstructures. Due to the internal electric field, the charge carriers move in opposite ways. SnO<sub>2</sub> was chosen for this investigation due to its inexpensive cost, low toxicity, and chemical

resistance across the full pH range. Its conduction band (CB), which sits halfway between BC and Cr(VI), should make it easier for electrons to travel to bound Cr(VI) species [14]. It is commonly recognised that the electron stimulation from the conduction band (CB) to the valance band (VB) influences the semiconductor material's photocatalytic performance. An excited electron (e<sup>-</sup>) in CB and a hole (h<sup>+</sup>) in VB are the consequences of this photo-generated excitation.

Highly hazardous Cr (VI) can be successfully detoxified into low-toxic Cr (III) by removing electrons from semiconductor surfaces that have already been activated by light. The separated electrons produced by the SnO<sub>2</sub> can convert Cr(VI) species to Cr(III), which can subsequently be removed as a solid precipitate, as shown in Eqs. (1) to (4) [15]:



The described Cr(VI) reduction process can only be enabled to take place when the CB potential of semiconductors rich in electrons is more negative than the reduction potential of Cr(VI)/Cr(III) (0.82 V vs NHE) [15].

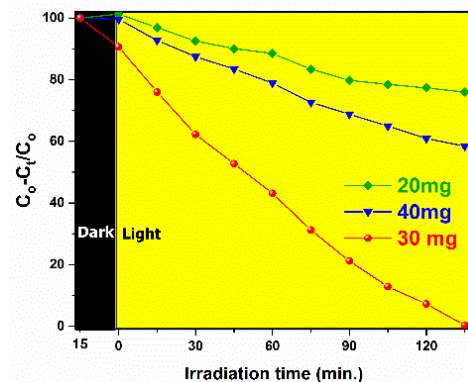


Figure 5. Effect of initial SnO<sub>2</sub>/BCr content on the Cr (VI) removal as a function of time.

After being reduced by photogenerated e<sup>-</sup> species, the surface-adsorbed Cr (VI) was stabilized on SnO<sub>2</sub>/BC composites. The composites first had Cr (VI) adsorbed on surfaces of BC, and SiO<sub>2</sub>'s photogenerated electrons were then passed over to the SnO<sub>2</sub>/BC composites. The reduced Cr (VI) was then electrostatically attracted to the BC surface

groups, where it was converted to Cr (III), and finally attached permanently. The whole methodology and relevant reactions for reducing Cr (VI) to Cr (III) are outlined by Rajapaksha et al. (2018) who discovered that Cr (VI) was highly adsorbed on BC at low pH values (2–5) and that this adsorption declined as pH increased, which was in close consistency with the surface charge of both SnO<sub>2</sub>/BC composite and Cr (VI) species [16].

#### 4. Conclusions

In this study, the use of biochar and n-SnO<sub>2</sub> together to potentially remove toxic Cr (VI) from aqueous solutions was investigated. The new biochar material showed an exceptional ability to remove Cr (VI), and the highest adsorption capacity of SnO<sub>2</sub>/BC was obtained.

SnO<sub>2</sub>/BC contributes significantly to the improvement of photocatalytic performance by offering a perfect surface for the accumulation of dispersed nanoparticles, increasing the active surface area and quantity of active sites of the catalyst, and enhancing the transfer of electrons from the CB of SnO<sub>2</sub> to the surface of BC. Photocatalytic experiments show that SnO<sub>2</sub> nanoparticle inclusion enhances the degradation activity of BC. It was discovered that employing SnO<sub>2</sub>/BC nanocomposite, photooxidation under UV light for 135 minutes can obtain approximately 100% degradation efficiency of 10 ppm Cr (VI) solution. When the pH of the solution was adjusted to 2.0, Cr(VI) dissociation is sufficient compared to the higher pH values of the solution.

#### References

1. J. Singh, S. Sharma, Aanchal, S. Basu, Synthesis of Fe<sub>2</sub>O<sub>3</sub>/TiO<sub>2</sub> monoliths for the enhanced degradation of industrial dye and pesticide via photo-Fenton catalysis, *Journal of Photochemistry and Photobiology A: Chemistry*, 376 (2019), 32-42.
2. S. Xia, Z. Song, P. Jeyakumar, S.M. Shaheen, J. Rinklebe, Y.S. Ok, N. Bolan, H. Wang, A critical review on bioremediation technologies for Cr (VI)-contaminated soils and wastewater, *Critical Reviews in Environmental Science and Technology*, 49 (2019), 1027-1078.
3. B. Cui, Z. Chen, F. Wang, Z. Zhang, Y. Dai, D. Guo, W. Liang, Y.J.N. Liu, Facile Synthesis of Magnetic Biochar Derived from Burley Tobacco Stems towards Enhanced Cr (VI) Removal: Performance and Mechanism, 12 (2022), 678.
4. P. Miretzky, A.F. Cirelli, Cr (VI) and Cr (III) removal from aqueous solution by raw and modified lignocellulosic materials: a review, *Journal of Hazardous Materials*, 180 (2010), 1-19.
5. D. Kalderis, M. Kotti, A. Méndez, G. Gascó, Characterization of hydrochars produced by hydrothermal carbonization of rice husk, *Solid Earth*, 5 (2014), 477-483.
6. A. Dbik, S. Bentahar, M. El Khomri, N. El Messaoudi, A. Lacherai, Adsorption of Congo red dye from aqueous solutions using tunics of the corm of the saffron, *Materials Today: Proceedings*, 22 (2020), 134-139.
7. E. Pehlivan, S. Cetin, Sorption of Cr (VI) ions on two Lewatit-anion exchange resins and their quantitative determination using UV-visible spectrophotometer, *Journal of Hazardous Materials*, 163 (2009), 448-453.
8. S. Parlayici, V. Eskizeybek, A. Avci, E. Pehlivan, Removal of chromium (VI) using activated carbon-supported-functionalized carbon nanotubes, *Journal of Nanostructure in Chemistry*, 5 (2015), 255-263.
9. D. Gümüş, F. Akbal, Photocatalytic degradation of textile dye and wastewater, *Water, Air, Soil Pollution*, 216 (2011), 117-124.
10. G. Elango, S.M. Roopan, Efficacy of SnO<sub>2</sub> nanoparticles toward photocatalytic degradation of methylene blue dye, *Journal of Photochemistry Photobiology B: Biology*, 155 (2016), 34-38.
11. Q. Wang, X. Shi, J. Xu, J.C. Crittenden, E. Liu, Y. Zhang, Y. Cong, Highly enhanced photocatalytic reduction of Cr (VI) on AgI/TiO<sub>2</sub> under visible light irradiation: influence of calcination temperature, *Journal of Hazardous Materials*, 307 (2016), 213-220.
12. M. Waqas, A.S. Aburizaiza, R. Miandad, M. Rehan, M.A. Barakat, A.S. Nizami, Development of biochar as fuel and catalyst in energy recovery technologies, *Journal of Cleaner Production*, 188 (2018), 477-488.
13. E. Keles, M. Yildirim, T. Öztürk, O. Altintas Yildirim, Hydrothermally synthesized UV light active zinc stannate:tin oxide (ZTO:SnO<sub>2</sub>) nanocomposite photocatalysts for photocatalytic applications, *Materials Science in Semiconductor Processing*, 110 (2020), 104959.
14. L. Li, C. Guo, J. Shen, J. Ning, Y. Zhong, Y. Hu, Construction of sugar-gourd-shaped CdS/Co<sub>1-x</sub>S hollow hetero-nanostructure as an efficient Z-scheme photocatalyst for hydrogen generation, *Chemical Engineering Journal*, 400 (2020), 125925.
15. G. Zhang, D. Chen, N. Li, Q. Xu, H. Li, J. He, J.J.A.C.B.E. Lu, Preparation of ZnIn<sub>2</sub>S<sub>4</sub> nanosheet-coated CdS nanorod heterostructures for efficient photocatalytic reduction of Cr (VI), 232 (2018), 164-174.
16. A.U. Rajapaksha, M.S. Alam, N. Chen, D.S. Alessi, A.D. Igalavithana, D.C. Tsang, Y.S. Ok, Removal of hexavalent chromium in aqueous solutions using biochar: chemical and spectroscopic investigations, *Science of the Total Environment*, 625 (2018), 1567-1573.

## High throughput DFT calculations and UHS sintering on high entropy diboride ceramics

**Mubashir Mansoor<sup>1,2</sup>, Sina Kavak<sup>1,3</sup>, Amir Akbari<sup>1,3</sup>, Mehya Mansoor<sup>1,4</sup>, Maryam Mansoor<sup>1,5</sup>, Volkan Dedeoğlu<sup>8</sup>, Zuhale Er<sup>2,6</sup>, Kamil Czelej<sup>7</sup>, Lütfi Öveçoğlu<sup>1</sup>, Mustafa Ürgen<sup>1\*</sup>, Duygu Ağaoğulları<sup>1,3\*</sup>**

<sup>1</sup> Department of Metallurgical and Materials Engineering, Istanbul Technical University, Maslak, Istanbul, Türkiye

<sup>2</sup> Department of Applied Physics, Istanbul Technical University, Maslak, Istanbul, Türkiye

<sup>3</sup> Prof. Dr. Adnan Tekin Materials Science and Production Technologies Applied Research Center (ATARC), Istanbul Technical University, Maslak, Istanbul, Türkiye

<sup>4</sup> Department of Geological Engineering, Istanbul Technical University, Maslak, Istanbul, Türkiye

<sup>5</sup> Department of Mining Engineering, Istanbul Technical University, Maslak, Istanbul, Türkiye

<sup>6</sup> Maritime Faculty, Istanbul Technical University, Tuzla, Istanbul, Türkiye

<sup>7</sup> Institute of complex system modeling, Warsaw University, Warsaw, Poland

<sup>8</sup> CSIRO Data61, Brisbane, Australia

\*Corresponding authors. Assoc. Prof. Dr. Duygu Ağaoğulları ([bozkurtdu@itu.edu.tr](mailto:bozkurtdu@itu.edu.tr))

Prof. Dr. Mustafa Ürgen ([urgen@itu.edu.tr](mailto:urgen@itu.edu.tr))

Cite as: Mansoor, M., Kavak, S., Akbari, M., Mansoor, M., Mansoor, Dedeoğlu, V., Er, Z., Czelej, K., Öveçoğlu, L., Ağaoğulları, D., Ürgen, M., High throughput DFT calculations and UHS sintering on high entropy diboride ceramics. *Int. Conf. Advanced. Mater. Sci. & Eng. HiTech. and Device Appl. Oct. 27-29 2022, Ankara, Turkey*

### Abstract

High entropy materials have become a cornerstone of rapid advancements in the materials world with novel and enhanced properties when compared to traditional multicomponent systems, making high entropy materials an active area of research for a variety of applications [1]. Diborides are especially interesting amongst the high entropy ceramics, due to their superb hardness that can be in excess of 30 GPa, and high melting temperatures, as well as the phase stabilities at low pressures, thus making it possible to synthesize super-hard material that do not require high pressure high temperature (HPHT) conditions, unlike diamond [2]. However, considering the vast phase space of the high entropy diborides, it is not feasible to explore the possibilities using traditional trial and error based experimentation and characterization [3]. We have conducted a high-throughput computation on the possible equimolar high entropy diboride compositions that can be formed from the nine B-group refractory elements (Hf, Mo, Ti, W, Zr, V, Nb, Cr, and Ta) and boron, in the AlB<sub>2</sub> hexagonal crystal structure. The mechanical properties including elastic constants and moduli, thermal expansion, hardness, and fracture toughness have been calculated through ab-initio density functional theory (spin polarized DFT), similar to the successful ab-initio methodology we have recently applied on (HfTiZrW)<sub>2</sub>B<sub>2</sub> ceramics [4]. The most promising of the diborides were then synthesized experimentally by using the ultra-fast high temperature sintering method (UHS) [5], followed by their characterizations. We demonstrate new Ashby diagrams on the diboride phase space, and experimentally validate the computed data on a number of promising compositions.

**Keywords:** DFT, high-throughput, diborides, high entropy ceramics, UHS.

© 2022 Published by ICMATSE

### References

1. Ma, Y., Ma, Y., Wang, Q., Schweidler, S., Botros, M., Fu, T., Hahn, H., Brezesinski, T., & Breitung, B. (2021). High-entropy energy materials: challenges and new opportunities. *Energy and Environmental Science*, 14(5), 2883–2905. <https://doi.org/10.1039/d1ee00505g>
2. Zhang, Y., Guo, W. M., Jiang, Z. B., Zhu, Q. Q., Sun, S. K., You, Y., Plucknett, K., & Lin, H. T. (2019, April). Dense high-entropy boride ceramics with ultra-high hardness. *Scripta Materialia*, 164, 135–139. <https://doi.org/10.1016/j.scriptamat.2019.01.021>
3. Mitra, R., Bajpai, A., & Biswas, K. (2022, June). Machine learning based approach for phase prediction in high entropy borides. *Ceramics International*, 48(12), 16695–16706. <https://doi.org/10.1016/j.ceramint.2022.02.218>
4. Kavak, S., Bayrak, K. G., Mansoor, M., Kaba, M., Ayas, E., Balci-Çağiran, Z., Derin, B., Öveçoğlu, M. L., & Ağaoğulları, D. (2022, October). First Principles Calculations and Synthesis of Multi-Phase (HfTiWZr)<sub>2</sub>B<sub>2</sub> High Entropy Diboride Ceramics: Microstructural, Mechanical and Thermal Characterization. *Journal of the European Ceramic Society*. <https://doi.org/10.1016/j.jeurceramsoc.2022.10.047>
5. Wang, C., Ping, W., Bai, Q., Cui, H., Hensleigh, R., Wang, R., Brozena, A. H., Xu, Z., Dai, J., Pei, Y., Zheng, C., Pastel, G., Gao, J., Wang, X., Wang, H., Zhao, J. C., Yang, B., Zheng, X. R., Luo, J., . . . Hu, L. (2020, May). A general method to synthesize and sinter bulk ceramics in seconds. *Science*, 368(6490), 521–526. <https://doi.org/10.1126/science.aaz7681>

## **OPERATION of PbSe DETECTORS IN THE PLASMIC MEDIA**

**H. Hilal Yücel KURT**

*Department of Physics, Faculty of Science, Gazi University, 06500 Teknikokullar, Ankara, Turkey, , ORCID: 0000-hkurt@gazi.edu.tr ORCID: 0002-9709-516X*

**Selçuk UTAŞ**

*Department of Physics, Faculty of Science, Gazi University, 06500 Teknikokullar, Ankara, Turkey, selcuk.utas@gmail.com, ORCID: 00 0000-0002-9709-516X*

*Cite this paper as: KURT, H. Hilal, UTAŞ, Selçuk. OPERATION OF DETECTORS IN THE PLASMIC MEDIA. Int. Conf. Advanced. Mater. Sci. & Eng. HiTech.and Device Appl. Oct. 27-29 2022, Ankara, Turkey*

### **Abstract.**

Infrared radiation-sensitive device development not only increases its popularity today but also hosts many different devices and applications. The importance of semiconductor materials in the market, industry, space research, fiber optic structures, defense, and weapon industry is increasing with the developing technology. Semiconductor technology has gained an advantageous position with dc, ac, and rf power supplies, with the composition of group VI elements from II and its usage in plasmas. By using semiconductors in plasmas, the infrastructure of Tokamak and fusion energies, which are currently under construction, and are considered an unlimited power source, is also provided.

**Keywords:** PbSe Detector, Comsol Multiphysic, Migrative Electron Flux, Electron Density  
© 2022 Published by ICMATSE

### **Introduction**

Lead selenide (PbSe) with IV-VI semiconductor composition is a semiconductor material. They can operate at room temperature without the need for cooling from any external source. It has a direct band gap of 0.27 eV. It is used in the manufacture of infrared detectors for thermal imaging [1]. The mineral clostalite is a naturally occurring lead selenite. It can be formed by the reaction between lead and selenium. PbSe was one of the first materials to be found to be sensitive to infrared radiation used for military applications, and it is suitable for use from nanostructures to all high-tech structures with developing technology. For the first time, PbSe devices were used by the Germans, Americans, and British during and immediately after the Second World War. Infrared detonators and Passive Infrared Marking systems (PICs) have been used as photodetectors [2]. As an infrared radiation-sensitive material, PbSe can detect IR radiation in wavelengths from 1.5 to 5.2  $\mu\text{m}$  (medium wave

infrared window, abbreviated MWIR). Due to its quantum nature, it also offers a very fast response, making this material an excellent candidate as a detector of low-cost, high-speed infrared imagers [3]. Lead selenite is a photoconductive material. The detection mechanism is based on the change of conductivity of the polycrystalline thin film of the active material when photons arrive. These photons are absorbed within the PbSe microcrystals and then cause electrons to rise from the valence band to the conduction band. Lead selenide is a thermoelectric material. Lead selenide nanocrystals embedded in various materials can be used as quantum dots [4], for example, in nanocrystalline solar cells.

There is great interest in lead crystals because they have a number of interesting physical properties as well as numerous potential applications. Peak sensitivity is temperature dependent and ranges from 3.7–4.7  $\mu\text{m}$ .

### Result and Discussion

Plasma consists of partially excited gas, electrons, negative ions, positive ions, and various excited atomic molecules [5].

We used Ar (Argon) gas and data in our study. Because Argon gas has strong discharge features at the point of interest and easily reacts with the III-V group and II-VI group semiconductor materials [6].

The average free path (speed) is the average distance traveled charges in an electric field before collisions. The average free path calculated for an air medium at 1 atm (760 Torr) pressure is  $0.07 \mu\text{m}$ .

In our research, detector performance will be examined by using a PbSe semiconductor as a cathode, with a width of  $D=0.025 \mu\text{m}$  and different anode-cathode distances, without exceeding atmospheric pressure. For this aim, electron density and migrative electron density will be taken as the basis.

As seen in Fig. 1, the electron density value increases with the increase in pressure. While it was  $1.07 \times 10^{19} \text{ 1/m}^3$  under 22 Torr pressure, it became  $1.23 \times 10^{19} \text{ 1/m}^3$  under 300 Torr pressure. The system, which radiates in the Faraday space region at low pressure, glows brightly in the cathode glow region with the increase in pressure and is under the influence of hot electrons. The plasma acted like a conductive wire and this plasma mode corresponds to the arc region.

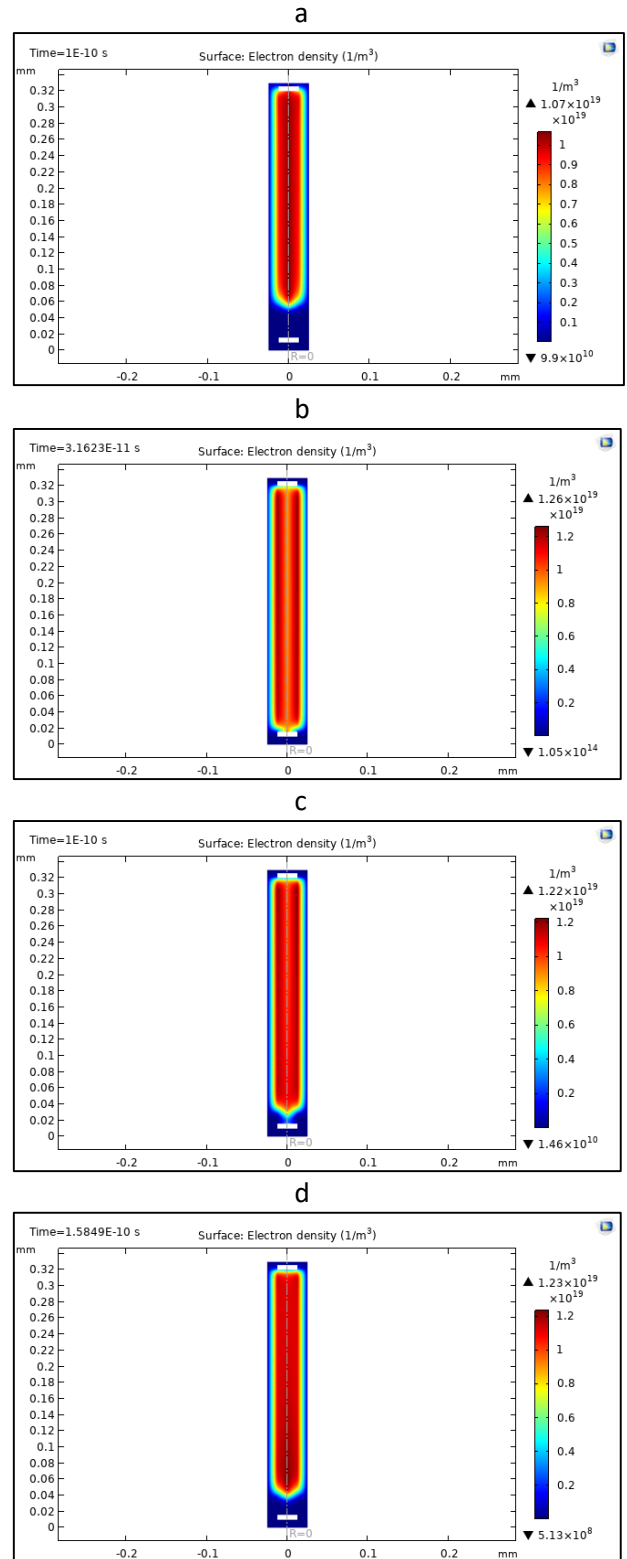


**Figure 1.**  $D=0.025 \mu\text{m}$   $d=300 \mu\text{m}$  Electron Density a)For  $p=22 \text{ Torr}$  b)For  $p=100 \text{ Torr}$  c)For  $p=220 \text{ Torr}$  d)For  $p=300 \text{ Torr}$

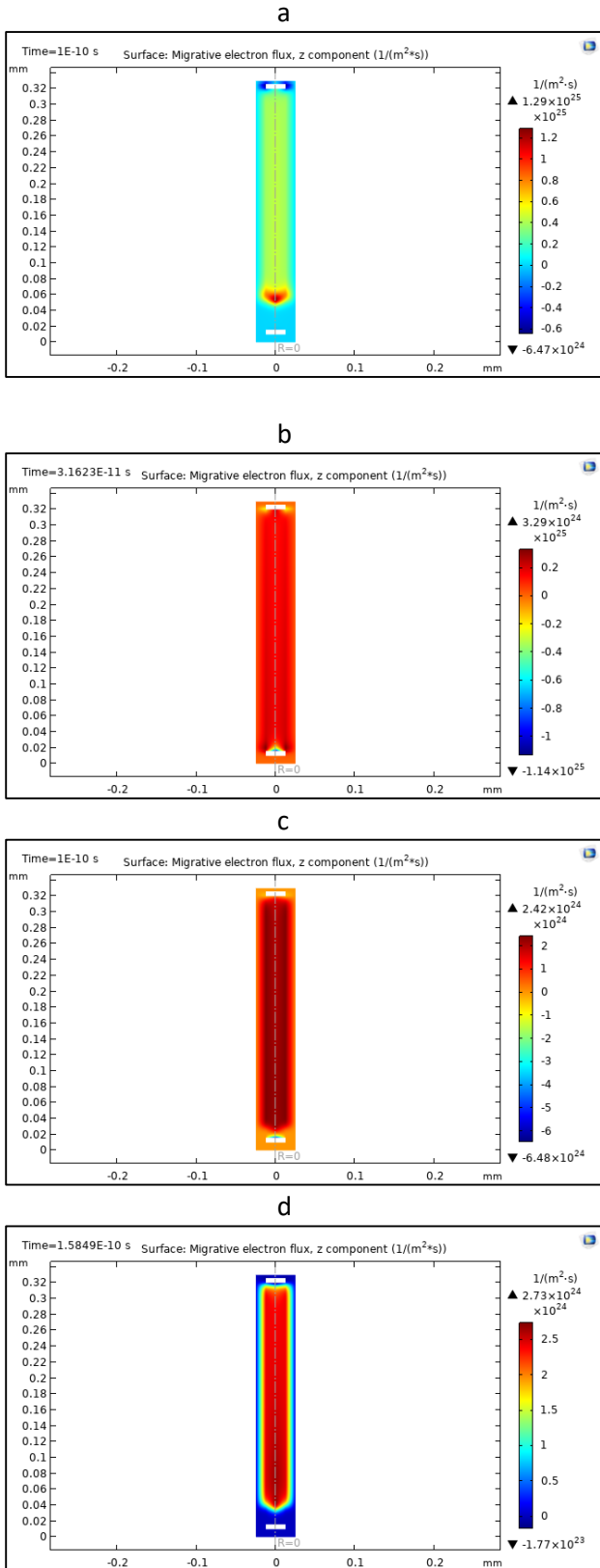


**Figure 2.**  $D=0.025 \mu\text{m}$   $d=300 \mu\text{m}$  Electron Density  
a)For  $p=22$  Torr b)For  $p=100$  Torr c)For  $p=220$  Torr  
d)For  $p=300$  Torr

Although the electrons that flow between the anode and the cathode and form the plasma do not provide a complete plasma transition under low pressure, they are partially under the influence of cold electrons, but when

the pressure value is 300 Torr, they operate in the glow working region.

In Fig. 3, when the pressure exceeds the atmospheric pressure at the same  $D$  and  $d$  distances, the system goes to the arc region and a small glow is seen in the plasma system.

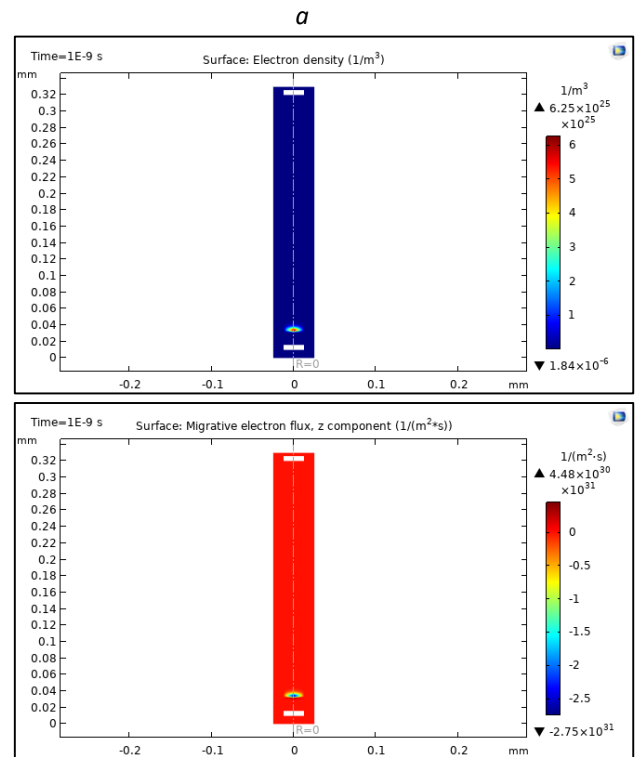


**Figure 3.**  $D=0.025 \mu\text{m}$   $d=300 \mu\text{m}$  Electron Density and Migrative Electron Flux

### Conclusion

Studies continue to eliminate any possible intolerance in the use of plasma systems and semiconductor materials, as well as the operation and spectral range of semiconductor material, by determining its use as detector diaphragms. The PbSe material was able to operate the plasma in the glow region by showing a good detector property under atmospheric pressure at dc operating power. Our study was carried out using the Comsol Multiphysics program. With the development of technology and nanotechnology, very powerful electronic circuits, high-speed chips, optimization, data security systems, cancer treatments, disinfection systems, thin film coating systems, and powerful lasers will be further developed. That will cause the development of many types of equipment, weapons, and, other vehicles used in military technology.

## References

- [1] Lawson, William D. "A method of growing single crystals of lead telluride and lead selenide." *Journal of Applied Physics* 22.12 (1951): pp. 1444-1447.
- [2] DEJENE, ABDI. *INFLUENCE OF SODIUMHYDROXIDE (NaOH) CONCENTRATION ON THE STRUCTURAL, OPTICAL AND ELECTRICAL PROPERTIES OF LEAD SELENIDE (PbSe) THIN FILM DEPOSITED BY CBD METHOD*. Diss. 2019.
- [3] Vergara, Germán, et al. "Polycrystalline lead selenide: the resurgence of an old infrared detector." *Opto-Electronics Review* 15.2 (2007): 110-117.
- [4] Shuklov, Ivan A., and Vladimir F. Razumov. "Lead chalcogenide quantum dots for photoelectric devices." *Russian Chemical Reviews* 89.3 (2020): 379.
- [5]. Schmidt, Martin, Ralf Schneider, and Hans-Erich Wagner. *Nonthermal plasma chemistry and physics*. Ed. Jürgen Meichsner. Boca Raton: CRC press, 2013.
- [6] Kurt, H. Hilal. "Optoelectronic Properties of GaAs, GaP, and ZnSe Cathodes in a Plasma–Semiconductor Cell." *Advances in Optoelectronic Materials*. Springer, Cham, 2021. 145-174.

## UNDER ATMOSPHERIC PRESSURE PLASMA RESULTS OF THE MICRODISCHARGE CELL WITH GaSb CATHODE

**H. Hilal Yücel KURT**

*Department of Physics, Faculty of Science, Gazi University, 06500 Teknikokullar, Ankara, Turkey,  
hkurt@gazi.edu.tr  
ORCID: 0002-9709-516X*

**Selçuk UTAŞ**

*Department of Physics, Faculty of Science, Gazi University, 06500 Teknikokullar, Ankara, Turkey,  
selcuk.utas@gmail.com  
ORCID: 00 0000-0002-9709-516X*

*Cite this paper as: KURT, H. Hilal, UTAŞ, Selçuk. UNDER ATMOSPHERIC PRESSURE PLASMA RESULTS OF THE MICRODISCHARGE CELL WITH GaSb CATHODE. *Int. Conf. Advanced. Mater. Sci. & Eng. HiTech.and Device Appl.Oct. 27-29 2022,Ankara, Turkey**

### Abstract

In this study, simulations were made with the help of Comsol Multiphysics program under atmospheric pressure placed in a plasma system using GaSb material. Space charge densities were found at different anode-cathode distances and between 0.05 mm cathode diameter. Thus, the spectral working range required for a plasma system and the operation of GaSb material in the field of optics and IR were investigated.

**Keywords:** GaSb Wafer, Microplasma device, atmospheric pressure plasma systems  
© 2022 Published by ICMATSE

### Introduction

GaSb is an important material due to its increasing applications in optics, electronics, and detector technology. It is of great importance in high-speed electronics, space exploration, photonic devices, and fiber optic technology [1]. GaSb, a group III-V semiconductor material, is encouraged to be used in microplasma cells. GaSb is a narrow band gap semiconductor material with direct absorption from the valence band to the conduction band. When the material is used as a cathode in plasma systems, it gives priority to this material due to its high-speed optoelectronic response to incoming radiation. The properties of the plasma are directly proportional to the quality of the cathode material and the optical properties of the material. With the effect of electrons, ions, and photons interacting with the gas in the plasma tube, the disintegration mechanism takes place between the cathode and the anode [2,3]. This process is also called self-sustaining

discharges. On the other hand, optical, electrical, and IR wave absorption of the material used in the process, also known as the secondary electron emission mechanism, affects plasma formation very significantly. As it is known, plasma systems do not occur in all time intervals, at all wavelengths, at all pressures, and at the distance between each anode and cathode. GaSb has a lattice-matched energy gap between 0.36 eV and 1.61 eV [4,5]. They can work at room temperature.

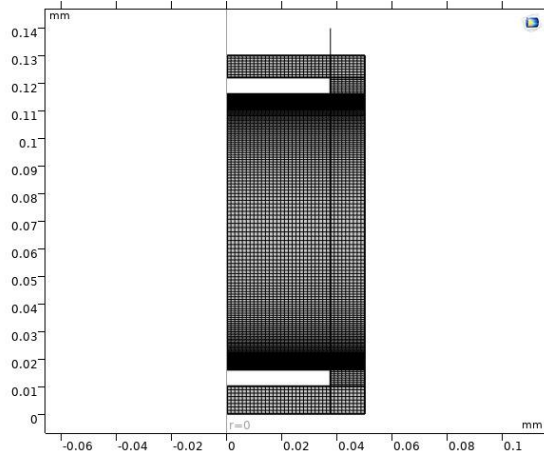


**Figure 1.** The mesh structure of the plasma system

As a result of many successive ionizations in the plasma range, the gas emits light in the visible range depending on the gas type and external conditions [6, 7]. In this study, we used commercial GaSb semiconductor wafers. We made our analysis with the help of the Comsol simulation program in the Argon environment.

The optimal mesh structure required for the plasma solution is suitable for plasma and approximately 76,800 mesh is used with the infinite element method.

There are two types of electron populations, slow and fast. Fast electrons are electrons that are near the cathode. Slow electrons are those that are released as a result of the ionization effect. The red color represents hot energetic electrons, and the blue and yellow colors represent cold low energetic electrons.

**Table 1.** Illumination region color formations in DC discharge

Gas	Cathode Limit	Negative Glow	Positive Column
Argon	Pink	Dark Blue	Dark Red

When an ion hits the cathode surface, an electron is emitted from the cathode surface with the specified probabilities. These electrons then ionize when they gain enough energy to initiate a strong electric field near the cathode. The electrons gained due to the wall and secondary emission effects are lost to the wall due to random motion within a few mean free paths. The electron flux [8] condition resulted in the following limit:

$$n \Gamma_e = \left( \frac{1}{2} \right) v_{e,th} n_e - \sum_p \gamma_p (\Gamma_p n) \quad (1)$$

and the electron energy flux,

$$n \Gamma_\epsilon = \left( \frac{5}{6} \right) v_{e,th} n_e - \sum_p [\epsilon_p \gamma_p (\Gamma_p n)] \quad (2)$$

$n$ , number of electrons reaching the anode;  $\gamma_p$ , contribution margins from my potential release to total yield;  $\Gamma_p$ , positive ion flux;  $M$ , reaction that contributes to growth;  $v_{e,th}$ , moving mass velocity

The chemical reactions occurring in the gas discharge tube cell [9] are given in the table below.

**Table 2.** Types of collisions and reactions that take place in the gas discharge tube

Collisions	Collision type	$\Delta\epsilon$ (eV)	Fixed used
e+Ar=>e+Ar	Elastic	0	Boltzman
e+Ar=>e+Ar <sup>s</sup>	Excitation	11,5	Boltzman
e+Ar <sup>s</sup> =>e+Ar	Superelastic	-11,5	Boltzman
e+Ar=>2e+Ar <sup>+</sup>	Ionization	15,8	Boltzman
e+Ar <sup>s</sup> =>2e+Ar <sup>+</sup>	Ionization	4,24	Boltzman
Ar <sup>s</sup> +Ar <sup>s</sup> =>e+Ar+Ar <sup>+</sup>	Penning Ionization	-	$6.2 \times 10^{-10} \text{ cm}^3 \cdot \text{s}^{-1}$
Ar <sup>s</sup> +Ar=>Ar+Ar	Stable damping	-	$1.0 \times 10^7 \text{ s}^{-1}$

## Result and Discussion

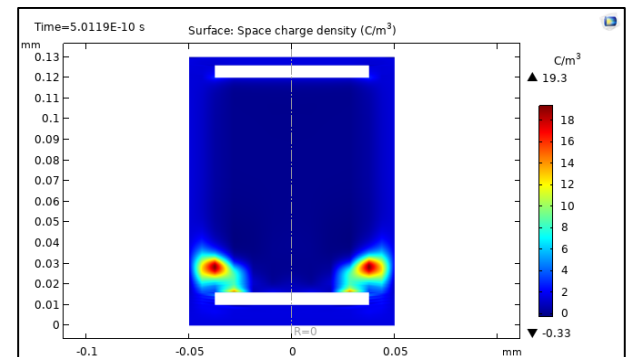


**Figure 2.**  $d=100 \mu\text{m}$   $p=760 \text{ Torr}$  Space Charge Density  $V=2000 \text{ V}$

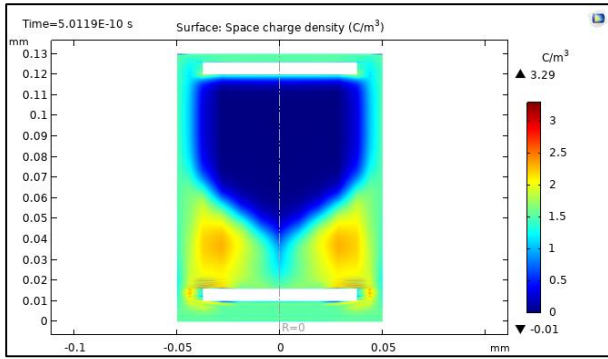


**Figure 3.**  $d=100 \mu\text{m}$   $p=760$  Torr Space Charge Density  $V=1500$  V

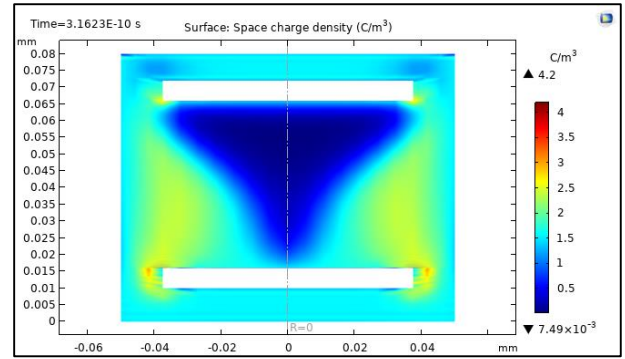


**Figure 5.**  $d=50 \mu\text{m}$   $p=760$  Torr Space Charge Density  $V=2000$  V

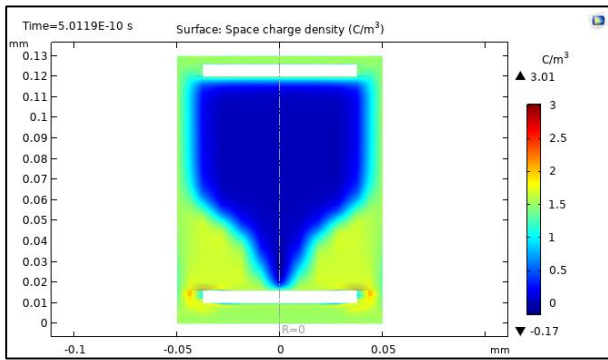


**Figure 4.**  $d=100 \mu\text{m}$   $p=760$  Torr Space Charge Density  $V=1000$  V

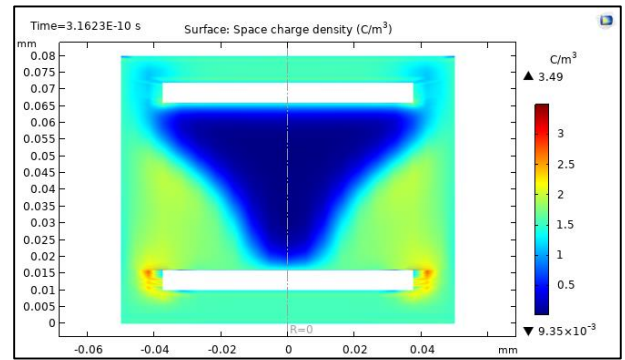


**Figure 6.**  $d=50 \mu\text{m}$   $p=760$  Torr Space Charge Density  $V=1500$  V

Fig. 1, Fig.2, and Fig.3 have been obtained for the same distance between the anode and cathode ( $d=100 \mu\text{m}$ ) and under the same pressure  $p=760$  Torr (approximate atmospheric pressure). Space charge density decreases when the voltage decreases from  $V=2000$  V to  $1000$  V. The space charge density is  $19.3 \text{ C/m}^3$  for  $2000$  V and  $3.29 \text{ C/m}^3$  for  $1500$  V and  $3.01 \text{ C/m}^3$  for  $1000$  V. Under  $2000$  V, plasma formation is observed with the accumulation of hot electrons (marked in red) in the region near the cathode, while plasma formation is observed at  $1500$  V and  $1000$  V values in the glow region. This formation shows us that the system can operate in this voltage and pressure range at room temperature without the need for cooling from any external source.

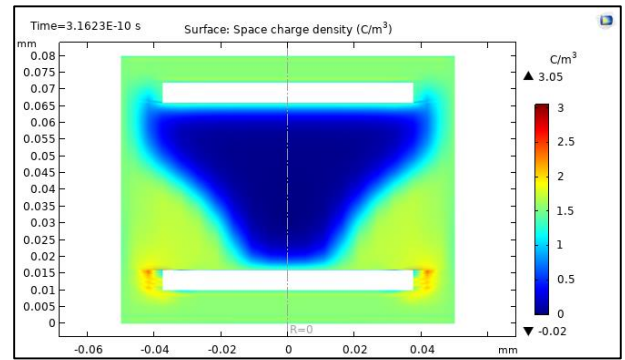


**Figure 7.**  $d=50 \mu\text{m}$   $p=760$  Torr Space Charge Density  $V=1000$  V

When the distance between the anode and the cathode was  $50 \mu\text{m}$ , the space charge density in the system increased under  $2000$  V DC power compared to  $100 \mu\text{m}$ . However, when compared with a distance of  $100 \mu\text{m}$ , GaSb material containing a direct band gap in the range of  $1000$ - $1500$ - $2000$  V, completely under the influence of cold electrons and without cryogenic water cooling, was found suitable for plasma.

## Conclusion

The formation and distribution of plasma depend on time and plasma conditions. Space charge accumulation at the cathode is the main reason for the secondary electron emission from the cathode. These charges make the

electric field unstable and cause inhomogeneous electric field distribution throughout the plasma. We used the Comsol simulation program to obtain space charge accumulation in front of the GaSb cathode. We have noticed that space charges are directly related to the plasma voltage. GaSb is a very good material for the plasma cells when they are used as cathode.

## References

- [1] P. S. Dutta, H. L. Bhat. Kumar, ". *The physics and technology of gallium antimonide: An emerging optoelectronic material,*" *J. Appl. Phys*, 81 (1997), pp. 5821-5870.
- [2] Y. P. Raizer, M. S. Mokrov. Physical mechanisms of self-organization and formation of current patterns in gas discharges of the Townsend and glow types. *Physics of Plasmas*, 20(10) (2013), pp. 101604.
- [3] M. C. Penache. Study of high-pressure glow discharges generated by micro-structured electrode (MSE) arrays. *Johann Wolfgang Goethe Universität (2002)*.
- [4] M. A. Kinch. State-of-the-art infrared detector technology. SPIE (2014).
- [5] N. Medvedev, I. Milov. Electron-phonon coupling in metals at high electronic temperatures. *Physical Review B*, 102(6) (2020), pp. 064302.
- [6] J. D. Freels, P. K. Jain (2011, October). Multiphysics Simulations of the Complex 3D Geometry of the High Flux Isotope Reactor Fuel Elements Using COMSOL. In *COMSOL Conference, Newton, Mass.*.
- [7] Y. Sadiq, H. Y. Kurt, A. O. Albarzanji, S. D. Alekperov, B. G. Salamov, B. G. Transport properties in semiconductor-gas discharge electronic devices. *Solid-state electronics*, 53(9) (2009), pp. 1009-1015.
- [8] I. Rafatov, E. A. Bogdanov, A. A. Kudryavtsev. On the accuracy and reliability of different fluid models of the direct current glow discharge. *Physics of Plasmas*, 19(3) (2012), pp. 033502.
- [9] A. Bogaerts, E. Neyts, R. Gijbels, J. Van der Mullen. Gas discharge plasmas and their applications. *Spectrochimica Acta Part B: Atomic Spectroscopy*, 57(4) (2002), pp. 609-658.

## ENERGY EXCHANGE VIA GaAs ELECTRODE IN A PLASMA SYSTEM

**H. Hilal Yücel KURT**

*Department of Physics, Faculty of Science, Gazi University, 06500 Teknikokullar, Ankara, Turkey,  
hkurt@gazi.edu.tr  
ORCID: 0002-9709-516X*

**Selçuk UTAŞ**

*Department of Physics, Faculty of Science, Gazi University, 06500 Teknikokullar, Ankara, Turkey,  
selcuk.utas@gmail.com  
ORCID: 00 0000-0002-9709-516X*

*Cite this paper as: KURT YÜCEL, H. Hilal, UTAŞ, Selçuk. ENERGY EXCHANGE VIA GaAs ELECTRODE  
IN A PLASMA SYSTEM. Int. Conf. Advanced. Mater. Sci. & Eng. HiTech. and Device Appl. Oct. 27-29  
2022, Ankara, Turkey*

### Abstract.

The GaAs electrode has been used as a cathode which is near Infrared material that causes the conversion of the Infrared energy to the visible one in the pressure range between 22 Torr and 760 Torr. It has a direct narrow band gap. Electron-based energy graphs and plasma formations were calculated with the COMSOL simulation program. The Energy Exchange mechanism between the cathode and plasma occurs when the appropriate plasma conditions are reached in the system.

**Keywords:** GaAs cathode, Comsol Multiphysics plasma module, Mean electron energy, Energy exchange  
© 2022 Published by ICMATSE

### INTRODUCTION

GaAs is one of the most common semiconductors in the III-V group, which is used in photon energy conversion systems that provide costly quantum efficiency, which is mostly used in high concentration photovoltaic systems [1,2]. In microdistance plasma systems, it is effective in improving the absorption of incoming light through the enhancement of light beams in the microchannel plates (MCP). The system transforms with the microplasma unit and provides the energy increase and electro-multiplication with the MCP structure. These devices also form the basis of night vision devices and are also the head of multiplier systems. This research focused on the scientific understanding of the energy conversion process and plasma formations by examining microchannel plasma devices with average mean electron energies for various interelectrode distances and gas pressures.

GaAs-containing multi-joint cells are the most suitable PV cells that provide 47.1% efficiency with their triple structure. They have been developed from the smallest electronic equipment to the largest satellites and for special applications such as space exploration. Simultaneous coupling of three or more in the growth

process results in high quantum efficiency, and also cultivation methods such as metal-organic chemical vapor deposition technique contribute to their high yields [3]. GaAs FETs are also widely used in power amplifiers and receiver amplifiers and frequency converter applications [4-5]. The performance of the converters is a result of the high electron mobility of group III-V materials. Moreover, the TIRS focal plane houses three sensor chip groups consisting of GaAs quantum well IR detectors related to the electronic structure of GaAs and the design of the system [6].

In this work, an effort has been made to find undefined plasma parameters such as mean electron energy and electron current density and migrated electron flux by incorporating the flow of gas using the plasma module of COMSOL multi-physics to make clear energy conversion. Model results clarified the complex behavior of the plasma. By analyzing mean electron energies, electron densities also current densities, the contributions of the different plasma parameters for the optimal operation range in the material and device physics are studied.

## 2. RESULT AND DISCUSSION

In our system, semiconductor materials are defined as cathodes, while SnO<sub>2</sub> coated- glass is defined as the anode. In the first stage, the geometric structure was created. Then, argon gas and semiconductor have been chosen from the material library. COMSOL Multiphysics package gives the facility for the modelling of semiconductor-plasma systems. The numerical calculation is an important tool to improve our knowledge based on the plasma behavior inside the micro discharge cell with GaAs electrode and it is also important to increase the knowledge in the field of Dc micro discharges used for deposition or etching [7, 8]. The optimal mesh numbers used 42.560 elements. The programme uses gas discharge formalism and the required material constants to find the steady-state solutions for the defined simulation cell [9]. It should be noted that there are limited theoretical studies on the semiconductor- plasma structures.

Townsend discharge is the gas ionization process via electrons accelerated in a sufficiently strong electric field, causing the change in electrical conductivity due to the increasing avalanche mechanism. When a decrease occurred in the number of free charges or weakened in the electric field, this stops the Townsend discharge. Townsend discharge got its name from John Sealy Townsend and is also known as the "Townsend avalanche mechanism". Avalanche means a successive reaction process in the plasma area for a sufficiently high electric field. This reaction takes place in an ionizable medium, such as air. When the atoms or molecules were ionized in an applied electric field, the positive ions move toward the cathode while the free electrons move toward the anode. If the electric field is strong enough, the electrons gain enough energy to release more free charge. With the collision of electrons with another atom or molecule, more electrons are released when it reaches a sufficient energy level. The two free electrons move together after advancing a little in the electric field and gaining energy before another collision occurs. This is an effective chain reaction of electron formation. The number of electrons moves towards the anode, increasing to  $2n$  in each collision. Here  $n$  is a collision. The limit of the number of avalanche multipliers is known as the Raether limit [10].

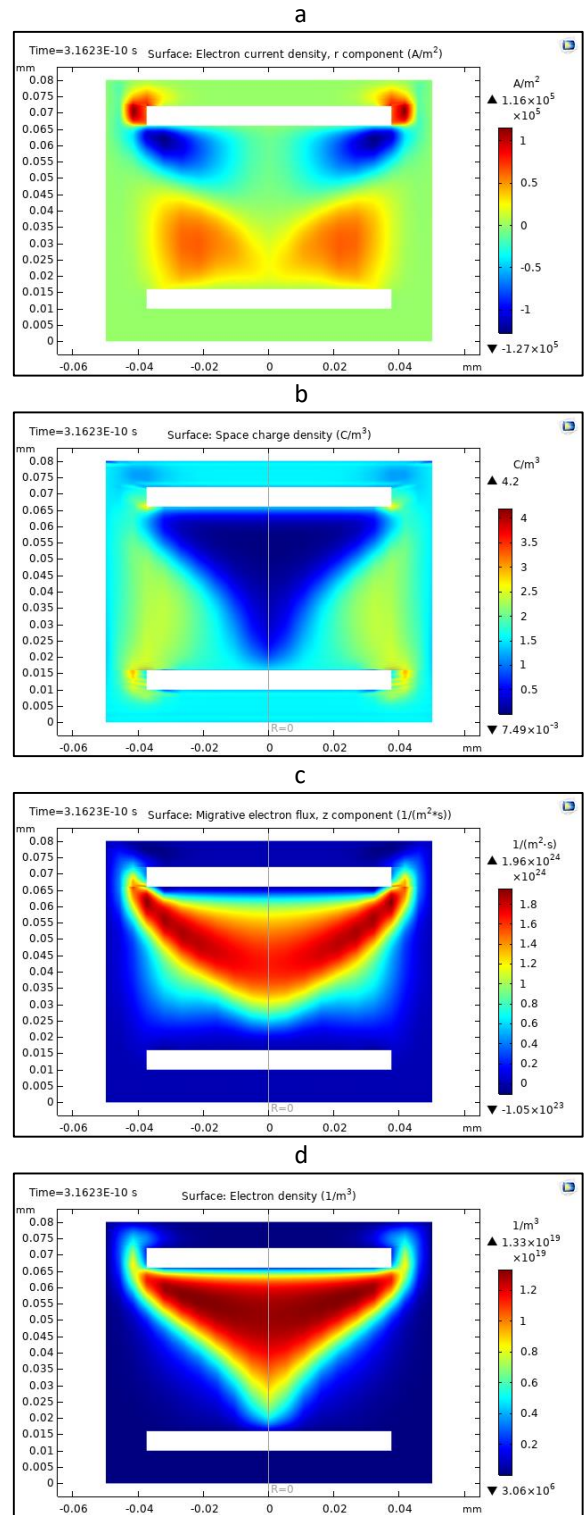


**Figure. 1 (a-d).** a) Surface electron current densities; b) Surface space charge densities; c) Migrative electron fluxes d) Surface electron densities for 50  $\mu\text{m}$  under pressure of 760 Torr

a

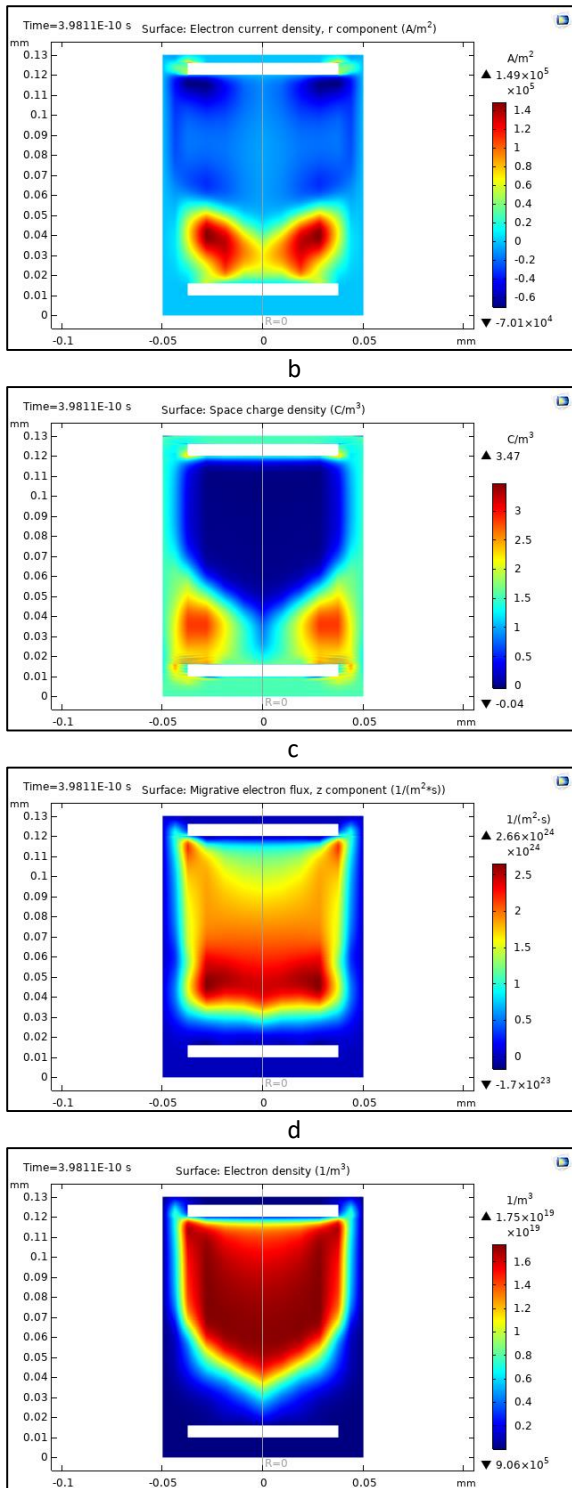


**Figure. 2 (a-d).** a) Surface electron current densities; b) Surface space charge densities; c) Migrative electron fluxes d) Surface electron densities for 100  $\mu\text{m}$  under pressure of 760 Torr

Distribution of the surface electron current densities, surface electron densities, surface space charge densities and migrative electron fluxes are shown for 760 Torr (atmospheric pressure) in Fig.2. In Fig. 1(a) and fig.1(a), the evolution of current density patterns is shown for 50  $\mu\text{m}$  and 100  $\mu\text{m}$ . As seen from the figure, the current is distributed on the cathode in the form of two symmetric parts. For 100  $\mu\text{m}$ , the whole current is on the cathode and has the magnitude of  $1.49 \times 10^5 \text{ A/m}^2$  and  $1.16 \times 10^5 \text{ A/m}^2$  for 50  $\mu\text{m}$ .

Self-organized electron flux patterns have complex plasma chemistry due to nonlocal Electric field strength in a glow discharge. Fig. 1(c) and fig. 2(c) shows migrative electron flux for two  $d$  values for 760 Torr. It has higher value for 100  $\mu\text{m}$  ( $2.66 \times 10^{24} 1/(\text{m}^2.\text{s})$ ) than that of 50  $\mu\text{m}$  ( $1.96 \times 10^{24} 1/(\text{m}^2.\text{s})$ ) for 760 Torr

## CONCLUSION

The 3D MEE maps were calculated and drawn by the COMSOL simulation program, depending on the average electron energies of the plasma and the plasmic formation stages, the variation of the gap distance  $d$  and the gas pressure. COMSOL uses binomial Boltzmann constants and sub-equations to calculate electron energy distributions for plasma [10]. When microplasma occurs, plasma species production is found with reduced local electric field strength  $E/n$  and electron density [11]. Regular plasma patterns form at the plasma boundaries. It was observed that MEE increased with gas pressure. In a Dc discharge gas system with GaAs cathode, different electron energy distributions are observed in argon.

## REFERENCES

- [1] Nakao, Akihiro, Yoshikazu Tanaka, and Ari Ide-Ektessabi. "Discharge properties of a micro plasma cell with an MgO–NiO protecting layer." *Surface and Coatings Technology* 203.17-18 (2009): 2731-2734.
- [2] Knechtli, Ronald C., Robert Y. Loo, and G. Sanjiv Kamath. "High-efficiency GaAs solar cells." *IEEE Transactions on electron devices* 31.5 (1984): 577-588.
- [3] Iles, Peter A. "Photovoltaic Conversion: Space Applications." (2004): 25-33.
- [4] Berger, Jim. "Perceived neutrality of technology and its potential impact: Recontextualizing technology into adult learning settings using a cultural studies approach." *Encyclopedia of information communication technologies and adult education integration*. IGI Global, 2011. 810-823.
- [5] Knott, Arnold, et al. "Evolution of very high frequency power supplies." *IEEE Journal of Emerging and Selected Topics in Power Electronics* 2.3 (2013): 386-394.

- [6] Markham, Brian L., et al. "Landsat program." *Comprehensive remote sensing 1* (2018): 27-90.
- [7] Andersen, Hans Henrik, and Helge L. Bay. "Sputtering yield measurements." *Sputtering by particle bombardment I* (1981): 145-218.
- [8] Delcroix, Jean-Loup, and Armando Rocha Trindade. "Hollow cathode arcs." *Advances in Electronics and Electron Physics*. Vol. 35. Academic Press, 1974. 87-190.
- [9] Kurt, H. Hilal, and Evrim Tanriverdi. "Electrical properties of ZnS and ZnSe semiconductors in a plasma-semiconductor system." *Journal of Electronic Materials* 46.7 (2017): 3965-3975.
- [10] Kao, Chih-cheng, and Yu-cheng Liu. "Intense green emission of ZnS: Cu, Al phosphor obtained by using diode structure of carbon nano-tubes field emission display." *Materials chemistry and physics* 115.1 (2009): 463-466..
- [11] Mohammadi, Kyana. "Décharge électrique à l'interface de deux liquides: application à la synthèse de nanoparticules." (2022).

## Production and Characterization of Commercially Pure (Cp-Ti) and Alloy (Ti64) Porous Titanium Medical Implants using Laser Powder Bed Fusion (L-PBF) Technology Surgery

**Fatma Nur Depboylu**

Department of Bioengineering, Hacettepe University Institute of Science and Technology, Beytepe,  
06800, Ankara, Turkey, Fatmanur.depboylu@gmail.com  
ORCID: 0000-0003-0401-5923

**Özgür Poyraz**

Department of Mechanical Engineering, Eskişehir Technical University, 26555, Eskişehir, Turkey,  
poyrazozgur@gmail.com  
ORCID: 0000-0001-9892-5738

**Evren Yasa**

Department of Mechanical Engineering, Eskişehir Osmangazi University, 26480, Eskişehir, Turkey,  
ebalyasa@gmail.com / eyasa@ogu.edu.tr  
ORCID: 0000-0001-5443-3598.

**Feza Korkusuz**

Faculty of Medicine, Department of Sports Medicine, Hacettepe University, Sıhhiye, 06100, Ankara, Turkey,  
feza.korkusuz@gmail.com  
ORCID: 0000-0001-9486-3541

*Cite this paper as: Depboylu, FN, Poyraz, Ö, Yasa, E, Korkusuz, F. Production and Characterization of Commercially Pure (Cp-Ti) and Alloy (Ti64) Porous Titanium Medical Implants using Laser Powder Bed Fusion (L-PBF) Technology Surgery. Int. Conf. Advanced. Mater. Sci. & Eng. HiTech. and Device Appl. Oct. 27-29 2022, Ankara, Turkey*

### Abstract.

Titanium is preferred for biomedical implants since suitable for biocompatibility and mechanical strength. But recently, the decreasing bulk weight without losing biomechanical properties is rising for ideal metallic implants. The PorousSLM project aimed to design and develop gyroid lattice structures in titanium plates for tissue integration using laser powder bed fusion (L-PBF) technology and to optimize L-PBF manufacturing parameters for thin lattice titanium structures. Mechanical properties of gyroid lattice structure designs which have different porosity rates were obtained by finite element analysis to compare literature and experimental data. Also manufacturing process development was completed in 3 steps from determined optimum energy density parameter to the fine tuning parameters to achieve almost full dense parts production. Cleaning process was developed to remove unmelted powders which adhered to the part surface without detrimental degradation which causes mechanical strength loss. Gyroid lattices in titanium mini plates are investigated to match the mechanical properties of current commercial plates.

**Keywords:** Osteosynthesis Miniplate, Titanium, Gyroid, Laser Powder Bed Fusion

© 2022 Published by ICMATSE

### Introduction

Ti6Al4V alloy osteosynthesis implants made with traditional methods in the market cannot show ideal

implant properties due to disadvantages such as high mechanical strength, stress protection effect and low ductility [1]. Commercial pure titanium (cp-

Ti) implants, which are free of Al and V toxic effects and have controlled pores that can achieve the mechanical properties of bone, can be produced with L-PBF (Fig. 1) to solve disadvantages of Ti6Al4V [2]. The aim of this study is to manufacture high-density cp-Ti parts and to develop a process for creating thin walled gyroid lattice structures that eliminate defects that may occur during the process. Then, the cleaning process is applied to remove unmelted powder from strut surface of porous structure without detrimental degradation which causes mechanical strength loss.

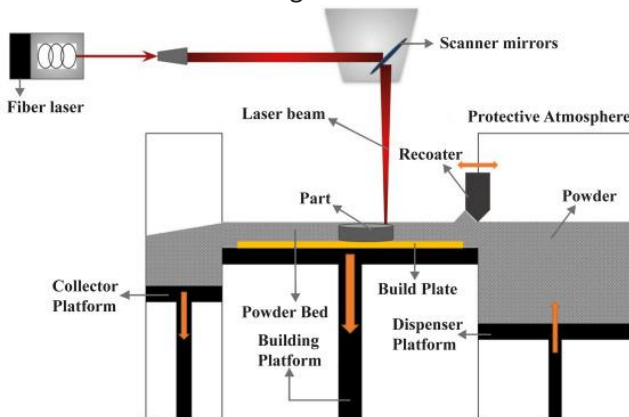


**Figure 1.** Laser Powder Bed Fusion technology Process and Equipment [3]

### Methods

Gyroid latticed cubic designs were created with 3 mm unit cell size (UCS) and various strut thickness (ST) from 0,3 to 0,7 mm by nTopology Software. Compression tests of created gyroid cubic models were completed with adding 2 solid plates to up and down of gyroids via Finite element analysis (FEA) in ANSYS software. Elastic modulus values were calculated and investigated with different porosity rates of gyroid designs. Manufacturing process development started with thin wall and L-PBF manufacturing parameter optimization using with ASTM F67 cp-Ti (EOS TiCP Grade 2) powder in L-PBF process (EOS M290) to reach full dense parts. Then gyroid lattice structures were manufactured with fine tuning parameters to improve dimensional accuracy. Stereomicroscope and metallography density measurements were made for post production characterization. Chemical etching was applied to gyroid parts into acid solution following with ultrasonic bath and dried for cleaning process. Mass loss and strut thickness loss were investigated.

### References

1. Ataee, A., Li, Y., Brandt, M., & Wen, C. (2018). *Acta Materialia*, 158, 354-368,
2. Wysocki, B., Maj, P., Krawczyńska, A., Roźniatowski, K., Zdunek, J., Kurzydowski, K. J., & Świążkowski, W. (2017). *Journal of Materials Processing Technology*, 241, 13-23
3. Depboylu, F. N., Yasa, E., Poyraz, Ö., Minguella-Canela, J., Korkusuz, F., & De los Santos López, M. A. (2022). Titanium based bone implants production using laser powder bed fusion technology. *Journal of Materials Research and Technology*.

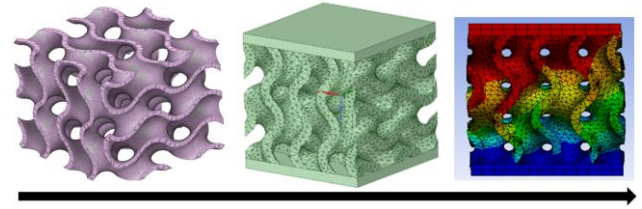


**Figure 2.** (Left) Gyroid lattice design, (Middle) Gyroid model with 2 solid plate for FEA compression test, (Right) Compression FEA deformation of gyroid.

### Results

As the porosity increased, the elastic modulus ratio decreased (Table 1). Obtained data was consistent with the hook's law. In addition, FEA results were consistent with the gyroid titanium lattice structures given in the literature.

**Table 1.** Elastic modulus values of gyroid designs at different porosity rates via FEA

Design	Porosity Rate (%)	Elastic Modulus (GPa)
3 mm UCS-0,3 ST	80,63	3,1
3 mm UCS-0,5 ST	67,63	6,0
3 mm UCS-0,7 ST	54,44	9,9

As a result of production parameter optimization, the production of the parts with almost fully dense (Fig. 3) and geometric accuracy (Fig. 4) was achieved. In addition, the cleaning process test will be repeated in less than 12 minutes since unwanted micro-pits are formed on the surface.

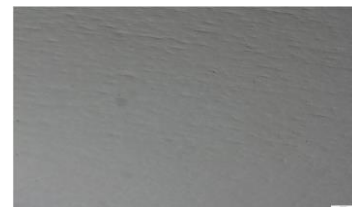


**Figure 3.** Produced part which has almost full dense.



**Figure 4.** Produced gyroid lattice part.

### Conclusion

The design and production final parameters have been determined, and the gyroid lattice structure will be integrated into the mini plate and produced at the specified L-PBF production parameters.

## Creating an innovation culture in research and development in a volatile world

**Dr Nasar Ali**

(i) Institute for Personal and Professional Development, Young Professionals Society; (ii) NANOSMAT, Cheshire, England, UK, [n.ali@nanosmat.co.uk](mailto:n.ali@nanosmat.co.uk)  
ORCID: 0000-0001-5959-2926

**Dr Mikael Syväjärvi**

(i). ALMINICA AB, Sweden, [mikael@alminica.se](mailto:mikael@alminica.se); (ii) ICM Research Institute, Sweden  
ORCID: 0000-0003-2912-7665

**Abstract.** Here, we speak about the importance of adopting creativity and innovation in research and development to solve challenging global problems such as climate change, pandemics, energy crisis, etc. Typically in PhD projects, researchers aim to complete their doctoral work by publishing research papers in peer reviewed journals and working on some form of novelty (big or little), which is introducing something new, either new process, new material, new characterisation technique or even application. However, novelty is different from innovation. We will give examples of the difference in the two in the presentation. Novelty is simply described as an incremental change to an existing product, process etc. Whereas, innovation is the successful implementation of new creative ideas to develop something brand new. True innovation changes the way industries operate and is a game changer for business creation and societal impact. Substantially more needs to be done to support researchers wanting to do innovative work and to consider entrepreneurship to translate innovative research to market and commercialisation, and over time contribute to global sustainable development goals.

**Keywords:** Innovation, Creativity, Novelty, Trailblazer, Game-Changer  
© 2022 Published by ICMATSE

It's very important to understand why one needs to innovate. We innovate to solve problems. In the last 2 years, we see how the different innovative covid vaccinations have been helping to save millions of lives around the world by providing protection to humans from the deadly coronavirus. To innovate, it's crucial to come up with creative and novel ideas. It's better to collaborate with more people to come up with 'best' ideas. Ideas are the powerhouse for your invention. It's not necessary that you use sophisticated techniques to innovate. The discovery of graphene took place using a simple scotch tape method, and persistence.

Researchers publishing papers in journals are making a limited impact because publishing is a slow process and not everyone reads journal papers, especially the public and entrepreneurs. We work in the lab each day and encounter problems, which if we don't solve could be a risk, however, we solve them without actually thinking about it (Figure 1). Some of these steps can be 'inventive'. This means we are doing innovation daily and with time we are doing more and more. By sharing our experiences with others we create usefulness, and with this chain

continuing to grow in spreading innovative steps and innovation a momentum is created which impacts the scientific community and the society (Figure 2).

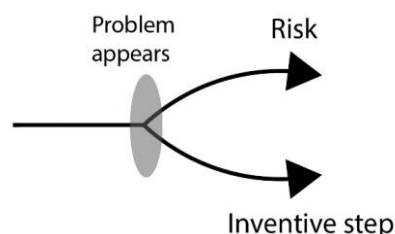


**Figure 1.** Outcomes of solving/not-solving problems.

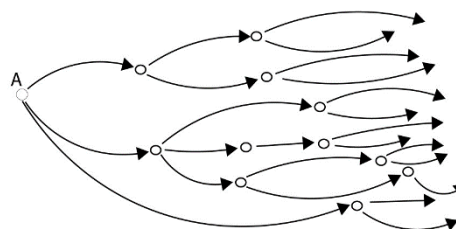


**Figure 2.** Building a growing momentum in taking more inventive steps and doing more innovation by sharing experiences

## Hyaluronate-Based Thermo-sensitive Hydrogel for Vitreous Body Substitute

*Feng-Huei Lin (double)*

*Company name-* Institute of Biomed Eng & Nanomed, NHRI, Zhu Nan, Taiwan, Institute of Biomedical Engineering, National Taiwan University, Taipei, Taiwan

[double@ntu.edu.tw](mailto:double@ntu.edu.tw)

*Cite this paper as: Lin Feng-Hue Hyaluronate-Based Thermo-sensitive Hydrogel for Vitreous Body Substitute.Int. Conf. Advanced. Mater. Sci.& Eng. HiTech.and Device Appl.Oct. 27-29 2022,Ankara, Turkey*

**Abstract.** Human vitreous is a gelatinous substance that is predominantly composed of collagen fibril, hyaluronic acid (HA) and water (97–99%). Vitreous substitutes are needed to tamponade the detached retina after vitrectomy when treating retinal detachments. However, several drawbacks associated with current vitreous substitutes have been reported. In the present study, we developed a colorless, transparent and injectable hydrogel as a vitreous substitute that was formed by oxidated HA (oxi-HA) and adipic acid dihydrazide (ADH). The results of biodegradation demonstrated that the hydrogel could maintain its gel matrix over at least 35 days depending on the ADH concentration. In addition, the biocompatibility was evaluated on a retina pigmented epithelium (RPE) cell culture following ISO 10993-5 (tests for in vitro cytotoxicity), and the hydrogel was found to be nontoxic. This study suggested that the injectable oxi-HA/ADH hydrogel could fulfill many critical elements that are desirable in vitreous substitutes.

**Keywords:**

© 2022 Published by ICMATSE



**INTERNATIONAL CONFERENCE ON  
ADVANCED MATERIALS SCIENCE &  
ENGINEERING AND  
HIGH TECH DEVICE APPLICATIONS**

**ISBN: 978-625-00-1052-5**

**October 27- 29 2020  
Gazi University Ankara / TURKEY  
[icmatse.org](http://icmatse.org)**

